

EXPERIMENTAL INVESTIGATION AND NUMERICAL SIMULATION OF AN
UNREINFORCED MASONRY STRUCTURE WITH FLEXIBLE DIAPHRAGMS

A Thesis
Presented to
The Academic Faculty

by

Tianyi Yi

In Partial Fulfillment
of the Requirements for the Degree
Doctor of Philosophy in
Civil and Environmental Engineering

Georgia Institute of Technology
February 2004
Copyright © Tianyi Yi 2004

EXPERIMENTAL INVESTIGATION AND NUMERICAL
SIMULATION OF AN UNREINFORCED MASONRY STRUCTURE
WITH FLEXIBLE DIAPHRAGMS

Approved by:

Roberto T. Leon, CEE, Chairman

Lawrence F. Kahn, CEE

James I. Craig, AE

Reginald DesRoches, CEE

Laurence J. Jacobs, CEE

Date Approved: ____02/19/2004

To my parents

ACKNOWLEDGEMENTS

In completing this doctorate dissertation, I would like to express my gratefully appreciation to the tremendous help from many professors, fellow students and other friends.

I am appreciative and thankful for the support of my dissertation advisor, Dr. Reoberto Leon, and Dr. Kahn, and other members of my committee. Without their support this dissertation would not have been written.

I would also like to express my thanks and appreciation to Dr. Germanovich, Georgia Institute of Technology, and Dr. Lange, University of Illinois. They have provided valuable advice for my research.

I would also like to express appreciation to my friend, Dr. Franklin Moon. Over the past three and a half years, we have been working together as a wonderful research team.

I would also like to express appreciation to my friend, Ruiting Wu. She has always been a strong support for me.

At last, I would like to express my thanks to the financial support of the National Science Foundation through the Mid-America Earthquake Center (award number EEC-9701785). I would also like to thank the Market Development Alliance of the FRP Composites Industry (MDA) for the additional financial support. Cherokee Brick and Tile Company donated all the bricks used in the test structure. Lafarge Cement donated all cement and lime used for the mortar. Dur-O-Wal Inc. donated the masonry

prestressing rods and hardware. Simpson Strong-Tie donated the joist anchors and associated hardware. The MDA donated the FRP retrofit systems. These donations were gratefully appreciated and acknowledged.

The conclusions and opinions appeared herein are those of the author and do not necessarily represent those of the National Science Foundation or other sponsor organizations.

TABLE OF CONTENTS

DEDICATION	iii
ACKNOWLEDGEMENT	iv
LIST OF TABLES	xi
LIST OF FIGURES	xvii
LIST OF SYMBOLS	xxx
SUMMARY	xxxvi
CHAPTER 1 INTRODUCTION	1
1.1 Need for research	1
1.2 Objectives and scope of research	6
1.3 Outline of the research	7
CHAPTER 2 LITERATURE REVIEW	10
2.1 General	10
2.2 Masonry material	11
2.3 URM in-plane walls	14
2.4 URM out-of-plane walls	21
2.5 Flexible floor and roof diaphragms	22
2.6 Experimental and analytical research for URM buildings	24
2.7 Summary	44
CHAPTER 3 MECHANICAL KEY MODEL FOR THE FAILURE CRITERIA OF MASONRY	46
3.1 Introduction	46
3.2 Shear behavior of masonry bed joints	52
3.3 Proposed mechanical key model for interface shear strength and tensile strength	60
3.4 Experimental verification	65
3.5 Failure envelope for strong unit-weak mortar masonry assembly based on the mechanical key model	70
3.6 Reevaluation of FEMA 356 strength parameters based on the mechanical key model	74
3.7 The assessment of the diagonal compression test based on the	77

mechanical key model	
3.8 Conclusions	82
CHAPTER 4 EFFECTIVE PIER MODEL FOR THE NONLINEAR IN-PLANE ANALYSIS OF INDIVIDUAL URM PIERS	84
4.1 Introduction	84
4.2 External forces	86
4.3 Internal stress distribution	87
4.4 URM pier failure modes	90
4.5 Deformation of URM piers	99
4.6 Elastic modulus of masonry	101
4.7 Comparison with FEMA 356	101
4.8 Comparison with experimental results	110
4.9 Conclusions	121
CHAPTER 5 FLANGE EFFECTS FOR THE NONLINEAR BEHAVIOR OF INDIVIDUAL URM PIERS	123
5.1 Introduction	123
5.2 Modification of the effective pier model to consider the flange effects	124
5.3 The ultimate strengths corresponding to four typical failure mechanisms of a URM pier considering flange effects	132
5.4 Determination of the flange width	144
5.5 Other possible failure mechanisms for a URM pier with flange	148
5.6 Conclusions	150
CHAPTER 6 DESIGN OF THE ST-11 BUILDING	152
6.1 Introduction	152
6.2 Objectives	152
6.3 Material properties	155
6.4 Design of the test structure	159
6.5 Construction	175
6.6 Rehabilitation of the test structure	177
6.7 Loading sequences	178
6.8 Summary	179
CHAPTER 7 TESTS OF ROOF DIAPHRAGM AND OUT-OF- PLANE WALLS	180

7.1	Introduction	180
7.2	Test on one-half of the diaphragm parallel to the joists	183
7.3	Interaction mechanisms between diaphragm and masonry walls parallel to the joists	191
7.4	Interaction mechanisms between diaphragm and masonry walls perpendicular to the joists	208
7.5	Conclusions	220
CHAPTER 8	IN-PLANE WALL TESTS PARALLEL TO WALLS 1 AND 2	224
8.1	Introduction	224
8.2	Test setup	225
8.3	Crack propagation, damage accumulation and kinematic mechanisms of the test structure	235
8.4	Coupling between Walls 1 and 2	293
8.5	Flange effects	296
8.6	Global overturning movement	303
8.7	Effective secant elastic modulus, natural period, and vibration modes	307
8.8	Discussions	310
8.9	Conclusions	311
CHAPTER 9	IN-PLANE WALL TESTS PARALLEL TO WALLS A AND B	314
9.1	Introduction	314
9.2	Test setup	314
9.3	Crack propagation, damage accumulation and kinematic mechanisms	319
9.4	Flange effects	357
9.5	Mixed behavior: global overturning and local rocking	366
9.6	Effective piers in a perforated wall	368
9.7	Comparison between the behavior of Walls A and B	374
9.8	Effective secant elastic modulus, natural period, and vibration modes	377
9.9	Discussions	378
9.10	Conclusions	381
CHAPTER 10	PRELIMINARY ANALYSES OF ST-11 BUILDING	385
10.1	Introduction	385

10.2	Three dimensional elastic finite element analysis	386
10.3	Dynamic analysis based on a conceptual model	398
10.4	Seismic evaluation of the test structure based on FEMA 356 methodology	409
10.5	Ultimate strength based on rigid body analysis	424
10.6	Discussions	430
10.7	Conclusions	434
CHAPTER 11	NONLINEAR FINITE ELEMENT ANALYSIS OF URM STRUCTURE	435
11.1	Introduction	435
11.2	Two dimensional nonlinear FE model	438
11.3	Three dimensional nonlinear FE model	456
11.4	Conclusions	481
CHAPTER 12	NONLINEAR PUSHOVER ANALYSIS OF PERFORATED URM IN-PLANE WALLS	483
12.1	Introduction	483
12.2	Modeling of URM perforated in-plane wall and pier-spandrel interaction	489
12.3	Overturning effects	492
12.4	Flange effects	499
12.5	Nonlinear properties of URM piers	500
12.6	External lateral seismic excitations	507
12.7	Nonlinear pushover analysis of the test structure	509
12.8	Conclusions	525
CHAPTER 13	RECOMMENDATIONS FOR THE URM SECTION OF FEMA 356	526
13.1	Introduction	526
13.2	Material properties and condition assessment (FEMA 356 Section 7.3)	527
13.3	Engineering properties of masonry walls (FEMA 356 Section 7.4)	531
13.4	Proposed mathematical model for a three dimensional URM building	537
13.5	Other issues	539
13.6	Summary	540

CHAPTER 14	CONCLUSIONS AND FUTURE RESEARCH	541
14.1	URM materials	541
14.2	URM structural components	543
14.3	Structural characteristics of URM building	544
14.4	Modeling of URM buildings	548
14.5	FEMA 356 provisions	550
14.6	Additional research needs	551
APPENDIX A.	QUAD CHARTS FOR RELATED MAE CENTER PROJECTS	554
APPENDIX B.	DETERMINATION OF TYPE K' MORTAR	573
APPENDIX C.	DESIGN OF FOUNDATION SLABS	577
APPENDIX D.	LINEAR STATIC PROCEDURE FOR THE TEST STRUCTURE	580
APPENDIX E.	NONLINEAR STATIC PROCEDURE FOR THE TEST STRUCTURE	591
APPENDIX F.	RIGID BODY ANALYSIS FOR THE TEST STRUCTURE	601
REFERENCES		617
VITA		634

LIST OF TABLES

Table 2.1	Mortar compositions by volumes	12
Table 2.2	Masonry unit strengths	13
Table 2.3	Ultimate drift of URM pier corresponding to different failure modes	19
Table 3.1	Masonry bed joint shear strength	56
Table 4.1	Comparison between test results and the effective pier model	119
Table 5.1	Definitions for the effective flange length	145
Table 6.1	Objectives for Project ST-11	153
Table 6.2	Different grade of masonry mortar used prior to 1950 (ASTM 1958)	157
Table 6.3	Material properties of the test structure	158
Table 6.4	Opening ratios of each wall	167
Table 6.5	Pier sizes and aspect ratios	168
Table 7.1	Lists of test runs, loading direction parallel to the joists	187
Table 7.2	Tangential stiffness of the half roof diaphragm at the end of pushing loading (by mid-span displacement)	191
Table 7.3	Lists of Test Runs Parallel to Joists	194
Table 7.4	Out-of-plane elastic stiffness of Walls A and B	201
Table 7.5	Axial stiffness of the diaphragm	206
Table 7.6	Lists of test runs perpendicular to the joists	211
Table 7.7	Lateral stiffness of the entire diaphragm perpendicular to the joists	214
Table 7.8	Out-of-plane elastic stiffness of Walls 1 & 2	216
Table 7.9	Experimental and predicted force distributions between the diaphragm and the masonry walls	217
Table 8.1	Measured maximum displacement values in each test cycle	229
Table 8.2	Lateral displacement ratios of Piers 2-7 and 2-9 in the push direction (Cycles 3a to 5a)	244

Table 8.3	Lateral displacement ratios of Piers 2-7 and 2-9 in the pull direction (Cycles 3a to 5a)	245
Table 8.4	Lateral displacement ratios of Piers 2-7 and 2-9 in the push direction (Cycles 6 to 8a)	254
Table 8.5	Lateral displacement ratios of Piers 2-7 and 2-9 in the pull direction (Cycles 6 to 8a)	254
Table 8.6	Uplift of the first floor piers during the tests	258
Table 8.7	Lateral displacement ratios of Piers 2-7 and 2-9 in the push direction (Cycles 10 to 10a)	260
Table 8.8	Lateral displacement ratios of Piers 2-7 and 2-9 in the pull direction (Cycles 10 to 10a)	260
Table 8.9	Displacements and base shears of the test building in Cycle 9	294
Table 8.10	Displacements and base shears of the test building in Cycle 8a	295
Table 8.11	Uplift of Wall 1 during the tests	305
Table 8.12	Uplift of Wall 2 during Test cycles 8 to 10a	307
Table 8.13	Elastic modulus of masonry (ksi)	306
Table 8.14	Natural periods and vibration modes of Wall 1 and Wall 2	309
Table 9.1	Displacement values of each test cycle	315
Table 9.2	Lateral displacement of Piers B-7 and B-10 in the push direction	326
Table 9.3	Lateral displacement ratios of Piers B-7 and B-10 in the pull direction	327
Table 9.4	Rigid movements of Wall B first floor spandrel when loaded in the push direction (Cycles 22a – 25a)	332
Table 9.5	Rigid movements of Wall B first floor spandrel when loaded in the pull direction (Cycles 22a – 25a)	333
Table 9.6	Rigid movements of First floor spandrel of Wall A when loaded in the push direction (Cycles 22a to 25a)	350
Table 9.7	Rigid movements of First floor spandrel of Wall A when loaded in the pull direction (Cycles 22a to 25a)	350
Table 9.8	Elastic modulus of the test structure parallel to Walls A and B	377

Table 9.9	Natural periods and vibration modes of Walls A and B	378
Table 10.1	Gravity stresses in the piers	389
Table 10.2	Out-of-plane stiffness of the masonry walls (kips/in)	391
Table 10.3	Calculated in-plane stiffness of the masonry walls (kips/in)	394
Table 10.4	In-plane stiffness of the masonry walls with and without flange effects (kips/in)	395
Table 10.5	Structural properties used in analysis with Walls A and B in-plane	400
Table 10.6	Elastic stiffness used for sensitivity analysis (Walls A and B in-plane)	401
Table 10.7	Natural periods of the conceptual model (Walls A and B in-plane)	401
Table 10.8	Structural properties used in analysis with Walls 1 and 2 in-plane	403
Table 10.9	Elastic stiffness used for sensitivity analysis (Walls 1 and 2 in-plane)	404
Table 10.10	Natural periods (seconds) of the conceptual model (Walls 1 and 2 in-plane)	404
Table 10.11	Maximum displacements of the URM structure under seismic load	407
Table 10.12	Maximum base shears of the URM structure and each component under seismic loads	408
Table 10.13	Response acceleration parameters (g) (BSE-1)	409
Table 10.14	Response acceleration parameters (g) (BSE-2)	410
Table 10.15	Pseudo seismic lateral load V (kips)	412
Table 10.16	The maximum strengths and the corresponding failure modes for each wall	413
Table 10.17	Performance level of each wall (BSE-1: 10% /50 year) (based on FEMA 356 equations)	414
Table 10.18	Performance level of each wall (BSE-2: 2% /50 year) (based on FEMA 356 equations)	414

Table 10.19	The observed maximum strengths and failure modes for each wall	416
Table 10.20	Performance level of each wall (BSE-1: 10% /50 year) (based on test data)	416
Table 10.21	Performance level of each wall (BSE-2: 2% /50 year) (based on test data)	417
Table 10.22	Target displacement, δ_t (in)	418
Table 10.23	Design displacement drift of each component (%) (BSE-1)	420
Table 10.24	Design displacement drift of each component (%) (BSE-2)	420
Table 10.25	Force-deformation parameters for the first story piers	422
Table 10.26	Performance level of each component (BSE-1)	423
Table 10.27	Performance level of each component (BSE-2)	424
Table 10.28	Weight calculation for the rigid body analysis for Wall 2	427
Table 10.29	Ultimate strength of each wall (kips)	429
Table 11.1	Calculated ultimate strength of Wall 1	449
Table 11.2	Calculated ultimate strength of Wall 2	451
Table 11.3	Calculated ultimate strengths of Walls A and B	454
Table 12.1	Working states and the corresponding identification tag of a URM	506
Table 12.2	Failure mechanisms of Walls A and B	521
Table B.1	Summary of diagonal compression test results (Type N)	573
Table B.2	Summary of diagonal compression test results (Type O)	574
Table B.3	Summary of direct shear tests	576
Table C.1	Dimensions and weights of the RC slabs	577
Table D.1	Seismic forces for the test structure at the BSE-1 level	582
Table D.2	Seismic forces for the test structure at the BSE-2 level	583
Table D.3	Design earthquake actions for each wall at the BSE-1 level	584
Table D.4	Design earthquake actions for each wall at the BSE-2 level	584
Table D.5	The maximum strengths and the corresponding failure modes for each wall	585
Table D.6	Factors for determining the design actions of the test structure	586

Table D.7	Design actions for each wall at BSE-1 level (in kips)	587
Table D.8	Design actions for each wall at BSE-2 level (in kips)	587
Table D.9	m factor for Wall 2	588
Table D.10	Performance level of each wall (BSE-1)	588
Table D.11	Performance level of each wall (BSE-2)	588
Table D.12	The observed maximum strengths and failure modes for each wall	589
Table D.13	Design actions for each wall at the BSE-1 level (based on test, in kips)	589
Table D.14	Design actions for each wall at the BSE-2 level (based on test, in kips)	590
Table D.15	m factor for each wall	590
Table D.16	Performance level of each wall (based on test, BSE-1)	590
Table D.17	Performance level of each wall (based on test, BSE-2)	590
Table E.1	Target displacements for the test structure at the BSE-1 level	592
Table E.2	Target displacements for the test structure at the BSE-2 level	593
Table E.3	Design displacements for each component (in.) (BSE-1 and K=1)	594
Table E.4	Design displacement for each component (in.) (BSE-1 and K=0.5)	595
Table E.5	Design displacement for each component (in.) (BSE-2 and K=1)	595
Table E.6	Design displacements for each component (in.) (BSE-1 and K=0.5)	596
Table E.7	Design displacement drift for each component (%) (BSE-1)	597
Table E.8	Design displacement drift for each component (%) (BSE-2)	597
Table E.9	Force-deformation relationships for all the first-story piers	599
Table E.10	Performance of each component (BSE-1)	600
Table E.11	Performance of each component (BSE-2)	600
Table F.1	Weight used in the right body analysis for Wall 2 (push direction)	602

Table F.2	Weights used in the right body analysis for Wall 1 (push direction)	605
Table F.3	Weights used in the right body analysis for Wall 1 (pull direction)	608
Table F.4	Weights used in the right body analysis for Walls A and B (kips)	610
Table F.5	Analyzed vs. measured maximum strengths for Walls A and B	610
Table F.6	Weights used in the right body analysis for Wall B sliding (kips)	613
Table F.7	Analyzed vs. measured maximum strengths for Wall B	613
Table F.8	Weights used in the right body analysis for Wall A (push direction) (kips)	615

LIST OF FIGURES

Figure 1.1	Charleston fire station	6
Figure 2.1	Typical URM building under earthquake excitation (Modified from Figure 2 of Bruneau 1994a)	11
Figure 2.2	Typical masonry pier	12
Figure 2.3	A typical perforated in-plane wall	15
Figure 2.4	Different crack patterns for the URM piers	16
Figure 2.5	Crack observed in the spandrel of Wall B (Magenes et al. 1995)	20
Figure 2.6	Specimen House 1 in Clough's test (Clough et al. 1979)	27
Figure 2.7	Specimen House 2 in Clough's test (Clough et al. 1979)	28
Figure 2.8	Layout and dimensions of the tested models (units in cm) (Tomazevic et al. 1993)	30
Figure 2.9	Floor and Roof systems of the tested models (units in cm) (Tomazevic et al. 1993)	31
Figure 2.10	Distribution of displacements along the top floor (Tomazevic 1993)	33
Figure 2.11	Window wall and out-of-plane wall of the tested structure S1 (Costley and Abrams 1996)	34
Figure 2.12	Configuration of perforated in-plane walls (Costley and Abrams 1996)	35
Figure 2.13	Tested single-story URM building (Paquette and Bruneau 2002)	38
Figure 2.14	Final crack pattern in the dynamical tested specimen (Costley and Abrams 1996)	42
Figure 2.15	Final crack pattern in static tested specimen (Magenes et al. 1995)	43
Figure 3.1	Biaxial strength of solid clay unit masonry (Page 1981, 1983)	47
Figure 3.2	Modes of failure of solid clay unit masonry under biaxial loading (Dhanasekar et al. 1985a)	48
Figure 3.3	Masonry shear test configurations (Atkinson et al. 1989)	54
Figure 3.4	Typical failure criterion (in terms of $\tau - \sigma_n$) (Page et al. 1982)	55
Figure 3.5	Shear crack at the interface between masonry units and mortar	59

Figure 3.6	Typical mortar and clay unit interface (Lange et al. 1999)	60
Figure 3.7	Mechanical key model	62
Figure 3.8	4-brick direction shear test set up	66
Figure 3.9	Measured initial shear strength with different lateral confining stresses	67
Figure 3.10	Changing of lateral compressive force with the initiation of shear sliding cracks on the bed joints	69
Figure 3.11	Break down and separation of the mechanical key	69
Figure 3.12	Failure criteria for masonry bed joints	72
Figure 3.13	Failure mode of masonry with the tensile stress parallel to the bed joint	74
Figure 3.14	Two different types of diagonal cracking (Epperson et al. 1992)	77
Figure 3.15	A diagonal compression specimen	79
Figure 3.16	Distribution of the bed joint shear stress in the masonry panel	80
Figure 3.17	Distribution of the bed joints normal stress in the masonry panel	80
Figure 3.18	Distribution of the normal stress parallel to the bed joints	81
Figure 4.1	External forces applied on a pier	86
Figure 4.2	Distribution of the internal stresses in a URM pier with flexural cracks	88
Figure 4.3	Effective pier after toe crushing and flexural cracking	95
Figure 4.4	Stress-strain relationship of masonry before and after diagonal tension cracks	98
Figure 4.5	Effective pier at an angle to the vertical line	99
Figure 4.6	Predicted base shear strength by the effective pier model vs. FEMA 356 equation	105
Figure 4.7	Predicted toe crushing strength by the effective pier model vs. FEMA 356 equation	108
Figure 4.8	Calculated and measured lateral force – displacement curve of specimen 1F (Franklin et al. 2001)	112
Figure 4.9	Calculated and measured lateral force – displacement curve of specimen 1S (Erbay et al. 2002)	114
Figure 4.10	Calculated and measured lateral force – displacement curve of specimen MI3 (Magenes and Calvi 1992)	116

Figure 4.11	Calculated and measured lateral force – displacement curve of specimen (W1, Manzouri et al. 1995)	118
Figure 5.1	Non-rectangular URM pier section	123
Figure 5.2	A typical URM pier with transverse wall	125
Figure 5.3	External forces applied on a non-rectangular section URM pier	127
Figure 5.4	Contribution of transverse wall to the rocking strength of a URM pier with zero effective length	135
Figure 5.5	Contribution of transverse wall to the rocking strength of a URM pier with the effective length of $0.15L$	136
Figure 5.6.	Toe crushing strength of non-rectangular section URM pier ($\omega = 0.1$)	141
Figure 5.7	Toe crushing strength of non-rectangular section URM pier ($\omega = 0.3$)	141
Figure 5.8	Toe crushing strength of non-rectangular section URM pier ($\omega = 0.5$)	142
Figure 5.9	Elevation showing the effective flange width for the transverse wall in tension	147
Figure 5.10	Effective flange width for the transverse wall in compression	148
Figure 5.11	Unreinforced masonry corner wall separated during shaking tests (Tomazevic, 1999)	149
Figure 6.1	3D exploded view of the test structure	155
Figure 6.2	Two different types of bricks	156
Figure 6.3	Test setup for the measurement of elastic modulus of masonry (5 brick specimen)	159
Figure 6.4	Overview of the test structure with the L strong walls	160
Figure 6.5	Plan view of the ST-11 test structure	161
Figure 6.6	Elevation view of Wall 1	162
Figure 6.7	Elevation view of Wall 2	163
Figure 6.8	Elevation view of Walls A and B	164
Figure 6.9	Detail of American bond	165
Figure 6.10	Common bond used to ensure adequate connection strengths (Stoddard 1946)	168
Figure 6.11	Detail of arch lintels	169
Figure 6.12	Detail of steel lintels	170
Figure 6.13	ST-11 roof/floor diaphragm	172

Figure 6.14	Simpson connections (taken from www.strongtie.com)	173
Figure 6.15	Photo of the stud wall together with the foundation	174
Figure 6.16	Opening left at the top of Wall 1	176
Figure 6.17	Assembly of the floor systems	177
Figure 7.1	Typical diaphragm components	181
Figure 7.2	The tested roof diaphragm	183
Figure 7.3	Test setup for the one-half diaphragm test	184
Figure 7.4	Setup of the loading system for the one-half diaphragm test	185
Figure 7.5	Loading history for the one-half diaphragm test	186
Figure 7.6	Typical force-displacement curve of the half roof diaphragm	188
Figure 7.7	Total external force-displacement curve for the out-of-plane Wall A	190
Figure 7.8	Test set up for the entire roof diaphragm test parallel to the joists	192
Figure 7.9	Instrumentation set up for the roof diaphragm test parallel to the joists	193
Figure 7.10	Conceptual model for the structure in the direction parallel to the joists	196
Figure 7.11	Simplified conceptual model for the structure in the direction parallel to the joists	196
Figure 7.12	Typical displacements of roof diaphragm and the masonry walls when loaded parallel to the joists	197
Figure 7.13	Loading phase for calculating the secant stiffness of the out-of-plane Wall A (Run 8)	199
Figure 7.14	Loading phases for calculating the secant stiffness of the out-of-plane Wall A (Run 18)	200
Figure 7.15	Long distance between the loading point and the masonry wall helps to uniformly distribute the force on the boundary	202
Figure 7.16	Deformation profiles of the out-of-plane walls at the roof level	203
Figure 7.17	Deformation profile of the out-of-plane walls along the vertical centerline	204
Figure 7.18	Sliding between the joists and the out-of-plane wall (Run 17 with tension ties and Run 18 without tension ties)	207
Figure 7.19	Set up of the loading system for the diaphragm test perpendicular to the joists	209

Figure 7.20	Instrumentations set up for the roof diaphragm test perpendicular to the joists	210
Figure 7.21	Interaction between the roof and the masonry walls in the direction perpendicular to the joists	213
Figure 7.22	Conceptual model for the structure perpendicular to the joists	213
Figure 7.23	Lateral deformation profile of the diaphragm perpendicular to the joists	214
Figure 7.24	Interaction forces between the roof and the out-of-plane wall in the direction perpendicular to the joists	218
Figure 7.25	Relative movement between the joist and the masonry wall	220
Figure 8.1	Connection details for connecting the actuators to the masonry walls, view looking east	226
Figure 8.2	Modified stiffness displacement control scheme	227
Figure 8.3	Loading history	229
Figure 8.4	Instrumentations of the in-plane tests parallel to Walls 1 and 2	232
Figure 8.5	Instrumentations of Pier	234
Figure 8.6	Axial displacements of Pier 2-7 and Pier 2-9	237
Figure 8.7	Strains at the base of Pier 2-7	237
Figure 8.8	The constant tensile strain at the base of Pier 2-7 in Test cycle 3a indicated possible flexural cracks	239
Figure 8.9	Crack pattern of Wall 2 at the end of Cycle 5b (looking eastward)	240
Figure 8.10	The base shear-lateral roof displacement curves for Wall 2 during Cycles 2g to 5b	241
Figure 8.11	Vertical displacements of Pier 2-7 upper boundary	242
Figure 8.12	Upward displacement of the upper boundary of a pier due to rocking of individual pier	244
Figure 8.13	Crack pattern of Wall 2 and adjacent Wall A (left) and Wall B (right) at the end of Cycle 8a	247
Figure 8.14	Rocking of Pier 2-9 in different directions	248
Figure 8.15	The base shear-lateral roof displacement curves for Wall 2 up to Cycles 8b	250
Figure 8.16	Vertical displacements of Pier 2-7 upper boundary	251
Figure 8.17	Lateral displacements of Pier 2-7	252
Figure 8.18	Vertical movement of Pier 2-8	253

Figure 8.19	Crack pattern of Wall 2 and adjacent Wall A (left) and Wall B (right) at the end of Cycle 10a.	256
Figure 8.20	Rocking of the first floor piers in Wall 2 and upward movement of the second story wall	257
Figure 8.21	The base shear-lateral roof displacement curves for Wall 2 during the entire load cycles	257
Figure 8.22	Lateral displacements of Pier 2-7	259
Figure 8.23	Base shear-lateral roof displacement of Wall 1 up to Cycle 5b	261
Figure 8.24	The average vertical strains in Pier 1-6 and Pier 1-7 when the wall was loaded in the push direction	262
Figure 8.25	The average vertical strains in Pier 1-6 and Pier 1-7 when the wall was loaded in the pull direction	263
Figure 8.26	The base vertical strains in Pier 1-6 and Pier 1-7 when the wall was loaded in the push direction	263
Figure 8.27	The base vertical strains in Pier 1-6 and Pier 1-7 when the wall was loaded in the pull direction	264
Figure 8.28	Vertical movements of Pier 1-6 in Cycles 2g, 3a, and 5a	265
Figure 8.29	Vertical movements of Pier 1-7 in Cycles 2g, 3a, and 5a	266
Figure 8.30	Crack pattern of Wall 1 and adjacent Wall B (left) and Wall A (right) at the end of Cycle 8a.	267
Figure 8.31	Lifting up of Wall B due to the flange effects	269
Figure 8.32	Rocking of Wall 1 as two piers when the wall was loaded in the pull direction	270
Figure 8.33	Rocking of Wall 1 when loaded in the push direction (southward)	271
Figure 8.34	Wall 1 was separated from Wall A when it was pushed to the left (southward)	272
Figure 8.35	Base shear-lateral roof displacement of Wall 1 up to Cycle 8a	273
Figure 8.36	Vertical displacements of the upper boundaries of Pier 1-6 and Pier 1-7 before and after cracking	275
Figure 8.37	Vertical strain at the base of Pier 1-6 in Cycles 5b, 6, 7, and 8 when the building was loaded in the pull direction	276
Figure 8.38	Vertical displacements of the upper boundaries of Pier 1-6 in Cycles 5b, 6, 7, and 8 when the building was loaded in the pull direction	277
Figure 8.39	Vertical strain at the base of Pier 1-7 in Cycles 5b, 6, 7, and 8 when the building was loaded in the pull direction	278

Figure 8.40	Vertical displacements of the upper boundaries of Pier 1-7 in Cycles 5b, 6, 7, and 8 when the building was loaded in the pull direction	279
Figure 8.41	Inclined compressive force transferred in Pier 1-7 when the building was loaded in the pull direction	279
Figure 8.42	Vertical displacements of the upper boundaries of Pier 1-6 in Cycles 5b, 6, 7, and 8 when the building was loaded in the push direction	280
Figure 8.43	Vertical strains at the base of Pier 1-6 in Cycles 5b, 6, 7, and 8 when the building was loaded in the push direction	281
Figure 8.44	Lateral displacements of Pier 1-6 in Cycle 5b	282
Figure 8.45	Lateral displacements of Pier 1-6 in Cycle 8	282
Figure 8.46	Vertical strain at the base of Pier 1-7 in Cycles 5b, 6, 7, and 8 when the building was loaded in the push direction	284
Figure 8.47	Vertical displacements at the base of Pier 1-7 in Cycles 5b, 6, 7, and 8 when the building was loaded in the push direction	284
Figure 8.48	Crack pattern of Wall 1 and adjacent Wall B (left) and Wall A (right) at the end of Cycle 10a	286
Figure 8.49	Switching failure modes of Pier 1-6 from rocking to sliding when the wall was loaded in the pull direction (northward) in Cycle 10	287
Figure 8.50	Base shear –lateral roof displacement of Wall 1 up to Cycle 10a	288
Figure 8.51	Sliding of Pier 1-6 captured by Potentiometer P1-6S when Wall 1 was loaded in the pull direction in Cycle 10	289
Figure 8.52	Vertical displacements of the upper boundaries of Pier 1-6 before and after sliding	289
Figure 8.53	Vertical strains at the base of Pier 1-6 before and after sliding	290
Figure 8.54	Vertical displacements of the upper boundaries of Pier 1-7 before and after sliding of Pier 1-6	291
Figure 8.55	Vertical strains at the base of Pier 1-7 before and after sliding of Pier 1-6	291
Figure 8.56	Sliding of Pier 1-6 in Cycle 10 and Cycle 10a	293
Figure 8.57	Shear flow in the tested structure	297
Figure 8.58	Vertical stress distribution in a solid tube structure	298
Figure 8.59	Vertical stress distribution in a perforated tube structure	298
Figure 8.60	Vertical strain distribution at the base of the tested building	301

Figure 8.61	Vertical strain distribution at the base of the tested building (Cycle 10)	302
Figure 8.62	Vertical movements of Wall 1	304
Figure 8.63	Rocking behavior of Wall 1 in Cycle 7	304
Figure 8.64	Vertical movements of Wall 1 (Cycle 8)	306
Figure 9.1	Instrumentations of the in-plane wall tests parallel to Walls A and B	317
Figure 9.2	Lateral roof displacement-base shear curve for Wall B (Cycles 20c to 21b)	320
Figure 9.3	Existing cracks in Wall B before test (looking north)	321
Figure 9.4	The vertical movements of the upper boundaries of the four first story piers in Wall B when loaded in the push direction to maximum deflection	322
Figure 9.5	The vertical movements of the upper boundaries of the four first story piers in Wall B when loaded in the pull direction to maximum deflection	323
Figure 9.6	Reading of strain gages of Pier B-9 in Cycle 21b	324
Figure 9.7	Lateral displacements of Pier B-10 (Cycle 21b)	326
Figure 9.8	Crack pattern of Wall B and adjacent Wall 2 (left) and Wall 1 (right) at the end of Cycle 25b	329
Figure 9.9	Lateral displacement- base shear force curves for Wall B up to Cycle 25b	330
Figure 9.10	Vertical movements of Wall B first floor spandrel when loaded in the push direction to maximum deflection (Cycles 22a – 25a)	331
Figure 9.11	Vertical movements of Wall B first floor spandrel when loaded in the pull direction to maximum deflection (Cycles 22a – 25a)	333
Figure 9.12	Crack pattern of Wall B and adjacent Wall 2 (left) and Wall 1 (right) at the end of Cycle 26b	335
Figure 9.13	Kinematic mechanism of Wall B when loaded in the push direction	336
Figure 9.14	Kinematic mechanism of Wall B when loaded in the pull direction	338
Figure 9.15	Vertical movements of the Wall B first floor spandrel (up to Cycle 26a)	339
Figure 9.16	Lateral displacement – shear force curves for Wall B in all the test cycles	340

Figure 9.17	Initial cracks in Wall A and adjacent Wall 1 (left) and Wall 2 (right)	342
Figure 9.18	Lateral roof displacement-base shear of Wall A (Cycles 20c to 21b)	343
Figure 9.19	Crack pattern of Wall A and adjacent Wall 1 (left) and Wall 2 (right) at the end of Cycle 25b.	344
Figure 9.20	Base shear vs. lateral roof displacement for Wall A up to Cycle 25b	347
Figure 9.21	Vertical displacement of the first floor spandrel for Wall A when loaded in the push direction to maximum deflection (Cycles 22a to 25a)	349
Figure 9.22	Vertical displacement of the first floor spandrel for Wall A when loaded in the pull direction to maximum deflection (Cycles 22a to 25a)	349
Figure 9.23	Crack pattern of Wall A and adjacent Wall 1 (left) and Wall 2 (right) at the end of Cycle 26b	352
Figure 9.24	Temporary support for the arch lintel, Pier A-10 on the left (view from inside the building toward north)	353
Figure 9.25	Kinematic mechanism of Wall A when loaded in the push direction.	354
Figure 9.26	Kinematic mechanism of Wall A when loaded in the pull direction.	355
Figure 9.27	Vertical movements of the first floor spandrel of Wall A (up to Cycle 26a)	356
Figure 9.28	Base shear-lateral roof displacement of Wall A in all the test cycles	357
Figure 9.29	Pier flange and spandrel flange in the tensile side of a pier	359
Figure 9.30	Pier flange and spandrel flange on the compressive side of a pier	360
Figure 9.31	Effective area of a pier flange	361
Figure 9.32	Effective area for the pier flange and the spandrel flange in the tensile side of a pier	362
Figure 9.33	Effective area for the pier flange and the spandrel flange in the compressive side of a pier	364
Figure 9.34	Effective flange area for a in-plane pier with adjacent opening in the out-of-plane wall	365
Figure 9.35	Vertical movements of the masonry walls	368
Figure 9.36	Effective pier of a door pier when loaded from left to right	369

Figure 9.37	Effective pier of a door pier when loaded from right to left	370
Figure 9.38	Different configurations of window piers	371
Figure 9.39	Effective pier of an interior window	371
Figure 9.40	Effective pier of a door pier when loaded from left to right	372
Figure 9.41	Effective pier of an exterior door pier when loaded from right to left	373
Figure 9.42	Effective pier of an exterior door pier when loaded from left to right	374
Figure 9.43	Comparison of Wall A and Wall B	376
Figure 9.44	Typical cracks in an arch lintel	379
Figure 9.45	Picture of the damaged arch lintel in Wall A (over Wall A first-story door opening)	380
Figure 10.1	Three-dimensional model of the ST-11 building	387
Figure 10.2	Out-of-plane loading of the masonry wall	390
Figure 10.3	Different loading cases for calculation of the in-plane stiffness of masonry walls	393
Figure 10.4	Maximum Von Mises stresses in the Wall 1 under in-plane loading (looking west)	397
Figure 10.5	Maximum Von Mises stresses in the Wall 2 under in-plane loading (looking east)	397
Figure 10.6	Maximum Von Mises stresses in Walls A and B under in-plane loading (looking south)	397
Figure 10.7	Conceptual model of an URM structure	399
Figure 10.8	Vibration modes for the test structure (Walls A and B in-plane)	402
Figure 10.9	Vibration modes for the test structure (Walls 1 and 2 in-plane)	404
Figure 10.10	Artificial Mid-America ground motion (rock site)	406
Figure 10.11	Artificial Mid-America ground motion (soil site)	406
Figure 10.12	Elastic model for each perforated wall	412
Figure 10.13	Nonlinear model for each perforated wall	419
Figure 10.14	Generalized force-deformation relationship for a URM pier	421
Figure 10.15	Kinematic mechanism of Wall 1 when loaded in the north direction	426
Figure 10.16	Internal force distribution of Wall 1	427
Figure 11.1	Flexural moments and shear forces applied on a spandrel	440
Figure 11.2	Teeth configurations of the head joints	440

Figure 11.3	Schematic of a contact element	441
Figure 11.4	Normal forces transmitted between the pair of surfaces	442
Figure 11.5	Shear force-relative sliding displacement relationship for contact elements	443
Figure 11.6	Modeling of a perforated wall with contact elements and stabilizing truss elements	444
Figure 11.7	Force-displacement response of Wall 1 with different bed joint shear friction coefficients	447
Figure 11.8	Deformed shapes of Wall 1	448
Figure 11.9	Stress contour of Wall 1	448
Figure 11.10	Force-displacement response of Wall 1 with different material properties	449
Figure 11.11	Force-displacement response of Wall 2 with different friction coefficients	450
Figure 11.12	Deformed shapes of Wall 2	451
Figure 11.13	Force-displacement response of Wall 2 with different masonry properties	452
Figure 11.14	Force-displacement response of Walls A and B with different friction coefficients	453
Figure 11.15	Deformed shapes of Walls A and B	453
Figure 11.16	Definition of the possible crack pattern in the test structure	458
Figure 11.17	ABAQUS 3D contact model for the test structure	460
Figure 11.18	Failure mechanisms of Wall 2	462
Figure 11.19	3D FE analysis vs. measured base shear-lateral roof displacement relationship for Wall 2	463
Figure 11.20	Failure mechanism of Wall 1	465
Figure 11.21	3D FE analysis vs. measured base shear-lateral roof displacement relationship for Wall 1	466
Figure 11.22	Distribution of base shear force parallel to Walls 1 and 2 among four walls	468
Figure 11.23	Distribution of base shear force perpendicular to Walls 1 and 2 among four walls	469
Figure 11.24	Distribution of vertical compressive force among four walls	469
Figure 11.25	Failure mechanism of Wall B	471
Figure 11.26	3D FE analysis vs. test observation of the base shear-lateral roof displacement relationship for Wall B	473

Figure 11.27	Failure mechanisms of Wall A	475
Figure 11.28	3D FE analysis vs. test observation of the base shear-lateral roof displacement relationship for Wall A	477
Figure 11.29	Distribution of base shear force parallel to Walls 1 and 2 among four walls	478
Figure 11.30	Distribution of base shear force perpendicular to Walls 1 and 2 among four walls	479
Figure 11.31	Distribution of vertical compressive force among four walls	479
Figure 12.1	Solid spandrel-cracked pier perforated URM wall model	486
Figure 12.2	Solid pier-cracked spandrel perforated URM wall model	486
Figure 12.3	Park's simple lumped parameter model (2002)	488
Figure 12.4	Concepts of elastic spandrel-nonlinear pier model	490
Figure 12.5	Effect of overturning moments on different structure configurations	494
Figure 12.6	Internal forces in an idealized perforated wall	495
Figure 12.7	Distribution of vertical stress under gravity load and lateral force	497
Figure 12.8	Lateral force-drift relationship for rocking	502
Figure 12.9	Lateral force-drift relationship for sliding	503
Figure 12.10	Lateral force-drift relationship for diagonal tension pier	504
Figure 12.11	Lateral force distributions for all runs in Paulson (1990)'s test	508
Figure 12.12	Base shear-lateral displacement relationships of Wall 2	512
Figure 12.13	Failure mechanisms of Wall 2	512
Figure 12.14	Calculated vertical stress variations in Wall 2 first story piers	513
Figure 12.15	Calculated base shear distribution among Wall 2 first story piers	513
Figure 12.16	Base shear-lateral displacement relationships of Wall 1	516
Figure 12.17	Failure mechanism of Wall 1 predicted by the effective pier model	517
Figure 12.18	Failure mechanism of Wall 1 predicted by the simplified model	517
Figure 12.19	Calculated vertical stress variations in Wall 1 first story piers (by the effective pier model)	518
Figure 12.20	Calculated base shear distribution among Wall 1 first story piers (by the effective pier model)	518

Figure 12.21	Base shear-lateral displacement relationships of Wall A	520
Figure 12.22	Base shear-lateral displacement relationships of Wall B	521
Figure 12.23	Vertical stress variations in Wall A first story piers (by the effective pier model)	523
Figure 12.24	Vertical stress variations in Wall B first story piers (by the effective pier model)	523
Figure 12.25	Base shear distribution among Wall A first story piers (by the effective pier model)	524
Figure 12.26	Base shear distribution among Wall B first story piers (by the effective pier model)	524
Figure B.1	Photograph of shear failure through brick	575
Figure C.1	Plan view of foundation layout (dimensions are in inches)	578
Figure C.2	Reinforcement details of the foundation slabs (dimensions are in inches)	579
Figure D.1	Analytical model for the URM wall	585
Figure E.1	Nonlinear pushover model for a perforated URM wall	594
Figure E.2	Force-displacement relationship for a URM pier	598
Figure F.1	Kinematic movement of Wall 2 when loaded in the push direction	601
Figure F.2	Internal force distribution in Wall 2 when loaded from left to right	603
Figure F.3	Kinematic movements and internal force distribution in Wall 1 when loaded in the push direction	605
Figure F.4	Kinematic movement of Wall 1 before Pier 1-6 slides (pull direction)	606
Figure F.5	Internal force distribution in Wall 1 before Pier 1-6 slides (pull direction)	608
Figure F.6	Kinematic movement of Wall B when loaded in the push direction	610
Figure F.7	Internal force distribution in Wall B when loaded in the push direction	611
Figure F.8	Knematic movement of Wall B with sliding between spandrel and piers (push direction)	612
Figure F.9	Kinematic movement of Wall A (push direction)	615
Figure F.10	Internal force distribution in Wall A (push direction)	616

LIST OF SYMBOLS

A	Area of section
A_e	Area of effective section
A_f	Section area of the transverse wall
a_f	The distance between the center of the transverse wall and the compression edge at the bottom of the pie
a_i	The distance between the inertia center and the edge of the entire section
D_{Li}	The reading of LVDT i
d_{dia}	The lateral displacement of the roof diaphragm measured at its center point
d_{out}	The lateral deformation of the out-of-plane wall
$d_{out,i}$	The out-of-plane deformation of Wall i
E	Elastic modulus of masonry
G	Shear modulus of masonry
f_m	Compressive strength of masonry
f_m^\perp	The compressive strengths perpendicular to the bed joints
f_m^\parallel	The compressive strengths parallel to the bed joints
$f_m(\phi)$	The compressive strengths at an angle ϕ to the bed joint
f_m^n	Characteristic stress in the mechanical key
f_m^l	The lateral compressive stress in the mechanical key

f_t	Tensile strength of masonry
f_t^d	Diagonal tensile strength of masonry
f_t^\perp	The tensile strengths perpendicular to the bed joints
$f_t(\phi)$	The tensile strengths at an angle ϕ to the bed joint
f_t^\parallel	The tensile strengths parallel to the bed joints
f_t^m	Maximum tensile strength of a mechanical key
h	Height of the pier
K	Lateral stiffness of the pier
K_a	The axial stiffness of the diaphragm
K_{dia}	The lateral stiffness of the roof diaphragm
K_{do}	The stiffness of the connection between the joists and the out-of-plane walls
K_o	The stiffness of the out-of-plane wall
$K_{o,i}$	The out-of-plane stiffness of Wall i
K_{og}	The stiffness of the out-of-plane wall due to the support of the ground
K_{oi}	The stiffness of the out-of-plane wall due to the support of the in-plane wall
K_i	The stiffness of the in-plane wall
K_{ij}	The coupling stiffness between in-plane walls
L	Length of the pier
L_f	Length of the flange (transverse wall)
L_{crush}	Length of the failed portion of the pier
L_e	Effective length

L_{e_top}	Lengths of the uncracked sections at the top of the pier
L_{e_bottom}	Lengths of the uncracked sections at the bottom of the pier
M	External moment
M_{cr}	Cracking moment
M_b	Moment applied at the bottom of the pier
M_t	Moment applied at the top of the pier
P	External axial force
P_b	Axial force applied at the bottom of the pier
P_t	Axial force applied at the top of the pier
r_c	The ratio of the total interface area of the channel keys to the gross area of the interface
r_w	The ratio of the total interface area of the wedge keys to the gross area of the interface
S_S	Shear strength of diagonal compression specimen
t	Thickness of the pier
t_f	Thickness of the flange (transverse wall)
U_v	The vertical displacement of the upper boundary of a pier
U_θ	The rotation of the upper boundary of a pier
U_L	The lateral displacement of the upper boundary of a pier
u_{center}	The out-of-plane displacement of the masonry wall at the center point of the roof level
u_i	The in-plane lateral roof displacements of the in-plane walls
V	The external shear force

V_i	The lateral in-plane forces applied on Wall i
V_{bjs}	Bed-joint shear strength of a URM pier
V_{bjs}^{FEMA}	Bed-joint shear strength given by FEMA
V_{dt}	Diagonal tension strength of a URM pier
V_{dia}^{FEMA}	Diagonal tension strength given by FEMA
V_r	Rocking strength of a URM pier
V_{s2}	The remaining sliding strength of a bed joint
V_r^{FEMA}	Rocking strength given by FEMA
V_{tc}	Toe crushing strength of a URM pier
V_{tc}^{FEMA}	Toe crushing strength given by FEMA 356
W	Self weight of the pier
W_i	Weight of the in-plane wall
W_i	Weight of the in-plane rigid bodies
W_{if}	Weight of the flanges
W_o	Weight of the out-of-plane wall
W_d	Weight of the diaphragm
W_f	Self weight of the flange.
σ	Compressive stress of masonry
σ_{avg}	Average vertical compressive stress at the inflection point level
σ_{cb}	Maximum vertical compressive stresses at the bottom of the pier
σ_{ct}	Maximum vertical compressive stresses at the top of the pier

σ_n	Axial stress normal to the bed joint
$\sigma_{n \max}$	Maximum compressive stress in this section
σ_1	Maximum principle tensile stress
σ_2	Maximum principle compressive stress
σ_m^1	Maximum principle tensile stress in the mechanical key
τ	Average shear stress on the bed joint
τ_b	Shear stresses at the bottom of the pier
τ_d	Average shear stress at the inflection point level
τ_t	Shear stresses at the top of the pier
τ_u	Maximum shear strength of the bed joint
τ_m^s	The effective shear stress in each mechanical key
τ_o	Initial cracking shear strength of the bed-joint
δ_t	The target displacement at the top of the building
μ	Internal frictional coefficient at the brick-mortar interface
μ_1	The shear friction coefficient for the cracked bed joint
α	A coefficient determining the position of the inflection point along the height of a pier
β	Stress distribution factor
ζ	Shear stress distribution factor
χ	A factor that accounts for the effects of the aspect ratio to the lateral confining stress

χ	A factor dependent on the lateral deformation shape of the wall
θ	Inclined angle of an effective pier
Δ	Lateral deformation of the pier
$\Delta_{in-plane}$	The maximum displacement of the in-plane wall relative to the ground
$\Delta_{out-of-plane}$	The maximum displacement of the out-of-plane wall relative to the ground
$\Delta_{diaphragm}$	The maximum displacement of the diaphragm relative to the in-plane wall
γ	Boundary coefficient
ε	Compressive strain of masonry
ε_m	Axial strain corresponding to the maximum compressive stress
κ	The length to height ratio of masonry unit

SUMMARY

Unreinforced masonry (URM) construction, which has been widely used in the United States, presents a large threat to life safety and regional economic development because of its poor seismic resistance. In this research, the nonlinear seismic properties of URM structures were investigated via a quasi-static test of a full-scale two-story URM building and associated analytical and numerical studies.

The tests of the 24ft. by 24ft. in plan 22ft. high URM building revealed that the damage was characterized by (1) the formation of large discrete cracks in the masonry walls and (2) the rocking and sliding of URM piers. Both of these results were consistent with the predictions based on individual component properties obtained in previous research. However, the tests also revealed significant global behavior phenomena, including flange effects, overturning moment effects, and the formation of different effective piers in a perforated wall. This global behavior greatly affected the response of the URM building tested.

In order to understand the nonlinear behavior of the test structure, a series of analytical studies were conducted. First, at the material level, a mechanical key model was proposed to describe the failure of URM assemblages under a biaxial state of stress. Second, at the component level, an effective pier model was developed to illustrate the mixed failure modes of a URM pier and its nonlinear force-deformation relationship. Third, at the structure level, a nonlinear pushover model was built using the mechanical models at the material and component levels to describe the nonlinear properties of a URM building. This nonlinear pushover model and a three-dimensional finite element

model were employed to analyze the test structure. Both gave results in good agreement with the test data. Improvements to current provisions for the evaluation of existing masonry structures were proposed.

CHAPTER 1

INTRODUCTION

1.1. NEED FOR RESEARCH

Existing unreinforced masonry (URM) buildings have been long recognized for their seismic hazard. Previous major earthquakes have shown that the damage and collapse of URM construction is one of the primary failure modes for building systems (Bruneau 1994a, 1994b, 1995). In the United States, URM structures had been widely used as residential, commercial and essential facilities buildings until the 1933 Long Beach earthquake revealed their seismic vulnerability (Bruneau 1994a). Following that event, URM construction was outlawed in all public buildings in California and some other West Coast states. However, a large number of old URM buildings are still being used in California and other Western states, and URM structures have continued to be constructed in other regions which were considered as non-seismic areas until very recently. These seismically deficient buildings present a threat to life safety. Research to develop effective and economic seismic hazard mitigation methods for these URM buildings is urgently needed.

The seismic hazard of old URM structures stems from their many unique structural characteristics. First, at the material level, URM is a composite material composed of masonry units and mortar with a certain bond scheme (most old URM buildings in America were constructed in standard American bond, i.e., with a header course every sixth course). In addition, no reinforcement is added to enhance its

performance. As a result, URM is a brittle, anisotropic material. Moreover, weak mortar was typically used in most old URM construction. The elastic modulus and strength of the mortar are lower than those of masonry units, and there is normally a weak interface between the masonry unit and the mortar. This type of masonry is usually called strong unit-weak mortar masonry. Its material properties are controlled by the interface between masonry units and mortar. Second, the composite characteristics and the weak interface of URM material contribute to the distinctive behavior of URM at the component level. At this level, four typical failure modes, rocking, sliding, diagonal cracking and toe crushing dominate the nonlinear in-plane behavior of URM piers. Third, at the structure level, URM buildings exhibit high stiffness and low lateral strength. They also typically incorporate flexible floor and roof diaphragms made of wood or steel joists, and these flexible floor and roof diaphragms can lead to distinctive structural behavior in URM buildings, including lack of coupling and torsion.

In response to the seismic vulnerability of URM structures, a large amount of experimental and analytical research has been conducted on the behavior of URM structures in areas of high seismicity. In the United States, the research became particularly intensive after the 1933 Long Beach earthquake and the 1971 San Fernando earthquake, both of which reemphasized the vulnerability of the URM structures. After the latter earthquake, a mitigation methodology known as the ABK method was developed specifically for URM structures (ABK 1984). This methodology has been widely used since the early 1980s to reduce seismic hazard in existing URM buildings, and has been adopted with minor modification by several standards and prestandards, such as ATC-14 (ATC, 1987), ATC-22 (ATC, 1989), and FEMA (FEMA 1992a,b, ATC

1997a,b, 1999a,b, 2000). Numerous experimental and analytical investigations on URM structures have also been conducted in Europe, especially in Yugoslavia and Italy as a consequence of the 1964 Skopje and 1976 Friuli earthquakes. The research results from Europe, together with those obtained in United States provide reasonable guidelines for the seismic assessment and rehabilitation of URM buildings in areas of high seismicity.

However, although a large amount of research has been conducted to understand URM behavior, the knowledge obtained from previous research is difficult to synthesize. In experimental research, this is due primarily to the lack of uniformity in test protocols and difficulties associated with testing stiff brittle systems. In analytical research, this is due primarily to the difficulties in tracking cracking in a heterogeneous medium, numerical stability associated with contact problems and stiff system behavior, and the large models needed to track the behavior properly. These problems have their origin, again, on our inability to properly model the problem at the three required scales: material, component, and structure levels.

At the material level, although many tests have been conducted on the shear strength of URM, the shear behavior of URM is still unclear because it is a quite complex cracking problem at the interface between masonry units and mortar. In addition, there is still no conclusive knowledge about the relationship among several critical strength parameters: the bed-joint tensile strength, the diagonal tensile strength, the initial bed joint shear strength, and the shear friction factor along the cracked bed joint surface. The lack of this knowledge does not permit a complete understanding of the nonlinear behavior of URM. A similar problem exists at the component level. For instance, even though numerous experiments have been conducted on the strength and the failure modes

of individual masonry piers under in-plane loads, and several formulas have been proposed for the strength of a URM pier corresponding to certain failure mode based on these experimental research results (see FEMA 273/356 (ATC 1997, 2000)), no comprehensive theory is available to explain the interactions of different failure modes and the corresponding load-displacement relationship of a single URM pier. The lack of such theory makes it difficult to extrapolate the knowledge obtained from piers with a given configuration to other piers with different configurations, and from the isolated piers to the piers existing in a perforated wall. At the structure level, the problem is more daunting. Due to the large demands on the experimental facilities and funding, tests of entire URM structures, especially of full-scale URM structures, are seldom conducted. As a result, little knowledge is available on the structural behavior of URM buildings at the 3D structural level. These issues include the governing mechanisms for a perforated wall, the effects of flexible diaphragms on the performance of the entire URM building, the coupling effects between perpendicular walls, and the building torsion.

Another important problem is the special aspects of seismic hazard for URM buildings in Mid-America. Until recently, most of the research on URM buildings has been conducted in the areas of high seismicity. However, the URM problem in Mid-America has its own peculiar aspects. First, the design of most URM structures in Mid-America did not consider seismic loads. Most of these URM structures are stiff, massive buildings that are well suited to resist wind loads. Their mass and lack of ductility, however, make them highly vulnerable to ground motions. What is worse, because seismic hazard was not a consideration, numerous critical structures, including fire stations, police offices, and emergency response centers were built as URM structures

(Figure 1.1). These structures present a critical threat to adequate response and recovery efforts after a major earthquake. Second, the tectonic characteristics of Mid-America are likely to produce ground motions with significantly different attenuation and frequency content characteristics than those in the Western US. Thus, much of what has been learned through non-linear dynamic analysis of URM subjected to Western ground motions (1940 El Centro, for example) needs to be verified for the ground motions expected in Mid-America. Finally, it is not clear whether the methodologies developed and employed for retrofit of URMs in the Western US are applicable, both from the economic and technical points of view, in Mid-America. This is due primarily to the long return periods of strong earthquakes in this region, which make most retrofits economically unviable except for historic or critical structures. All these aspects point to the need of special research on URM buildings in Mid-America area.

In order to develop strength evaluation and rehabilitation strategies for URM buildings in the Mid-America area, a group of research projects sponsored by the Mid-America Earthquake (MAE) Center were conducted at several universities in the 1996-2001 period. Those projects investigated URM structures from many different aspects, including the characterization of the URM building inventory in Mid-America (SE-1¹), in-plane strength and retrofit tests on URM piers (ST-6) and their analyses (ST-4), URM out-of-plane wall test (ST-10) and their analyses (ST-9), and testing on flexible wood diaphragm tests (ST-8) and their analyses (ST-5). As a capstone of those projects, a full-scale quasi-static experiment of a two-story URM structure was conducted at Georgia

¹ The project numbers shown in parenthesis are those used by the MAE Center. A brief description of these projects, in the form of so-called quad charts, is given in Appendix A.

Tech (ST-11). Meanwhile, a parallel reduced-scale shaking table test was conducted at the US Construction Engineering Research Laboratory (CERL) (ST-22).



Figure 1.1. Charleston fire station

1.2. OBJECTIVES AND SCOPE OF RESEARCH

The research presented in this dissertation is based on the full-scale experiment of the project ST-11. This research centers on the seismic behavior of low-rise URM structures in the Mid-America area. These URM structures are made of strong unit-weak mortar masonry materials and flexible wood floor and roof diaphragms. This research is aimed at systemically investigating the nonlinear seismic behavior of these URM structures at the material level, the component level, and the structure level. The seismic behavior of URM structures is investigated via full-scale, quasi-static testing of a two-

story URM building, associated material tests, and advanced nonlinear numerical analyses.

1.3. OUTLINE OF THE RESEARCH

The dissertation is organized into 14 chapters, reflecting the major thrusts of this research.

Chapter 2 gives a brief literature review of previous research on URM structures. The review covers three different levels: the material level, the component level, and the structure level. The main focus of the review is on the previous experimental research on URM structures.

In order to fully understand the critical characteristics of URM materials, the results of an extensive investigation in the governing behavior of strong unit-weak mortar masonry is reported in Chapter 3. A micro-model, labeled the mechanical key model, is developed in this chapter to illustrate the failure modes and maximum strengths of masonry bed joints under different combinations of normal stress and shear stress. This model is then expanded to explain the failure mechanism for the entire strong unit-weak mortar masonry assemblage.

Based on the knowledge obtained at the material level, a macro-model, termed the effective pier model, is developed in Chapter 4 to describe the nonlinear properties of individual URM in-plane piers. The model addresses the mixed failure modes, and it can be used to predict both the maximum strength and the deformation capacity. This model is compared with the ultimate strength equations given by FEMA 356 and previous experimental results.

Most of previous research on URM in-plane pier, including what has been done in Chapter 4 is applicable only to rectangular cross-section in-plane piers. However, many of the in-plane piers in a URM building are connected to adjacent transverse walls. The adjacent transverse walls may significantly affect the behavior of the in-plane piers, leading to so-called flange effects. In order to consider the flange effects, the effective pier model proposed in Chapter 4 is modified in Chapter 5. A simple method also is proposed to calculate the effective flange width.

Chapters 6 through 9 discuss the quasi-static test of a full-scale two-story URM building, which is the center of the dissertation. Specifically, Chapter 6 introduces the design of this test, which includes the test objectives, the design of the test building (termed ST-11 building), the associated material tests, the construction procedure, and the loading sequence. Chapter 7 introduces the initial testing which was aimed at investigating the interaction between flexible diaphragms and masonry walls by laterally loading the roof diaphragm. Some specific characteristics of the test building, such as the stiffness values of the masonry walls and diaphragm, as well as the behavior of the connections between wall and diaphragm, also were measured in these initial tests. Following the initial low-force level tests, two more series of tests were conducted to investigate the nonlinear properties of the test structure. The results of the first set of tests, which focused on the nonlinear properties of the test structure parallel to Walls 1 and 2, are presented in Chapter 8. The second set of tests, which focused on the nonlinear properties of the test structure parallel to Walls A and B, are discussed in Chapter 9. Some unique features of the test structure discovered in the experimental research, such

as the contribution of the flange effects and the overturning moment effects, are also discussed in the two chapters.

Chapters 10 through 12 present a series of analytical studies for the test building. These studies were aimed at fully understanding the behavior of the test building and developing robust analytical tools for the nonlinear response of URM structures. Specifically, a set of preliminary analyses, including a 3D finite element (FE) elastic model, a simplified dynamic conceptual model, the FEMA 356 pre-standard procedure, and a simple rigid body analysis, are utilized in Chapter 10 to evaluate both the elastic properties and the nonlinear responses of the test structure. These preliminary analyses provided directions for more complex nonlinear analyses. The latter include a nonlinear 2D FE analysis and a nonlinear 3D FE analysis as presented in Chapter 11, and a simplified pushover analysis method as presented in Chapter 12.

As an application of this research, the proposed changes to the FEMA 356 pre-standard procedure, based on the experimental, theoretical and numerical investigations, are discussed in Chapter 13. The conclusions of the research are summarized in Chapter 14.

CHAPTER 2

LITERATURE REVIEW

2.1. GENERAL

A typical URM building under earthquake excitation is shown in Figure 2.1. To simplify the problem, earthquake excitation is assumed parallel to one pair of masonry walls. These walls are called the in-plane walls. The masonry walls perpendicular to the seismic excitation direction are called the out-of-plane walls. The in-plane walls and out-of-plane walls, together with the flexible floor and roof diaphragms, comprise a typical URM building. Many research projects have been conducted on the properties of the three basic components and the overall URM building. Section 2.3 gives a brief introduction on the properties of masonry materials. Sections 2.4 to 2.6 discuss research for the three basic components of a URM building. Section 2.7 emphasizes previous research on entire URM buildings.

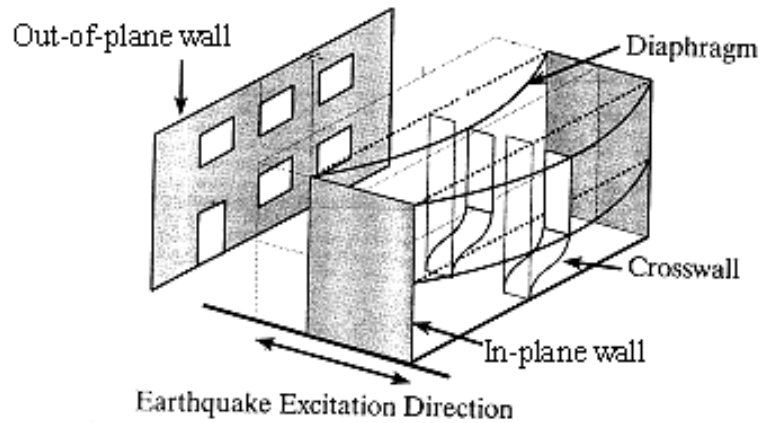


Figure 2.1. Typical URM building under earthquake excitation (Modified from Figure 2 of Bruneau 1994a)

2.2. MASONRY MATERIAL

A close-up view of a typical masonry pier is shown in Figure 2.2. Masonry is a composite construction material consisting of masonry units and mortars built following certain pattern. The mechanical properties of masonry vary considerably due to variable material properties of units and mortars. For example, mortar is typically composed of cement, lime, sand and enough water to produce a plastic, workable mixture. Several different types of mortars have been widely used in the construction, as shown in Table 2.1 (ASTM 1958).

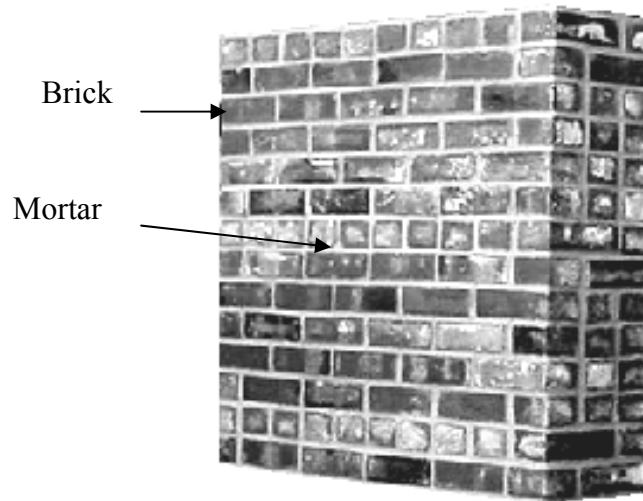


Figure 2.2 . Typical masonry pier

Table 2.1. Mortar compositions by volumes

Type	Ratio (cement: lime: sand)	Compressive strength (psi)
M	1:0:3	2500
S	0.5-1 :0.25-0.5: 4.5	1800
N	1: 0.5-1.25: 6	750
O	1: 2: 9	350
K*	0.5: 2: 7.5	75

* No longer used for construction after 1960's

Brick, concrete masonry units, clay tile, and stone have all been used for the masonry units in previous practice. Brick masonry is the focus of this research, because it makes up majority of the existing URM buildings. The strengths of brick masonry unit vary significantly, as shown in Table 2.2 (ASTM 1992).

Table 2.2. Masonry unit strengths

Designation	Minimum compressive strength (brick flatwise), gross area (psi)	
	Average of 5 brick	Individual
Grade SW	3000	2500
Grade MW	2500	2200
Grade NW	1500	1250

The mechanical properties of masonry as a composite material are functions primarily of the mechanical properties of the individual masonry units, mortars, and the bond characteristics between units and mortar. Strictly speaking, URM construction results in an anisotropic material. However, for a simplified design approach, the elastic properties of URM materials are usually considered as isotropic. These elastic, isotropic properties are taken as those determined from tests on masonry prisms perpendicular to the bed joints. The elastic modulus of masonry is controlled by the combined elastic modulus of masonry units and mortar (Hamid et al. 1987). Previous research indicates a large scatter in the measured elastic modulus of masonry, with the reported values ranging from 500 ksi to 2000 ksi (Sinha 1978, Magenes and Calvi 1992, Calvi et al. 1996). Two reasons explain the large scatter. First, the material properties of masonry units and mortar vary significantly by themselves. Second, different workmanship factors may contribute to the variation as well. The European code (EC6 1995) gives the following formulae for calculating Young's modulus E and shear modulus G of masonry material for a design purpose (Tomazevic 1999):

$$E_1(f_m) = 1000 f_m, \quad G = 0.4 E \quad (2.1)$$

where f_m is the characteristic compressive strength of masonry. Some other researchers recognized that masonry is actually a nonlinear material and thus its elastic modulus

varies with different stress level (Naraine and Sinha 1989, AlShebani and Sinha 1999). These models will be discussed in more detail in Chapter 4.

The nonlinear properties of masonry, such as ultimate strength and ductility, are also direction-depended. Specifically, several critical strength values, such as the compressive strength perpendicular to the bed joints, the tensile strength perpendicular to the bed joints, and the shear strength of the bed joints, are generally utilized to describe the nonlinear properties of masonry. Extensive research has been conducted on this topic. Detailed description of the research can be found in Chapter 3. A new model, which can illustrate the relationship of these critical strength values, will also be presented in Chapter 3.

2.3. URM IN-PLANE WALLS

A typical perforated in-plane wall is composed of piers between window and door openings, and spandrels above and below the openings (Figure 2.3). Most of previous research on the in-plane behavior of URM wall was concentrated on the piers, because the final collapse of a URM structure is most often due to pier failure (Calvi et al. 1995). The pier works like a column restrained by the spandrels at the top, and the ground or another spandrel at the bottom. The boundary conditions for the pier are usually modeled as either fixed-fixed or fixed-free, depending on the relative stiffness between the piers and the spandrels.

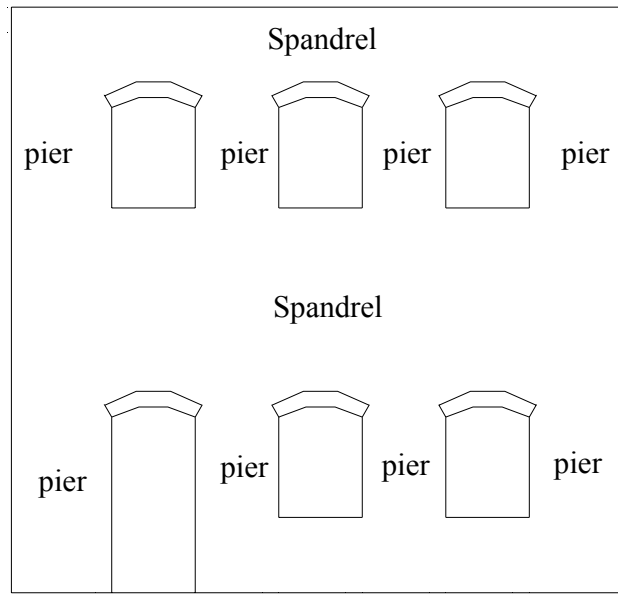


Figure 2.3. A typical perforated in-plane wall

2.3.1. In-plane URM Piers

Many experiments have been conducted to investigate the in-plane properties of URM piers (Abrams and Shah 1992, Anthoine et al. 1995, Epperson and Abrams 1989, Magenes and Calvi 1992, Manzouri et al. 1995). In-plane component tests of masonry piers are typically performed under a given constant axial load, and with the application of a monotonic or cyclic lateral force or displacement in a quasi-static fashion. FEMA 307 (ATC 1999) lists the results of some recent tests on URM piers. These tests provided data on damage progression, ultimate strength, and drift response of the piers under investigation. This resource is a good reference for detailed descriptions of the load-displacement response of URM piers under in-plane forces, and for the development of

the FEMA strength equations. Some of these experimental data will be discussed in detail in Chapter 4.

These experiments described in FEMA 307 have shown that URM piers can have considerable deformability and ductility if certain failure mechanisms prevail. Axial stress, aspect ratio, boundary conditions, and relative strength between mortar joints and units determine the failure mechanisms of masonry piers. FEMA 273 (ATC 1997) gives four typical crack patterns and failure modes for the URM piers as shown in Figure 2.4.

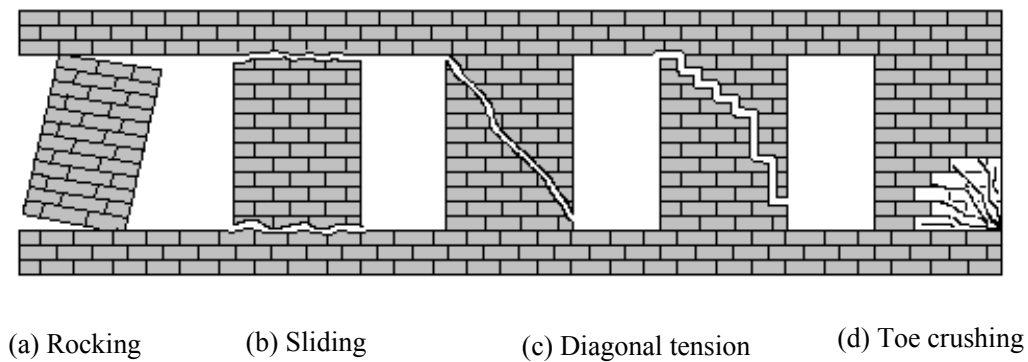


Figure 2.4. Different crack patterns for the URM piers

- A large flexural moment can cause wide flexural cracks at the top or the bottom of the pier. After that the pier may undergo rigid body rotation (rocking) about one corner of the pier (Figure 2.4a).
- When the shear force in a pier is larger than the bed joints shear strength, sliding cracks develop in the bed joints, and the wall undergoes relative sliding movement along the bed joints (Figure 2.4b).

- When the principal tensile stress due to external forces exceeds the tensile strength of masonry, diagonal tension cracks develop in the pier (Figure 2.4c). The cracks are stepped cracks propagating along the mortar bed joints and head joints in the case of strong unit-weak mortar masonry. These cracks are straight cracks and go through the units if the strength of the unit is similar to that of the mortar.
- When the principal compressive stress due to external forces exceeds the compressive strength of masonry, compressive failure develops in the pier. Since the toe of a pier is usually the zone with high concentrated compressive stress, the compressive failure always develops at the toe area (Figure 2.4d). Therefore this failure mode is also labeled as “toe crushing”.

Rocking and sliding exhibit large deformation capacities. The stepped diagonal tensile cracks propagating along the bed joints and head joints also display large deformation capacity, since the units slide between each other and lead to large energy dissipation. Conversely, the diagonal cracks going through the units make the masonry pier unstable and consequently lead to rapid strength deterioration, which represents a very brittle failure mode. Toe crushing is another brittle failure mode, because the crushing zone rapidly loses its strength. FEMA 273, 306, and 356 (ATC 1997, 1999, 2000) give equations to calculate the strength of URM piers corresponding to different failure modes. It needs to be pointed out, however, that these failure modes are not mutually exclusive. The failure of an in-plane masonry pier is often a combination of these modes. Based on the above considerations, FEMA 306 (ATC 1999) gives 7

different failure modes to describe possible single or combined failure modes of URM piers under different loading conditions. These failure modes are:

- URM2A: Wall-pier rocking
- URM2B: Bed-joint sliding
- URM2K: Preemptive diagonal tension
- URM2L: Preemptive toe crushing
- URM1H: Flexural cracking/Toe crushing
- URM1F: Flexural cracking/Toe crushing/ Bed joint sliding
- URM2G: Flexural cracking/diagonal tension

Detailed descriptions of these failure modes can be found in FEMA 306 (ATC 1999).

The elastic stiffness of masonry piers can be calculated based on classical elastic theory considering flexural and shear deformation as follows (FEMA 274, ATC 1997):

$$K_e = Gt \frac{L}{1.2h \left[1 + \alpha \left(\frac{G}{E} \right) \left(\frac{h}{L} \right)^2 \right]} \quad (2.1)$$

where t is the thickness of pier; h is the height of pier; L is the length of pier, and α is a coefficient determining the position of the inflection point along the height of pier (α is equal to 0.83 in the case of fixed-fixed wall, and 3.33 in the case of a cantilever wall).

Based on the test data collected by FEMA 307 (ATC 1999), the deformation capacity corresponding to each failure mechanism can be estimated as in Table 2.3.

Table 2.3. Ultimate drift of URM pier corresponding to different failure modes

Failure mode	Ultimate drift (%)	References
Rocking	0.6% to 1.3%	Anthoine (1995), Magenes & Calvi (1995), Costley & Abrams (1996)
Bed-joint sliding	0.6% to 2.4%	Magenes & Calvi (1995), Abrams & Shah (1992)
Rocking/Toe Crushing	0.8%	Abrams & Shah (1992)
Flexural Cracking/Toe Crushing/Bed-joint Sliding	0.8% to 1.3%	Manzouri et al (1995)
Flexural Cracking/Diagonal tension	0.5% to 0.8%	Anthoine (1995), Magenes & Calvi (1992), Magenes & Calvi (1995)
Flexural Cracking/Toe crushing	0.2% to 0.4%	Abrams & Shah (1992), Epperson and Abrams (1989)

The table clearly shows that the type of failure mode determines the deformation capacity of URM piers. For example, if rocking or sliding occurs before the URM pier fails in diagonal tension or toe crushing, the ultimate drift capacity is rather large, around 1% to 2%. In contrast, if the pier fails in diagonal tension or toe crushing without rocking or sliding preceding them, the ultimate drift capacity of pier is rather small, around 0.5%.

FEMA 306 (ATC 1999) utilizes a series of empirical formulae to identify the mixed failure modes of a URM pier. However, the rationale behind these formulae is not provided. A method based on the mechanical mechanism of a URM pier will be presented in Chapter 4 to describe its mixed failure mode.

2.3.2. URM Spandrels

Not much research has been conducted on the behavior of URM spandrels. The behavior of a spandrel is very different from that of a pier. One of the primary reasons is that the loading conditions of a spandrel are different from that of a pier. For example, the axial force in a spandrel is very small compared with that of a pier. To simplify the design, some researchers have assumed that the spandrel is always elastic and free of damage (Boussabah 1992). On the other hand, field studies and experimental research show that cracks can develop in the spandrel (Figure 2.5). These cracks will influence the behavior of the URM piers, and that of overall URM structure.

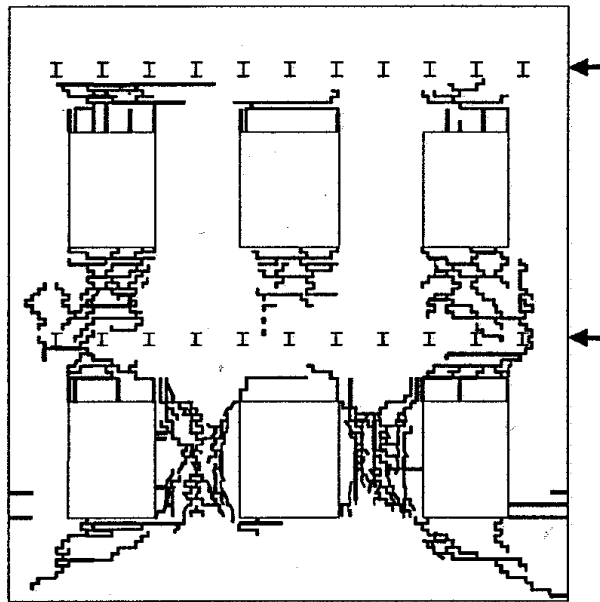


Figure 2.5. Crack observed in the spandrel of Wall B (Magenes et al. 1995)

FEMA 306 (ATC 1999) distinguishes between two different failure modes of spandrels, which are spandrel joint sliding (URM3D) and spandrel unit cracking (URM3I). Formulae are provided in the report to calculate the strength of spandrel corresponding to different failure mechanisms. However, no reference, or justification, or supporting experimental data is provided for the formulas. Further detailed discussions on the possible failure mechanisms of spandrel will be given in Chapter 11.

2.4. URM OUT-OF-PLANE WALL

The out-of-plane wall works like a thin plate supported on the edges adjacent to the in-plane walls, the connections with the roof and floor systems, and the ground acting as the boundary elements. During an earthquake, the out-of-plane wall vibrates under the seismic force induced by its own mass and the forces transferred from roof, floor and in-plane walls. The vibration and the associated bending deformation may lead to the cracking and out-of-plane collapse of the wall. Many experiments, including both dynamic and static tests, have been carried out to assess the out-of-plane behavior of masonry walls (ABK 1981a, out-of-plane, Prawel and Lee 1990b, Bariola et al. 1990, ST10 2000, Drysdale 1988, Zhang et al. 2001). These experiments verified that out-of-plane seismic dynamic stability is one of the most important problems for out-of-plane walls (Boussabah 1992). When not properly connected to roof, floor and in-plane walls, the out-of-plane masonry wall can easily become unstable and collapse under out-of-plane vibrations, as has been observed in the case of many old masonry buildings during earthquakes (Bruneau 1994b). On the other hand, if the supports of the out-of-plane wall, especially the connections between the wall and the floor and roof diaphragms, have

sufficient strength, the supports transform the out-of-plane behavior of the URM wall from an unrestrained cantilever beam to a series of one-story-high panels dynamically excited at each end of floor diaphragms. As a result the URM wall can resist more severe earthquakes than predicted by traditional static analysis methods (Bruneau 1994, Boussabah 1992). After cracking, each portion of this properly supported wall behaves as a rigid-body member rocking on the wall's through-cracks. If the gravity forces of the wall are sufficient to prevent overturning of these individual bodies through the entire earthquake, a condition of dynamic stability of the out-of-plane walls exists. Detailed literature review of past experimental and analytical research on URM out-of-plane wall can be found in the intermediate ST-11 report (Yi et al. 2002).

Another important role an out-of-plane wall plays in a URM building is its influence on the response of in-plane walls. The existing of out-of-plane walls may increase the stiffness and the strength of in-plane walls. This effect is well known as "flange effects". However, not much research has been conducted on this topic. A theoretical investigation on the flange effects will be given in Chapter 5. Results of experimental research on this topic will be presented in Chapters 8 and 9.

2.5. FLEXIBLE FLOOR AND ROOF DIAPHRAGMS

A wood diaphragm is an assemblage that typically includes three elements: sheathing, joists and blocks. Some experimental research has been conducted on flexible wood diaphragm (APA 1985, 1986, Contryman 1952, 1955, Tissell 1967, Jonhson 1956, ABK 1981a, Zagajeski 1984, Peralta et al. 2000). MAEC Project ST-8 report (Peralta et al. 2000) gives a detailed review of those tests. These experiments revealed that the wood

diaphragm exhibits some distinct characteristics that have significant effects on the behavior of a URM building.

First, instead of acting as a hinge support to the out-of-plane wall, as is the case for a rigid diaphragm, the flexibility of a wood diaphragm makes its support to the out-of-plane masonry walls a spring support. The interaction between the flexible wood diaphragm and the out-of-plane walls will affect the response of the out-of-plane wall. If the diaphragm is not properly connected to the masonry wall, the diaphragm may pound the URM out-of-plane wall during an earthquake, and make the wall develop out-of-plane cracks (Bruneau 1994b).

Second, a wood diaphragm has large deformation capacity and high strength relative to its mass. The failure of a wood diaphragm itself has rarely been observed in previous earthquakes. Instead, several other failure mechanisms dominate the failure of a wood diaphragm. For example, lack of connections or weak connections unrelated to seismic concerns (star anchors and government anchors for example) between the diaphragm and the masonry walls in existing URM buildings usually play an important role in the nonlinear behavior of diaphragm. Moreover, when the masonry walls vibrate in the out-of-plane direction and tend to separate from the roof or floor diaphragm under seismic excitation, the diaphragm may slip off its supports and collapse if the diaphragm is not or inadequately connected to the masonry walls (Bruneau 1994b).

Third, while the flexibility of a wood diaphragm produces an amplification of up to 3 or 4 times the input acceleration in the elastic range, the wood diaphragm may have a highly nonlinear hysteretic behavior when the peak ground acceleration is high. This has

a positive effect on reducing the diaphragms' peak accelerations and velocities (Bruneau 1994b).

Previous experimental research on flexible diaphragm mainly focused on the linear and nonlinear properties of flexible diaphragm itself. However, the contribution of flexible diaphragm to the response of the entire URM building comes from the interaction between flexible diaphragm and masonry walls. This interaction is governed by not only the stiffness of the flexible diaphragm and masonry walls, but also the strength and stiffness of the connections between these two components. This topic will be addressed in Chapter 7.

2.6. EXPERIMENTAL AND ANALYTICAL RESEARCH FOR URM BUILDINGS

The interactions between the three basic components: the in-plane walls, the out-of-plane walls, and the roof and floor diaphragms, determine the behavior of a URM building. Under a seismic excitation, the in-plane walls are generally excited with little amplification because of their large stiffness and low natural period. In contrast, the out-of-plane walls are excited with rather large amplification, due to their relative low stiffness and high natural period. The floor and roof diaphragms are excited through the connections between the walls and the diaphragms, and usually exhibit large amplification. However, the low mass of the diaphragms means that the acceleration of the floor or roof system results in relatively small forces compared to those developed in the walls.

Post-earthquake investigations and experimental research have showed that the typical failure modes of a URM building can be grouped into the following categories (Deppe 1988, Boussabah 1992, Bruneau 1994a, 1994b, 1995, Tomazevic 1999, Peralta et al. 2000):

- Lack of anchorage between masonry walls and diaphragms
- Anchor failure
- Out-of-plane failures of masonry walls
- In-plane failures of URM walls
- Combined in-plane and out-of-plane failures, including cracks at the wall intersections
- Diaphragm related failures

Of the different failure modes discussed above, the potential out-of-plane failure of URM elements, including out-of-plane structural walls and other non-structural components, constitutes the most serious life-safety hazard for this type of construction. However, this type of failure can be prevented by properly anchoring the masonry walls to the floor and roof system. In this case, the in-plane failure of URM walls is the dominating failure mode for the URM building, which is the main research focus of this Ph.D. work.

2.6.1. Experimental research on URM structures

Reduced-scale dynamic tests (Clough et al. 1979, Gulkan et al. 1979, 1990, Tomazevic 1990, 1993, Costley and Abrams 1996), pseudo-dynamic tests (Paquette and

Bruneau, 2000 and 2003), and large-scale quasi-static tests (Magenes et al. 1995) have been conducted on URM structures.

The first dynamic tests on a URM structure were conducted by Clough et al. (1979). Four one-story masonry houses, with both unreinforced and partially reinforced masonry wall panels, were tested on a shake table. The objectives of this experiment were to determine the maximum earthquake intensity that could be resisted by a typical URM house, and to evaluate the additional resistance that would be provided to the structure by partial reinforcement.

In this test, the masonry units, the size of the wall components, and the roof-to-wall connections were full-scale to represent the behavior of a real masonry building. On the other hand, the plan areas of the building were one-ninth those of a reasonable prototype due to the capacity of the shake table. To represent the realistic gravity stresses in the masonry pier, weights were added at the roof level. The first specimen was designed with a panel in the middle of each four sides, and with a corner component located at each corner (Figure 2.6). The other three specimens were designed with four perforated walls and no direct connections between adjacent wall panels (Figure 2.7). All four specimens were made from standard two-core hollow concrete block or two-core hollow clay brick and type S mortar. A typical timber truss roof system was used for all the four specimens.

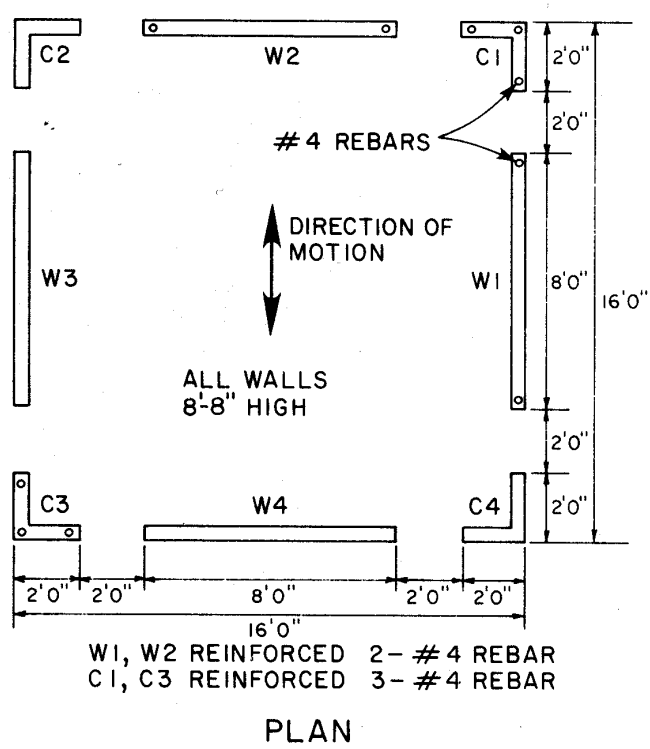


Figure 2.6. Specimen House 1 in Clough's test (Clough et al. 1979)

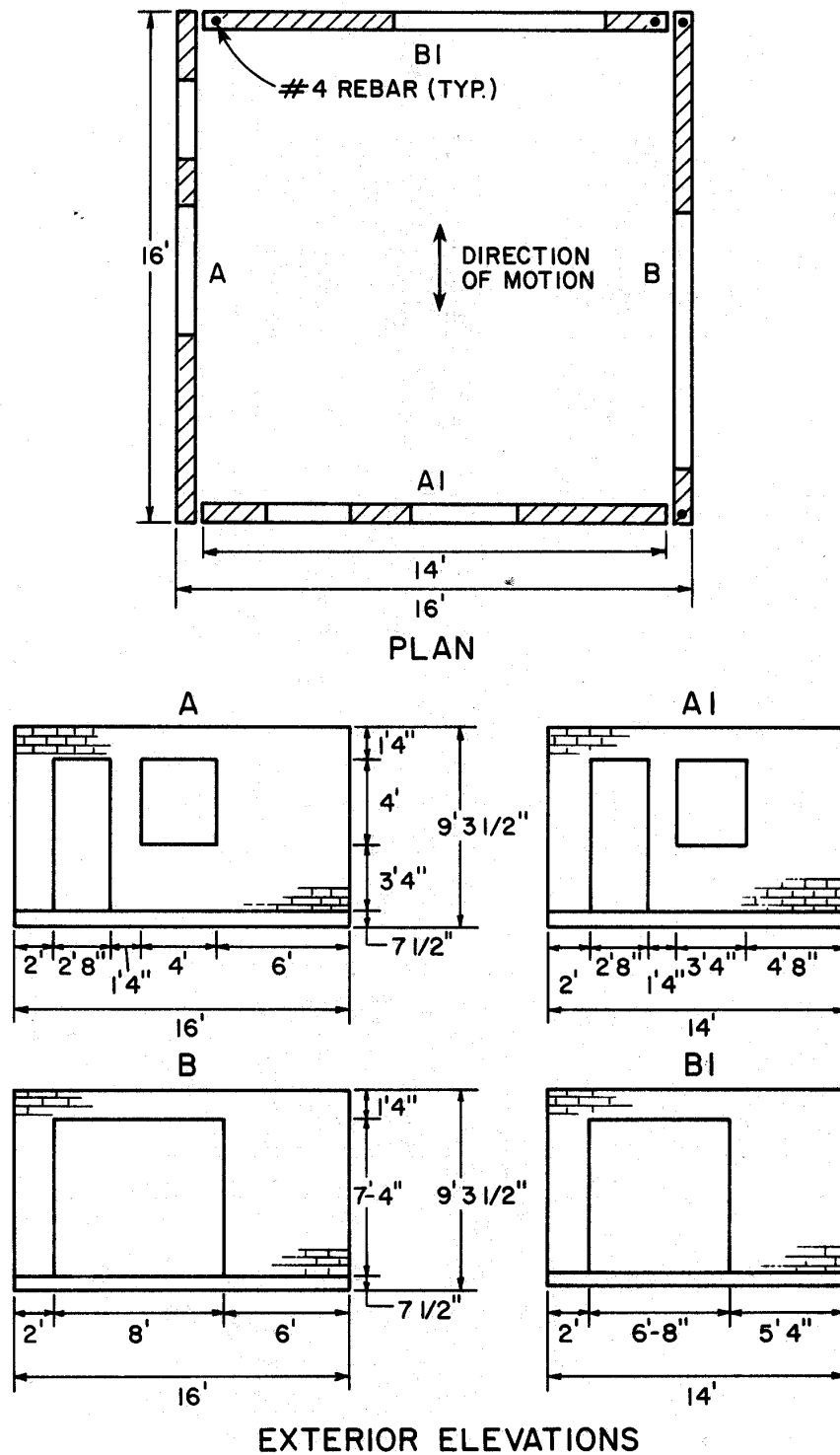


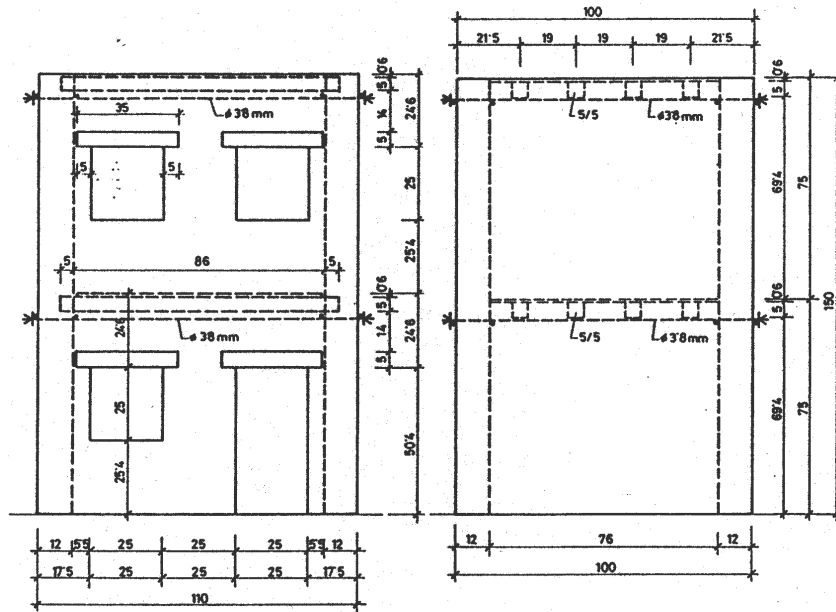
Figure 2.7. Specimen House 2 in Clough's test (Clough et al. 1979)

The following phenomena were observed in these tests (Clough et al. 1979):

- Since the stiffness of the in-plane walls were much larger than that of the out-of-plane walls, the in-plane walls resisted the majority of the seismic forces.
- The masonry structure was so stiff that the motions of the test structures followed the shake table motions very closely, with the deformation of the structure generally being proportional to, and in phase with the base accelerations. The amplification of ground motion due to the flexibility of structure was rather small. As a result, the peak acceleration, instead of the frequency characteristics, was a major factor to be considered when assessing the damage of a URM building.
- If one in-plane wall was stiffer than the other, the two in-plane walls might develop different lateral displacements under lateral earthquake excitation, with a resulting tendency to cause rotation of the roof. If the roof had sufficient membrane rigidity, it would rotate as a rigid unit, and consequently induced out-of-plane deformations in the in-plane walls, and in-plane deformations in the out-of-plane walls. However, if the stiffness of the roof diaphragm was much smaller than that of the masonry walls, the masonry walls would resist this tendency and forced the roof to develop shear distortions to accommodate the unequal displacements at the top of the in-plane walls.

Based on the prototypes of old urban masonry residential houses in the earthquake-prone areas of central Europe and Mediterranean, four 1:4 scale simplified two-story URM models were constructed and tested in a one-degree vibration shake table by Tomazevic et al. (1993). The URM structures were composed of stone and cement mortar (cement: lime: sand in the proportion of 0.5:4:12). The structural configurations of

the masonry walls in all the four models were identical: the in-plane walls oriented in the direction of the shake table motion were solid loading-bearing walls, while the out-of-plane walls were perforated walls with window and door openings (Figure 2.8). The diaphragms were different for the four models (Figure 2.9). Model A had wooden floors made of freely supported wood joists without steel ties. The diaphragms of Model C were identical to those of Model A, except that the masonry walls were tied with steel ties at the floor and roof levels. The diaphragms of Model D were similar to those of Model C, except that a brick vault replaced the wooden roof. The diaphragms in Model B consisted of RC slabs with bond-beams along the walls.



(a) Out-of-plane wall

(b) In-plane wall

Figure 2.8. Layout and dimensions of the tested models (units in cm) (Tomazevic et al. 1993)

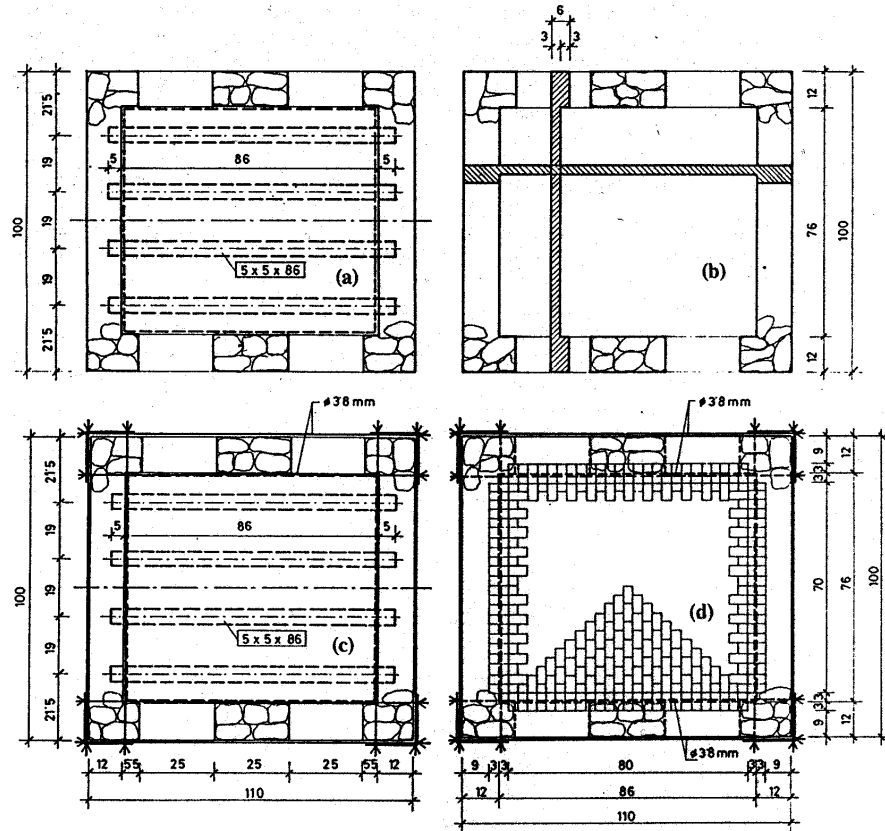


Figure 2.9. Floor and Roof systems of the tested models (units in cm) (Tomazevic et al. 1993)

The behavior of Model A was as follows. At the beginning of the test, rocking was observed along the cracks at the joints between the walls and the foundation slab. With increasing ground motion, more and more horizontal and diagonal cracks developed in the first floor walls. After that, the walls in the second story disintegrated, and all the upper corner walls separated. Vertical cracks and horizontal cracks were also observed in the second-story out-of-plane walls. Masonry units began to fall off. Meanwhile, the cracks in the first floor continued to propagate. The test was stopped when one of the corner walls at the second floor collapsed.

The behavior of Models B, C, and D were similar. All of them collapsed because of the severe damage developed in the walls in the first story, whereas no significant damages to the second story walls were observed. At the beginning of the test, the models were observed rocking and vibrating along the crack at the joints between the walls and the foundation slab. Then horizontal cracks developed all around the models just below the floor diaphragm. With increasing ground motion, the damage accumulated in the first floor walls, while the second story walls vibrated like a monolithic box placed on the top of the first floor walls with little damage. Finally, severe diagonal cracks developed in the first-story in-plane walls. Also, vertical cracks developed at the corners of the first-story in-plane walls because of the sliding and rocking of the upper second-story box.

The lateral deformation shapes were also obtained in this experiment. Figure 2.10 shows the distribution of the displacements at three locations along the roof. The displacements of the in-plane walls and the out-of-plane walls were almost the same in the elastic range for the different diaphragms, possibly due to the large thickness of the masonry walls. However, with increasing ground motion, the differences between the lateral displacements of the in-plane walls and that of the out-of-plane wall increased. As observed in the experiment, there was out-of-plane failure in Model A, but not in Model B, C, and D. It indicates a rigid diaphragm or simply tying the masonry walls at the floor and roof levels can prevent the out-of-plane damage of masonry walls.

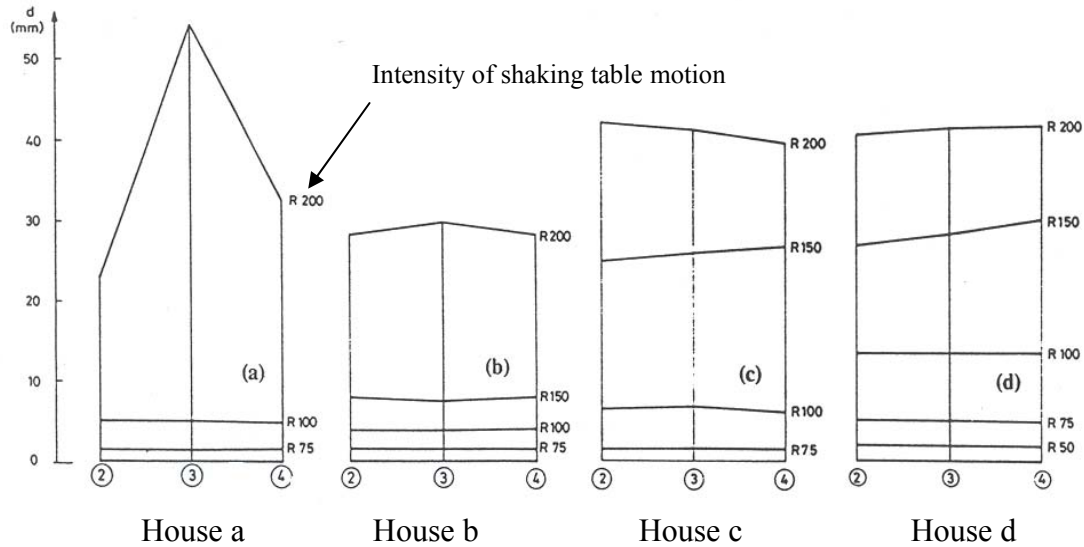


Figure 2.10. Distribution of displacements along the top floor (Tomazevic 1993)
(Locations: 2, 4 the in-plane walls, 3 center of the out-of-plane wall)

The other important conclusions also obtained from this test are (Tomazevic 1993):

- The structural characteristics of the floor and roof diaphragms and the tying of structural walls represented decisive parameters to the seismic resistance of masonry walls.
- For a URM structure without ties to prevent the separation of the walls, the out-of-plane walls cracked easily. As a result, the out-of-plane walls might collapse before severe damage developed in other parts of the structure. In addition, the failure of out-of-plane walls was easy to develop in the upper story.
- If the failure of the out-of-plane walls were prevented by a strong floor system, the damage would concentrate on the first story in-plane walls. When the upper structure rocked and slid on the top of the first floor, the corner of the first floor failed early in the tests.

More recently, two reduced-scale URM buildings were constructed and tested at the University of Illinois by Costley and Abrams (1996). The box-type structures had two perforated shear/bearing in plane walls (window wall and door wall), and two solid out-of-plane walls (Figures 2.11 and 2.12). For both test structures S1 and S2, the two out-of-plane walls and the window wall were continuous, forming a C-shape, while the door wall was separated by a full-height gap with the width of one mortar joint. A steel diaphragm with attached additional weights was used to represent the flexible wood diaphragm. The diaphragm was simply supported on the in-plane walls through special details so that it could transfer the shear forces as well as the vertical forces. The floor system was also tied to the out-of-plane walls by rods and nuts. Only the first building S1 is discussed here, since the second building was rebuilt from the first one and exhibited similar behavior.

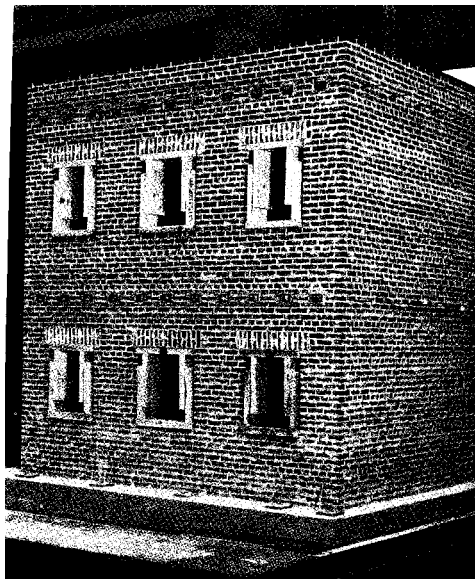
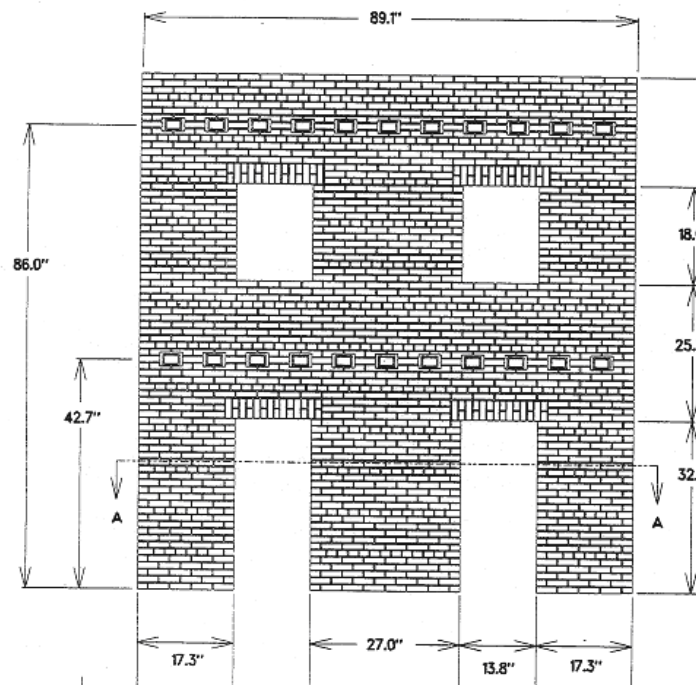
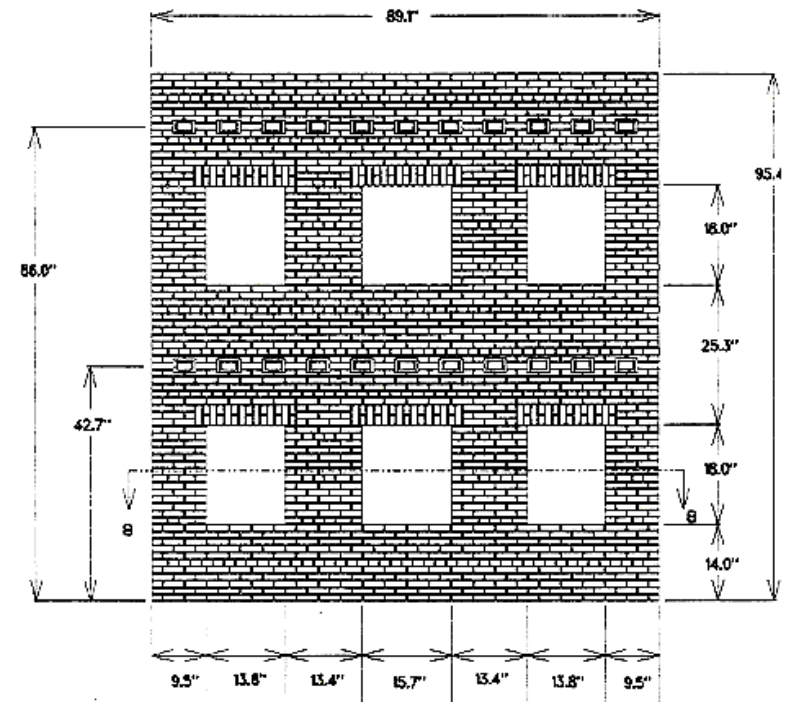


Figure 2.11. Window wall and out-of-plane wall of the tested structure S1 (Costley and Abrams 1996)



(a) Door wall



(b) Window wall

Figure 2.12. Configuration of perforated in-plane walls (Costley and Abrams 1996)

The first cracks observed in this building were the debonding cracks between two out-of-plane walls and the concrete foundation. With increasing base acceleration, more and more cracks developed in both the in-plane walls and the out-of-plane walls. In the door wall, the outside piers rocked, and the central pier slid. In the window wall, some cracks were observed initiating from the corner of the window opening, and propagating as diagonal cracks into the piers. The entire top portion of this test structure appeared to be fixed in space as the first-story walls moved back and forth below with the base excitation.

As expected for a flexible diaphragm system, little coupling was observed between the parallel shear walls. Individual walls vibrated independently of each other with no torsion induced by the diaphragm. In some cases, the deflection of the door wall was two times larger than that of the window wall. The acceleration ratios for the model structure were also interesting. Prior to cracking, both the ratio between the wall acceleration and the base acceleration and the ratio between the diaphragm acceleration and the wall acceleration were appreciable, on the order of 1.2-1.7 and 1.7-2.5, respectively. After substantial cracks developed in the walls, both of the two ratios decreased to almost 1:1, which means little amplitude existed.

The test also showed that the equivalent roof level seismic force was almost the same as that at the floor level. For the structure in elastic range, the phenomenon could be explained by the fact that the masonry walls might be very stiff. After cracks developed in the structure, these results might also be expected since the upper portion (including both diaphragms) of the structure remained intact and moved as a rigid body on the top of the first floor.

Compared to the reduced-scale dynamic experiments, full-scale tests of URM structures are seldom conducted due to the cost and test capacity demands. Recently, a research program was conducted at the University of Ottawa to investigate the flexible-floor-rigid wall interaction in old URM buildings (Paquette and Bruneau, 2002). A test of a single-story full-scale URM building was conducted. This building was composed of two symmetric perforated in-plane walls and two solid out-of-plane walls, which were constructed from solid bricks and Type O mortar (Figure 2.13). The two out-of-plane walls and the east in-plane wall were continuous, forming a C-shape, while the west in-plane wall was separated from the out-of-plane walls by a gap. This was used to investigate the effect of out-of-plane walls on the in-plane walls. The flexible diaphragm of this building was constructed with wood joists and covered with diagonal boards with a straight board overlay. The diaphragm was also anchored to the wall with through-wall bolts in accordance with UCBC (ICBO, 1997). The building was tested in a pseudo-dynamic fashion by using one actuator to apply pseudo-dynamic force at the center of the diaphragm. One interesting finding in this test is that during the initial low intensity seismic motion, different stiffness for the east and west walls were observed. However, after the cracks fully developed in the building, the hysteretic curves for these two shear walls during a higher intensity seismic motion became very similar. This suggests that the effect of continuous or discontinuous corners becomes less significant during high intensity seismic motion.



Figure 2.13. Tested single-story URM building (Paquette and Bruneau 2002)

Another full-scale test of URM structure was conducted by Magenes et al. (1995) in Italy. The specimen tested in their experiment was a replica of the reduced-scale dynamic specimen tested by Costley and Abrams (1996). The geometry of the large-scale static (LS) test structure was almost identical to that of the reduced-scale dynamic (RD) specimen. The floor and roof systems of the LS specimen were the same as those used in the RD specimen, consisting of 11 isolated steel beams directly embedded into the masonry walls. However, different materials were used in the two tests. Clay brick and Type O mortar were used for the RD model, while clay brick and lime mortar were used for the LS structure. Furthermore, the gravity stresses in the first floor piers of the LS structure were 60 to 70 psi, which were larger than the gravity stresses of 33 to 48 psi in the first floor piers of the RD model.

The lateral loads were applied to the in-plane walls of the LS specimen under displacement control. The roof drifts of the two in-plane walls were controlled and were set equal to each other. The displacement at the floor level of each wall was controlled such that the applied force at the floor level was equal to that at the roof level. The equal roof and floor forces loading scheme was based on the test results of the RD test.

Some interesting results can be obtained by comparing the different failure modes observed for the two test specimens. The final crack pattern for the RD specimen S1 is shown in Figure 2.14. The out-of-plane walls cracked prior to the in-plane walls. Cracks in the out-of-plane walls were mainly horizontal, which means that the out-of-plane walls worked more like the flange of the in-plane walls. All the cracks in the in-plane walls concentrated on the first floor. Flexural horizontal cracks developed at the bottom and top of each pier. Some cracks also developed in the portion below the window opening in the window wall. On the other hand, no diagonal cracks were observed in the piers, and no cracks were observed in the spandrel. The final crack pattern for the LS specimen is shown in Figure 2.15. The crack pattern of the out-of-plane walls was similar to that of the RD specimen. However, the crack pattern of the in-plane walls was different from that of RD specimen. Initially, cracking was limited to the spandrels between the openings in both the two in-plane walls. As cracks developed in the spandrels, the coupling between masonry piers decreased. Eventually, the cracks in the spandrels ceased to propagate further, and more and more cracks were observed in the piers. At the maximum drift level, the failures of all the first floor piers in the door wall were dominated by shear. On the other hand, although the central first-story pier of the window wall failed in shear cracks, its two exterior first-story piers rocked.

Both the RD test and the LS test showed that the damage of the first floor was much severe than that of the second floor, and that the damage of the in-plane walls was much severe than that of the out-of-plane walls. The two in-plane walls worked as two separate walls, because the flexible floor and roof diaphragms could not provide much coupling between the parallel masonry walls. However, significant differences existed between the two specimens, which can be summarized as follows:

- The damage of the LS specimen was much extensive and severe than that of the RD specimen.
- The failures of the first floor piers of the LS specimen were dominated by diagonal cracks, which were not observed in the RD specimen.
- The spandrel of LS specimen, especially the area right above the first-story opening, showed extensive damage, which was not observed in the RD specimen.
- The out-of-plane walls in the LS specimen worked more like the flanges of in-plane walls, since the external force was transmitted to them through in-plane walls. This was different from the RD specimen, where the out-of-plane walls had to resist their own inertia force.

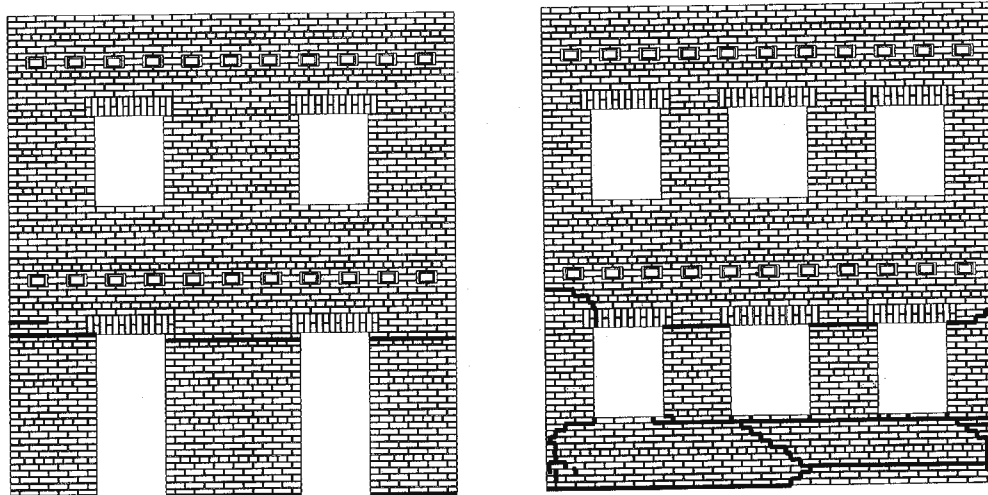
Significant differences for the lateral drifts between the RD specimen and the LS specimen were also observed. Although the story drifts associated with the initiation of cracking for both the RD specimen and the LS specimen were approximately 0.1%, the drifts associated with the nonlinear behavior were different for the two specimens. The maximum lateral force of the LS structure was initially achieved at a drift of approximately 0.2%, and the static test was terminated when significant damage developed at a maximum drift of approximately 0.4%. As a comparison, the RD structure

reached its maximum lateral strength at a first floor drift of approximately 0.5%, and the test was terminated with a maximum first floor drift of approximately 1.0%.

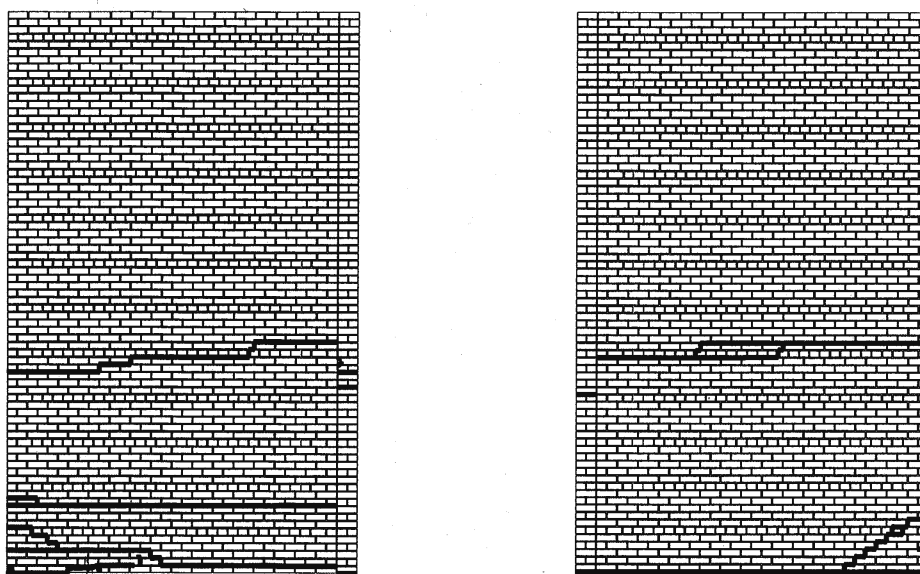
The different behaviors observed for the RD test and the LS test are probably due to the following reasons:

- The different materials and gravity stresses used in the two structures may lead to different failure modes in the pier.
- The concentrated lateral forces applied in the LS test will cause different force distributions in the masonry walls compared with that induced by the relatively uniform lateral inertia forces in the RD test, and consequently lead to different failure modes.
- The LS test allows more time for the cracks to propagate. As a result, the damage of the LS specimen is more severe than that of the RD specimen.

Another important phenomenon observed in the LS test but not in the RD test is the different directions of diagonal cracks in the first floor piers of the door wall (see Figure 2.5). The diagonal cracks in the central pier propagate in two opposite directions and exhibited an X configuration. Conversely, the diagonal cracks in the two exterior piers propagated only in one direction, parallel to the large compressive force induced by the external overturning moment. This indicates that the overturning moment has significant influence on the nonlinear behavior of URM walls. More detailed discussion on the effects of external overturning moment will be found in Chapters 8 and 9.



(a) In-plane wall



(b) out-of-plane wall

Figure 2.14. Final crack pattern in the dynamical tested specimen (Costley and Abrams 1996)

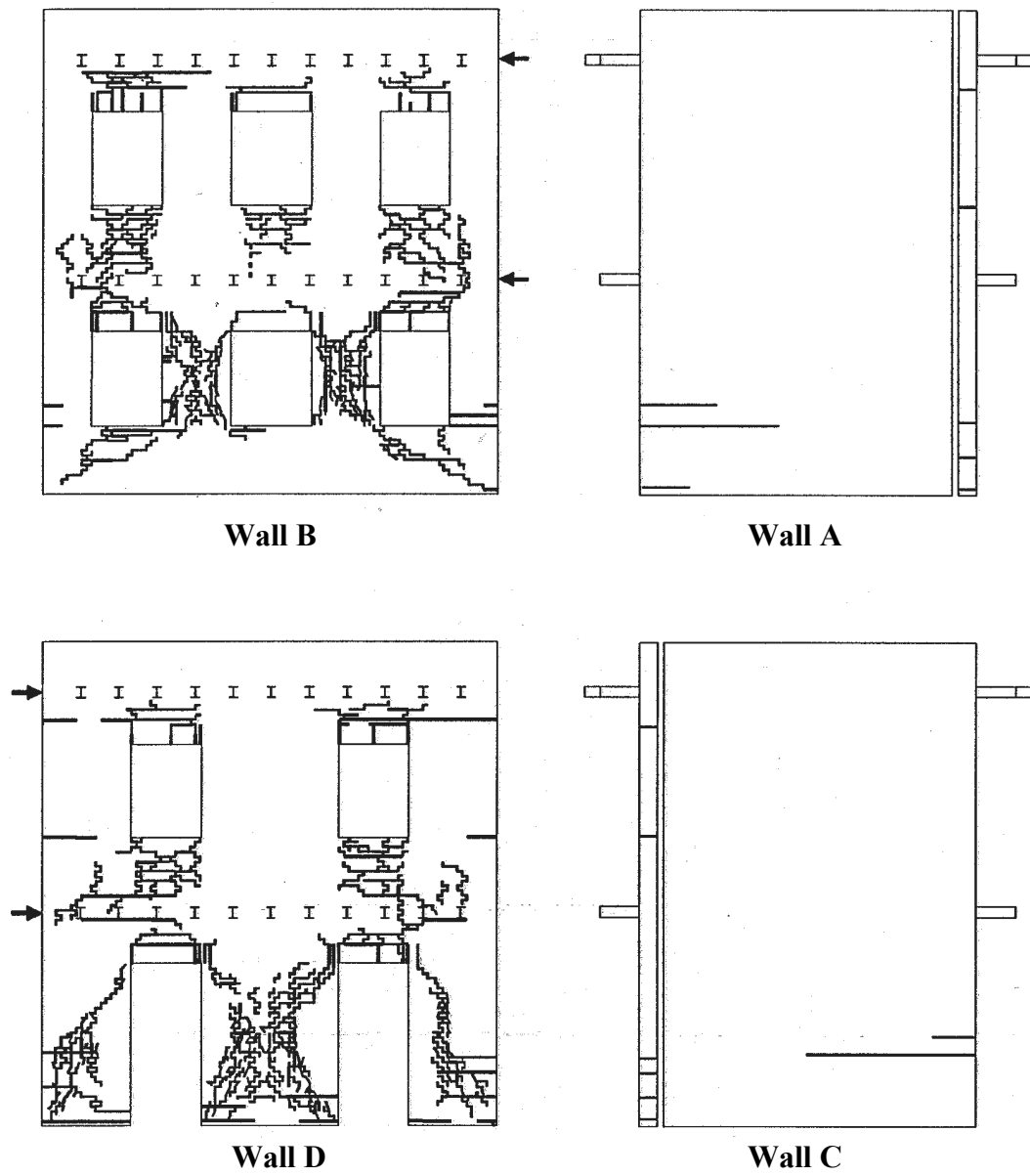


Figure 2.15. Final crack pattern in static tested specimen (Magenes et al. 1995)

2.6.2. Analytical research on URM structures

Associated with the experimental research described above and elsewhere, extensive analytical research has also been conducted to predict the nonlinear response of URM structures. The analysis of URM structure can be divided into two categories: 1) analyses based on detailed nonlinear FE models, and 2) analyses based on simplified models.

Commonly used nonlinear FE models for URM structures can be further subdivided into discrete crack models and smeared crack models. The difference between these two types of models is the methodology to treat the opening and closing of the cracks in masonry. Further discussion of the two types of models can be found in Chapter 11.

The detailed nonlinear FE analysis methods are usually not suitable for the analysis of an entire URM structure, simply because they are too time-consuming. As an alternative, simplified methods were also widely used in previous research. The simplified methods can be further categorized into the simplified methods to model a perforated URM in-plane wall and the simplified methods to model an entire URM building. Further discussion on the two types of models can be found in Chapter 12.

2.7. SUMMARY

A general picture of the research on URM structure has been given in this chapter. Specifically, previous experimental research on the performance of entire URM structures was reviewed in detail. Previous research reveals that URM structure is a very unique structure type with its specific structural characteristics. Detailed investigation on

the nonlinear behavior of URM buildings should be conducted at three different levels - the material level, the component level, and the structure level, which will be discussed in the subsequent chapters.

CHAPTER 3

MECHANICAL KEY MODEL FOR THE FAILURE CRITERIA OF MASONRY

3.1. INTRODUCTION

Masonry, a composite material made up of masonry units and mortar, exhibits distinct directional properties because of the influence of mortar joints. In the case of strong unit-weak mortar masonry, this phenomenon is more significant because the mortar joints act as planes of weakness. For example, depending on the orientation of the joints to the applied stresses, cracks can occur in the joints alone, or in some form of combined mechanism involving both the mortar and the masonry unit. Therefore, the material properties of masonry under in-plane loads, such as the failure modes and the ultimate strength, are determined by not only the principal stresses σ_1 and σ_2 , but also their respective orientations to the bed joint, θ and $\theta+90$ (Page et al. 1982).

The most complete set of experimental data for masonry subjected to proportional biaxial loading were provided by Page (1981, 1983). These tests verified that both the orientation of the principal stresses with regard to the bed joints and the principal stress ratio influence the failure mode and strength. The biaxial strengths obtained in these tests on half-scale solid clay units are shown in Figure 3.1. The different modes of failure are illustrated in Figure 3.2.

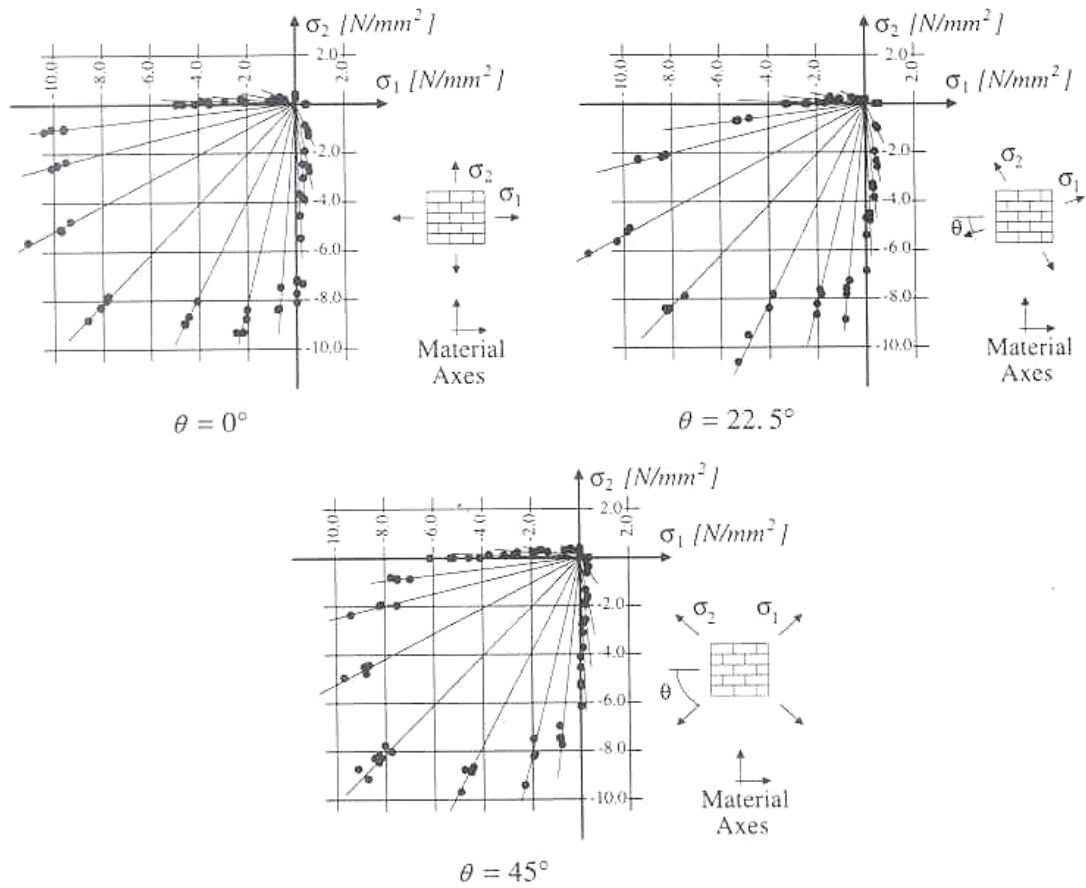


Figure 3.1. Biaxial strength of solid clay unit masonry (Page 1981, 1983)

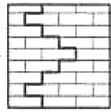
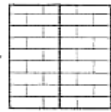
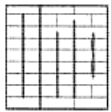
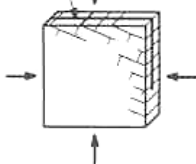

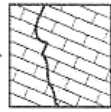

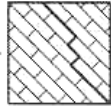
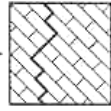

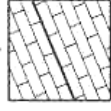



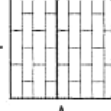
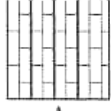
Angle θ	Uniaxial tension	Tension/compression	Uniaxial compression	Biaxial compression
0°				
22.5°				
45°				
67.5°				
90°				

Figure 3.2. Modes of failure of solid clay unit masonry under biaxial loading (Dhanasekar et al. 1985a)

The observed failure modes for the in-plane masonry are as follows. When masonry was loaded in uniaxial tension, failure occurred by cracking and sliding of the head and bed joints. When masonry was loaded in uniaxial compression, the failure mode was more sensitive to the orientation of the bed joints with respect to the applied load. For uniaxial compression parallel to the bed joint, failure occurred by splitting in the vertical head joints due to lateral spreading of the panel. For uniaxial compression

perpendicular to the bed joint, failure involved a combined mechanism with vertical cracks in both head joints and bricks. When the uniaxial compressive force was applied at an angle to the bed joints, the failure modes included possible splitting cracks in both the masonry joints and the bricks, and stair-step cracks in both the bed joints and the head joints.

When masonry was loaded in a tension-compression biaxial loading condition, failure occurred either by cracking and sliding of the joints alone or in a combined mechanism involving both units and joints. In contrast, in a biaxial compression loading condition failure typically occurred by splitting of the specimen at mid-thickness, in a plane parallel to its free surface, regardless of the orientation of the principal stresses. Meanwhile, the maximum compressive strength increased by 1.2 – 1.6 as compared with uniaxial compression.

Summarizing the above test data and others from the experiments conducted by other researchers (Johnson and Thompson (1969), Ganz and Thurlimann (1982), Samarasinghe (1980), Samarasinghe and Hendry (1982), Ganz (1985,1989), Hamid and Drysdale (1981), Tassios and Vachliotis (1989)), it was found that three fundamental failure modes exist for masonry, which are: (1) sliding of the mortar joints, (2) cracking of the bricks and splitting of the joints, and (3) splitting in the middle plane (Andreass and Ceradini 1992).

Several failure criteria have been proposed to explain the failure mechanisms of masonry under biaxial in-plane loading (Sinha and Hendry (1969), Yokel and Fattal (1976), Hegemeir et al. (1978), Hamid and Drysdale (1980, 1981), Mann and Muller (1982), Samarasinghe and Hendry (1982), Ganz and Thurlimann (1982,1984), Drysdale

and Hamid (1984), Dhanasekar et al. (1985a, 1985b), Ganz (1985, 1989), Dialer (1991), Andraus (1996)). Among them, Andraus (1996) gave the most comprehensive failure criteria. In his model, a modified Mohr-Coulomb frictional law was used to illustrate the shear strength corresponding to the sliding of the mortar joint; a maximum tensile strain criterion was used to account for the splitting of bricks or joints; and a maximum compressive stress criterion was used for the splitting in the middle plane. These criteria have been embedded into a FE analysis program to analyze the nonlinear behavior of masonry (Andraus 1996).

Although many different comprehensive failure criteria have been proposed for analyzing the nonlinear behavior of masonry and they have indeed provided much valuable insight into the properties of masonry, these approaches have always some constraints in general due to the following reasons. First, all the failure criteria utilized in previous research were originally proposed for continuous and homogeneous material. They require that the damage be uniform across the volume of material being considered. This however is not the case for URM assemblies. Instead of having relative uniform damage, URM assemblies usually exhibit concentrated damage in the form of several large cracks. As a result, several distinctive failure modes observed for masonry in the field and in the experiments, such as rocking and sliding, cannot be captured by a nonlinear FE analysis employing these uniform failure criteria. Second, the failure criteria used for masonry are usually not coded in commercial nonlinear FE analysis packages. Therefore, in order to use these failure criteria, specific FE codes need to be written, which makes the evaluation of the different criteria proposed quite difficult. Third, as for other nonlinear FE analyses, this method requires detailed knowledge of

nonlinear FE analysis, and thus is quite impractical for structural design and analysis by the majority of structural engineers.

Based on this consideration, FEMA prestandards use a different approach to illustrate the nonlinear in-plane behavior of masonry (ATC 1999). Instead of focusing on the failure of local masonry materials, FEMA prestandards took each individual masonry element, such as pier and spandrel, as the analysis subject. Several possible failure modes, which are based on the field observation, are given for each individual masonry element (ATC 1997a, 1997b, 2000). The corresponding force-displacement curve is also given for each failure mode (ATC 1999a, 1999b). Therefore, it is quite easy to utilize these failure criteria at the component level to analyze the nonlinear behavior of a masonry wall.

Associated with these failure modes, FEMA prestandards adopt several representative material properties for masonry. These representative material properties are as follows (ATC 1997a, 1997b, 1999a, 1999b, 2000):

- The bed joint tensile strength: f_t
- The diagonal tensile strength: f_t^d
- The compressive strength: f_m
- The initial bed joint shear strength: τ_o
- The shear friction coefficient for the cracked bed joint: μ_1
- The elastic modulus: E

Some of these material properties are easy to understand and identify. For example, the bed joint tensile strength, the compressive strength, and the elastic modulus have been characterized through previous research. On the other hand, although extensive

research has been conducted on masonry bed joint shear strength, this value is still unclear. In addition, no clear definition has been given for the diagonal tensile strength in the FEMA reports or elsewhere in the literature.

The component-level approach adopted by FEMA prestandards is an appropriate method for analyzing the nonlinear behavior of URM structures from the practice point of view. However, in order to use this approach the critical strength parameters discussed above need to be clarified. In this chapter, the tensile and shear properties of the interface between masonry unit and mortar will be first reexamined, as these properties are believed to be the controlling parameters required to understand the behavior of the entire masonry assembly. A mechanical key model will be proposed to illustrate the possible failure modes of the unit-mortar interface. The model will be calibrated using the results of previous tests and those conducted by the author. This model is then expanded to describe the failure modes and maximum strengths of the entire masonry assembly. Finally, as an application, the critical strength parameters adopted by FEMA and a typical material test method (the diagonal compression test) will be reexamined.

3.2. SHEAR BEHAVIOR OF MASONRY BED JOINTS

Previous experiments have shown that the failure of strong unit-weak mortar masonry is dominated by splitting or sliding of masonry joints for most loading cases expect large compressive stresses. Therefore, the tensile and shear properties of the masonry joints are the dominating characteristics for masonry. In the case of strong unit-weak mortar masonry, the tensile strength of masonry joints has usually been found to be very small, ranging in value from 0 – 60 psi.

The shear strength of masonry bed joints has been widely investigated (Atkinson et al. 1989). The test methods employed to characterize it include a prismatic masonry specimen that contains a bed joint at an angle to the applied compressive load (Figure 3.3a), a diagonal compressive specimen (Figure 3.3b), a racking test (Figure 3.3c), a 4-brick direct shear test (Figure 3.3d), and a 3-brick direct shear test (Figure 3.3e). The advantages and disadvantages of each test method were discussed in Atkinson et al. (1989). Based on previous experimental investigation and FE analysis, the 4-brick direct shear test seems to be one of the most promising test methods for measuring the shear strength of masonry bed joint, because: (1) it gives a relative uniform distributed shear stress and lateral compressive stress on the bed joints, and (2) it is quite easy to build and to test.

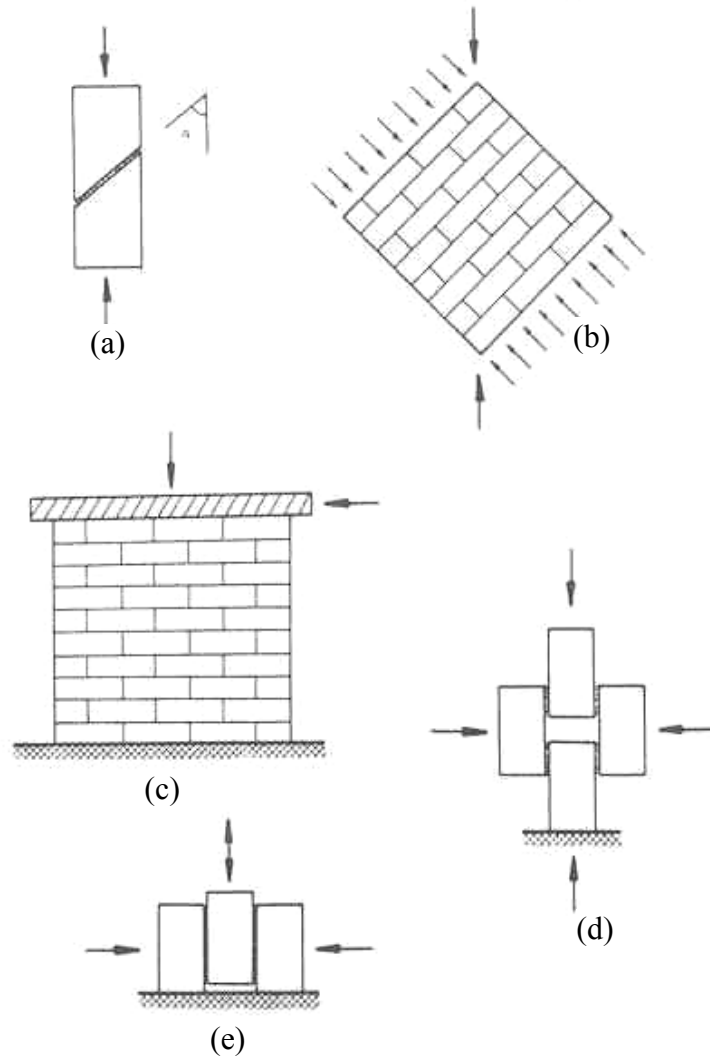


Figure 3.3. Masonry shear test configurations (Atkinson et al. 1989)

These previous investigations revealed that the failure of a bed joint is a function of applied shear force and normal force. The complete failure criterion for a masonry bed joint in terms of shear stress (τ) and normal stress (σ_n) is conceptually illustrated by Page et al. (1982) as shown in Figure 3.4. Region 1 corresponds to a large shear stress to compressive normal stress ratio, where the failure of the bed joint is dominated by shear sliding of the bed joint. Region 2 corresponds to a small shear stress to compressive

normal stress ratio, where the failure of the specimen is dominated by the compressive failure of the entire specimen.

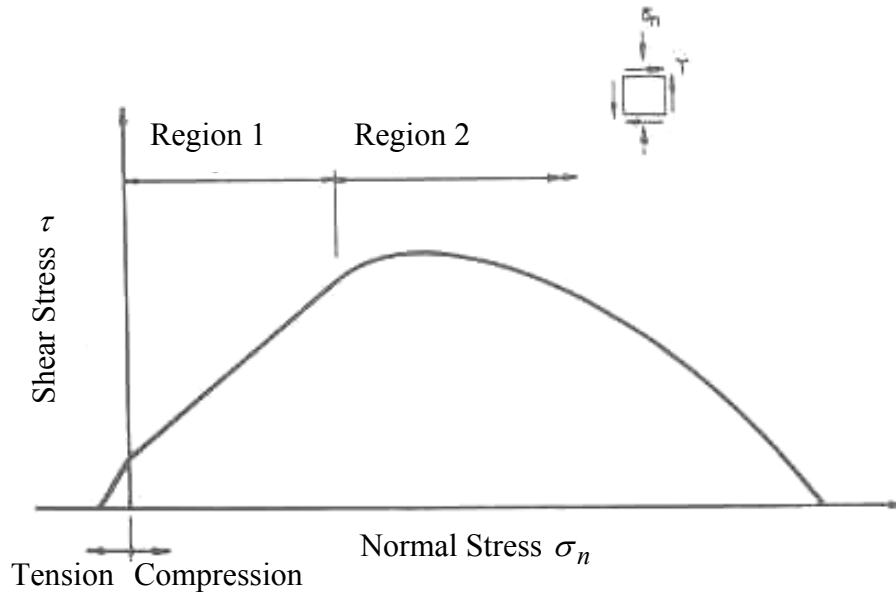


Figure 3.4. Typical failure criterion (in terms of $\tau - \sigma_n$) (Page et al. 1982)

Previous research also showed that the shear strengths of bed joints vary significantly with different masonry units and mortar materials. On the other hand, there is a relative linear relationship between the shear strength of a bed joint and the applied compressive normal stress. Most researchers attributed the increase in bed joint shear strength with an increased compression normal force to a frictional resistance at the brick-mortar interface. As a result, a Mohr-Coulomb frictional law has been widely used to illustrate the shear capacity of masonry bed joint:

$$\tau = \tau_0 + \mu\sigma \text{ (psi)} \quad (3.1)$$

where τ_0 is the shear bond strength, σ is the compressive normal stress, and μ is the internal frictional coefficient at the brick-mortar interface.

An extensive survey of the existing test data on the bed joint shear strength has been given by Atkinson et al. (1989). The test data from Atkinson and some other test data collected in the current research, is listed in Table 3.1 in terms of Eq. 3.1 Some tests measured the frictional coefficient for a cracked bed joint surface, which is also listed in the table under the column μ_1 is.

Table 3.1. Masonry bed joint shear strength

Source	Masonry Unit	Mortar	τ_0 (Psi)	μ	μ_1
Benjamin et al. (1958)	brick	Three different mortars	150	0.73	-
Pieper (In Mayes and Clough 1975)	Brick	1:2:8	29	0.84	-
Nuss et al. (1978)	Brick	1:2:9	160	0.77	-
Nuss et al. (1978)	Brick	1:0.5:4.5	686	0.75	-
Nuss et al. (1978)	Brick	1:0.25:3	705	0.76	-
Drysdale et al. (1979)	Brick	1:0.5:4	83	0.9	-
Hamid et al. (1980) ¹	brick	1:0.25:2.81	103	0.97	1.12
Hamid et al. (1980) ¹	brick	1:0.5:4.0	110	0.86	1.18
Hamid et al. (1980) ¹	brick	1:1.25:6.75	103	0.91	1.11
Hamid et al. (1979)	Concrete block	S	76	1.07	-
Hegemier et al. (1978)	Concrete block	S	36	0.89	-
Kariotis et al. (1985)	Old Brick	Sand –lime	48	1.15	-
Pook et al. (1986)	Concrete block	S	110	0.7	-
Stockl and Hofmann (1986)	Brick	1:0.68:15	138	0.7	-
Stockl and Hofmann (1986)	Brick	1:0.0:9.7	210	0.56	-
Atkinson et al. (1989)	Old Brick	1:2:9	25	0.67	0.69

Table 3.1 (cont'd).

Source	Masonry Unit	Mortar	τ_0 (Psi)	μ	μ_1
Atkinson et al. (1989)	New Brick	1:1.5:4.5	118	0.75	0.75
Riddington et al. (1990) ²	Brick	1 masonry cement : 3.5 sand by weight	157	1.13	-
<p>Note:</p> <p>1. The original paper didn't give the maximum shear strength in terms of Eq. (3.1). τ_0 and μ were calculated by the author based on the test data given in the original paper. Also, the test data revealed nonlinear relationship between the shear strength and the normal stress, especially when the normal stress is quite high (1000 psi). It was probably due to the prior mortar failure because of the large lateral compressive stress, as pointed out in the original paper. Therefore, only the test data with a normal stress less than 500 psi were used to calculate the shear strength.</p> <p>2. Two sets of tests were conducted in this research. One with a precompression normal stress up to 300 psi, another one with a precompression normal stress up to 1015 psi. Only the first set of test data was used for the same reason discussed above. Furthermore, only the test results obtained from Test Scheme A and B were used, because these two test set ups led to uniform normal stress in the bed joint. Detailed description of the test set up can be referred to the original paper (Riddington et al. 1990).</p>					

This table shows that the initial shear bond strength τ_0 varied substantially, due to the wide range of masonry units and mortars tested. On the other hand, the internal frictional coefficient (μ) has much less scatter, with the majority of the reported data falling in the range 0.7 to 1.0. Atkinson et al. (1989) proposed a value of 0.7 as the lower bound estimate for the bed joint friction coefficient.

Much of the existing test data does not distinguish between the bed joint friction coefficient before and after cracking. Only the experiments conducted by Hamid et al. (1979) and Atkinson et al. (1989) measured the bed joint friction coefficient after cracking. This limited test data shows quite large scatter.

Reviewing the previous experimental data, several questions remain to be answered insofar as the bed joint shear strength of masonry:

- Although the linear Mohr-Coulomb frictional law fits well with the existing test data for the initial bed joint shear strength, this formula is basically an empirical criterion. Originally, the Mohr-Coulomb frictional law was used to illustrate the nonlinear behavior of particulate materials such as soil. It is not necessarily a straightforward extrapolation to simply extend this criterion to the interface strength between brick and mortar. Furthermore, no attempt has been reported to correlate the bed joint shear strength with the bed joint tensile strength, although intuitively there should be some relationship between these two strength values.
- The shear resistance of a cracked bed joint is determined by its shear friction coefficient (μ_1), while the shear resistant for an intact surface is related to the internal frictional coefficient (μ). A common assumption is that the two values are the same. However, no rationales have been provided.

An alternative hypothesis to the Mohr-Coulomb criterion has been proposed by Smith et al. (1971) to explain the shear failure of the masonry bed joint. This theory suggests that the shear failure of masonry bed joint is actually due to the tensile failure of mortar. However, later research has shown that this hypothesis gives poor predictions for

the masonry bed joint shear strength with different precompression normal stress (Hamid et al. 1982).

Previous experimental research showed that the shear failure usually does not occur in the masonry unit or in the mortar. Instead, the shear crack develops at the interface between masonry unit and mortar. An example for this type of shear crack is shown in Figure 3.5. This interface crack explains why the hypothesis given by Smith et al. (1971) cannot capture the shear behavior of masonry, since Stafford's theory only applies to a crack inside the mortar joint. On the other hand, this interface crack reveals that a mechanical model for the shear strength of masonry could be established related to the strength of the interface between masonry unit and mortar.

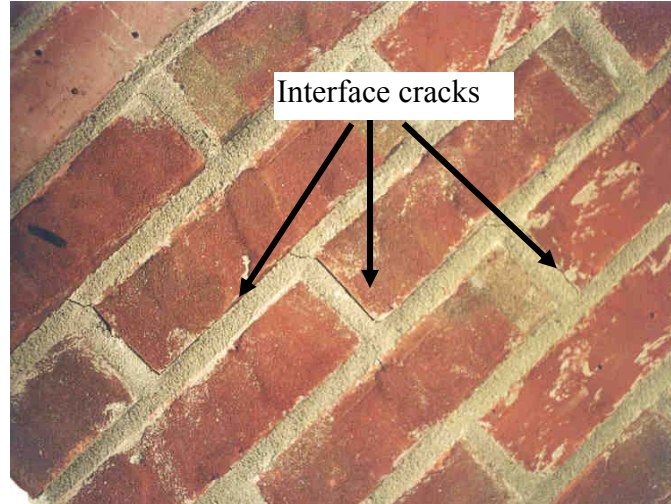


Figure 3.5. Shear crack at the interface between masonry units and mortar

3.3. PROPOSED MECHANICAL KEY MODEL FOR INTERFACE SHEAR STRENGTH AND TENSILE STRENGTH

Microscopy techniques can give a different perspective into the strength of the interface between masonry unit and mortar from a micro-structural point of view. Several microscopy studies have been carried out on the masonry unit-mortar interface (Lawrence et al. 1987, Abell et al. 1998, Lange et al. 1999). One important finding in the previous research is that mechanical interlock instead of chemical adhesion is the principal force bonding mortar to masonry units (Lange et al. 1999). A typical micro-image of the interface between masonry unit and mortar is shown in Figure 3.6. The mortar goes into the existing voids at the surface of masonry units. This volume of mortar then works as a mechanical key to connect masonry units with mortar. Previous research has also shown that if the surface of masonry unit is so smooth and solid that the mechanical keys cannot develop at the surface, the bond strength between the masonry units and the mortar is very small (Kampf 1963).



Figure 3.6. Typical mortar and clay unit interface (Lange et al. 1999)

Based on these considerations, a mechanical key model is proposed herein. A conceptual illustration of this model is shown in Figure 3.7. The following assumptions are employed:

- The mechanical keys are formed by the mortar going into the voids on the surface of the masonry units.
- There are two different kinds of mechanical keys at the interface between masonry unit and mortar. The first one is a wedge key (Figure 3.7a), and another one is a channel key (Figure 3.7b). The two different types of mechanical keys reflect the different idealized shapes of voids on the surface of masonry unit.
- There is no bond strength between masonry unit and mortar. Therefore, the interface strength is controlled only by the strength of the mechanical keys.
- The ratio of the total interface area of the wedge keys to the gross area of the interface is defined as r_w , and the ratio of the total interface area of the channel keys to the gross area of the interface is defined as r_c . It is assumed that r_w is equal to r_c .
- The fracture of the mechanical keys can be illustrated by maximum tensile stress criterion. That is, when the maximum tensile stress in a mechanical key reaches its maximum tensile strength of this key (f_t^m), the mechanical key breaks.

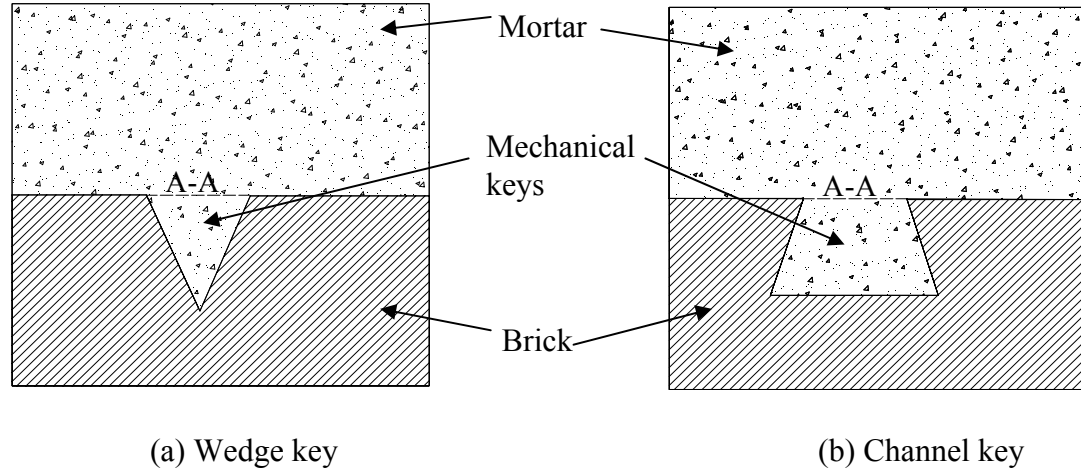


Figure 3.7. Mechanical key model

Based on this model, the interface strengths such as the pure tensile strength, the pure shear strength, and the shear strength associated with normal stress can be investigated.

For example, when the interface is loaded by a pure tensile force normal to the interface, the tensile force is resisted by the mechanical keys. However, since the bond strength between masonry unit and mortar is assumed as zero, the wedge mechanical key cannot take any force. Therefore, the external tensile force is resisted only by the channel keys, and thus the tensile stress (f_m^n) induced in the channel keys can be calculated by:

$$f_m^n = \frac{P}{r_c A} \quad (3.2)$$

where P is the tensile normal force applied on the interface, A is the gross area of the interface. When the calculated tensile stress is equal to the maximum tensile strength of the mechanical key, the mechanical key breaks in tension. The equivalent tensile strength for the interface can then be calculated as:

$$f_t = r_c \cdot f_t^m \quad (3.3)$$

When the interface is loaded with pure shear force, the effective shear stress τ_m^s in each mechanical key can be calculated as:

$$\tau_m^s = \frac{V}{(r_w + r_c)A} \quad (3.4)$$

where V is the total lateral shear force applied on the interface. The Mohr's circle approach shows that for a pure shear loading case, the principal tensile stress in the mechanical key has the same value as the shear stress. Therefore, the initial shear bond strength for the masonry interface without prescompression force can be calculated as:

$$\tau_0 = \frac{V}{A} = (r_w + r_c)f_t^m \quad (3.5)$$

Comparing Eq. (3.3) and Eq. (3.5), and recalling that r_w is equal to r_c , it can be concluded that the initial shear bond strength (τ_0) is roughly twice of the bed joint tensile strength. Page (1981) used triplet test and couple tests to measure the initial shear bond strength and the tensile bond strength of masonry bed joints. Based on his test data, Page (1981) pointed out that for brickwork, the typical ratio of shear to tensile bond strength was around 2.31. It is close to the value predicted by the mechanical key model.

When a precompressive normal force P is applied to the interface, the compressive stress introduced in each mechanical key is:

$$f_m^n = \frac{P}{(r_w + r_c)A} \quad (3.6)$$

Note that the elastic modulus of the mortar is usually smaller than that of masonry unit. Thus the masonry unit actually provides confinement to the mechanical key. As a result, the external compressive normal force introduces not only a normal compressive

stress f_m^n but also a lateral compressive stress f_m^l in the mechanical keys. As a simplification, the value of the lateral compressive stress f_m^l is assumed equal to the compressive normal stress: f_m^n . This assumption is correct when the stiffness of the masonry unit is much larger than that of mortar and the mortar completely fills in the voids.

Considering the lateral confining stress, the maximum principal tensile stress in a mechanical key under lateral shear force V and normal compressive force P can be calculated based on Mohr's circle as:

$$\begin{aligned} f^{\max} &= \frac{-f_m^n - f_m^l}{2} + \sqrt{\frac{(f_m^n - f_m^l)^2}{4} + \tau_m^s} \\ &= -f_m^n + \tau_m^s \end{aligned} \quad (3.7)$$

The interface reaches its maximum shear strength when f^{\max} is equal to f_m^t . Substituting Equations (3.4) and (3.6) into (3.7) gives:

$$V = (r_w + r_c) A f_t^m + P \quad (3.8)$$

Rewriting Eq. (3.8) in term of stress, and substituting Eq. (3.5) gives:

$$\tau = \tau_0 + 1.0 \cdot \sigma \quad (3.9)$$

Eq. (3.9) gives the same formula as the linear Mohr-Coulomb frictional law. However, this method is based on a rational explanation for the interface failure. Note that the equivalent internal friction coefficient obtained by this method is 1.0, which is consistence with previous test results. It should also be pointed out that Eq. (3.9) is obtained by assuming that the confining compressive stress f_m^l is equal to the normal compressive stress f_m^n . In many real cases, since the voids in the brick cannot be fully

filled by the mortar, and the stiffness of masonry unit is not infinitely larger than that of the mortar, the value of f_m^l should be less than f_m^n . Therefore, Eq. (3.9) gives an upper-bound estimate for the initial bed joint shear strength.

In the case that both tensile normal force and lateral shear force are applied on a masonry unit-mortar interface. The tensile normal force will cause a tensile stress in the channel keys, which can be calculated by Eq. (3.3). Meanwhile, the shear stress induced in the channel keys by the lateral shear force can be calculated by Eq. (3.4). Again, based on Mohr's circle, the principal tensile stress in the channel key can be calculated as:

$$\sigma_m^1 = \frac{P}{2Ar_c} + \sqrt{\frac{P^2}{4A^2r_c^2} + \frac{V^2}{4A^2r_c^2}} \quad (3.10)$$

By equating Eq. (3.10) to the maximum tensile strength of the mechanical key, and introducing both the maximum pure tensile strength f_t and the maximum pure shear strength τ_0 given by Eq. (3.3) and Eq. (3.5), respectively, the failure criterion for the masonry bed joint under tensile normal stress and lateral shear stress can be written as:

$$\left(\frac{\tau}{\tau_0}\right)^2 + \frac{\sigma}{f_t} = 1 \quad (3.11)$$

3.4. EXPERIMENTAL VERIFICATION

A 4-brick direct shear test was employed to investigate the bed joint shear properties before and after cracking and to verify the proposed mechanical key model. A picture of the test set up is shown in Figure 3.8. It is a simplified configuration of the test set up used by Hamid et al. (1979). The compressive force is applied by a jack at the top of the center top brick, which introduces shear forces at the two vertically placed bed

joints, and causes shear-sliding cracks in the bed joints. At the same time, instead of using jack, a special plate-rod system composed of four steel rods and two steel plates is employed to apply lateral compressive force to the specimen. Two strain gages were used for each steel rod to monitor the tensile force in the rod. The plate-rod system is also used to monitor the displacement of the specimen normal to the bed joint during the sliding of the bed joint.

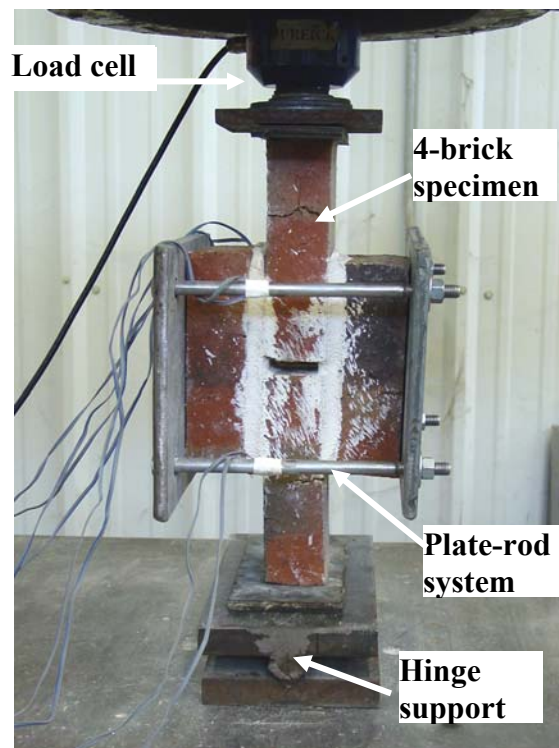


Figure 3.8. 4-brick direction shear test set up

The tested specimen is composed of solid clay bricks and Type K' mortar with a Portland cement to lime to sand ratio of 0.5:2:9. This masonry assembly is assumed to be a representative of the strong unit-weak mortar masonry material observed in existing URM buildings. A total of 21 specimens were tested. The applied lateral compressive stress to these specimens ranged from zero to 100 psi. The observed failure modes were always shear-sliding cracks along the bed joint interface between brick and mortar. The measured maximum initial shear strength corresponding to different lateral compressive stresses is shown in Figure 3.9. It can be seen that the measured initial shear bond strength was around 60 psi, and the measured equivalent internal shear friction coefficient was around 1.1. These test results verified that Eq. (3.9), as proposed by the mechanical key model, gives good results.

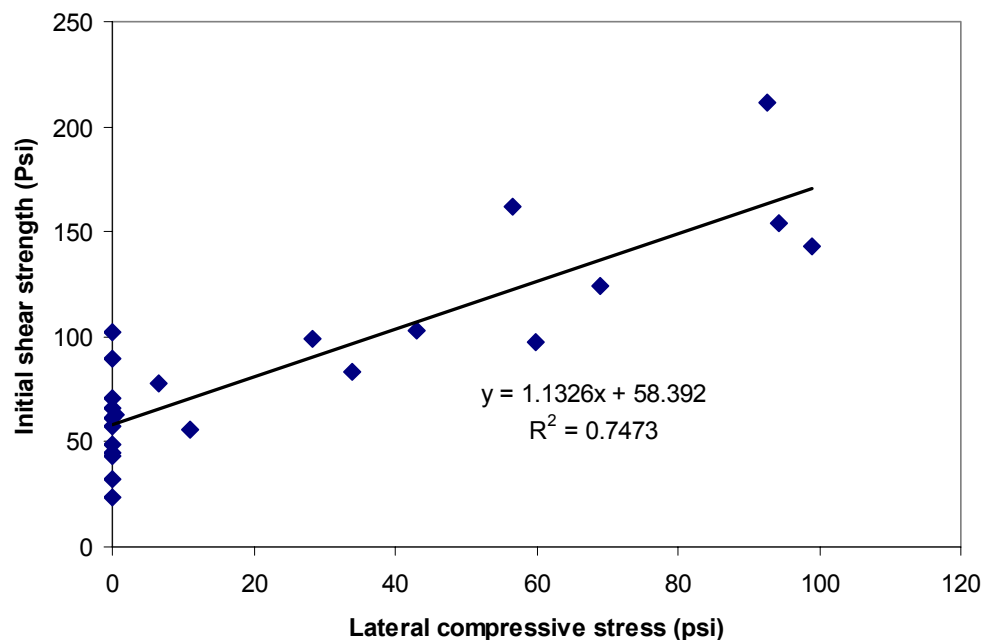


Figure 3.9. Measured initial shear strength with different lateral confining stresses

After shear cracks fully developed, the specimens were reassembled and tested again with various lateral confining stresses. These tests were repeated several times to investigate the effects of the number of deformation cycles on the shear friction coefficient of the cracked bed joint surfaces. It was found that the shear friction coefficient for the tested cracked bed joint surfaces were not sensitive to the lateral confining stress values (ranging from 0 to 100 psi) or to the deformation cycle number (ranging from 1 to 4). The shear friction coefficient had a measured value close to 1.0. Therefore, for the specific masonry tested, the shear friction coefficient for the cracked bed joint surface is close to the equivalent internal shear friction coefficient.

Another interesting phenomenon observed during the tests is the variation of the lateral compressive confining force, which is an indication of the lateral movement of the specimen. One typical lateral force-vertical force relationship corresponding to the beginning of shear sliding cracks on the bed joints is shown in Figure 3.10. The lateral confining force remained relatively constant until the point that shear-sliding crack began. With the initiation of the shear-sliding crack, the measured lateral confining force showed a large increase. This indicated a sudden lateral tension movement of the interface, apparently due to the break down and separation of the mechanical keys at the interface, as shown in Figure 3.11. After that, the vertical force dropped off quickly due to the loss of the specimen stiffness (Region II). With increasing shear-sliding deformation, the lateral confining force gradually increased again (Region III), which was due to the dilatancy movement of the sliding surface. This type of movement has been commonly observed in the relative movement of rock joints (Goodman 1980).

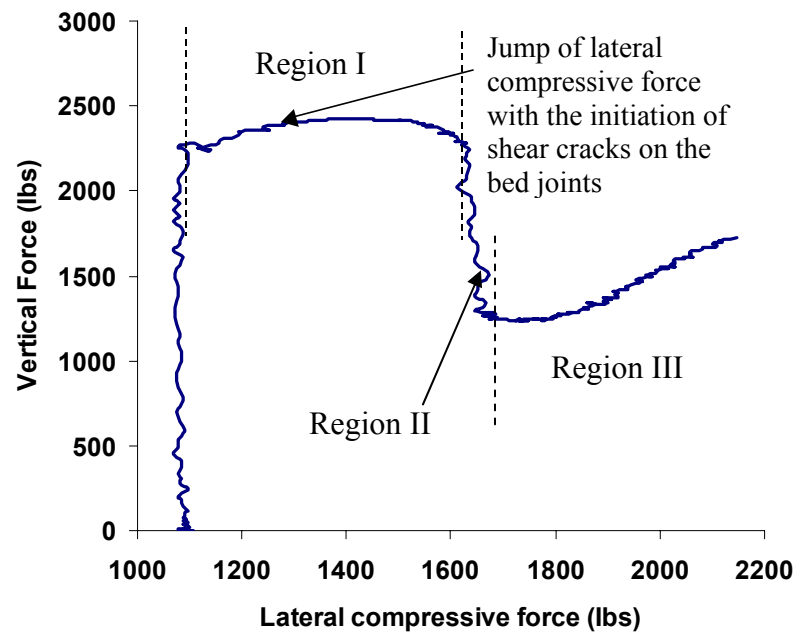


Figure 3.10. Changing of lateral compressive force with the initiation of shear sliding cracks on the bed joints

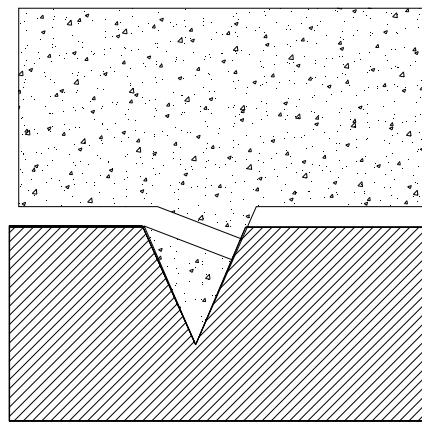


Figure 3.11. Break down and separation of the mechanical key

3.5. FAILURE ENVOPOLE FOR STRONG UNIT-WEAK MORTAR MASONRY ASSEMBLY BASED ON THE MECHANICAL KEY MODEL

By combining Eq. (3.9) and Eq. (3.11), the complete failure criterion for the splitting/sliding failure of a masonry bed joint can be built as shown in Figure 3.12. Note that when the compressive normal stress becomes large, the failure mode of masonry gradually translates to a compressive failure of the masonry. Therefore, another failure criterion is also plotted in Figure 3.8 as the cut-off for Eq. (3.9). As discussed before, extensive experimental research has been conducted for the compressive failure of masonry and several failure criteria have been proposed (Page et al. 1982, Andreaus 1996). The failure of masonry in the compressive region can be divided into two categories, compression-tension stress state and compression-compression stress state. When masonry is in a compression-tension stress state, the compressive strength of masonry decreases rapidly with increasing lateral tensile stress (Page 1981, 1983). Usually, a linear equation has been used to illustrate the compressive failure of masonry under compression-tension biaxial stress state:

$$\frac{\sigma_1}{f_t} + \frac{\sigma_2}{f_m} = 1 \quad (3.12)$$

where σ_1 and σ_2 are the principal tensile stress and the principal compressive stress for the in-plane loaded masonry, respectively. f_t and f_m are the masonry tensile strength and compressive strength, respectively. Note that the values of f_t and f_m are dependent on the angle between the loading direction and the bed joint (Page 1981), although some researchers did not consider this fact for the sake of simplicity (Syrmakezis C.A. et al. 1995, Bull J.W. 2001). A simple treatment is proposed herein to consider this issue.

Assuming the uniaxial compressive strengths for the masonry are f_m^\perp and f_m^\parallel corresponding to the direction of the compressive force perpendicular and parallel to the bed joints, respectively, the uniaxial compressive strength for masonry corresponding to the direction of the compressive force at an angle ϕ to the bed joint can be simply calculated as:

$$f_m(\phi) = f_m^\parallel + (f_m^\perp - f_m^\parallel) \cdot \frac{2\phi}{\pi} \quad (3.13)$$

Similarly, assuming that the uniaxial tensile strengths for the masonry are f_t^\perp and f_t^\parallel corresponding to the direction of the tensile force perpendicular and parallel to the bed joints, respectively, the uniaxial tensile strength for masonry corresponding to the direction of the tensile force at an angle θ to the bed joint can be calculated as:

$$f_t(\phi) = f_t^\parallel + (f_t^\perp - f_t^\parallel) \cdot \frac{2\phi}{\pi} \quad (3.14)$$

Substituting Eqs. (3.13) and (3.14) into Eq. (3.12), the maximum compressive strength of masonry at compression-tension stress state corresponding to the principal compressive stress at an angle of θ to the bed joint can be calculated as:

$$\frac{\sigma_1}{f_t^\perp + (f_t^\parallel - f_t^\perp) \frac{2\phi}{\pi}} + \frac{\sigma_2}{f_m^\parallel + (f_m^\perp - f_m^\parallel) \cdot \frac{2\phi}{\pi}} = 1 \quad (3.15)$$

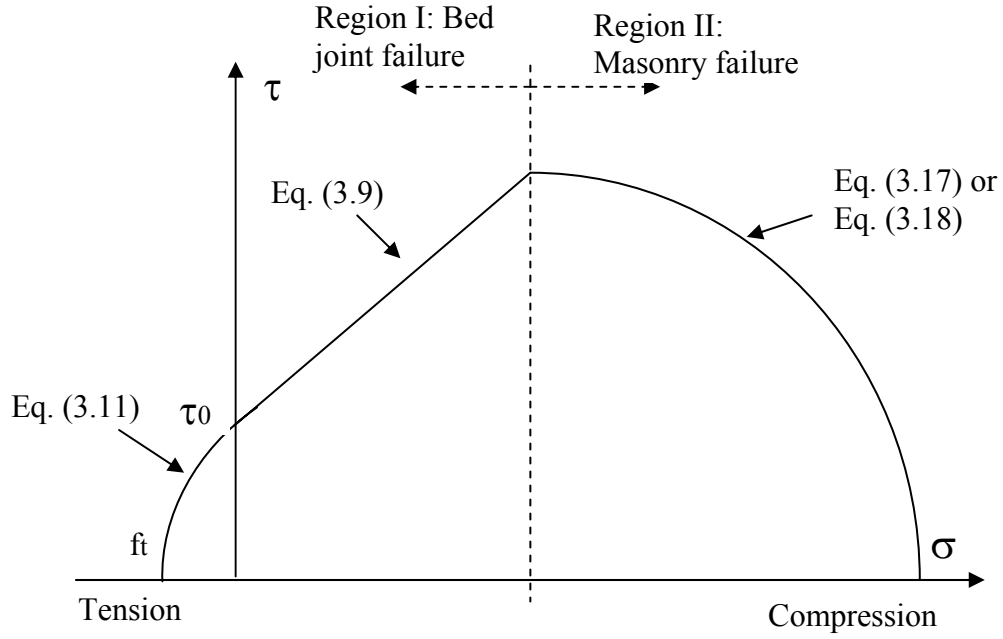


Figure 3.12. Failure criteria for masonry bed joints

It should be pointed out that f_t^\perp and f_m^\perp are the well-known masonry bed joint tensile strength and masonry compressive strength, respectively, and can be obtained from standard material tests. On the other hand, tests have seldom been conducted to measure the value of f_m^\parallel . Therefore, not much information is available for this value. However, Page's tests (Page 1981) showed that it is roughly 0.7 of f_m^\perp for brick masonry.

The value of f_t^\parallel is determined by the initial shear bond strength of the bed joint if the strength of the head joint is ignored (See Figure 3.13). Therefore, The value of f_t^\parallel can be calculated by:

$$f_t^\parallel = 0.5\kappa\tau_0 \quad (3.16)$$

where κ is the length to height ratio of masonry unit, which is around 3.2 for common size brick unit. Considering these values Eq. (3.15) can be simplified to:

$$\frac{\sigma_1}{f_t^\perp + (1.6\tau_0 - f_t^\perp)\frac{2\phi}{\pi}} + \frac{\sigma_2}{f_m^\perp\left(0.7 + \frac{0.6\phi}{\pi}\right)} = 1 \quad (3.17)$$

When masonry is in a compression-compression stress state, as discussed before, the failure of masonry is not so sensitive to the directions of the principal stresses. Therefore, a simple equation proposed by Naraine (1991) can be used:

$$CJ_2 + (1 - C)I_1 + CI_2 = 1 \quad (3.18)$$

where J_2 , I_1 , I_2 are principle stress invariants defined as:

$$J_2 = \left(\frac{\sigma_{avg}}{f_m^\perp} - \frac{\sigma_{lateral}}{f_m^\parallel} \right)^2, \quad I_1 = \left(\frac{\sigma_{avg}}{f_m^\perp} + \frac{\sigma_{lateral}}{f_m^\parallel} \right), \quad I_2 = \left(\frac{\sigma_{avg}}{f_m^\perp} - \frac{\sigma_{lateral}}{f_m^\parallel} \right) \quad (3.19)$$

and C is a constant defining the shape of the failure envelope. When C is equal to 1.0, Eq. (3.18) reduces to the Von Mises yield criterion. When C is equal to 1.6, Eq. (3.18) fits well with the existing experimental data (Naraine 1991).

Based on the above discussion, the failure criterion for Region II in Figure 3.12 can be determined by Eqs. (3.17) and (3.18). This failure criterion, together Eqs (3.9) and (3.11), forms a complete failure envelope for a masonry bed joint under in-plane stress state. Given that for strong unit-weak mortar URM assembly, its behavior is controlled by the properties of bed joints, it is reasonable to expand the proposed mechanical key model to illustrate the behavior of masonry at large scale. Note that when using Eqs. (17) and (18) to determine the compressive failure envelope, the values of σ_1 , σ_2 , and θ can be determined by the normal stress and shear stress applied on the bed joint based on Mohr's circle.

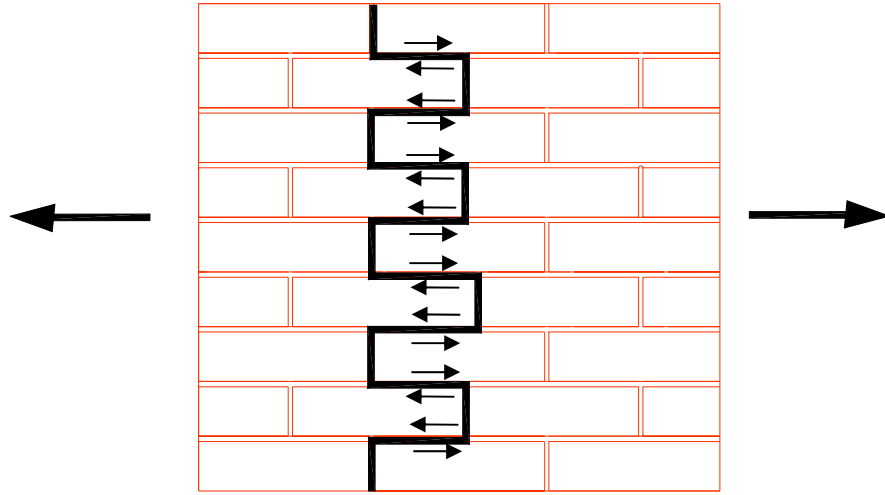


Figure 3.13. Failure mode of masonry with the tensile stress parallel to the bed joint

3.6. REEVALUATION OF FEMA 356 STRENGTH PARAMETERS BASED ON THE MECHANICAL KEY MODEL

As an application of the mechanical key model, the validity of the strength parameters adopted by FEMA 356 can be assessed. As discussed before, three controlling strength parameters are needed in the mechanical key model. They are:

- The bed joint tensile strength: f_t
- The compressive strength of masonry perpendicular to the bed joint: f_m
- The initial bed joint shear bond strength: τ_0

These three parameters are also adopted in FEMA 356. In addition, another strength parameter, the diagonal tensile strength (f_t^d), is utilized in FEMA 356 as well. At present, several standard material tests are available to determine the values of the first three strength parameters. For example, ASTM E72 method and couple test can be used to determine the ultimate and design flexural tensile strengths for masonry. Prism test is

usually utilized to determine the compressive strength of masonry (ASTM E447). Racking load test, diagonal compression test, and 4-brick direct shear test are usually used to measure the shear strength of masonry (ASTM E72, ASTM E519). On the other hand, no test method has been specified to measure the diagonal tension strength.

Both FEMA 356 and the mechanical key model point out that masonry shear strength is dependent on both the initial bed joint shear bond strength and the shear friction coefficients. The mechanical model further points out that the value of the initial bed joint bond shear strength is roughly double of the bed joint tensile strength.

One significant difference between FEMA prestandards and the mechanical key model is that FEMA 356 does not distinguish between the equivalent internal shear friction coefficient for an uncracked bed joint and the shear friction coefficient for a cracked bed joint. Conversely, the mechanical key model points out that these two values are associated with different mechanical phenomena. The internal shear friction coefficient is an equivalent value that incorporates the effect of the confining compressive stress on the mechanical key induced by the lateral stress. For a perfect strong unit-weak mortar masonry, μ is equal to 1.0. Considering the possibility that many voids are not completely filled, a reduced value, say 0.8-0.9, should probably be used. In contrast, the shear friction coefficient for a cracked joint corresponds to the true sliding friction between brick and mortar. Its value depends on the configuration of the interface between the masonry unit and the mortar, which can also be determined by 4-brick direct shear test or triplet test.

Another significant difference between FEMA prestandards and the mechanical key model is that FEMA 356 uses the diagonal tensile strength (f_t^d) to determine the

possible diagonal cracking in a masonry panel. However, whether this diagonal cracking is due to splitting and/or sliding of masonry joints or the compressive failure of masonry is not clearly specified. Nevertheless, ASTM equates the diagonal tension strength with the shear stress (ASTM E519), and FEMA 356 uses the initial bed joint shear strength for the diagonal tensile strength (ATC 2000).

In contrast, the mechanical key model reveals the true working mechanism for a diagonal cracking in a masonry panel. This model points out that both the sliding and splitting of the masonry joints are attributable to the tensile failure of the interface between the masonry unit and mortar. Therefore, when the calculated combination of the normal stress and the shear stress on the bed joints satisfies Eq. (3.9) or Eq. (3.11), a diagonal cracking will occur in the masonry. This crack is associated with sliding and splitting of both the bed joints and the head joints. On the other hand, when the compressive stress in masonry is quite large, and the calculated combination of the normal stresses satisfies Eqs. (3.17) or (3.18), another type of diagonal cracking will occur. This type of diagonal cracking involves cracks in both masonry units and mortar. Both types of diagonal cracking were observed in previous tests and field investigations. One example is the specimen E3 tested by Epperson et al. (1992), as shown in Figure 3.14. Note that the diagonal cracks developed at both the top right corner and the left bottom corner of this pier when the pier was pushed from right to left. The external moments caused a larger compressive stress at the left bottom corner than at the top right corner. As a result, sliding/splitting-type diagonal tensional cracks developed at the top right corner, while compression-type diagonal cracks developed at the bottom left corner. In a nutshell, the mechanical key model considers that a diagonal cracking in masonry

assembly is either due to the sliding and splitting of the masonry joints, or due to the large compressive stress in the masonry. Both cases can be analyzed by employing the mechanical key model. Therefore, no specific diagonal tensile strength is needed to illustrate the possible diagonal cracking in masonry.

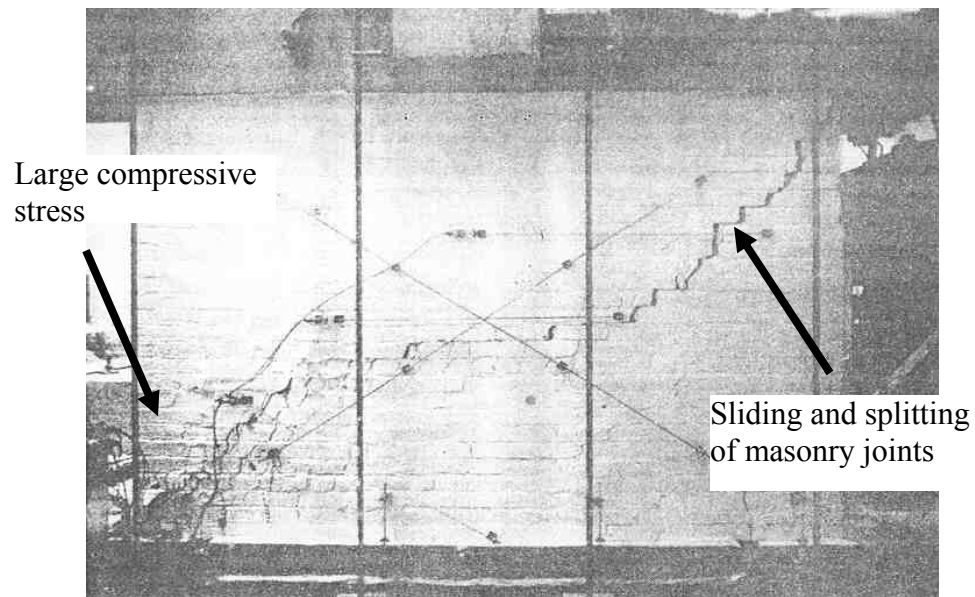


Figure 3.14. Two different types of diagonal cracking (Epperson et al. 1992)

3.7. THE ASSESSMENT OF THE DIAGONAL COMPRESSION TEST BASED ON THE MECHANICAL KEY MODEL

The second example for the application of the mechanical key model is the assessment of a typical masonry material test method: the diagonal compression specimen. ASTM 519 specifies that a diagonal compressive test can be used to determine

the shear strength of masonry. And the shear strength of the test specimen can be calculated by the following equation:

$$S_s = \frac{0.707P}{A} \quad (3.20)$$

where P is the applied concentrated diagonal load, and A is the cross section area of the specimen.

However, previous research has shown that the concentrated diagonal load used in this test creates a complex state of stress in the specimen. For example, both normal and shear stresses are introduced on the bed joints. The additional normal compressive stress might improve the shear strength of the specimen. Therefore, it is quite interesting to use the mechanical key model to examine the values of strength obtained from a diagonal compressive test. In order to do this, a FE analysis was conducted as the first step. This analysis was used to obtain the critical stress parameters in the specimen such that the proposed mechanical key model can be used to predict the maximum strength.

The diagonal compression specimen analyzed is shown in Figure 3.15. It is a one-wythe wall composed of 9 courses with 3 bricks in each row. For the analysis, the height (h) is taken as 23.25 in, the length (L) is taken as 24.75in, and the thickness (t) is taken as 3.375 in. A two-dimensional square linear quadrilateral element was used to mesh the masonry panel, with a mesh size of 0.22 inches. Such a small mesh size is needed to give a good estimation for the stress distribution in the masonry joints, since the thickness of the masonry joints is around 0.375 in. The effect of the different elastic moduli for the masonry units and mortar is considered in this analysis. The elastic moduli used for the brick and mortar are 1704 ksi and 40 ksi, respectively. These are specified as typical values by Sahlin (1971). A steel angle section was included on the top left and the

bottom right of the specimen to simulate the loading steel shoes used in the test. A typical elastic modulus of 29000 ksi was used for the steel shoes. The Poisson ratio for masonry was assumed to be 0.25. Fixed boundary conditions were assumed at the face of the bottom steel shoe, and a uniform pressure was applied at the top steel shoe.

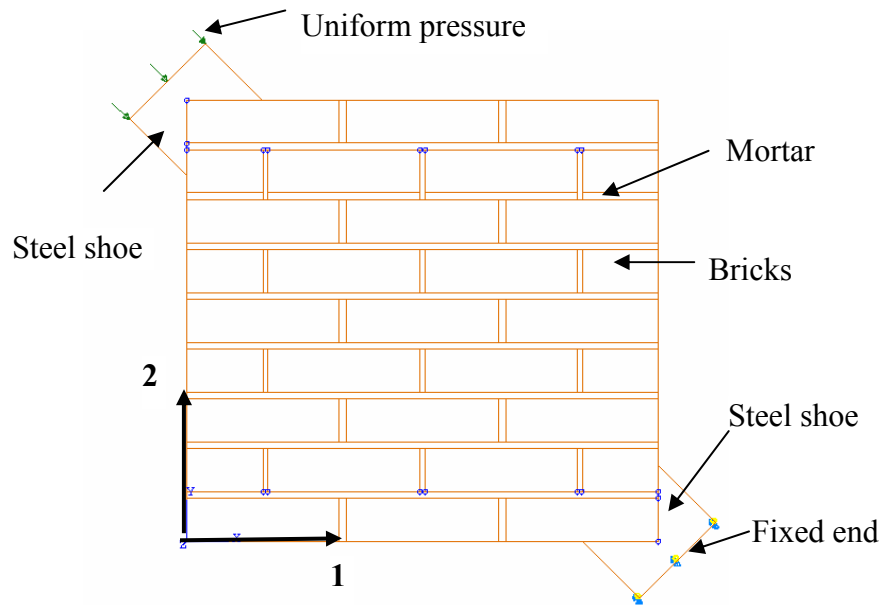


Figure 3.15. A diagonal compression specimen

Assuming a 1 kip compressive force is applied on the top left steel shoe, the normal stress perpendicular to the bed joints (S22), the normal stress parallel to the bed joints (S11), and the shear stress in the bed joints (S12), are shown in Figures 3.16 to 3.18. The figures show that the normal stress perpendicular to the bed joints and the shear stress in the bed joints are relative uniform at the mid of the panel. These values are -8 psi and 13 psi, respectively. On the other hand, the normal stress parallel to the bed joints

(S11), is quite different between the mortar joints and the masonry units, due to their different elastic modulus. An average value of -8 psi is calculated over the two different components. Note that the minus sign for the normal stress means a compressive stress.

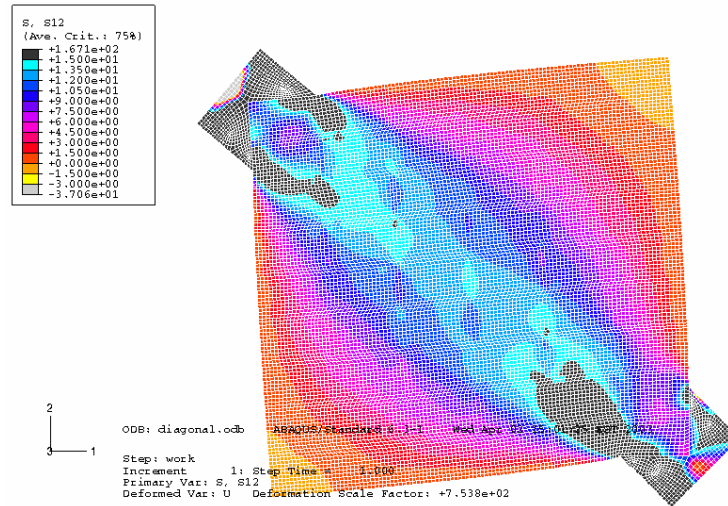


Figure 3.16. Distribution of the bed joint shear stress in the masonry panel

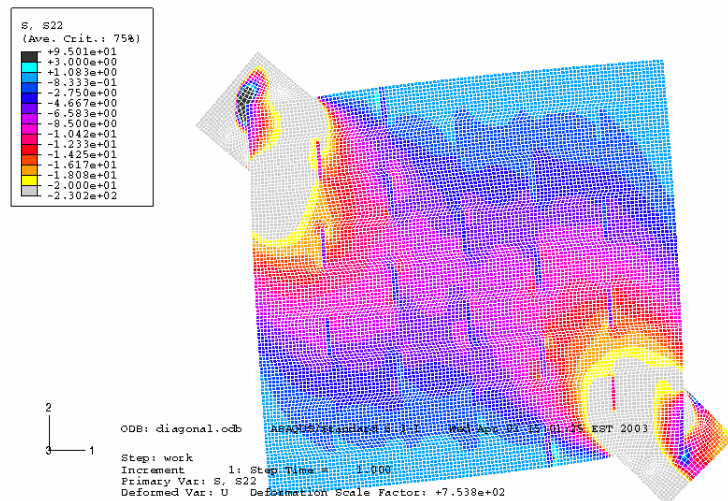


Figure 3.17. Distribution of the bed joints normal stress in the masonry panel

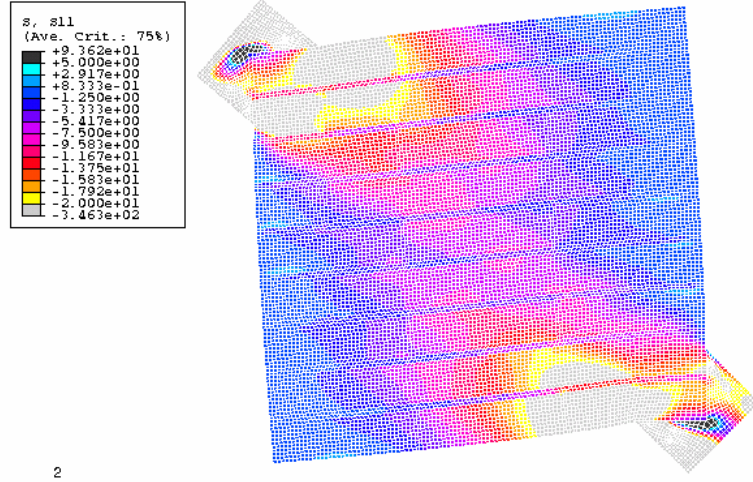


Figure 3.18. Distribution of the normal stress parallel to the bed joints

When a compressive force of P Kips is applied on the top left steel shoe, based on Eq. (3.9) the splitting/sliding type diagonal cracking failure will occur if the follow equation is satisfied:

$$P = \tau_0 / (13 - 8\mu) \quad (3.21)$$

On the other hand, the values and the directions of the principal stresses at the mid area of the specimen can be calculated based on the stress values S_{11} , S_{22} , and S_{12} given by the FE analysis. Substituting these values into Eq. (3.17) gives the governing equation for the compressive-tensional type diagonal cracking failure for the specimen analyzed here. The equation is as the follows:

$$\frac{5P}{0.8\tau_0 + 0.5f_t^\perp} + \frac{24.7P}{f_m^\perp} = 1 \quad (3.22)$$

The failure modes and the corresponding maximum strength for a diagonal compression specimen can be determined from the three equations (3.21) and (3.22).

Based on the mechanical key model, f_t^\perp is roughly half of τ_0 . For a typical strong unit-weak mortar masonry, one can assume that f_m^\perp is 10 times τ_0 . In this case, Eq. (3.21) can be simplified as:

$$P = 0.138\tau_0 \quad (3.23)$$

Eqs. (3.22) and (3.23) give similar P values. If μ is equal to 1.0, the compression-tension type diagonal cracking dominates the failure of the specimen. On the other hand, if μ is equal to 0.7, the sliding/splitting type diagonal cracking dominates the failure of the specimen. This indicates that the maximum strength obtained by the diagonal compressive test does not necessarily correspond to one specific critical strength value.

3.8. CONCLUSIONS

A mechanical key model is proposed in this section to illustrate the tensile and shear strength of the interface between masonry unit and mortar. This model reveals that both the tension failure and the shear failure of the interface can be attributed to the tensile failure of the mechanical key. By combining the model with a biaxial masonry failure criterion, the model can be used to illustrate the complete failure envelope of a masonry bed joint. This envelope is reflected as Eqs. (3.9), (3.11), and (3.17) or (3.18). For a strong unit-weak mortar masonry, the masonry bed joints control the properties of masonry. In this case, the mechanical key model can be expanded to explain the failure mechanism for the entire masonry assembly.

Several direct conclusions from the mechanical key model are:

- A distinction needs to be made between the initial equivalent internal shear friction coefficient for the uncracked bed joint and the shear friction factor for the cracked bed joints, since they are associated with different mechanical behavior.
- The upper-bound estimate for the initial equivalent internal shear friction coefficient is about 1.0, while the lower-bound estimate for the initial equivalent internal shear friction coefficient is about 0.7.
- The initial bed joint shear bond strength is roughly double that of the initial bed joint tensile strength.

Both the previous experimental data and the tests conducted as part of this project show the robustness and accuracy of the proposed model.

The strength parameters adopted by FEMA 356 and a typical masonry material test method (the diagonal compression test) were reviewed based on the proposed model. It was found that:

- Diagonal cracking in a masonry assembly is either due to the sliding and splitting of masonry joints, or due to the large compressive stress in the masonry. The two modes of failure can be analyzed employing the mechanical key model. No diagonal tensile strength is needed to assess the possible diagonal cracking in masonry.
- The strength measured from the diagonal compression test does not necessarily correspond to one specific critical strength value, and thus is difficult to illustrate.

CHAPTER 4

EFFECTIVE PIER MODEL FOR THE NONLINEAR IN-PLANE ANALYSIS OF INDIVIDUAL URM PIERS

4.1. INTRODUCTION

Due to the poor seismic performance of unreinforced masonry (URM) structures, the use of URM construction has been discouraged in seismic regions in the United States for many decades. However, numerous URM structures remain in service in those areas, especially in the regions that have only recently been recognized as having significant seismic risk. In order to assess the threat to life safety presented by these structures, effective analytical tools are required. To that end, numerous investigations aimed at understanding the nonlinear behavior of URM structures have been conducted.

The nonlinear in-plane behavior of individual URM piers has been investigated in many experimental studies (Abrams and Shah 1992, Anthoine et al. 1995, Epperson and Abrams 1989, Magenes and Calvi 1992, Manzouri et al. 1995 for example). Typically, tests impose lateral displacements to a single URM pier with idealized boundary conditions (i.e. cantilever or fixed-fixed) and a constant vertical stress. Experimental results have identified several in-plane failure mechanisms for a URM pier, such as rocking, sliding, toe crushing, and diagonal tension. These past studies provide a sound basis for the understanding of the in-plane behavior of individual URM piers.

In addition to the experimental research, several analytical studies aimed at quantifying the nonlinear in-plane response of URM piers have been conducted,

including those by McDowell et al. (1956), Abrams (1992), and Tomazevic (1999) to name a few. McDowell et al. (1956) proposed an arching action theory to explain the lateral strength of masonry walls constrained between rigid supports. Later, a similar but simpler model was used by other researchers to describe the rocking behavior of a URM pier (Abrams 1992, Tomazevic 1999). FEMA 356 (ATC 2000) provided design equations for the calculation of the strength of a URM pier corresponding to each of the four typical failure modes. However, experimental results have shown that the actual failure mode of a URM pier was typically a combination of several different primary failure modes. For example, specimen W1 in Manazouri's test (Manazouri et al. 1995) was observed to fail due to a combination of toe crushing and bed-joint sliding. As a result, eight failure modes, which consisted of the four typical failure modes and combinations thereof, were proposed in FEMA 306 (ATC 1999) to describe the damage of URM piers under different loading conditions.

The majority of analytical research to date has been based on observed experimental results rather than on fundamental mechanistic theories and constitutive models. Currently, there is no simple but comprehensive methodology available to describe the progression of damage in a URM pier and its corresponding nonlinear lateral force–deformation curve under varying loading and end support conditions. The lack of an appropriate analytical model for the nonlinear behavior of an individual URM pier hinders the understanding of the nonlinear mechanism of URM walls with multiple piers and openings, and ultimately of entire URM buildings.

Based on the above considerations, an effective pier macro-model is proposed here to describe the nonlinear behavior of an individual URM pier subjected to external

forces. Specifically, the model is intended to be used to predict the crack pattern, failure mechanisms, maximum strength, and lateral force–displacement curve of a single URM pier.

4.2. EXTERNAL FORCES

Before the nonlinear mechanisms of a URM pier can be addressed, the externally applied forces need to be defined. Figure 4.1 illustrates the externally applied forces considered by the effective pier model.

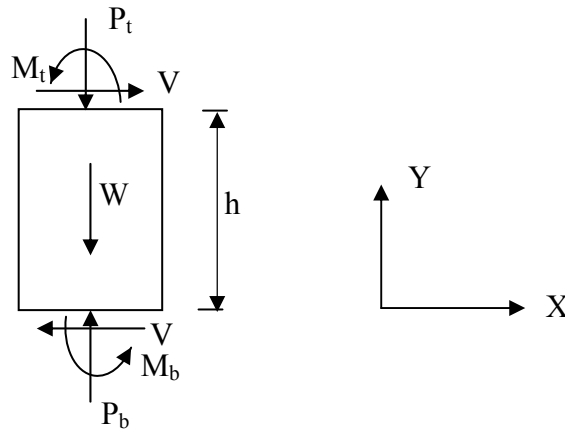


Figure 4.1. External forces applied on a pier

where, V is the applied shear force; P_t is the axial force applied at the top of the pier; P_b is the axial force applied at the bottom of the pier; M_t is the moment applied at the top of the pier; M_b is the moment applied at the bottom of the pier; and W is the self weight of the pier.

The equilibrium equations give:

$$P_b = P_t + W \quad (4.1)$$

$$V \cdot h = M_t + M_b \quad (4.2)$$

where, h is the height of the pier. If the height (h) and the weight (W) of a pier are known, Eqs. (4.1) and (4.2) indicate that three independent external forces exist for a pier.

4.3. INTERNAL STRESS DISTRIBUTION

The assumed distribution of internal stresses in a URM pier is shown in Figure 4.2, where, L is the length of the pier; L_{et} and L_{eb} are the lengths of the uncracked sections at the top and the bottom of the pier; σ_{ct} and σ_{cb} are the maximum vertical compressive stresses at the top and the bottom of the pier; τ_t and τ_b are the shear stresses at the top and the bottom of the pier; σ_{avg} and τ_d are the average vertical compressive stress and shear stress at the inflection point level, respectively; and f_t is the tensile strength of masonry perpendicular to the bed joint.

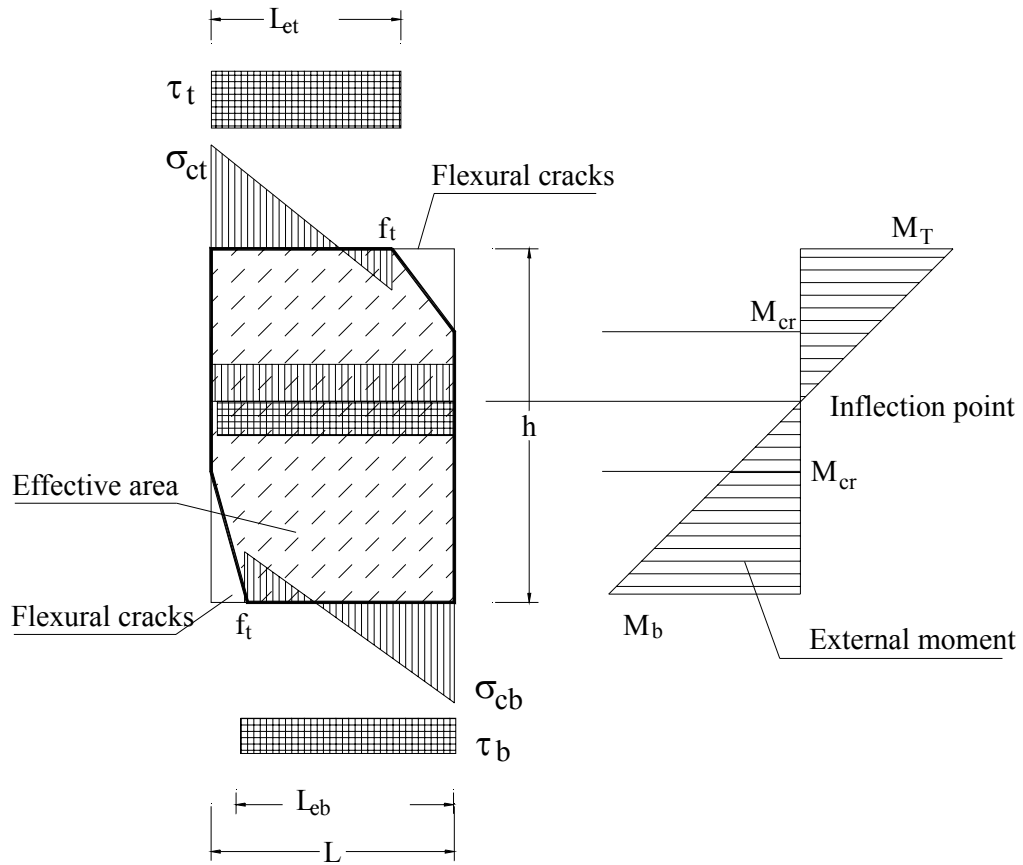


Figure 4.2. Distribution of the internal stresses in a URM pier with flexural cracks

The following assumptions are made in relation to the internal stress distribution:

- The external forces applied at the top of the pier cause cracking of some portion of the top section if the calculated maximum tensile stress is larger than masonry bed joint tensile strength, f_t . The effective section at the top of the pier is defined as the uncracked portion of the pier. Similar assumptions are used at the bottom.
- The effective pier is defined by linearly connecting the top and bottom effective sections to the original pier boundaries at the points with a cracking moment of M_{cr} (Figure 4.2). If the inflection point is located outside the boundaries of the

pier, the effective pier is simply defined by linearly connecting the top and bottom effective sections.

- The axial stress normal to the bed joint, σ_n , varies linearly across the effective section.
- The shear stress is uniformly distributed over each effective section.

The length of the effective section and the stress distribution at both the top and the bottom of a URM pier can be calculated based on the equilibrium equations and the above assumptions. For example, the externally applied forces at the top section of the pier are the moment M , the axial force P , and the shear force V . Based on the assumption of linear stress distribution in this section, the effective length L_e will be less than the length of the pier, provided that the following inequality is satisfied (i.e. the tension strength, f_t , is less than the maximum tensile stress):

$$\frac{6M}{L^2 t} - \frac{P}{Lt} - f_t \geq 0 \quad (4.3)$$

where, t is the thickness of the pier. In this case, applying equilibrium in the y-direction yields:

$$P = \frac{1}{2} (\sigma_{n \max} - f_t) L_e t \quad (4.4)$$

where, $\sigma_{n \max}$ is the maximum compressive stress in this section. Furthermore, moment equilibrium gives:

$$M = P \left(\frac{L}{2} - \frac{L_e}{3} \right) + \frac{1}{6} f_t L_e^2 \quad (4.5)$$

From Eq. (4.5), the effective length can be calculated as:

$$L_e = \frac{P - \sqrt{P^2 - f_t t (3PL - 6M)}}{f_t t} \quad (4.6)$$

The maximum compressive stress and the average shear stress at this section can then be calculated as:

$$\sigma_{n \max} = \frac{2P}{L_e t} + f_t \quad (4.7)$$

$$\tau = \frac{V}{L_e t} \quad (4.8)$$

Conversely, if the inequality (4.3) is not satisfied, the effective length L_e will be equal to the length of the pier. In this case, the maximum compressive stress and the average shear stress at this section can be calculated as:

$$\sigma_{n \max} = \frac{6M}{L^2 t} + \frac{P}{Lt} \quad (4.9)$$

$$\tau = \frac{V}{Lt} \quad (4.10)$$

Similarly, the length of the effective section and the stress distribution at the bottom of a URM pier can also be calculated based on Eqs. (4.3) through (4.10). By equating inequality (4.3) to zero, the cracking moment M_{cr} shown in Figure. 4.2 can be calculated. After that, the length of the effective section along the height of the pier can be determined, and the axial stress and shear stress at any level can be calculated following the same procedure.

4.4. URM PIER FAILURE MODES

Based on past experimental research, the four main failure modes of a URM pier are rocking, sliding, diagonal tension, and toe crushing. In order to properly model the

behavior of a URM pier, each of these failure modes must be addressed. The following section describes how the effective pier model considers each failure mode.

4.4.1. Rocking

A rocking failure is characterized by large flexural cracks at the bottom and the top of the pier. As the displacement increases the pier deforms as a rigid body rotating about the compressive toe. When force reversals occur, the flexural cracks close and the pier behaves as an uncracked pier until the flexural cracks open in the other direction. As a result, rocking can be considered as a “working” condition rather than a failure mode. Therefore, no material failure criterion needs to be employed as the effective pier model inherently describes this type of mechanistic behavior.

4.4.2. Bed-joint Sliding

A bed-joint sliding failure is identified by the formation of horizontal cracks on the bed-joint interface between masonry units and mortar, and a relative displacement between the masonry units above and below the bed joint. The pier deforms by sliding along the bed-joint with resistance offered by friction alone. Similar to rocking, a pier that displays bed-joint sliding will typically experience large deformations without significant vertical or lateral strength deterioration. However, due to the frictional resistance a large amount of energy is dissipated. As a result, bed-joint sliding is better defined as a “plastic working mechanism” as opposed to an ultimate strength failure mode.

In order to address bed-joint sliding, the mechanical key model proposed in Chapter 3 is employed. The mechanical key model gives the same equation as the Coulomb friction model (Chapter 3, Eq. 3.9). Previous experiments have shown that this linear equation given by the mechanical key model or the Coulomb friction model effectively describes the behaviors of bed-joint sliding (Meli 1973, Hegemier et al., 1978, Hamid et al.1980, Atkinson et al.1989). Based on the mechanical key model, bed joint sliding occurs when the following inequality is satisfied:

$$\tau \geq \tau_u \quad (4.11)$$

where, τ is the average shear stress on the bed joint, which can be calculated by Eq. (4.8) or (4.10); and τ_u is the maximum shear strength of the bed joint, which is given by:

$$\tau_u = \tau_0 + \mu\sigma_{avg} \quad (4.12)$$

where, τ_0 is the initial shear bond strength of the bed-joint; μ is the internal shear friction coefficient. Previous experiments have shown that μ varies between 0.7 and 1.0 (Hegemier et al. 1978, Hamid 1980, Atkinson 1989). Atkinson (1989) proposed a value of 0.7 as the lower bound estimate. The mechanical key model reveals that 1.0 is the upper bound estimate. σ_{avg} is the average vertical compressive stress on the bed joint, which can be calculated by:

$$\sigma_{avg} = \frac{P}{L_e t} \quad (4.13)$$

After sliding occurs, the residual shear strength is supplied by friction alone, and can be written as:

$$\tau_u = \mu_0\sigma_{avg} \quad (4.14)$$

where μ_0 is the true shear friction coefficient on the cracked bed joints.

4.4.3. Toe Crushing

Unlike rocking and sliding, a toe crushing failure leads to the loss of strength and stiffness in a pier. Toe crushing is defined as a compressive failure of masonry occurring at the toe of the pier. This failure occurs when the maximum compressive stress exceeds the maximum compressive strength of masonry:

$$\sigma_{n \max} \geq \beta \cdot f_m \quad (4.15)$$

where, $\sigma_{n \max}$ is the maximum compressive stress calculated by Eq. (4.7) or (4.9); f_m is the compressive strength of masonry; and β is a factor that accounts for the erroneous assumption of a linear stress distribution along the length of the pier (i.e., β should be larger than 1). To be consistent with the equivalent stress block analogy as outlined in MSJC 530-02, β should be taken as 1.28. MSJC (ACI 530-02) specified that for the design purpose, “masonry stress of $0.8 f_m$ shall be assumed uniformly distributed over an equivalent compressive zone”. The length of this compressive zone is 0.8 of the real length of the section in compression. This is equivalent to a linear distribution of compressive stress over the real compressive length with the maximum compressive stress at the edge of the section equal to $1.28 f_m$.

In order to consider toe crushing, the portion of masonry where the vertical compressive stress is larger than $\beta \cdot f_m$ is assumed to retain no strength. Based on the assumptions outlined previously, the length of the failed portion of the pier (L_{crush}) can be written as:

$$L_{crush} = \frac{\sigma_{n \max} - \beta f_m}{\sigma_{n \max} + f_t} L_e \quad (4.16)$$

Figure 4.3 illustrates the assumed internal stress distribution in a pier after toe crushing has occurred. From the figure it is apparent that when the toe crushing area propagates, the effective area of the pier decreases. Strictly speaking this is incorrect, as the compressive strength of masonry does not immediately drop to zero after the strength has been exceeded. However, this assumption greatly simplifies the problem and results in conservative strength estimates. If this simple loss model is unacceptable for a specific application, a Todeschini stress distribution (Todeschini et al. 1964), which accounts for the nonlinear stress strain behavior of masonry, can be employed.

It should be pointed out that if toe crushing occurs, the equation for calculating the effective length of the pier should be modified from Eq. (4.6) to:

$$L_e = \frac{P - \sqrt{P^2 - f_t t (3P(L - 2L_{crush}) - 6M)}}{f_t t} \quad (4.6b)$$

Several iterations may be needed to obtain the correct L_e and L_{crush} values from Eq. (4.7), (4.16) and (4.6b).

If the effective length obtained by Eq. (4.6b) is less than $L - L_{crush}$, the maximum compressive stress and the average shear stress at this section can still be calculated from Eqs. (4.7) and (4.8), respectively. Otherwise, they have to be calculated as:

$$\sigma_{\max} = \frac{6M}{(L - L_{crush})^2 t} + \frac{P(L + 2L_{crush})}{(L - L_{crush})^2 t} \quad (4.9b)$$

$$\tau = \frac{V}{(L - L_{crush}) \cdot t} \quad (4.10b)$$

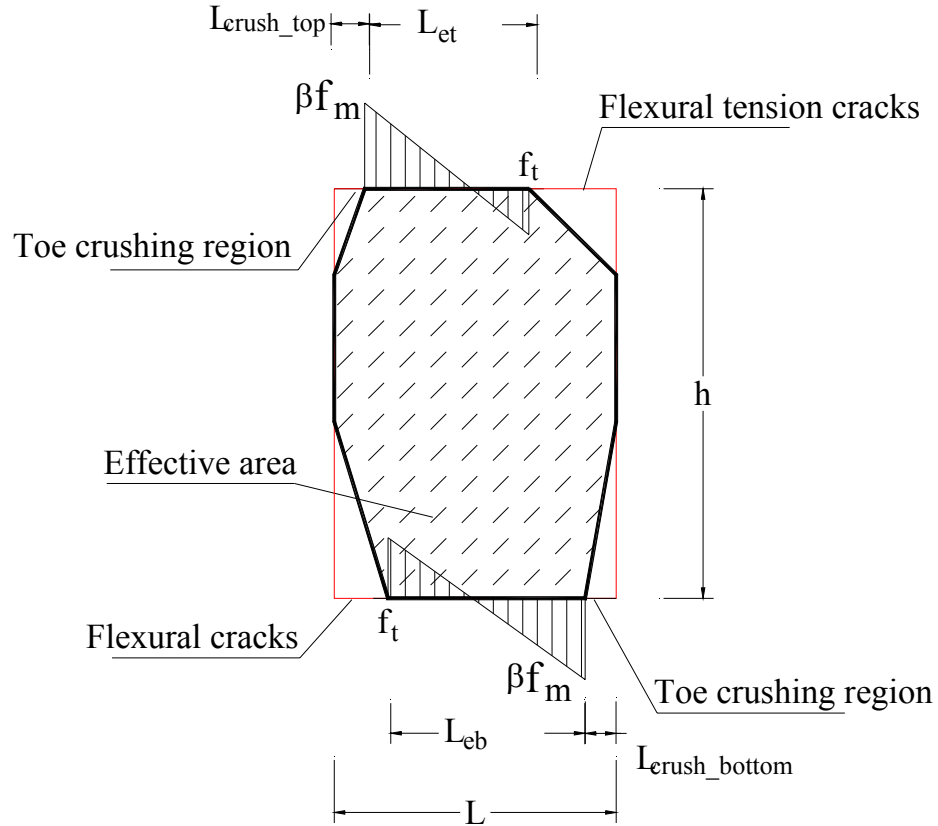


Figure 4.3. Effective pier after toe crushing and flexural cracking

4.4.4. Diagonal Cracking

Diagonal tension cracks usually develop at the mid-height of a URM pier and propagate diagonally. Previous experimental research showed that there are two different types of diagonal cracks: 1) stair-step cracking going along bed joints and head joints; and 2) diagonal cracks going through both masonry units and mortar joints. The mechanical key model reveals that different mechanisms exist for the two types of diagonal cracks. The first type of diagonal crack is due to the sliding and splitting of masonry joints, which can be expressed by Eq. (4.12). The second type of diagonal crack

is due to the biaxial failure of masonry as a whole. If masonry is in a principal compression – principal tension stress state, the corresponding failure criterion can be expressed as (Chapter 3 Eq. 3.17):

$$\frac{\sigma_1}{f_t + (1.6\tau_0 - f_t)\frac{2\theta}{\pi}} + \frac{\sigma_2}{f_m\left(0.7 + \frac{0.6\theta}{\pi}\right)} = 1 \quad (4.17)$$

where σ_1 is the principle tensile stress, σ_2 is the principle compressive stress, and θ is the angle between the direction of σ_2 and the bed joint. If masonry is in compression – compression state, i.e., both σ_1 and σ_2 are compression, Naraine's equation (Naraine 1991) can be used:

$$CJ_2 + (1 - C)I_1 + CI_2 = 1 \quad (4.18)$$

where J_2 , I_1 , I_2 are principle stress invariants defined as:

$$J_2 = \left(\frac{\sigma_{avg}}{f_m^\perp} - \frac{\sigma_{lateral}}{f_m^\parallel} \right)^2, \quad I_1 = \left(\frac{\sigma_{avg}}{f_m^\perp} + \frac{\sigma_{lateral}}{f_m^\parallel} \right), \quad I_2 = \left(\frac{\sigma_{avg}}{f_m^\perp} - \frac{\sigma_{lateral}}{f_m^\parallel} \right)$$

and C is a constant defining the shape of the failure envelop. When C is equal to 1.0, Eq. (4.18) reduces to the Von Mises yield criterion. When C is equal to 1.6, Eq. (4.18) fits with the existing experimental data (Naraine 1991).

The actual diagonal tension failure mode is determined by Eqs. (4.12), (4.17) and (4.18). To utilize these equations to calculate the diagonal cracking strength of masonry, the representative stress state at the mid-height of a UMR pier, which include the average vertical compressive stress σ_{avg} , the average lateral confining stress $\sigma_{lateral}$, and the average shear stress τ , have to be calculated. For simplicity, the diagonal tension strength is assumed to be unaffected by the externally applied moment. Therefore, the

three stress values can be calculated at the inflection point. For example, σ_{avg} can be calculated by Eq. (4.13) with L_e equal to L , and τ can be calculated as the follows:

$$\tau = \frac{\zeta V}{Lt} \quad (4.19)$$

where ζ is a shear stress factor that accounts for the erroneous assumption of a constant shear stress distribution. For slender piers ($L/h < 0.5$), the horizontal shear stress distribution is a parabola, which implies ζ is equal to 1.5. For stout piers ($L/h > 2$), the horizontal shear stress distribution approaches a constant value, which implies ζ is equal to 1.0.

Similarly, the average lateral confining stress $\sigma_{lateral}$, which is induced by the lateral force applied on a URM pier, can be calculated as the follows:

$$\sigma_{lateral} = \frac{\chi V}{ht} \quad (4.20)$$

where χ is a factor that accounts for the effects of the aspect ratio. If $L/h > 1$, the lateral confining stress is assumed uniform distributed along the height of the pier, χ is equal to 1.0. When $L/h < 0.5$, there is no lateral confining force in the mid-height of the pier, because is away from the boundary. In this case, χ is equal to zero.

The first type of diagonal crack (stair-step sliding and splitting of mortar joints) is very similar to bed joint sliding. Therefore, the response of masonry pier after this type of diagonal cracking is similar to that after bed joint sliding. The pier can still maintain a large amount of lateral resistance and vertical resistance. In contrast, the propagation of the second type of diagonal tension cracks causes a rapid deterioration of strength. To consider its effect, a smeared crack technique is employed, due to the difficulty to

consider the effect of discrete diagonal cracks on overall pier behavior. It is assumed that even after the second type of diagonal cracks develop inside the mid-height portion of the pier, the effective area of the pier remains continuous. However, the effective tangent modulus of elasticity of masonry will become negative because of the rapid and unstable propagation of the diagonal tension cracks. One possible stress-strain relationship of masonry before and after the development of diagonal tension cracks is shown in Figure 4.4. It can be seen that the post-cracking behavior of the masonry is quite different for two different types of diagonal cracks. Also notice that since no test data are available for the softening behavior of URM piers after the second type diagonal cracking, the tangent modulus of URM piers with diagonal tension crack is set equal to $-0.1E$, where E is the initial elastic modulus of masonry.

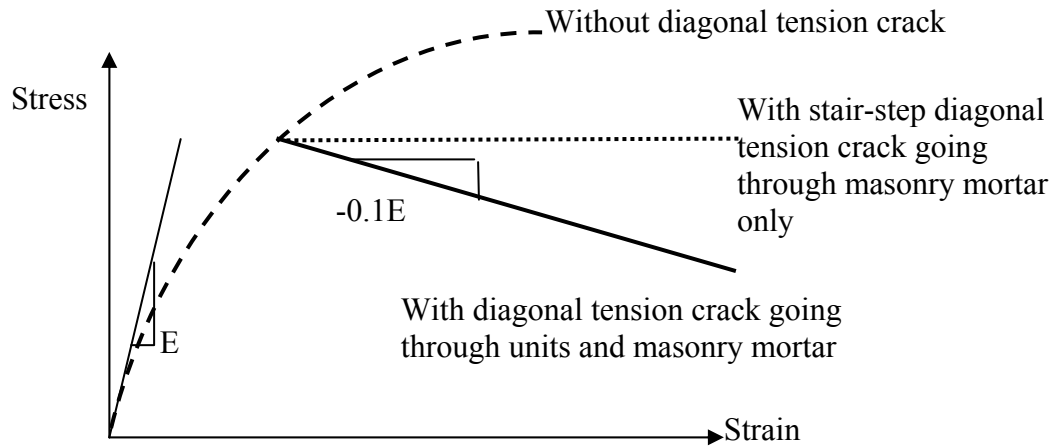
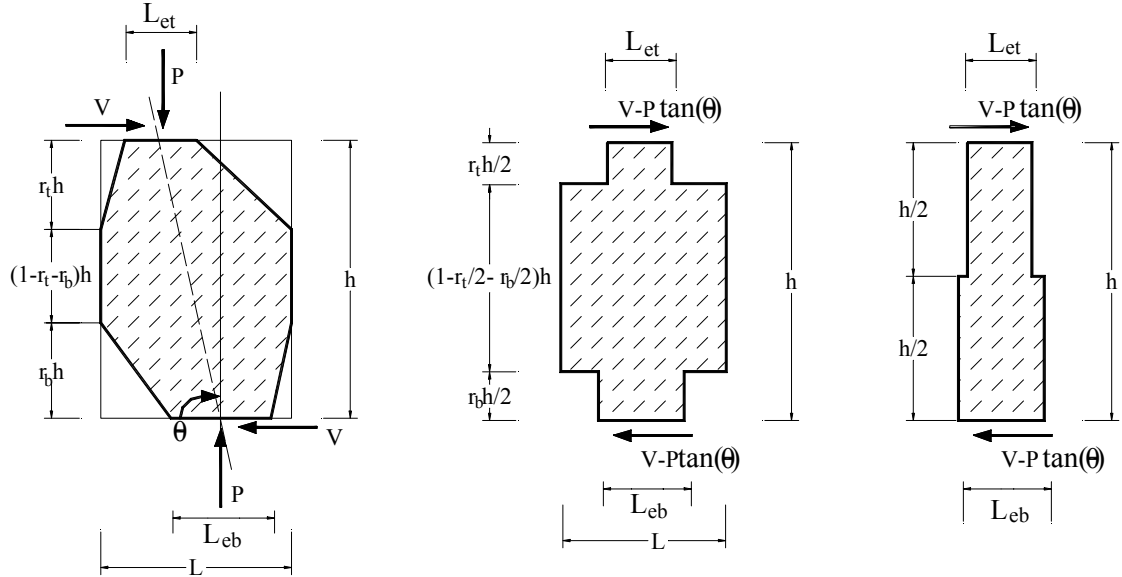


Figure 4.4. Stress-strain relationship of masonry before and after diagonal tension cracks

4.5. DEFORMATION OF URM PIERS

The effective pier model can also be used to obtain the deformation behavior of a URM pier under lateral force. As shown in Figure 4.5a, a URM pier may experience a loss of section due to either tensile or compressive failure, which must be considered when calculating displacements. The remaining pier will typically be inclined at some angle, that is, the central axis of the pier is not vertical. The angle θ between the central axis of the pier and the vertical line can be calculated by:

$$\theta = \arctan\left(\frac{L - L_{crush_bottom} - L_{crush_top} - 0.5L_{et} - 0.5L_{eb}}{h}\right) \geq 0 \quad (4.21)$$



a) Inclined effective area of the pier (b) Three-section effective pier (c) Two-section effective pier

Figure 4.5. Effective pier at an angle to the vertical line

Since the central axis of the pier is not vertical after cracking, a portion of the lateral force will be resisted through axial deformation not flexural and shear deformation. Therefore, the lateral force that causes shear and flexural deformation is $V - P \tan(\theta)$. When calculating the shear and flexural deformation, the inclined effective pier as shown in Figure 4.5(a) can be further simplified as a three-section vertical effective pier, as shown in Figure 4.5(b). This simplified effective pier consists of a top portion with a length of L_{et} and a height equal to half the distance from the top to the point with a moment of M_{cr} , a bottom portion with a length of L_{eb} and a height equal to half the distance from the bottom to the point with a moment of M_{cr} , and a mid portion with a length of L . In the case that the inflection point is out of the pier, the three-section vertical effective pier is transmitted into a two-section pier, as shown in Figure 4.5(c).

Assuming the lateral deformation of the pier induced by its axial deformation can be ignored, the lateral deformation of the pier is then determined by its flexural deformation and shear deformation, which can be calculated by:

$$\Delta = \frac{V - P \tan(\theta)}{K} \quad (4.22)$$

where, Δ is the lateral deformation of the pier; and K is the lateral stiffness of the pier, which is dependant on the dimensions, boundary conditions, and elastic modulus of the pier. For an initial elastic URM pier, K can be calculated as:

$$K = \frac{GtL}{\left[1.2h \left(1 + \gamma \left(\frac{G}{E} \right) \left(\frac{h}{L} \right)^2 \right) \right]} \quad (4.23)$$

where, γ is a coefficient that describes the boundary conditions of the pier (γ is equal to 0.83 for fixed–fixed end conditions, and 3.33 for cantilever end conditions); E is the

elastic modulus of masonry; and G is the shear modulus of masonry, which is taken as $0.4E$. After the URM pier experiences a loss of section, the lateral stiffness of the effective URM pier (Figure 4.5a) can be calculated based on the three-section or two-section models as shown in Figures 4.5b and 4.5c.

4.6. ELASTIC MODULUS OF MASONRY

Past research has shown that masonry displays significant nonlinear stress-strain behavior even at very low stress levels (Naraine and Sinha 1989, AlShebani and Sinha 1999). In order to consider this behavior, the following stress-strain relationship proposed by Naraine and Sinha (1989) is used in this research:

$$\sigma = \frac{f_m \varepsilon}{\varepsilon_m} \exp\left(1 - \frac{\varepsilon}{\varepsilon_m}\right) \quad (4.24)$$

where ε_m is the axial strain corresponding to the maximum compressive stress. It depends on the type of masonry units and mortar used for the construction of masonry. When no other information is available, the design values of 0.0035 for clay masonry and 0.0025 for concrete masonry provided by MSJC 530-02 can be used. σ and ε are the compressive stress and strain of masonry, respectively. Based on Eq. (4.24), the secant elastic modulus of masonry can be calculated as:

$$E = \frac{\sigma}{\varepsilon} = \frac{f_m}{\varepsilon_m} \exp\left(1 - \frac{\varepsilon}{\varepsilon_m}\right) \quad (4.25)$$

4.7. COMPARISON WITH FEMA 356

Currently, FEMA 356 (a revision of FEMA 273) represents a state-of-the-art in URM seismic design guidelines. Four separate equations for calculating the maximum

in-plane strength of a URM pier corresponding to the four primary failure modes are presented in that document. In addition, equations for calculating the strength of a URM pier corresponding to some combinations of these failure modes are also given. For simplicity, only the four primary failure modes of URM piers are used for comparisons between FEMA 356 and the effective pier model.

4.7.1. Rocking Capacity

To compare rocking strengths, a URM pier with only flexural horizontal cracks at the top and/or the bottom of the pier is assumed. As a result, Eqs (4.3) through (4.10) can be used to calculate the internal stress distribution of the pier. In order to aid in the comparison, the following relationship (given by FEMA 356) between the moments at the top and bottom of the pier is adopted:

$$M_t = (2\alpha - 1)M_b \quad (4.26)$$

where α is a factor reflecting the boundary conditions of a URM wall. For a fixed-free cantilever wall, α is taken as 0.5 and M_t is equal to zero; for a fixed-fixed pier, α is equal to 1.0 and M_t is equal to M_b .

Substituting Eq. (4.26) into Eq. (4.2) gives:

$$V = \frac{2\alpha}{h} M_b \quad (4.27)$$

Since there are flexural horizontal cracks developing at the top and/or bottom of the pier, the effective length at the top and/or bottom of the pier should be less than the length of the pier. Therefore, the moment at the bottom: M_b can be calculated by Eq. (4.5). For simplicity, the tensile strength of the bed joint is neglected. Substituting Eq. (4.5) into Eq. (4.27) gives the lateral strength of the pier in terms of vertical forces as:

$$V_r = \left(1 - \frac{2}{3} \frac{L_b}{L}\right) \alpha(P_t + G) \frac{L}{h} \quad (4.28)$$

Based on FEMA 356, the following expression gives the rocking strength of a URM pier:

$$V_r^{FEMA} = 0.9 \alpha(P_t + G) \frac{l}{h} \quad (4.29)$$

Comparing Eq. (4.28) and (4.29) it is apparent that they are identical when L_b is equal to $0.15L$. That is, FEMA 356 defines rocking as a failure mode when the horizontal flexural cracks extend through 85% of the pier's length. In contrast, the effective pier model points out that the rocking strength of a URM pier increases with the crack propagation. As an ultimate example, when the URM pier is fully cracked and l_b is equal to zero, the rocking strength predicted by Eq. (4.28) is 1.11 times the FEMA predicted value.

4.7.2. Bed-Joint Sliding Capacity

The critical shear sliding section is at either the bottom or the top of the pier depending on the values of L_{eb} and L_{et} , because the effective length is the smallest at those locations. For comparison purposes, it is assumed that $L_{eb} < L_{et} < L$, as a result, the critical shear sliding section is at the bottom of the pier. Assuming $f_t=0$, the effective length at the bottom section can be calculated from Eq. (4.5) as:

$$L_{eb} = 3 \left(\frac{L}{2} - \frac{M_b}{P_t + W} \right) \quad (4.30)$$

The average vertical stress in the effective length of bed joint is:

$$\sigma_{avg} = \frac{P_t + W}{L_{eb} \cdot t} \quad (4.31)$$

Substituting Eqs. (4.30), (4.31) and (4.8) into (4.11), and considering (4.12), the shear force at which bed-joint sliding will commence can be written as:

$$V_{bjs} = 3 \left(\frac{L}{2} - \frac{M_b}{P_t + W} \right) t \tau_0 + \mu(P_t + W) \quad (4.32)$$

Eq. (4.32) indicates that the bed-joint sliding strength of a URM pier depends on not only the vertical forces, the friction coefficients, and the initial shear strength, but also the moment applied to the pier. Specifically, the lengths of the horizontal flexural cracks, which are caused by the moment, affect the bed-joint shear strength.

As a comparison, if the safety factor is not considered, the sliding strength given by FEMA 356 is:

$$V_{bjs}^{FEMA} = 0.75 L t \tau_0 + \mu(P_t + W) \quad (4.33)$$

Comparing Eq. (4.32) and Eq. (4.33) shows that the two equations are similar. However, the equation given by FEMA 356 does not consider the effect of moment. That is, the reduction in the effective length of the pier due to the presence of horizontal flexural cracks is not considered in FEMA 356.

In order to more clearly illustrate the difference between the effective pier model and the FEMA equation, the ratio of V_{bjs}/V_{bjs}^{FEMA} is plotted vs. the vertical force eccentricity at the base, $M_b/(L(P_t + W))$, in Figure 4.6. The influence of the ratio k between the cracked bed joint shear resistance and the initial shear resistance, $\mu(P_t + W)/L t \tau_0$, is also shown in this figure. This figure shows that when the vertical force eccentricity is equal to 0.25, which corresponds to an effective length of 0.75L at

the base of the pier based on Eq. (4.5), the effective pier and the FEMA equation give the same prediction for the shear strength of the URM pier. On the other hand, when the external moment applied to the base of the pier increases, the effective pier model predicts that the shear strength of the pier decreases, because the uncracked effective length at the base of the pier becomes smaller. Figure 4.6 also shows that with increasing vertical force (P_t+W), the difference between the effective pier model and the FEMA equation becomes smaller, since the effect of the external moments becomes relatively smaller.

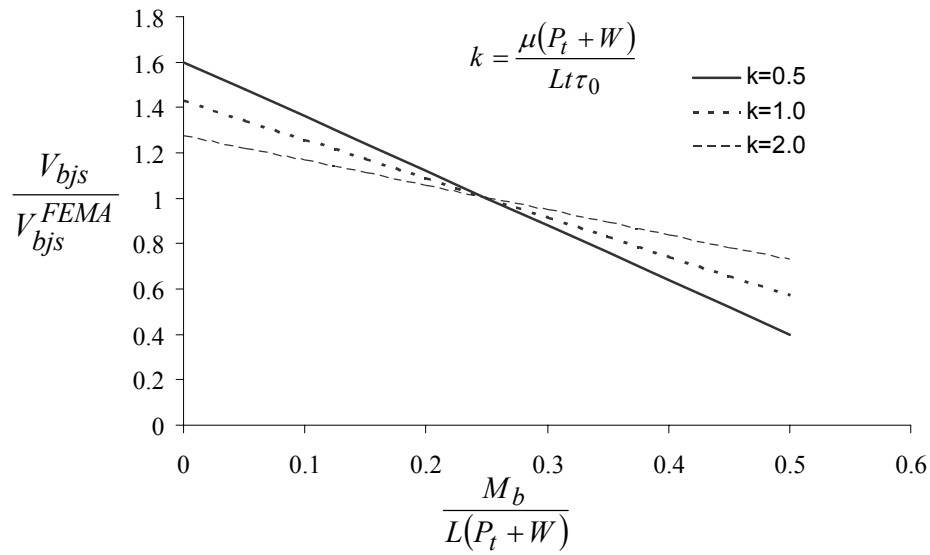


Figure 4.6. Predicted base shear strength by the effective pier model vs. FEMA 356 equation

4.7.3. Toe-Crushing Capacity

According to Inequality (4.15), toe crushing occurs when the compressive stress at the toe of the pier exceeds the compressive strength of masonry. The maximum compressive stress in a pier is determined by the greater values of the maximum compressive stresses at the top and the bottom of the pier: σ_{ct} and σ_{cb} . Again for comparison purposes it is assumed that $L_{eb} < L_{et} < L$ and $f_t=0$; therefore, according to Eq. (4.7), $\sigma_{ct} < \sigma_{cb}$. As a result, a toe crushing failure mode is controlled by the maximum compressive stress at the bottom of the pier.

Considering Eq. (4.7) and Eq. (4.30), the inequality (4.15) can be rewritten as:

$$P_t + W \geq \frac{1}{4} \left(3 - 6 \frac{M_b}{L \cdot (P_t + W)} \right) \cdot \beta L l t f_m \quad (4.34)$$

Considering again the relationship between the moment applied on the top of the pier and that applied on the bottom of the pier, substituting Eq. (4.27) into Eq. (4.34) gives the strength corresponding to toe crushing:

$$V_{tc} \geq \alpha (P_t + W) \left(\frac{L}{h} \right) \left(1 - \frac{(P_t + W)/(Lt)}{0.75 \beta f_m} \right) \quad (4.35)$$

As a comparison, the toe crushing strength given by FEMA 356 is:

$$V_{tc}^{FEMA} = \alpha (P_t + W) \left(\frac{L}{h} \right) \left(1 - \frac{(P_t + W)/(Lt)}{0.7 f_m} \right) \quad (4.36)$$

It can be seen that FEMA 356 gives a nearly identical expression for the toe-crushing strength of a URM pier, except that the value 0.7 was given instead of 0.75β . This implies that FEMA 356 assumes β is equal to 0.93. Recall that the equivalent stress

block analogy of MSJC 530-02 points out that β should be larger than 1, the equation given by FEMA 356 may underestimate the toe crushing strength of a URM pier.

FEMA 356 considers toe-crushing failure mode as a force-control action, and the value of f_m used in Eq. (4.36) should be the expected value divided by 1.6 (ATC 2000). However, as discussed before, rocking is actually a working condition of a URM pier. A URM pier always works with the opening or closing of flexural cracks under external force. Eq. (4.7) indicates that in order to obtain large compressive stress at the toe of a pier, generally a large flexural crack has already developed in the pier. Based on this consideration, it is apparent that toe crushing is actually a limit of the rocking behavior. As a result, the penalty factor 1.6 should not be employed to decrease the toe crushing strength of a URM pier.

In order to further compare the effective pier model and the FEMA 356 equation, the ratio of V_{tc}/V_{tc}^{FEMA} is plotted vs. the compressive strength increase factor β , and the normalized vertical compressive stress at the base of the pier, $r = (P_t + W)/Ltf_m$ in Figure 4.7 (the penalty factor 1.6 is not used in the FEMA 356 equation). This figure shows that with the increasing β value, the effective pier predicts higher toe crushing strength compared with the FEMA equation. On the other hand, when the vertical compressive stress at the base of the pier is smaller ($r = 0.1$), the difference between the effective pier model and the FEMA equation is small (less than 10%). With increasing base vertical compressive stress, the difference between the two methods becomes more significant.

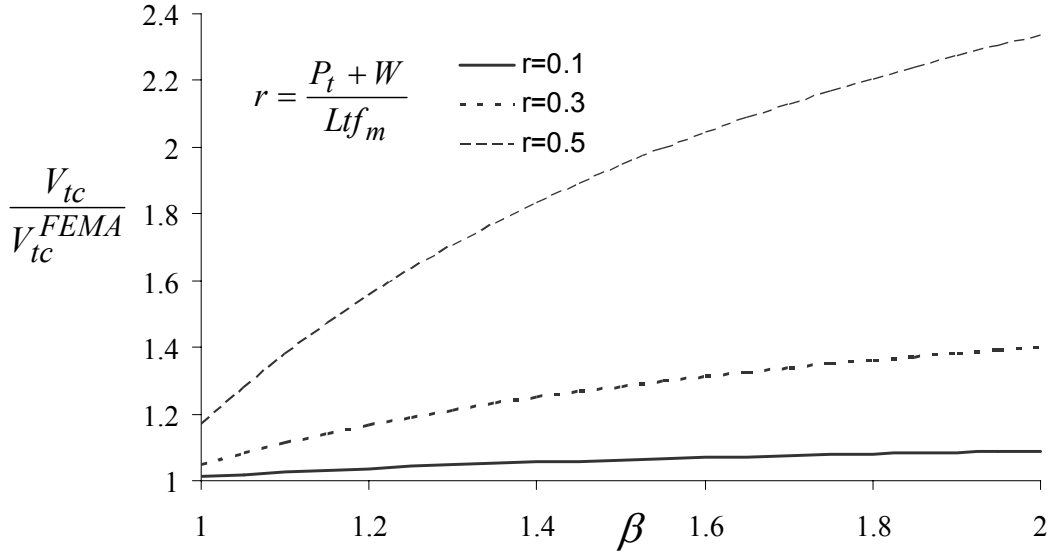


Figure 4.7. Predicted toe crushing strength by the effective pier model vs. FEMA 356 equation

4.7.4. Diagonal Tension Capacity

Eqs. (4.12), (4.17) and (4.18) express the strength corresponding to diagonal tension cracks. As the modification of FEMA 356, FEMA 306 gives the diagonal tension strength of a URM pier as:

$$V_{dt}^{FEMA} = \beta (l t f_t^d) \sqrt{1 + \frac{P_b}{l t f_t^d}} \quad (4.37)$$

where, f_t^d is the diagonal tensile strength. β is equal to 0.67 for $L/h < 0.67$, L/h when $0.67 \leq L/h \leq 1.0$, and 1.0 when $L/h > 1.0$.

Comparing between Eqs. (4.12), (4.17), (4.18) and Eq. (4.37), it is apparent that the effective pier model and FEMA 307 give different expressions. Specifically, FEMA 306 utilized a strength parameter: diagonal tensile strength, while the effective pier model

uses the compressive strength, the bed joint tensile strength, and the shear strength of masonry to determine the diagonal cracking strength of a URM pier.

To explore the validity of the FEMA equation for diagonal tension, another failure criterion, the maximum tensile stress criterion, will be employed to calculate the diagonal cracking strength. Based on this criterion, diagonal tension cracks are considered to occur when the maximum principle tensile stress in masonry is larger than the tensile strength of masonry. The criterion is:

$$\sigma_1 \geq f_t^d \quad (4.38)$$

where, σ_1 is the maximum principle tensile stress, and f_t^d is the tensile strength of masonry at an angle to the bed joint. Similar to the treatment for the effective pier model, the average vertical stress and shear stress corresponding to the inflection point level can be used to calculate the maximum principle tensile stress, which leads to:

$$\sigma_1 = \sqrt{\left(\frac{\sigma_{avg}}{2}\right)^2 + (\zeta\tau)^2} - \frac{\sigma_{avg}}{2} \quad (4.39)$$

Substituting Eq. (4.39) into Eq. (4.38), and rewriting it in terms of forces, the diagonal tension strength of a URM pier given by the maximum tensile stress criterion is:

$$V_{dt} = \frac{1}{\zeta} (L t f_t^d) \sqrt{1 + \frac{P_b}{L t f_t^b}} \quad (4.40)$$

Recalling that for a slender pier ($L/h < 0.5$), the value of $1/\zeta$ approaches 0.67; and for a stout pier ($L/h > 2$), the value of $1/\zeta$ approaches 1.0. Therefore, Eq. (4.40) actually gives the equation of FEMA 306.

Material level research has shown that the diagonal failure of masonry is a complex failure phenomenon consisting of several different failure modes. Therefore, masonry strength should not be explained simply by the maximum tensile strength. Furthermore, as discussed in Chapter 3, the exact mechanism and value of the diagonal tensile strength employed by FEMA 306 is quite difficult to determine. Considering this, the effective pier model is a more rational approach to explain the diagonal failure mechanism of URM piers compared with the FEMA method.

4.8. COMPARISON WITH EXPERIMENTAL RESULTS

Based on the effective pier model presented, a nonlinear pushover program was developed and used to analyze several test specimens of past experiments (Abrams and Shah 1992, Anthoine et al. 1995, Epperson and Abrams 1989, Magenes and Calvi 1992, Manzouri et al. 1995, Franklin et al. 2001, Erbay et al. 2002). In order to illustrate the ability of the effective pier model to predict all of the primary failure modes, a detailed comparison was made first with test specimens that exhibited primarily only one failure mode. In addition, a specimen was chosen that exhibited multiple failure modes to assess the ability of the effective pier model to predict mixed modes.

4.8.1. Rocking Behavior

The ability of the effective pier model to predict rocking and toe crushing behavior was examined by comparing results with URM brick specimen 1F tested by Franklin et al. (2001). This test pier consisted of an inverted T-section with idealized cantilever boundary conditions. The specimen had a height of 59 in, width of 33 in, and

was tested with a constant vertical stress of 42 psi. Initial cracking was observed in the bed joint at the base of the pier at 0.10% drift and 3.02 kips of lateral load. The wall exhibited typical rocking behavior until approximately 2% drift at which point toe crushing was observed. The maximum strength was 3.2 kips at 0.5% drift.

To analyze specimen 1F, the following material properties were used. First, based on the material test results, the compressive strength of masonry was set to be 1140 psi. Second, to match the initial elastic modulus value gotten from the material tests, ϵ_m was assumed as 0.005. This gives an initial elastic modulus of 620 ksi based on Eq. (4.24). Furthermore, since no other material properties are available, the initial bed-joint shear strength and the bed joints tensile strength were assumed to be 100 psi and 40 psi, respectively. Both the equivalent initial shear friction coefficient and the shear friction coefficient for the cracked bed joint were assumed to be 0.7. These values are the common values observed in many material tests and are proposed by Atkinson (1989) as the lower-bound estimate. The shear stress factor ζ was assumed to be 1.5 for the tested slender pier, and the compressive strength factor β was assumed to be 1.28 to be consistent with the equivalent stress block analogy recommended by MSJC 530-02.

The results obtained from the effective pier model predicted the initiation of rocking at a drift of 0.93% and a lateral force of 2.97 kips (Figure 4.8). The calculated maximum strength was 3.11 kips at the drift of 3.1%, as the pier was displaced past 3.1% toe crushing was predicted. The error between the calculated and measured maximum strength was 2.8%. Since the test was concluded at a maximum drift of 2.0%, the calculated lateral force-displacement curve is plotted together with the measured lateral

force-displacement envelope only up to 2% (Figure 4.8). It is apparent that the lateral force-displacement curve given by the analysis is close to that obtained from the test.

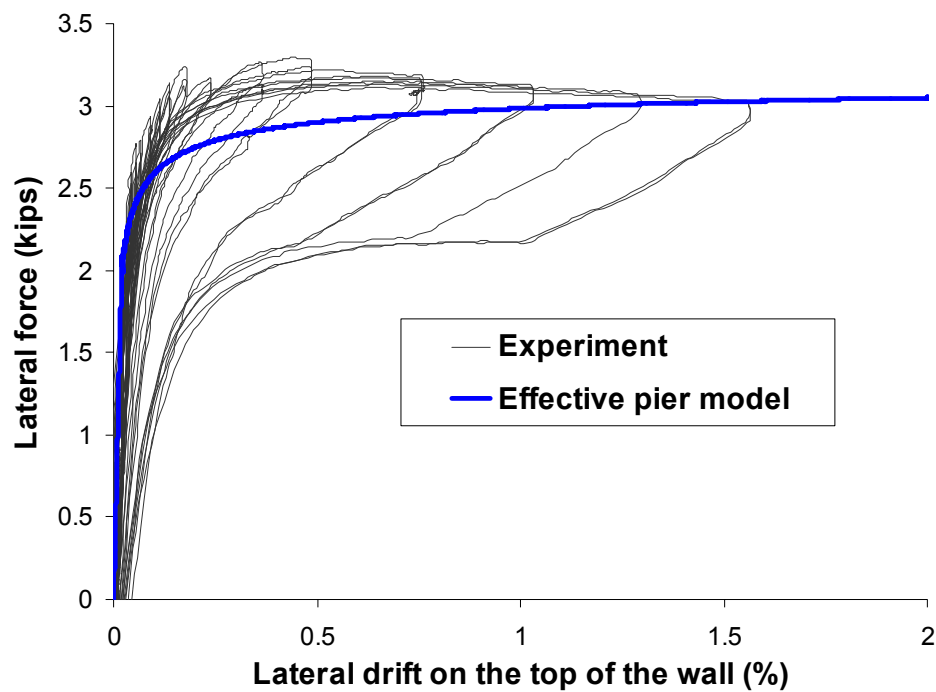


Figure 4.8. Calculated and measured lateral force – displacement curve of specimen 1F (Franklin et al. 2001)

4.8.2. Sliding Behavior

Specimen 1S tested by Erbay et al. (2002), which exhibited a typical sliding failure mode, was chosen to assess the ability of the effective pier model to predict sliding. The height and the length of the specimen were 77.0 in and 156.0 in, respectively. The pier was tested with cantilever boundary conditions and a constant vertical stress of 90 psi. Masonry properties for Specimen 1S were identical to those of

specimen 1F. Flexural cracking was observed in the bed joint at the base of the pier at about 0.02% drift. The failure modes observed for this specimen were classified as sliding degrading to toe crushing at a drift of 0.3% (Figure 4.9). The maximum strength for the specimen was 120.6 kips. The test was concluded at 0.3% drift.

The shear factor ζ was assumed to be 1.0 because the aspect ratio (h/l) of this pier was 0.5; all other assumptions about the masonry material properties are the same as for Specimen 1F. The effective pier model predicted the initiation of a flexural crack at a drift of 0.03 % and a lateral force of 54.4 kips. The calculated maximum strength was 101.2 kips at the drift of 0.29%, at which point the model predicted bed-joint sliding at the base of the pier. The error between the calculated and measured maximum strength was 16.1 %. The calculated lateral force-displacement curve is plotted together with the measured lateral force-displacement curve in Figure 4.9. The effective pier model underestimates the maximum strength of the specimen. However, it does give a fairly close prediction for the strength corresponding to the ultimate drift. The effective pier model predicted a sharp drop of the lateral strength when the pier began to slide, which was not observed in the test. Apparently, the assumed shear friction coefficient of 0.7 for the cracked surface is too low for the tested specimen. Therefore, another shear friction coefficient of 1.0 for the cracked surface was used for the analysis again. The result is also plotted in Figure 4.9, which fits better with the experimental results. The analysis cannot capture the toe crushing failure at the end of the test. However, the analysis shows that the maximum compressive stress at the toe is 1063 psi at the end of loading, which is rather close to the compressive strength of masonry (1140 psi). Therefore, it is fair to say

that a toe crushing failure is possible considering the possible variation of material properties.

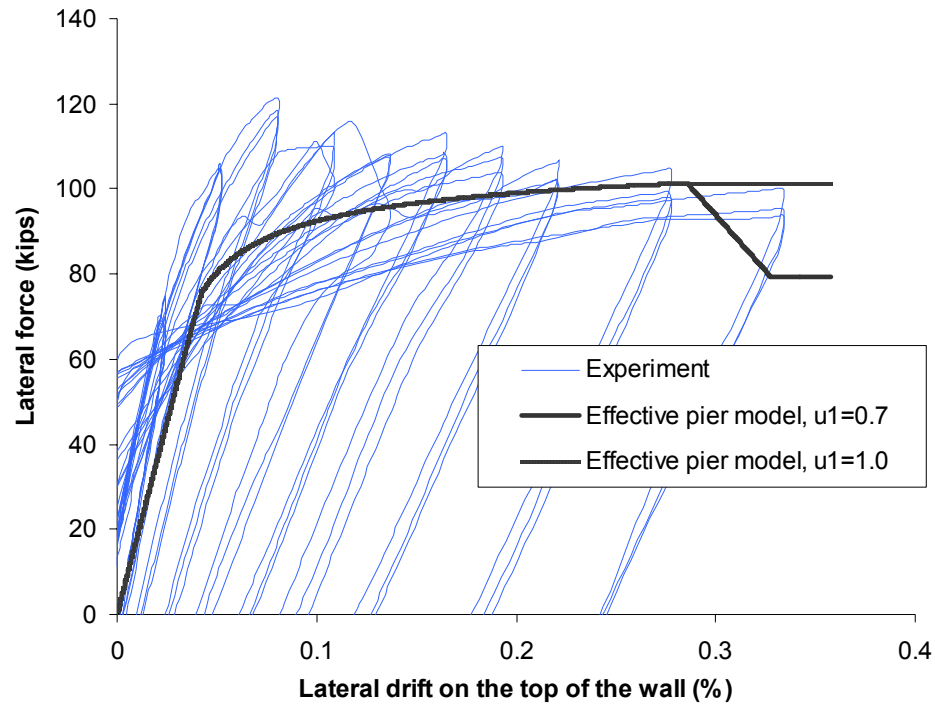


Figure 4.9. Calculated and measured lateral force – displacement curve of specimen 1S (Erbay et al. 2002)

4.8.3. Diagonal Tension Behavior

Specimen MI3 tested by Magenes and Calvi (1992) was used to assess the ability of the effective pier model to predict diagonal tension behavior. The height, length, and thickness of this specimen were 118 in, 59 in, and 15 in, respectively. The specimen was tested with fixed-fixed end conditions and a constant vertical stress of 180 psi. The reported compressive strength of the brick masonry was 1145 psi. Specimen behavior

was classified as flexural cracking degrading to diagonal tension cracking with a peak load of 41.6 kips and a final drift of 0.5%.

For analysis, the compressive strength was assumed as 1145 psi, and ε_m was assumed to be 0.01 as per FEMA 307 (ATC 1999). Furthermore, both the initial bed-joint shear strength and the bed joint tensile strength were all assumed to be 40.0 psi. Both the initial equivalent bed joint friction coefficient and the shear friction coefficient for the cracked bed joints were taken as 0.81. All the values are consistent with reported values (ATC 1999). The compressive strength-increase factor β was assumed to be 1.28 and the shear factor ζ was assumed to be 1.5.

The calculated lateral force-displacement curve is plotted together with the measured lateral force-displacement envelope in Figure 4.10. The effective pier model predicted that the initial flexural crack initiates at a drift of 0.083 % and a lateral force of 31.0 kips. The analysis also predicted that the specimen would fail due to diagonal tension cracking with a maximum strength of 51.3 kips and a drift of 0.18%. The calculated maximum strength is 19% larger than the measured value. It should be pointed out that the analysis showed that the diagonal cracking is the compression type diagonal cracking. Therefore, the strength of the specimen dropped quickly after it reached its peak point.

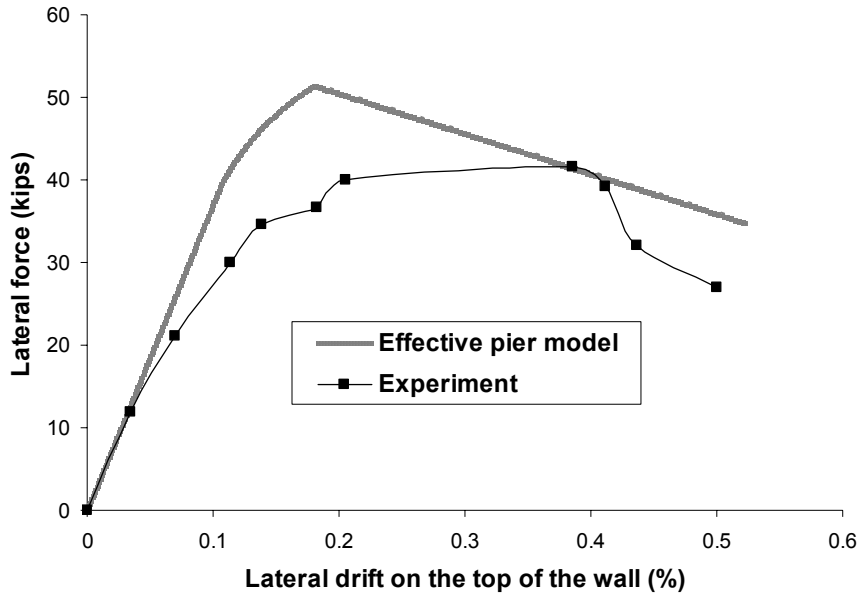


Figure 4.10. Calculated and measured lateral force – displacement curve of specimen MI3 (Magenes and Calvi 1992)

4.8.4. Mixed Modes Behavior

Specimen W1 tested by Manzouri et al. (1995) was used to investigate the ability of the effective pier model to predict mixed failure modes. The height, length, and thickness of this specimen were 60 in, 102 in, and 13 in, respectively. The specimen was tested as a cantilever column with constant vertical stress of 150 psi. The reported compressive strength of masonry was 2000 psi. No other material properties were reported. Specimen behavior was characterized as flexural cracking at 88 kips degrading to toe crushing and eventually bed-joint sliding at 156 kips with a final drift of 1.3%.

Since no other material properties were reported, the properties of masonry were taken as those assumed in FEMA 307. Specifically, ϵ_m was taken as 0.01 and the initial bed-joint shear strength and the bed joint tensile strength were assumed to be 85 psi and

40 psi, respectively. Both the initial equivalent bed joint friction coefficient and the shear friction coefficient for the cracked bed joints were taken as 0.7. The compressive strength factor β was assumed to be 1.2 and the shear stress factor ζ was assumed to be 1.0 for the tested stout pier.

The calculated lateral force-displacement curve is plotted together with the measured lateral force-displacement envelope in Figure 4.11. The analysis predicted the initiation of a flexural crack at a drift of 0.046% and a lateral force of 73.3 kips. The model also predicts the specimen will display toe crushing at a drift of 0.66% and a lateral force of 156 kips. As the specimen is displaced further the model predicted that specimen would begin to rock at a drift of 0.74% and a lateral force of 156.7 kips. Finally the specimen would slide along the bed joint at a drift of 0.92% and a lateral force of 158.4 kips, which also corresponded to the maximum strength of the specimen. The effective pier model correctly captured the mixed failure modes and predicted the lateral force-displacement envelope of the tested specimen accurately.

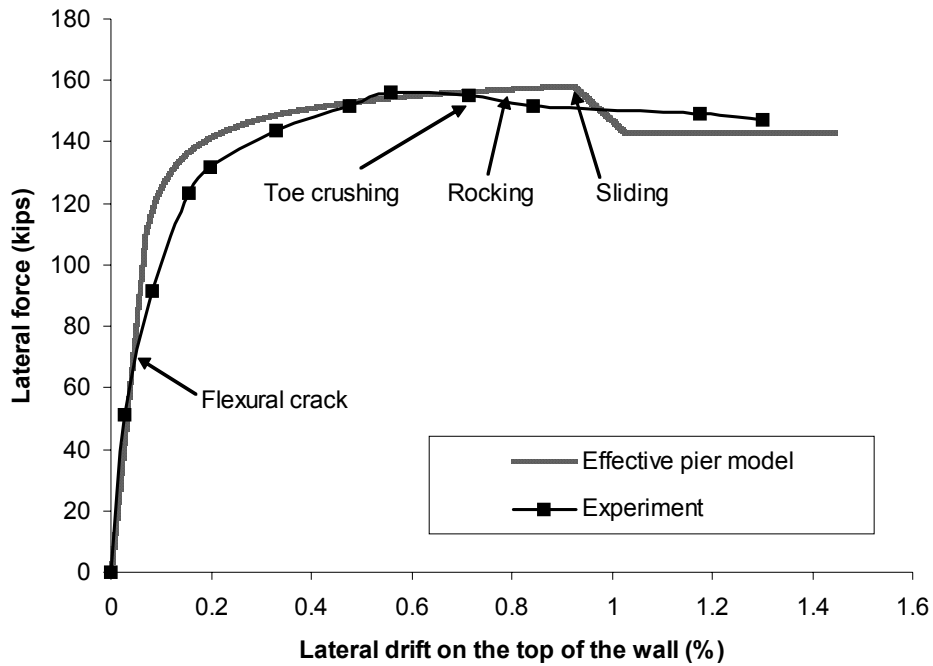


Figure 4.11. Calculated and measured lateral force – displacement curve of specimen (W1, Manzouri et al. 1995)

4.8.5. Comparison with other experimental results

Several other URM piers investigated in past experiments were analyzed using the effective pier model. Both the experimental and analytical results are given in Table 4.1. The difference between the experimental and analytical results was also expressed by the ratio of analytical minus experimental results divided by the experimental results (termed “error”). The majority of the tests chosen for comparison were summarized in FEMA 307 (ATC 1999). The material properties used for the analyses were consistent with those given or assumed in FEMA 307 (ATC 1999). Table 4.1 shows that the maximum strengths predicted by the effective pier model are consistently within +/-30% of the experimentally determined values. Considering the lack of reported material properties for many of these specimens, this error is relatively small. Furthermore, in

some of the experiments, the applied axial load varied significantly from the desired nominal values; applied axial load greatly affects the lateral capacities (FEMA 307, ATC 1999).

In addition, Table 4.1 shows that the effective pier model correctly predicted the failure modes of 16 of the 21 test piers. It should be pointed out that some researchers reported rocking failure modes while others reported flexural cracking. As pointed out by the effective pier model, there is no clear distinction between rocking and flexural cracking. Furthermore, researchers reported two different types of diagonal cracking. The first type was the traditional diagonal cracking through masonry units while the second type was classified as stair-stepped bed-joint sliding. For weak mortar-strong unit masonry, it is very difficult to identify the cause of a stair-stepped bed-joint sliding failure since both the maximum principle tension stress as well as the bed-joint shear stress can cause this behavior.

Table 4.1. Comparison between test results and the effective pier model

Test Specimens	Maximum Strength: kips (kN)			Failure Modes	
	Exp. Results	EFP Model	Error (%)	Exp. Results	Effective pier model
High Wall (Anthoine et al 1995)	16.2 (72.1)	15.2 (67.6)	-6.8	Rocking	Flexural cracking ending with toe crushing
1F (ST-6)	3.38 (15.0)	3.1 (13.8)	-8.8	Rocking	Flexural cracking ending with rocking
2F (ST-6)	1.85 (8.2)	1.96 (8.7)	5.9	Rocking	Flexural cracking ending with rocking
6F (ST-6)	5.85 (26.0)	5.82 (25.9)	-0.5	Rocking	Flexural cracking, then toe crushing, then rocking

Table 4.1. (cont'd)

Test Specimens	Maximum Strength: kips (kN)			Failure Modes	
	Exp. Results	EFP Model	Error (%)	Exp. Results	Effective pier model
MI4 (Magenes and Calvi 1992)	34.4 (153.0)	33.8 (150.4)	-1.7	Stair-stepping bed joint sliding	Flexural cracking, then diagonal tension cracking
W1 (Abrams and Shah 1992)	92 (409.2)	80.7 (359.0)	-12.3	Bed joint sliding	Flexural cracking, then toe crushing, then sliding
MI2 (Magenes and Calvi 1992)	51 (226.9)	46.4 (206.4)	-9.0	Bed joint sliding at top course, then stair-stepped bed-joint sliding	Flexural cracking, then diagonal tension cracking
IS (ST-6)	121.2 (539.1)	101.2 (450.2)	-16.5	Bed Joint sliding	Flexural cracking, then sliding
W1 (Manzouri et al. 1995)	156 (693.9)	156.3 (695.3)	0.2	Toe crushing, then bed joint sliding	Flexural cracking, then toe crushing, then rocking, then sliding
W2 (Manzouri et al. 1995)	68 (302.5)	63.4 (282.0)	-6.8	Toe crushing, diagonal cracking, then bed joint sliding	Flexural cracking, then rocking
W3 (Manzouri et al. 1995)	80 (355.9)	79 (351.4)	-1.3	Toe crushing, then bed joint sliding	Flexural cracking, then sliding
W3 (Abrams and Shah 1992)	20 (89.0)	14.2 (63.2)	-29.0	Rocking then toe crushing	Flexural cracking, then rocking, then toe crushing
Low Wall (Anthoine et al. 1995)	18.8 (83.6)	18.3 (81.4)	-2.7	Diagonal tension	Flexural cracking, then diagonal tension cracking
MI3 (Magenes and Calvi 1992)	41.6 (185.1)	47 (209.1)	11.0	Diagonal tension	Flexural cracking, then diagonal tension cracking
MI 1 (Magenes and Clavi 1992)	58.2 (258.9)	62.1 (276.2)	6.7	Diagonal tension	Flexural cracking, then diagonal tension cracking

Table 4.1. (cont'd)

Test Specimens	Maximum Strength: kips (kN)			Failure Modes	
	Exp. Results	EFP Model	Error (%)	Exp. Results	Effective pier model
W2 (Abrams and Shah 1992)	44 (195.7)	32.1 (144.1)	-26.4	Toe crushing	Flexural cracking, then rocking, then toe crushing
E1 (Epperson and Abrams 1989)	120 (533.8)	123.4 (548.9)	2.8	Toe crushing	Flexural cracking, then toe crushing, then rocking
E3 (Epperson and Abrams 1989)	164 (729.5)	198.4 (882.5)	21.0	Toe crushing	flexural cracking, then toe crushing, then rocking
E5 (Epperson and Abrams 1989)	154 (685.0)	164.4 (731.3)	6.8	Toe crushing	Flexural cracking, then rocking
E6 (Epperson and Abrams 1989)	150 (667.2)	154.9 (689.0)	3.3	Toe crushing	Flexural cracking, then rocking
E7 (Epperson and Abrams 1989)	157 (698.4)	186.9 (831.4)	19.0	Toe crushing	Flexural cracking, then rocking, then toe crushing

4.9. CONCLUSIONS

A macro-model termed the effective pier model was established to describe the nonlinear in-plane behavior of individual URM piers. With some simplifications to the model, strength expressions were derived for URM piers corresponding to each of the four primary failure modes. These strength expressions were in close agreement with FEMA 356.

On the other hand, compared with FEMA 356, the effective pier model provided different explanations for the four primary failure modes. The effective pier model showed that the rocking mechanism was actually a normal working mechanism of URM piers and that the toe-crushing failure mode was actually a limit for the rocking mechanism. Therefore, the penalty factor adopted by FEMA for the toe crushing failure mode should not be used, and the design toe crushing strength of a URM pier should be increased.

A nonlinear pushover analysis program based on the effective pier model was developed and used to analyze 21 URM piers investigated in previous experiments. Strength, force-displacement behavior and failure modes were all in close agreement with observed behavior. The effective pier model was able to accurately describe both single and mixed failure modes of URM piers, which cannot be modeled by current analytical procedures, such as the one outlined by FEMA 356.

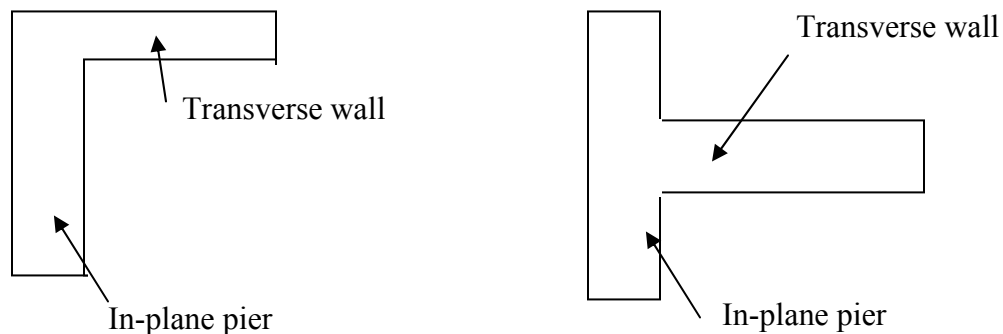
The effective pier model developed in this chapter can be embedded into a pushover analysis program and used to analyze the nonlinear behavior of perforated URM walls. With minor modifications the effective pier model can account for flange effects, which have been shown to be substantial in certain cases (Moon et al. 2003, Yi et al. 2003).

CHAPTER 5

FLANGE EFFECTS FOR THE NONLINEAR BEHAVIOR OF INDIVIDUAL URM PIERS

5.1. INTRODUCTION

Numerous experimental projects and analytical studies have been conducted on the nonlinear in-plane behavior of URM piers. An effective pier model, proposed in the previous chapter to illustrate the nonlinear behavior of rectangular-section URM piers, has been shown to give good agreement with previous experimental results. However, some URM piers in a URM building do not have a rectangular section, such as the piers at the corner of the building (Figure 5.1a) or those connected with an adjacent interior wall (Figure 5.1b). Obviously, these adjacent transverse walls will move together with the in-plane piers during dynamic excitation, and thus possibly increase both the initial stiffness and maximum strength of the in-plane piers.



(a) URM pier at the corner

b) URM pier connected with adjacent interior wall

Figure 5.1. Non-rectangular URM pier section

Although several experimental research projects have been conducted on the effects of transverse walls on the response of in-plane walls at the structural level (Tomazevic et al. 1993, Costley and Abrams 1996, Paquette and Bruneau 1999), the current literature review reveals that little research has been done for the effects of transverse walls on the response of an individual pier. This lack of research hinders the full understanding of the effects of the transverse walls. The effective pier model proposed in the previous chapter is modified in this chapter to account for the contribution of adjacent transverse walls to the response of in-plane walls.

5.2. MODIFICATION OF THE EFFECTIVE PIER MODEL TO CONSIDER THE FLANGE EFFECTS

5.2.1. Basic assumptions

A typical URM pier with a transverse wall is shown in Figure 5.2. The height, length, and thickness of the in-plane pier are h , L , and t , respectively. The height and thickness of the transverse wall are h and t_f , respectively. The length of the transverse wall is L_f .

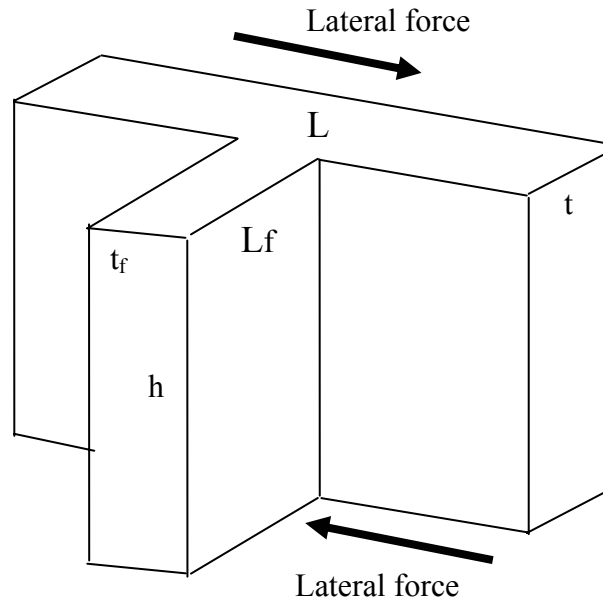


Figure 5.2. A typical URM pier with transverse wall

The existence of the transverse wall significantly increases the complexity of the response of the URM pier. In order to modify the effective pier model to illustrate the nonlinear behavior of this non-rectangular section URM pier, several assumptions have to be made:

- Although it is recognized that the response of a non-rectangular pier is no longer purely in-plane, the possible torsional behavior is ignored. In general, the resultants of the external forces don't necessarily go through the shear center of this non-rectangular section, and thus torsion will be induced. However, ignoring these torsional forces will not introduce a significant error since in most cases the pier is laterally supported by the floor system and large torsional deformations are prevented.

- A length of L_f is assumed for the transverse wall. However, in many cases the length of the transverse wall will be very long compared with the height of the in-plane pier. For such cases, only part of the transverse wall will participate in the response of the in-plane pier. Therefore, an effective length of L_f has to be determined. It is assumed herein that the long transverse wall will crack prior to the failure of the in-plane pier, and the corresponding effective length (L_f) can be calculated based on the crack pattern in the transverse wall. The determination of the effective flange width L_f is discussed in Section 5.5.
- The connection between the in-plane pier and the transverse wall is assumed strong enough to ensure the two walls work together as a single pier.
- External forces are applied in the plane of the in-plane pier.
- The assumptions used for the rectangular-section URM pier effective model, such as the linear vertical stress distribution in the section, still apply.

5.2.2. Effective length and internal stress distribution

The externally applied forces and the dimensions for a URM pier with a transverse wall are illustrated in Figure 5.3. V is the applied shear force; P_t is the axial force applied at the top of the URM pier; P_b is the axial force applied at the bottom of the pier; M_t is the moment applied at the top of the pier about the inertia center of the entire section; M_b is the moment applied at the bottom of the pier about the inertia center of the entire section; W is the self weight of the in-plane pier; and W_f is the self weight of the transverse wall. The distance between the center of the transverse wall and the

compression edge at the bottom of the pier is a_f ; the distance between the inertia center and the edge of the entire section is a_i ; the section area of the transverse wall is A_f .

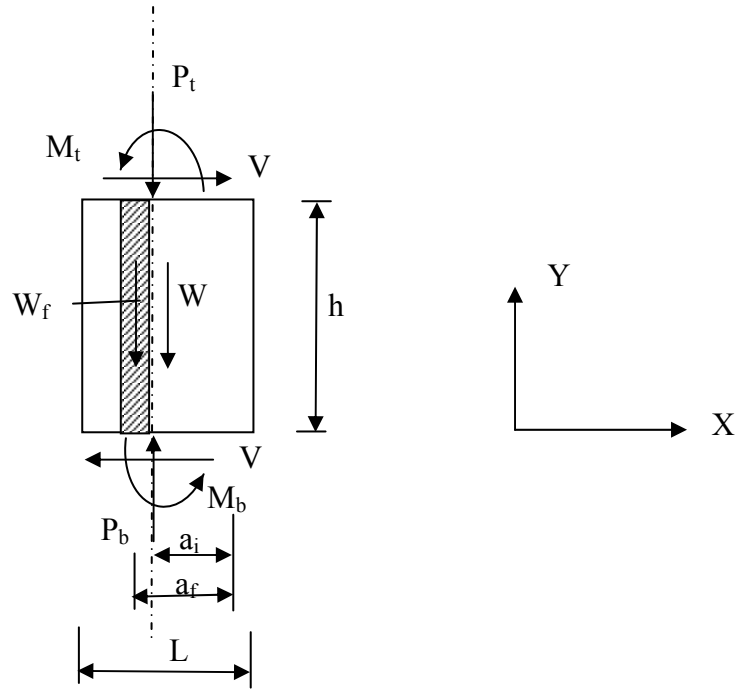


Figure 5.3. External forces applied on a non-rectangular section URM pier

The equilibrium equations give:

$$P_b = P_t + W + W_f \quad (5.1)$$

$$V \cdot h = M_t + M_b \quad (5.2)$$

Similar to the effective pier model for a rectangular section URM pier, the stress distribution and the length of the effective section at both the top and the bottom of the non-rectangular section URM pier can be calculated based on the equilibrium equations and the linear vertical stress distribution assumption. Taking the bottom section for

example, assuming that the effective length L_e is less than the length of the in-plane pier and the transverse wall is within the effective length, the vertical force and the flexural moment can be calculated based on the internal vertical stress distribution as:

$$P_b = \frac{1}{2}(\sigma_{n \max} - f_t)L_e t + A_f \left[\sigma_{n \max} - \frac{f_t + \sigma_{n \max}}{L_e}(a_f) \right] \quad (5.3)$$

$$M_b = \frac{1}{6}L_e^2 t \left(\frac{\sigma_{n \max} + f_t}{2} \right) + \frac{1}{2}(\sigma_{n \max} - f_t)L_e t \cdot \left(a_i - \frac{L_e}{2} \right) + A_f \left[\sigma_{n \max} - \frac{f_t + \sigma_{n \max}}{L_e}(a_f) \right] \cdot (a_i - a_f) \quad (5.4)$$

where $\sigma_{n \max}$ is the maximum compressive stress in this section. Solving Eqs. (5.3) and (5.4) simultaneously gives L_e and $\sigma_{n \max}$. If the value of calculated L_e is smaller than a_f , the transverse wall is out of the effective length. In this case the values of L_e and $\sigma_{n \max}$ have to be recalculated by the following equations:

$$P_b = \frac{1}{2}(\sigma_{n \max} - f_t)L_e t \quad (5.3b)$$

$$M_b = \frac{1}{6}L_e^2 t \left(\frac{\sigma_{n \max} + f_t}{2} \right) + \frac{1}{2}(\sigma_{n \max} - f_t)L_e t \cdot \left(a_i - \frac{L_e}{2} \right) \quad (5.4b)$$

On the other hand, if the value of calculated L_e based on Eqs. (5.3) and (5.4) is larger than L , the entire section is uncracked. In this case, $L = L_e$, and the maximum compressive stress $\sigma_{n \max}$ can be calculated as:

$$P_b = \frac{1}{2}(\sigma_{n \max} - \sigma_t)Lt + A_f \left[\sigma_{n \max} - \left(\frac{\sigma_t + \sigma_{n \max}}{L} \right) a_f \right] \quad (5.3c)$$

$$\begin{aligned}
M_b = & \frac{1}{6} L^2 t \left(\frac{\sigma_{n \max} + \sigma_t}{2} \right) - \frac{1}{2} (\sigma_{n \max} - \sigma_t) L t \cdot \left(a_i - \frac{L}{2} \right) \\
& + A_f \left[\sigma_{n \max} - \left(\frac{\sigma_t + \sigma_{n \max}}{L} \right) a_f \right] \cdot (a_i - a_f)
\end{aligned} \tag{5.4c}$$

where σ_t is the maximum vertical tensile stress at the tensile side of the section.

After the effective length of this section is determined by the above equations, the average shear stress over this effective length can be simply calculated by:

$$\tau = \frac{V}{L_e t} \tag{5.5}$$

Note that the transverse wall is ignored for the shear stress distribution. This simplification is based on the fact that the thickness of the transverse wall parallel to the loading direction is very small compared with the in-plane panel.

Similarly, the effective length and the stress distribution at the top of a URM pier can also be calculated based on Eqs. (5.3a) through (5.5). For the rest of the pier, the length of the effective section can be determined by linearly interpolating between the effective sections at the top and bottom of the pier to the original pier boundaries at the points with a cracking moment of M_{cr} . Once the effective section is determined, the axial stress and shear stress at any level can be calculated following the same procedure as for the original model.

5.2.3. Failure criteria

After the internal stress distribution in a non-rectangular section URM pier is obtained, the same failure criteria employed in Chapter 4 can be applied to calculate the

possible failure mechanism of the URM pier. However, the following issues should be required attention:

- When dealing with a bed joint shear failure mode, the calculation of the average vertical compressive stress on the bed joint σ_{avg} should include the possible effects of the transverse walls. Therefore,

If $L_e \geq a_f$,

$$\sigma_{avg} = \frac{P}{L_e t + A_f} \quad (5.6a)$$

Otherwise,

$$\sigma_{avg} = \frac{P}{L_e t} \quad (5.6b)$$

- When toe crushing leads to a decrease of the effective length, the effective length of the section should be recalculated based on the reduced section and the equilibrium equations. For example, if a length of L_{crush} is lost at the compression side of the bottom section due to toe crushing and the transverse wall is assumed to still be within the effective length, the effective length at the bottom section can be calculated by:

$$P_b = \frac{1}{2}(\beta f_m - f_t)L_e t + A_f \left[\beta f_m - \frac{f_t + \beta f_m}{L_e} (a_f - L_{crush}) \right] \quad (5.7)$$

- It is assumed that a possible diagonal tensile failure will occur only in the in-plane wall. Therefore, three representative stresses at the mid-height of a UMR pier, which include the average vertical compressive stress σ_{avg} , the average lateral confining stress $\sigma_{lateral}$, and the average shear stress τ , can be used to check the

diagonal tensile failure. Elastic mechanics theory shows that the shear stress in a transverse wall is small under lateral shear force. As a result, the calculation of the average shear stress and the average lateral confining stress ignores the contribution of the transverse wall, and is thus the same as that for the rectangular section pier. The calculation of the average vertical compressive stress should include the contribution of the transverse wall, and is:

$$\sigma_{avg} = \frac{P}{Lt + A_f} \quad (5.8)$$

5.2.4. Deformation of URM pier

The deformation of a non-rectangular section URM pier can be calculated following the same procedure as that for a rectangular section URM pier. A three-section or two-section vertical effective pier can be used to calculate the flexural and shear deformations. Again, the lateral stiffness of the pier (K) is dependant on the dimensions, boundary conditions, elastic and shear moduli of the pier. The initial elastic stiffness can be calculated as:

$$K = \frac{1}{\frac{h^3}{\zeta EI} + \frac{h}{GA}} \quad (5.9)$$

where, ζ is a coefficient that describes the boundary conditions of the pier (ζ is equal to 12 for fixed–fixed end conditions, and 3 for cantilever end conditions); E is the elastic modulus of masonry; G is the shear modulus of masonry, which is taken as $0.4E$; I is the moment of inertia of this non-rectangular section; and A is its section area.

5.3. THE ULTIMATE STRENGTHS CORRESPONDING TO FOUR TYPICAL FAILURE MECHANISMS OF A URM PIER CONSIDERING FLANGE EFFECTS

In order to investigate the effects of transverse wall on the lateral strength of a non-rectangular section URM pier, the maximum strengths corresponding to four primary failure modes of a cantilever URM pier are calculated based on the modified effective pier model.

5.3.1. Rocking Capacity

To simplify the problem, the bed joint tensile strength is assumed to be zero. Meanwhile, the transverse wall is first assumed to lie within the effective length. Therefore, the equilibrium equations at the base of the pier can be derived from Eqs. (5.3) and (5.4) as the follows:

$$P_b = \frac{1}{2} \sigma_{n \max} L_e t + A_f \left[\sigma_{n \max} - \frac{\sigma_{n \max}}{L_e} a_f \right] \quad (5.3d)$$

$$M_b = \frac{1}{6} L_e^2 t \frac{\sigma_{n \max}}{2} + \frac{1}{2} \sigma_{n \max} L_e t \cdot \left(a_i - \frac{L_e}{2} \right) + A_f \left[\sigma_{n \max} - \frac{\sigma_{n \max}}{L_e} a_f \right] \cdot (a_i - a_f) \quad (5.4d)$$

Note that the lateral shear force for this URM pier can be explained in terms of the flexural moment at the bottom of the pier as:

$$V = \frac{M_b}{h} \quad (5.10)$$

Solving Eqs. (5.3d), (5.4d), and (5.10) simultaneously gives the lateral strength of the pier in terms of vertical forces as:

$$V = \frac{1}{h} P_b \frac{\frac{1}{2} L_{eb} a_i t - \frac{1}{6} L_{eb}^2 t + (a_i - a_f) A_f \left(1 - \frac{a_f}{L_{eb}}\right)}{\frac{L_{eb} t}{2} + A_f \left(1 - \frac{a_f}{L_{eb}}\right)} \quad (5.11)$$

where L_{eb} is the effective length at the bottom of the pier.

If the area of the transverse wall is zero, the non-rectangular section pier reverts to a rectangular section pier, and Eq. (5.11) reduces to:

$$V = \left(1 - \frac{2}{3} \frac{L_{eb}}{L}\right) (P_t + W) \frac{L}{2h} \quad (5.12)$$

Eq. (5.12) is the same as Eq. (4.28) given in the previous chapter for a rectangular section pier.

If the transverse wall is at the compressive toe of the pier, then

$$a_f = 0 \quad (5.13)$$

Noticing that the inertia center of the non-rectangular section is determined by:

$$a_i = \frac{W_f \cdot a_f + 0.5W \cdot L}{W_f + W} \quad (5.14)$$

and introducing the ratio between the section area of the transverse wall to the in-plane panel as:

$$\psi = A_f / (Lt) = W_f / W \quad (5.15)$$

and substituting Eqs. (5.13), (5.14), and (5.15) into Eq. (5.11) yields:

$$V = \left(\frac{W}{W + W_f} - \frac{2}{3} \cdot \frac{(L_{eb}/L)^2}{L_{eb}/L + 2\psi} \right) (P_t + W + W_f) \frac{L}{2h} \quad (5.16)$$

If the transverse wall is not within the effective length, the equilibrium equations have to follow Eqs. (5.3b) and (5.4b), which can be simplified as:

$$P_b = \frac{1}{2} \sigma_{n \max} L_e t \quad (5.3e)$$

$$M_b = \frac{1}{12} L_e^2 t \sigma_{n \max} + \frac{1}{2} \sigma_{n \max} L_e t \cdot \left(a_i - \frac{L_e}{2} \right) \quad (5.4e)$$

Solving Eqs. (5.3e), (5.4e), and (5.10) simultaneously gives the lateral strength of the pier in terms of vertical forces as:

$$V = \left(\frac{a_i}{L} - \frac{1}{3} \cdot \frac{L_b}{L} \right) (P_t + W + W_f) \frac{L}{h} \quad (5.11b)$$

As an example, when the transverse wall is at the heel side of the pier,

$$a_f = L \quad (5.13b)$$

Considering Eqs. (5.13b) and (5.14), Eq. (5.11b) can be simplified as:

$$V = \left(1 - \frac{2}{3} \cdot \frac{L_b}{L} + \frac{W_f}{2(W_f + W)} \right) (P_t + W + W_f) \frac{L}{2h} \quad (5.17)$$

Comparing Eqs. (5.12), (5.16), and (5.17), it can be seen that the rocking strength of a non-rectangular URM pier is affected by the transverse wall. Specifically, Eq. (5.17) shows that when the transverse wall is at the heel side of a pier, the rocking strength of the pier is remarkably increased.

Eq. (5.17) also indicates that the contribution of a transverse wall to the rocking strength of a URM pier increases with the decreasing of effective length (L_{eb}). When the effect length at the base of the URM pier is zero, the contribution of the transverse wall reaches maximum, and the corresponding rocking strength of a cantilever URM pier can be derived from Eq. (5.11b) as:

$$V_{rock} = \left(1 + 2\psi \frac{a_f}{L} \right) \bar{V}_{rock} \quad (5.18)$$

where \bar{V}_{rock} is the rocking strength of a cantilever URM pier without transverse wall.

The effects of a transverse wall on the rocking strength of a URM pier, which are shown by Eqs. (5.11) and (5.11b), are also illustrated in terms of the non-dimensional

values $\frac{a_f}{L}$ vs. $\frac{V}{\frac{W}{W_f + W} P_b \frac{L}{2h}}$ in Figures. 5.4 and 5.5. In Figure 5.4, the effective length

at the bottom of the pier is assumed to be zero. This can be considered as the ultimate state of rocking. In Figure 5.5, the effect length at the bottom of the pier is assumed to be 0.15l, which is the value adopted by FEMA 356.

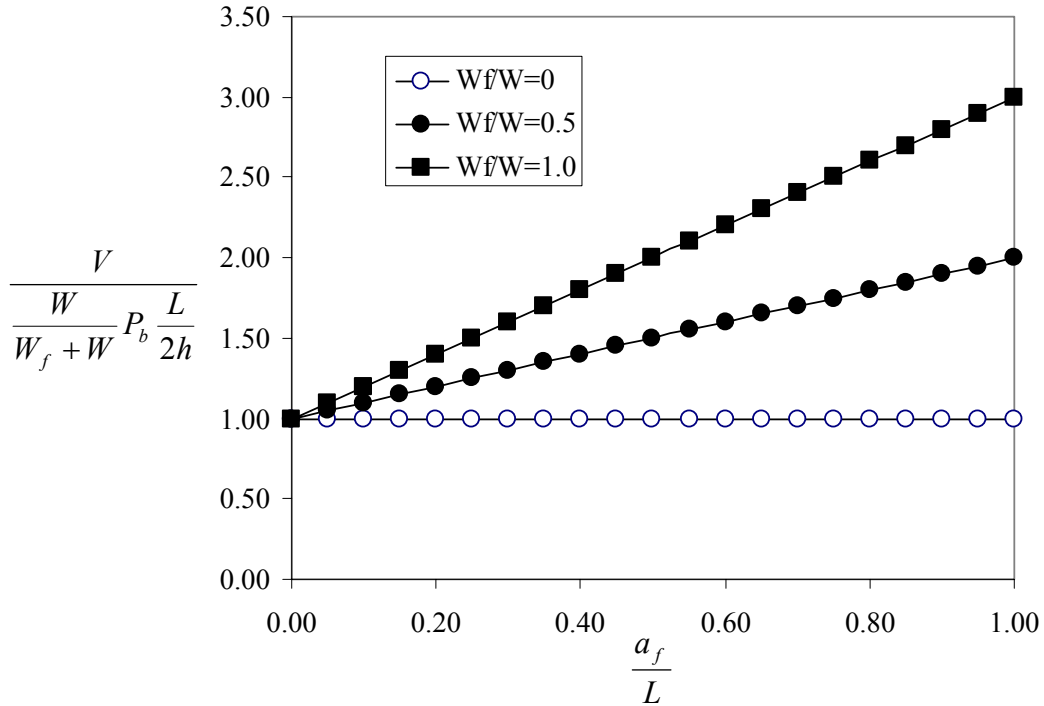


Figure 5.4. Contribution of transverse wall to the rocking strength of a URM pier with zero effective length

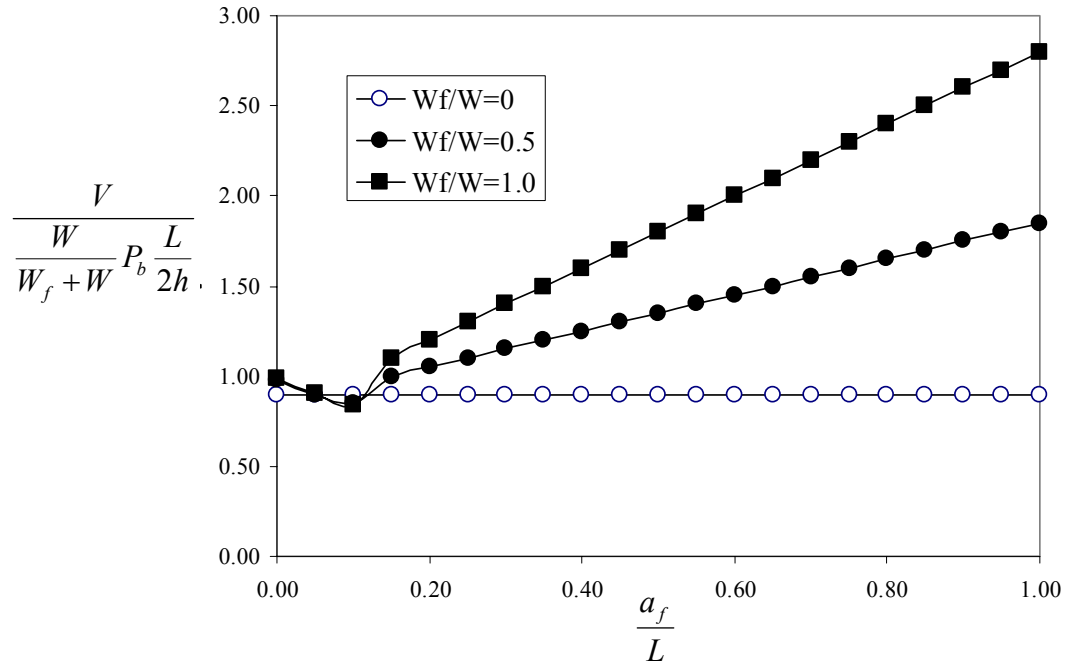


Figure 5.5. Contribution of transverse wall to the rocking strength of a URM pier with the effective length of $0.15L$

Figure 5.4 shows that the effect of a transverse wall is dependent on its weight and its location with respect to the compression toe. The larger the weight of the transverse wall is, the more significant its effect is. On the other hand, when the transverse wall is at the compressive toe, it has no contribution to the rocking strength of the URM pier. When the transverse wall moves away from the compression toe, the rocking strength of the pier increases in a linear fashion. Specifically, when the transverse wall is at the heel end ($\frac{a_f}{L}=1.0$), the model gives the largest increase in the rocking strength.

Figure 5.5 gives similar trends for the flange effects of the transverse wall on the rocking strength of a URM pier as those shown in Figure 5.4. However, the increment in the rocking strength due to the transverse wall is slightly smaller when compared with Figure 5.4. This is due to the fact that the lever arm from the transverse wall to the rocking center is smaller in Figure 5.5.

5.3.2. Bed-Joint Sliding Capacity

As discussed in the previous chapter, there are two different types of bed joint sliding capacities, which are the bed joint sliding capacity for an uncracked bed joint and the bed joint sliding capacity for a cracked bed joint. If the bottom section of a cantilever URM pier has fully cracked during previous loading, the bed joint sliding strength of this URM pier depends only on the vertical compressive force and the shear friction. In this case, the bed joint sliding capacity for a URM pier with a transverse wall can be calculated as:

$$V_{sliding} = \mu_1 \cdot (P_t + W + W_f) \quad (5.19)$$

Eq. (5.19) shows that the additional weight due to the transverse wall increases the sliding capacity of a cracked URM bed joint.

On the other hand, for an uncracked bed joint surface, the bed joint sliding strength is determined by not only the vertical compressive force and the initial internal shear friction coefficient, but also the uncracked bed joint area:

$$V = A_e \tau_0 + \mu(P_t + W + W_f) \quad (5.20)$$

In order to calculate the effective area at the bottom section of a URM pier, the effective length L_e has to be calculated first by solving Eqs. (5.3b) and (5.4b) or Eq.

(5.3d) and (5.4d). After obtaining L_e , the effective area at the bottom section A_e can be calculated as:

If $L_e \geq a_f$,

$$A_e = L_e t + A_f \quad (5.21a)$$

Otherwise,

$$A_e = L_e t \quad (5.21b)$$

As an example, when the transverse wall is not within the effective length, the bed joint sliding capacity for a cantilever URM pier can be calculated from Eqs. (5.11b), (5.20), and (5.21b) as:

$$V_{sliding} = \frac{\mu(P_t + W + W_f) + 3a_i t \tau_0}{1 + \frac{3ht\tau_0}{(P_t + W + W_f)}} \quad (5.22)$$

Eq. (5.22) shows again the increase in shear sliding capacity of a URM pier with the added weight of the transverse wall. On the other hand, Eq. (5.22) also indicates that the shear sliding capacity increases when the transverse wall moves away from the compression toe (increasing a_i).

When the transverse wall is within the effective length, the bed joint sliding capacity for a cantilever URM pier can be obtained similarly from Eqs. (5.11), (5.20), and (5.21a). However, no closed-form solution can be obtained from these equations and a numerical technique has to be utilized to obtain a solution.

It needs to be pointed out that for a URM building under seismic excitation, the cyclic nature of the seismic load usually leads to fully cracking of bed joint prior to any

sliding occurring. In this case, the contribution of the transverse wall to the sliding strength of a URM pier can be rewritten from Eq. (5.19) as:

$$V_{sliding} = (1 + \psi) \bar{V}_{sliding} \quad (5.23)$$

where $\bar{V}_{sliding}$ is the sliding strength of a cantilever URM pier without transverse wall.

5.3.3. Toe-Crushing Capacity

As discussed in the previous chapter, toe crushing occurs when the compressive stress at the toe of the pier reaches the compressive strength of masonry:

$$\sigma_{n \max} = \beta \cdot f_m \quad (5.24)$$

If the transverse wall is within the effective length, substituting Eq. (5.24) into Eq. (5.3d) gives the effective length at the base of the wall as:

$$L_{eb} = \frac{(P_b - A_f \cdot \beta \cdot f_m) + \sqrt{(A_f \cdot \beta \cdot f_m - P_b)^2 + 2(\beta \cdot f_m)^2 A_f a_f t}}{\beta \cdot f_m t} \quad (5.25)$$

Substituting Eq. (5.25) into Eq. (5.11) gives the corresponding toe-crushing capacity.

On the other hand, if the transverse wall is not within the effective length, substituting Eq. (5.24) into Eq. (5.3e) gives the effective length at the base of the wall as:

$$L_{eb} = \frac{2P_b}{\beta \cdot f_m t} \quad (5.26)$$

Substituting Eq. (5.26) into Eq. (5.11b) gives the corresponding toe-crushing capacity as:

$$V = \left(\frac{a_i}{L} - \frac{2}{3} \cdot \frac{P_b}{\beta \cdot f_m L t} \right) (P_t + W + W_f) \frac{L}{h} \quad (5.27)$$

The flange effects of a transverse wall on the toe crushing strength of a URM pier are illustrated in terms of the non-dimensional values $\frac{a_f}{L}$ vs. $\frac{V}{\frac{W}{W_f + W} P_b \frac{L}{2h}}$ for different W_f/W ratios and different vertical stress ratios ($\omega = P_b / ((1 + \psi) \beta f_m L t)$), as shown in Figures 5.6 to 5.8. The figures show that the transverse wall generally increases the toe crushing strength. However, this increment is dependent on the W_f/W ratio, the ω ratio, as well as the location of the transverse wall. When the vertical compressive stress is small ($\omega = 0.1$), the transverse wall at the heel side of the pier increases the toe crushing strength significantly. In contrast, when the vertical compressive is large ($\omega = 0.5$), the transverse wall at the toe side of the pier increases the toe crushing strength significantly. Figures 5.6 to 5.8 also indicate that the contribution of a transverse wall is not linearly dependent on the weight of the transverse wall.

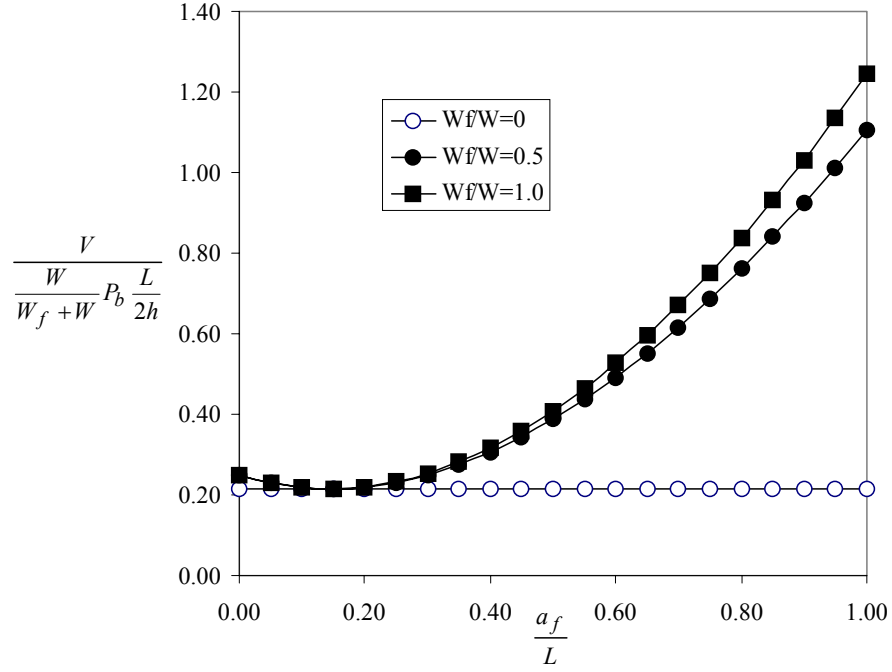


Figure 5.6. Toe crushing strength of non-rectangular section URM pier ($\omega = 0.1$)

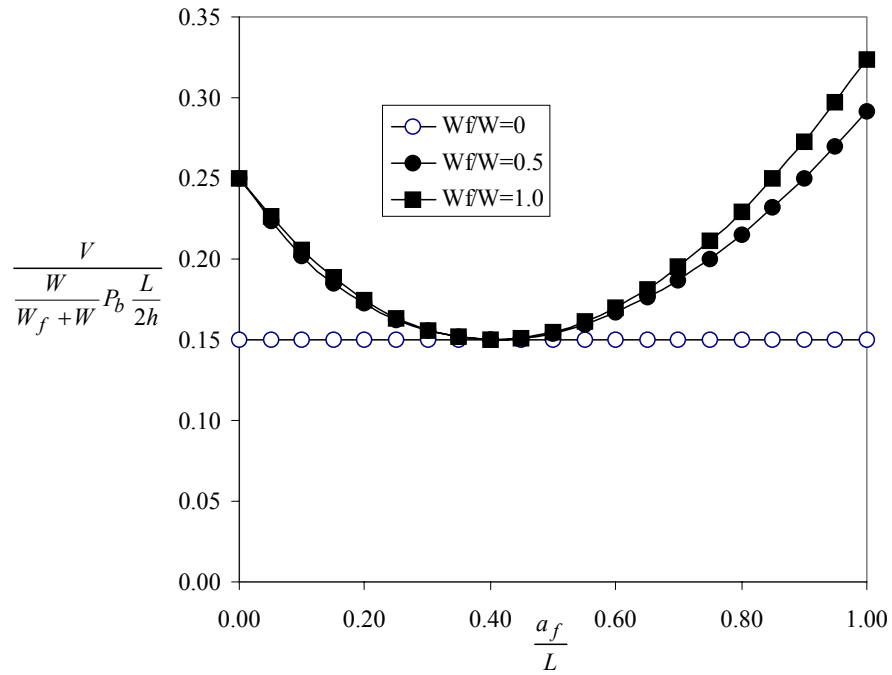


Figure 5.7. Toe crushing strength of non-rectangular section URM pier ($\omega = 0.3$)

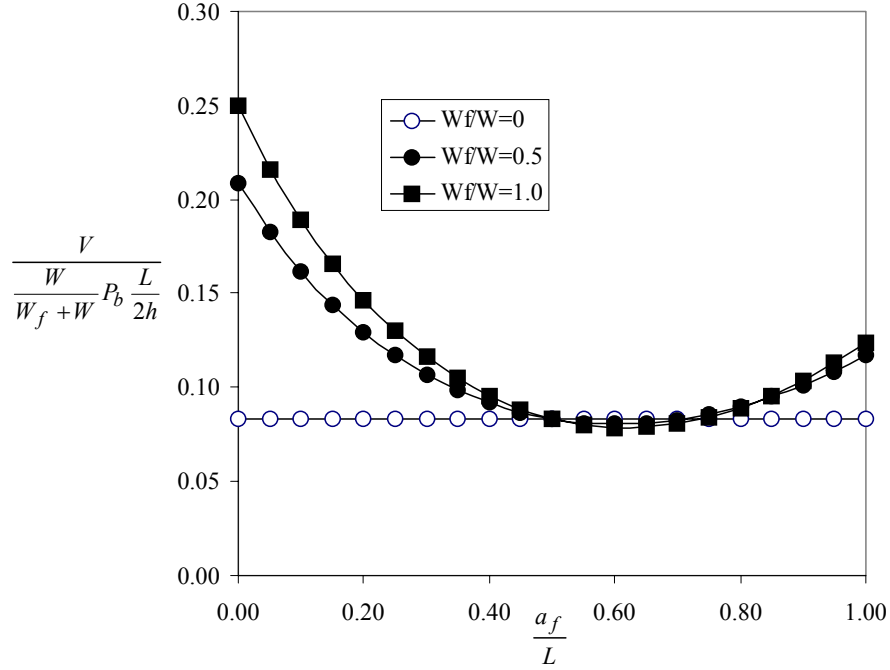


Figure 5.8. Toe crushing strength of non-rectangular section URM pier ($\omega = 0.5$)

5.3.4. Diagonal Tension Capacity

As discussed in Chapter 4, the diagonal tension failure mode of a URM pier is controlled by the following Equations:

- (1) Stair-stepped bed joint sliding:

$$\tau_u = \tau_0 + \mu \sigma_{avg} \quad (5.28)$$

- (2) Compression-tension principal stress state masonry failure criterion

$$\frac{\sigma_1}{f_t + \left(1.6\tau_0 - f_t\right) \frac{2\theta}{\pi}} + \frac{\sigma_2}{f_m \left(0.7 + \frac{0.6\theta}{\pi}\right)} = 1 \quad (5.29)$$

- (3) Compression-compression principal stress state masonry failure criterion

$$CJ_2 + (1 - C)I_1 + CI_2 = 1 \quad (5.30)$$

where J_2 , I_1 , I_2 are principal stress invariants defined as:

$$J_2 = \left(\frac{\sigma_{avg}}{f_m^\perp} - \frac{\sigma_{lateral}}{f_m^\parallel} \right)^2, \quad I_1 = \left(\frac{\sigma_{avg}}{f_m^\perp} + \frac{\sigma_{lateral}}{f_m^\parallel} \right), \quad I_2 = \left(\frac{\sigma_{avg}}{f_m^\perp} - \frac{\sigma_{lateral}}{f_m^\parallel} \right)$$

In order to use the above failure criteria, three representative stresses at the mid-height of a URM pier: the average vertical compressive stress σ_{avg} , the average lateral confine stress $\sigma_{lateral}$, and the average shear stress τ , have to be used. As discussed in Section 5.2.3, $\sigma_{lateral}$ and τ are considered not affected by the existence of transverse wall. On the other hand, the value of σ_{avg} can be calculated by Eq. (5.8) to incorporate the effect of transverse wall. Specifically, if the vertical compressive stress applied on the top of the transverse wall is the same as that on the top of the in-plane section, Eq. (5.8) indicates that the value of σ_{avg} for a URM pier is not affected by the existence of the transverse wall. As a result, it can be concluded that the diagonal tension capacity of a URM pier is not affected by its transverse wall.

5.3.5. Mixed failure modes

The effects of transverse wall on the ultimate strength of a cantilever pier corresponding to the four typical failure modes were discussed in previous sections. The transverse wall does not affect the diagonal tension strength of a URM pier, but typically increases the rocking strength, the sliding strength, and the toe crushing strength of a URM pier. Therefore, considering the participation of transverse wall, the failure modes of a URM pier should tend to shift towards a brittle diagonal tension failure mode. The analysis for mixed failure modes of a URM pier with transverse wall is a complex job. A

simple set of equations can not be derived to address this task. Instead, an analysis program based on the primary equations discussed before must be used for this purpose. Such a program is discussed in Chapter 12.

5.4. DETERMINATION OF THE FLANGE WIDTH

In the above sections, the width of the transverse wall is assumed to be known, and the vertical stress in the transverse wall is assumed to be uniformly distributed. However, for a real case, the vertical stress is nonlinearly distributed in a transverse wall because of the phenomenon known as shear lag. Owing to the shear deformation of the walls, the longitudinal displacements away from the junction of the in-plane wall and the transverse wall will lag behind those at the junction(s). As a result, high stresses are concentrated at the junction, and the stresses decrease in value at locations away from the junction. In order to take into account the nonlinear stress distribution in the transverse wall, an effective flange length is needed.

The effect of shear lag in linear elastic systems has been investigated using the theory of elasticity (Timoshenko and Goodier 1970). This method, however, is too complex to be used for estimating the effective flange width in practical engineering problems. Approaches employing empirical approximations have proved to be more successful in developing simplified equations to estimate the effective flange width. For example, based on experimental observations, Reisner (1964) made effective width calculations by assuming that the distribution of flexural normal stresses in a flange plate can be approximated by a second order parabolic curve. Other semi-empirical methods developed to deal with the shear lag problem include the harmonic analysis method

(Kristek et al. 1981), the folded-plate method (Kristek 1979), the finite stringer analysis (Evans et al. 1980), and the single Fourier series approach (Tahan et al. 1997).

When nonlinearity in material behavior needs to be considered, the effective flange width can no longer be accurately calculated using elastic techniques. Many research studies have been conducted on the effective flange width in reinforced concrete T-sections beams and shear walls as well as reinforced masonry shear walls (Ehsani and Wight 1985, Pantazopoulou and Moehle 1990, Qi and Pantazopoulou 1991, Shahrooz and Pantazopoulou 1992, Hosoyama et. al. 1995, Priestley and He 1995, Pantazopoulou and French 2001, and Hassan and EI-Tawil 2003).

Based on previous research, various definitions have been proposed for the effective flange width of shear wall for the design purposes. Some of these definitions are listed in Table 5.1. The notations used in the Table are shown in Figure 5.2. Table 5.1 shows that the calculation of effective flange width is quite different for different material and different building codes.

Table 5.1. Definitions for the effective flange length

Standards	Subjects	Specifications
ACI 530-02 Section 1.9.4.2	Reinforced masonry wall	L_f be less than: - $6t_f$ -Actual flange length
ACI 318-02 Section 21.7.5.2	Reinforced concrete wall	L_f be less than: -1/2 the distance to an adjacent shear wall -25% of the total wall height
EC6	Reinforced masonry wall	L_f be less than: -20% of the total wall height -1/2 the distance to an adjacent shear wall -The distance to the end of the wall. - Half the storey height.

The above definitions are based primarily on data pertaining to the tension flange effective width, but they are also suggested as applicable to a flange under compression (ACI Committee 318, 2002).

In contrast to many studies conducted for the flange widths of reinforced concrete shear walls and reinforced masonry shear walls, little research on the flange widths of unreinforced masonry walls has been found in the literature review. Moreover, the definitions proposed for reinforced concrete or masonry shear walls cannot be simply extended to URM walls, since the rationales employed are different for the different materials. For example, previous research has shown that with increasing lateral drifts, the effective flange width of a reinforced concrete shear wall will increase due to yielding of reinforcement. Obviously, this cannot be applied to brittle URM walls.

For a URM pier, a simple approach is proposed herein to calculate the effective flange width. Assuming the transverse wall is at the tensile side of a URM pier, and a large moment will be introduced at the base of the transverse wall. As a result, tensile stress will be introduced at the base and the direction of the principle tensile stress will be 45° in respect to the base. Elastic analysis shows that the maximum tensile stress concentrates at the conjunction between the in-plane wall and the transverse wall. Therefore, a tensile crack will initiate from that corner and propagate diagonally upward, as shown in Figure 5.9. This 45° crack propagate to the top of the pier or join with another crack propagating from another adjacent shear wall. It is assumed that the trapezoid area or the triangular area above the 45° crack will move together with the in-plane wall. Therefore, this area is considered as the effective flange area. The

corresponding effective width for a rectangular tension flange can be calculated as the follows:

$$\text{If } L_i > 2h, \quad L_f = h/2$$

$$\text{If } L_i \leq 2h, \quad L_f = \frac{(4h - L_i) \cdot L_i}{8h} \quad (5.31)$$

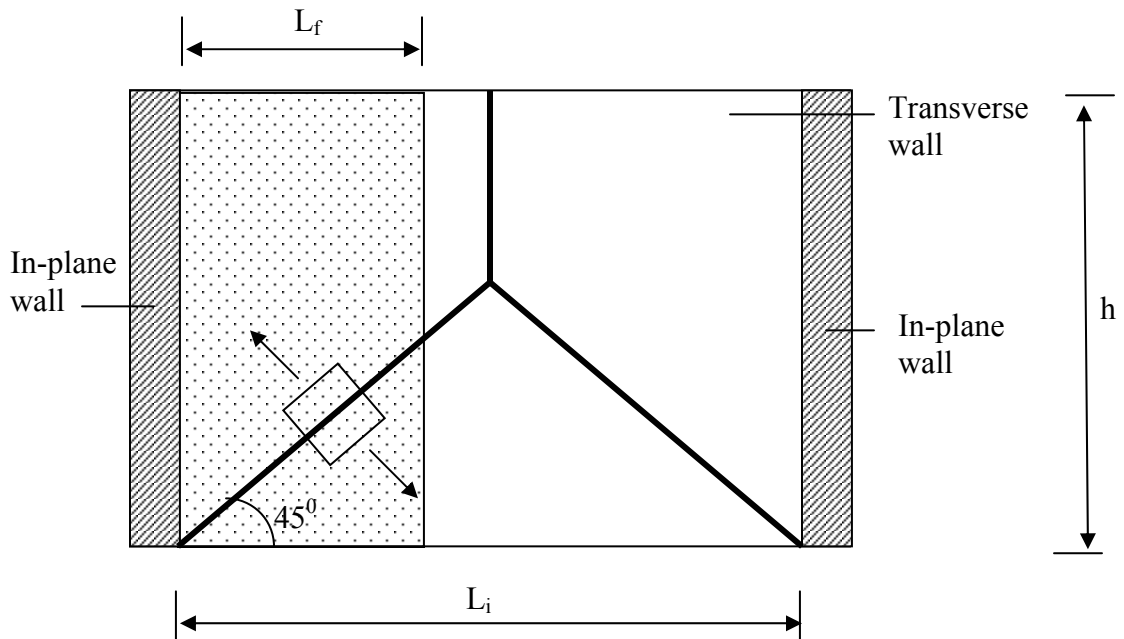


Figure 5.9. Elevation showing the effective flange width for the transverse wall in tension

If the transverse wall of a URM pier is at the compression side under external lateral force, the external moment will introduce additional vertical compressive stress in the transverse wall. The transfer of the additional compression force from the in-plane wall to the transverse wall roughly follows a 45° path, as shown in Figure 5.10.

Therefore, the equivalent width for this rectangular compression flange can be also calculated by Eq. (5.31). When the transverse wall is at other locations, the corresponding effective flange width is also defined by Eq. (5.31) for simplicity.

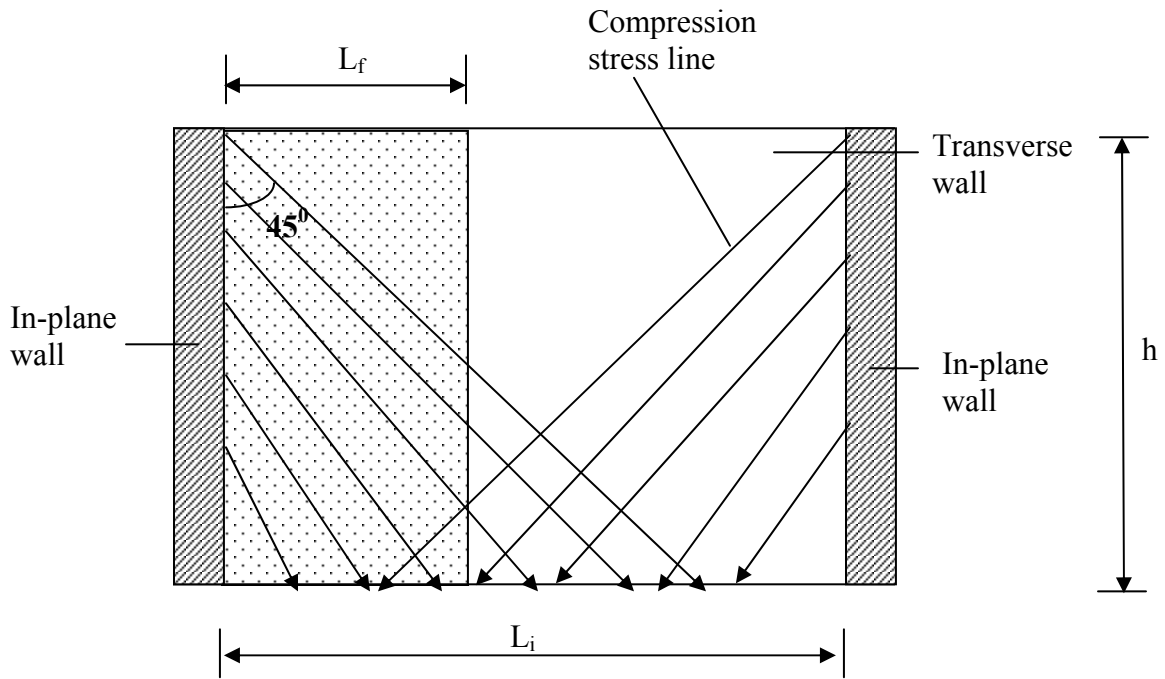


Figure 5.10. Effective flange width for the transverse wall in compression

5.5. OTHER POSSIBLE FAILURE MECHANISMS FOR A URM PIER WITH FLANGE

A basic assumption adopted by the proposed model is that the connection between the in-plane pier and the transverse wall is strong enough to ensure that the two walls work together as a single pier. In order to have a good connection between two adjoining

walls, some details are specified in modern construction. These requirements, however, are not always satisfied in existing URM buildings. Particularly, when the transverse wall is on the compression side, the large outward force transferred from the in-plane wall may cause separation of the corner, as shown in Figure 5.11. Nevertheless, since this type of failure mechanism usually occurs after severe damage has developed in the wall, it is not considered in the current model.

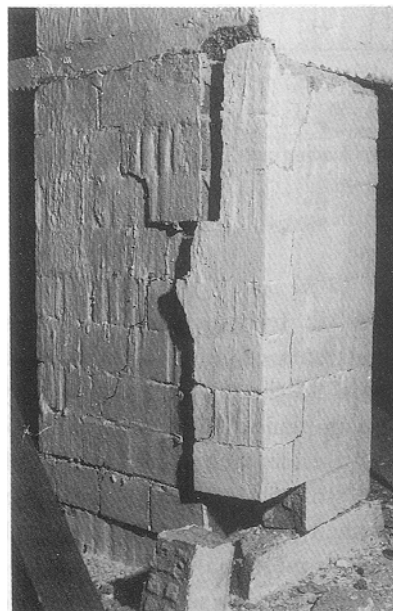


Figure 5.11. Unreinforced masonry corner wall separated during shaking tests (Tomazevic, 1999)

Another possible failure mechanism not considered by the proposed model occurs when the length of the in-plane pier (L) is smaller than the width of the transverse wall (L_t). In this case the in-plane pier may crack prior to the damage of the transverse wall.

Therefore, the response of this URM pier is controlled by the out-of-plane behavior of the transverse wall, which is not the research focus of the proposed analytical model.

5.6. CONCLUSIONS

Previous research indicates that flange effects due to the participation of transverse walls have significantly influence on the response of a URM pier. The effective pier model proposed for a rectangular section URM pier in Chapter 4 is modified to consider the flange effects. Based on this modified effective pier model, the maximum strengths of a URM pier corresponding to the four fundamental failure modes are assessed. It is found that flange effects significantly increase the rocking strength, the shear sliding strength, and the toe crushing strength of a URM pier. In contrast, it has no noteworthy effects on the diagonal tension strength of a URM pier. Furthermore, the analysis also reveals that the location of the transverse wall has remarkable influence on the response of a URM pier.

The contribution of flange effects largely depends on the effective width of the flange. A simple method based on a reasonable crack pattern in a URM pier is proposed in this chapter to calculate the effective flange width. It can be applied for both tension-flange piers and compression-flange piers.

The modified effective pier model can be embedded into a pushover analysis program and used to analyze the nonlinear behavior of perforated URM walls; this is discussed in Chapter 12. However, the reliability of the proposed model needs to be validated through future experimental research. The parameters for such proposed

experimental research should include the effective width and the locations of the transverse wall, and the vertical stress value applied on the URM pier.

CHAPTER 6

DESIGN OF THE ST-11 BUILDING

6.1. INTRODUCTION

A quasi-static test of a full-scale two-story URM building was conducted at Georgia Tech as the main experimental part of this research. This test was sponsored by the National Science Foundation (NSF) through the Mid-America Earthquake Center (MAEC) Project ST-11. This chapter introduces the design and construction of this URM building, and is organized as follows: First, the objectives of this experimental research are briefly reviewed. Second, the extensive material tests performed in order to select appropriate materials for the construction of the full-scale test structure are described. Next, the design of the test structure is presented, including the design of the masonry walls, the timber roof and floor system, and the foundation. After that, the construction of the building and the proposed rehabilitation techniques are summarized. Finally, the loading sequence for testing the building is presented. Test results are discussed in Chapters 7 through 9.

6.2. OBJECTIVES

The goal of the ST-11 project was to examine the structural characteristics of existing unreinforced masonry buildings and to explore the effectiveness of several rehabilitation techniques. The categorized research objectives are listed in Table 6.1.

Table 6.1. Objectives for Project ST-11

	Objectives
Existing URM	<ul style="list-style-type: none"> (1) Verify the validity of extrapolating from individual component behavior to the overall response in a URM building system (2) Experimentally identify the critical components in order to develop a systematic method for evaluation and rehabilitation of URM structures (3) Experimentally validate current code provisions (FEMA 356) as well as advanced analysis tools for URM structures (4) Compare the full-scale quasi-static test with the half-scale dynamic test (MAEC project ST-22)
Rehabilitated URM	<ul style="list-style-type: none"> (5) Examine the relative effectiveness of different rehabilitation approaches (6) Assess the effectiveness of selective rehabilitation of individual components on overall system performance. (7) Experimentally validate standard code, as well as advanced analysis tools for rehabilitated URM structures (8) Compare the full-scale quasi-static test with half-scale dynamic test
Others	<ul style="list-style-type: none"> (9) Aid in the improvement of code provisions and the development of rehabilitation guidelines

The research presented herein is focused on existing URM, which covers Objectives 1, 2, 3, and 9 listed in Table 6.1. Objective 1 is to verify the extrapolation of individual component behavior to the overall response of the building system. This objective is based on the parallel research conducted under other MAEC projects that investigated the behavior of individual components, such as project ST-6 (URM wall piers, Franklin et al. 2001, Erbay et al. 2001) and project ST-8 (Flexible wood diaphragms, Peralta, et al. 2000). Detailed description of these projects can be found in Appendix A. Specifically, the ST-11 test was used to investigate the following two issues:

- Determination of the contribution of each masonry pier to the strength of the entire perforated wall;
- Assessment of the contribution of the flexible wood roof and floor diaphragm to the overall response of the building system.

Objective 2 is to experimentally identify critical components in order to develop a systematic method to evaluate existing URM structures and to apply rehabilitation approaches. Figure 6.1 shows typical components of a URM building. The following critical components or behavior were investigated in the ST-11 test:

- The diaphragm-to-wall connections,
- The out-of-plane behavior of URM walls,
- The torsional behavior of a URM building with unsymmetrical layout,
- The progressive damage of piers in a perforated URM wall,
- The behavior of secondary elements,
- The behavior of different lintels.

Objective 3 is to experimentally validate available code provisions (FEMA 356, ATC 1999), as well as advanced analysis tools for evaluating the seismic resistance of unreinforced masonry structures. The ST-11 test structure represents a realistic configuration for URM structures in Mid-America, and thus constitutes a good test for FEMA 356 provisions as well as for advanced analysis tools. The test results will help to improve the standard codes and rehabilitation guidelines for existing URM structure, which is Objective 9 of this research.

The other objectives of the ST-11 test project, such as the comparison of the full-scale quasi-static test with half-scale dynamic test (Objectives 4 and 8) and the

rehabilitation of the test structure (Objectives 5, 6, and 7), are out of the scope of the research presented herein; it can be found elsewhere (Moon 2004).

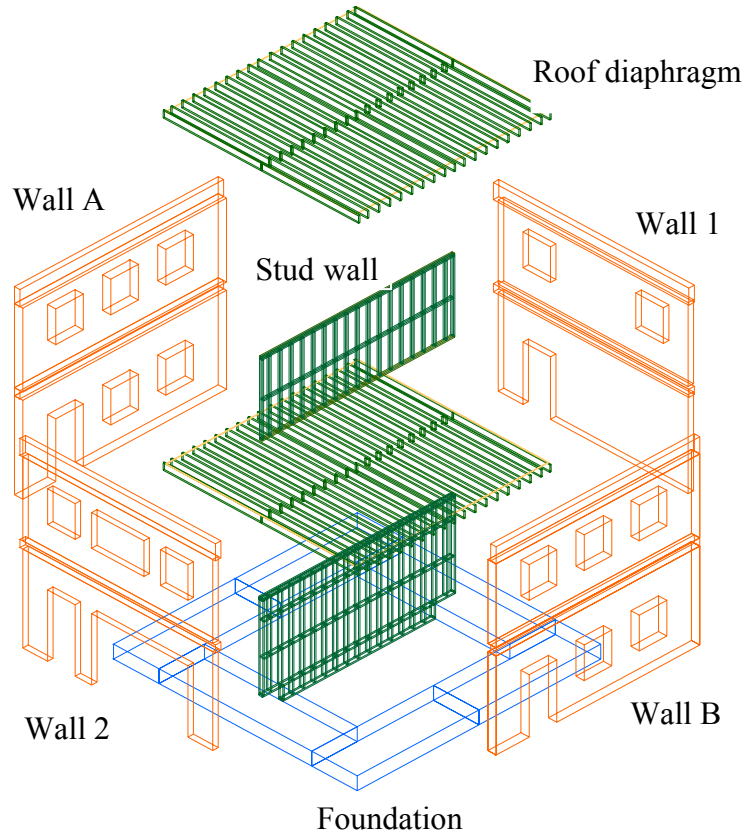


Figure 6.1. 3D exploded view of the test structure

6.3. MATERIAL PROPERTIES

6.3.1. Bricks

The bricks used for construction were donated by the Southern Brick Institute and supplied by a local company (CHEROKEE Brick and Tile). Two different types of bricks, including both solid bricks and cored bricks, were employed (Figure 6.2).

Nominal dimensions of both types of bricks were 7.75 in length, 3.5 in width, and 2.25 in thickness. The cored bricks contained a longitudinal hole through the center, with a nominal diameter of 0.875 in.

Measured compressive strengths for the solid brick and the core brick were 6030 psi and 5285 psi, respectively. These were determined according to ASTM C67. In an attempt to minimize the influence of this strength difference, the solid bricks were used for the lower 54 courses of the test structure and the cored bricks were used for the remainder of the structure. The analyses predicted that most of the damage would concentrate on the first floor and thus the solid bricks were used in that area. Solid bricks were employed for all header courses.



Figure 6.2. Two different types of bricks

6.3.2. Masonry mortar

The choice of an appropriate masonry mortar was the main task of the material characterization work. A survey of existing buildings in Mid-America by the Southern Brick Institute revealed that strong unit-weak mortar masonry was widely used in construction prior to 1950. Analyses conducted at Clemson University of mortar samples taken from existing structures in Mid-America showed a very low amount of Portland cement (Clemson University, 2000). This suggested that masonry with low-strength mortar is common in existing URM structures in Mid-America.

The grades of masonry mortar used prior to 1950 are listed in Table 6.2. To represent strong unit-weak mortar masonry, a weak mortar such as pre-1950 Type O or Type K mortar needed to be simulated in the lab.

Table 6.2. Different grade of masonry mortar used prior to 1950 (ASTM 1958)

Type	Ratio (cement: lime: sand)	Compressive Strength (psi)
M	1:0:3	2500
S	0.5-1 :0.25-0.5: 4.5	1800
N	1: 0.5-1.25: 6	750
O	1: 2: 9	350
K	0.5 : 2 : 7.5	75

Based on a series of material tests, a mortar mix in the ratio of 0.5: 2: 9 (Portland cement: lime: sand) was chosen to represent the weak mortar. The compressive strength of this type of mortar was 41 psi, which is close to the value for Type K mortar given in Table 6.2. Since the designed mortar mixture is close to that specified for Type K mortar,

this mortar is designated as a Type K' mortar. Detailed descriptions of this series of material tests can be found in Appendix B.

6.3.3. Material properties of masonry

Masonry prism specimens and 4-brick direct shear specimens were constructed simultaneously with the construction of building. Several critical material parameters, including the compressive strength, the initial bed joint shear strength, the equivalent internal shear coefficient, and the shear-sliding coefficient for the cracked bed joint, were measured by prism tests and 4-bricks direct shear tests. The results are listed in Table 6.3. It should be pointed out that the compressive strength is different for solid brick and hollow brick, while the other strength parameters are the same for the two different types of bricks.

Table 6.3. Material properties of the test structure

Strength parameters	Number of tests	Mean	COV	R ²
Compressive strength (solid brick)	3	1458 psi	0.25	-
Compressive strength (hollow brick)	3	593 psi	0.09	-
Initial bed joint shear bondage strength	21	60 psi	-	0.75
Equivalent internal shear coefficient	21	1.1	-	0.75
Shear sliding coefficient for cracked bed joint	21	1.0	-	0.75

The elastic modulus of masonry also was measured by prism test. The test setup is shown in Figure 6.3. Four LVDTs were used to account for effects of possible eccentric loading. The specimens were loaded up to a maximum compressive stress of about 500

psi. A total of 16 specimens were tested. The measured mean value of elastic modulus was 1168 ksi.

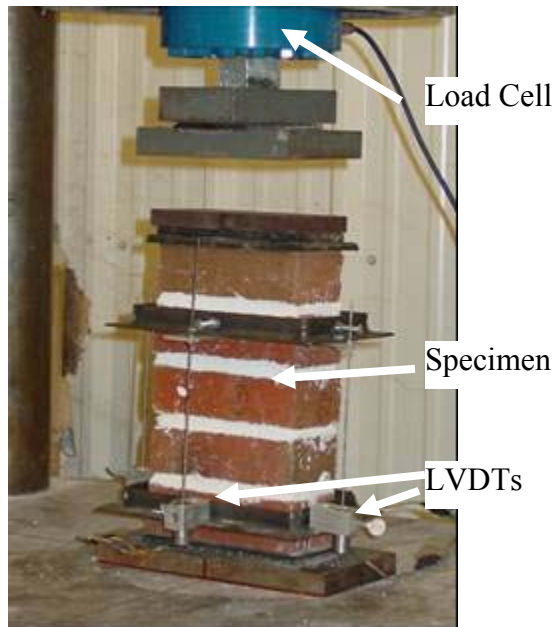


Figure 6.3. Test setup for the measurement of elastic modulus of masonry (5 brick specimen)

6.4. DESIGN OF THE TEST STRUCTURE

6.4.1. Overall design

The ST-11 test structure was a two-story URM bearing wall structure with timber floor and roof diaphragms. It was intended to represent a typical existing URM building in Mid-America. The URM building was constructed to fully utilize the L-shaped strong wall in the Structural Engineering Laboratory at Georgia Tech. The dimensions of the building were 24ft by 24ft. in plan with story heights of 12 ft. for the first story and 10 ft. for the second story (Figure 6.4). In order to facilitate the use of the same floor system

investigated in MAEC project ST-8 (Peralta et al. 2000), a stud wall was constructed through the center of the structure to support the joists. The test structure was constructed on top of a set of reinforced concrete slab foundations, which were post-tensioned to the strong-floor. The design of each component of this building is discussed in the following sections.



Figure 6.4. Overview of the test structure with the L strong walls

6.4.2. Masonry walls

The plan view of the test structure is shown in Figure 6.5. The elevation views of each of the walls are shown in Figure 6.6 through Figure 6.8. The building was composed of four URM masonry walls, which are named Walls A, B, 1 and 2, respectively. For the

purpose of explanation, the piers and spandrels in each wall are named as X-Y, where X is the name of the wall and Y is the number of the pier or spandrel in this wall. For example, Pier 1-6 means Pier 6 in Wall 1 (Figure 6.6). The masonry walls were constructed in standard American bond with a header course every sixth course (Figure 6.9).

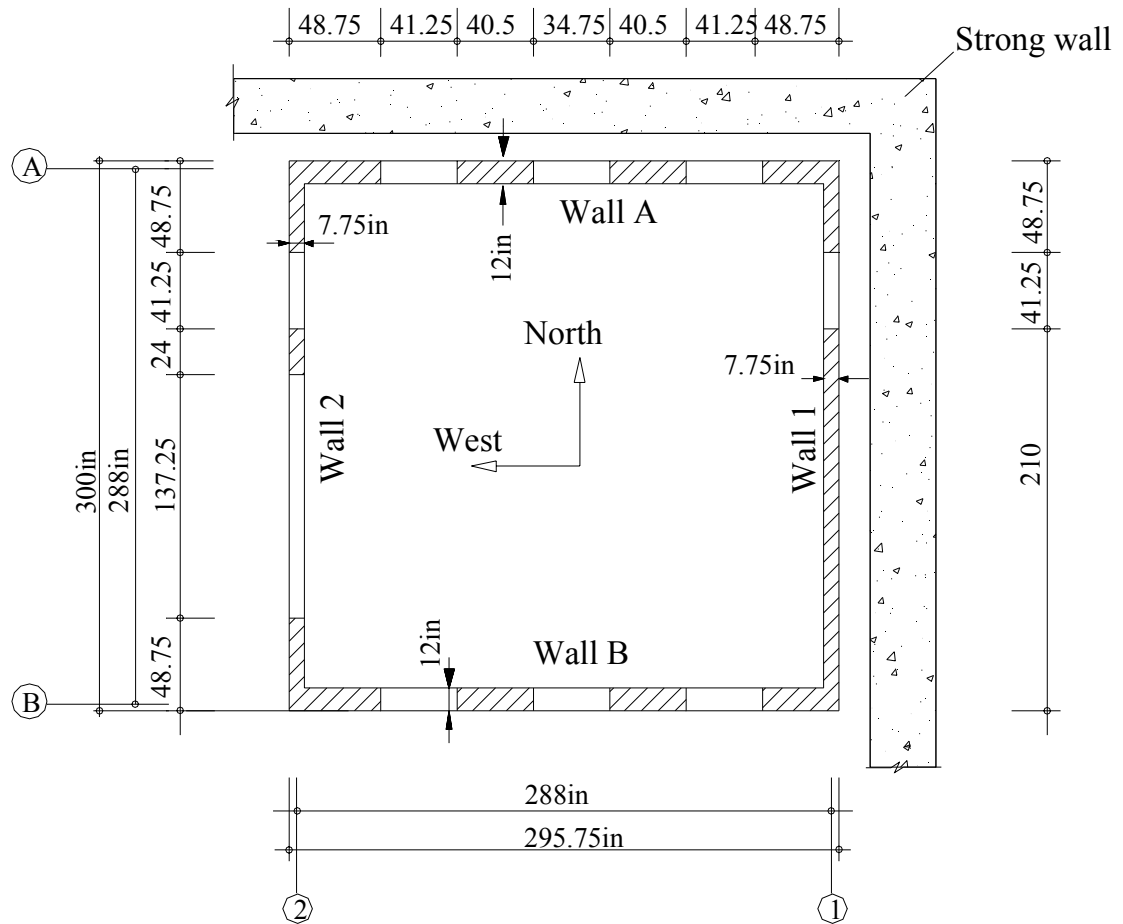


Figure 6.5. Plan view of the ST-11 test structure

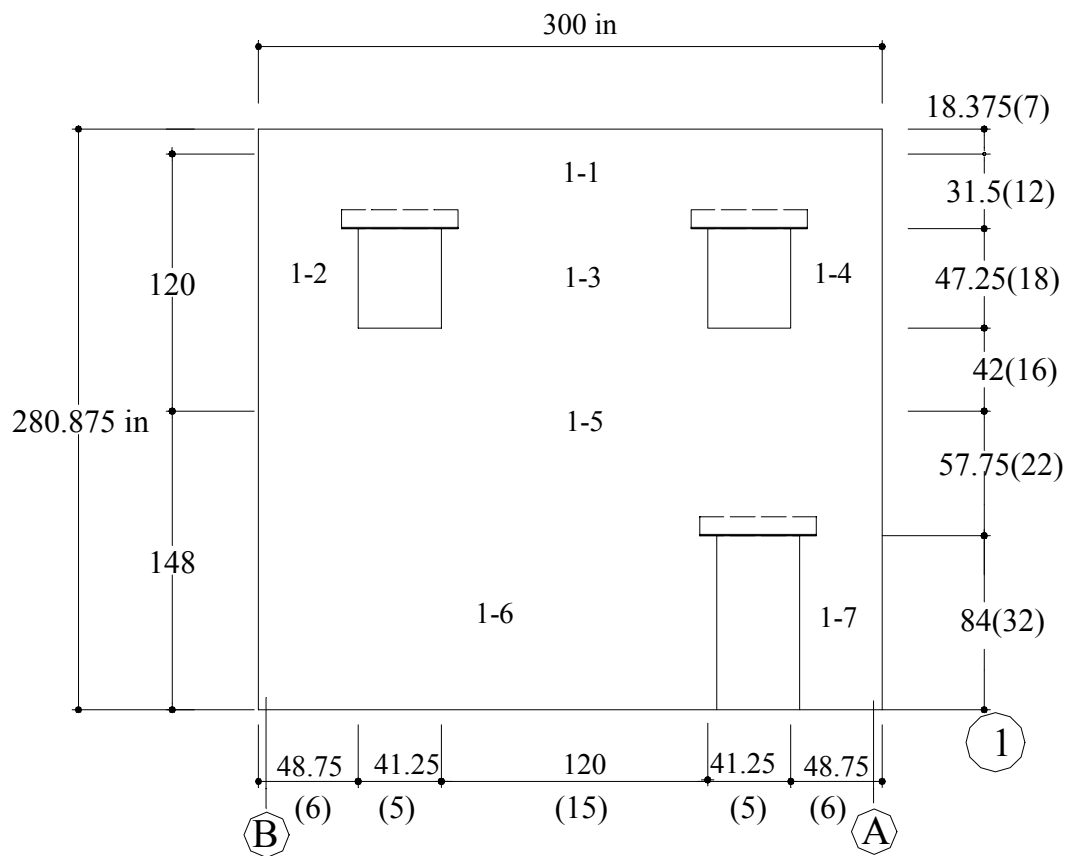


Figure 6.6. Elevation view of Wall 1
(Number in the parenthesis indicates the number of masonry units)

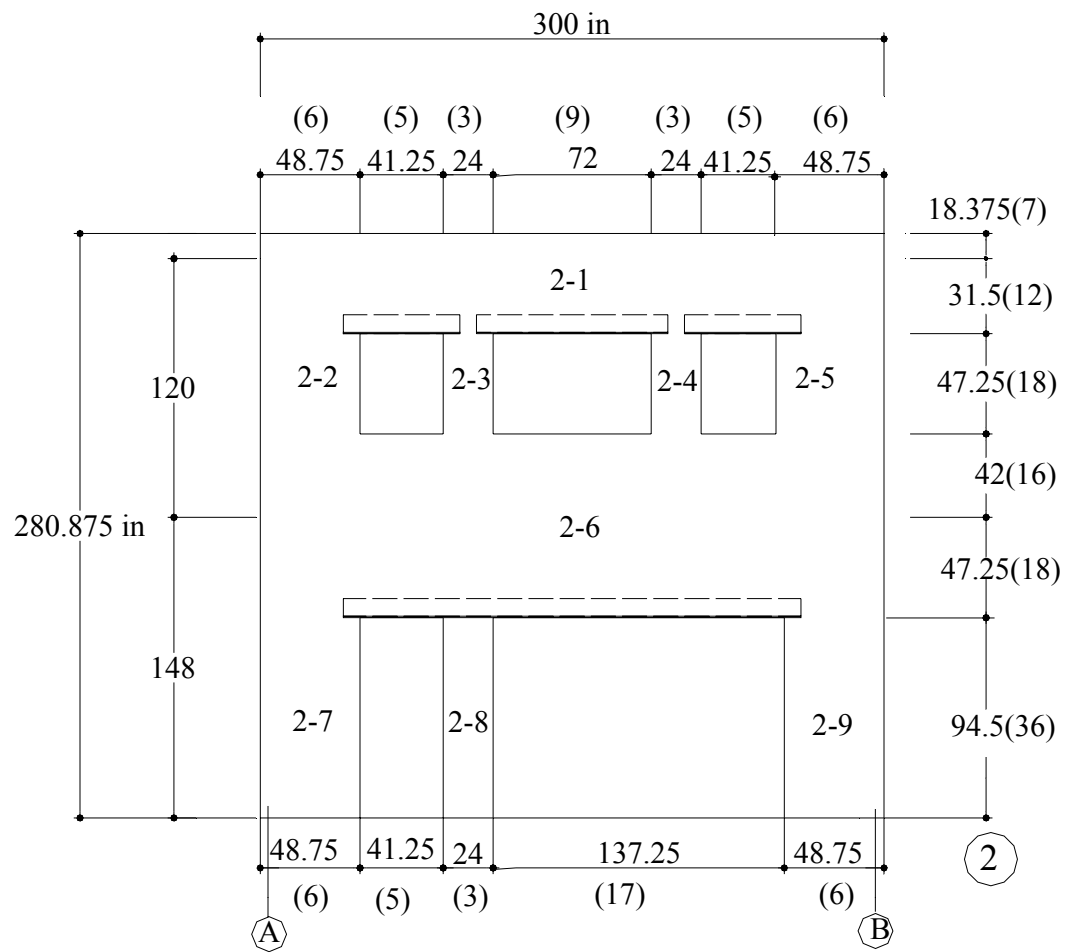


Figure 6.7. Elevation view of Wall 2
(Number in the parenthesis indicates the number of masonry units)

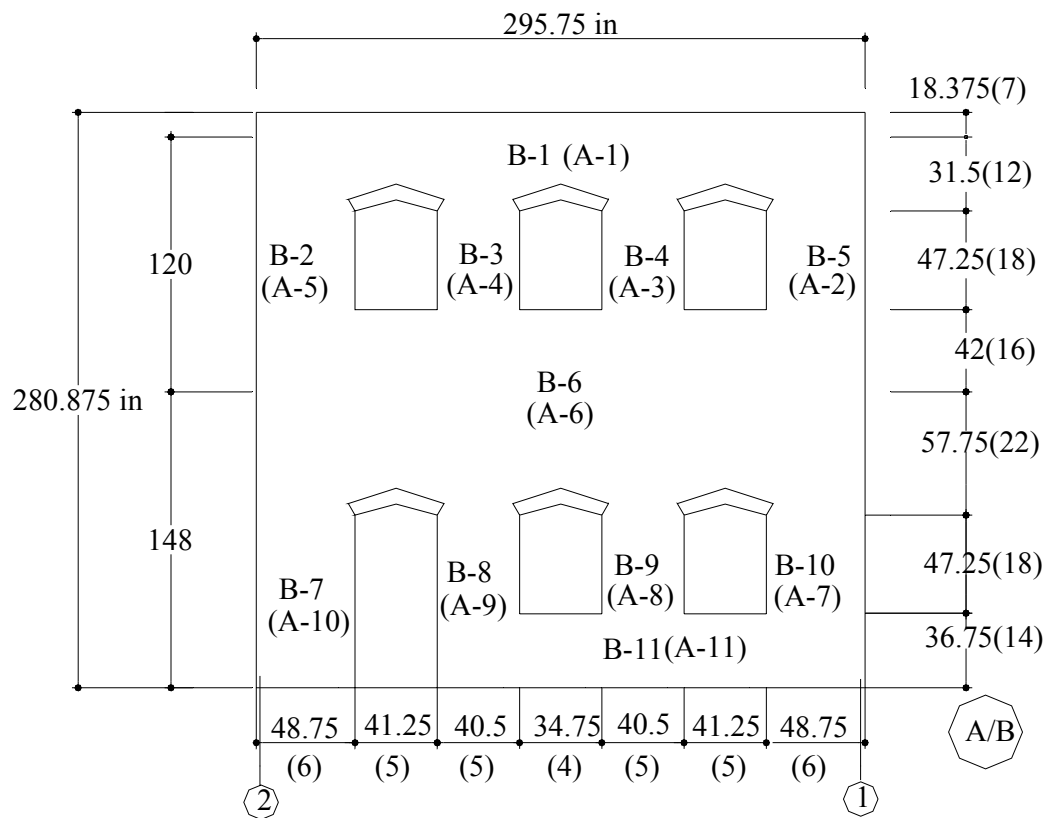


Figure 6.8. Elevation view of Walls A and B
(Number in the parenthesis indicates the number of masonry units)

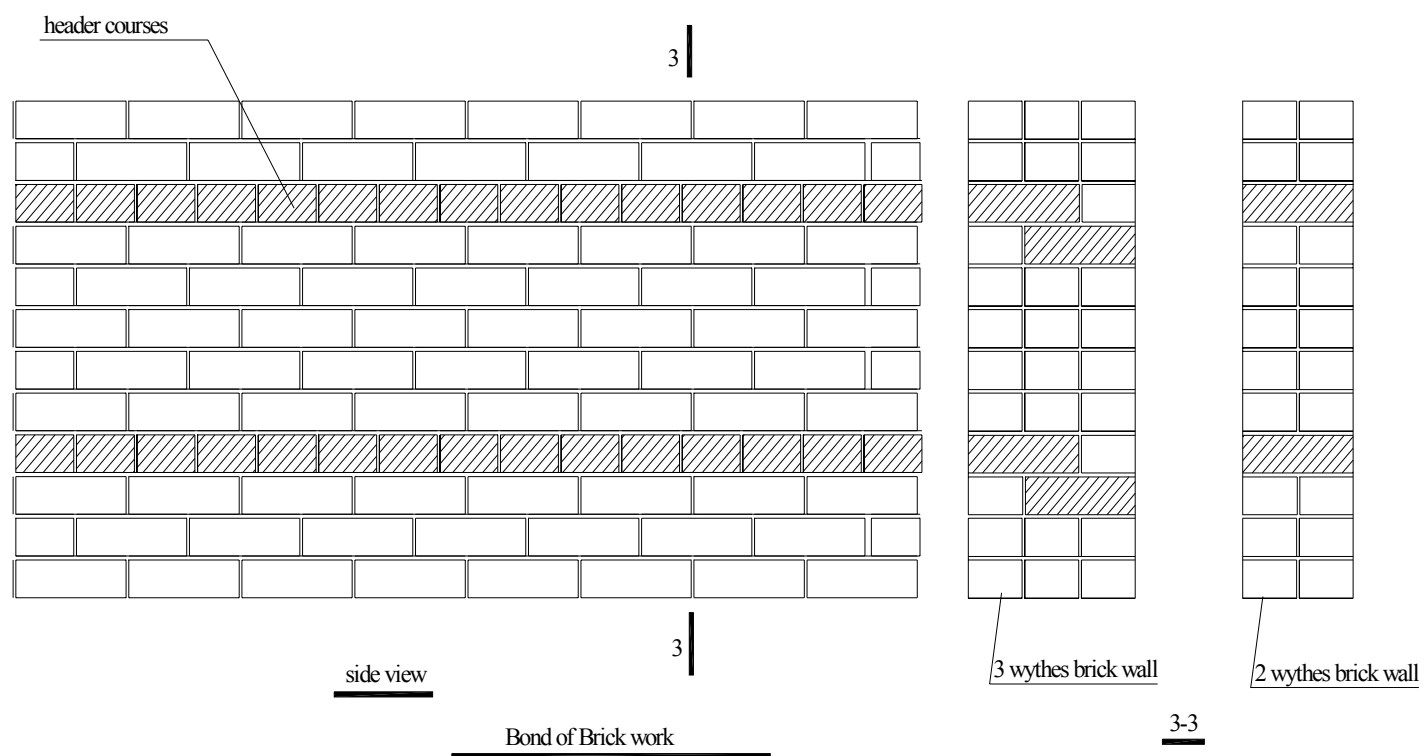


Figure 6.9. Detail of American bond

Walls A and B were composed of three wythes of masonry giving a nominal thickness of 12 in., while Walls 1 and 2 were composed of two wythes of masonry giving a nominal thickness of 8 in. The latter (8 in.) is the minimum thickness for masonry bearing walls more than one story high (Masonry Standards Joint Committee, 2002), and 12 in. is a typical thickness for low rising masonry building walls. The use of two and three-wythe walls for the test structure also ensured that the stability of masonry wall was not an issue.

The opening ratios for each wall are listed in Table 6.4. This table shows that the opening ratios of Walls 1 and 2 are quite different. Wall 2 contained a large door opening (indicative of the front of a firehouse), and was designed to represent a strong spandrel-weak pier type perforated wall. Wall 1 had relatively small openings, and was designed to represent a strong pier-weak spandrel type perforated wall. Furthermore, many structures in Mid-America contain parallel walls with large differences in stiffness. As a result, the behavior of URM structures with flexible diaphragms subject to torsion is of interest. Walls 1 and 2 allowed this type of behavior to be investigated. Walls A and B had moderate opening ratios, which were observed in many existing URM buildings. In addition, Walls A and B were identical except that four vertical holes were left in Wall A to allow a post-tensioning retrofit to be investigated. Since the two walls are identical, direct comparisons can be made on the relative effectiveness of different retrofit techniques. Walls A and B supported the floor system.

Table 6.4. Opening ratios of each wall

No. of wall	Story	Rough area (in ²)	Opening area (in ²)	Opening ratio
A/B	Second	40924	5600	13.7%
	First	43771	7106	16.2%
2	Second	41513	7336	17.7%
	First	44400	16940	38.2%
1	Second	41513	3875	9.3%
	First	44400	3444	7.8%

The pier sizes and h/L ratios are listed in Table 6.5. The aspect ratios of piers in the test structure ranged from 0.4 to 4.0. This range of pier aspect ratios was selected in order to allow both the “shear” and “flexural” piers such as those tested in MAEC project ST-6 to be investigated. Two types of wall piers were investigated in Project ST-6: (1) cantilever flexural members with a h/L ratio of 1.77 and a vertical stress ranging from 25 psi to 75 psi; and (2) cantilever shear members with a h/L ratio of 0.5 and a vertical stress of 65 psi or higher (Erbay et al. 2001, Franklin et. al. 2001). For design, the piers in the first floor were assumed to act as “fixed-fixed” columns or walls. Following this assumption, the piers with h/L ratios between 3.0 and 4.0 in the first floor were equivalent to the flexure piers tested in ST-6. Similarly, piers with h/L ratios of 1.0 employed in the first floor were representative of the shear piers tested in ST-6. Thus, the behavior of both types of individual piers tested with idealized boundary conditions in project ST-6 could be investigated in the context of an entire, realistic structure as part of the ST-11 building.

Table 6.5. Pier sizes and aspect ratios

Pier	Length (in)	Height (in)	H/L	Pier	Length (in)	Height (in)	H/L
A/B-2	48.375	47.25	1.0	1-4	48.375	47.25	1.0
A/B-3	40.25	47.25	1.2	1-6	48.375	84	1.7
A/B-4	40.25	47.25	1.2	1-7	210.625	84	0.4
A/B-5	48.375	47.25	1.0	2-2	48.375	47.25	1.0
A/B-7	48.375	84	1.7	2-3	24	47.25	2.0
A/B-8	40.25	47.25	1.2	2-4	24	47.25	2.0
A/B-9	40.25	47.25	1.2	2-5	48.375	47.25	1.0
A/B-10	48.375	47.25	1.0	2-7	48.375	94.5	2.0
1-2	48.375	47.25	1.0	2-8	24	94.5	4.0
1-3	121.25	47.25	0.4	2-9	48.375	94.5	2.0

The four masonry walls were connected with each other at the corners. The corners were built following normal standards (Structural Clay Products Institute, 1949) to ensure adequate connection strengths (Figure 6.10). This also allowed flange effects to be investigated. In particular, Wall 1 was designed so that the area of the flange for Wall B (Pier 1-6) was much larger than that for Wall A (Pier 1-7, Figure 6.6). Thus, the effects of different size flanges were investigated.

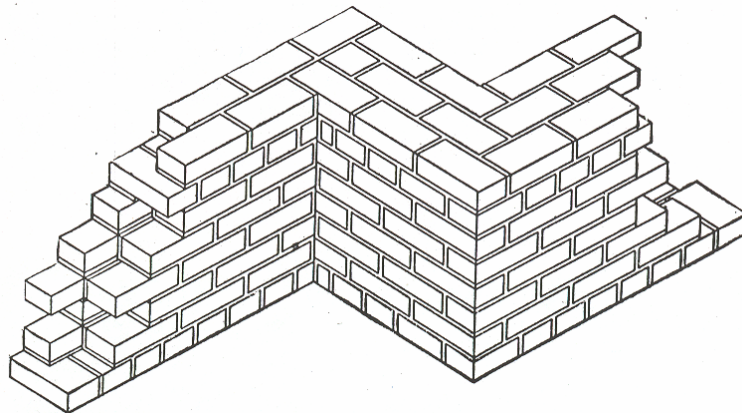


Figure 6.10. Common bond used to ensure adequate connection strengths (Stoddard 1946)

Walls A and B employed URM arch lintels (Figure 6.11), while Walls 1 and 2 employed steel lintels (Figure 6.12). Both of the two lintels are representative of typical lintels used for existing URM structures (Stoddard 1946).

Another interesting feature for the designed structure is that no additional weight was added on the roof and the floor to simulate the live load. Thus a lower bound for the strength of the building was obtained, as the axial compression stress on the walls was minimized. However, the pre-set post-tensioning ducts in Wall A allowed the effects of potential additional vertical load on the behavior of the building to be investigated.

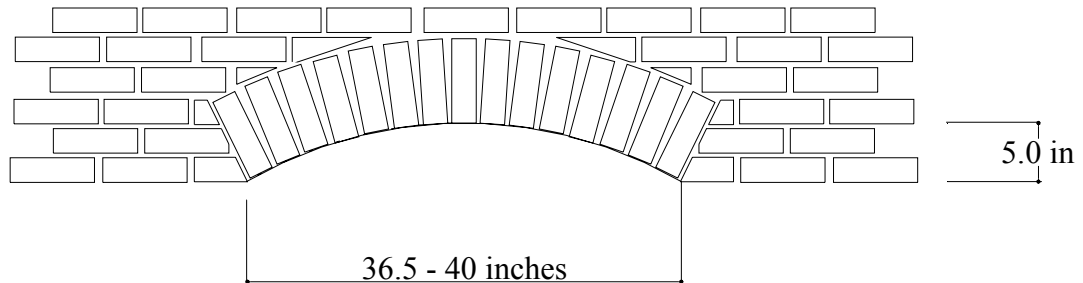


Figure 6.11. Detail of arch lintels

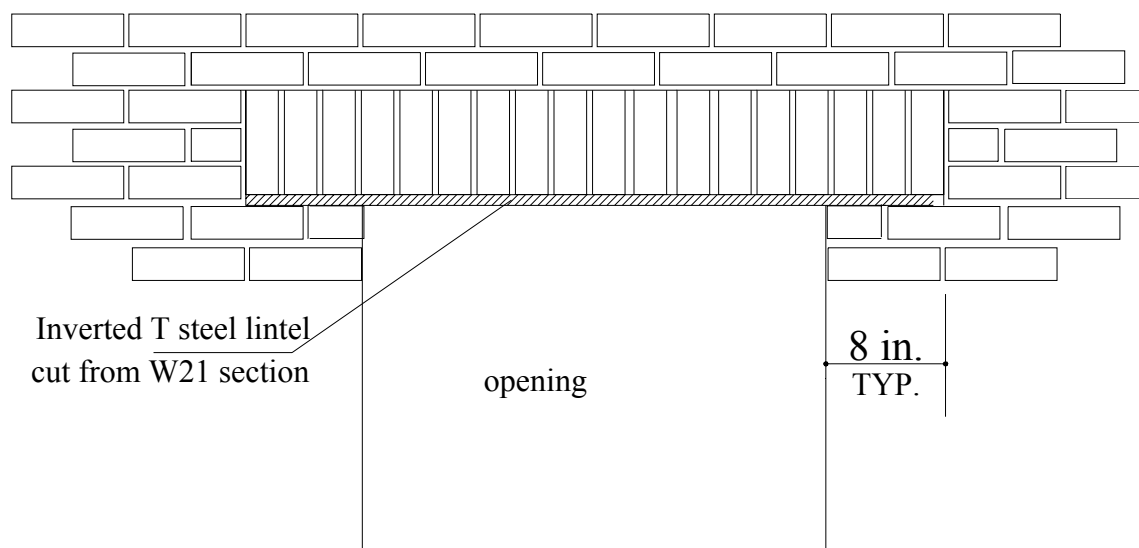


Figure 6.12. Detail of steel lintels

6.4.3. Timber roof and floor diaphragm

Surveys of pre-1950 URM buildings in Mid-America indicated that timber diaphragm and steel diaphragm were widely used for floor and roof systems (MAEC SE-1, see Appendix A). Timber roof and floor diaphragms were chosen for use in the ST-11 test structure since it could be considered to model a lower bound of strength and stiffness for existing diaphragms. In order to utilize the test results obtained from other parallel MAE center projects, diaphragms similar to the “MAE-2” diaphragm tested in MAEC ST-8 (Peralta et al. 2000) were used for the ST-11 test specimen.

The configuration of the roof diaphragm is shown in Figure 6.13. The framing of the diaphragm was composed of 2x10 joists spanning 12 ft. and spaced 16 in. on center. The joists were laterally supported by full depth blocking spaced at approximately 4 ft. on center, and simply supported on Walls A and B as well as on the stud wall built

through the center of the building. The joists rested directly on the inner wythe of Walls A and B in masonry “pockets”. The joists did not have a diagonal “fire-cut” end. The joists and blocks were nailed together with 16d common nails. In order to anchor the roof diaphragm to the masonry walls, 5/8” threaded rods were used as shear ties, and Simpson Strong-TieTM system with 5/8” thread rods were used as tension ties (Figure 6.14). The number and locations of these ties were varied for different loading cases (see Chapter 7). Straight sheathing was provided by using 1x6 square edge boards, staggered symmetrically with respect to the diaphragm mid-span. Three 8d common nails were used at the supported end and two at interior joist support locations for each sheathing board.

The floor diaphragm is identical to the roof diaphragm except that 3/8” Plywood instead of 1x6 square edge boards was used for the sheathing. The sheathing was nailed to the joists by 8d common nails.

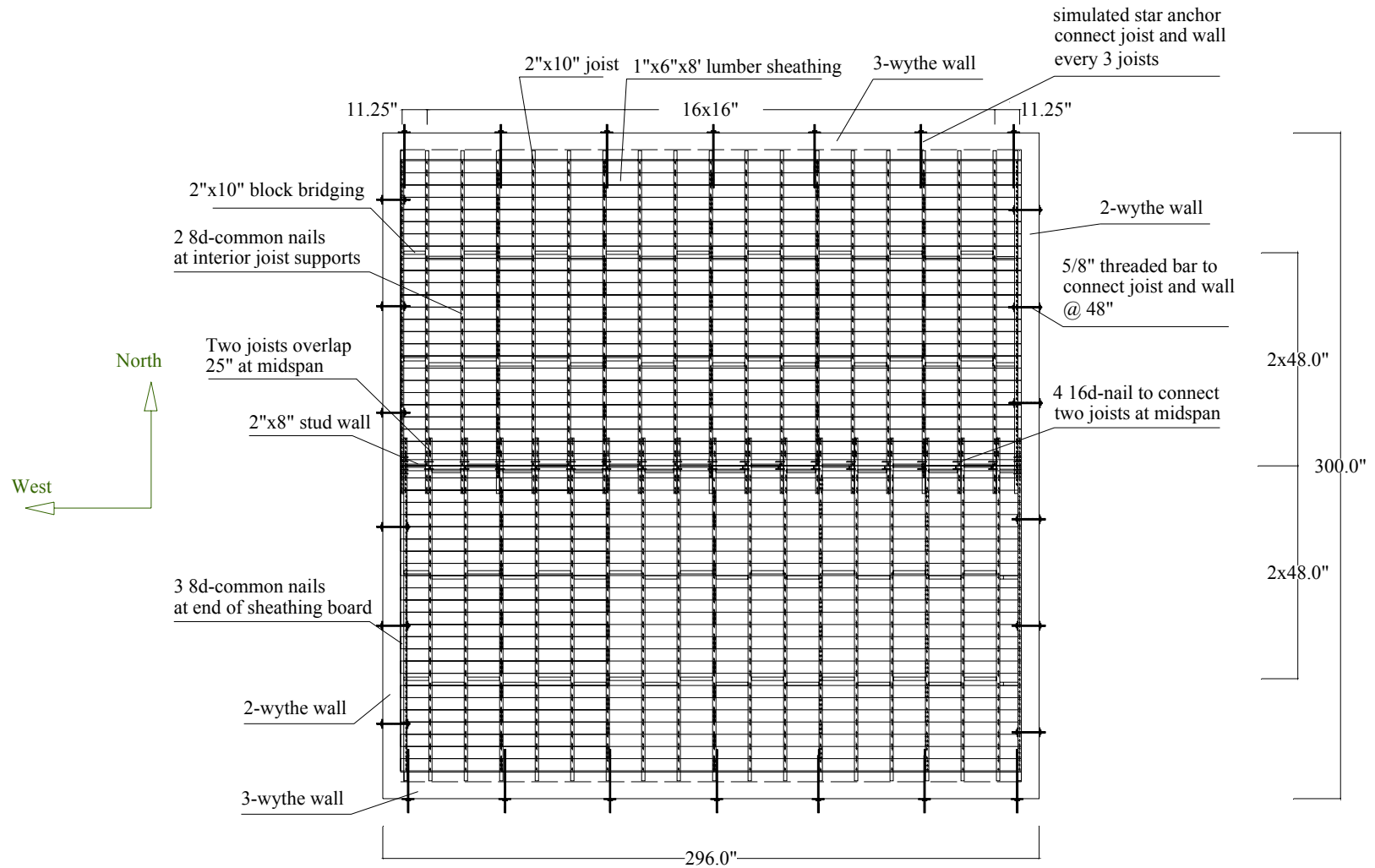


Figure 6.13. ST-11 roof/floor diaphragm

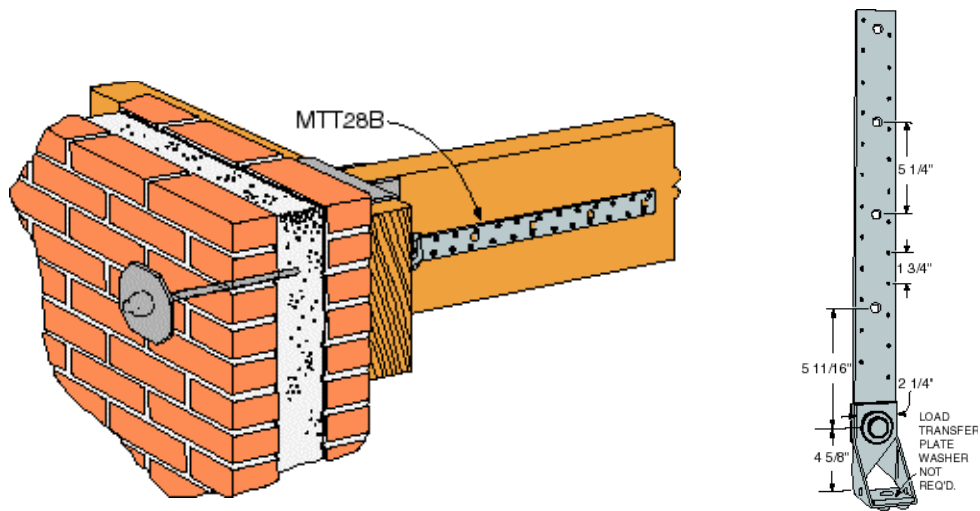


Figure 6.14. Simpson connections (taken from www.strongtie.com)

6.4.4. Timber Stud Wall

The floor system tested in MAEC ST-8 (Peralta et al. 2000) contained 2x10 joists spaced at 16 in on center. This type of floor system is only capable of spanning 12 ft. However, the distance between bearing walls of the ST-11 test structure was 24 ft. As a result, a timber stud wall was provided in the center of the structure to reduce the required span to 12 ft. and to allow the 2x10 joists, as used in ST-8, to be employed. Both the first and the second floor stud walls were constructed of 2x6 studs spaced at 16 in. on center with 2 by 6 blocking supplied at 4 ft. on center (Figure 6.15). Since these walls were only intended as vertical load carrying members, they contain no sheathing. The stud wall in the first floor was fixed to the strong-floor at the base, and nailed to the

floor joists at the top. The stud wall in the second floor was nailed to the floor joists at the bottom and to the roof joists at the top.



Figure 6.15. Photo of the stud wall together with the foundation

6.4.5. Reinforced Concrete Foundation Slabs

A reinforced concrete foundation composed of six individual RC slabs was used to transfer the base shear of the structure to the strong floor and to anchor the post-tensioning tendons used for retrofit. The thickness of these RC slabs was 20 in. The design of these RC slabs can be found in Appendix C.

6.5. CONSTRUCTION

Prior to the construction of the ST-11 test structure, the reinforced concrete foundation slabs were first cast and post-tensioned to the strong-floor with high strength Dywidag bars. Then the timber stud walls and joist floor systems were built on the ground and ready to be moved into place with the overhead cranes. The formwork for the arch lintels was also constructed and the inverted steel T section used for the lintels in Walls 1 and 2 were cut to the proper lengths. The ST-11 test structure was constructed by experienced masons. The masons were permitted to adjust the amount of water used in the mortar until the desired consistency was achieved. The masonry walls were built using the standard American running bond pattern, with a header course every sixth course. This bond pattern continued through the piers and floor levels to the top course. For the three-wythe walls, the outside two wythes were tied at the same course as the two-wythe walls, while the inside two wythes were tied at the next course (Figure 6.9). Four holes were left at the corners of the structure at the floor and roof levels to allow the post-tensioning tendons used to attach the actuators to the structure. To facilitate the loading of the roof diaphragm, step-back openings were left in the center of Wall A and Wall 1 at the roof level (Figure 6.16). These openings were filled prior to the in-plane wall tests.

Construction of the walls was temporarily halted at the floor and roof levels to allow the floor systems to be placed by the overhead crane (Figure 6.17). Once the floor systems were aligned properly on Walls A and B, the pockets were built around the end of the joists to ensure proper fit. After the floor systems were assembled, sheathing was nailed to the top of the joists. At the same time, construction of the masonry wall

continued in order to keep the construction schedule. The construction of the entire building took approximately 1 month. Three masonry prism specimens and three 4-brick direct shear specimens were constructed per day (about 100 ft² of surface area) throughout the construction of building.

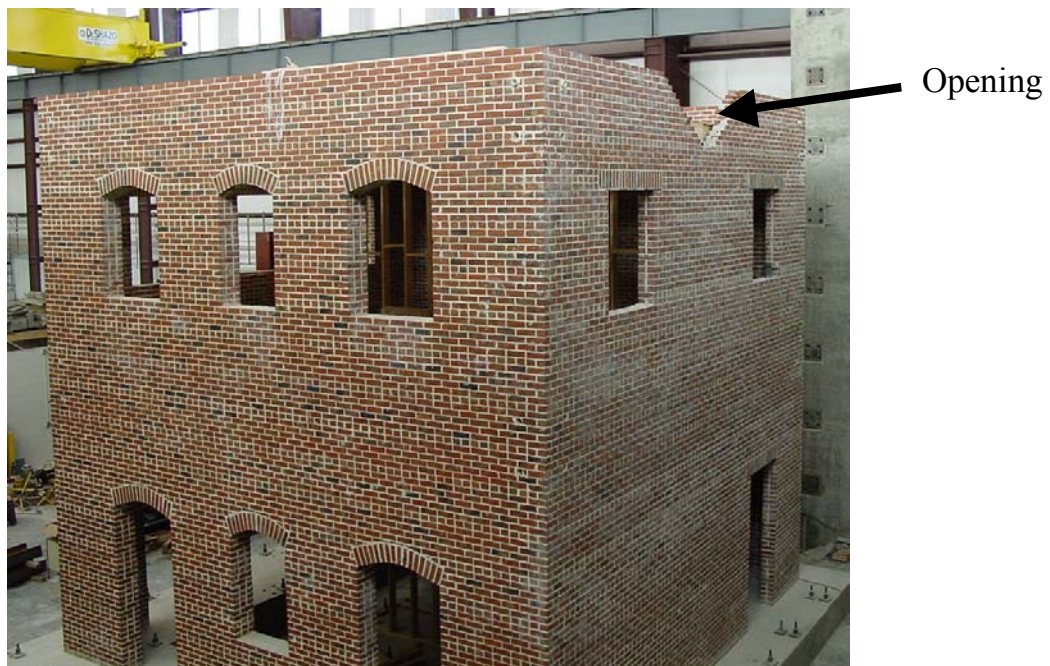


Figure 6.16. Opening left at the top of Wall 1



Figure 6.17. Assembly of the floor systems

6.6. REHABILITATION OF THE TEST STRUCTURE

Several different rehabilitation methods were designed and applied to the test structure. These rehabilitation methods included:

- the Saint-Gobain cementitious mortar–glass fiber reinforcement mesh system for Wall 2,
- the Clarke-Schwebel Tech Fab prefabricated glass fiber for Wall 1,
- the A&P glass fiber system for Wall B,
- the Hughes Brothers NSM Rods system for Wall B, and
- a post-tension system for Wall A.

Detailed descriptions of these rehabilitation systems can be found elsewhere (Moon 2004).

6.7. LOADING SEQUENCE

In order to fully investigate the structural performance of the test structure, a series of different loading steps were performed (Yi et al. 2002):

STEP 1: Low-level cyclic displacements were applied to (a) half and (b) the entire roof diaphragm to investigate its elastic properties and those of the masonry out-of-plane walls. The roof diaphragm was first loaded parallel to Walls A and B, then loaded parallel to Walls 1 and 2. The objectives of this series of tests included the determination of diaphragm stiffness, out-of-plane wall stiffness, and insight into the connection between the out-of-plane wall and the diaphragm. Detailed description of the test set up and the test results can be found in Chapter 7.

STEP 2: Lateral cyclic displacements were applied simultaneously to Walls 1 and 2 until fully developed failure mechanisms for these two walls were observed. The objectives for this test step included:

- Measure the in-plane elastic stiffness of Walls 1 and 2.
- Investigate the torsion behavior and the coupling behavior of the test structure that is characterized by containing weak in-plane walls and strong out-of-plane walls, and two in plane walls with very different stiffness.
- Investigate the nonlinear properties of Walls 1 and 2, including the maximum strengths, the deformation capacities, the crack patterns and the failure modes, the flange effect due to the out-of-plane walls, and the interaction between the piers and the spandrels, etc.

Detailed description of the test set up and the test results can be found in Chapter 8.

STEP 3: Lateral cyclic displacements were applied simultaneously to Walls A and B until fully developed failure mechanisms for these two walls were observed. The objectives for this test step were to:

- Measure the in-plane elastic stiffness of Walls A and B.
- Investigate the coupling behavior of the test structure with two identical strong in-plane walls and two weak out-of-plane walls.
- Investigate the nonlinear properties Walls A and B, similar to these for Walls 1 and 2.

Detailed descriptions of the test set up and the test results can be found in Chapter 9.

Each test step discussed above was accompanied with a retrofit of the test structure and a series of retests after the tests for the URM building were finished. Detailed descriptions of these retrofits and corresponding tests can be found elsewhere (Moon 2004).

6.8. SUMMARY

The design of the test structure is described in this Chapter. It includes the design objectives, characterizations of the masonry materials, design of the masonry walls, design of the flexible roof and floor diaphragms, design of the stud walls, and design of the RC foundation. The construction and the loading sequence for the test structure are also briefly discussed. Detailed descriptions of test set up and test results are given in the following three chapters.

CHAPTER 7

TESTS OF ROOF DIAPHRAGM AND OUT-OF-PLANE WALLS

7.1. INTRODUCTION

Horizontal roof and floor diaphragms in a building distribute lateral seismic forces or wind forces to the building's vertical resist components (moment frames or shear walls). The distribution of the lateral forces through the horizontal diaphragms is dependent on the in-plane stiffness of the diaphragms. In the case of a rigid diaphragm such as a reinforced concrete slab, the in-plane stiffness of the diaphragm is so large that the distribution among several vertical components is affected only by the lateral stiffness and the locations of these vertical components. In contrast, a timber roof or floor diaphragm in a URM building, which is composed of sheathing, joists and blocks (Figure 7.1), characterizes large flexibility. It usually exhibits significant bending and shear deformations under lateral forces. As a result, the distribution of lateral forces in a URM building is dependent on the interaction between the flexible diaphragms and the masonry walls.

The nonlinear properties of flexible timber roof or floor diaphragm itself have been investigated in several previous experimental research projects (APA 1985, 1986, Contryman 1952, 1955, Tissell 1967, Jonhson 1956, ABK 1981a, Zagajeski 1984, Peralta et al. 2000). For example, in the 1950s, a series of tests were conducted at the Forest Products Laboratory at Oregon State University to determine the strength and stiffness of timber diaphragms at various deformation levels. Parameters such as plywood thickness,

lumber sheathing humidity, nailing pattern, type of boundary members, bridging, blocking, connections, openings and width-to-length ratios were varied in this study (Johnson 1956). In the early 1980s, quasi-static tests and dynamic in-plane shaking tests for timber diaphragms were conducted by the ABK group (ABK 1981). These tests revealed the highly nonlinear and hysteretic stiffness characteristics of timber diaphragms. Recently, a MAEC Project ST-8 (Peralta et al. 2000) tested three full-scale timber diaphragm specimens, which were representatives of the timber diaphragms built in pre-1950's URM buildings. The goal of that research was to investigate the behavior of existing and rehabilitated timber diaphragms in URM buildings under lateral in-plane loads. Based on these experimental results, several design equations and analysis models have been proposed for the design and analysis purpose (Peralta et al. 2000, Kim et al. 2002).

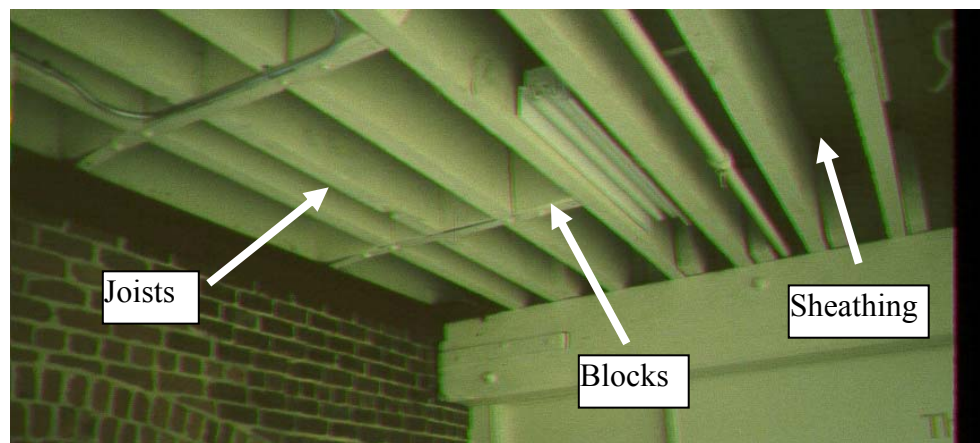


Figure 7.1. Typical diaphragm components

In contrast to the many experimental tests conducted to ascertain the nonlinear properties of flexible diaphragms, not many experimental tests have been carried out to investigate the role a flexible diaphragm plays in the response of an entire building. Fonseca (1997) tested two reinforced concrete tilt-up structures with plywood diaphragms to investigate the strength and deformation capacity of this type of structure. Paquette and Bruneau (2000, 2004) conducted a pseudo-dynamic testing on a full-scale one-story URM specimen with a timber roof diaphragm, aiming at investigating the flexible floor-rigid wall interaction in old URM buildings. Results from these experiments, together with some other observations from the field (Bruneau 1994) confirmed that the interaction between flexible timber diaphragms and masonry walls has a significant influence on the behavior of a URM building. More conclusions on the interaction between flexible diaphragm and masonry walls obtained from previous experimental investigation can be found in Section 2.5.

Based on the above context, it is clear that an experimental investigation of the interaction between flexible roof or floor diaphragm and masonry walls is very important for understanding the response of an entire URM building with flexible roof and floor diaphragms. The first part of ST-11 experiment was meant to address this issue by testing the timber roof diaphragm of the ST-11 building. Several parameters that may affect the interaction between flexible roof and floor diaphragm and masonry walls were investigated in these tests. These parameters include the relative stiffness of masonry walls and timber roof diaphragm, the connection behavior between masonry walls and timber roof diaphragms, and the overall working mechanisms. A picture of the tested roof diaphragm is shown in Figure 7.2.



Figure 7.2. The tested roof diaphragm

In order to investigate the interaction between the roof diaphragm and the masonry walls, a lateral load was applied at the center of the roof diaphragm. Deformations of both the diaphragm and the masonry walls were measured during the test. The loading sequence of this test consisted of the following three steps:

- Testing of half of the diaphragm parallel to the joists.
- Testing of the entire diaphragm parallel to the joists.
- Testing of the entire diaphragm perpendicular to the joists.

The test setup and the test results for the above three test series are presented in the following sections. Conclusions are given at the end.

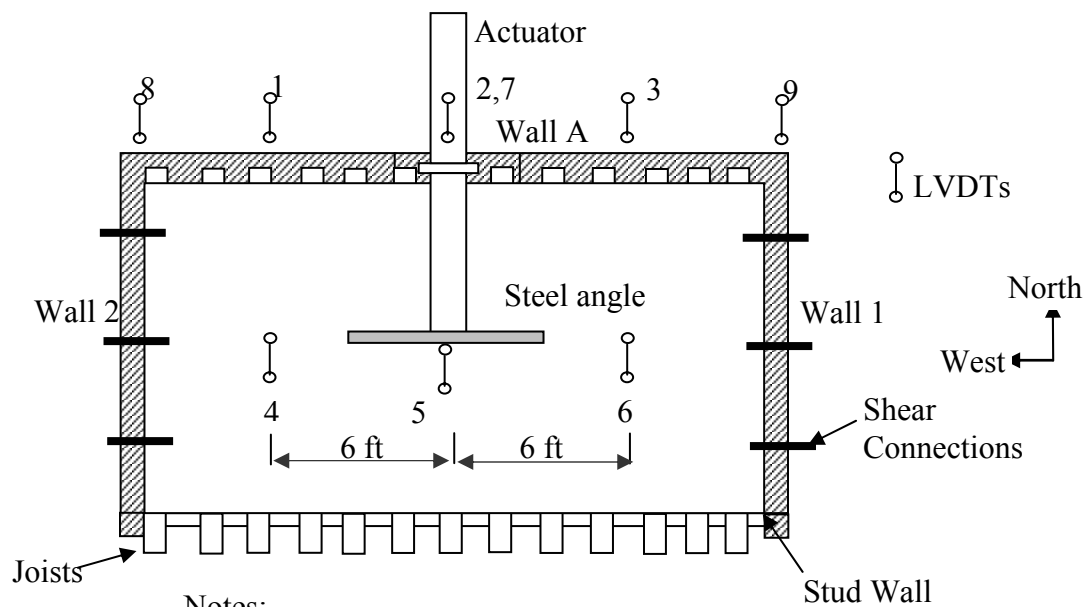
7.2. TEST ON ONE-HALF OF THE DIAPHRAGM PARALLEL TO THE JOISTS

Roof sheathing was first nailed to the 12-ft long joists simply supported on Wall A and the stud wall. These joists were not connected with the joists next to Wall B. As a result, no connections existed between this one-half roof diaphragm and Wall B. This one-half roof diaphragm was then tested parallel to the joists. This test aimed at

determining the elastic stiffness of a rectangular roof diaphragm with a span to length ratio of 2.0, and at comparing the obtained results with the test results of specimen MAE2 obtained from MAEC project ST-8 (Peralta et al. 2000).

7.2.1. Test Setup

The test setup is schematically shown in Figure 7.3. The diaphragm was simply supported on Wall A and the stud wall. It was also laterally supported on Walls 1 and 2 by shear connections made from 5/8" diameter threaded rods. The configuration of the roof diaphragm can be found in Section 6.4.3.



Notes:
LVDT 7 is at the floor level, the other LVDTs are at the roof level.

Figure 7.3. Test setup for the one-half diaphragm test

Two 4 ft long 2x10 timbers were used to reinforce the central joist (Figure 7.4a), and two other 4 ft long 2x10 timbers are nailed to the sheathing right above the central joist (Figure 7.4b). Thus a strong loading line was formed along the test diaphragm. Four Simpson tension ties were used to connect these 2x10 timbers pieces to the steel angle attached to a loading actuator through an opening at the middle of the top of Wall A. In some test runs a steel angle with a length of 8 ft was bolted to the diaphragm at the end of the top 2x10 timbers. This additional angle was used to alter the force distribution in the diaphragm, and to check the effect of different force distribution on the behavior of the diaphragm.

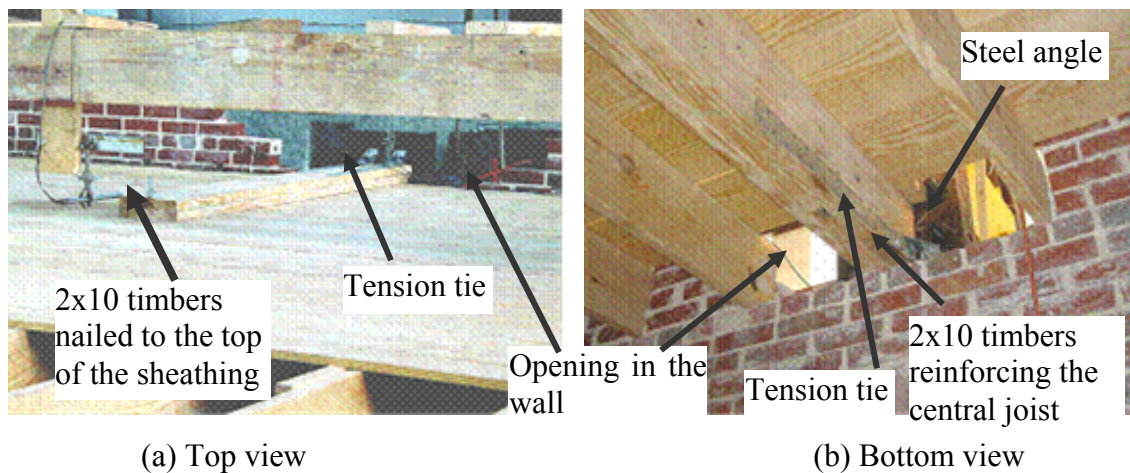


Figure 7.4. Setup of the loading system for the one-half diaphragm test

The diaphragm was loaded with displacement control. The typical loading history is given in Figure 7.5. Each test run is a complete load cycle with a maximum

displacement of 0.2 in. This loading history was applied to all the test series discussed later, although the initial loading direction was different in some test runs.

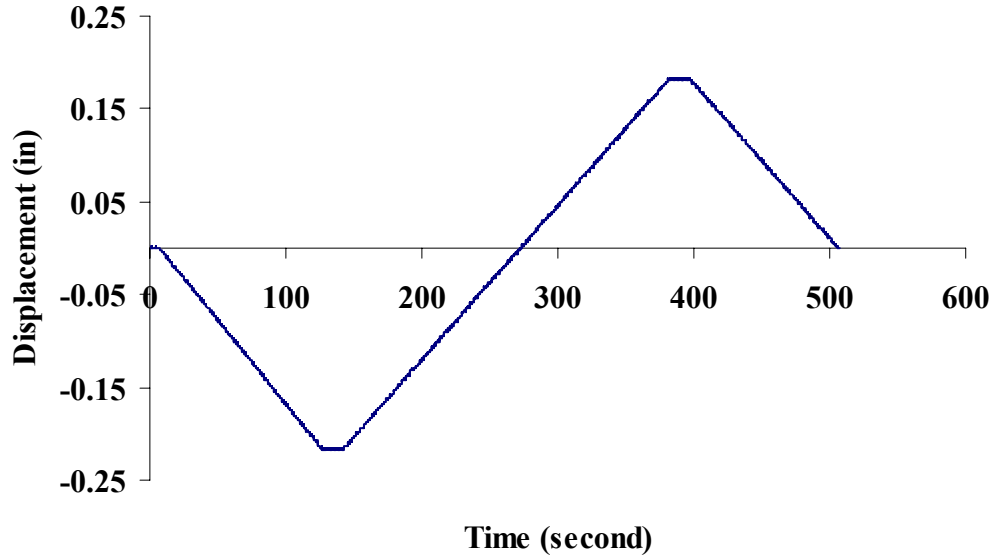


Figure 7.5. Loading history for the one-half diaphragm test

Several LVDTs were used to monitor the response of the structure during the test (Figure 7.3). Specifically, LVDTs 4, 5 and 6 were used to measure the lateral displacement of the diaphragm. LVDTs 1, 2, 3 and 7 were used to monitor the possible out-of-plane deformation of Wall A. LVDTs 8 and 9 were used to measure the lateral displacement of the in-plane Walls 1 and 2.

7.2.2. Test runs

Four test runs were conducted to investigate the response of this half diaphragm (Table 7.1). Two series of parameters, different loading patterns and different initial loading directions, were examined in these test runs.

Table 7.1. Lists of test runs, loading direction parallel to the joists

ID	Description
Run 8	Half diaphragm, steel angle ¹ , pull direction ² , no connections ⁴
Run 9	Half diaphragm, steel angle, push direction ³ , no connections
Run 10	Half diaphragm, point load, pull direction, no connections
Run 11	Half diaphragm, point load, push direction, no connections

1: Steel angle was used at the end of the 2x10 woods to distribute the force.

2: Pull direction: the roof was pulled toward Wall A.

3: Push direction: the roof was pushed away from Wall A.

4: No tension connections were provided between Wall A and the roof diaphragm.

7.2.3. Test results

A typical force-lateral displacement curve for the half diaphragm is shown in Figure 7.6 (Run 8). The maximum lateral displacement at the center of the roof was about 0.15 in., which means that about 25% of the control displacement imposed by the loading actuator was lost due to the flexibility of the loading system. The observed roof stiffness in the negative direction (the sign of the force is negative when the roof is pulled toward the north) is much higher than that in the positive direction (the sign of the force is positive when the roof is pushed toward the south). This can be explained by the different interaction behavior between the roof diaphragm and Wall A as follows.

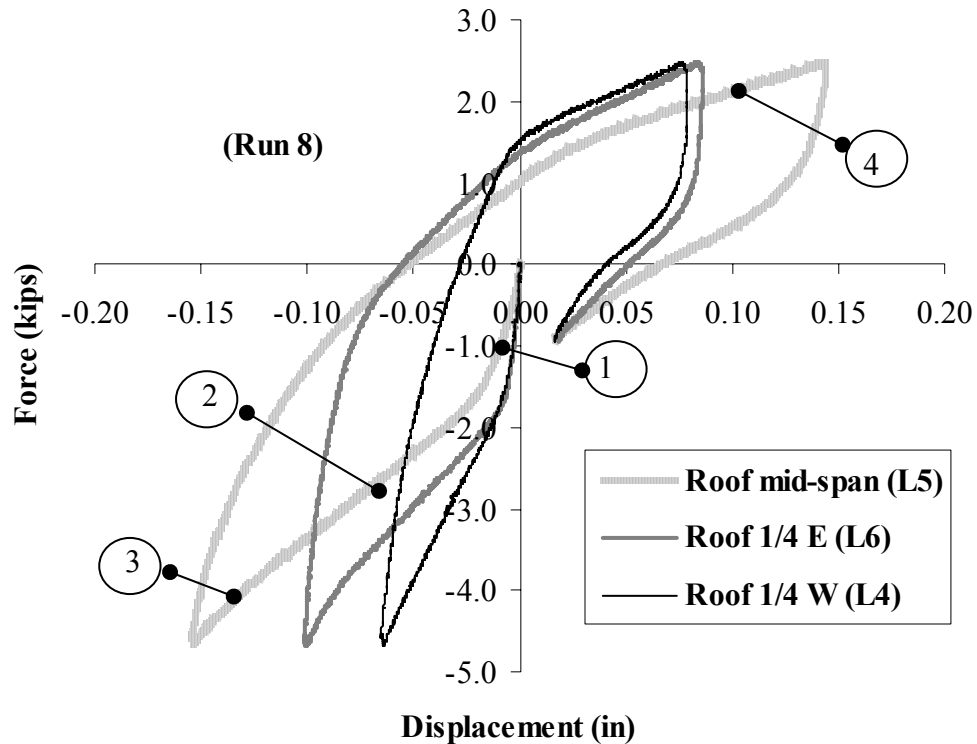


Figure 7.6. Typical force-displacement curve of the half roof diaphragm

Since the lateral stiffness of the stud wall was negligible, the lateral supports to the diaphragm were provided by the shear connections and Wall A. When the roof diaphragm started to be pulled toward Wall A (force is negative), the external force was not large enough to overcome the bond forces and the friction forces between the end of the joists and the masonry wall. As a result, the out-of-plane Wall A deformed together with the diaphragm, which increased the observed stiffness of the diaphragm and caused a large initial stiffness section (stage 1) in Figure 7.6. With increasing external lateral force, the bond between the end of the joists and the masonry wall was gradually broken and the friction forces were progressively overcome. Sliding occurred between the joists

and the masonry wall, leading to a decrease of the observed stiffness of the roof diaphragm (stage 2). However, when the ends of the joists touched the masonry wall after sliding, Wall A gradually picked up more force, and consequently the observed stiffness of the roof diaphragm increased (stage 3).

It should be noted that a typical shear connection between the timber diaphragm and the masonry in-plane wall being tested displayed rather large flexibility compared with Wall A. As a result, the lateral forces transferred from the diaphragm to the shear connection were small. Furthermore, although the lateral deflection of the diaphragm exhibited a large value at the mid-span, only a small displacement was observed at each end of the diaphragm. This caused even less force being transferred to the shear connections. Consequently, it is reasonable to assume that all the external lateral forces were transferred from the diaphragm to the out-of-plane walls, while no forces went directly into the in-plane Wall A. One interesting result of this assumption is that the lateral shear stiffness of the diaphragm does not play important role in the response of the diaphragm when loaded parallel to the joists. This assumption applies to not only the half diaphragm, but also the entire diaphragm, especially for the case that the pockets housing the ends of the joists are grouted, which is discussed later.

When the roof diaphragm was pushed away from Wall A, the interaction between the roof and the masonry wall was different from that in the previous case. With increasing lateral displacement and gradual sliding between the joists and the out-of-plane wall, less and less external forces were transferred from the diaphragm to the out-of-plane Wall A, while more and more forces were transferred to the in-plane Walls 1 and 2 through the shear connections. This can be seen from the softening behavior of the

diaphragm (stage 4) in Figure 7.6, and also the stiffening stage of the total external force-displacement curve (stage 1) for the out-of-plane Wall A as shown in Figure 7.7. Although Figure 7.7 indicates that Wall A still took some forces at the end of push loading, the force was small. Therefore, the upper-bound estimation for the lateral stiffness of the half roof diaphragm can be obtained by assuming all the incremental external forces were transferred directly to the in-plane wall, and calculating the tangential stiffness at the end of the push loading. The calculated lateral stiffness of the half roof diaphragm in each test series are listed in Table 7.2. Note that the calculated stiffness includes both the flexural deformation and the shear deformation of the diaphragm.

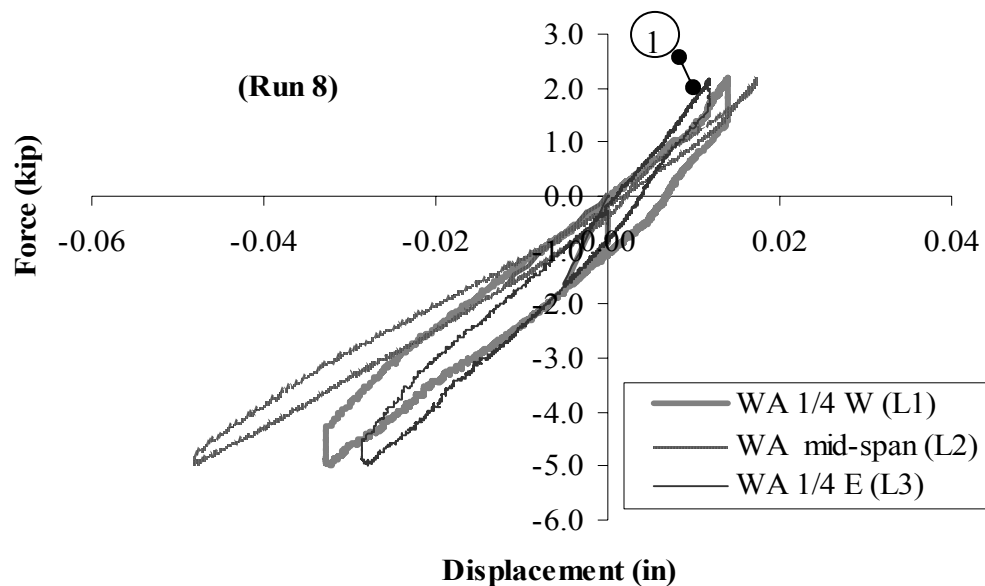


Figure 7.7. Total external force-displacement curve for the out-of-plane Wall A

Table 7.2. Tangential stiffness of the half roof diaphragm at the end of pushing loading
(by mid-span displacement)

Test Run	Stiffness (kips/in) (by 0.05 inch increment)
Run 8	9
Run 9	10
Run 10	6
Run 11	6

Table 7.2 shows that the steel angle increased the stiffness of the diaphragm because it better distributed the force into the diaphragm (Runs 8 and 9). The measured stiffness of the diaphragm (10 kips/in.) is smaller than the value obtained in ST-8 test (20.6 kips/in). This is reasonable given that ST-8 applied two point loads instead of one point load.

It should also be pointed that the readings of LVDTs 8 and 9 were very small, which indicated that the deformation of the in-plane walls was negligible. This phenomenon was observed in all the other test runs that will be discussed later.

7.3. INTERACTION MECHANISMS BETWEEN DIAPHRAGM AND MASONRY WALLS PARALLEL TO THE JOISTS

After the test for the one-half diaphragm was completed, the remaining half diaphragm was built with an identical configuration to the first part. Again, shear connections made from 5/8" diameter threaded rods were used to connect the roof diaphragm with in-plane Walls 1 and 2. The entire diaphragm was tested again in the direction parallel to the joists.

7.3.1. Test setup

The test setup is shown in Figure 7.8. Similar to the half diaphragm test, 2x10 timber sections were used to strengthen the central joist and were nailed to the sheathing. A 100-kip actuator was connected to these 2x10 timbers sections with Simpson tension ties. This resulted in a point load to the diaphragm, which is referred as the “point load” case in the following discussion. In some test runs, a timber diamond frame made from 2x10 sections was bolted to the center of the diaphragm. It was used to produce a relative uniform displacement at the center quarter of the diaphragm. This is referred as the “uniform load” case in the following discussions. In some other cases, Joist anchors made from Simpson tension ties were used to connect the roof diaphragm with the out-of-plane Walls A and B. No shear connections were provided between the roof diaphragm and the masonry in-plane Walls 1 and 2.

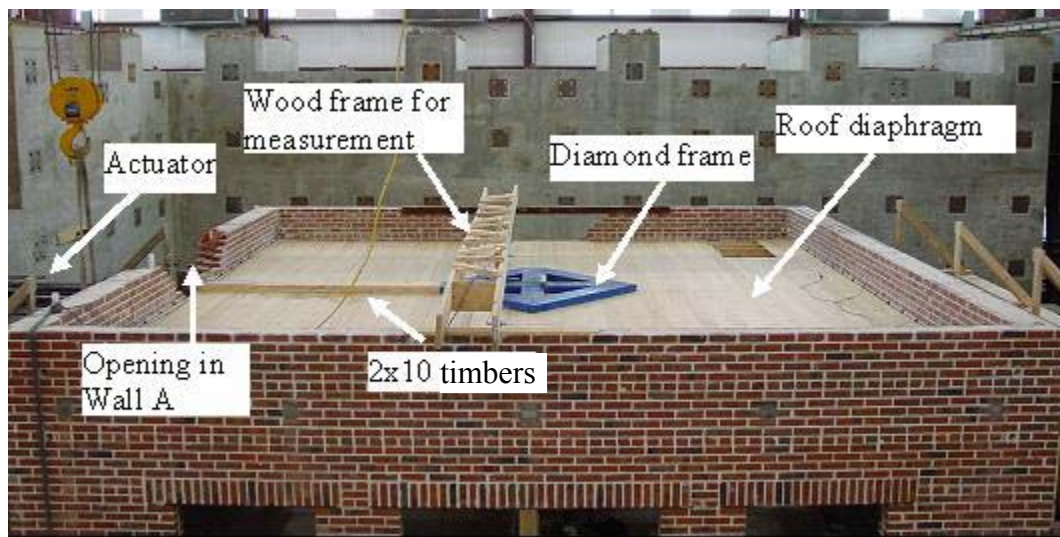
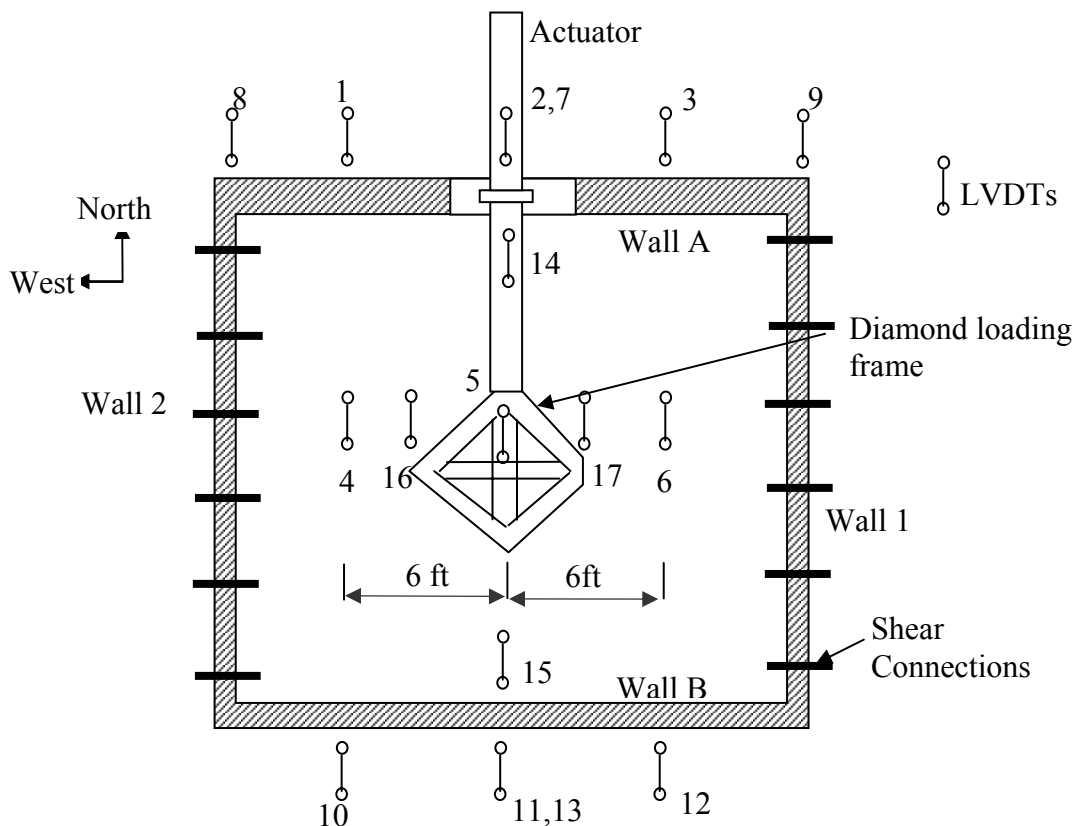


Figure 7.8. Test set up for the entire roof diaphragm test parallel to the joists

The instrumentation set up for the test is shown in Figure 7.9. LVDTs 4, 5, 6, 16, 17 were used to measure the lateral displacement of the diaphragm. LVDTs 1, 2, 3 and 7 were used to measure the out-of-plane deformations of Wall A. LVDTs 10, 11, 12 and 13 were used to measure the out-of-plane deformations of Wall B. LVDTs 8 and 9 were used to measure the out-of-plane deformations of Wall B. LVDTs 8 and 9 were used to measure the lateral displacement of in-plane walls 1 and 2. LVDTs 14 and 15 were used to measure the relative sliding between the center joist and the masonry walls.

The diaphragm was loaded with displacement control. The typical loading history is shown in Figure 7.5.



Notes: LVDTs 7 and 13 are at the floor level, the other LVDTs are at the roof level.

Figure 7.9. Instrumentation set up for the roof diaphragm test parallel to the joists

7.3.2. Test runs

Six test runs, each run a full displacement cycle with a maximum actuator displacement of 0.2 in, were conducted on the full diaphragm in the direction parallel to the joists. The controlling features for each test run are listed in Table 7.3. Note that several small-displacement test runs were conducted prior to the main test runs to tune the test system, and thus the reported runs start with Run 17. Among these test runs, Runs 17 to 20 were intended to investigate the interaction between the diaphragm and the masonry walls with different loading patterns and with or without tension connections between the diaphragm and out-of-plane walls. The contribution of the touching between the 1x6 sheathing and the out-of-plane walls to the interaction between the diaphragm and the masonry walls also is of interest in this test. Therefore, a 3-in. width gap was left between the 1x6 sheathing of the diaphragm and Wall B in Runs 21b and 22. When analyzing the test results, the results from the previous test runs 8 to 11 are also utilized.

Table 7.3. Lists of Test Runs Parallel to Joists

ID	Description
Run 17	Full diaphragm, uniform displacement, pull direction*, with tension connections**
Run 18	Full diaphragm, point load, pull direction, with tension connections
Run 19b	Full diaphragm, point load, pull direction, no tension connections
Run 20	Full diaphragm, uniform displacement, pull direction, no tension connections
Run 21b	Full diaphragm, uniform displacement, pull direction, no tension connections, with gap adjacent to Wall B
Run 22	Full diaphragm, point load, pull direction, no tension connections, with gap adjacent to Wall B

* Pull direction: the roof is pulled toward Wall A.

** Locations of the tension connections between the roof diaphragm and Walls A and B refer to Figure 7.9.

7.3.3. Working mechanism for the diaphragm-wall system parallel to the joists

Interesting behavior for the diaphragm-wall system parallel to the joists was observed during this test step. Due to the same reasons discussed for the one-half diaphragm test (see Section 7.2.3), the shear connections between the diaphragm and the in-plane walls transferred only small percentage of lateral forces. Most of the lateral forces were transferred from the diaphragm to the out-of-plane walls. As a result, for analysis purpose the diaphragm-wall system can be simplified to the model shown in Figure 7.10. The diaphragm is only connected to the out-of-plane walls, while the out-of-plane walls are supported by both the ground and the in-plane walls. M_d , M_o and M_i are the lumped mass of the diaphragm, the out-of-plane wall, and the in-plane wall, respectively. K_a is the axial stiffness of the diaphragm. K_{do} represents the stiffness of the connection between the joists and the out-of-plane walls. K_{og} is the stiffness of the out-of-plane wall due to the support of the ground; K_{oi} is the stiffness of the out-of-plane wall due to the support of the in-plane wall; and K_i is the stiffness of the in-plane wall. Under an earthquake excitation, the in-plane wall is excited by its own mass and the forces transferred from the out-of-plane walls. Since the stiffness of the in-plane walls are much larger than those of the diaphragm and of the out-of-plane walls, the in-plane walls can be considered as an infinitely stiff part of this structure, and the conceptual model in Figure 7.10 can be further simplified to that shown in Figure 7.11, in which the stiffness of the out-of-plane wall K_o is the sum of K_{og} and K_{oi} .

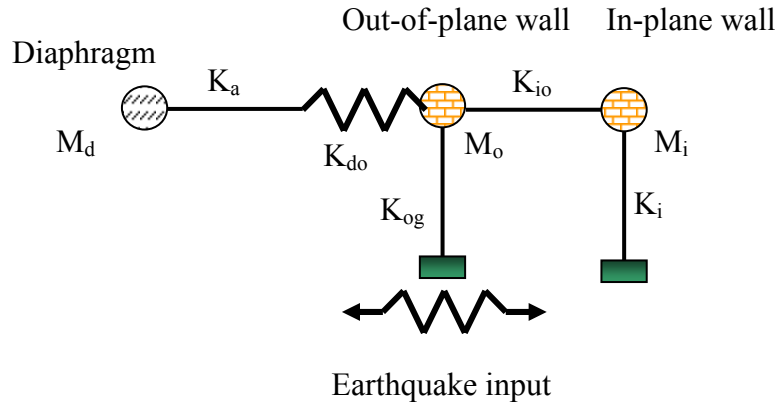


Figure 7.10. Conceptual model for the structure in the direction parallel to the joists

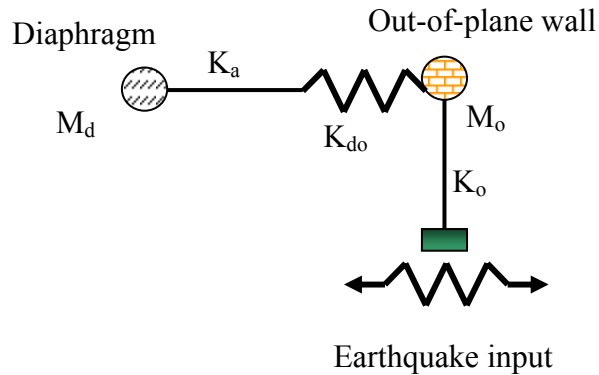


Figure 7.11. Simplified conceptual model for the structure in the direction parallel to the joists

The observed typical displacements of the roof diaphragm and the masonry walls under cyclic loading are shown in Figure 7.12. L5 is the measured lateral displacement at the mid-point of the roof diaphragm, while L11 is the measured lateral displacement at the middle of the top of Wall B. The signs for both the two displacements are positive when moving away from the strong wall (Southward). L15 is the measured relative displacement between Wall B and the diaphragm. Its sign is positive when the relative

displacement is separation. Figure 7.12 shows that when the diaphragm was pushed toward the south (both the force and L5 are positive), the out-of-plane wall B was also pushed toward the south (L11 is positive). However, there was a closing movement between Wall B and the diaphragm, and thus L15 was negative. The displacements were the opposite when the diaphragm was loaded toward the north. This type of movement is represented by the conceptual model shown in Figure 7.11. The values of these displacements are dependent on the value of the external forces, K_a , K_{od} , and K_o . Detailed discussion for these stiffness values is given in the following sections.

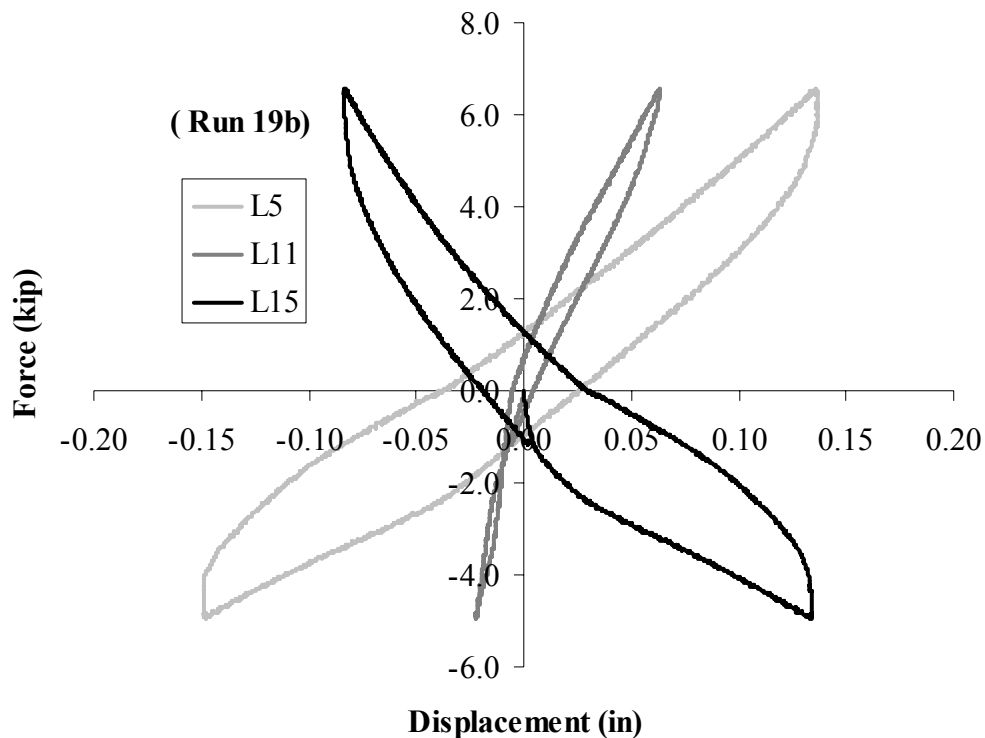


Figure. 7.12. Typical displacements of roof diaphragm and the masonry walls when loaded parallel to the joists

7.3.4. Elastic response of the out-of-plane Walls A & B

The out-of-plane elastic stiffness of Walls A and B can be obtained from Test Runs 8 through 11 and 17 through 22 as follows:

- Since Wall A and Wall B are identical three-wythe walls, the out-of-plane stiffness of the two walls is assumed to be the same.
- In the test runs 8 to 11 for the half diaphragm, the out-of-plane stiffness of Wall A can be obtained from the loading portion of the load-displacement curve when the diaphragm is pulled against Wall A (negative direction). The secant stiffness corresponding to a 2 kips force increment at the end of the “pull” portion of the loading as shown in Figure 7.13 is used as the representing elastic stiffness of the wall. It can be calculated as:

$$K_A = \Delta F / \Delta D_2 \quad (7.1)$$

where K_A is the out-of-plane stiffness of Wall A. ΔF is the force increment measured by the load cell in the actuator. ΔD_2 is the incremental deformation at the middle of the top of Wall A measured by LVDT 2.

- In the test runs 17 to 22, i.e. the full diaphragm tests, the lateral force is resisted by both Wall A and Wall B no matter which direction the actuator is acting. As a result, the out-of-plane stiffness of Wall A and Wall B can be calculated as:

$$K_A \cdot \Delta D_2 + K_B \cdot \Delta D_{11} = \Delta F \quad (7.2)$$

where K_A , ΔF and ΔD_2 are the same as in Eq. (7.1). K_B is the out-of-plane stiffness of Wall B. ΔD_{11} is the displacement increment measured in LVDT 11.

Since K_A is assumed equal to K_B , Eq. (7.2) can be rewritten as:

$$K_A = \Delta F / (\Delta D_2 + \Delta D_{11}) \quad (7.3)$$

To assess the variability of this stiffness, the secant stiffness was calculated for the following three portions of each test run: a) maximum positive load, b) maximum negative load, and c) zero load (Figure 7.14). As for the previous calculations, this was a secant stiffness corresponding to an external force increment of approximately 2 kips.

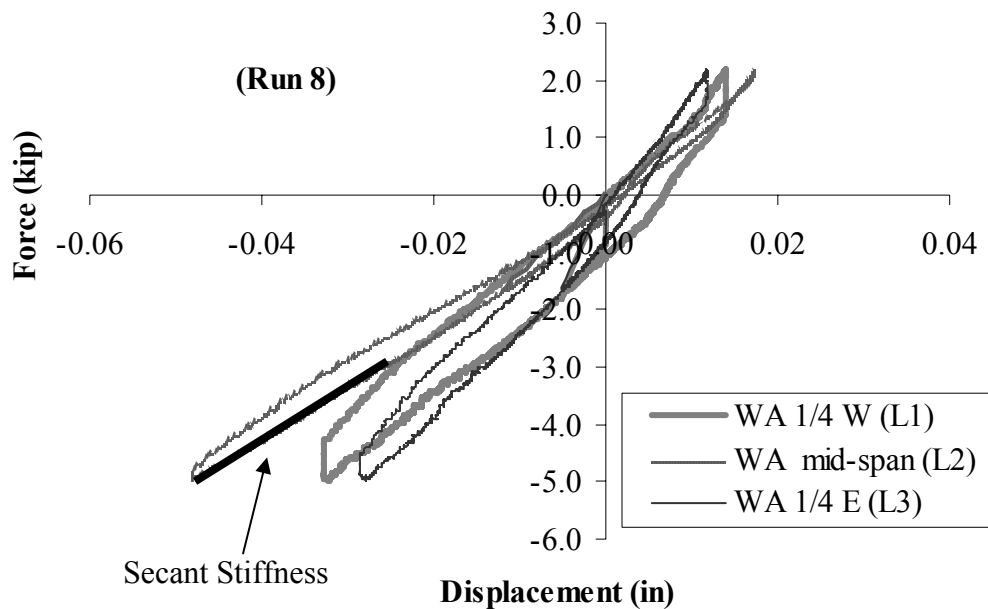


Figure 7.13. Loading phase for calculating the secant stiffness of the out-of-plane Wall A (Run 8)

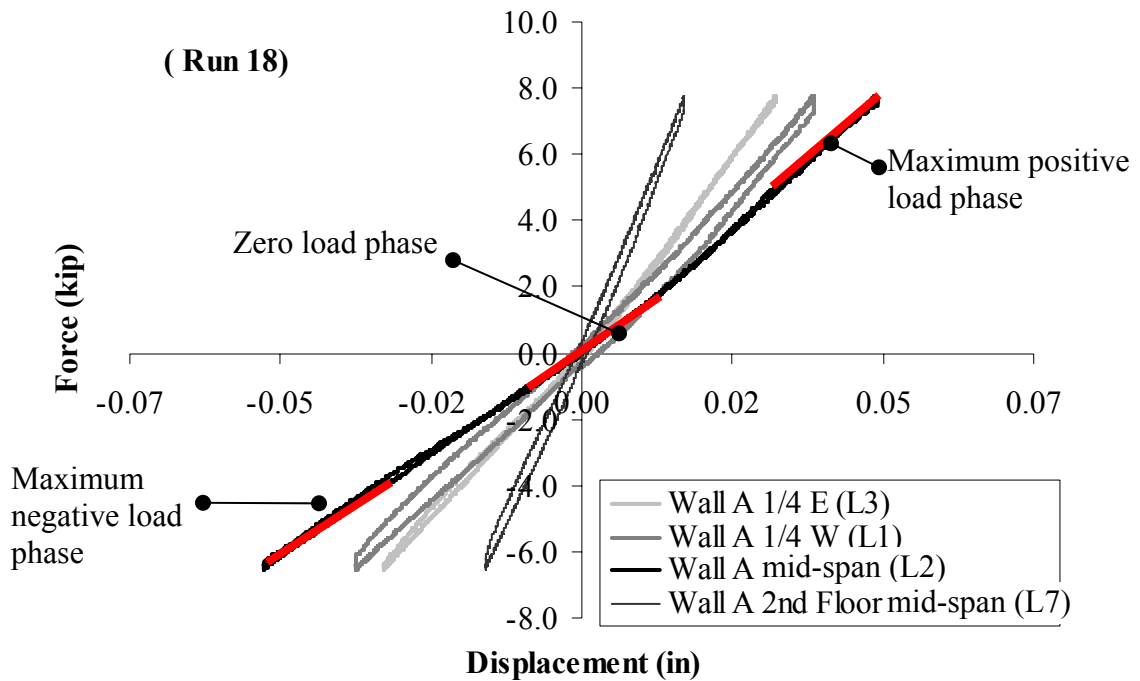


Figure 7.14. Loading phases for calculating the secant stiffness of the out-of-plane Wall A (Run 18)

The measured stiffness of the out-of-plane walls A and B are listed in Table 7.4. This table shows that the stiffness of the out-of-plane wall was not significantly affected by the loading pattern (uniform or point load cases) in the full diaphragm tests. The rather long distance between the loading point and the out-of-plane wall (12ft) might help to even out the forces transferred from the diaphragm to the out-of-plane wall, no matter what type of load was applied at the center of the diaphragm (Figure 7.15). In contrast, since there was a quite short distance between the loading point and the out-of-plane masonry wall in the half diaphragm test, the steel angle noticeably increased the observed stiffness of the out-of-plane wall.

Table 7.4. Out-of-plane elastic stiffness of Walls A and B

Test Run	Load Case	Loading Phases	Connections	Diaphragm	Stiffness (kips/in)	Mean of Stiffness (kips/in)
8	Steel Angle	To Wall A	No	Half	89.0	89.0
9	Steel Angle	To Wall A	No	Half	94.3	94.3
10	Point	To Wall A	No	Half	76.9	76.9
11	Point	To Wall A	No	Half	74.0	74.0
17	Uniform	To Wall A	Yes	Full	71.5	69.4
		To Wall B			68.5	
		Zero			68.2	
18	Point	To Wall A	Yes	Full	70.3	68.2
		To Wall B			68.7	
		Zero			65.7	
19b	Point	To Wall A	No	Full	78.3	74.0
		To Wall B			71.9	
		Zero			71.7	
20	Uniform	To Wall A	No	Full	79.3	73.8
		To Wall B			72.2	
		Zero			70.0	
21b	Uniform, Gap	To Wall A	No	Full	80.0	78.3
		To Wall B			76.2	
		Zero			78.6	
22	Point, Gap	To Wall A	No	Full	76.1	75.3
		To Wall B			74.2	
		zero			75.5	

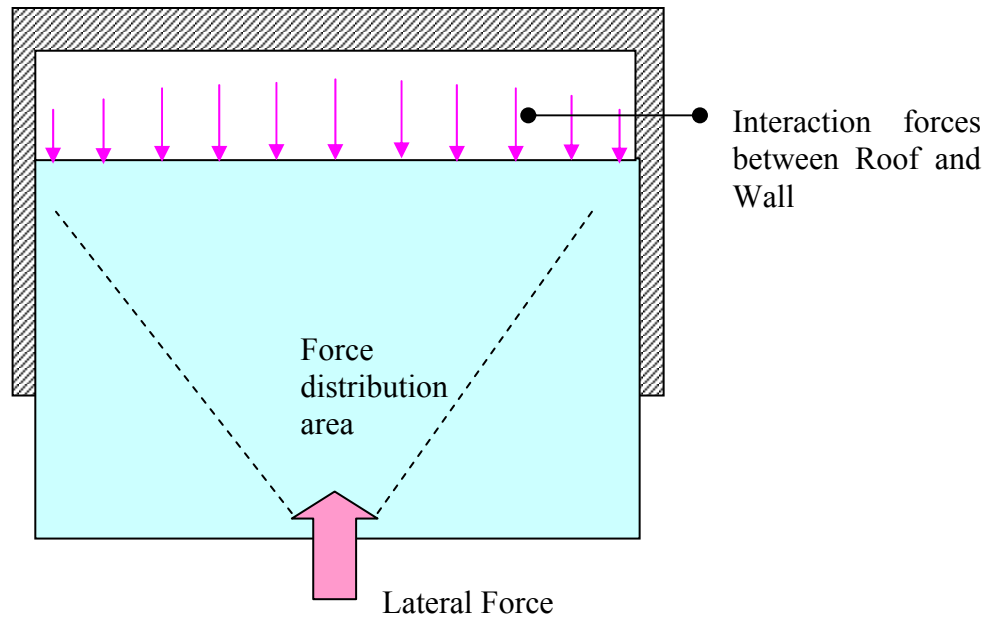
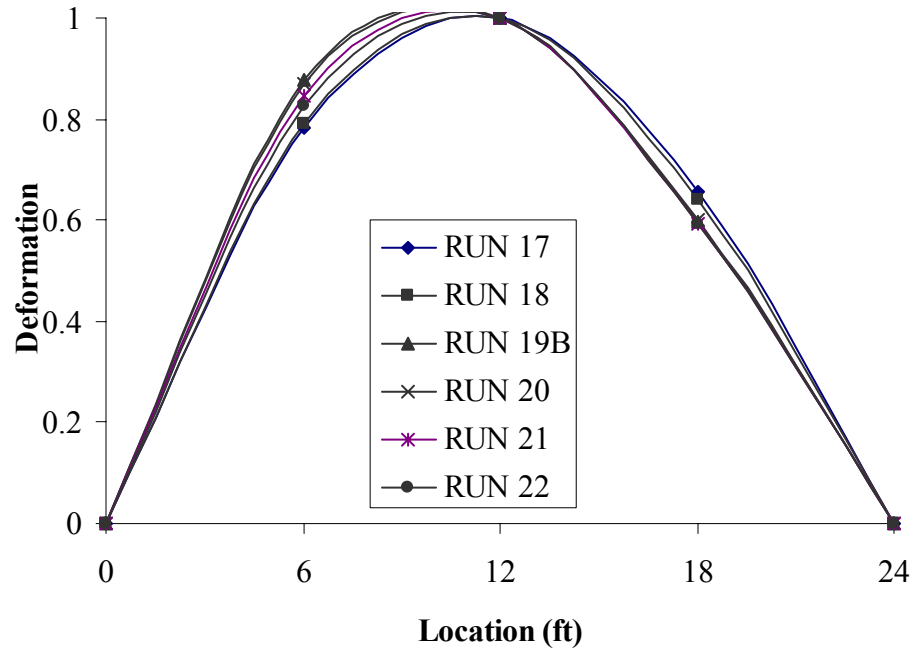


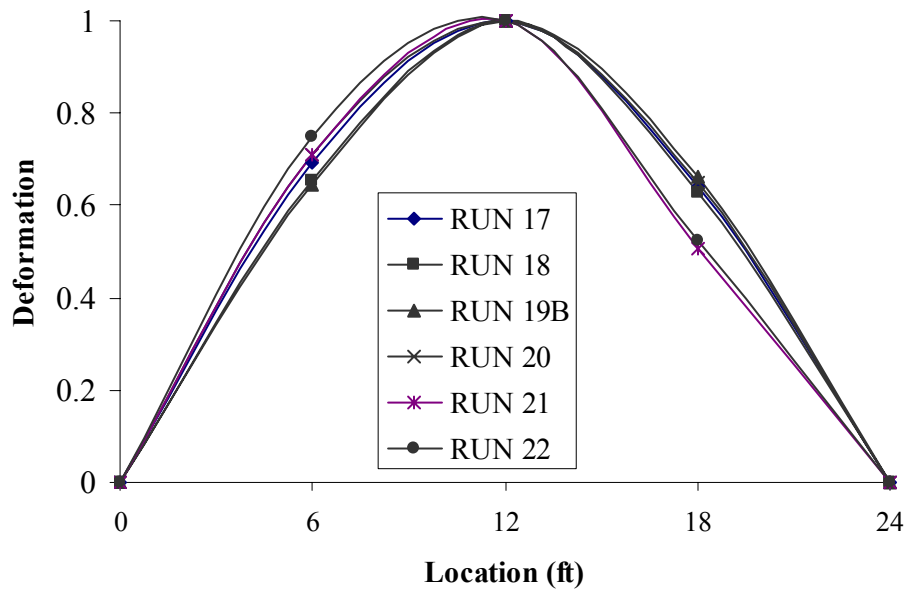
Figure 7.15. Long distance between the loading point and the masonry wall helps to uniformly distribute the force on the boundary

Nevertheless, except for Runs 8 and 9, all the other test runs provided rather consistent values for stiffness, ranging from 68.2 to 78.3 kips/in for the out-of-plane stiffness of Walls A and B. If the lateral force transferred from the roof diaphragm to the out-of-plane walls A and B is assumed close to a uniform force distribution, an elastic FE analysis showed that the corresponding elastic modulus of the masonry was around 900 to 1100 ksi (see Section 10.2.3).

The horizontal deformation profiles for Walls A and B at the roof level are shown in Figure 7.16. Both of them exhibit a typical flexural deformation profile. The lateral deformation profiles for Walls A and B along the vertical centerline of the wall are shown in Figure 7.17. Both of them also exhibit a typical flexural deformation profile.

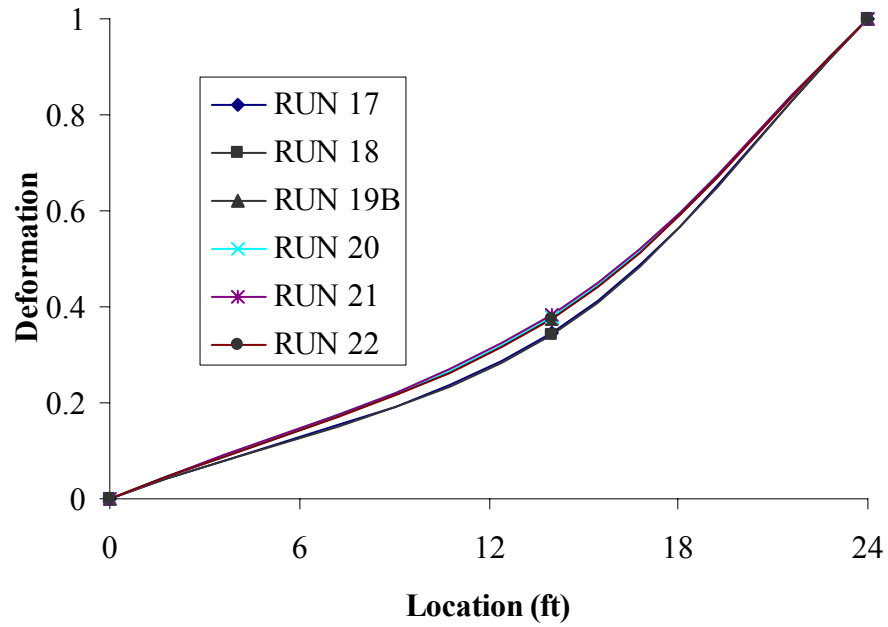


(a) Deformation Profile of Wall A (Horizontal, roof level)

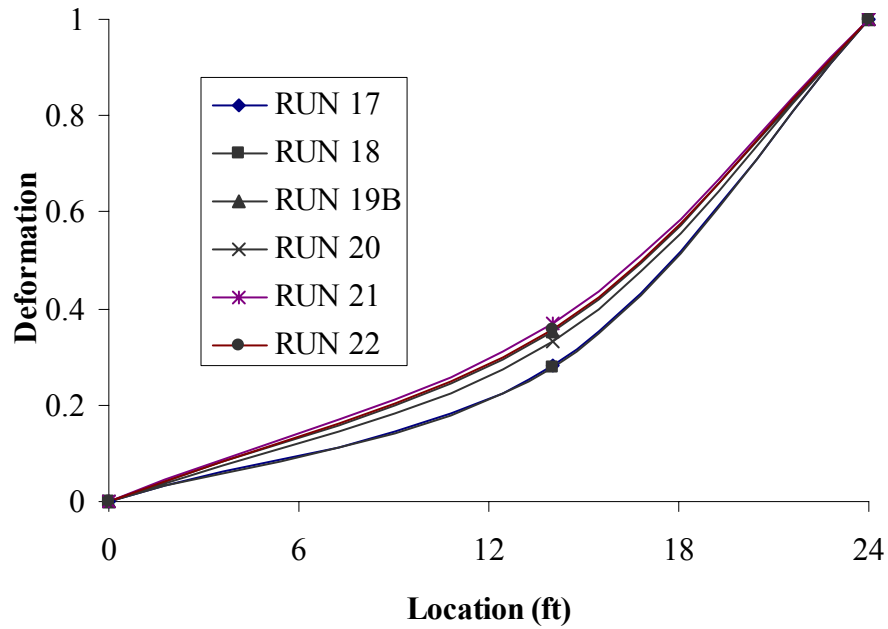


(b) Deformation Profile of Wall B (Horizontal, roof level)

Figure 7.16. Deformation profiles of the out-of-plane walls at the roof level



(a) Deformation Profile of Wall A (Vertical, center)



(b) Deformation Profile of Wall B (Vertical, center)

Figure 7.17. Deformation profile of the out-of-plane walls along the vertical centerline

7.3.5. Elastic axial stiffness of the diaphragm parallel to the joists

The axial deformation of the diaphragm can be obtained by calculating the relative displacements measured by the LVDTs as:

$$D_{dab} = D_{L15} + D_{L11} - D_{L14} - D_{L2} \quad (7.4)$$

where D_{L15} , D_{L14} , D_{L11} and D_{L2} are readings obtained from LVDTs L15, L14, L11 and L2, respectively (Figure 7.9).

The axial stiffness of the roof diaphragm parallel to the joists can be calculated as:

$$K_a = \frac{F_{wallb}}{D_{dab}} = \frac{K_{wallb} \cdot L11}{D_{dab}} \quad (7.5)$$

where F_{wallb} is the lateral force applied to the out-of-plane wall B introduced by the diaphragm. K_{wallb} is the out-of-plane stiffness of Wall B, which is assumed as 73 kips/in from Table 7.4.

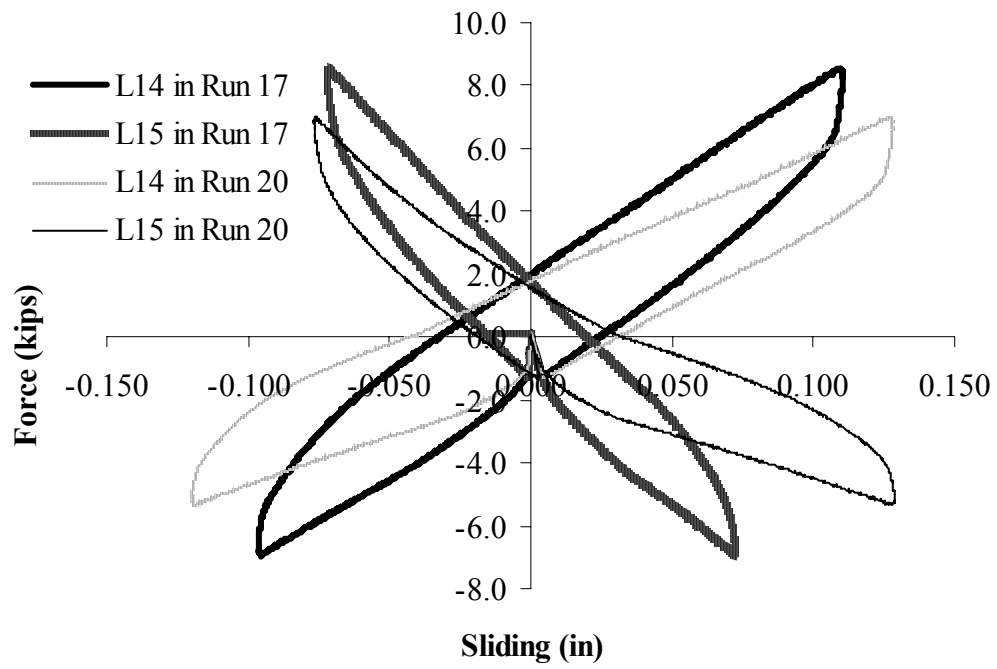
The secant stiffness obtained from connecting the maximum positive and the maximum negative displacement points was used as the representative axial stiffness of the roof diaphragm. The resulting values of the axial stiffness are listed in Table 7.5. This table shows that the axial elastic stiffness of the tested diaphragm was about 200 kips/in, which is about two to three times the out-of-plane stiffness' of Walls A and B. The presence of tension ties between the roof diaphragm and the masonry walls did not have a significant influence on the axial stiffness of the roof diaphragm. On the other hand, the gap between the 1x6 sheathing of the roof and the masonry Wall B significantly reduced the observed axial stiffness of the roof diaphragm.

Table 7.5. Axial stiffness of the diaphragm

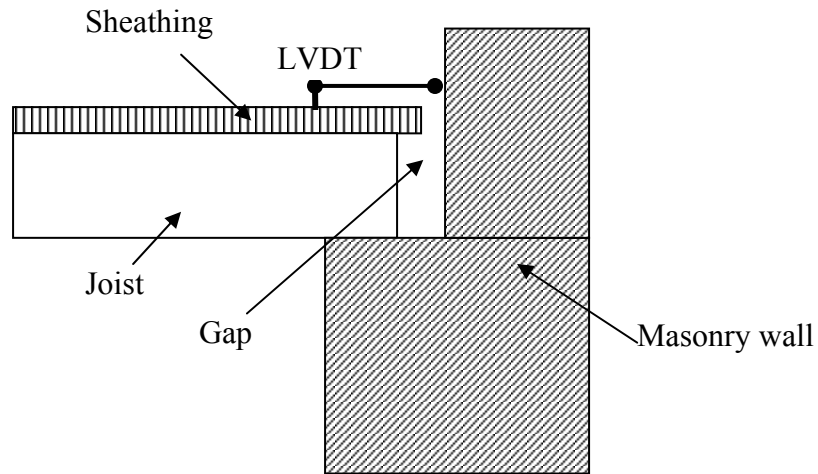
Test run	Load case	Tension tie connections	Stiffness (kips/in))
17	Uniform	Yes	182.1
18	Point	Yes	192.3
19b	Point	No	224.0
20	Uniform	No	203.1
21b	Uniform, Gap	No	102.6
22	Point, Gap	No	110.1

7.3.6. Sliding behavior between the joists and the out-of-plane walls

Figure 7.18a shows the relative sliding between the joists and the masonry out-of-plane walls, which were obtained from LVDTs L14 and L15. There was a large amount of sliding between the joists and the masonry walls during the test runs with an ungrouted-pocket connection detail (Figure 7.18b). Compared to the no tension tie case (Run 20), the tension ties between the diaphragm and the wall (Run 17) helped to reduce the sliding between the joists and the walls. It should be noted that the sliding behavior is very sensitive to the construction details and external forces. If the pocket is grouted and the lateral force is not large enough to break the grout, sliding should not occur. Furthermore, if the ends of the joists touch the masonry wall, the sliding will stop.



(a) Force-sliding displacement curves



(b) Joist-masonry wall connection details

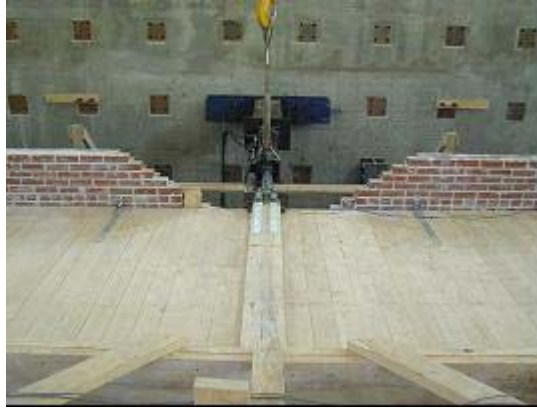
Figure 7.18. Sliding between the joists and the out-of-plane wall (Run 17 with tension ties and Run 18 without tension ties)

7.4. INTERACTION MECHANISMS BETWEEN DIAPHRAGM AND MASONRY WALLS PERPENDICULAR TO THE JOISTS

After being tested in the direction parallel to the joists, the diaphragm was loaded again in the direction perpendicular to the joists.

7.4.1. Test setup

The test setup is shown in Figure 7.19. As before, shear connections made from 5/8" diameter threaded rods were used to connect the roof diaphragm with in-plane Walls A and B. In some test cases Simpson tension ties were used to connect the roof diaphragm with the out-of-plane Walls 1 and 2. An opening was left at the middle of the top and parapet of Wall 1 to allow the actuator to be connected. The actuator was attached to two 2x10 timber sections nailed to the top of the diaphragm and the stud wall underneath the diaphragm through tension ties. In addition, in order to strengthen this connection, blocking was inserted between the diaphragm and the stud wall, nailed to the joists, and bolted to the stud walls through steel angles (Figure 7.19b). This provided a point load to the diaphragm. In some test runs a timber diamond frame made from 2x10 timber sections was bolted to the center of the diaphragm. As before, this configuration was used to produce a relatively uniform displacement at the center quarter of the diaphragm.



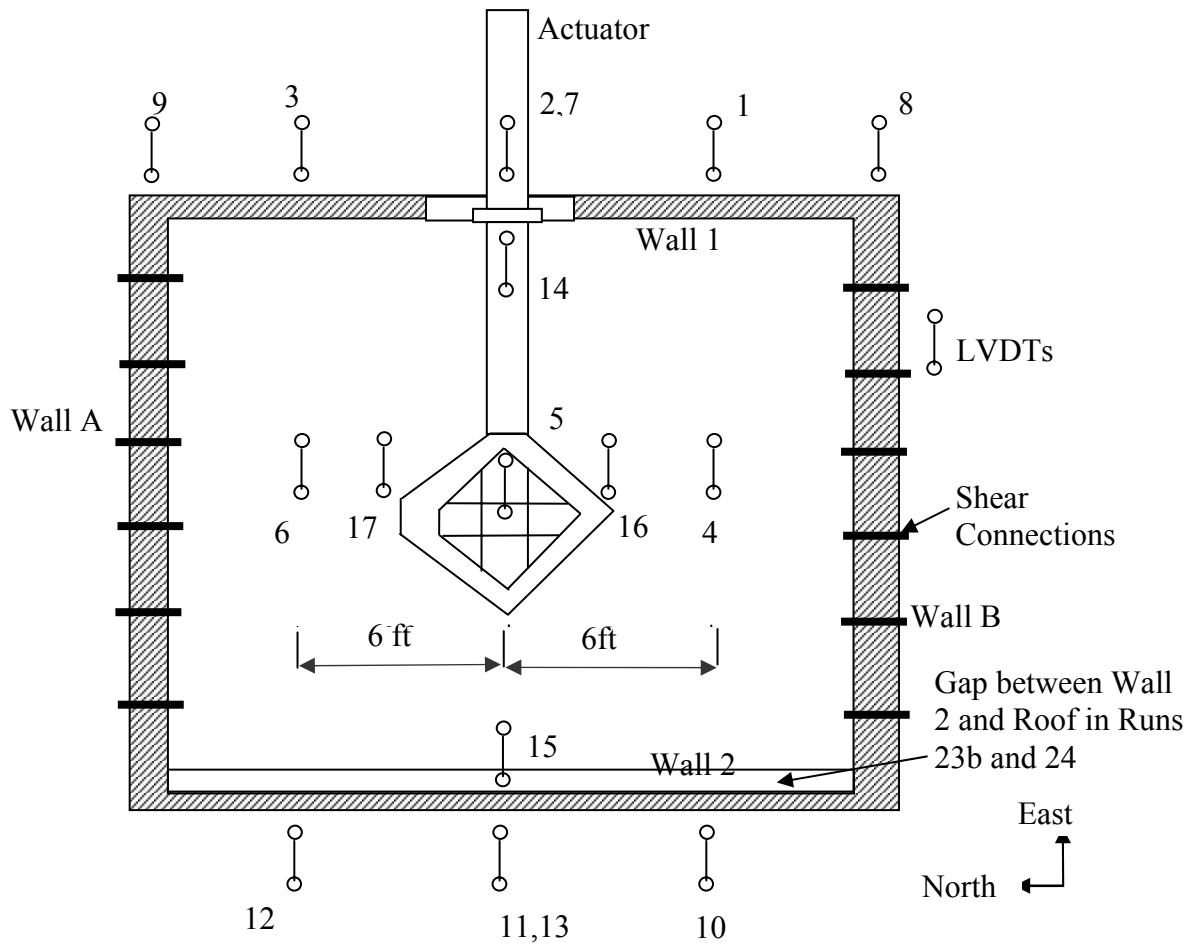
(a) Top view (looking east)



(b) Bottom view (looking north)

Figure 7.19. Set up of the loading system for the diaphragm test perpendicular to the joists

The instrumentation set up for the test is shown in Figure 7.20. LVDTs 4, 5, 6, 16, 17 were used to measure the lateral displacement of the diaphragm. LVDTs 1, 2, 3 and 7 were used to measure the out-of-plane deformation of Wall 1. LVDTs 10, 11, 12 and 13 were used to measure the out-of-plane deformation of Wall 2. LVDTs 8 and 9 were used to measure the lateral displacements of in-plane walls A and B. LVDTs 14 and 15 were used to measure the relative movement between the masonry out-of-plane wall and the joist next to it.



Notes: LVDTs 7 and 13 are at the floor level, the other LVDTs are at the roof level.

Figure 7.20. Instrumentations set up for the roof diaphragm test perpendicular to the joists

The diaphragm was loaded with displacement control. The typical loading history is shown in Figure 7.3.

7.4.2. Test runs

Ten test runs 23b through 32, as listed in Table 7.6, were conducted to investigate the behavior of the roof diaphragm perpendicular to the joists. In Runs 23b and 24, a 6 in. gap was cut through the sheathing and blocks to separate the roof diaphragm from Wall 2

(see Figure 7.20). As a result, these two test runs can be used to determine the lateral shear stiffness of the roof diaphragm. After that, the gap was filled in, and thus the interaction between the diaphragm and the masonry walls could be investigated. Runs 25 to 28 were used to investigate the interaction between the roof diaphragm and the masonry walls with different loading patterns (point and uniform) and with or without tension tie connections between the diaphragm and the out-of-plane walls. Runs 29 to 32 were used to investigate the effect of pocket grouting of the connections between the joists and Walls A and B. It should be pointed out that an initial damage occurred to the out-of-plane Wall 2 between Run 27 and Run 28 because of a malfunction of the TestStar loading system. This issue is discussed in detail later.

Table 7.6. Lists of test runs perpendicular to the joists

ID	Description
Run 23b	Gap between Wall 2 and the roof diaphragm, uniform displacement (Diamond)
Run 24	Gap between Wall 2 and the roof diaphragm, point displacement
Run 25	No gap between Wall 2 and the roof diaphragm, point displacement, no tension ties
Run 26	No gap between Wall 2 and the roof diaphragm, point displacement, With tension ties between the roof diaphragm and Walls 1 and 2
Run 27	No gap between Wall 2 and the roof diaphragm, uniform displacement, With tension ties between the roof diaphragm and Walls 1 and 2
Run 28*	No gap between Wall 2 and the roof diaphragm, uniform displacement, no tension ties
Run 29*	No gap, pockets grouted, no tension ties, uniform displacement
Run 30*	No gap, pockets grouted, with tension ties, uniform displacement
Run 31b*	No gap, pockets grouted, with tension ties, point displacement
Run 32*	No gap, pockets grouted, no tension ties, point displacement

* After the initial damage occurred to the out-of-plane wall 2

7.4.3. Behavior of the diaphragm-wall system perpendicular to the joists

The interaction mechanism between the diaphragm and the masonry walls in the direction perpendicular to the joists was different from that parallel to the joists. In the direction perpendicular to the joists, the diaphragm developed lateral flexural and shear deformation because it worked as a beam with its ends simply supported on the in-plane walls (Walls A and B). At the same time, the deformed diaphragm pushed or pulled the out-of-plane walls (Walls 1 and 2) and forced the out-of-plane walls to deform. As a result, part of the external lateral forces was directly transferred from the diaphragm to the in-plane walls, while the other part was transferred to the out-of-plane walls. The force transferred to the out-of-plane walls was then further transferred to the ground or to the in-plane walls because of the flexural deformation of the out-of-plane walls. The above mechanism is explained conceptually by the model shown in Figure 7.21. Note that a slip element is used again to account for the imperfect connection between the diaphragm and the out-of-plane walls.

A conceptual model as shown in Figure 7.22 can be used to illustrate the interaction mechanism between the diaphragm and the masonry walls discussed above. In this model, M_i , M_o , and M_d are the lumped masses of the in-plane wall, out-of-plane wall, and floor or roof diaphragm, respectively. K_i is the stiffness of the in-plane wall, which can be simply assumed as infinite. K_o is the stiffness of the out-of-plane wall, K_a is the axial stiffness of the roof diaphragm perpendicular to the joists, K_{di} is the lateral stiffness of the roof diaphragm, and K_{do} stands for the effective stiffness of the slip element. This model indicates that the values of K_o , K_a , K_{di} , and K_{do} determine the response of this diaphragm-masonry wall system.

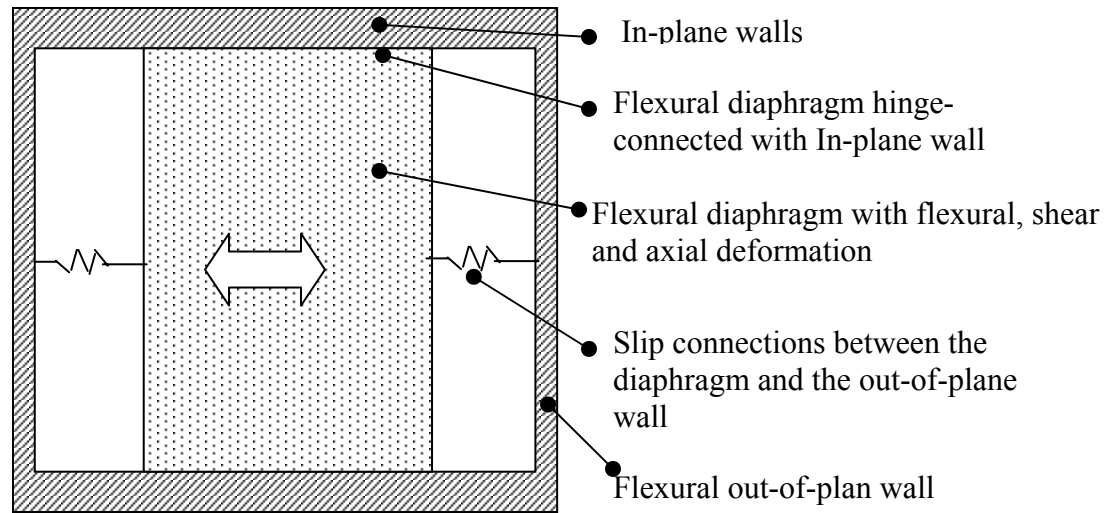


Figure 7.21. Interaction between the roof and the masonry walls in the direction perpendicular to the joists

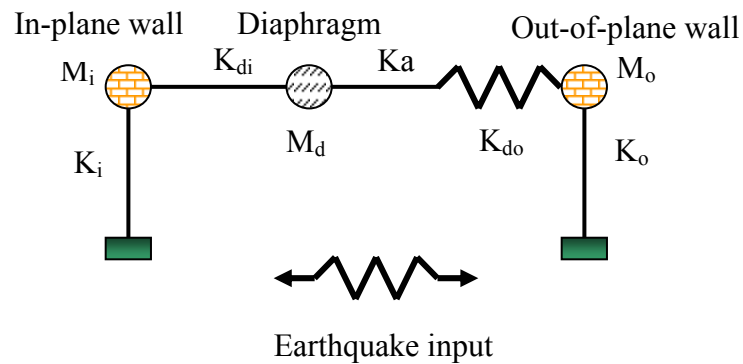


Figure 7.22. Conceptual model for the structure perpendicular to the joists

7.4.4. Elastic lateral stiffness of the diaphragm perpendicular to the joists

The lateral stiffness of the diaphragm perpendicular to the joists was obtained by measuring the lateral displacement of the diaphragm in Test runs 23b and 24 when the diaphragm was pushed away from Wall 1. The secant behavior of the diaphragm at the

end of loading was used again to calculate the stiffness and the deformation profiles. The stiffness obtained in the two test runs are listed in Table 7.7. The profiles of the lateral deformation of the diaphragm are shown in Figure 7.23. It is apparent that the “diamond” loading frame notably changed the deformation profile of the diaphragm, while it only slightly increased the lateral stiffness of the diaphragm.

Table 7.7. Lateral stiffness of the entire diaphragm perpendicular to the joists

Test Run	Load Case	Diaphragm	Stiffness (kips/in)
23b	Uniform	Full	5.70
24	Point	Full	5.04

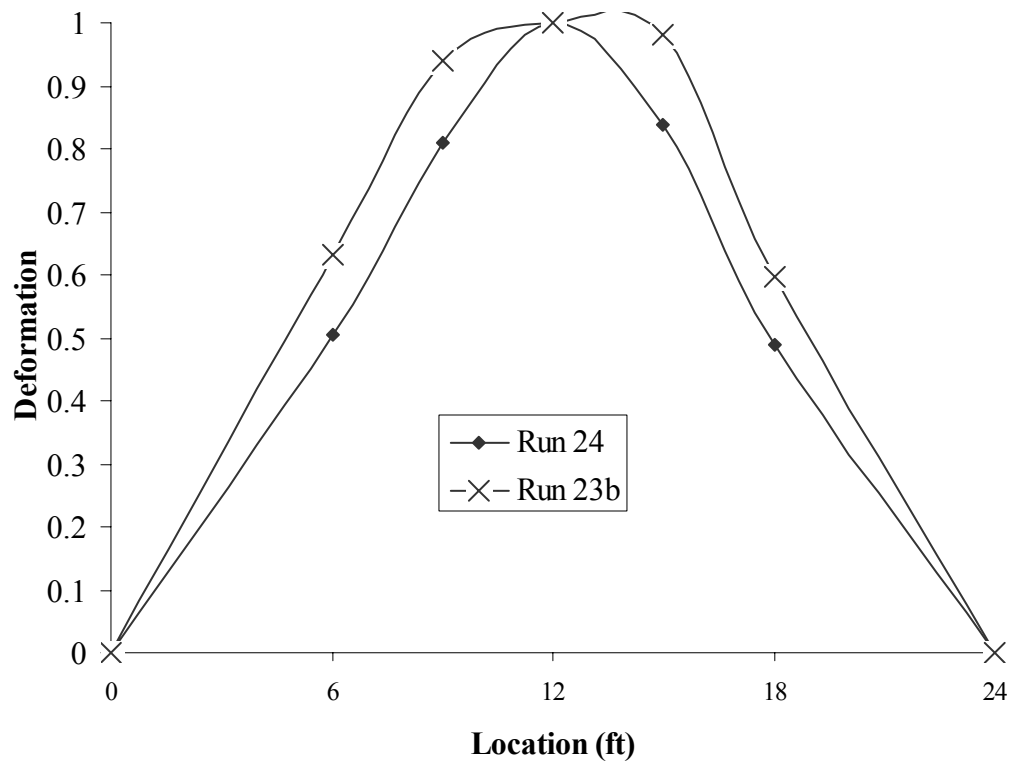


Figure 7.23. Lateral deformation profile of the diaphragm perpendicular to the joists

7.4.5. Elastic response of the out-of-plane Walls 1 and 2

Since the lateral stiffness of the diaphragm had been obtained in the test runs 23b and 24, the force directly transferred to the in-plane walls could be estimated as:

$$F_{in} = d_{dia} \cdot K_{dia} \quad (7.6)$$

where F_{in} is the force transferred to the in-plane wall; d_{dia} is the lateral displacement of the roof diaphragm measured at its center point; and K_{dia} is the lateral stiffness of the roof diaphragm, which is assumed as 5.7 kips/in based on Table 7.7.

After F_{in} is calculated, the force transferred from the diaphragm to the out-of-plane walls can be calculated by simply subtracting F_{in} from the total external force. As a result, the stiffness of the out-of-plane walls can be calculated.

In the test runs 23b, 24, 25, 28, 29, and 32, there were no tension ties connecting between the diaphragm and the masonry out-of-plane walls. As a result, there is only one out-of-plane wall resisting the lateral force, and thus the stiffness of the masonry wall in the push (compression) can be calculated by:

$$K_o = \frac{F - d_{dia} \cdot K_{dia}}{d_{out}} \quad (7.7)$$

where K_o is the out-of-plane stiffness of the masonry wall under consideration; F is the total external force, and d_{out} is the lateral deformation of the out-of-plane wall measured at the mid point at the roof level.

On the other hand, in the test runs 26, 27, 30, and 31b, there were tension ties connecting between the diaphragm and the masonry out-of-plane walls. As a result, both the two out-of-plane walls (Walls 1 and 2) worked together to resist the lateral forces. The equilibrium equation is given by:

$$F = K_{o,1} \cdot d_{out,1} + K_{o,2} \cdot d_{out,2} + d_{dia} \cdot K_{dia} \quad (7.8)$$

where $K_{o,i}$ is the out-of-plane stiffness of Wall i , and $d_{out,i}$ is the measured out-of-plane deformation of Wall i .

The out-of-plane stiffness of Walls 1 and 2 calculated from Test runs 23b, 24, 25, 28, 29, and 32 are listed in Table 7.8. This table shows that the measured stiffness for Wall 1 in all the test runs produced consistent results, with the mean value of 31.4 kips/in. Different loading patterns and the grouting of the pockets did not have significant effects on the out of-plane stiffness of the masonry wall. The out-of-plane stiffness of Wall 2 before initial damage was 24.0 kips/in. This value dropped to around 11.3 kips/in after the initial damage. This initial damage of Wall 2 occurred because of a malfunction of the TestStar controller system. The actuator overextended and pushed the diaphragm against Wall 2 by accident. However, since the limit detector for the displacement of the actuator was always set at 0.2 inches as a protective measure, no serious damage occurred to Wall 2. No visible cracks were observed after this damage. The decrease in the initial stiffness is believed due to some micro cracks developed in the walls.

Table 7.8. Out-of-plane elastic stiffness of Walls 1 & 2

Test Run	Load Case	Stiffness of Wall 1 (kips/in)	Stiffness of Wall 2 (kips/in)
23b	Uniform, Gap	27.2	-
24	Point, Gap	29.4	-
25	Point	30.0	24.0
28*	Uniform	33.8	12.5
29*	Uniform, Pockets grouted	37.2	12.6
32*	Point, Pockets grouted	30.5	8.8
Mean		31.4	24.0/11.3

* After the initial damage occurred to out-of-plane wall 2

Based on Table 7.8, it can be concluded that the out-of-plane stiffness of Wall 1 was about 31.4 kips/in, and the out-of-plane stiffness of Wall 2 was 24.0 kips/in before initial damage and 11.3 kips/in after initial damage. Using these values as well as the lateral stiffness of the roof diaphragm of 5.7 Kips/in obtained from previous tests (Table 7.7), the force distributions in the test runs 26, 27, 30, and 31b are calculated by employing Eq. (7.8) and the measured lateral displacements of the roof diaphragm and the walls. These predicted results are compared with the test results as shown in Table 7.9.

Table 7.9. Experimental and predicted force distributions between the diaphragm and the masonry walls

Test Run	Load Case	Loading Direction	Test Force Increment (kips)	Calculated force increment based on Eq. (7.8) (kips)	Error (%)
26	Point	To Wall 1	2.0	1.79	10.2
		To Wall 2	2.02	2.07	-2.5
		Zero	2.08	1.75	15.8
27	Uniform	To Wall 1	1.98	1.68	15.1
		To Wall 2	2.12	1.77	16.4
		Zero	1.98	1.82	8.0
30	Uniform, pocket grouted	To Wall 1	1.99	1.92	3.3
		To Wall 2	2.16	1.45	33.0
		Zero	1.99	1.95	1.9
31b	Point, pocket grouted	To Wall 1	2.0	1.97	1.1
		To Wall 2	2.01	1.80	10.2
		Zero	2.02	1.82	9.8

Table 7.9 shows reasonable correlation between the test results and the predicted results. It indicates that the predicted stiffness values for the masonry walls and the roof

diaphragm are rational. It should be pointed out the distribution of the interaction forces between the diaphragm and the out-of-plane wall in the direction perpendicular to the joists is different from that parallel to the joists. As illustrated in Figure 7.24, since the diaphragm works like a beam simply-supported on the in-plane walls in the direction perpendicular to the joists, the interaction forces between the diaphragm and the out-of-plane walls are large near the mid span of the wall. Based on elastic FE analysis, the corresponding elastic modulus of masonry was again calculated to be about 900 to 1100 ksi.

The lateral deformation profiles of the out-of-plane masonry Walls A and B at the roof level and along the vertical centerline were similar to those of Walls 1 and 2.

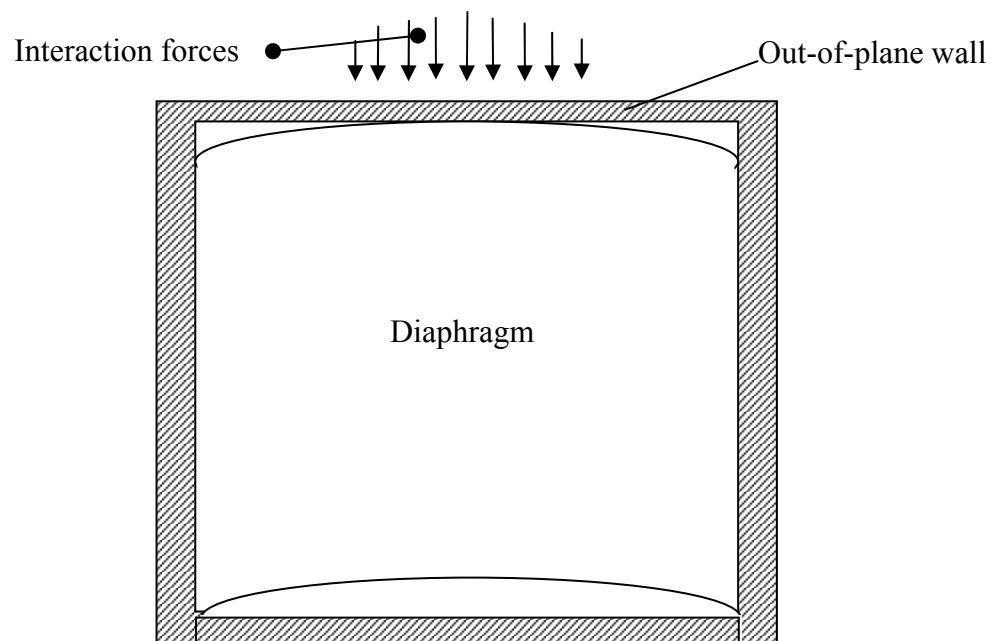
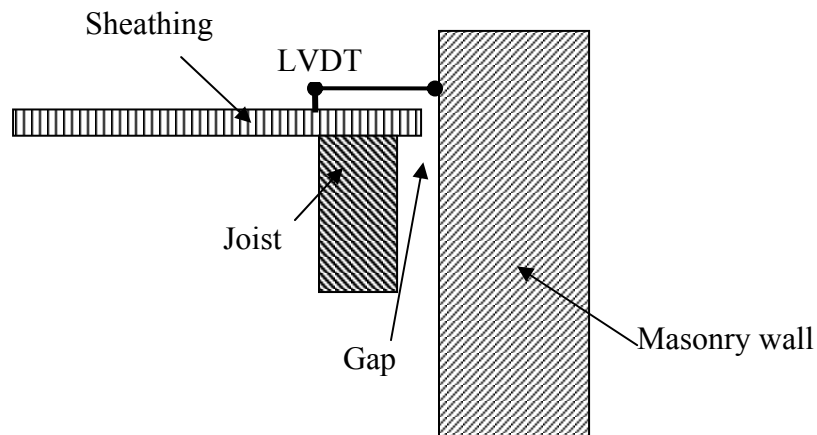


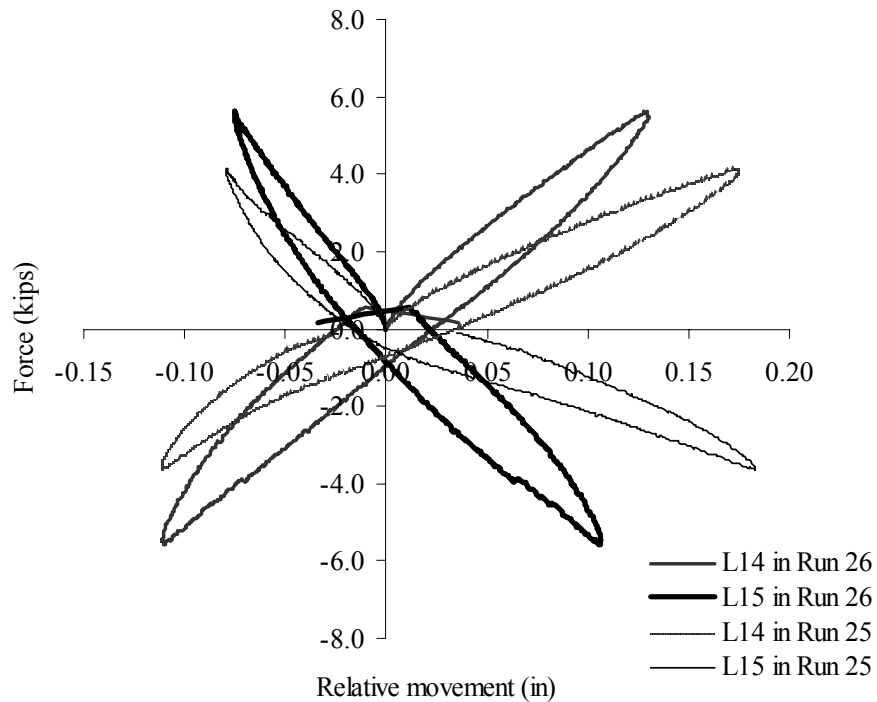
Figure 7.24. Interaction forces between the roof and the out-of-plane wall in the direction perpendicular to the joists

7.4.6. Relative movement between the outside joists and the out-of-plane wall

LVDTs L14 and L15 were mounted on the roof joists and measured the relative out-of-plane movements between the masonry out-of-plane wall and the joist next to it (Figure 7.25a). A typical relative movement is shown in Figure 7.25b. This figure shows that there is a large amount of relative movement between the joist and the masonry wall, which is due to the gap that forms between the joist and the wall. This gap is unavoidable due to construction tolerances. The figure also shows that the relative movement tends to stop when the roof diaphragm is pushed against the wall (positive force L15, and negative force for L14), and that the tension ties between the wall and the diaphragm help to reduce the relative movement.



(a) Details between masonry wall and exterior joist



(b) Force-displacement curves

Figure 7.25. Relative movement between the joist and the masonry wall

7.4.7. Elastic axial stiffness of entire diaphragm

The same method for calculating the axial deformation of the diaphragm parallel to the joists was tried to calculate the axial deformation of the diaphragm perpendicular to the joists. However, due to the large axial stiffness of the roof diaphragm, no reasonable values were obtained from these measurements.

7.5. CONCLUSIONS

The roof diaphragm of the ST-11 building was tested to investigate the interaction between flexible diaphragm and masonry walls. The test reveals that the stiffness of the

three basic components of a URM building (the in-plane walls, the out-of-plane walls, and the flexible diaphragms) together with the properties of the connections between the diaphragm and masonry walls, determine the response of this diaphragm-wall system. The interaction mechanisms between the roof diaphragm and the masonry walls were different in different directions (parallel to the joists and perpendicular to the joists). When the diaphragm was loaded parallel to the joists, the diaphragm was simply supported on the out-of-plane walls. Therefore, the lateral force was exclusively transferred from the diaphragm to the out-of-plane walls, and the lateral stiffness of the diaphragm did not play an important role in its response. In contrast, when the diaphragm was loaded perpendicular to the joists, the diaphragm was simply supported on the in-plane walls. As a result, not only the out-of-plane walls but also the in-plane walls resisted the lateral force. Two conceptual models can be used to illustrate the interaction mechanics in the two directions respectively, as shown in Figure 7.11 for the direction parallel to the joists, and Figure 7.22 for the direction perpendicular to the joists.

For the test structure, some critical structural characteristics were also determined:

- The out-of-plane stiffness of Walls A and B were about 73 kips/in. The out-of-plane stiffness of Wall 1 was around 31.4 kips/in. The out-of-plane stiffness of Wall 2 was around 24 kips/in before initial damage and 11.3 kips/in after initial damage. The corresponding elastic modulus of masonry was between 900 and 1100 ksi.
- The lateral stiffness of the half diaphragm when loaded parallel to the joists ranged from 6 to 10 kips/in. The axial stiffness of the entire diaphragm parallel to the joists ranged from 180 to 220 kips/in. The lateral stiffness of the full

diaphragm perpendicular to the joists was around 5.7 kips/in. It is apparent that the lateral stiffness of the diaphragm was smaller than that of the masonry out-of-plane wall, while the axial stiffness of the diaphragm was larger than that of the masonry out-of-plane wall.

- The stiffness of masonry in-plane wall was much larger than the stiffness of either the diaphragm or the masonry out-of-plane wall. As a simple assumption, the stiffness of the in-plane wall can be assumed as infinite.
- Due to the rather flexible connection details, there were large relative movements between the roof diaphragm and the masonry out-of-plane walls under lateral forces. This happened both when the diaphragm was loaded parallel to the joists and perpendicular to the joists. However, this phenomenon was observed at relatively small force and displacement levels (displacements less than 0.2 in). It can be assumed that the relative movement will decrease when the lateral displacement increases, and can be ignored at large displacement levels.

The test also revealed that connection details between masonry walls and diaphragm influence the response of the wall-diaphragm system. In particular, the test showed that:

- Tension rods tied the diaphragm and the masonry out-of-plane walls together, and helped to distribute the lateral forces from the diaphragm to both out-of-plane walls.
- Different loading patterns investigated in this test changed the deformation profile of the diaphragm, but they did not change the deformation values and profiles of the masonry out-of-plane wall significantly.

- Pocket grouting did not significantly affect the behavior of the diaphragm when loaded perpendicular to the joists.
- Shear connections between the joists and the masonry in-plane walls seemed to play a secondary role in the interaction behavior between the diaphragm and the masonry walls.

Finally, it is emphasized that the investigation was conducted at a relatively small force and displacement levels (displacements less than 0.2 in). Therefore, all the results obtained in this test should be considered as properties of the test structure in the elastic range. The interaction behavior of a flexible diaphragm-masonry wall system at large force and displacement levels should be investigated in future tests.

CHAPTER 8

IN PLANE WALL TESTS PARALLEL TO WALLS 1 AND 2

8.1. INTRODUCTION

The properties of URM materials and URM components have been investigated and reported in Chapters 3 to 5. The goal of these studies was to help understanding the properties of an entire URM building and thus to improve the performance of this type of structure. However, the behavior of a URM building cannot be assumed as simply the addition of the properties of its components and materials. In order to assess the seismic hazard of existing URM buildings, the URM building itself needs to be investigated as a unit. Several experimental research projects have been conducted on URM structures under quasi-static, pseudo dynamic or real-time dynamic testing regimes (Clough et al. 1979, Tomazevic 1990, 1993, Magenes et al. 1995, Costley and Abrams 1996, Paquette and Bruneau 2000). A detailed literature review of the past experiment research can be found in Section 2.6.

In spite of all these past research efforts, some important characteristics of URM building systems, such as the interaction between the in-plane walls and the out-of-plane walls, the influence of a flexible floor or roof diaphragm on the performance of the masonry walls, and the failure mechanisms of perforated masonry walls, are still unclear. To clarify some of these characteristics, the second phase of the ST-11 project test investigated the nonlinear properties of the test structure by laterally loading it parallel to Walls 1 and 2.

This series of tests are reported in this chapter. First, the test setup and the test sequence are introduced in Section 8.2. Then the observed nonlinear properties of the test structure, such as the crack propagation sequence, the damage accumulation, and the governing kinematic mechanisms, are presented in Section 8.3. Following that, some important structure behavior, such as the flange effects and the global overturning movements, are discussed in Sections 8.4 to 8.9. The conclusions obtained from this series of tests will be given in Section 8.10.

8.2. TEST SETUP

Following the roof diaphragm test, the ST-11 building was tested under external quasi-static lateral forces parallel to Walls 1 and 2. The configuration of the test structure was described in Chapter 6. The test set up for this test series is as follows.

8.2.1. External forces and loading scheme

In-plane lateral forces were applied to Walls 1 and 2 at the roof level and the second floor level. Two 220-kip hydraulic actuators were used at the roof level, and two 100-kip hydraulic actuators were used at the second floor level. In order to attach the actuators to the masonry walls, holes were drilled in the masonry wall at appropriated locations, and four 0.5 in. diameter Dywidag rods were placed through the holes and used to connect 0.5 in. thick steel plates on each side of the wall. A total force of 80 kips was applied to the rods to post-tension the steel plates horizontally to the wall. The actuators were then connected by bolts to the steel plate through pre-drilled holes in the steel plate. The other end of the actuators was pin-connected to the strong wall (Figure 8.1).

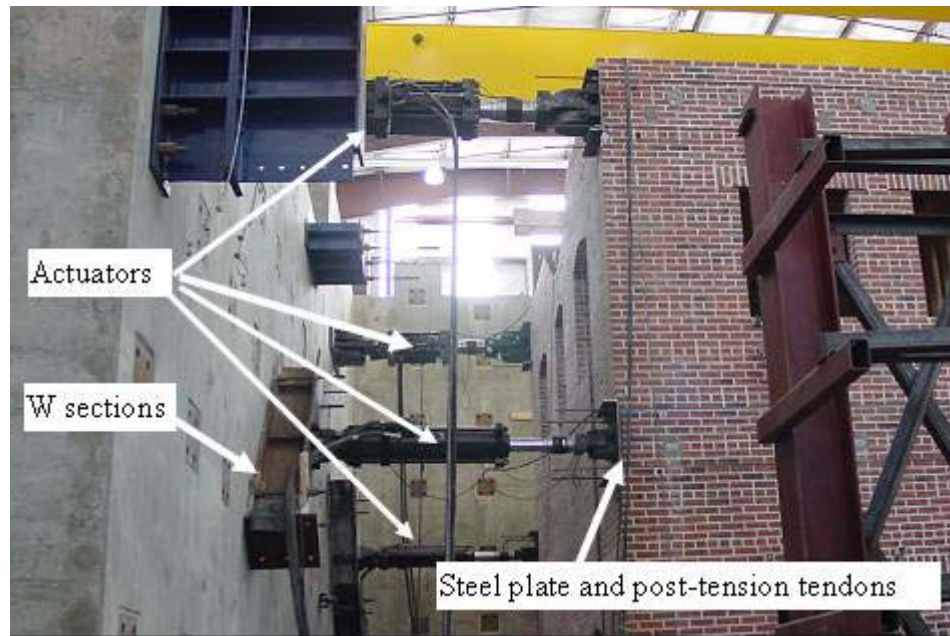


Figure 8.1. Connection details for connecting the actuators to the masonry walls, view looking east

The test was conducted in displacement control. A modified stiffness control scheme was employed to approximate the seismic forces on the structure. An outline of this control scheme is shown in Figure 8.2. Based on the results of the preliminary analysis and past experimental research, it can be assumed that the first vibration mode controls the response of low-rise URM buildings. However, it is important to notice that external forces cause damage accumulation in a building throughout loading history. This damage is typically not uniform distributed and thus leads to the change of the first vibration mode. Therefore, in order to apply realistic loads to the structure, this evolution of the first mode must be addressed. To accomplish this, the employed loading sequence for each of the walls began by imposing a displacement profile given by an elastic analysis. The structure was cyclically displaced in this profile to obtain the current desired maximum roof displacement (u_{li}). Based on these displacements and the applied

forces F_{1i} and F_{2i} , the stiffness matrix of an equivalent two-degree-of-freedom structure were back-calculated. Next, by assuming a mass matrix for the wall based on tributary area, the updated first mode shape, ϕ_i , were calculated. The subsequent cycles of displacements were then imposed based on the updated first mode shape.

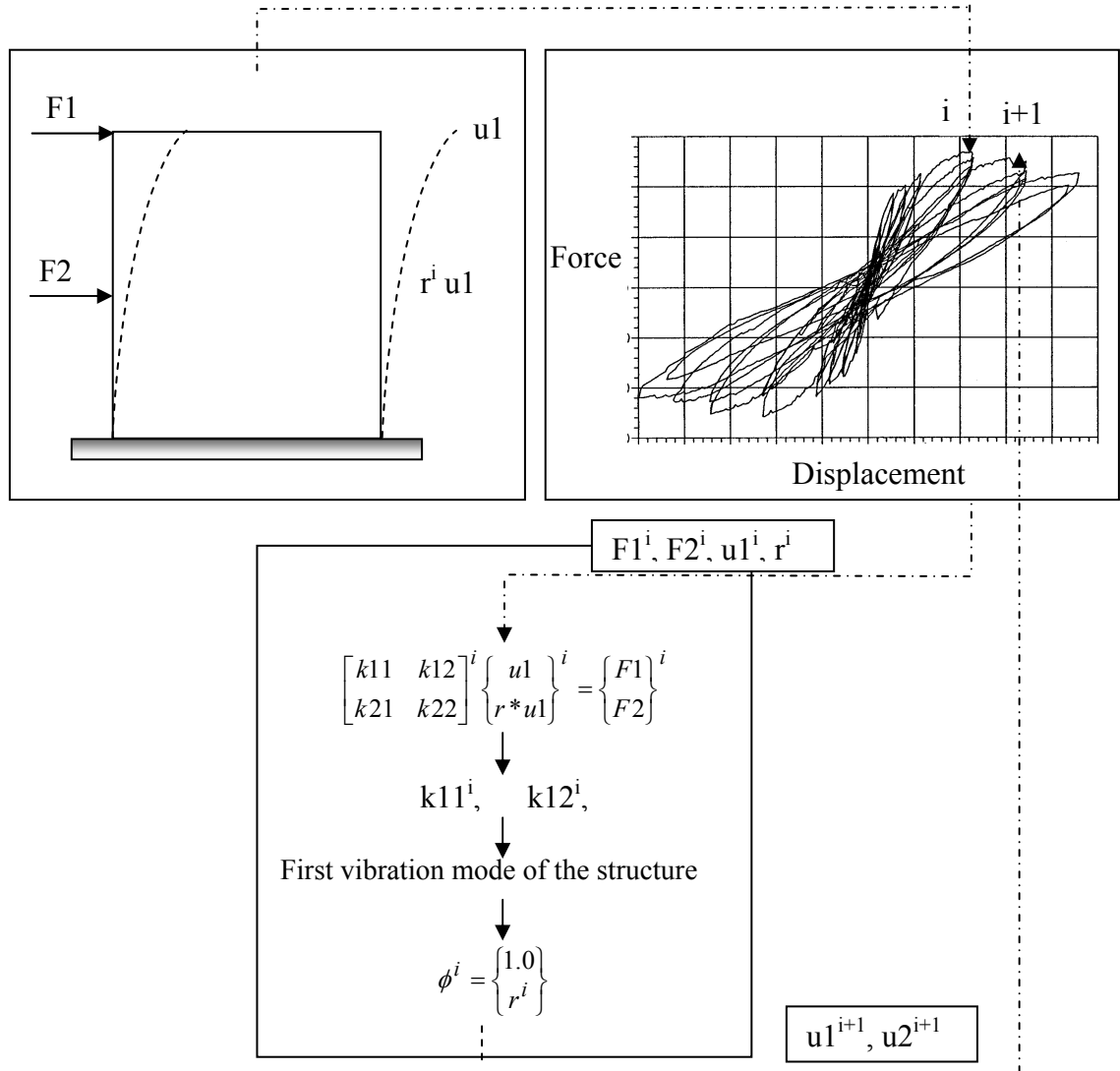


Figure 8.2. Modified stiffness displacement control scheme

No additional dead weight was applied to the building to simulate live load. This gave a worst-case scenario for the test structure as the beneficial effects of compressive stresses on the walls were minimized.

8.2.2. Testing procedure

For each target displacement, the building was first loaded following the loading history shown in Figure 8.3. After that, in most cases the building was loaded again with slight changes in the control displacements to achieve a better simulation of the targeted displacements and displacement profile. As a result, a series of tests comprised of 15 test cycles with different displacement levels were applied to the test structure. The maximum lateral displacement values measured at the roof level and the second floor level of Walls 1 and 2 corresponding to each test cycle are listed in Table 8.1. The reported test runs begin with 2g since several small-displacement test runs were conducted prior to the main test runs to tune the test system. Cycles 2g to 8a, 10 and 10a loaded the building with increasing lateral displacements, aiming at examining the gradual damage progression and the corresponding force-lateral displacement relationships of the test building. Cycle 9 held Wall 2 and loaded Wall 1, and was aimed at investigating the coupling behavior between Walls 1 and 2.

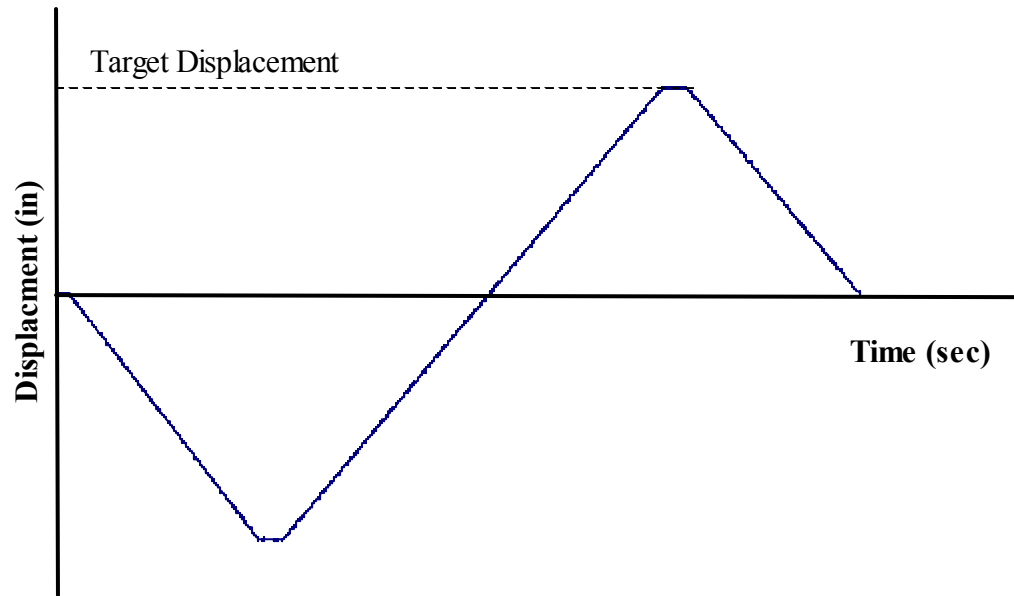


Figure 8.3. Loading history

Table 8.1. Measured maximum displacement values in each test cycle

Cycle	Maximum displacements at the push direction (toward south) (in.)				Maximum displacements at the pull direction (toward north) (in.)			
	Wall 1 roof	Wall 1 second floor	Wall 2 roof	Wall 2 second floor	Wall 1 roof	Wall 1 second floor	Wall 2 roof	Wall 2 second floor
2g	0.0077	0.004	0.017	0.012	-0.009	-0.005	-0.015	-0.010
3a	0.0186	0.011	0.046	0.033	-0.014	-0.008	-0.025	-0.019
3b	0.0192	0.011	0.045	0.033	-0.014	-0.008	-0.031	-0.024
4	0.0181	0.010	0.017	0.012	-0.018	-0.010	-0.021	-0.016
5	0.034	0.020	0.024	0.018	-0.024	-0.012	-0.031	-0.025
5a	0.0279	0.017	0.023	0.017	-0.030	-0.018	-0.035	-0.023
6	0.0421	0.024	0.064	0.059	-0.075	-0.046	-0.076	-0.062
6a	0.0453	0.027	0.063	0.056	-0.074	-0.060	-0.077	-0.046
7	0.0869	0.052	0.094	0.081	-0.118	-0.073	-0.097	-0.081
7a	0.102	0.061	0.096	0.085	-0.115	-0.071	-0.098	-0.083
8	0.135	0.081	0.144	0.119	-0.166	-0.104	-0.145	-0.128
8a	0.157	0.094	0.153	0.129	-0.161	-0.099	-0.145	-0.123
9	0.0486	0.033	0.011	0.006	-0.096	-0.057	-0.004	0
10	0.228	0.137	0.238	0.185	-0.262	-0.213	-0.247	-0.201
10a	0.242	0.168	0.257	0.202	-0.263	-0.222	-0.252	-0.198

8.2.3. Instrumentations

81 channels of instrumentations, including 29 LVDTs, 20 potentiometers, and 31 strain gages, were used to monitor both the global and local responses of the test structure (Figure 8.4). LVDTs have more accurate resolution (infinite) than potentiometers (0.05 in.). Therefore, LVDTs were used for important measurements, while potentiometers were used for less important locations or for redundancy. Specifically, LVDTs GW1R and GW12 were used to measure the lateral in-plane displacements of Wall 1 at the roof level and the second floor level, respectively (G means global behavior, W1 means Wall 1, R means roof, and 2 stands for the second floor). LVDTs GW2R and GW22 were employed to measure the lateral in-plane displacements of Wall 2 at the roof level and the second floor level, respectively. In addition, the global lateral in-plane displacements of Walls 1 and 2 were also monitored by Potentiometers GW12P, GW1RP, GW22P, and GW2RP (P stands for potentiometers), which duplicated the readings of the LVDTs to ensure the robustness of the data.

The lateral out-of-plane roof displacements of Wall A and Wall B were measured by LVDTs GOWAR and GOWBR, respectively. LVDT GOWB2 was used to measure the lateral out-of-plane displacement of Wall B at the second floor level. The global overturning movements of Wall 1 and Wall 2 were measured by Potentiometers GV1LP, GV1RP, GV2LP, and GV2RP. The possible sliding of Wall 1 was monitored by Potentiometer P1-6S. The forces applied to the building were measured by the load cells embedded in the actuators.

A typical LVDT setup shown in Figure 8.5 was used to measure the local response of each first story pier in Walls 1 and 2. In Figure 8.5, two vertical LVDTs and

two diagonal LVDTs are used. * represents the ID of the pier. VL and VR stand for the vertical LVDTs mounted at the left side and the right side of the pier, respectively; and XL, XR represent the diagonal LVDTs mounted at the left side and the right side of the pier, respectively.

The deformations of each pier were measured as follows. Assuming the bottom boundary (the foundation) of each first floor pier is rigid and fixed, the deformations of each pier can be determined by the movement of its upper boundary, which includes a vertical displacement (U_v), a rotation (U_θ), and a lateral displacement (U_L). Values for U_v and U_θ can be calculated as:

$$U_v = \frac{D_{*VL} + D_{*VR}}{2} \quad (8.1)$$

$$U_\theta = \arctan\left(\frac{D_{*VL} - D_{*VR}}{a}\right) \quad (8.2)$$

where D_i is the reading of LVDT i.

Three estimates can be given for the lateral movement U_L :

$$U_L^L = D_{*XL} \left(\frac{H1 + H2}{H2} \cdot \frac{\sqrt{a^2 + H1^2}}{a} \right) \quad (8.3a)$$

$$U_L^R = D_{*XR} \left(\frac{H1 + H2}{H2} \cdot \frac{\sqrt{a^2 + H1^2}}{a} \right) \quad (8.3b)$$

$$U_L^{avg} = (D_{*XL} + D_{*XR} - D_{*VR} - D_{*VL}) \left(\frac{H1 + H2}{H2} \cdot \frac{\sqrt{a^2 + H1^2}}{a} \right) \quad (8.3c)$$

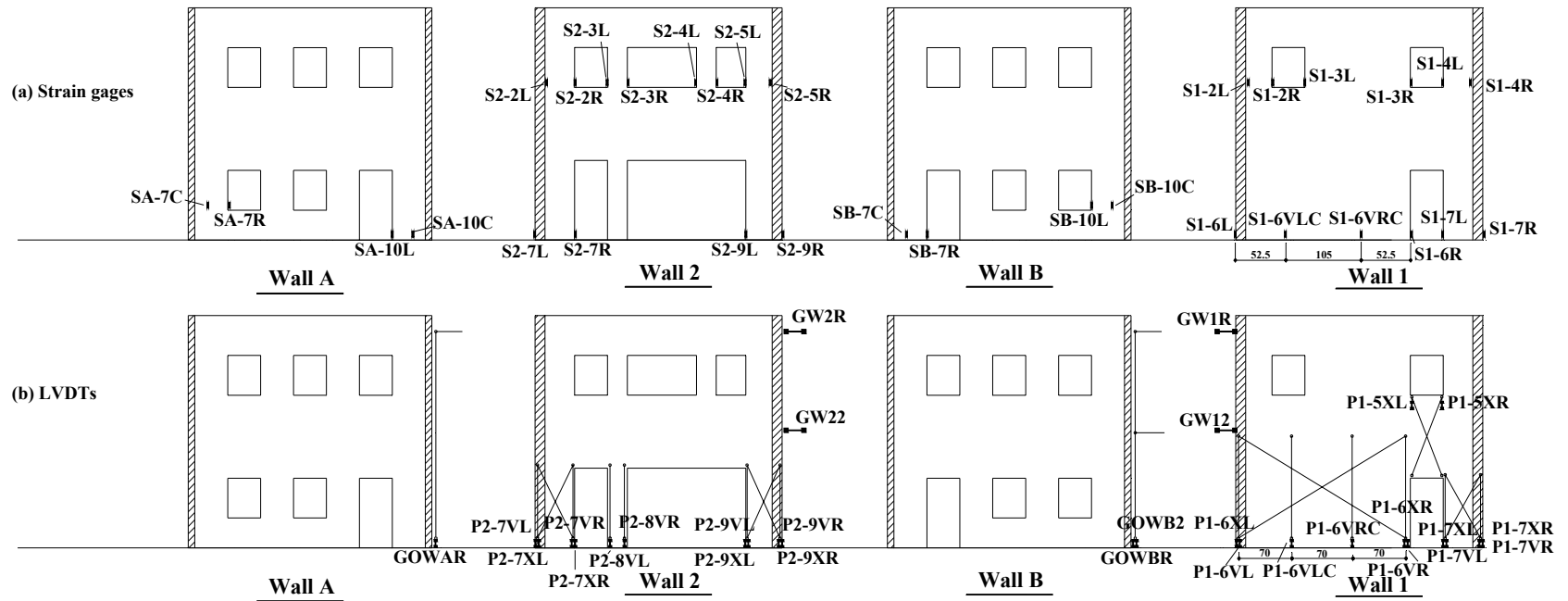


Figure 8.4. Instrumentations of the in-plane tests parallel to Walls 1 and 2

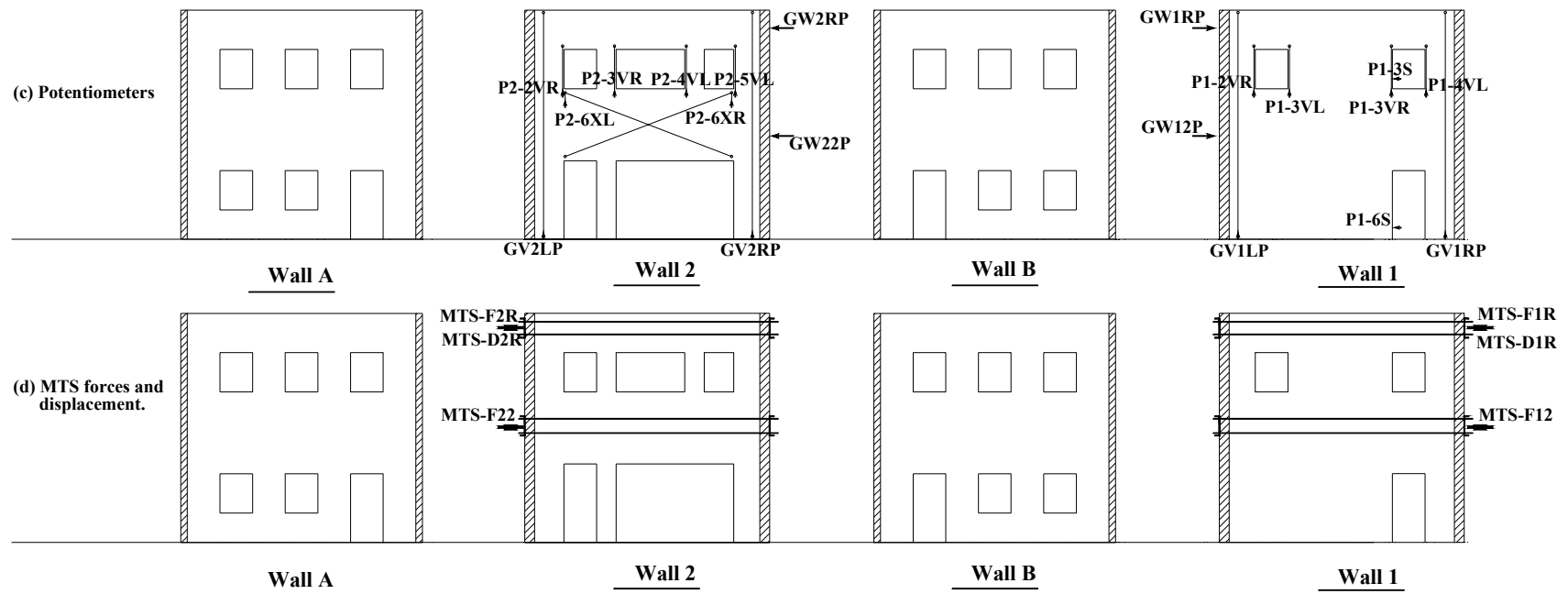


Figure 8.4. (cont'd)

All the three Eqs. (8.3a), (8.3b), and (8.3c) assume that the axial deformation of a URM pier is small compared with its lateral shear deformation. In the case of elastic range behavior, the three estimates give similar results. On the other hand, if large flexural cracks develop at the top and bottom of the pier, Eq. (8.3c) gives a more reasonable estimate for the shear deformation of the pier, since it subtracts the deformation induced by the flexural cracks.

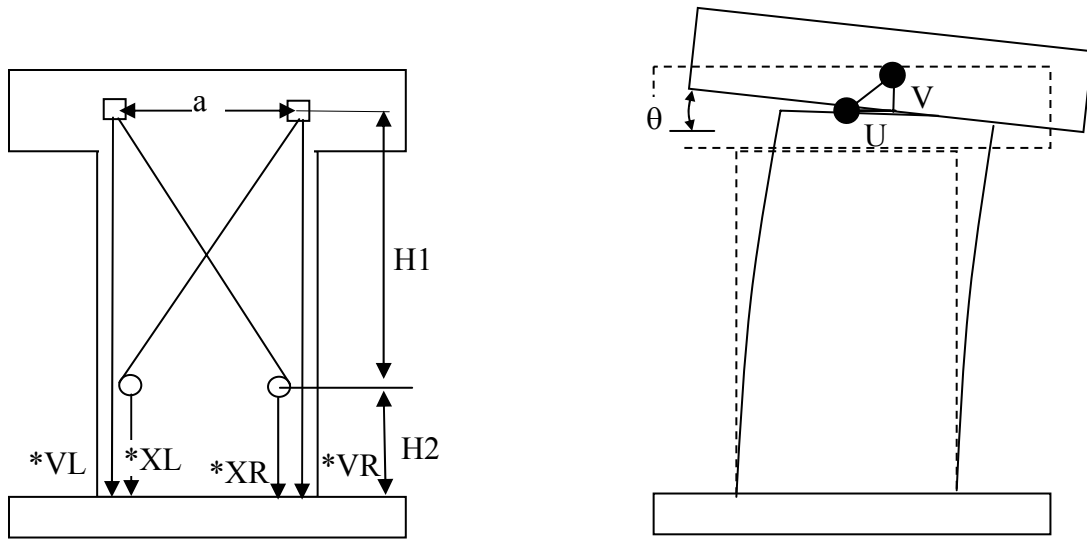


Figure 8.5 Instrumentations of Pier

Being slightly different from a typical pier, only vertical LVDTs were used for the slender pier 2-8 in Wall 2, because the shear deformation of this pier was assumed to be negligible. In the case of the large pier 1-6 in Wall 1, two more vertical LVDTs were placed at the third-points of the pier to measure the vertical deformation profile of this pier.

Possible shear deformation of the first floor spandrel in Wall 1 was monitored by two diagonal LVDTs (P1-5XL and P1-5XR). Shear deformation of the first floor

spandrel in Wall 2, and flexural deformation of all the piers in the second floor, were measured by potentiometers. In addition to the LVDTs and potentiometers, polyester backing foil strain gages with 1.2 in. gage length were also used at the bottom of each pier to measure the flexural deformation at the base of the pier (Figure 8.4).

8.3. CRACK PROPAGATION, DAMAGE ACCUMULATION AND KINEMATIC MECHANISMS OF THE TEST STRUCTURE

The in-plane tests clearly demonstrated the nonlinear properties of the test structure. This section gives a summary of the response of the test building through the entire test sequence.

Both experimental and analytical investigations have revealed little coupling behavior between masonry walls for flexible diaphragm cases (See Section 8.5 and 10.2.5). Therefore, the response of the test building is discussed separately for Walls 1 and 2. Since Wall 2 exhibited a relatively simple component-dominated response, its behavior is presented first in Section 8.3.1. Following that, the relatively complex global-dominated response of Wall 1 is discussed in Section 8.3.2.

8.3.1. Wall 2

The observed responses of Wall 2 clearly exhibited an evolution from elastic response (Cycle 2g with a maximum roof displacement of 0.017 in), to minor damage state (Cycles 3a through 5a, with a maximum roof displacement of 0.035 in), to a significant accumulation of damage in the structure (Cycles 6 through 8a, with a maximum roof displacement of 0.153 in), and finally to a matured failure mechanism

(Cycles 10 and 10a, with a maximum roof displacement of 0.257 in). As a result, the response of Wall 2 is discussed in the four different states.

8.3.1.1. Elastic response (Cycle 2g)

The response of Wall 2 in Cycle 2g was essentially elastic. No visual cracks or other damage were observed. The readings of the instrumentation in the first floor piers indicated that the response of the wall was a combination of global overturning behavior and local flexural and shear behavior. When the building was loaded in the push direction (southward, positive roof displacement), the upper boundary of Pier 2-7 displaced up, while the upper boundary of Pier 2-9 exhibited negligible vertical displacement (Figure 8.6). The uplift movement of Pier 2-7 was due to the additional axial tensile force induced by the overall overturning moment. On the other hand, the strain gages on opposite sides of Pier 2-7 and Pier 2-9 captured different signs of strains. When the building was loaded in the push direction, the strain gage on the left side of Pier 2-7 (S2-7L) measured tensile strain while the strain gage on the right side of this pier (S2-7R) measured compressive strain (Figure 8.7). The different signs of strains on the two sides of the pier indicated a local flexural deformation.

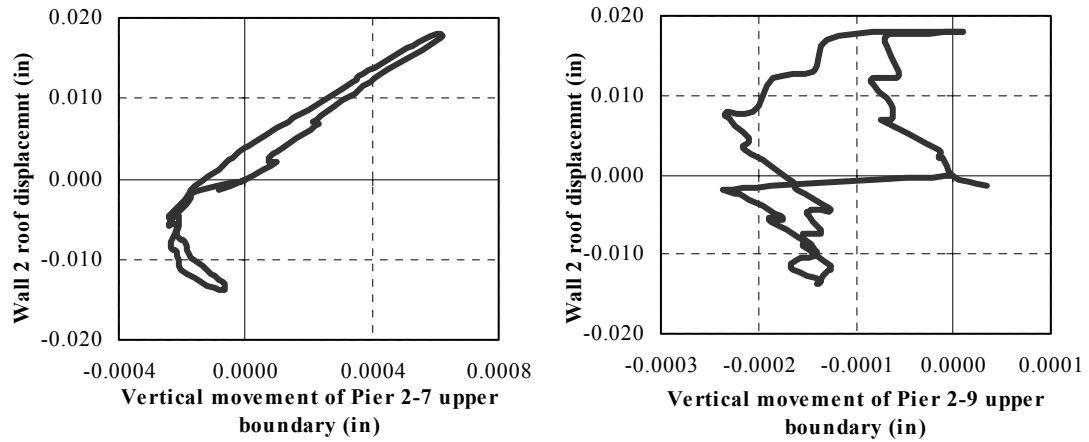


Figure 8.6. Axial displacements of Pier 2-7 and Pier 2-9

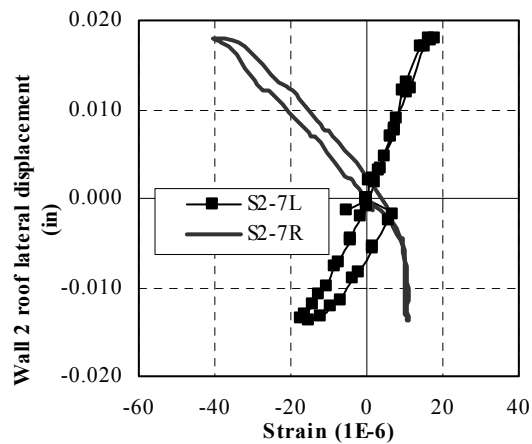


Figure 8.7. Strains at the base of Pier 2-7

The maximum lateral displacements for Pier 2-7 and Pier 2-9 were 0.0087 in. and 0.0126 in., respectively, in the push direction (southward); and they were -0.0073 in. and -0.0072 in., respectively, in the pull direction (northward). Note that the maximum lateral displacements at Wall 2, second floor level, were 0.012 in. the push direction and -0.01

in. the pull direction. Apparently most of the Wall 2 first story lateral deformation was concentrated in the piers.

Pier 2-8 was the small pier next to Pier 2-7. As a result of its small size, it had little contribution to the lateral resistance of Wall 2. The deformation of Wall 2 second floor was smaller than the resolution of employed potentiometers (0.05 in), and thus no valuable values were captured.

8.3.1.2. Minor damage (Cycles 3a to 5a)

The maximum lateral displacements imposed on the building in test cycles 3a –5b were not monotonically increasing with the cycle numbers. The maximum lateral push (southward) displacements for Wall 2 were obtained in Cycle 3a and Cycle 3b (0.046 in. at the roof and 0.033 in. at the second floor). The maximum lateral pull displacements (northward) for Wall 2 were obtained in Cycle 5a and Cycle 5b (-0.033 in. at the roof and -0.025 in. at the second floor).

In Cycle 3a, no damage or visual cracks were observed. However, the strain gage readings at the base of Pier 2-7 and Pier 2-9 indicated that possible flexural cracks were developing around the base of the piers. As shown in Figure 8.8 for Pier 2-7, at the beginning of the loading, the strains on the tensile side of this pier increased with increasing lateral roof displacement. This corresponded to an unloading of the initial compressive stress in the pier. However, when the measured tensile strains reached some limit values, the reading basically remained constant even though the lateral displacement of the building was still increasing. This indicated that some micro cracks were developing in the areas around the strain gages, which prevented masonry from taking more tensile stress. As expected from these trends, in Cycle 3b, the first flexural crack

was observed at the left toe of Pier 2-9 when the building was loaded in the push direction (Figure 8.9). This crack was due to the large tensile stress introduced by the local flexural moment.

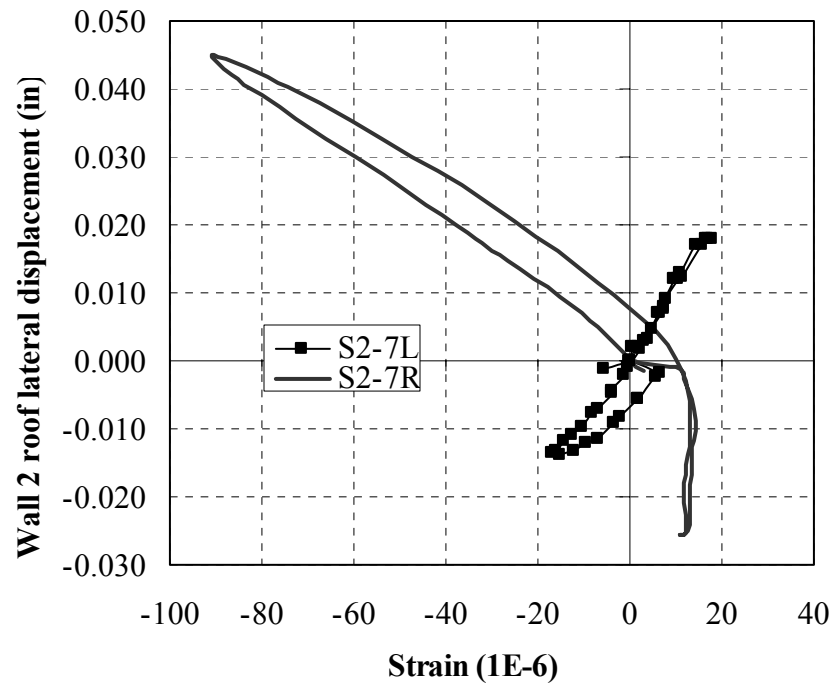


Figure 8.8. The constant tensile strain at the base of Pier 2-7 in Test cycle 3a indicated possible flexural cracks

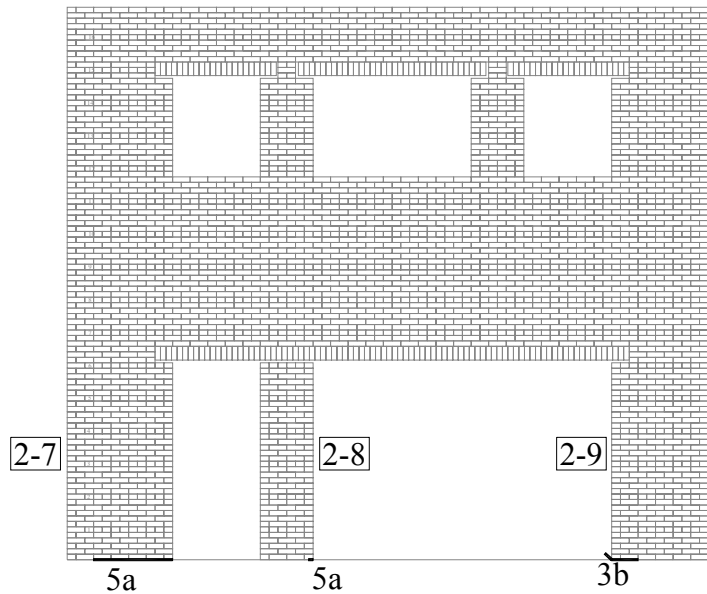


Figure 8.9. Crack pattern of Wall 2 at the end of Cycle 5b (looking eastward)

In Cycle 5a, when the building was loaded in the pull direction, new flexural cracks were observed in the other two first story piers: Pier 2-7 and Pier 2-8 (Figure 8.9). All the new cracks occurred at the right base of the piers, again due to the large tensile stresses introduced by the local flexural moments. No cracks were observed in the second floor wall. No more new cracks were observed in Cycle 5b.

Although several cracks were observed in this series of cycles, the damage to the wall was still minor, and its response was essentially elastic. This can be seen from the base shear–lateral roof displacement curves for Wall 2 as shown in Figure 8.10.

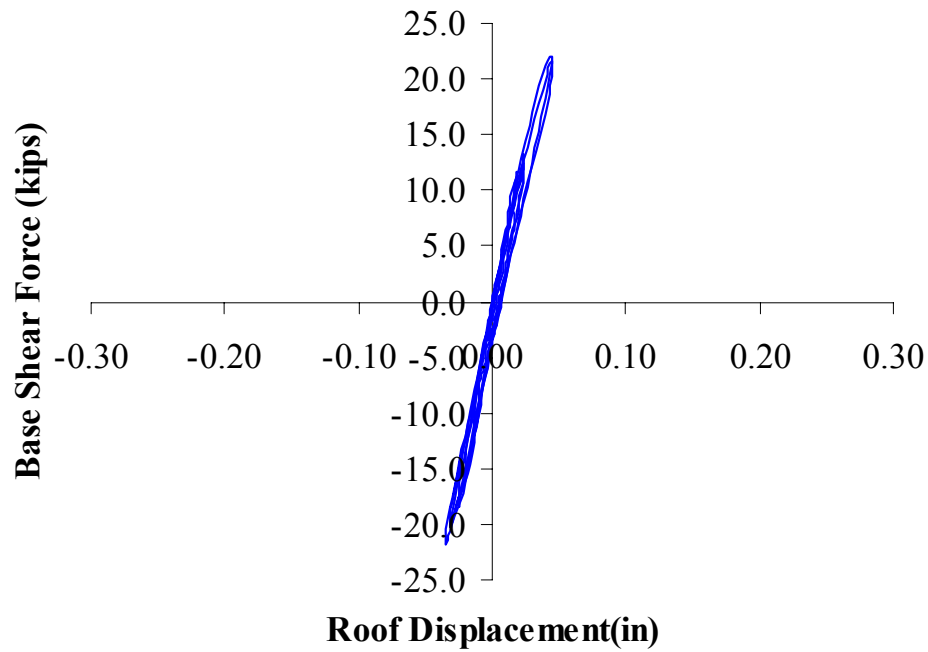


Figure 8.10. The base shear-lateral roof displacement curves for Wall 2 during Cycles 2g to 5b

Along with increasing lateral displacements, the behavior of Wall 2 was gradually changing. The three first story piers in Wall 2 worked more and more as three parallel rocking piers, while the effect of the global overturning moment gradually damped out. This trend can be clearly seen from the vertical displacements of the upper boundary of Pier 2-7 during Test Cycles 2g, 3a, and 5a, as shown in Figure 8.11.

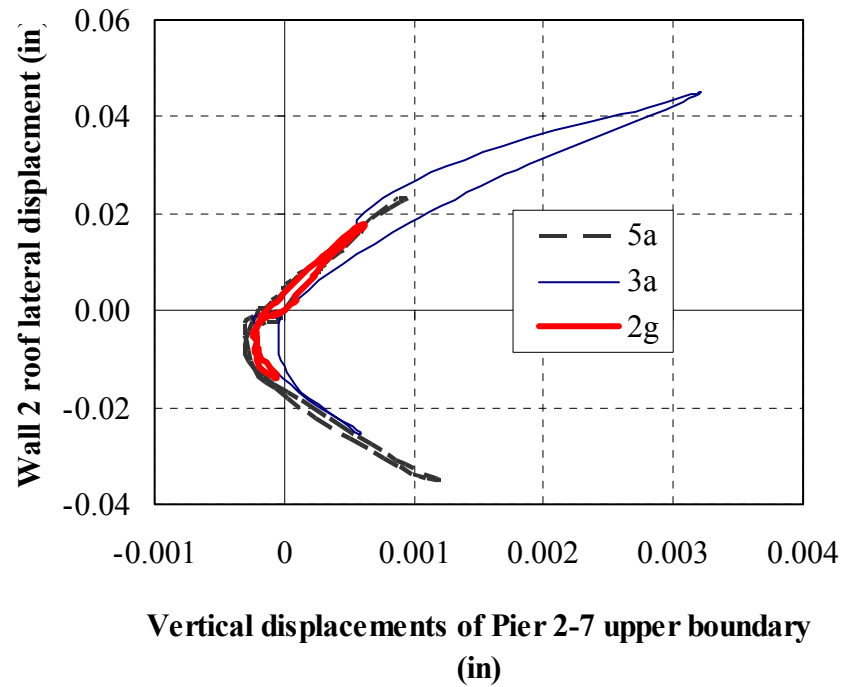


Figure 8.11 Vertical displacements of Pier 2-7 upper boundary

This figure shows that the vertical displacement of Pier 2-7 is dependent on both the value and the direction of the lateral displacement of Wall 2. When the building was loaded in the push direction (positive Wall 2 displacement, southward), the global overturning movement introduced a tensile vertical force in the pier and caused its upper boundary to displace upward. Meanwhile, the local pier flexural behavior also caused the upper boundary of Pier 2-7 to displace upward (Figure 8.12). These two factors added up and caused large upward displacements in the upper boundary of Pier 2-7. On the other hand, when the building was loaded in the pull direction (negative Wall 2 roof displacement), the global overturning movement caused the upper boundary of Pier 2-7 to displace downward, while the local flexural deformation of Pier 2-7 still caused its

upper boundary to displace upward. As a result, when the lateral pull displacement of Wall 2 was small, the vertical tensile deformation of Pier 2-7 induced by the global overturning movement was larger than the vertical compressive deformation induced by the local rocking, and thus the upper boundary of Pier 2-7 displaced downwards. However, when the roof lateral displacement reached around -0.01 in. (Figure 8.11), substantial flexural cracks were observed in Pier 2-7, and its rocking behavior caused large vertical uplift of its upper boundary. Therefore, the upper boundary of Pier 2-7 stopped displacing downwards and instead began to displace upwards with increasing roof lateral displacement.

The uplift of Pier 2-7 was around 0.002 in. for a Wall 2 lateral roof displacement of 0.035 in. in the push direction. This was almost double the uplift of Pier 2-7 of around 0.001 in. corresponding to a Wall 2 lateral roof displacement of -0.035 in. in the pull direction. This indicated that the effect of global overturning movement was still sizable in these cycles, although it was gradually damping out with increasing lateral displacements.

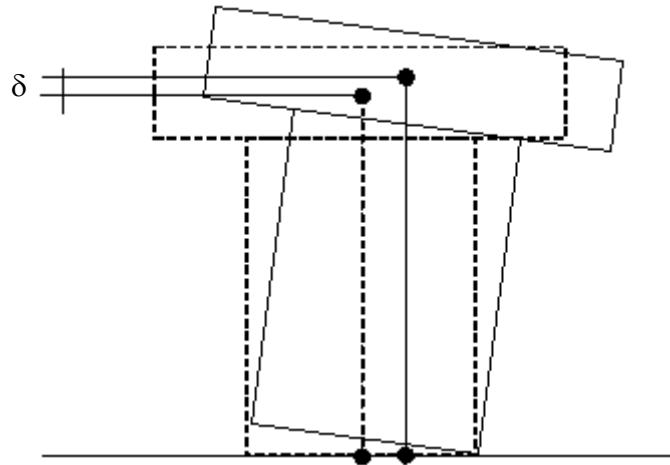


Figure 8.12. Upward displacement of the upper boundary of a pier due to rocking of individual pier

The ratios between the maximum lateral displacements of Pier 2-7, Pier 2-9 and the corresponding Wall 2 second floor lateral displacements are listed in Tables 8.2 and 8.3. Taking into account the possible errors of the measurements at such a small displacement level, it can be concluded that most of the Wall 2 first floor lateral deformation was concentrated in the piers.

Table 8.2. Lateral displacement ratios of Piers 2-7 and 2-9 in the push direction (Cycles 3a to 5a)

Maximum Wall 2 second floor lateral displacements in the push direction	Lateral displacement ratios for the piers	
	Pier 2-7	Pier 2-9
0.012 in.	73%	100%
0.018 in.	61%	98%
0.033 in.	65%	100%

Table 8.3. Lateral displacement ratios of Piers 2-7 and 2-9 in the pull direction (Cycles 3a to 5a)

Maximum Wall 2 second floor lateral displacements in the pull direction	Maximum lateral displacement ratios for the piers	
	Pier 2-7	Pier 2-9
-0.01 in.	73%	72%
-0.019 in.	71%	62%
-0.025 in.	90%	73%

8.3.1.3. Accumulation of damage (Cycles 6 to 8a)

Cracks began to develop and propagate quickly in Wall 2 during this series of test cycles (Figure 8.13). In Cycle 6, when the building was loaded in the push direction, a flexural crack with a length of around 8 in. initiated at the base of the corner between Wall A and Wall 2. When the building was loaded in the pull direction, flexural cracks developed at the right bottom corners of Pier 2-7 and Pier 2-8, and at the left top corner of Pier 2-8.

Meanwhile, a horizontal crack developed at the corner between Wall 2 and Wall B in the bed joint right above the first head course. This crack propagated to the left and down as a stair-step crack at an angle of approximately 45^0 for about 12 in. It propagated further to the ground in Cycle 6a when the building was loaded in the pull direction. At the same time, this crack also propagated into the out-of-plane wall B, opening the entire section of the flange pier B-7, and spreading horizontally into Pier 2-9 for about 8 in.

In Cycle 7, when the building was loaded in the push direction, a stair-step crack initiated at the right top corner of Pier 2-2 due to the tensile stress concentration. When the building was loaded in the pull direction, a crack opened at the left top corner of Pier 2-9 next to the end of the first floor steel lintel. This crack did not propagate further in the horizontal bed joint. Instead, it propagated at an angle of 45^0 to the left and up for about

34 in. This direction was perpendicular to the direction of the maximum tensile stress at the corner of opening.

This diagonal type of crack pattern was commonly observed in the following test cycles. It led to different effective aspect ratios of a pier when the pier was loaded in different directions. Taking Pier 2-9, as shown in Figure 8.14(a), for example, the rocking of this pier to the left (pull direction, northward) was different from that to the right (push direction, southward). When the pier rocked to the right, its aspect ratio was H/L (Figure 8.14(b)). When the pier rocked to the left, its aspect ratio was $(H+a)/L$ (Figure 8.14(c)). The different effective aspect ratios of a pier in push and pull directions lead to different behavior of this pier in the two loading directions. More detailed discussion on this topic can be found in Section 9.5.

Even though Cycle 7a was only a repeat of Cycle 7, several new cracks were observed. When the building was loaded in the push direction, the existing crack at the base of Pier A-10 propagated into Pier 2-7. Meanwhile, a stair-step crack initiated at the right top corner of Pier 2-7, and propagated at an angle of approximately 45° to the left and up for about 17 in. When the building was loaded in the pull direction, no more new cracks were observed.

In Cycle 8, when the building was loaded in the push direction, the existing diagonal crack at the right top corner of Pier 2-7 propagated farther for another 12 in. At the same time, another flexural crack developed in the bed joint one course above the existing crack at the base of Pier A-10. When the building was loaded in the pull direction, no more cracks developed.

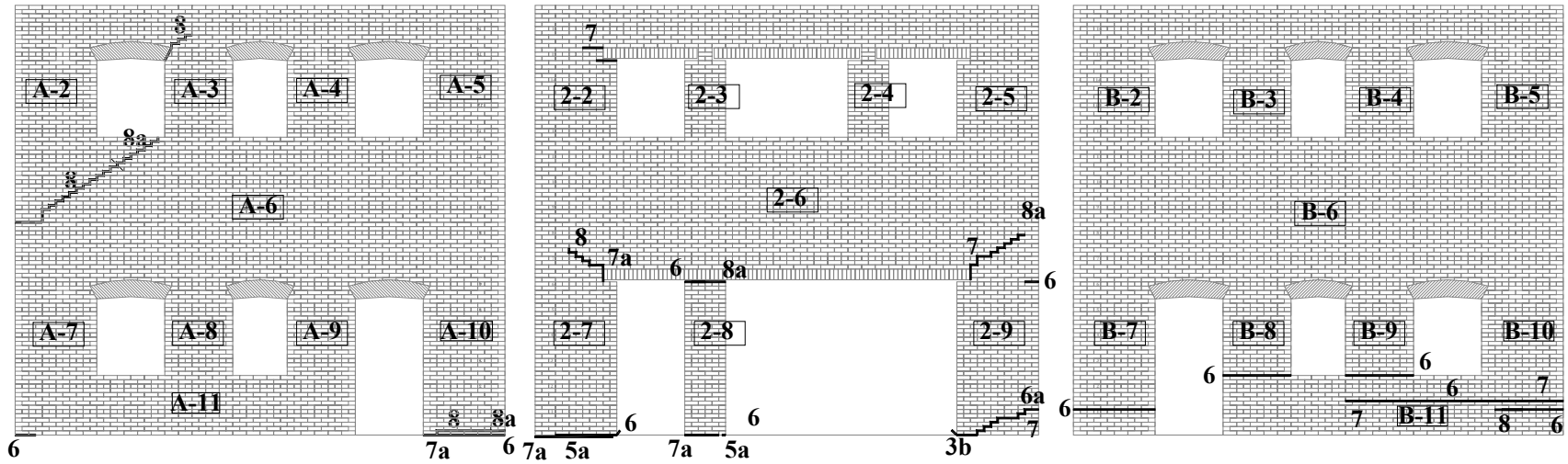


Figure 8.13. Crack pattern of Wall 2 and adjacent Wall A (left) and Wall B (right) at the end of Cycle 8a. The crack number corresponds to the test run number. Number IDs of each pier are given in the rectangles.

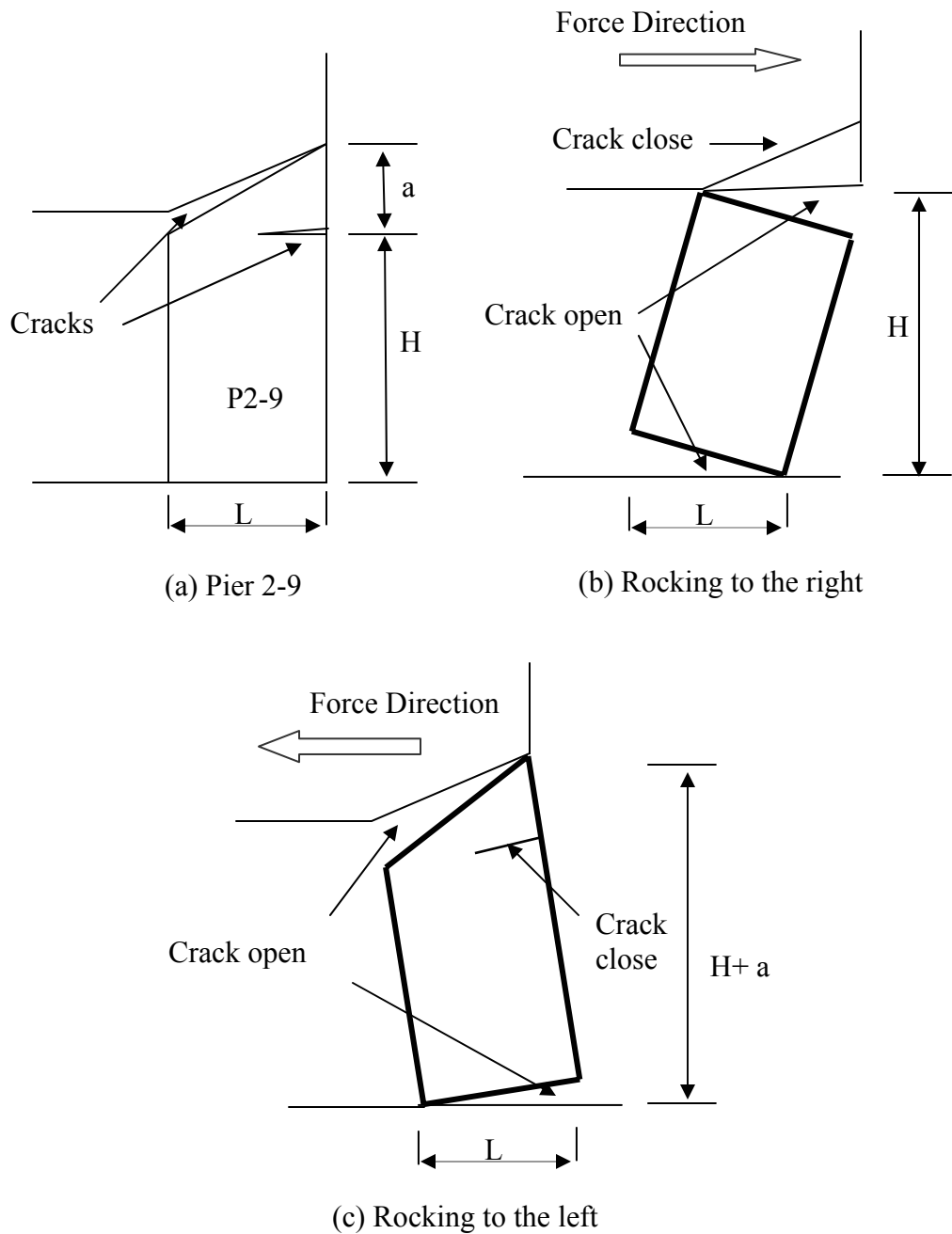


Figure 8.14. Rocking of Pier 2-9 in different directions

In Cycle 8a, when the building was loaded in the push direction, the existing crack at the base of Pier A-10 propagated a little more. Meanwhile, a flexural crack was

also observed between the top of Pier 2-8 and the bottom of the steel lintel. When the building was loaded in the pull direction, the existing diagonal crack at the left top corner of Pier 2-9 propagated farther for another 11 in.

All the cracks developed during this series of test cycles were apparently due to the large tensile stresses introduced by the flexural deformations of the piers. The cracks were concentrated around the top and the bottom of the first floor piers. This indicated that a working mechanism with the rocking of the first story piers was developing in the wall. Moreover, the flexural cracks that developed in Pier A-10 and Pier B-7 revealed a clear participation of the out-of-plane walls, which is discussed in Section 8.5.

The damage of the building can also be seen from the base shear-lateral roof displacement curves for Wall 2 in these test cycles (Figure 8.15). The response of Wall 2 became significantly nonlinear during Test cycles 6 to 8a. Specifically, when the lateral roof displacement reached 0.064 in. in the push direction, Wall 2 achieved its maximum lateral strength of 27.0 kips. This strength basically remained constant even when the lateral roof displacement increased from 0.064 in. to 0.144 in. in the following cycles.

Similar behavior occurred in the pull direction. When the lateral roof displacement reached -0.053 in., Wall 2 achieved its maximum lateral strength of around 24.4 kips. This strength remained constant when the lateral roof displacement increased from -0.053 in. in Cycle 6 to -0.145 in. in Cycle 8. Moreover, when the wall unloaded from its maximum lateral displacement, the rate of stiffness change increased as the lateral displacement approached zero. This force-displacement response indicated that a typical rocking response was developing in this wall.

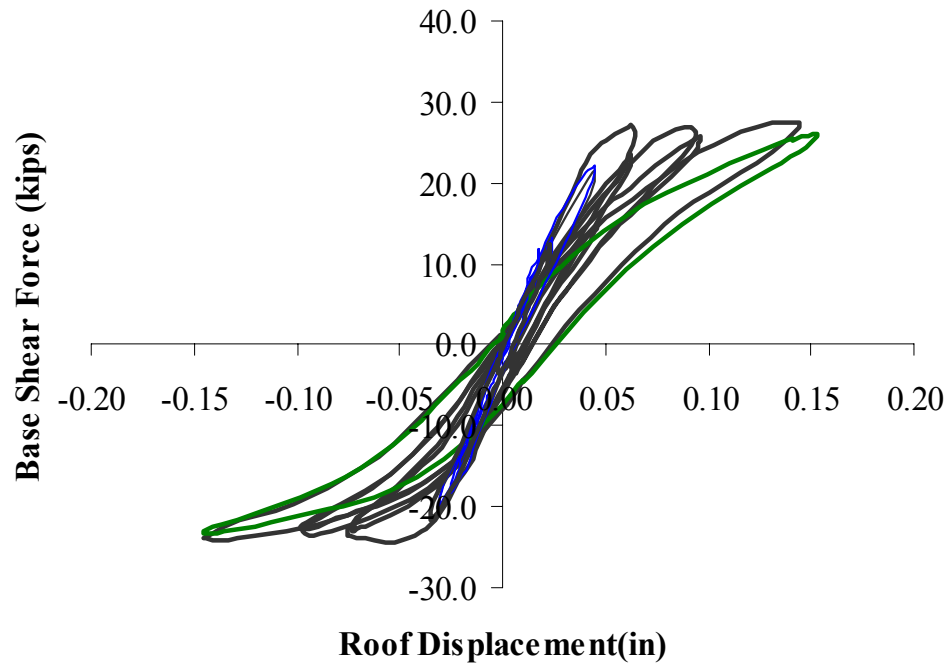


Figure 8.15. The base shear-lateral roof displacement curves for Wall 2 up to Cycles 8b

As indicated by the crack pattern, Wall 2 behavior was dominated by the individual rocking of the first story piers. This component-dominated behavior of Wall 2 was verified from the measured responses of the first floor piers. For example, the vertical movements of the upper boundary of Pier 2-7 in Cycle 5a, 6, 7, and 8 are shown in Figure 8.16. Regardless of which direction the building was loaded, the upper boundary of Pier 2-7 always displaced upwards due to the rocking of this pier. Note that these upward displacements were almost the same corresponding to a Wall 2 roof lateral displacement of 0.15 in. regardless of the loading direction. This indicated that the effect of overturning moment on the behavior of Pier 2-7 is negligible for such a displacement level.

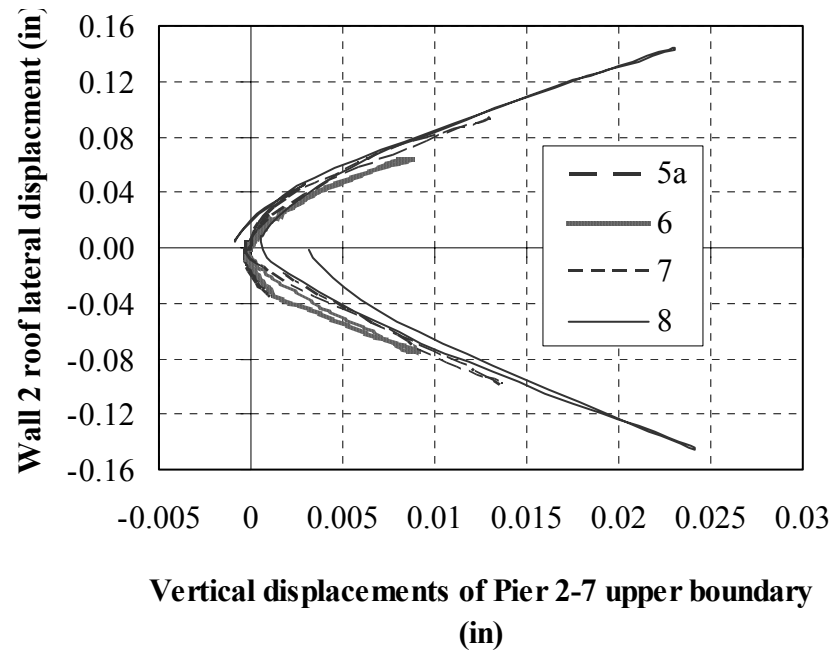
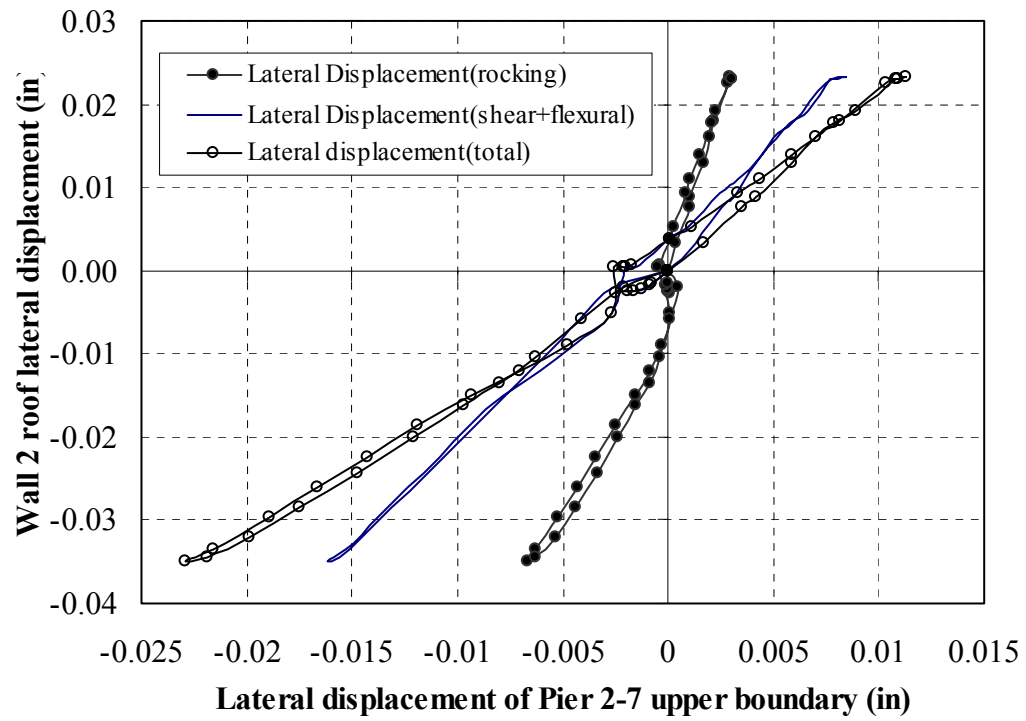
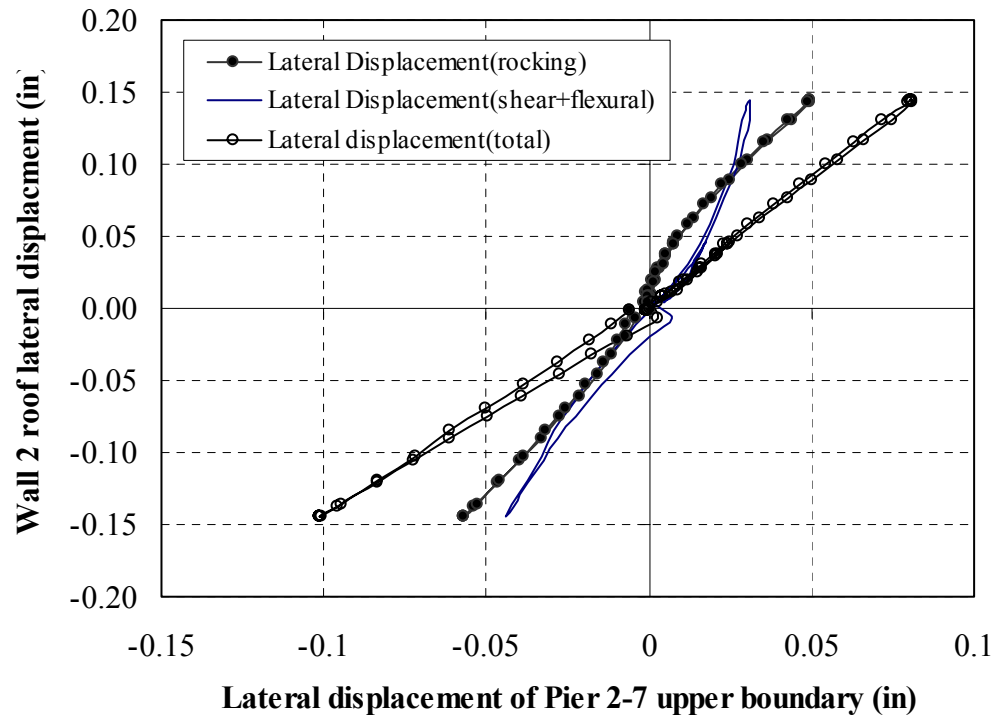


Figure 8.16. Vertical displacements of Pier 2-7 upper boundary

The evolution of the behavior of Wall 2 during this series of tests can also be seen from the lateral deformation components of each first story pier. Taking Pier 2-7 for example, its lateral displacement curves for Cycles 5a and 8 are shown in Figure 8.17. Note that the lateral displacement of a pier is composed of its rocking displacement, which was induced by the opening of the flexural cracks, and the shear and flexural displacement, which was accumulated inside the pier. Figure 8.17 shows that the behavior of this pier was quite different in these two test cycles. In Cycle 5a, the cracking of the pier was minor, and thus most of the lateral displacement of the pier was due to its shear and flexural deformation. Conversely, in Cycle 8, there were substantial crack propagations at the top and the bottom of Pier 2-7. As a result, a large portion of the lateral displacement of this pier was due to its rocking behavior.



(a) Cycle 5a



(b) Cycle 8

Figure 8.17. Lateral displacements of Pier 2-7

Another interesting phenomenon observed in this series of tests is that the response of Pier 2-8 was basically following the responses of Pier 2-7 and Pier 2-9. The upper boundary of Pier 2-8 always displaced upwards when the building was laterally displaced (Figure 8.18).

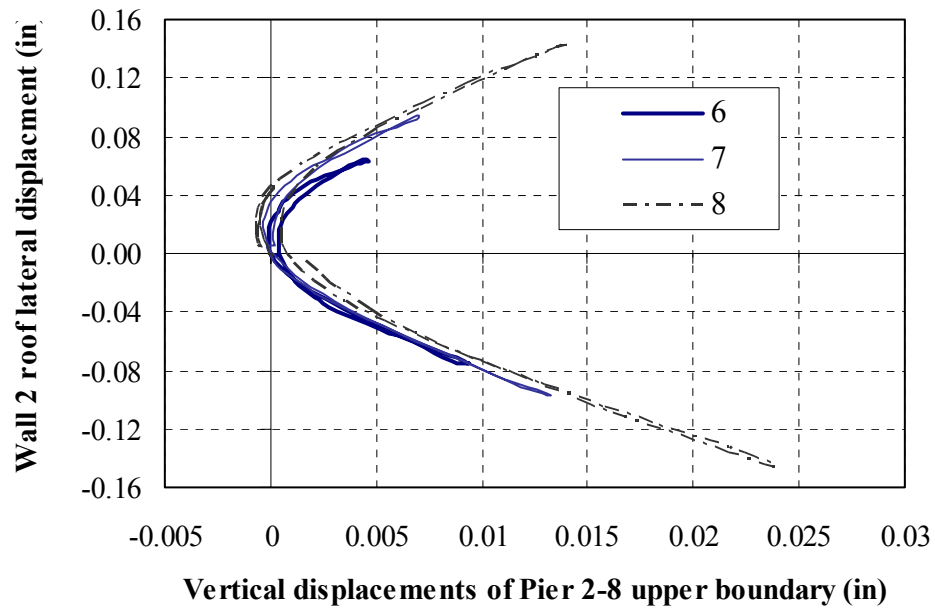


Figure 8.18. Vertical movement of Pier 2-8

Being similar to the previous cycles, the ratios between the maximum lateral displacements of Pier 2-7, Pier 2-9 and the corresponding Wall 2 second floor lateral displacements in this series of cycles indicated that most of the Wall 2 first floor lateral deformation was concentrated in the piers (Tables 8.4 and 8.5).

Table 8.4. Lateral displacement ratios of Piers 2-7 and 2-9 in the push direction (Cycles 6 to 8a)

Maximum Wall 2 second floor lateral displacements in the push direction	Maximum lateral displacement ratios for the piers	
	Pier 2-7	Pier 2-9
0.059 in.	70%	99%
0.081 in.	68%	100%
0.119 in.	67%	100%

Table 8.5. Lateral displacement ratios of Piers 2-7 and 2-9 in the pull direction (Cycles 6 to 8a)

Maximum Wall 2 second floor lateral displacements in the pull direction	Maximum lateral displacement ratios for the piers	
	Pier 2-7	Pier 2-9
-0.062 in.	77%	68%
-0.081 in.	79%	68%
-0.128 in.	79%	68%

8.3.1.4. Fully developed kinematic mechanism (Cycles 10 and 10a)

In Cycle 10, when the building was loaded in the push direction (southward), the existing diagonal crack at the right top corner of Pier 2-7 propagated farther for another 23 in., and moved into the out-of-plane Wall A. When the building was loaded in the pull direction (northward), a diagonal crack initiated at the upper left corner of Pier 2-5 and propagated to the upper right for about 45 in. This indicated that the second floor piers in Wall 2 began to rock.

In Cycle 10a, when the building was loaded in the push direction, a new crack developed at the left toe of Pier 2-9, three courses above the ground. This crack propagated to the right for about 16 in. and joined the existing cracks. When the building

was loaded in the pull direction, a horizontal flexural crack initiated at the upper left corner of Pier 2-7 and propagated to the right for about 24 in. (Figure 8.19).

With all these cracks formed, a kinematic mechanism was fully developed for Wall 2. The three first floor piers rocked when the building was laterally displaced (Figure 8.20). Specifically, since the size of Pier 2-8 was much smaller than those of Piers 2-7 and 2-9, Pier 2-8 gradually separated from the steel lintel when the wall was laterally loaded.

Although there was some evidence of rocking of the second floor piers, the damage to the second floor wall was minor compared with that to the first floor piers. The entire second floor masonry wall basically worked as a rigid box moving back and forth and displacing upwards on the top of the first floor piers. Moreover, the rocking of the first floor piers forced the flanges (Wall A and Wall B) to move together with the in-plane walls, and caused Walls A and B to crack. The flange effects due to the movement of Walls A and B provided a large contribution to the lateral resistances of the in-plane walls, as is discussed in more detail in Section 8.5.

Figure 8.21 shows the base shear-lateral roof displacement curves for Wall 2 during the entire set of test cycles. The lateral resistance of this wall exhibited little degradation with increasing lateral displacements. In addition, the energy dissipation of the wall was rather small. All these are consistent with the visual observation that the behavior of Wall 2 was governed by rocking.

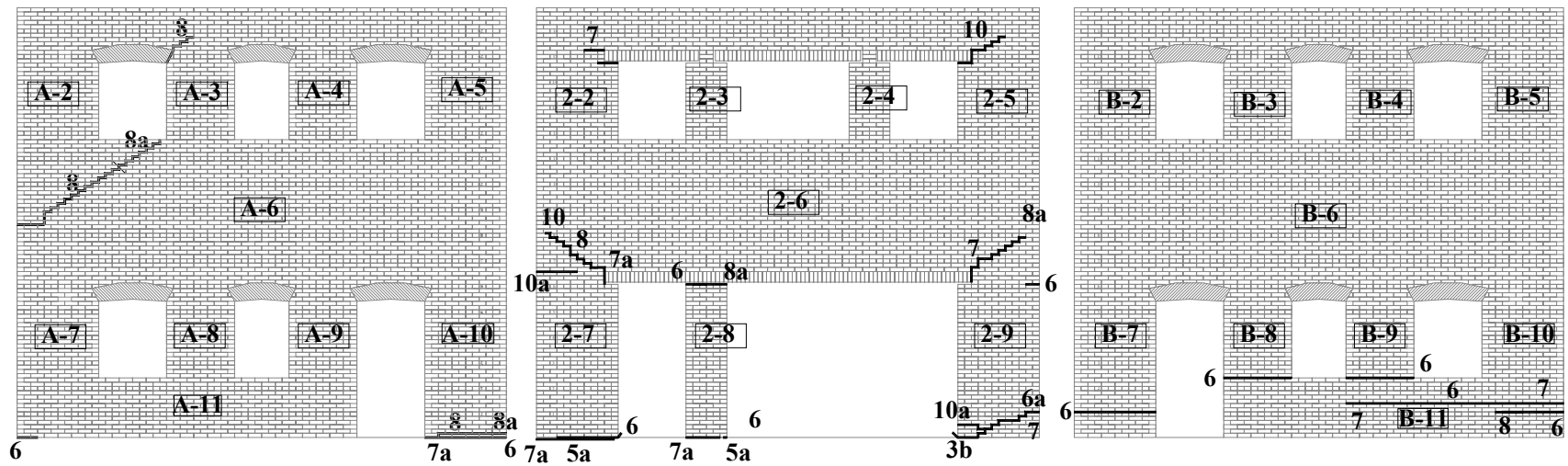


Figure 8.19. Crack pattern of Wall 2 and adjacent Wall A (left) and Wall B (right) at the end of Cycle 10a. The crack number corresponds to the test run number. Number IDs of each pier are given in the rectangles.

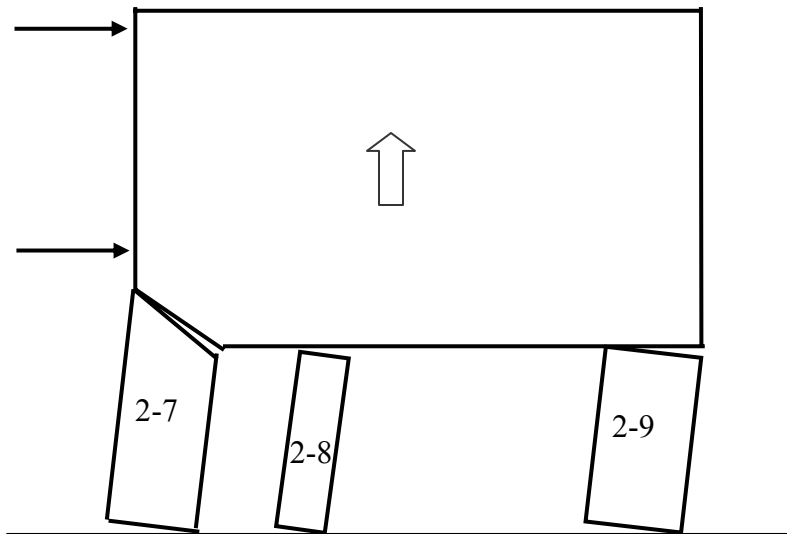


Figure 8.20. Rocking of the first floor piers in Wall 2 and upward movement of the second story wall

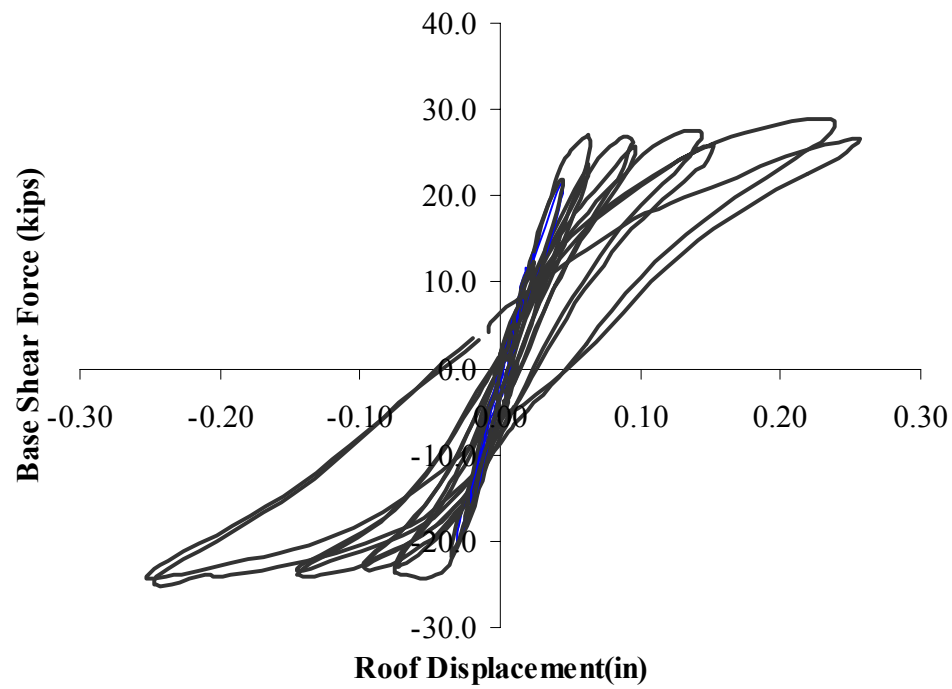


Figure 8.21. The base shear-lateral roof displacement curves for Wall 2 during the entire load cycles

The responses of the first floor piers in the last two test cycles were basically the same as in the previous cycles. The uplifts of the first floor piers corresponding to the maximum roof lateral displacements are listed in Table 8.6. The table shows that the uplifts of the first floor piers were close to each other, indicating an in-phase rocking of these piers. On the other hand, when the building was loaded in the push direction, the uplift of Pier 2-7 was still slightly larger than that of Pier 2-9, and vice versa when the building was loaded in the pull direction. This revealed that the global overturning movement still had an influence, albeit a small one, on the behavior of the piers.

Table 8.6. Uplift of the first floor piers during the tests

Roof lateral displacement (in.)	Uplifts of the piers (in.)		
	Pier 2-7	Pier 2-8	Pier 2-9
0.238 (10a)	0.045	0.033	0.039
0.257 (10b)	0.044	0.034	0.041
-0.247 (10a)	0.049	0.046	0.054
-0.252 (10b)	0.045	0.043	0.052

The displacement components of the first story piers were also similar with those in Cycles 8 and 8a. Figure 8.22 shows the lateral displacement response of Pier 2-7 in Cycle 10. The lateral displacements of the first story piers were dominated by their rocking behavior.

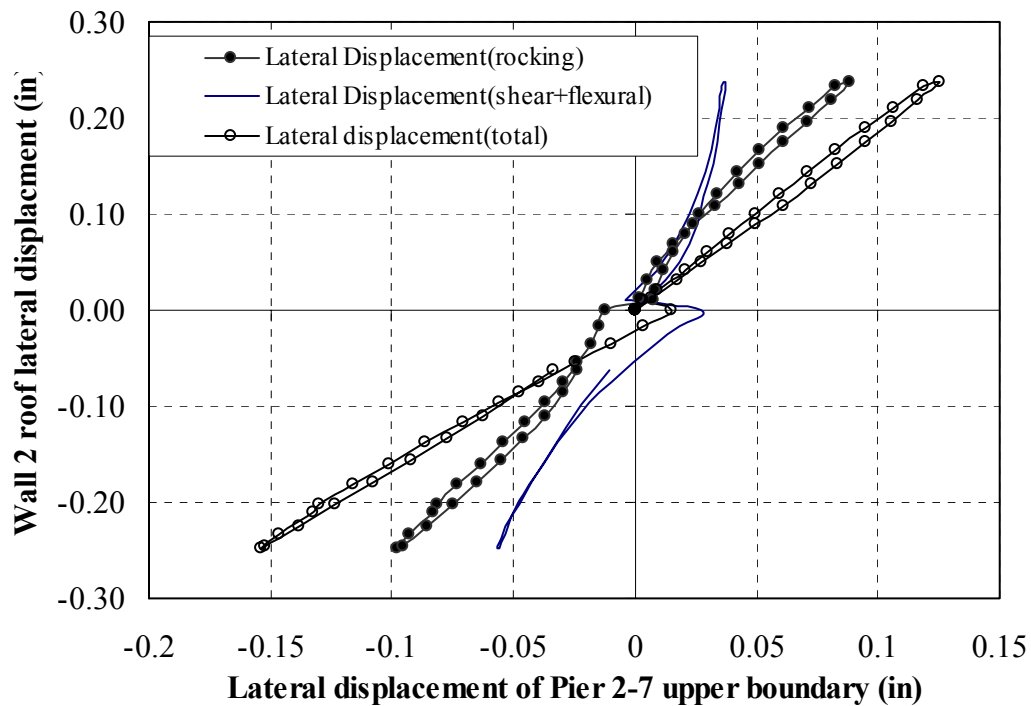


Figure 8.22. Lateral displacements of Pier 2-7

The ratios between the maximum lateral displacements of Pier 2-7, Pier 2-9 and the corresponding Wall 2 second floor lateral displacements are listed in Tables 8.7 and 8.8. Again, the tables show that most of the Wall 2 first floor lateral deformation was concentrated in the piers. This behavior was consistent with the readings of the diagonal potentiometers mounted in the spandrel 2-6, which could not pick up much deformation of the spandrel.

Table 8.7. Lateral displacement ratios of Piers 2-7 and 2-9 in the push direction (Cycles 10 to 10a)

Maximum Wall 2 second floor lateral displacements in the push direction	Maximum lateral displacement ratios for the piers	
	Pier 2-7	Pier 2-9
0.185 in.	68%	100%
0.202 in.	69%	100%

Table 8.8. Lateral displacement ratios of Piers 2-7 and 2-9 in the pull direction (Cycles 10 to 10a)

Maximum Wall 2 second floor lateral displacements in the pull direction	Maximum lateral displacement ratios for the piers	
	Pier 2-7	Pier 2-9
-0.201 in.	77%	65%
-0.198 in.	77%	68%

8.3.2. Wall 1

Being similar to Wall 2, the observed responses of Wall 2 exhibited an elastic or minor damage state in Cycles 2g to 5a (maximum roof displacement of 0.03 in.), a significant accumulation of damage in the structure (Cycles 6 through 8a, with a maximum roof displacement of 0.166 in), and a matured failure mechanism (Cycles 10 and 10a, with a maximum roof displacement of 0.263 in). As a result, the response of Wall 1 is discussed in the three different states.

8.3.2.1. Elastic response and minor damage (Cycles 2g to 5a)

The response of Wall 1 during Cycles 2g to 5a was essentially elastic. No visual cracks or other damage was observed in these test cycles. The base shear–lateral roof

displacement curves for Wall 1, shown in Figure 8.23, confirms the essentially linear elastic behavior observed.

The peak average vertical strains for Pier 1-6 and Pier 1-7 in Cycles 2g, 3a, and 5a are shown in Figures. 8.24 and 8.25 for the push direction (southward) and pull direction (northward), respectively. These figures show that the responses of Pier 1-6 and Pier 1-7 were basically the same in this series of test cycles. When the wall was loaded in the push direction, a compressive strain was introduced on the left side of the pier, while tensile strain was introduced on the right side of the pier, and vice versa in the pull direction. Note that the vertical strain distributions were similar for Pier 1-6 and Pier 1-7, which indicated that both walls participated in resisting the external lateral forces.

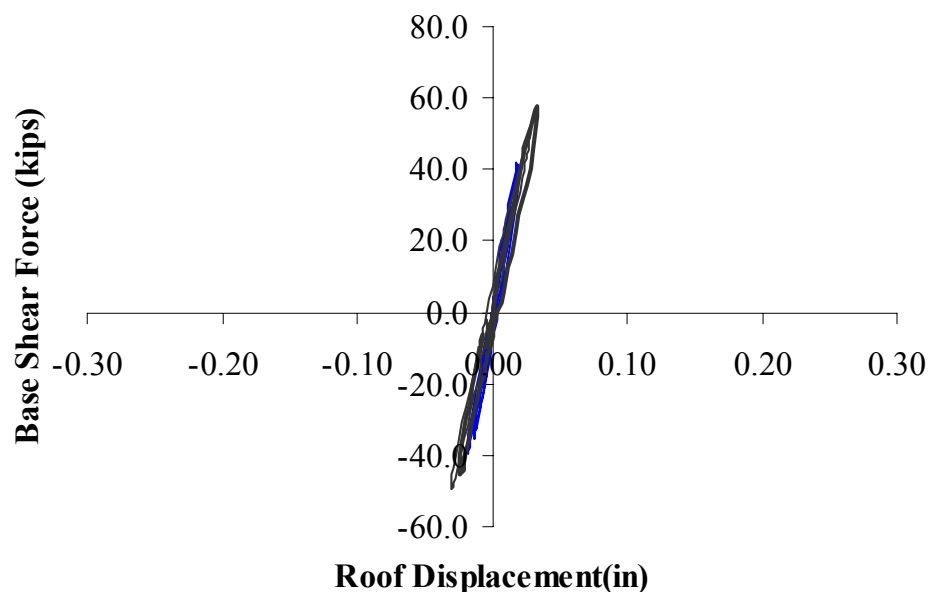


Figure 8.23. Base shear-lateral roof displacement of Wall 1 up to Cycle 5b

The peak vertical strain distributions at the base of the piers were picked up by the strain gages and are shown in Figures 8.26 and 8.27, corresponding to loaded in the push direction and pull direction, respectively. Typically, they exhibit similar trend as the average vertical strain distributions measured by the LVDTs. However, Figure 8.27 shows that when the wall was loaded in the pull direction in Cycle 5a, the strain gage on the left side of Pier 1-6 did not pick up any tensile strain. This indicated that a flexural crack was probably developing around that area, although no visual cracks had been observed. Similar behavior was observed in the strain gage on the right side of Pier 1-6 when the wall was loaded in the push direction, as shown in Figure 8.26.

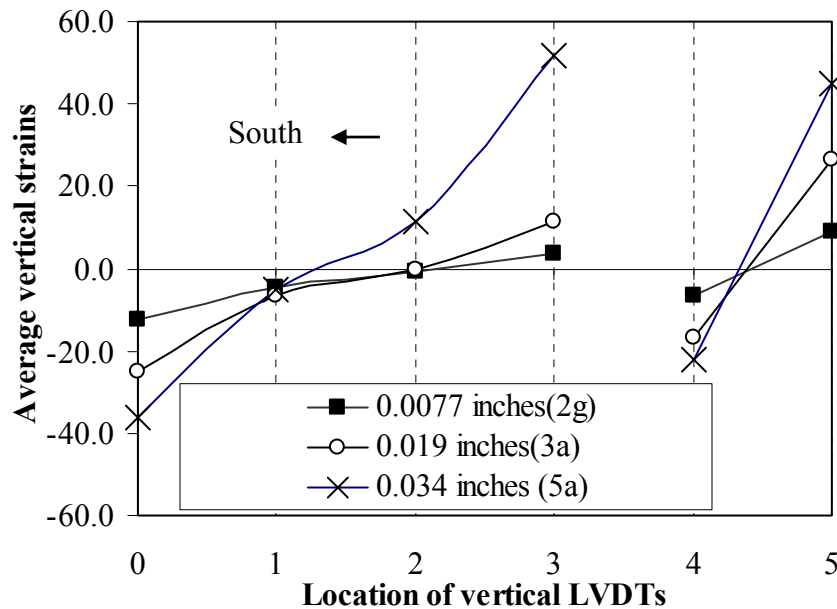


Figure 8.24. The average vertical strains in Pier 1-6 and Pier 1-7 when the wall was loaded in the push direction

X axis: 0: P1-6VL, 1: P1-6VLC, 2: P1-6VRC, 3:P1-6VR, 4:P1-7VL, 5:P1-7VR

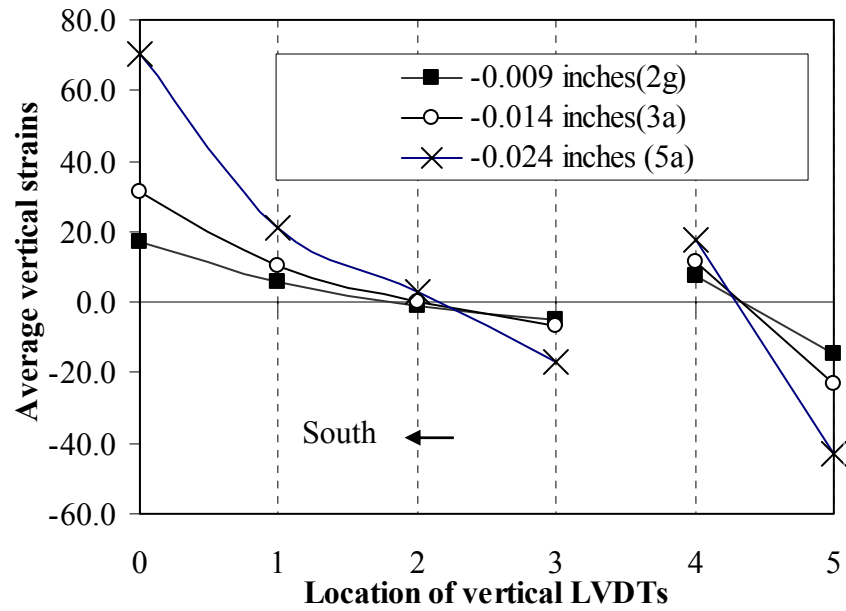


Figure 8.25. The average vertical strains in Pier 1-6 and Pier 1-7 when the wall was loaded in the pull direction
X axis: 0: P1-6VL, 1: P1-6VLC, 2: P1-6VRC, 3:P1-6VR, 4:P1-7VL, 5:P1-7VR

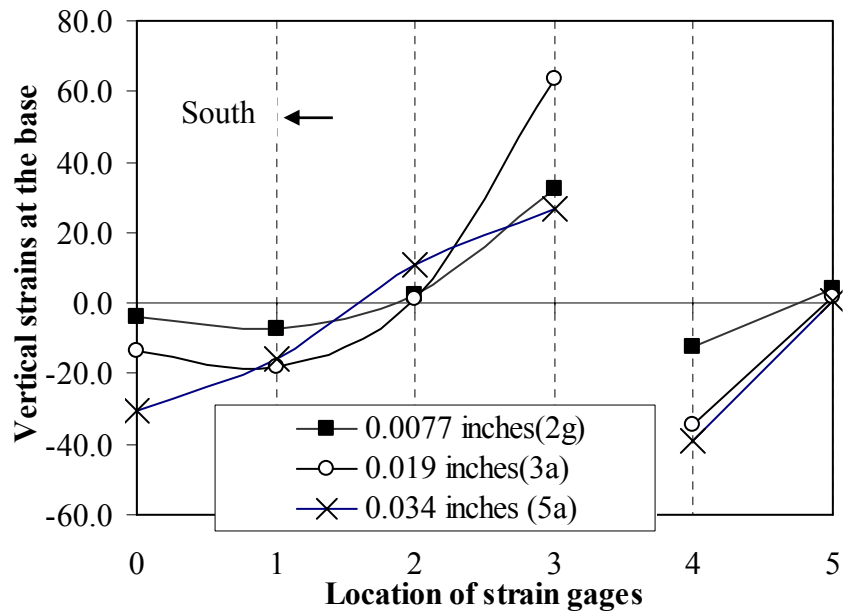


Figure 8.26. The base vertical strains in Pier 1-6 and Pier 1-7 when the wall was loaded in the push direction
X axis: 0: S1-6L, 1: S1-6VLC, 2: S1-6VRC, 3:S1-6R, 4:S1-7L, 5:S1-7R

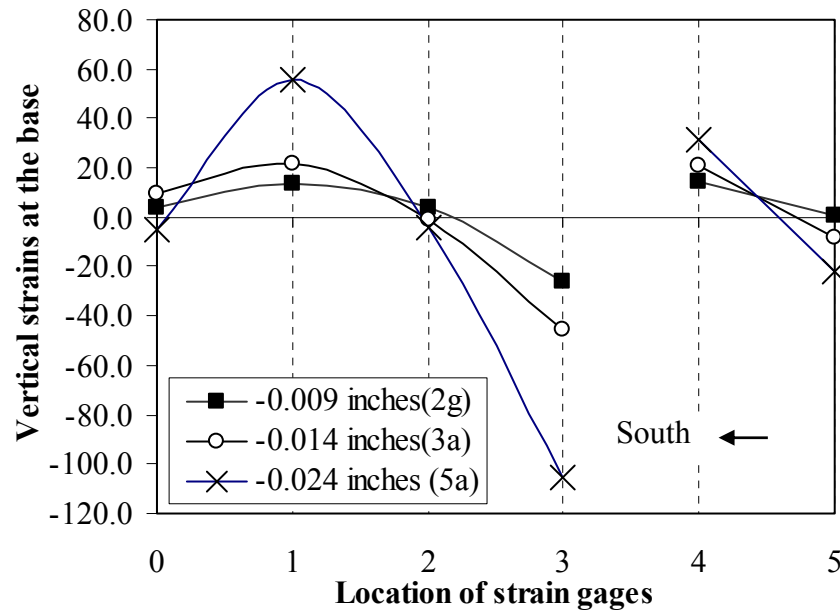


Figure 8.27. The base vertical strains in Pier 1-6 and Pier 1-7 when the wall was loaded in the pull direction
X axis: 0: S1-6L, 1: S1-6VLC, 2: S1-6VRC, 3:S1-6R, 4:S1-7L, 5:S1-7R

The vertical movement of the upper boundary of Pier 1-6 also reveals a possible damage at the end of this series of test cycles. As shown in Figure 8.28, during Cycles 2g and 3a, the upper boundary of Pier 1-6 displaced upwards when the wall was loaded in the pull direction (negative roof displacement), and displaced downwards when the wall was loaded in the push direction (positive roof displacement). This was due to the tensile or compressive vertical forces introduced by the global overturning moment.

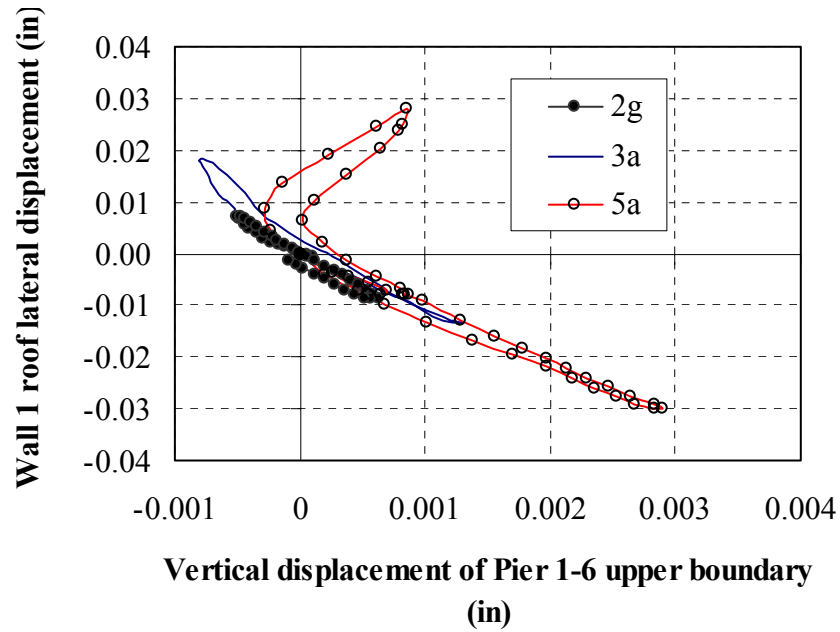


Figure 8.28. Vertical movements of Pier 1-6 in Cycles 2g, 3a, and 5a

In Cycle 5a, however, when the wall was loaded in the push direction, the upper boundary of Pier 1-6 first went down, and then lifted up. Referring to Figure 8.26, this phenomenon can be attributed to the large tensile deformation developed on the right side of the pier. This indicates that a flexural crack was probably developing at the right heel of Pier 1-6, and this pier was starting to rock about its left toe. In contrast, Pier 1-7 exhibited essentially elastic behavior, and the upper boundary of Pier 1-7 moved up and down due to the global overturning moment effects (Figure 8.29).

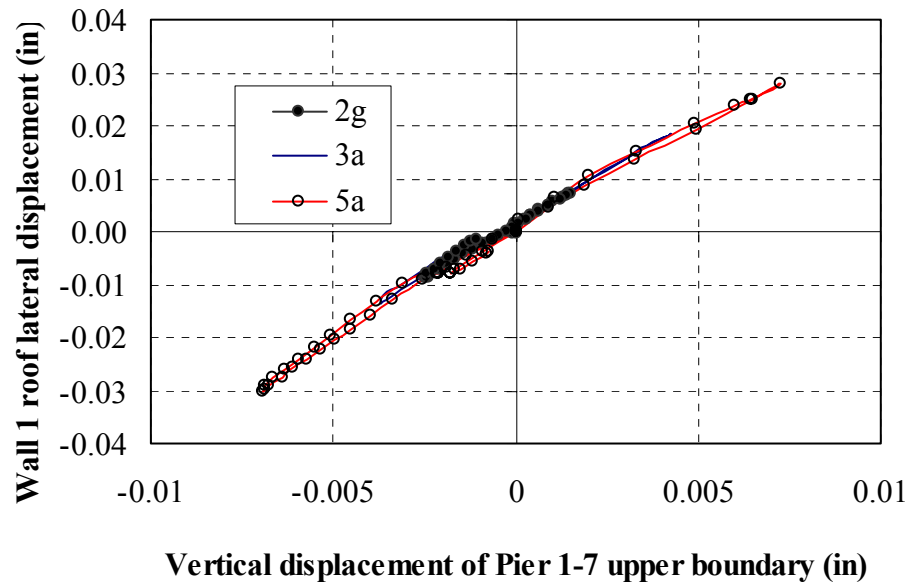


Figure 8.29. Vertical movements of Pier 1-7 in Cycles 2g, 3a, and 5a

8.3.2.2. Accumulation of damage – rocking of the wall (Cycles 6 to 8a)

Substantial damage developed in Wall 1 during test Cycles 6 to 8b. The crack patterns in Wall 1 after Cycle 8b are shown in Figure 8.30. The detailed description of the crack propagation is as follows.

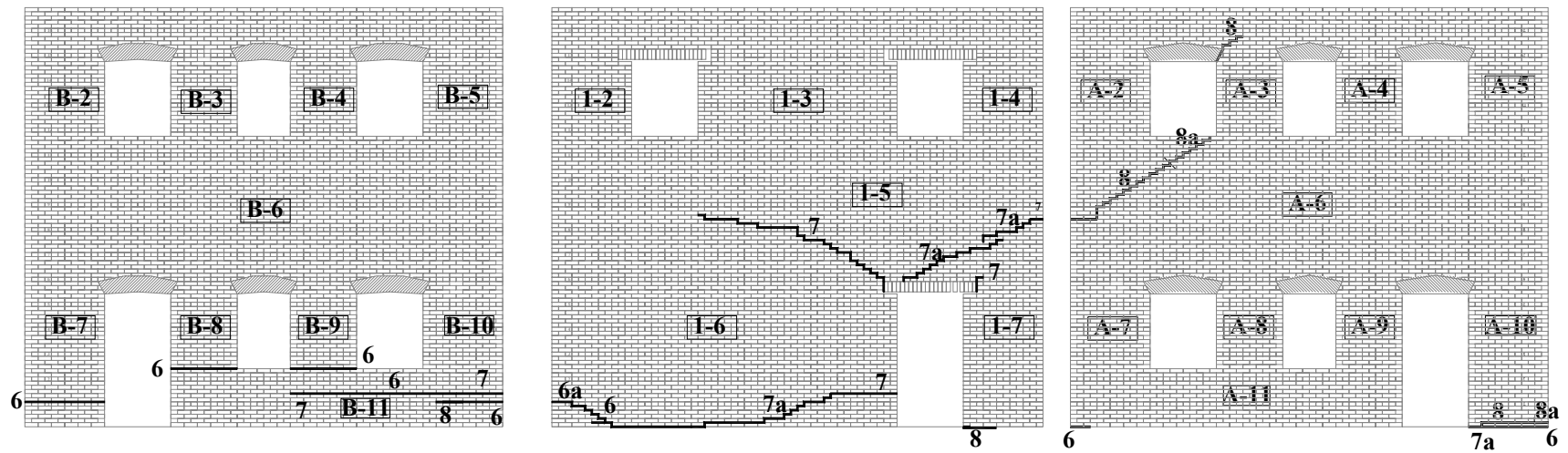


Figure 8.30. Crack pattern of Wall 1 and adjacent Wall B (left) and Wall A (right) at the end of Cycle 8a. The crack number corresponds to the test run number. Number IDs of each pier are given in the rectangles.

During Cycle 6, when the building was loaded in the push direction (southward), flexural cracks developed at the base corner between Wall A and Wall 1. On the other hand, when the building was loaded in the pull direction (northward), global overturning moment caused large tensile stresses at the corner between Wall 1 and Wall B. As a result, a horizontal crack initiated at the corner between Wall 1 and Wall B in the bed joint right above the first header course. This crack propagated horizontally into Wall 1 for about 12 in., then propagated as a stair-step crack at an angle of approximately 45° toward the ground until it reached the RC foundation. After that, it continued to propagate along the bed joint between the first course brick and the RC foundation to the right for about 48 in.

Meanwhile, since the flange effects introduced a large amount of tensile stresses in Wall B, this crack also propagated into Wall B. It spread into Wall B for about 36 in. and stopped. However, another crack developed in the bed joint two courses above the first crack and spread horizontally to the left until reaching the left side of Pier B-9. Meanwhile, several horizontal cracks propagated over the entire section of Pier B-8 and Pier B-9 at the bed joint right above the sill. These cracks continued to propagate in the following cycles. As a result, when the building was loaded in the pull direction (northward), the whole portion of Wall B above these cracks was essentially lifted up due to the large flange effects (Figure 8.31).

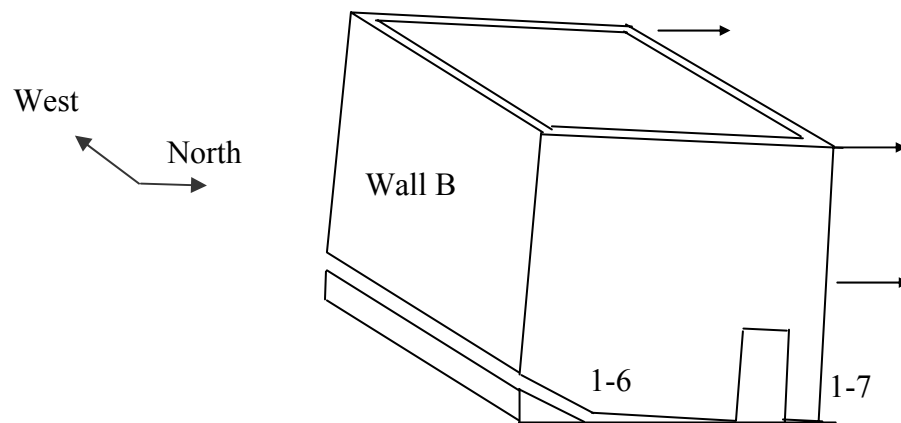


Figure 8.31. Lifting up of Wall B due to the flange effects

During Cycle 7, when the building was loaded in the push direction, two cracks developed at the top of Pier 1-7. One was a stair-step crack, and the other was a horizontal crack at the corner between Wall 1 and Wall A, two courses above the eighth header course. The latter crack was right below where the steel plate connected to the Wall 1 second floor actuator, which was probably induced by the large stress concentration around the loading point.

Also during Cycle 7, a flexural crack initiated in the bed joint at the right base of Pier 1-6 two courses above the first header course. This crack propagated into Pier 1-6 for about 40 in. It was apparently due to the large tensile stress induced by the rocking of Pier 1-6.

When the building was loaded in the pull direction, the existing horizontal cracks in Pier B-11 opened and propagated farther. Meanwhile, a large stair-step crack initiated at the right upper corner of Pier 1-6 next to the end of the first story steel lintel. This

crack propagated at an angle of 45° up and to the left for about 57 in., then gradually flattened down and grew for another 70 in. The flattening down of this crack was due to the lateral confining forces in the spandrel, introduced by the prestressing forces used to fix the Wall 1 second floor actuator. This large crack and the existing crack above Pier 1-7 basically separated Wall 1 into two piers and a large spandrel; and the two piers rocked about their individual right toes (Figure 8.32).

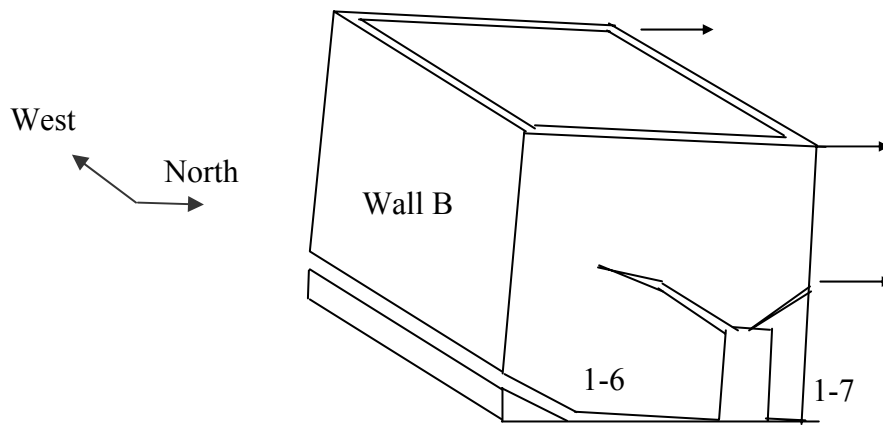


Figure 8.32. Rocking of Wall 1 as two piers when the wall was loaded in the pull direction

Even though Cycle 7a was only a repeat of Cycle 7, several new cracks were observed. When the building was loaded in the push direction (southward), the existing flexural crack at the right base of Pier 1-6 propagated farther at an angle of approximately 45° down and to the left until it reached the foundation. Then it continued to propagate to the left until it reached the existing crack at the left base of Pier 1-6. These new cracks fully cracked the base of Pier 1-6.

Also during Cycle 7a, the existing cracks at the top of Pier 1-7 continued to propagate diagonally and coalesce. These cracks tended to separate the large upper left portion of Wall 1 from Pier 1-7. As a result, when the building was loaded in the push direction, Pier 1-7 tended to be left behind while the remaining portion of Wall 1 rocked as a big pier about the left toe of Pier 1-6, as shown in Figure 8.33. When the building was loaded in the pull direction, no more new cracks were observed.

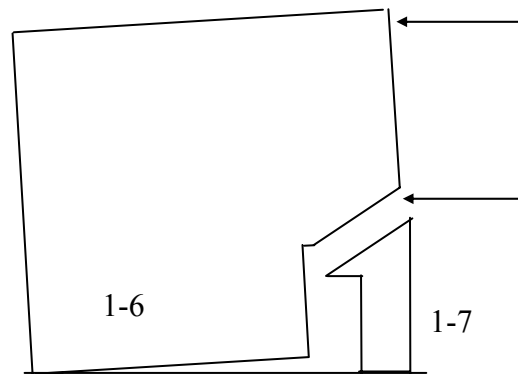


Figure 8.33 Rocking of Wall 1 when loaded in the push direction (southward)

During Cycle 8, when the building was loaded in the push direction, the existing diagonal crack on the top of Pier 1-7 propagated into Wall A, going up at an angle of approximate 45° toward the window opening at the second floor of Wall A. This crack stopped approximately 4 courses below the window. At the same time, a diagonal crack initiated at the left upper corner of Pier A-3 and went upwards and to the right for about 23 in.

In Cycle 8a, the crack below Wall A second story window propagated until it reached the window, and thus the cracks below and above the window were connected into a large crack. This crack separated Wall 1 from Wall A when the building was loaded in the push direction. As a result, the majority of Wall 1 except Pier 1-7 rocked together with the triangular portion of Wall A, about the left toe of Pier 1-6, as shown in Figure 8.34.

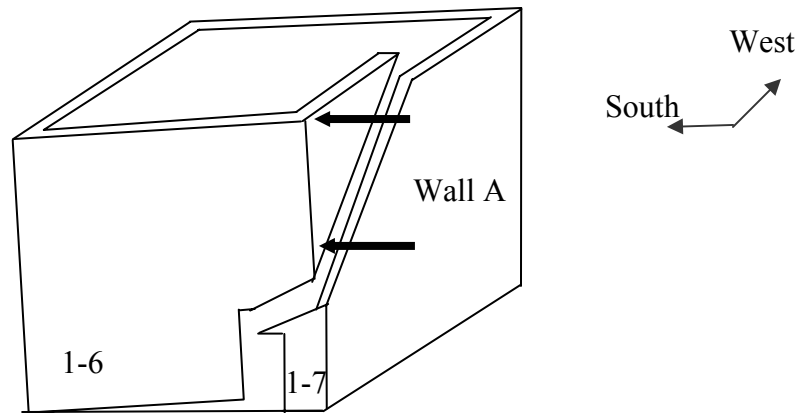


Figure 8.34. Wall 1 was separated from Wall A when it was pushed to the left (southward)

Along with the crack propagation described above, the base shear–lateral roof displacement curves for Wall 1 exhibited significant nonlinear behavior, as shown in Figure 8.35. Wall 1 reached its maximum strength of 59.7 kips when the lateral roof displacement was 0.042 in. in the push direction; and its maximum strength of -54.9 kips when the lateral roof displacement was -0.034 in. in the pull direction.

The small energy dissipation areas of the force-displacement curves indicate that rocking dominated the response of Wall 1. However, being different from Wall 2, Wall 1

exhibited quite significant strength degradation with increasing lateral roof displacement. In the push direction, its lateral strength decreased from 59.7 kips corresponding to a roof displacement of 0.042 in. to 48.2 kips corresponding to a roof displacement of 0.157 in. In the pull direction, its lateral strength decreased from -54.9 kips corresponding to a roof displacement of -0.034 in. to -51.8 kips corresponding to a roof displacement of -0.166 in.

These strength degradations can be attributed to the gradually loss of the flange effects. For example, when the building was loaded in the push direction, the crack propagation in Wall A caused a smaller portion of Wall A to work together with Wall 1, which consequently decreased the lateral strength of Wall 1. More detailed explanations of the changing of flange effects are given in Section 8.5. Its influence on the lateral strength of the test structure is discussed in Section 10.5.

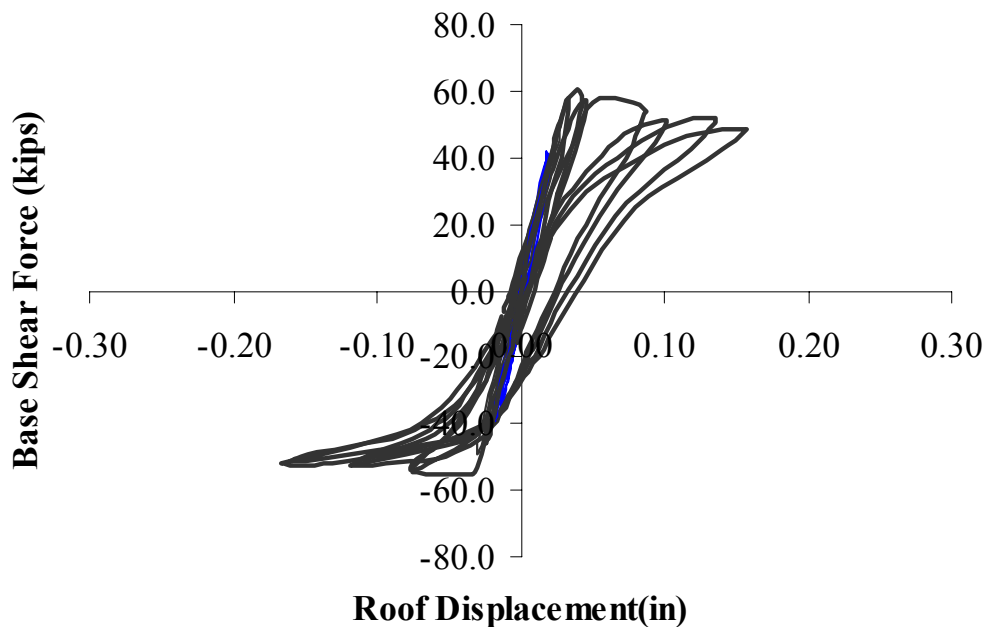
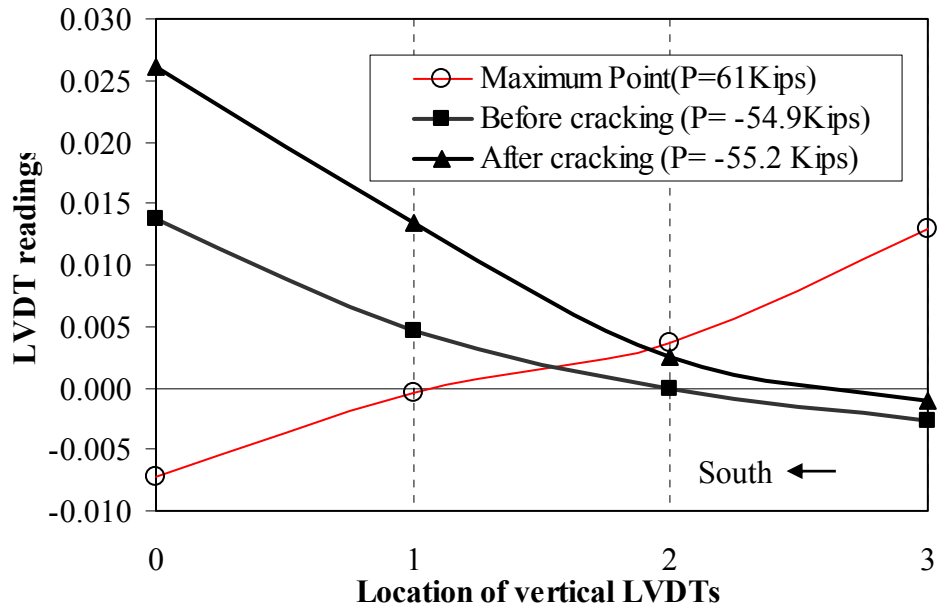


Figure 8.35. Base shear-lateral roof displacement of Wall 1 up to Cycle 8a

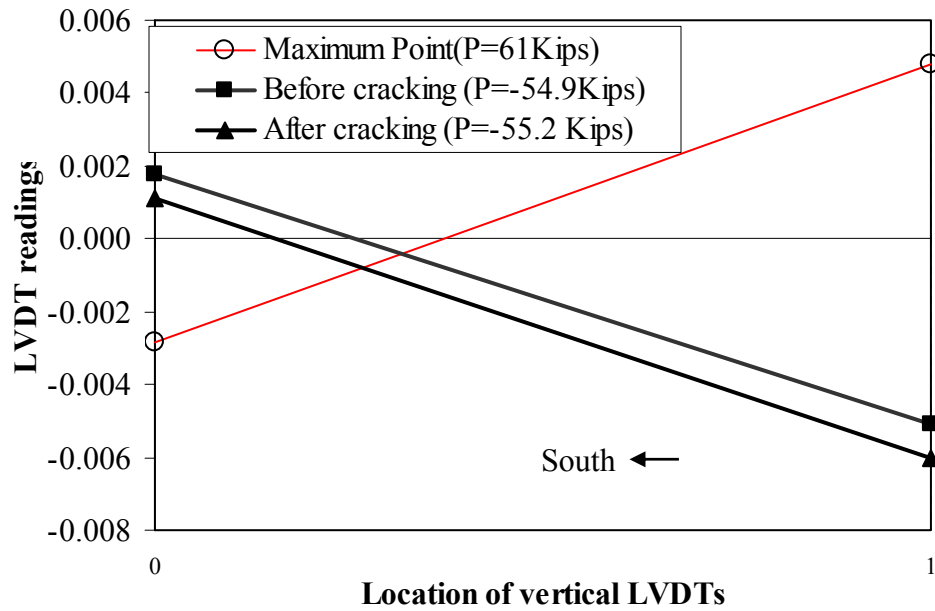
The evolution of the behavior of Wall 1 can also be seen from the displacement readings in Wall 1. To simplify the explanation, the behavior of Wall 1 in the pull direction is discussed first.

During Cycle 6, before the large crack developed at the left bottom of Pier 1-6, the behavior of Wall 1 was similar to that in the previous cycles. However, when the lateral roof displacement of Wall 1 reached -0.034 in. and its base shear force was -54.9 kips, a large crack separated the left side of Wall 1 from the foundation. As a result, significant force redistribution occurred. The vertical deformations of the upper boundaries of Pier 1-6 and Pier 1-7 right before cracking (the base shear of Wall 1 equaled -54.9 kips) and after cracking (the base shear of Wall 1 equaled -55.2 kips) are shown in Figure 8.36. The vertical deformations of the upper boundaries corresponding to the maximum push base shear forces are also shown in the figures as a comparison. The figure shows that when the flexural crack in Pier 1-6 occurred, the upper boundary of Pier 1-6 suddenly displaced up. Meanwhile, the upper boundary of Pier 1-7 moved down. This phenomenon can be explained as follows. Pier 1-6 and Pier 1-7 worked as a single beam section. The flexural crack in Pier 1-6 reduced the effective area and the moment inertia of the beam section. Since the external lateral force was essentially constant, both the compressive forces in Pier 1-7 and the tensile force in Pier 1-6 had to increase to resist the constant global overturning moment. As a consequence, the upper boundary of Pier 1-6 went up and the upper boundary of Pier 1-7 went down.



(a) Pier 1-6

X axis: 0: P1-6VL, 1: P1-6VLC, 2: P1-6VRC, 3: P1-6VR



(b) Pier 1-7

X axis: 0: P1-7VL, 1: P1-7VR

Figure 8.36. Vertical displacements of the upper boundaries of Pier 1-6 and Pier 1-7 before and after cracking

The behavior of Wall 1 in the pull direction changed again when the crack at the right top of the Pier 1-6 occurred. The reading of the base strain gages and the vertical LVDTs are plotted corresponding to the maximum lateral roof pull displacements for Cycles 5b, 6, 7 and 8 in Figures 8.37 and 8.38. The strain gage readings show that with increasing lateral roof pull displacement, a larger compressive stress was introduced at the right toe of Pier 1-6, and the flexural crack at the left base of the pier continued to open.

Meanwhile, the vertical LVDTs readings show that the entire upper boundary of Pier 1-6, including the right side of Pier 1-6, was lifting up. This indicated that the crack at the right top of Pier 1-6 was opening as well. The opening of the cracks at the right top and the left base of Pier 1-6, as well as the increasing large compressive stress at the right toe of Pier 1-6, indicated that Pier 1-6 was rocking about its right toe.

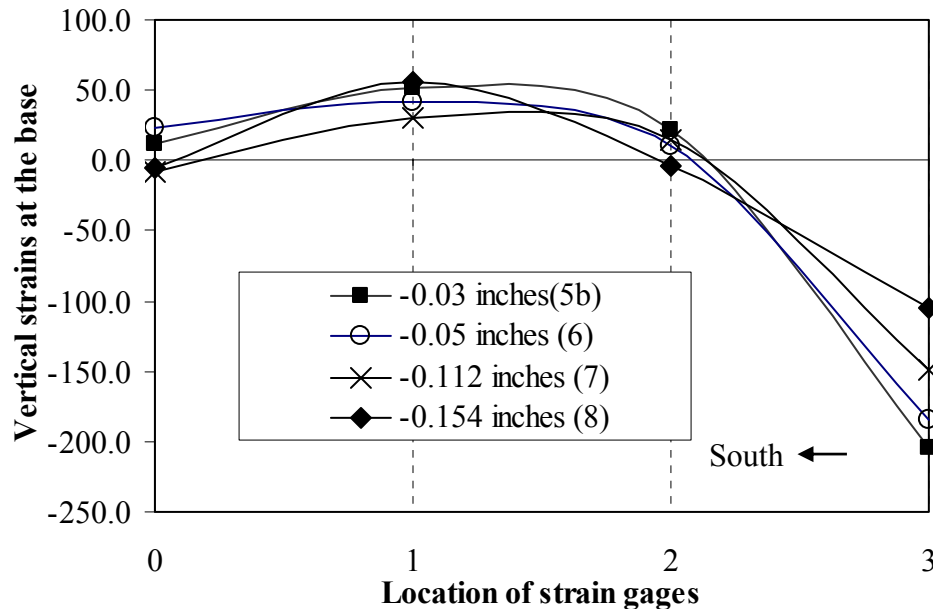


Figure 8.37. Vertical strain at the base of Pier 1-6 in Cycles 5b, 6, 7, and 8 when the building was loaded in the pull direction
X axis: 0: S1-6L, 1: S1-6VLC, 2: S1-6VRC, 3: S1-6R

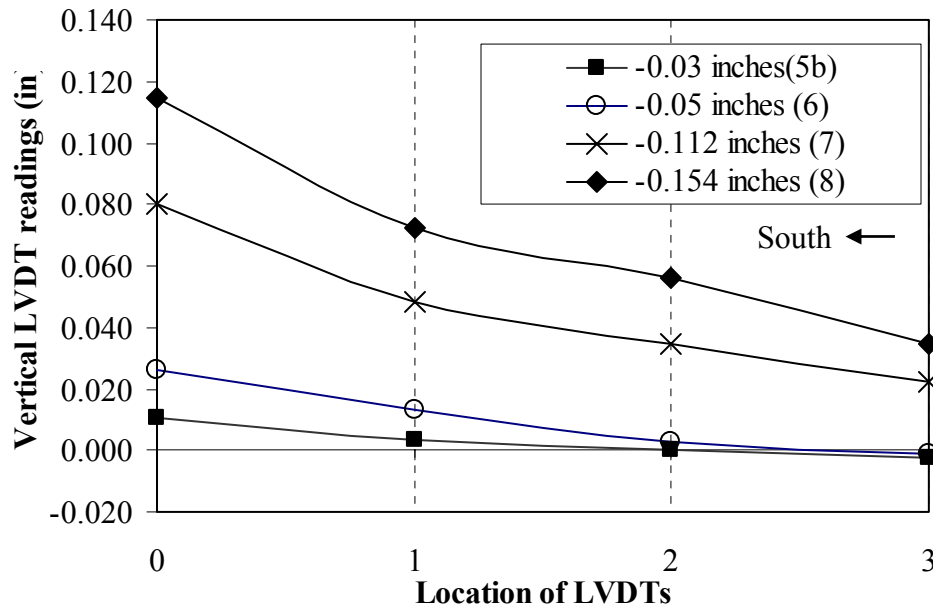


Figure 8.38. Vertical displacements of the upper boundaries of Pier 1-6 in Cycles 5b, 6, 7, and 8 when the building was loaded in the pull direction
X axis: 0: P1-6VL, 1: P1-6VLC, 2: P1-6VRC, 3:P1-6VR

The behavior of Pier 1-7 was different from that of Pier 1-6. The readings from the vertical LVDTs and the strain gages mounted in Pier 1-7 corresponding to the maximum lateral roof pull displacements in Cycles 5b, 6, 7, and 8, are plotted in Figures 8.39 and 8.40. Figure 8.39 shows that with increasing lateral roof displacement in the pull direction, the compressive stress at the right toe of Pier 1-7 increased, and the flexural crack at the left base of Pier 1-7 opened. This indicated that Pier 1-7 was rocking about its right toe.

However, at the same time, Figure 8.40 shows that the left side upper boundary of Pier 1-7 was pushed down, while the right side upper boundary of Pier 1-7 basically did not move vertically. This phenomenon is not a typical rocking behavior, and can be explained as the follows. As shown in Figure 8.41, when Wall 1 was loaded in the pull

direction, a large compressive force was applied on the top of Pier 1-7 due to the global overturning moment. This force was applied to Pier 1-7 at some angle. The horizontal component of this force (a shear force) caused this pier to rock about its right toe. As a result, a flexural crack developed at its left base. On the other hand, the vertical component of this force pushed the entire pier down. Since this inclined compressive force was close to the left side of the pier, the left side of the pier was pushed down more than its right side. In short, when Pier 1-7 was rocking about its right toe, a large amount of diagonal compressive force was also resisted by Pier 1-7. This compressive force may lead to a diagonal crack in this pier in the later tests.

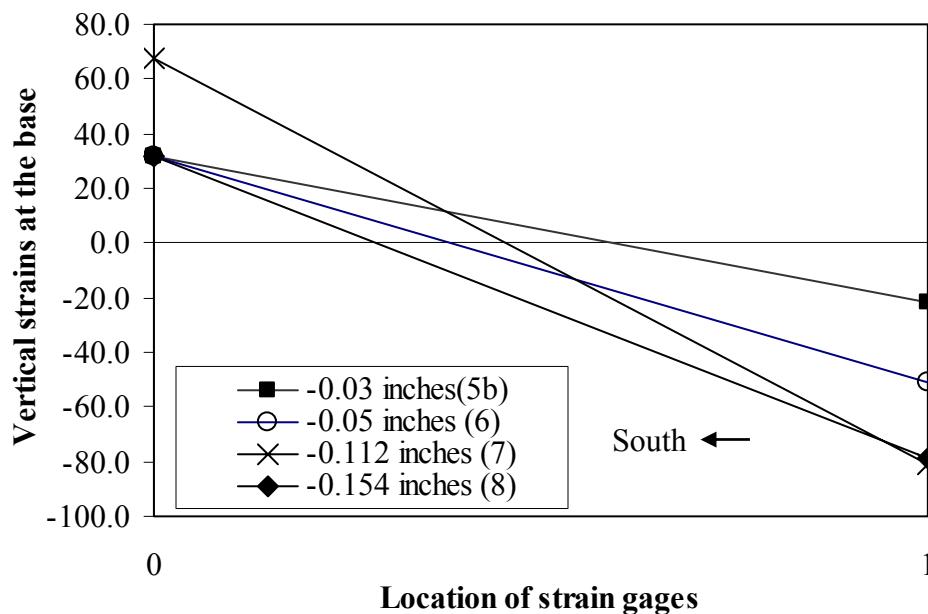


Figure 8.39. Vertical strain at the base of Pier 1-7 in Cycles 5b, 6, 7, and 8 when the building was loaded in the pull direction
X axis: 0:S1-7L, 1:S1-7R

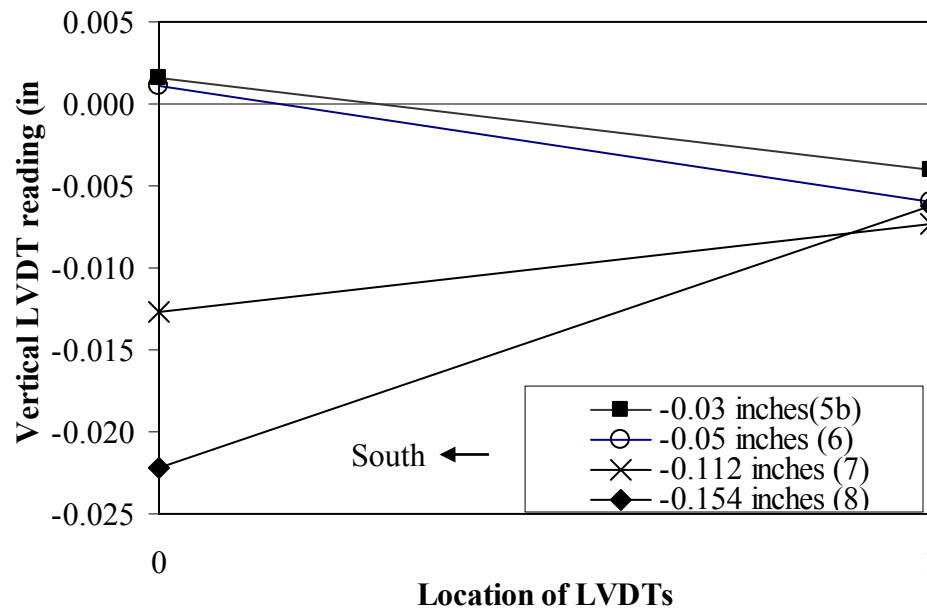


Figure 8.40. Vertical displacements of the upper boundaries of Pier 1-7 in Cycles 5b, 6, 7, and 8 when the building was loaded in the pull direction
X axis: 0:P1-7VL, 1:P1-7VR

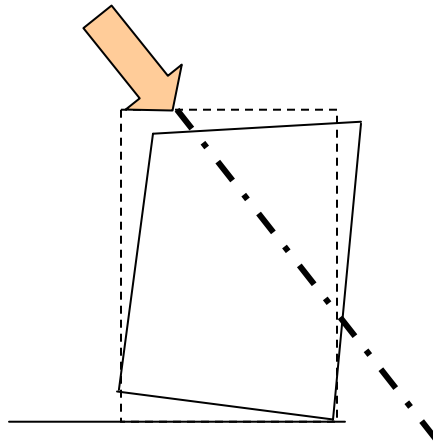


Figure 8.41. Inclined compressive force transferred in Pier 1-7 when the building was loaded in the pull direction

The behavior of Wall 1 was different in the push direction. The readings from the vertical LVDTs and the strain gages mounted in Pier 1-6 corresponding to the maximum lateral roof push displacements in Cycles 5b, 6, 7, and 8, are shown in Figures 8.42 and 8.43, respectively. The figures show that with increasing lateral roof displacement in the push direction, the flexural crack initiated from the right base of Pier 1-6 propagated towards the left toe of the pier. Meanwhile, the right side of Pier 1-6 was lifted up, while the left side of Pier 1-6 exhibited small compressive deformation. These observations indicated that Pier 1-6 was rocking about its left toe.

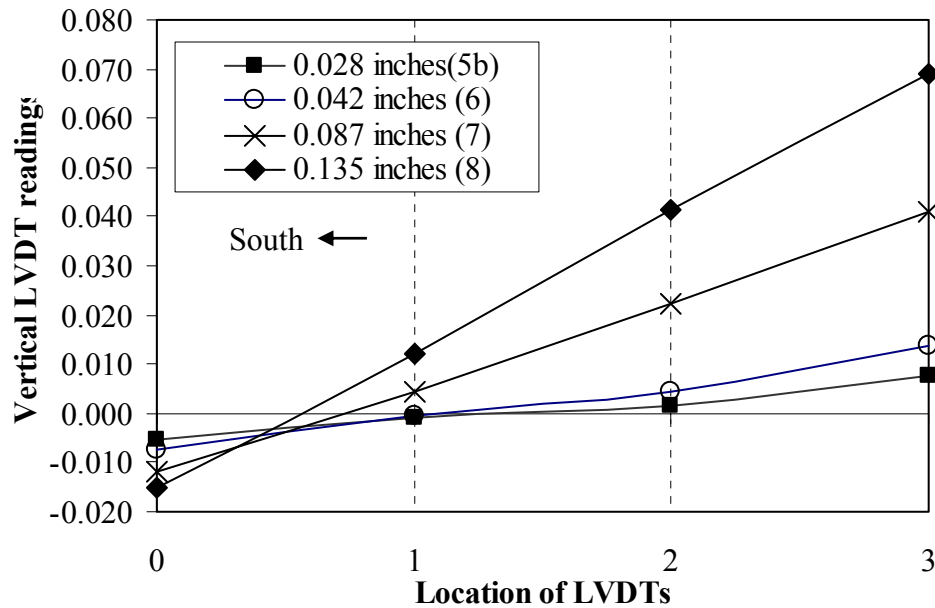


Figure 8.42. Vertical displacements of the upper boundaries of Pier 1-6 in Cycles 5b, 6, 7, and 8 when the building was loaded in the push direction
X axis: 0: P1-6VL, 1: P1-6VLC, 2: P1-6VRC, 3:P1-6VR

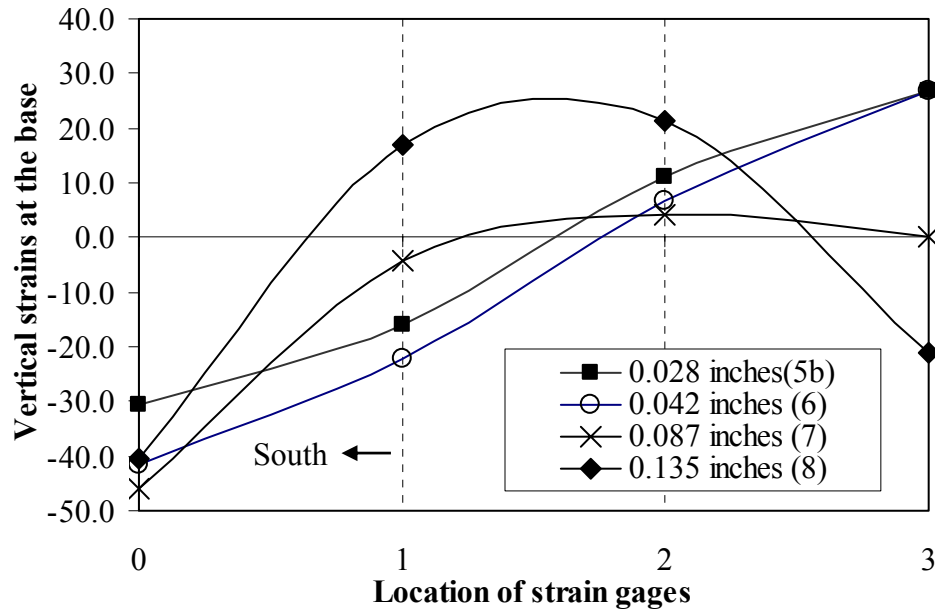


Figure 8.43. Vertical strains at the base of Pier 1-6 in Cycles 5b, 6, 7, and 8 when the building was loaded in the push direction
X axis: 0: S1-6L, 1: S1-6VLC, 2: S1-6VRC, 3:S1-6R

This rocking-dominated response of Pier 1-6 can also be seen from the lateral displacements of Pier 1-6 in Cycle 5b and Cycle 8 as shown in Figs. 8.44 and 8.45, respectively. Comparing these two figures, it is obvious that with the propagation of flexural cracks, the lateral displacement of Pier 1-6 was more and more dominated by its rocking behavior.

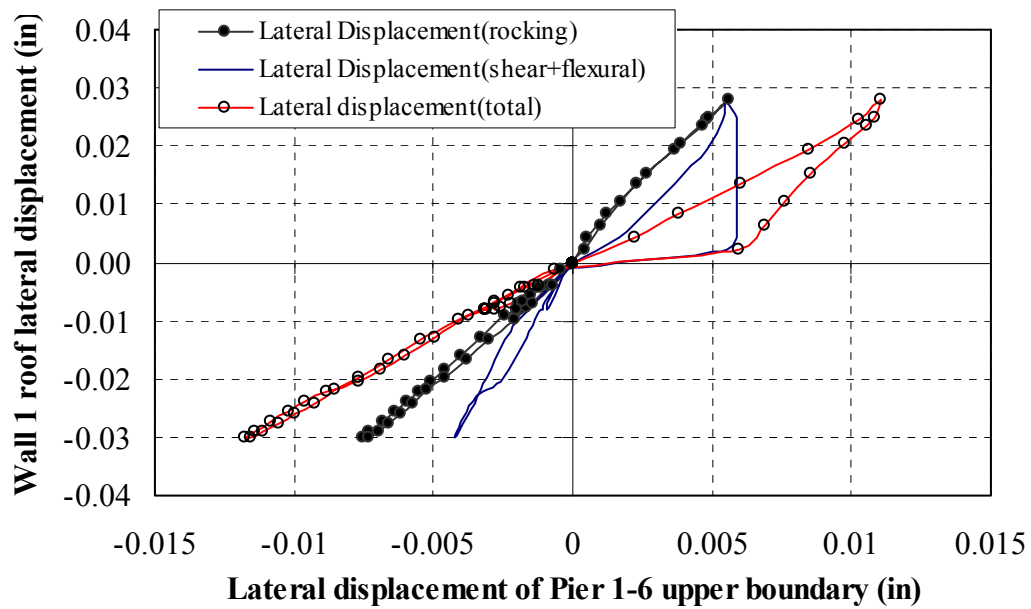


Figure 8.44. Lateral displacements of Pier 1-6 in Cycle 5b

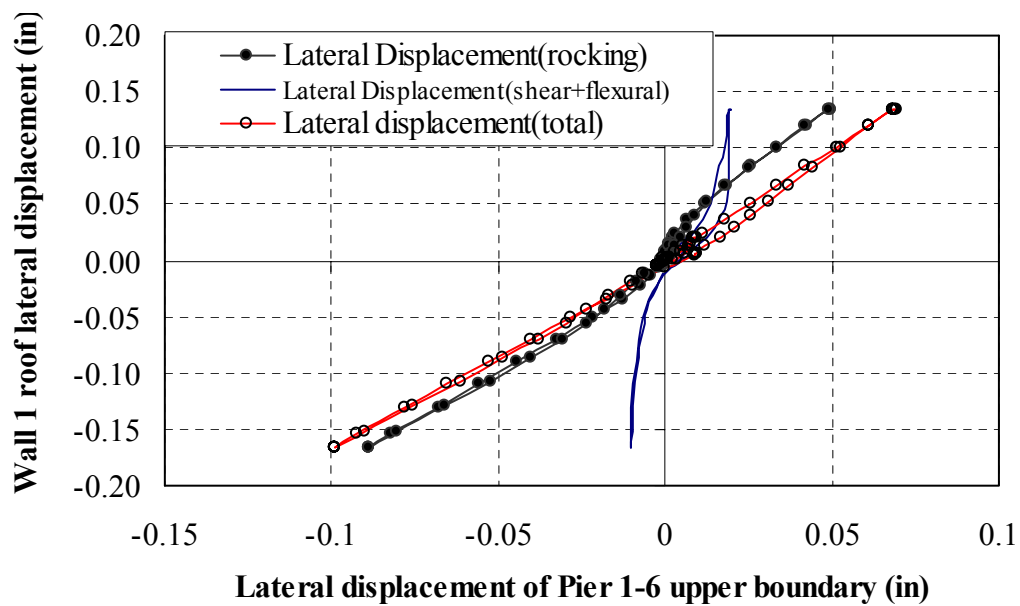


Figure 8.45. Lateral displacements of Pier 1-6 in Cycle 8

The observed behavior of Pier 1-7, (i.e., that this pier was being “left behind” when Wall 1 was loaded in the push direction), can also be seen from the measured lateral displacements of Pier 1-7 in Cycle 5b and Cycle 8. When the maximum Wall 1 second floor lateral displacement in the push direction increased from 0.017 in. in Cycle 5 to 0.081 in. in Cycle 8, the lateral displacement of Pier 1-7 only increased from 0.01 in. in Cycle 5 to 0.02 in. in Cycle 8. The readings of the vertical LVDTs and the strain gages of Pier 1-7 are plotted corresponding to the maximum lateral roof push displacements for Cycles 5b, 6, 7, and 8 in Figures 8.46 and 8.47, respectively. The figures show that although Pier 1-7 tended to be separated from the other portions of Wall 1 when the wall was loaded in the push direction, this isolation was not complete. As a result, some lateral forces were still transferred to Pier 1-7, and forced this pier to rock about its left toe. This rocking movement also caused the left side of Pier 1-7 to displace downwards, the right side of Pier 1-7 to displace upwards, and a large compressive stress to concentrate at the left toe.

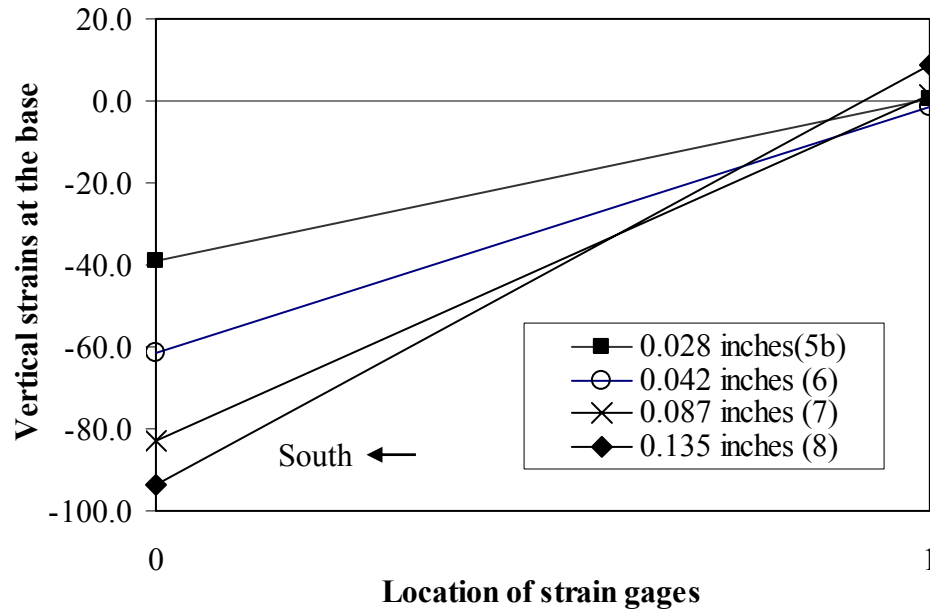


Figure 8.46. Vertical strain at the base of Pier 1-7 in Cycles 5b, 6, 7, and 8 when the building was loaded in the push direction
X axis: 0:S1-7L, 1:S1-7R

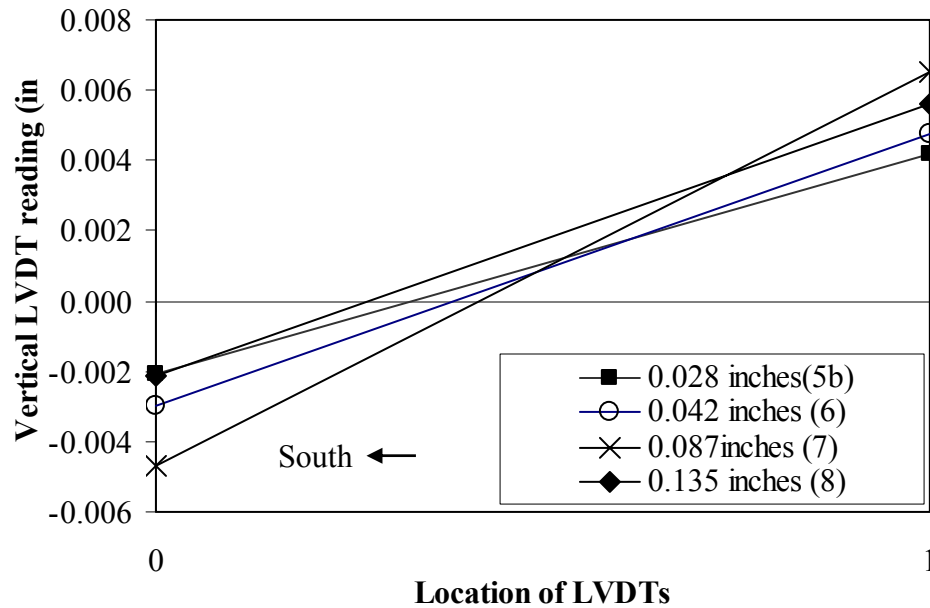


Figure 8.47. Vertical displacements at the base of Pier 1-7 in Cycles 5b, 6, 7, and 8 when the building was loaded in the push direction
X axis: 0: P1-7VL, 1:P1-7VR

8.3.2.3. Fully developed kinematic mechanism – sliding + rocking (Cycles 10 and 10a)

In Cycles 10 and 10a, the behavior of Wall 1 experienced another drastic change. In Cycle 10, when the building was loaded in the push direction (southward), Pier 1-6 rocked about its left toe. Meanwhile, more cracks developed in the area above the door opening and below the existing diagonal cracks in Wall 1 (Figure 8.48). This was probably due to the large tensile stress induced in this area when the main body of Wall 1 above Pier 1-7 was lifted by the external push forces.

When the building was loaded in the pull direction (northward), at first Wall 1 worked the same as that in the previous cycles, i.e., Pier 1-6 and Pier 1-7 rocked about their respective right toes. With increasing lateral displacements, more and more shear forces were introduced in Pier 1-6 and Pier 1-7. Meanwhile, the global overturning moment caused the vertical compressive force in Pier 1-6 to decrease. This decreasing vertical compressive force in Pier 1-6 led to the decreasing of its shear sliding strength. As a result, when the lateral roof displacement of Wall 1 reached -0.21 in., the base shear force in Pier 1-6 overcame its initial bed joint shear strength, and the pier suddenly began to slide. Sliding took place along a newly formed crack that initiated from the existing cracks at the left toe of Pier 1-6, stepped down to the foundation, and propagated all the way to the right toe of Pier 1-6 (Figure 8.48).

The loss of the initial bed joint shear bond strength along with the propagation of the bed joint shear crack caused the lateral strength of Wall 1 drop from -51.6 kips to -45.7 kips. The movement of the wall right before and after the formation of the crack is illustrated in Figure 8.49.

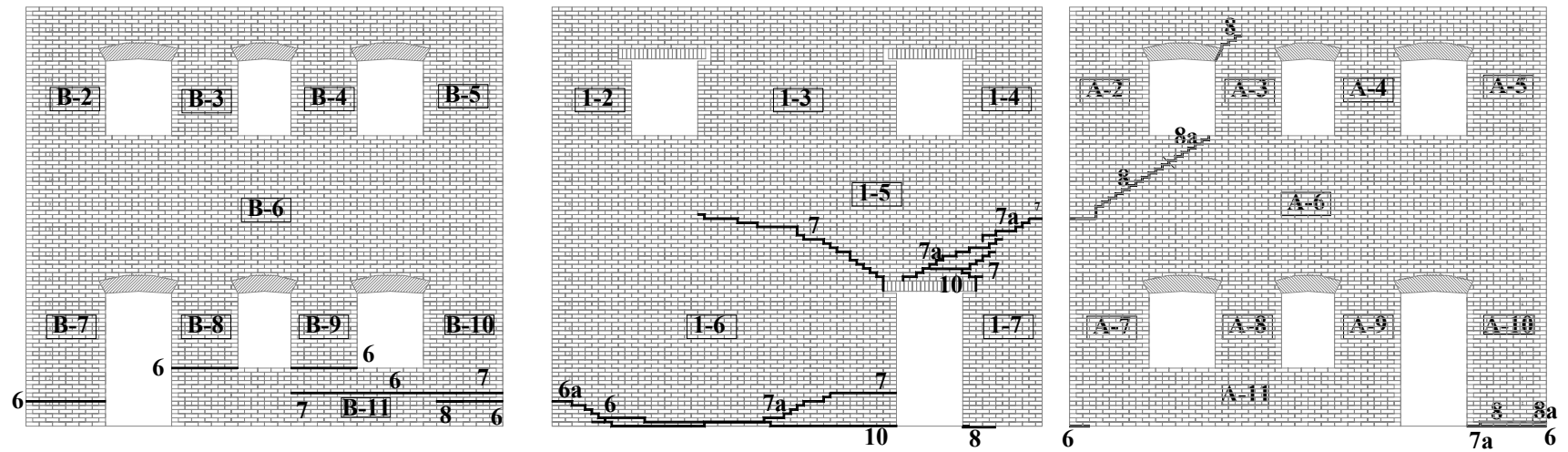


Figure 8.48. Crack pattern of Wall 1 and adjacent Wall B (left) and Wall A (right) at the end of Cycle 10a. The crack number corresponds to the test run number. Number IDs of each pier are given in the rectangles.

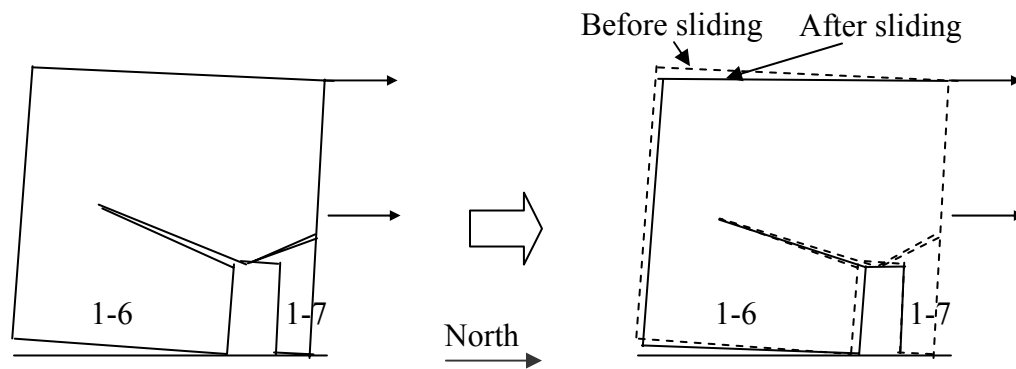


Figure 8.49. Switching failure modes of Pier 1-6 from rocking to sliding when the wall was loaded in the pull direction (northward) in Cycle 10

The change of behavior in wall 1 can also be seen from the base shear-lateral roof displacement curves for Wall 1, shown in Figure 8.50. When Wall 1 was loaded in the push direction in Cycle 10, the wall still behaved as a typical rocking component, since the unloading branch exhibited very small energy dissipation area. However, when Wall 1 was loaded in the pull direction, the drop of the total base shear from -51.6 kips to -45.7 kips corresponded to the beginning of sliding of Pier 1-6.

Afterwards, the unloading branch of Wall 1 exhibited a large energy dissipation area, which is a typical characteristic of sliding behavior. In the next cycle (Cycle 10a), the force-displacement curve of Wall 1 in the push direction also exhibited larger energy dissipation area as compared with the previous cycles. This indicated that the behavior of Wall 1 was a mixture of rocking and sliding in both the pull and push directions after the sliding crack was formed.

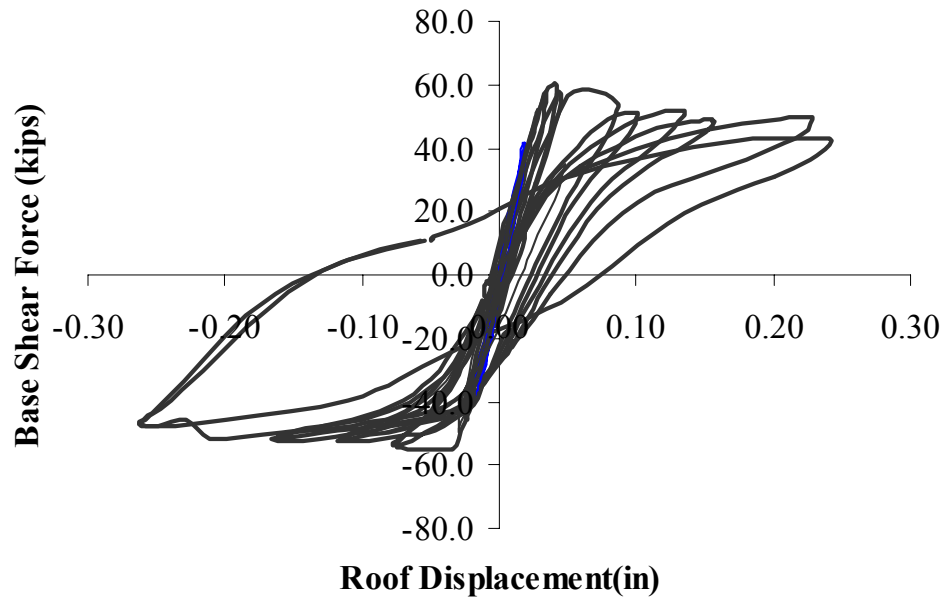


Figure 8.50. Base shear –lateral roof displacement of Wall 1 up to Cycle 10a

The shifting of Pier 1-6 behavior from pure rocking behavior to rocking and sliding mixed behavior was confirmed from the reading of the sliding potentiometer P1-6S, as shown in Figure 8.51. Meanwhile, due to the deformation compatibility requirements, the upper boundary of Pier 1-6 displaced down and rotated counterclockwise when Wall 1 was loaded in the pull direction. This can be seen from the readings of vertical LVDTs mounted in Pier 1-6 right before and after this rapid movement, shown in Figure 8.52. After Pier 1-6 displaced down, more area at the right toe of Pier 1-6 was in contact. Therefore, the compressive strain measured at the right toe of Pier 1-6 decreased from $-163 \mu\text{strain}$ to $-58 \mu\text{strain}$, as shown in Figure 8.53. The shifting of the kinematic mechanism of Wall 1 from rocking to sliding occurred during a very short period, and a loud sound was heard.

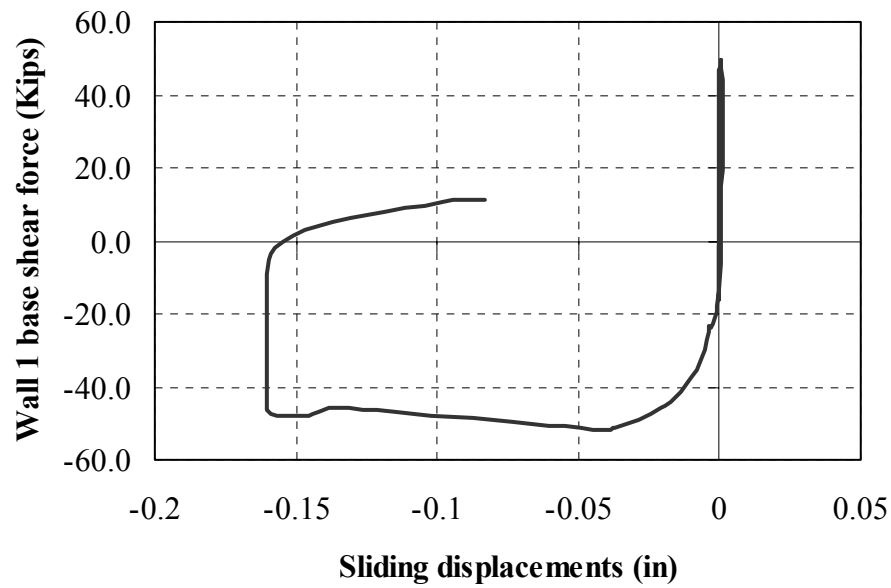


Figure 8.51. Sliding of Pier 1-6 captured by Potentiometer P1-6S when Wall 1 was loaded in the pull direction in Cycle 10

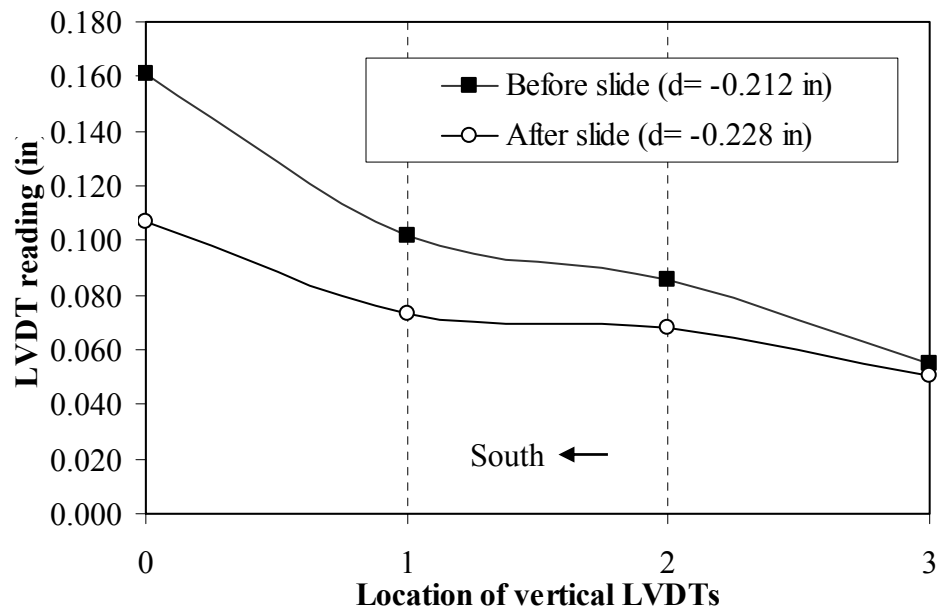


Figure 8.52. Vertical displacements of the upper boundaries of Pier 1-6 before and after sliding

X axis: 0: P1-6VL, 1: P1-6VLC, 2: P1-6VRC, 3:P1-6VR

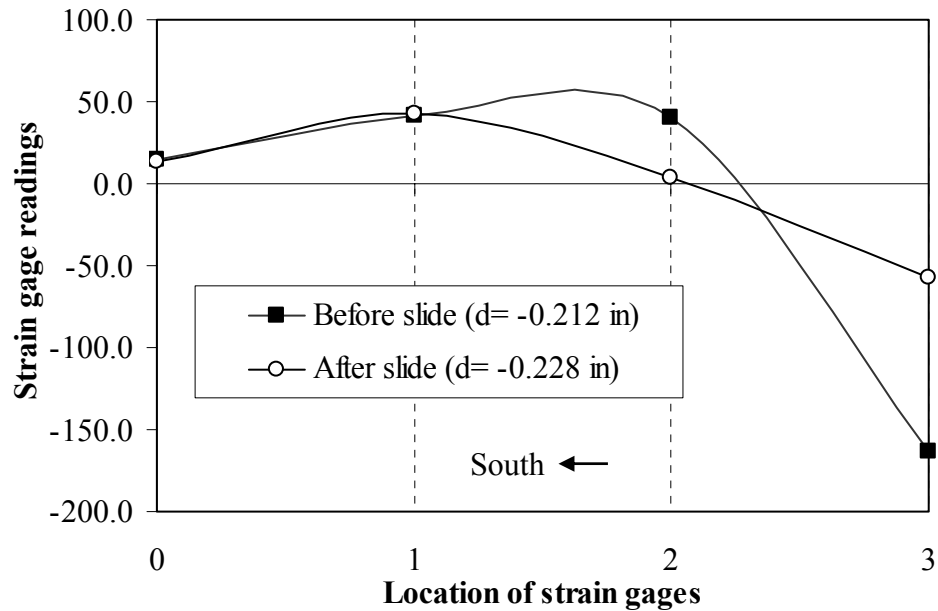


Figure 8.53. Vertical strains at the base of Pier 1-6 before and after sliding
X axis: 0: S1-6L, 1: S1-6VLC, 2: S1-6VRC, 3:S1-6R

With the settling down and sliding of Pier 1-6, the upper boundary of Pier 1-7 also displaced downwards and rotated counterclockwise (Figure. 8.54). As a result, more area at the right toe of Pier 1-7 was in contact, and the compressive strain measured at the right toe of Pier 1-7 decreased from -55 μ strain to -23 μ strain, as shown in Figure 8.55. Note that the reading of the compressive vertical deformation by the right diagonal LVDT P1-7XR increased from -0.00807 in. to -0.01486 in., and the reading of the tensile deformation by the left diagonal LVDT P1-7XL increased from 0.04954 in. to 0.0703 in. The rapidly increased shear deformation of Pier 1-7 indicated that more shear force was redistributed from Pier 1-6 to Pier 1-7.

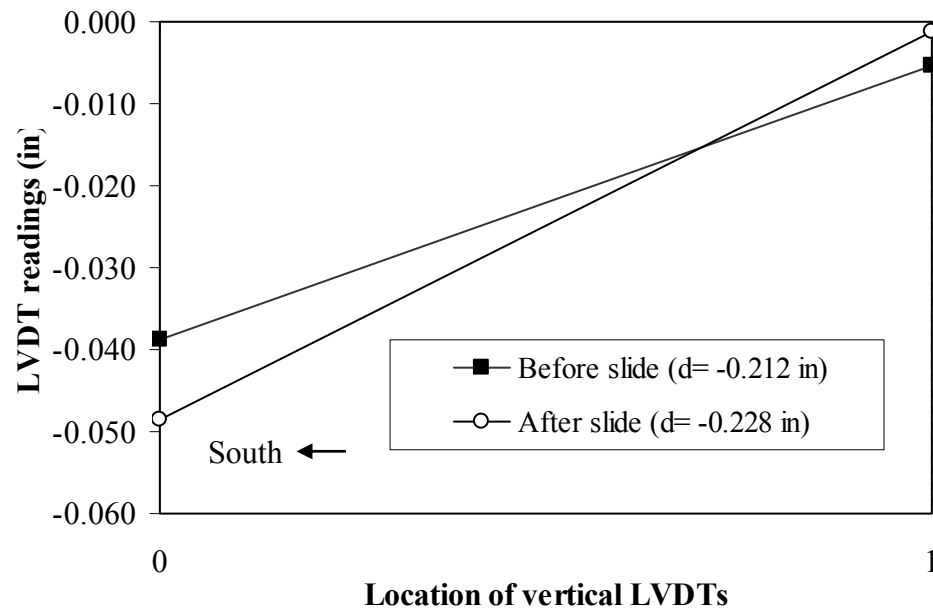


Figure 8.54. Vertical displacements of the upper boundaries of Pier 1-7 before and after sliding of Pier 1-6

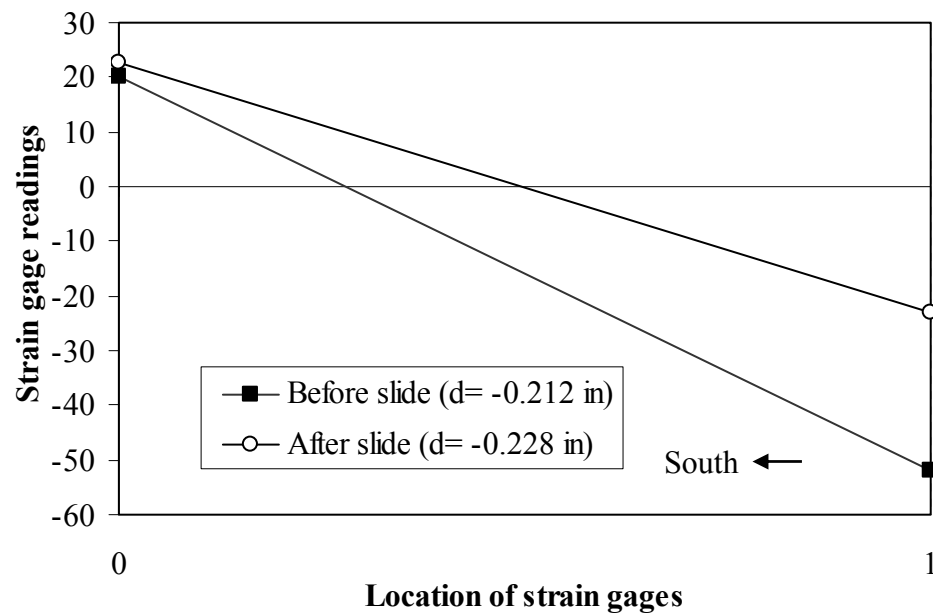


Figure 8.55. Vertical strains at the base of Pier 1-7 before and after sliding of Pier 1-6

After Pier 1-6 settled down, the lateral roof displacement of Wall 1 continued to increase from -0.228 in. to -0.260 in. During this period, Pier 1-6 kept on sliding to the right (Figure 8.51). At the same time, the upper boundary of Pier 1-6 lifted up and rotated clockwise. This revealed that Pier 1-6 was rocking as well as sliding. The behavior of Pier 1-7 was still governed by rocking and diagonal compression.

After the drastic shift in behavior in Cycle 10, the behavior of Wall 1 stabilized in Cycle 10a. When the building was loaded in the push direction, Pier 1-6 rocked about its left toe and slid along the bed joint. The sliding behavior was captured by the sliding potentiometer P1-6S, as shown in Figure 8.56. The rocking behavior of Pier 1-6 was captured by the four vertical LVDTs. The three vertical LVDTs at the right side of Pier 1-6 indicated large tensile deformations (maximum reading of P1-6VR was 0.12 in.) while the left one indicated a compressive deformation. The upper boundary of Pier 1-6 went up and rotated counterclockwise, which verified the rocking behavior of Pier 1-6. In contrast, the LVDTs in Pier 1-7 measured very little vertical movement (less than 0.005 in.) and rotation. This indicated that Pier 1-7 was separated from the majority of the wall and was not participating in the overall behavior of Wall 1.

When the building was loaded in the pull direction in Cycle 10a, Pier 1-6 rocked about its right toe, and slid along the bed joint. This mixed behavior was again captured by the vertical LVDTs in Pier 1-6 and the sliding potentiometer P1-6S. The response of Pier 1-7 was similar to that in Cycle 8 and 8a, dominated by rocking as well as diagonal compression.

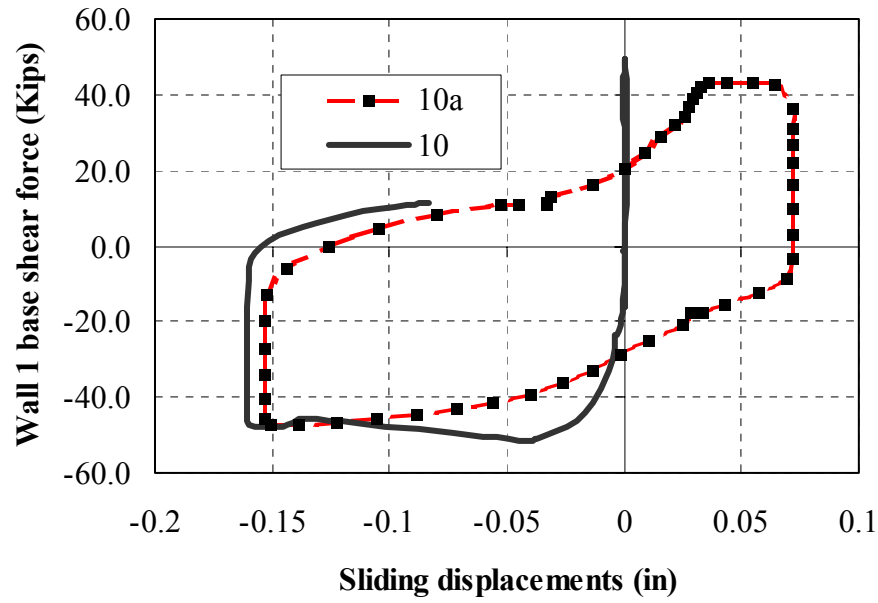


Figure 8.56. Sliding of Pier 1-6 in Cycle 10 and Cycle 10a

8.4. COUPLING BETWEEN WALLS 1 AND 2

In the previous section, the damage and behavior of the test building were explained in terms of Wall 1 and Wall 2, respectively. However, as a box structure, the response of this building may exhibit significant global behavior, due to the coupling behavior between the two parallel in-plane walls, the flange effects, and the global overturning behavior. The coupling effect observed during the test is discussed in this section. Other global effects are discussed in the next sections.

The coupling behavior between the two in-plane walls (Walls 1 and 2) can be described by:

$$\begin{Bmatrix} P1 \\ P2 \end{Bmatrix} = \begin{bmatrix} K11 & K12 \\ K21 & K22 \end{bmatrix} \begin{Bmatrix} U1 \\ U2 \end{Bmatrix} \quad (8.4)$$

where U_1 , U_2 are the lateral roof displacements of Walls 1 and 2, respectively. P_1 and P_2 are the base shear forces for Walls 1 and 2, respectively. K_{11} and K_{22} are the in-plane lateral stiffness of Walls 1 and 2, respectively. K_{12} and K_{21} are the coupling stiffness between the two walls. This stiffness results from the stiffness of the floor and roof diaphragms, and the stiffness of the out-of-plane walls.

Two important constraints exist for the stiffness matrix discussed above. First, the values of K_{11} and K_{22} should be positive, while the values of K_{21} and K_{12} should be negative and equal to each other. Second, in normal cases the absolute value of K_{12} should be less than that of K_{11} and K_{22} .

In order to investigate the coupling between Walls 1 and 2, a test cycle (Cycle 9) was employed. In this cycle, Wall 2 was held at the zero displacement position, while Wall 1 was displaced laterally. Therefore, the displacement values and the base shear values needed for Eq. (8.4) could be measured in the test. The results are listed in Table 8.9.

Table 8.9. Displacements and base shears of the test building in Cycle 9

Walls	Begin		End		Increments	
	Force (kips)	Roof Disp. (ins)	Force (kips)	Roof Disp. (ins)	Force (kips)	Roof Disp. (ins)
Wall 1	0	0	33.06	0.04408	33.06	0.04408
Wall 2	0	0	-0.825	-0.0041	-0.825	-0.0041

The stiffness matrix in Eq. (8.4) can then be estimated based on the displacement and force values provided in Table 8.8. Substituting these values into Eq. (8.4) gives:

$$0.04408 \cdot K_{11} - 0.0041 \cdot K_{12} = 33.06 \quad (8.5)$$

$$0.04408 \cdot K_{12} - 0.0041 \cdot K_{22} = -0.825 \quad (8.6)$$

In Eq. (8.6), since the value of K_{12} is negative, ignoring the second item ($0.0041K_{22}$) on the left side of the equation should give an upper bound estimate of K_{12} , which is:

$$K_{12} = -0.825 / 0.04408 = -18.7 \text{ kips/in} \quad (8.7)$$

Substituting the value of K_{12} into Eq. (8.5), a lower bound estimate of the stiffness of K_{11} can be calculated as 748 kips/in. On the other hand, if we assume K_{12} is equal to zero, from Eq. (8.5) the upper bound estimate for K_{11} is 750 kips/in. Therefore, the value of K_{11} can be estimated to be 749 kips/in.

The value of K_{22} cannot be calculated from Cycle 9, because the displacements applied on Wall 2 were so small that they may result in a large error in any calculation. However, the stiffness of K_{22} can be estimated from the previous cycle 8a. The force and displacement values of Walls 1 and 2 at the initial point and the point with the same Wall 1 base shear forces as those in Cycle 9 are listed in Table 8.10.

Table 8.10. Displacements and base shears of the test building in Cycle 8a

Walls	Begin		End		Increments	
	Force (kips)	Roof Disp. (ins)	Force (kips)	Roof Disp. (ins)	Force (kips)	Roof Disp. (ins)
Wall 1	0	0	33.96	0.0585	33.96	0.0585
Wall 2	0	0	18.69	0.0795	18.69	0.0795

Substituting the force and displacement values in Table 8.10 into Eq.(8.4), and assuming that the value of K_{12} is equal to -18.7 kips/in based on Eq. (8.7), the values of K_{11} and K_{22} can be calculated as 605 kips/in and 249 kips/in, respectively.

It can be concluded that the upper bound value of K_{12} is only 2.5% of K_{11} , and 7.5% of K_{22} . This verifies the assessment from the elastic 3D FE analysis that the coupling behavior between Walls 1 and 2 is small to negligible. Therefore, it is reasonable to discuss the behavior of Walls 1 and 2 separately, as in Section 8.3.

8.5. FLANGE EFFECTS

Flange effects were one of the most notable events observed during the tests. They can be explained in respect to elastic response and nonlinear response ranges separately.

The flange effects during an elastic response can be conceptually investigated by using thin wall structure theory. In the case of a tube structure such as the ST-11 building, the out-of-plane Walls A and B worked as flanges, while the in-plane walls 1 and 2 worked as webs. All the walls worked together as a box section to resist the external shear force and the overturning moment.

The internal shear flow in the box section of the structure is conceptually illustrated in Figure 8.57. Most of the external shear force is resisted by in-plane walls or webs (Walls 1 and 2), while the flanges provided by Wall A and Wall B do not contribute much to the shear resistance of the building.

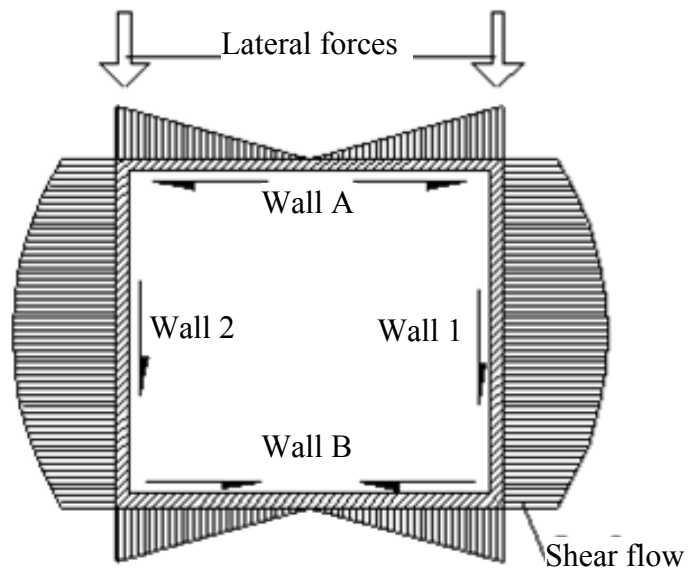


Figure 8.57. Shear flow in the tested structure

On the other hand, the vertical stress distribution in a solid box or tube structure due to the external overturning moment is shown in Figure 8.58. Both the in-plane and the out-of-plane walls participate in resisting the external overturning moment. In the case of a perforated tube structure, the shear force in the tube causes local flexural moment in each pier, which leads to a teeth-like vertical stress distribution in Walls 1 and 2. Meanwhile, the shear lag in the flanges prevents the flanges (Walls A and B) from fully functioning. Therefore, the vertical stress distribution at the base of ST-11 building before cracking would be similar to what is shown in Figure 8.59.

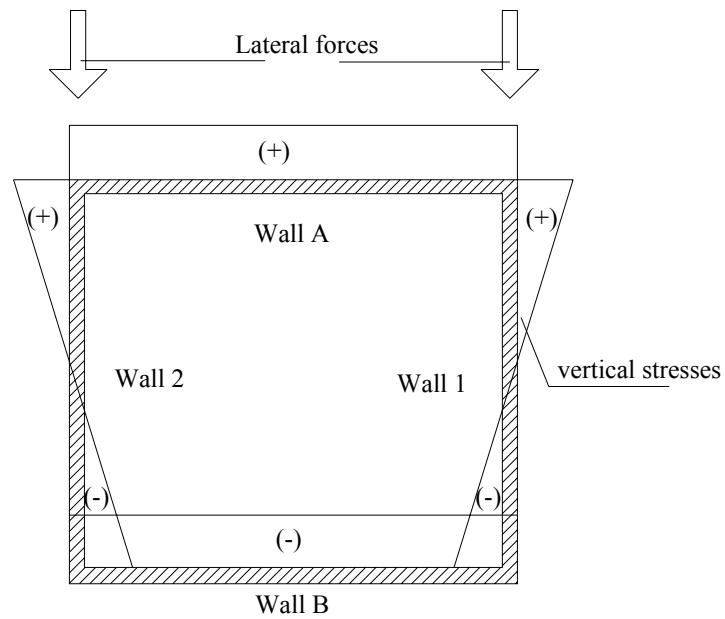


Figure 8.58. Vertical stress distribution in a solid tube structure

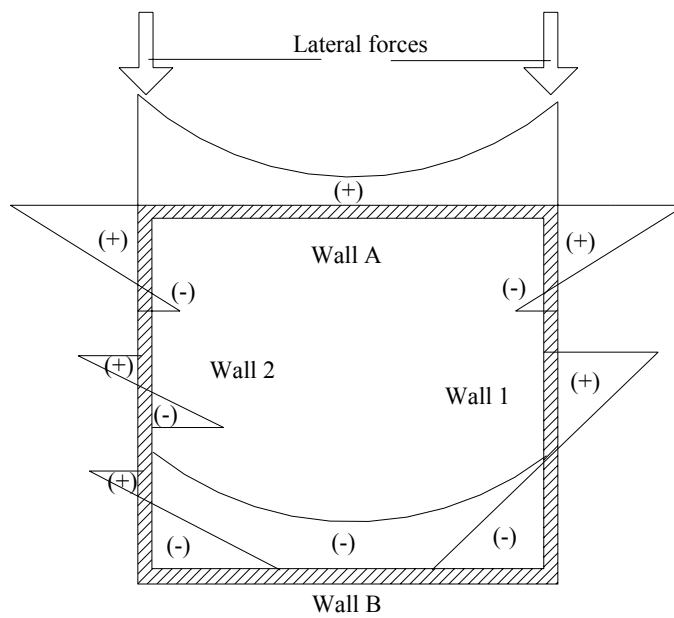
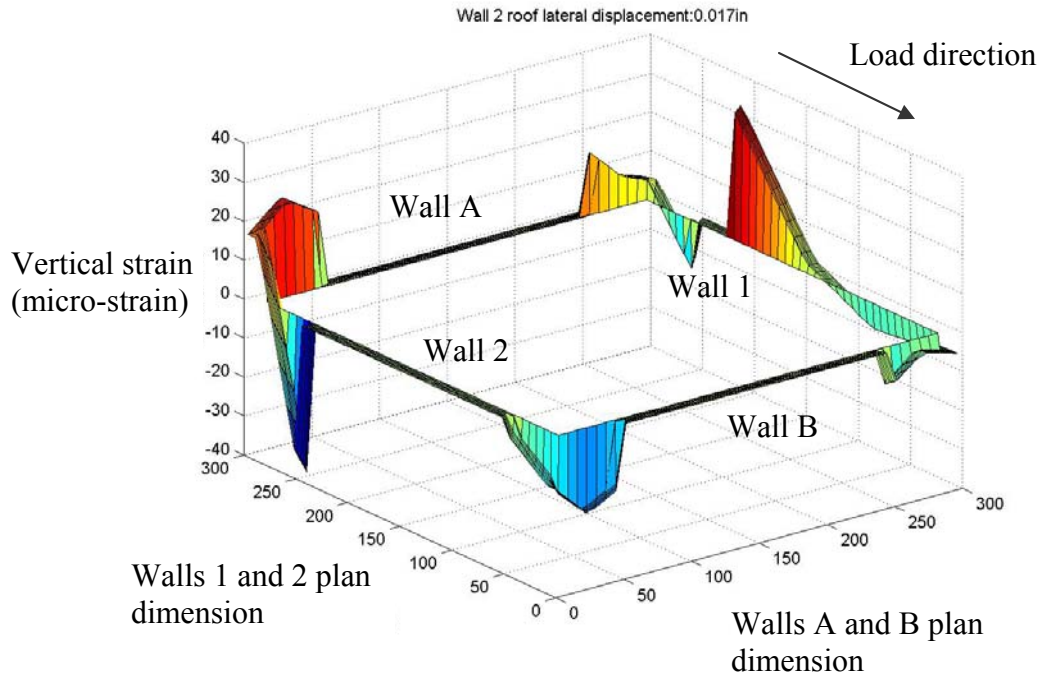


Figure 8.59. Vertical stress distribution in a perforated tube structure

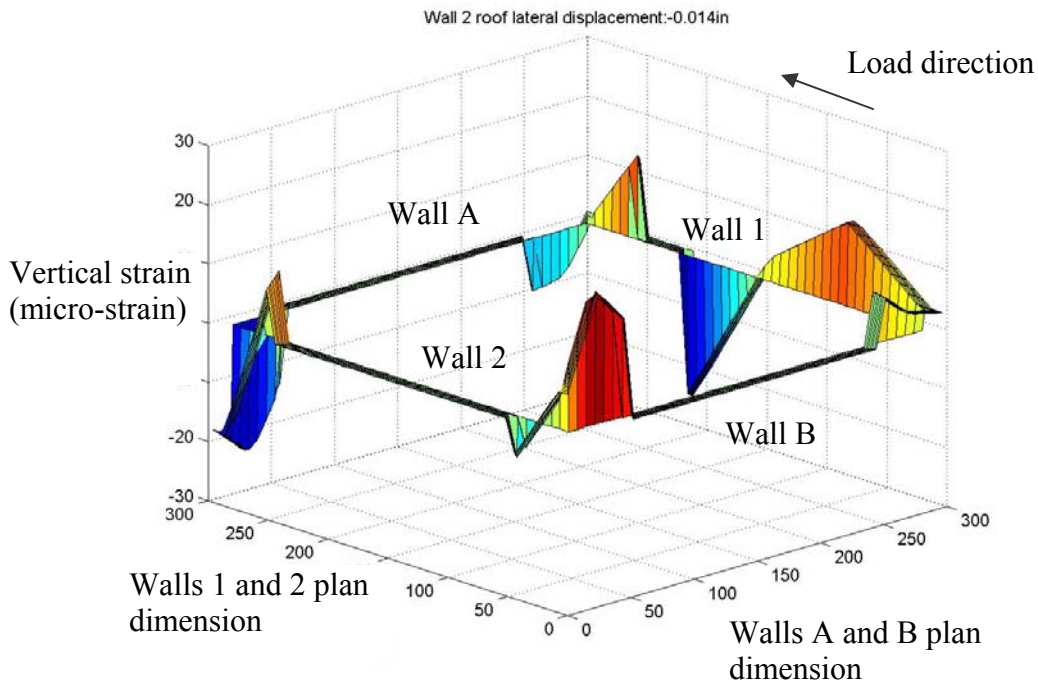
The vertical strain distribution at the base of the test building, obtained from the 18 strain gages mounted at the base of the first floor piers, is plotted vs. the maximum roof displacements in Figure 8.60 for Cycle 2g, in which no visible cracks were observed in the walls. The measured stress distribution shown in Figure 8.60 was similar to that shown in Figure 8.59. In addition, Figure 8.60 shows that a large vertical tensile stress was introduced in Wall A when the building was loaded in the push direction and in Wall B when the building was loaded in the pull direction. This indicated that a large portion of Wall A and Wall B participated in resisting the flexural moment induced by the global overturning movement or the pier rocking.

After substantial cracks developed in the walls, the flange effects were dependent on the crack patterns. The vertical strain distribution at the base of the test building is plotted vs. the maximum roof displacements in Figure 8.61 for Cycle 10. In this cycle, many flexural cracks had developed in the walls. Therefore, the strain gages could not pick up much tensile stress. However, significant opening of the flexural cracks observed in the test revealed the large flange effects due to the presence of Walls A and B. For example, in Cycles 6 to 8a, when the building was loaded in the pull direction, the entire Wall B was observed being lifted above the existing horizontal cracks in the first floor piers. This indicated that the entire Wall B was working as the flange for in plane Walls 1 and 2. Another example is in Cycles 8 to 10a, when the building was loaded in the push direction, the triangular portion of masonry wall at the second floor of Wall A adjacent to Wall 1 was lifted with the displacement of Wall 1. Therefore, this portion of masonry wall was working as the tension flange for Wall 1.

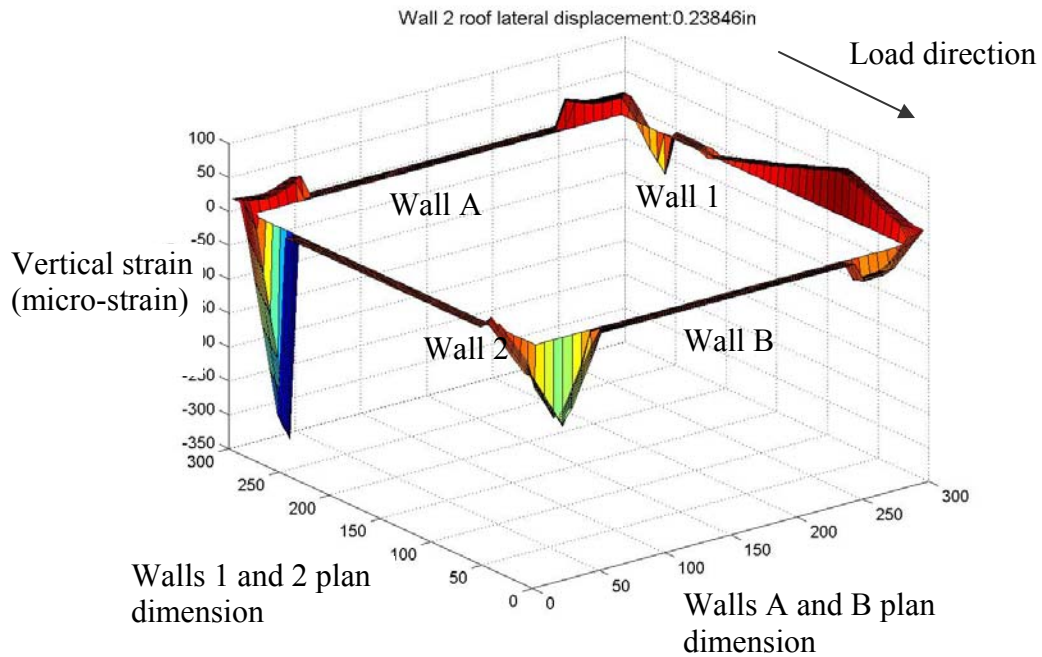
The flange effects introduced by Walls A and B increased the weight that Walls 1 and 2 had to carry when they rocked or slid. Therefore, this effect significantly increased the lateral strength of the test building. This topic is discussed in more detail in Section 9.4. Furthermore, the strain gage readings show that the compressive stress developed at the side of a pier without a flange was much larger than that at the side of a pier with additional flange (for example, the compressive stress developed at the right toe of Pier 2-7 when the building was loaded in the push direction was 5 times that developed at the left toe of Pier 2-7 when the building was loaded in the pull direction in Cycle 10a). This indicated that the flange also evened out the maximum compressive stress in the piers, and thus delayed the brittle toe crushing failure mode of the piers, as discussed previously in Section 5.3.3.



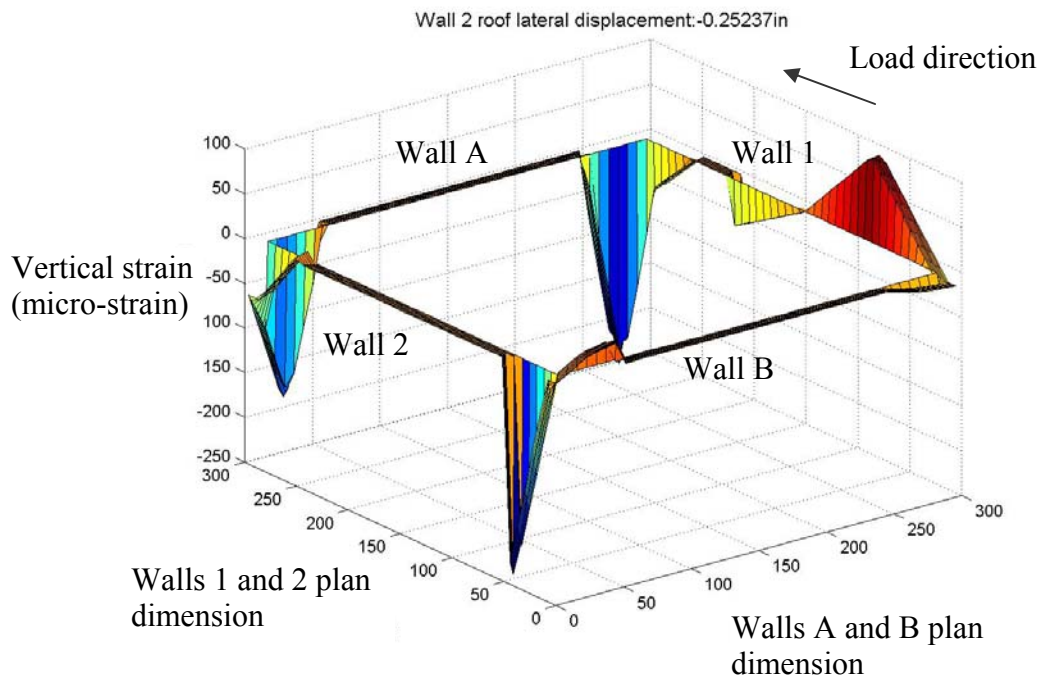
(a) Loaded in the push direction with Wall 2 lateral roof displacement of 0.017 in.



(b) Loaded in the pull direction with Wall 2 lateral roof displacement of -0.014 in.
Figure 8.60. Vertical strain distribution at the base of the tested building (Cycle 2g)



(a) Loaded in the push direction with Wall 2 lateral roof displacement of 0.239 in.



(b) Loaded in the pull direction with Wall 2 lateral roof displacement of -0.252in.
Figure 8.61. Vertical strain distribution at the base of the tested building (Cycle 10)

8.6. GLOBAL OVERTURNING MOVEMENT

The effects of global overturning movement were different for Wall 1 and Wall 2. In the case of Wall 1, in Cycle 7, the global overturning movement began to be detected by the two vertical potentiometers: GV1LP and GV1RP. When the building was loaded in the push direction, the right side of Wall 1 was lifted a large amount (0.15 in.) while the left side of Wall 1 did not displace vertically. When the building was loaded in the pull direction, the left side of Wall 1 was lifted up a large amount (0.06 in.) while the right side of Wall 1 had only small uplift (Figure 8.62). This clearly indicated the global overturning movement (rocking) of Wall 1, which can be further illustrated as follows. As shown in Figure 8.63(a), when Wall 1 was loaded in the push direction, the entire wall was rocking about its left toe. Therefore, its right side went up while its left side did not move much vertically. When Wall 1 was loaded in the pull direction, Pier 1-6 and Pier 1-7 rocked about their individual right toes. However, the aspect ratio of Pier 1-6 was much lower than that of Pier 1-7 (Figure 8.63(b)). As a result, when Pier 1-6 and 1-7 had the same lateral displacement, the top boundary of Pier 1-6 displaced up a large amount as compared to the top boundary of Pier 1-7.

The global overturning movements for Wall 1 were basically the same in Cycles 7a to 8a as for previous cycles. However, when the behavior of Pier 1-6 changed from rocking to sliding when the wall was loaded in the pull direction in Cycle 10, the uplift at the left side of Wall 1 decreased by about 30% (0.04 in). This indicated that the global rocking deformation of Wall 1 decreased when sliding occurred. After that, although the uplift at the left side of wall 1 was still observed, it was smaller than the previous cycles, which indicated that Pier 1-6 was rocking and sliding.

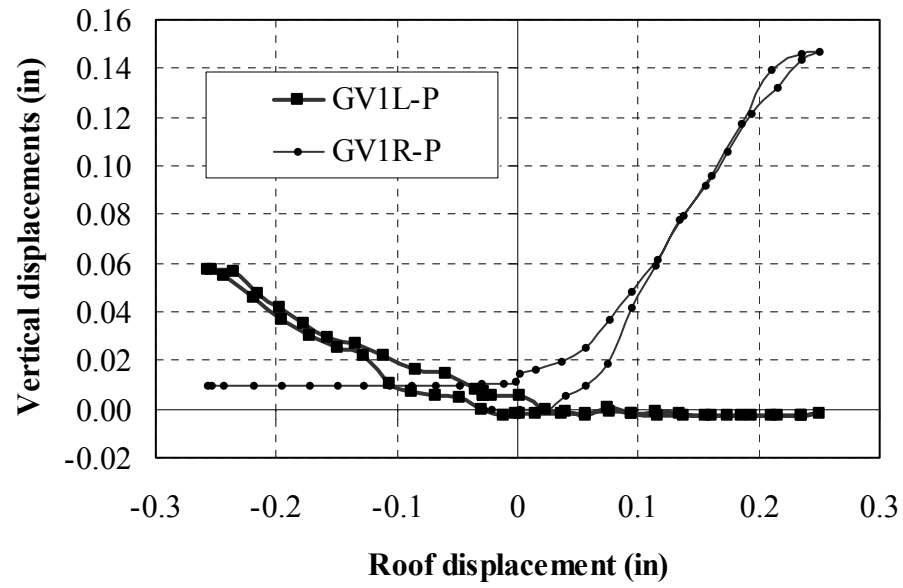


Figure 8.62. Vertical movements of Wall 1

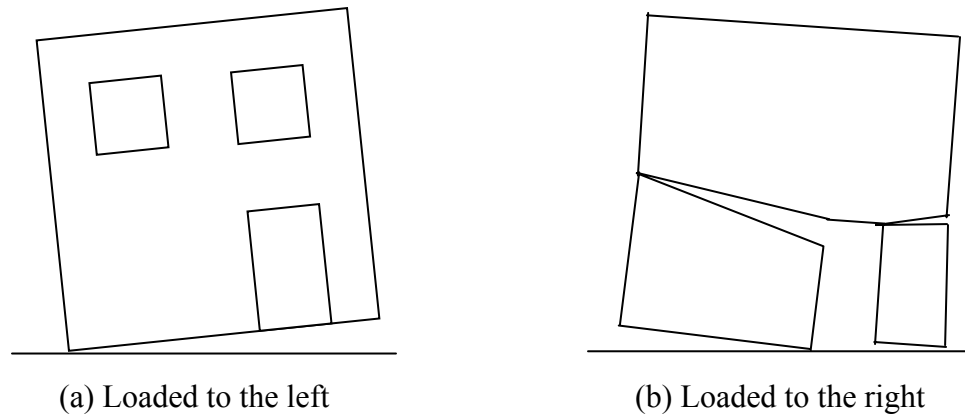


Figure 8.63. Rocking behavior of Wall 1 in Cycle 7

In order to more clearly show the transition, the maximum uplift for Wall 1 are listed in Table 8.11 together with the corresponding roof lateral displacements, where Δ_L is Wall 1 roof lateral displacement and Δ_V is Wall 1 vertical movement. The ratio

between the vertical movement and the roof lateral displacement is also listed in parentheses in the table. This table shows that before sliding occurred, with increasing lateral displacement, the uplift of Wall 1 at the tensile side was increasing. For example, the uplift at the right side of Wall 1 in the push direction increased from 46% of the roof lateral displacement in Cycle 7 to 82% of the roof lateral displacement in Cycle 10. This indicates that the flexural crack at the base of the wall was becoming larger and larger, causing the lateral deformation of the wall to be dominated more and more by its rocking behavior.

In Cycle 10a, Pier 1-6 rocked and slid, and thus the uplift at both sides of the wall decreased. However, the decrease at the left side was much larger than that at the right side, indicating that the sliding of Wall 1 was more significant in the pull than in the push direction.

Table 8.11. Uplift of Wall 1 during the tests

Cycle	Global overturning movement					
	Δ_L , positive, southward, (in.)	Δ_V , left side, south, (in.)	Δ_V , right side, north, (in.)	Δ_L , negative, southward, (in.)	Δ_V , left side, south, (in.)	Δ_V , right side, north, (in.)
7	0.0869	0	0.04 (46%)	-0.118	0.06 (51%)	0
7a	0.102	0	0.045 (44%)	-0.115	0.05 (44%)	0
8	0.135	0	0.07 (52%)	-0.166	0.11 (66%)	0
8a	0.157	0	0.087 (55%)	-0.161	0.106 (66%)	0
10	0.228	0	0.186 (82%)	-0.262*	0.107 (41%)	0
10a	0.242*	0	0.15 (62%)	-0.263*	0.06 (23%)	0

* Sliding Occurred

Compared to Wall 1, the different configuration of Wall 2 led to its different global behavior. Vertical movement was not detected until Cycle 8. In this cycle, Regardless of the loading direction, both sides of the top of Wall 2 were lifted, as shown in Figure 8.64. This indicates that the entire first floor spandrel and the second floor Wall 2 worked together as the upper boundary of the parallel piers in the first floor. They were lifted due to the local rocking of the first-story piers.

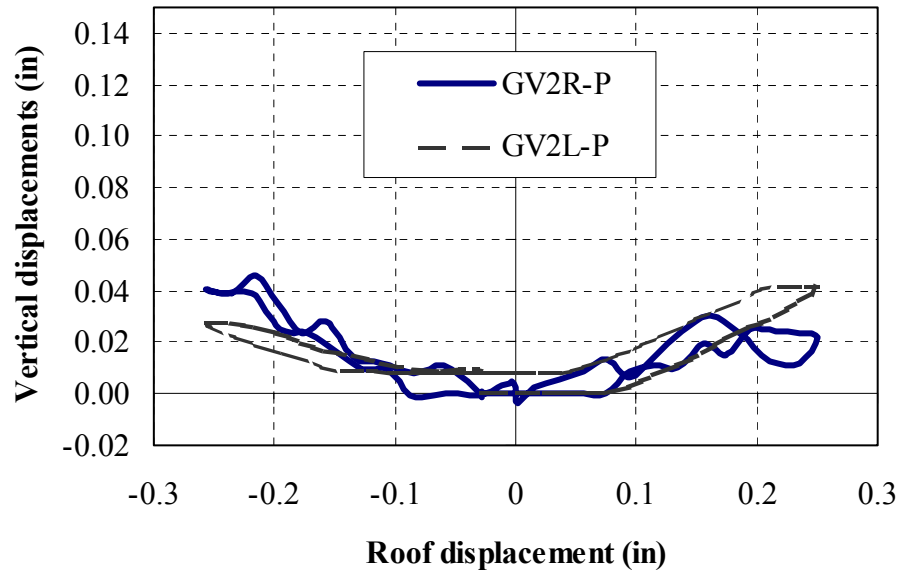


Figure 8.64. Vertical movements of Wall 1 (Cycle 8)

The global overturning movements of Wall 2 were basically the same in the cycles following Cycle 8. The uplift measured for Wall 2 in each cycle are listed in Table 8.12, where Δ_L is Wall 2 roof lateral displacement and Δ_V is Wall 2 vertical movement.

The ratio between the vertical movement and the rood lateral displacement is also listed in parentheses in the table. It can be seen that the uplift of Wall 2 was much smaller when compared with that of Wall 1. The reason is that the uplift of Wall 2 was controlled by the aspect ratios of its first floor piers, which were smaller than the aspect ratio of the entire Wall 1.

Table 8.12. Uplift of Wall 2 during Test cycles 8 to 10a

Cycle	Global overturning movement					
	Δ_L , positive, southward, (in.)	Δ_V , left side, south, (in.)	Δ_V , right side, north, (in.)	Δ_L , negative, southward, (in.)	Δ_V , left side, south, (in.)	Δ_V , right side, north, (in.)
8	0.144	0.015 (10%)	0.02 (14%)	-0.145	0.017 (12%)	0.032 (22%)
8a	0.153	0.007 (5%)	0.02 (13%)	-0.145	0.006 (4%)	0.016 (11%)
10	0.238	0.051 (21%)	0.035 (15%)	-0.247	0.04 (16%)	0.065 (26%)
10a	0.257	0.042 (16%)	0.031 (12%)	-0.252	0.027 (11%)	0.04 (16%)

8.7. EFFECTIVE SECANT ELASTIC MODULUS, NATURAL PERIOD, AND VIBRATION MODES

One way to monitor the damage of the test building is to measure the evolution of its typical structural characteristics, such as the effective secant stiffness, the natural period, and the corresponding vibration modes. The changing of these values with increasing lateral displacements traces the damage of the building.

The secant stiffness of the test structure and the corresponding effective masonry elastic modulus were measured as follows. First, the lateral forces applied on the building

were measured from the actuators in each test cycle. These lateral forces were then applied to a 3D elastic FE model to calculate the lateral displacements of the test building. Comparing the measured actual roof displacements of the building to the calculated elastic values, the effective secant elastic moduli of masonry were obtained. Following this approach, the effective secant elastic moduli of the structure were calculated for each test cycle, and are listed in Table 8.13. This table shows that the secant elastic moduli of the test structure decreased with increasing lateral displacements.

Table 8.13. Elastic modulus of masonry (ksi)

Cycles	Wall 2 (+)	Wall 2 (-)	Wall 1 (+)	Wall 1 (-)
2g	1000	1000	1000	1000
3b	689	845	885	1000
5a	804	800	678	700
6a	460	391	477	298
7a	320	293	186	201
8a	235	205	115	127
10a	134	125	76	77

On the other hand, considering the two walls as a two-degree-of-freedom system with lumped mass at the roof and at the second floor levels, the measured lateral displacements and lateral forces were used to calculate the first natural period and the corresponding vibration mode of these walls. The calculated results are listed in Table 8.14. The table shows that the natural periods of both Wall 1 and Wall 2 increased with increasing lateral roof displacements because of the accumulation of damage in the walls. Note that the natural period of Wall 1 jumped from 0.09 seconds in Cycle 8a to 0.15 seconds in Cycle 10a, which was due to the sudden shifting from rocking to sliding.

The change of the natural period is consistent with the change of the mode shape of the tested masonry walls. The mode shape of Wall 2 corresponding to the first natural period gradually increased from 0.8 to 0.9 with increasing lateral displacements. This was consistent with the fact that most of the damage was focused in the first floor piers and the response of Wall 2 was dominated by its individual components. In contrast, the mode shape of Wall 1 was around 0.6 – 0.7 before sliding occurred. This indicated that the response of Wall 1 was dominated by the global rocking. However, after the sliding developed at the base of Pier 1-6, the vibration mode of Wall 1 dramatically increased to 0.8 - 0.9, which was consistent with the sliding behavior of the wall.

Table 8.14. Natural periods and vibration modes of Wall 1 and Wall 2

		Wall 1		Wall 2	
		Natural Period (seconds)	Vibration mode (second floor/roof)	Natural Period (seconds)	Vibration mode (second floor/roof)
2g	+	0.028	0.63	0.054	0.81
	-	0.032	0.65	0.057	0.83
3b	+	0.032	0.58	0.064	0.83
	-	0.034	0.66	0.063	0.85
5a	+	0.036	0.56	0.061	0.83
	-	0.040	0.70	0.063	0.78
6a	+	0.046	0.57	0.080	0.88
	-	0.058	0.69	0.094	0.87
7a	+	0.069	0.55	0.095	0.9
	-	0.079	0.70	0.109	0.89
8a	+	0.089	0.53	0.115	0.92
	-	0.092	0.71	0.128	0.92
10a	+	0.154	0.80	0.164	0.86
	-	0.147	0.93	0.167	0.88

8.8. DISCUSSIONS

Besides the issues discussed in the above sections, three more issues need to be pointed out:

1) It is well known that a typical damage process for a reinforced masonry structure is characterized by many small cracks in the masonry walls. In contrast, the damage of this test URM structure was dominated by several large cracks. In addition, the locations of these cracks determined the nonlinear behavior of the entire URM structure.

2) When Wall 1 was loaded in the pull direction in Cycle 6, large cracks suddenly developed in the tension flange of Wall 1 (i.e., in Wall B). However, the total base shear for Wall 1 suffered only a small reduction (from –54.9 kips to –54.3 kips). This indicated that the bed joint tensile strength of masonry had negligible effect on the behavior of the test building. On the other hand, it also revealed that the tension flange area defined by the cracks was close to the flange area utilized by the in-plane wall before the crack developed.

3) Chapters 3 to 6 pointed out that four typical failure modes exist for a masonry wall: rocking, sliding, toe-crushing and diagonal tension. Note that the latter two failure modes were not significant in the tested structure. This can be attributed to the small gravity, vertical stresses applied to the structure and the relatively small lateral displacements imposed in the tests.

8.9. CONCLUSIONS

Quasi-static cyclic lateral displacements were applied on Walls 1 and 2 to investigate the behavior of the test building. The main conclusions obtained from this series of tests are as follows:

- For the test structure, the initial elastic modulus of masonry was around 1000 ksi. As a result, the test structure exhibited very stiff response before substantial cracking occurred. However, this stiffness rapidly decreased with increasing deformation and damage accumulation. The maximum lateral strengths of the test structure were 87 kips in the push direction (60 kips on Wall 1 and 27 kips on Wall 2), and 79 kips in the pull direction (55 kips on Wall 1 and 24 kips on Wall 2). The roof drifts corresponding to the maximum lateral strength were about 0.02%.
- The coupling stiffness between Wall 1 and Wall 2 was very small. Test cycle 9 revealed that this coupling stiffness was only 2.5% of the in-plane stiffness of Wall 1, and 7.5% of the in-plane stiffness of Wall 2. Therefore, it is reasonable to discuss the behavior of Wall 1 and Wall 2 separately.
- The test structure exhibited significant global response. One of the global responses was the flange effects introduced by the out-of-plane walls. Both the vertical strain distribution at the base of the building when the building behaved elastically, and the crack patterns of the test building after substantial cracking developed indicated the considerable flange effect provided by Walls A and B. More detailed discussion of the flange effects is given in Chapter 9.

- Another global behavior was the overturning movement of the test building. The overturning movement had a twofold effect on the behavior of the building. First, it introduced additional vertical compressive forces in the piers at the compressive side, and additional vertical tensile forces in the piers at the tensile side. Therefore, the URM piers behaved differently depending on whether it was at the compressive side or the tensile side of the building. This phenomenon was evident in the behavior of Pier 2-7 and Pier 2-9. Second, the overturning movement might lead to global rocking of the entire wall and, thus, affect the behavior of in-plane wall. This phenomenon was significant in Wall 1.
- The different configurations of Walls 1 and Wall 2 led to significantly different behavior between these two walls. Wall 2 had slender piers in the first floor, and damage of this wall was concentrated on the first floor piers. As a result, Wall 2 exhibited a component-dominated rocking mechanism. The ultimate working mechanism for Wall 2 under lateral displacements was that the three first-floor piers 2-7, 2-8, and 2-9 rocked, while the entire second floor walls and the first floor spandrel behaved as a monolithic portion moving laterally and vertically on the top of the first-story piers. Wall 2 also behaved quite symmetrically when the wall was loaded in different directions. Wall 1 was a solid wall with a door opening in the first floor. In contrast to the behavior of Wall 2, the behavior of Wall 1 was dominated by its global overturning movement, and exhibited a quite complex change throughout the load history. When the lateral displacements of Wall 1 were small (roof displacement was less than 0.15 in.), the behavior of this wall was characterized by global rocking. When Wall 1 was loaded in the push

direction, the majority of Wall 1 was lifted above Pier 1-7 and rocked about the left toe of Pier 1-6, while Pier 1-7 was basically left behind. When the wall was loaded in the pull direction, cracks isolated Pier 1-7 from Pier 1-7. As a result, each pier rocked about its right toe. On the other hand, the behavior of Wall 1 changed from rocking to sliding plus rocking when the lateral displacements of Wall 1 reached 0.25 in. When the wall was loaded in the push direction, Pier 1-6 slid and rocked along its bed joint, while Pier 1-7 was left behind. When the wall was loaded in the pull direction, Pier 1-6 slid and rocked along its bed joint, while a large amount of force was transferred to Pier 1-7. As a result, Pier 1-7 rocked about its right toe, and had the potential to develop diagonal cracking with increasing lateral displacement.

There were some other interesting phenomena observed in the test. For example, it was observed that the flexural cracks induced by the rocking of a pier generally did not propagate in the horizontal bed joint. Instead, these cracks propagated perpendicular to the direction of the maximum tensile stress at the corner of opening. This led to different effective aspect ratios of the pier when the pier was loaded in different directions and, consequently, altered the response of the pier. More discussions on the nonlinear properties of the test structure are given in Chapter 9.

CHAPTER 9

IN PLANE WALL TESTS PARALLEL TO WALLS A AND B

9.1. INTRODUCTION

This chapter presents the results of tests in which the ST-11 building was loaded parallel to Walls A and B. As a result of the prior in-plane loading tests of Walls 1 and 2, substantial cracks developed not only in Walls 1 and 2 but also in Walls A and B. Therefore, the tests parallel to Walls A and B should be considered as the tests for an existing URM building that already suffered some damage.

In this chapter, the test setup and the test sequence for Walls A and B is presented in Section 9.2. Then the nonlinear behavior of the test structure, including crack propagation, damage accumulation, and the global kinematic mechanisms, is presented in Section 9.3. Following that, some special issues such as the mixed modes of failure for Walls A and B, the determination of the flange effects, and the determination of the effective pier length in a perforated wall, are discussed in Sections 9.4 to 9.9. The conclusions obtained from the test are given in Section 9.10.

9.2. TEST SETUP

9.2.1. External forces and loading scheme

In-plane lateral forces were applied to Walls A and B at the roof level and the second floor level. The setup of the loading system and the design of the loading scheme

were the same as that used for the previous test series parallel to Walls 1 and 2, and a complete description can be found in Section 8.2.1.

9.2.2. Testing procedure

For most target displacements, two complete loading cycles were conducted for the test structure as was done in the previous tests on Walls 1 and 2. The test series on Walls A and B consisted of 13 test cycles. The measured maximum lateral displacement values at the roof and the second floor levels of Walls A and B for each of the test series are listed in Table 9.1. The maximum lateral roof displacement applied on the test structure was about 0.5 in.

Table 9.1. Displacement values of each test cycle

Cycle	Maximum displacements in the push direction (positive, westward, in.)				Maximum displacements in the pull direction (negative, eastward, in.)			
	Wall B roof	Wall B second floor	Wall A roof	Wall A second floor	Wall B roof	Wall B second floor	Wall A roof	Wall A second floor
20c	0.008	0.005	0.0083	0.005	-0.010	-0.006	-0.007	-0.004
21a	0.029	0.023	0.03	0.02	-0.030	-0.022	-0.03	-0.024
21b	0.029	0.023	0.03	0.022	-0.031	-0.023	-0.031	-0.023
22a	0.069	0.057	0.076	0.058	-0.072	-0.057	-0.071	-0.056
22b	0.069	0.058	0.077	0.060	-0.071	-0.056	-0.070	-0.054
23a	0.096	0.081	0.093	0.073	-0.096	-0.077	-0.105	-0.077
23b	0.094	0.081	0.096	0.077	-0.101	-0.079	-0.109	-0.079
24a	0.137	0.117	0.138	0.111	-0.153	-0.123	-0.159	-0.116
24b	0.147	0.125	0.145	0.117	-0.148	-0.119	-0.157	-0.115
25a	0.232	0.189	0.221	0.186	-0.273	-0.225	-0.278	-0.206
25b	0.226	0.195	0.190	0.163	-0.286	-0.237	-0.313	-0.237
26a	0.460	0.414	0.400	0.319	-0.521	-0.416	-0.604	-0.438
26b	0.488	0.436	0.423	0.369	-0.517	-0.442	-0.566	-0.422

9.2.3. Instrumentations

Ninety-six channels of instrumentations, including 30 LVDTs, 16 potentiometers, and 44 strain gages, were used to monitor both the global response and the local response of the test structure (Figure 9.1). LVDTs GVAR and GVA2 were used to measure the lateral in-plane displacements of Wall A at the roof level and at the second floor level, respectively. LVDTs GWBR and GWB2 were employed to measure the lateral in-plane displacements of Wall B at the roof level and at the second floor level, respectively. In addition, the global lateral in-plane displacements of Walls A and B were also monitored by potentiometers P-GVAR, P-GVA2, P-GWBR, and P-GWB2. The lateral out-of-plane roof displacements of Walls 1 and 2 were measured by LVDTs GOW1R and GOW2R, respectively. The global overturning movements of Walls A and B were measured by potentiometers P-GVAL, P-GVAR, P-GVBL, and P-GVBR. Possible sliding of the masonry walls were monitored by several dial-gages placed at some particular locations. The forces applied on the building were measured by the load cells embedded in the actuators.

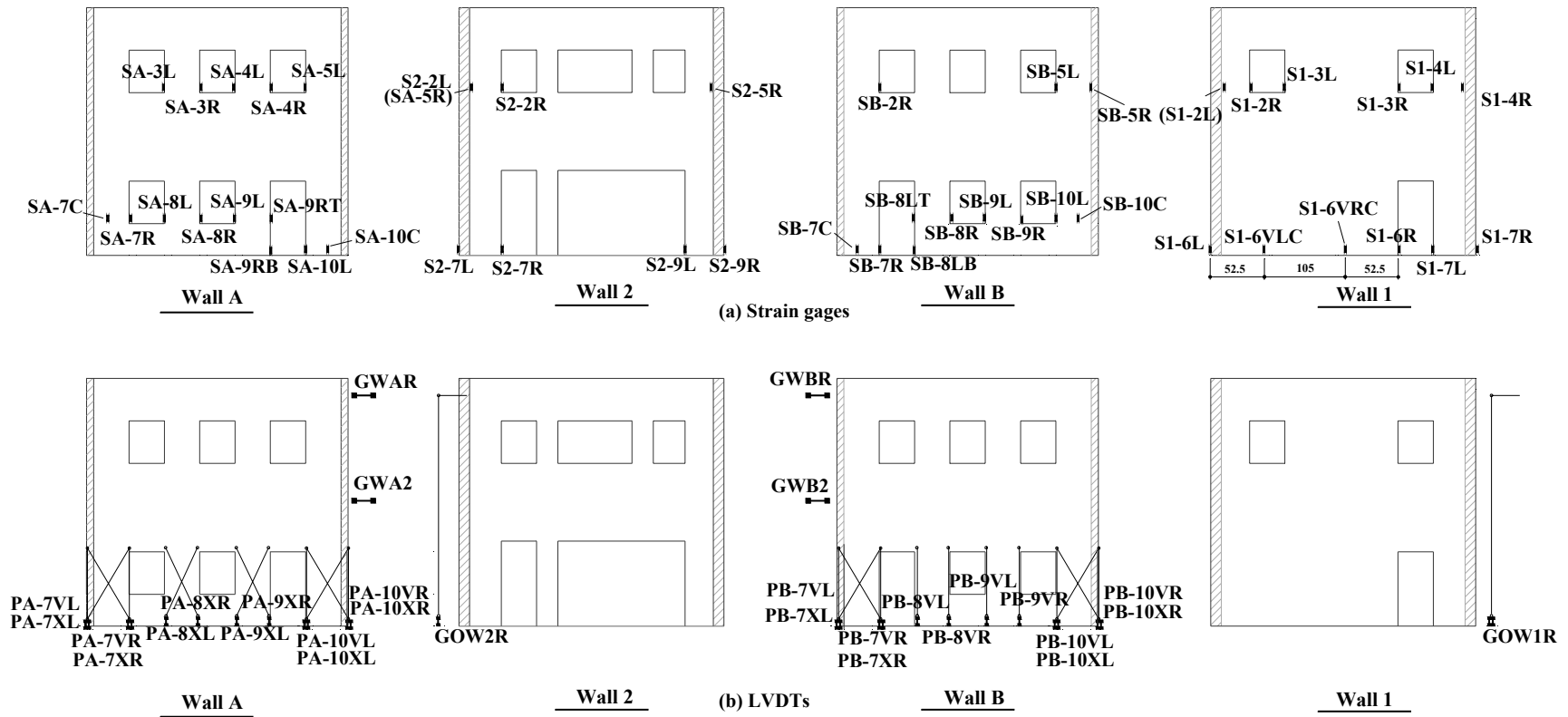
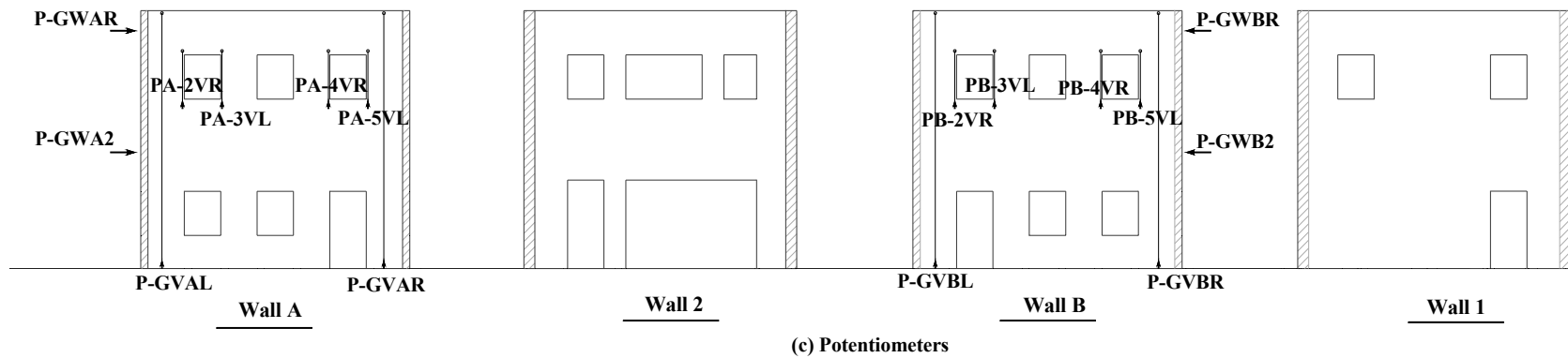
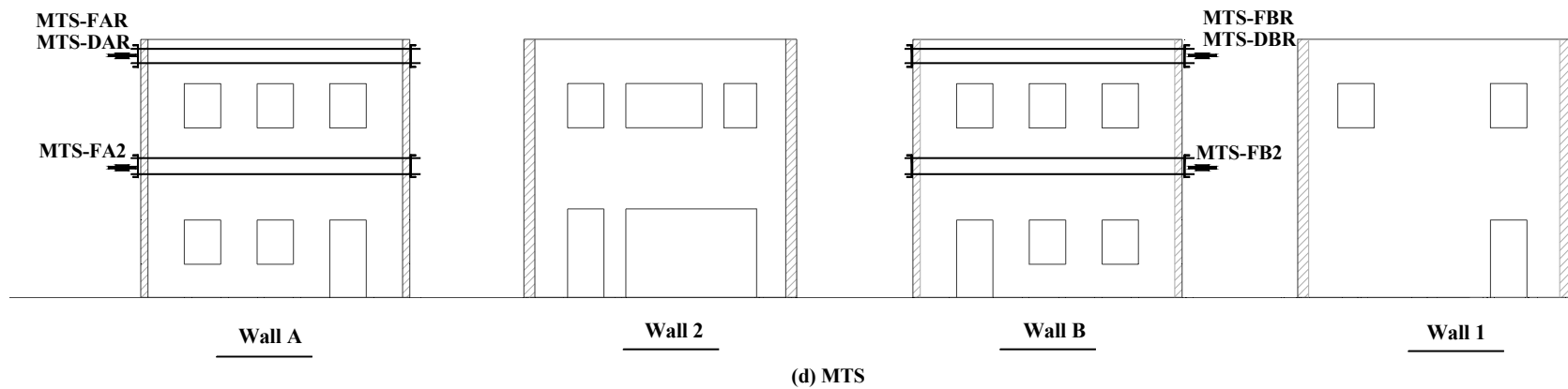


Figure 9.1. Instrumentation of the in-plane wall tests parallel to Walls A and B



(c) Potentiometers



(d) MTS

Figure 9.1. (cont'd)

In a similar manner as for the tests for Walls 1 and 2, the local response of the exterior first story piers in Walls A and B were measured by 2 vertical LVDTs and 2 diagonal LVDTs. However, given the different wall penetrations, two vertical LVDTs were used for the interior first story piers in Wall B, and two diagonal LVDTs were used for the interior first story piers in Wall A. Since the first floor spandrels in Walls A and B were quite deep, it was assumed that damage was unlikely to occur to these spandrels; and, thus, they were not instrumented. The flexural deformation of all the piers in the second floor was measured by potentiometers. In addition to the LVDTs and potentiometers, strain gages were used at the bottom of each pier to measure the vertical strains at the base of the pier.

9.3. CRACK PROPAGATION, DAMAGE ACCUMULATION AND KINEMATIC MECHANISMS

This section gives a summary of the response of the test structure throughout the test sequence. The crack propagation, damage accumulation, and the kinematic mechanisms are described at different damage levels, which include the response before the onset of further damage, the accumulation of damage in the walls, and the fully developed kinematic mechanisms. Similar to the previous tests parallel to Walls 1 and 2, little coupling was observed between the two parallel in-plane Walls A and B. As a result, the response of Walls B and A are discussed separately in Section 9.4.1 and Section 9.4.2.

9.3.1. Wall B

9.3.1.1. Response of Wall B before further damage (Cycles 20c through 21b)

The response of Wall B in Cycles 20c through 21b was essentially elastic. No cracks or other visual damage were observed. The base shear–lateral roof displacement curves for Wall B are shown in Figure 9.2, which exhibit linear elastic behavior.

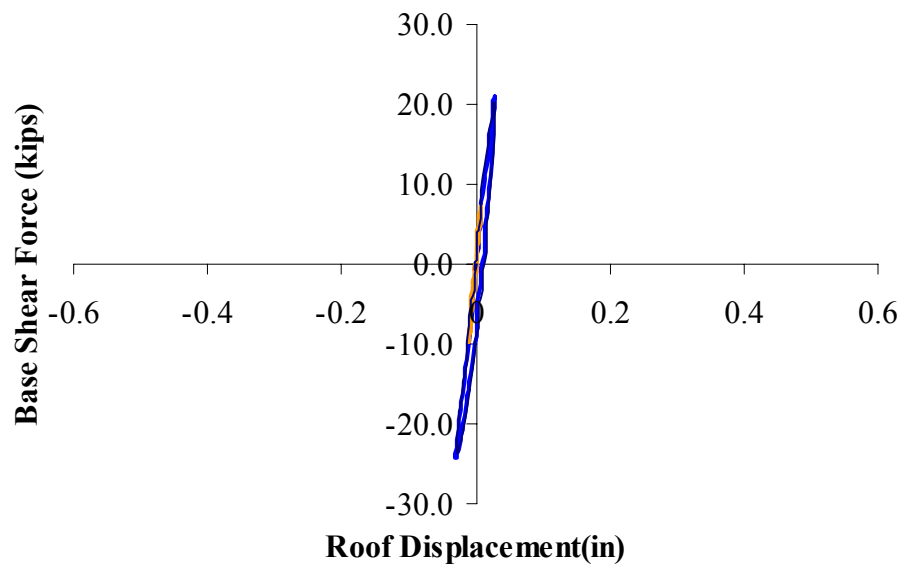


Figure 9.2. Lateral roof displacement-base shear curve for Wall B (Cycles 20c to 21b)

Some cracks already existed in Wall B due to previous tests on Walls 1 and 2. Majority of the existing cracks in Wall B were in the first story piers (Figure 9.3). Fully developed horizontal cracks existed in the bed joints at both the top and 6 courses above the bottom of Pier B-7. These cracks propagated into and almost fully cracked Pier 2-9. As a result, the effective portion of Pier B-7 was well defined as the portion between the top crack and the bottom crack. Similarly, fully developed horizontal cracks existed at

both the top and the bottom of Piers B-8 and B-9, and thus these two piers were also well defined. The existing cracks in Pier B-10 were more substantial. A diagonal crack existed inside Pier B-10, extending from the three-fourth height at the left side of this pier to the right toe of Wall B. Cracks also existed in the area of the wide pier B-11 below Piers B-9 and B-10.

These existing cracks drove the response of Wall B. If the applied lateral displacements for Wall B were not large enough to overcome the compressive stresses on the crack surfaces induced by the gravity load, the wall basically worked as an uncracked wall. Otherwise, it was very likely that Piers B-7, B-8, and B-9 would rock. Following the geometry defined by these existing cracks.

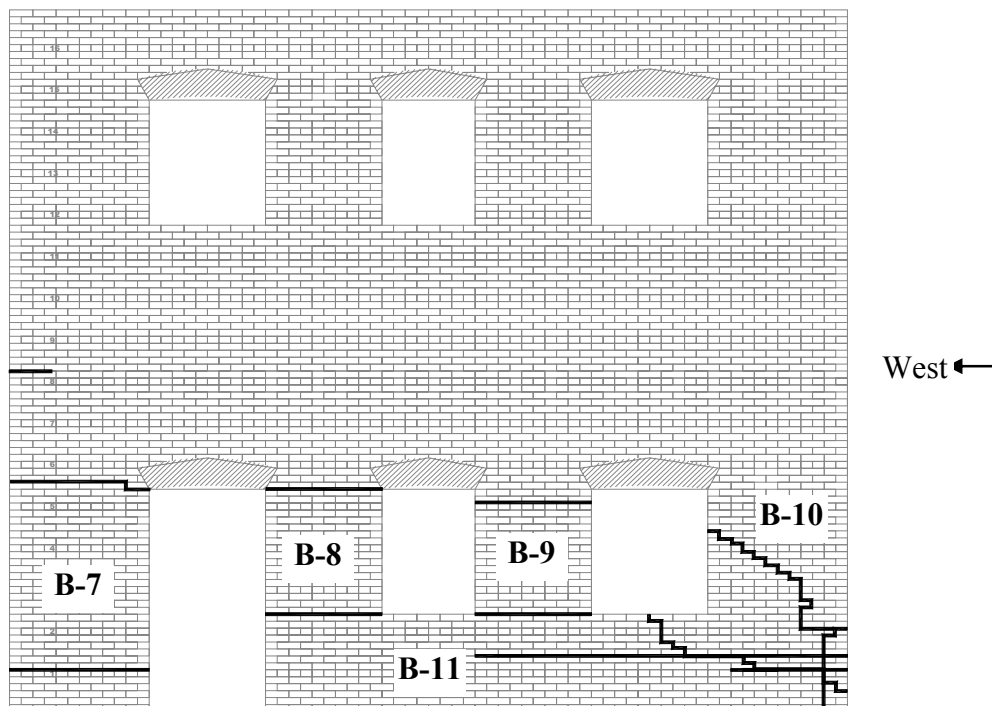


Figure 9.3. Existing cracks in Wall B before test (looking north)

In Cycles 20c to 21b, the effects of the global overturning movement were significant, as demonstrated by the vertical displacements of the upper boundaries of all the four first floor piers of Wall B, as shown in Figure 9.4 and Figure 9.5. In the two figures, the vertical movement of each pier is calculated by averaging the readings of the two vertical LVDTs in the pier. For example, the average of the readings of LVDTs PB-8VL and PB-8VR gives the vertical movement of the upper boundary of Pier B-8.

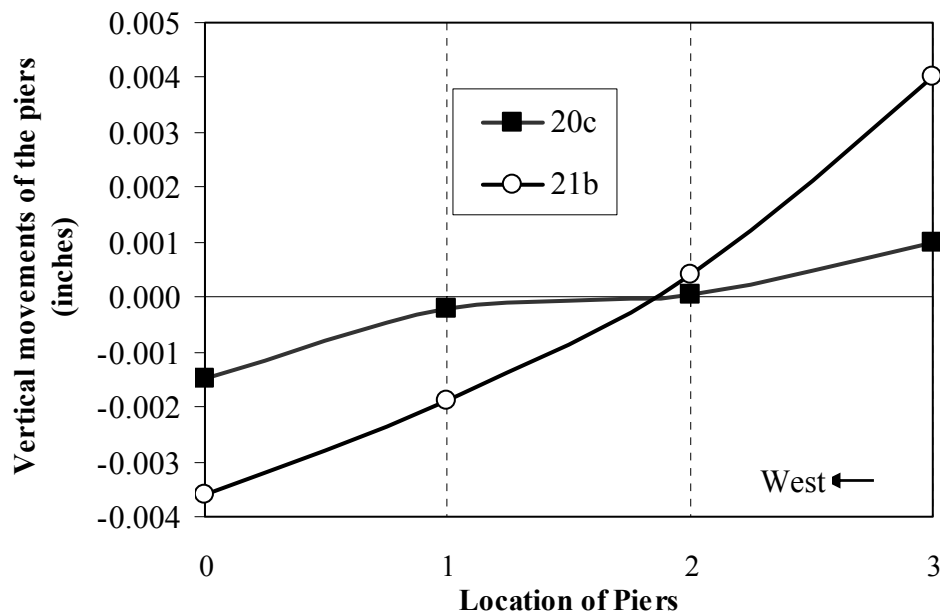


Figure 9.4. The vertical movements of the upper boundaries of the four first story piers in Wall B when loaded in the push direction to maximum deflection
X axis: 0 : Pier B-7, 1: Pier B-8, 2: Pier B-9, 3: Pier B-10

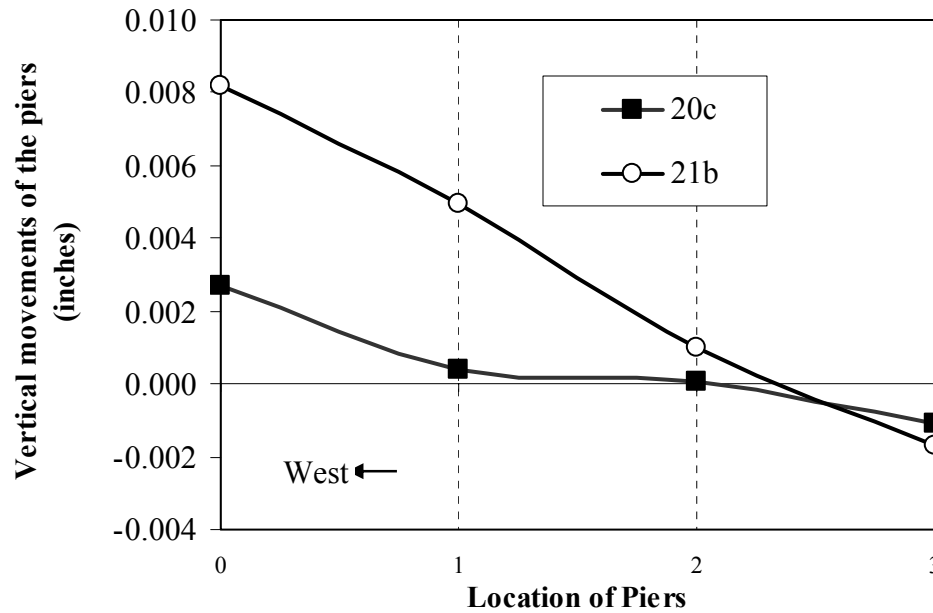


Figure 9.5. The vertical movements of the upper boundaries of the four first story piers in Wall B when loaded in the pull direction to maximum deflection
X axis: 0 : Pier B-7, 1: Pier B-8, 2: Pier B-9, 3: Pier B-10

Figure 9.4 shows that when Wall B was loaded in the push direction (westward), compressive deformations were introduced in Piers B-7 and B-8, while tensile deformations were introduced in Piers B-9 and B-10. The deformation values at the exterior piers were larger than those in the interior piers, and increased with increasing lateral displacements. The phenomena clearly shows the effect of the global overturning moment. Figure 9.5 shows similar effects when Wall B was loaded in the pull direction (eastward). A small difference is that in the latter case all the three left piers (B-7, B-8, and B-9) were in tension while only Pier B-10 was in compression. This was probably due to the fact that the left three piers were fully cracked in the previous test, and thus the center of moment of inertia of the entire wall section was shifted to the right. In addition, the existence of a large pier (Pier 1-6) provided a large flange at the right side of Wall B,

which also helped to shift the inertia center to the right. Figure 9.4 and Figure 9.5 also indicate that the entire first floor spandrel of Wall B rotated counterclockwise when the wall was loaded in the push direction, and rotated clockwise when the wall was loaded in the pull direction. This behavior was again due to the global overturning moment effects.

The instrumentation also revealed local rocking of the first story piers. For example, the readings of the strain gages at the base of Pier B-9 in Cycle 21b are shown in Figure 9.6. The figure shows that the left base of Pier B-9 was in compression and the right base was in tension when Wall B was loaded in the push direction, and vice versa when Wall B was loaded in the pull direction. This indicates that Pier B-9 was in bending or was rocking during this cycle.

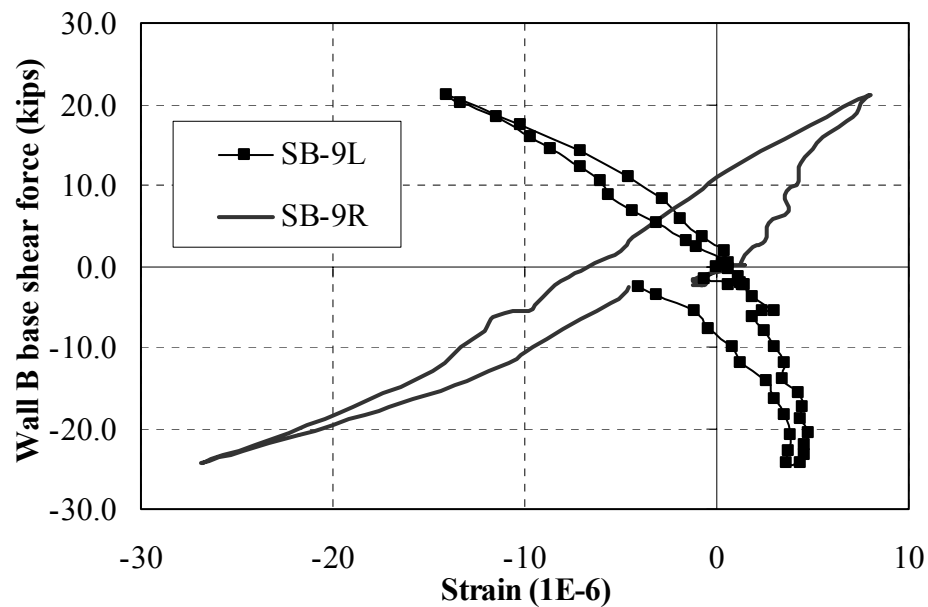


Figure 9.6. Reading of strain gages of Pier B-9 in Cycle 21b

This mixed behavior of Wall B, with both global overturning and local rocking, also can be deduced from the lateral displacements of the two exterior piers, Pier B-7 and Pier B-10. As discussed before, a typical lateral displacement of a pier is composed of rocking displacement and shear/flexural displacement. The ratio between the two displacement components was affected by the global overturning moment and was different when the wall was loaded in different directions. Taking Pier B-10 for example, as shown in Figure 9.7, when Wall B was loaded in the pull direction (negative displacement), Pier B-10 was in the compression side. As a result, its rocking deformation was quite small; and, thus, the majority of the lateral deformation of this pier was due to its shear and flexural deformation. In the contrast, when Wall B was loaded in the push direction (positive displacement), the entire pier B-10 tended to be lifted. As a result, this pier did not resist much external lateral shear force, and its shear and flexural deformations were rather small. The lateral displacement of the pier was thus controlled by rocking.

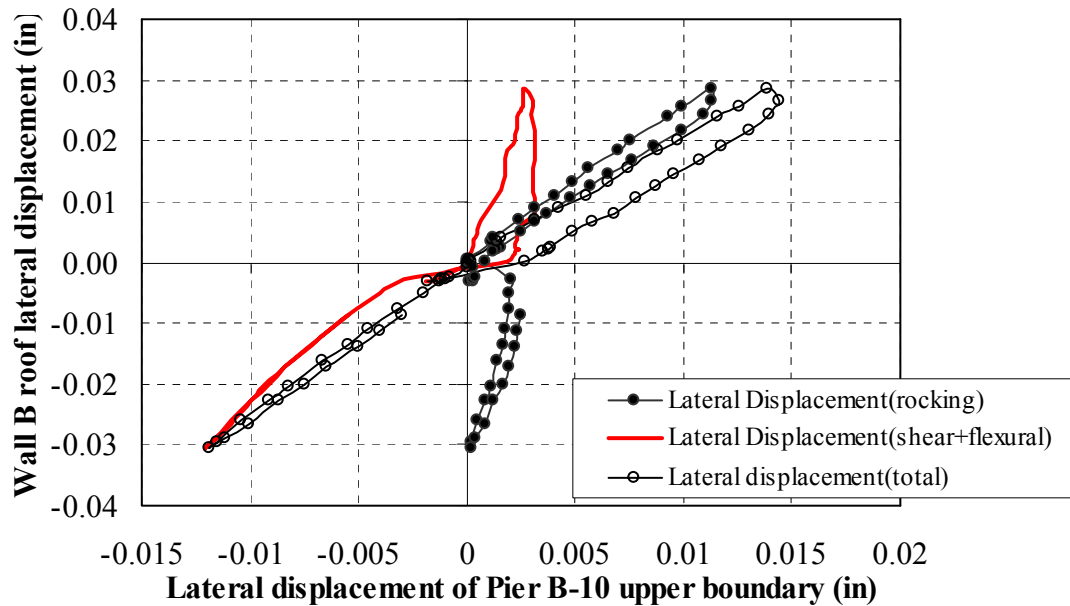


Figure 9.7. Lateral displacements of Pier B-10 (Cycle 21b)

The lateral displacements of Pier B-7 and Pier B-10, together with their controlling components, are listed in Tables 9.2 and 9.3. The tables show that Pier B-7 and Pier B-10 mirrored each other's behavior due to the effects of the global overturning moments. In addition, the tables show that the first story lateral deformation of Wall B was concentrated on these piers.

Table 9.2. Lateral displacement of Piers B-7 and B-10 in the push direction

Maximum Wall B second floor lateral displacements in the push direction	Maximum lateral displacements for the piers (in.)	
	Pier B-7	Pier B-10
0.005 in.	0.0045, shear + flexural	0.003, rocking
0.023 in.	0.018, shear + flexural	0.015, rocking

Table 9.3. Lateral displacement ratios of Piers B-7 and B-10 in the pull direction

Maximum Wall B second floor lateral displacements in the pull direction	Maximum lateral displacement ratios for the piers	
	Pier B-7	Pier B-10
-0.006 in.	-0.005, rocking	-0.004, shear + flexural
-0.023 in.	-0.02, rocking	-0.012, shear + flexural

9.3.1.2. Accumulation of damage in Wall B (Cycles 22a through 25b)

During Cycles 22a through 25b, the existing cracks at the top and bottom of the first floor piers opened or closed due to rocking of the individual piers. Besides this, new crack propagation and damage were observed in Wall B and its adjacent out-of-plane walls (Walls 1 and 2) (Figure 9.8).

When the wall was loaded in the push direction (westward) in Cycle 22a, a crack initiated at the left top corner of Pier B-10, and extended upward and to the right for about 15 in. This crack propagated farther with each cyclic excursion (Cycles 22b, 23a, and 24a), until it reached the out-of-plane Wall 1. This crack was apparently due to the effects of overturning moment, since the push moment tended to lift the right side of Wall B, and leave Pier B-10 behind.

When the wall was loaded in the pull direction (eastward), there were no new cracks observed in Cycles 22a and 22b. However, in Cycle 23a, the existing crack at the top of Pier 2-9 opened because of the overturning moment effects. This crack propagated farther to the left side of Pier 2-9, and fully cracked the top of this pier. Meanwhile, a crack initiated at the middle of the windowsill between Pier B-9 and Pier B-10, propagated at an angle of approximately 30° downward and to the right for about 70 in. This crack propagated farther to the foundation in Cycle 25a.

Besides the crack propagation in the in-plane walls, overturning moment also caused substantial cracks in the out-of-plane Wall 2. In Cycle 25b, a horizontal crack was observed at the mid-height of the Wall 2 first floor spandrel. This crack propagated to the left and right, and joined the existing cracks on both sides of the wall. As a result, the entire second floor of Wall 2 was lifted as the flange for Walls A and B.

During this series of test cycles, the propagation of cracks was confined mainly to the first floor. However, in Cycle 25a, when Wall B was loaded in the push direction, cracks developed at the top left corner of Piers B-4 and B-5, and at the right bottom of Pier B-3 and Pier B-4, due to the local rocking behavior of these piers (Figure 9.8).

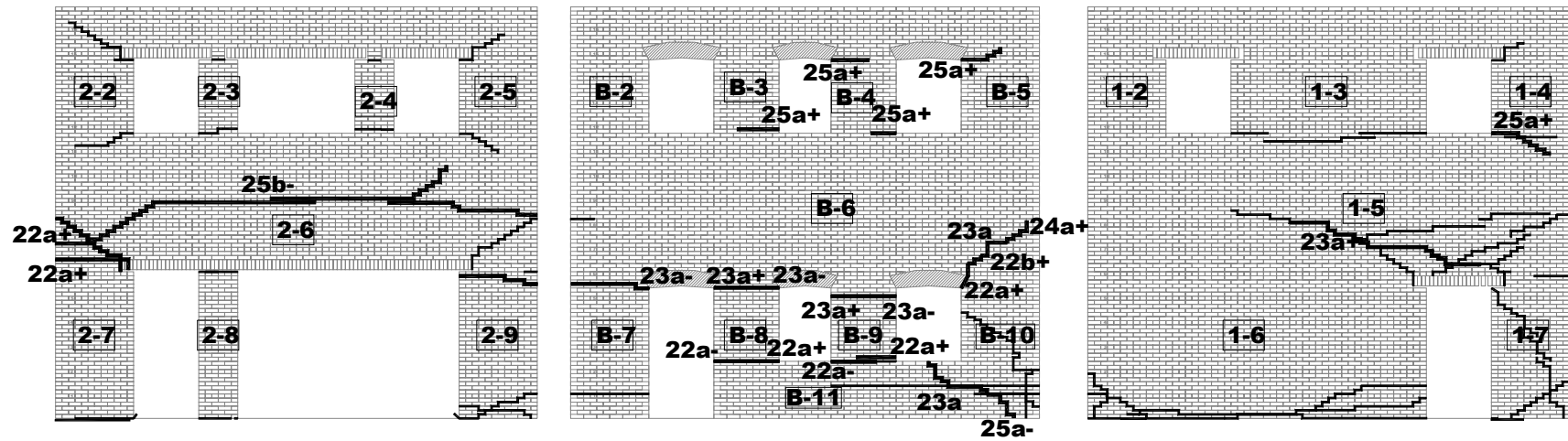


Figure 9.8. Crack pattern of Wall B and adjacent Wall 2 (left) and Wall 1 (right) at the end of Cycle 25b. The crack number corresponds to the test run number. Number IDs of each pier are given in the rectangles.

The lateral displacement–base shear force curves for Wall B up to Cycle 25b are shown in Figure 9.9. The response of Wall B exhibited significant nonlinear behavior. Wall B attained its maximum lateral strength of 43.0 Kips in the push direction at a roof displacement of 0.222 in., and its maximum lateral strength of -36.9 Kips in the pull direction at a roof displacement of -0.273 in. One interesting phenomenon is that although a large crack was developing in Wall 2 when the building was loaded in the pull direction, the load displacement curve for Wall B was smooth. This indicates that the bed joint tensile strength of masonry was small.

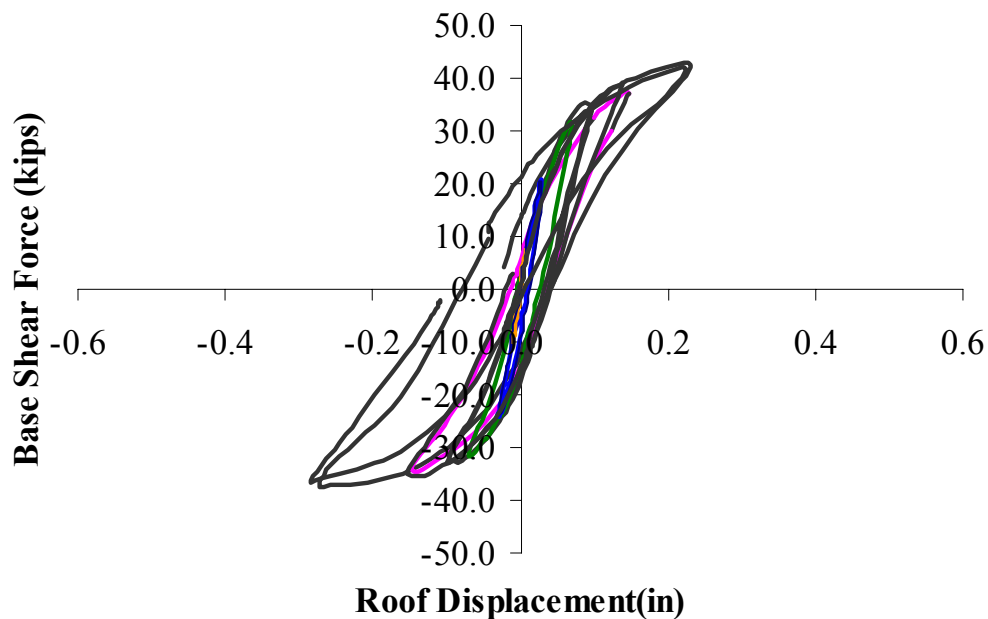


Figure 9.9 Lateral displacement- base shear force curves for Wall B up to Cycle 25b

The behavior of Wall B can be understood from the vertical movements of the upper boundaries of its four first story piers. Figure 9.10 shows the measured vertical movements of these upper boundaries in Cycles 22a through 25a corresponding to the maximum lateral push displacements. The first floor spandrel of Wall B worked pretty much like a rigidity body, exhibiting vertical displacement and rotation with increasing lateral displacement. To look more clearly into this issue, the displacement of this spandrel is illustrated by the vertical displacements on the left side of Wall B and its rotation angles, as listed in Table 9.4.

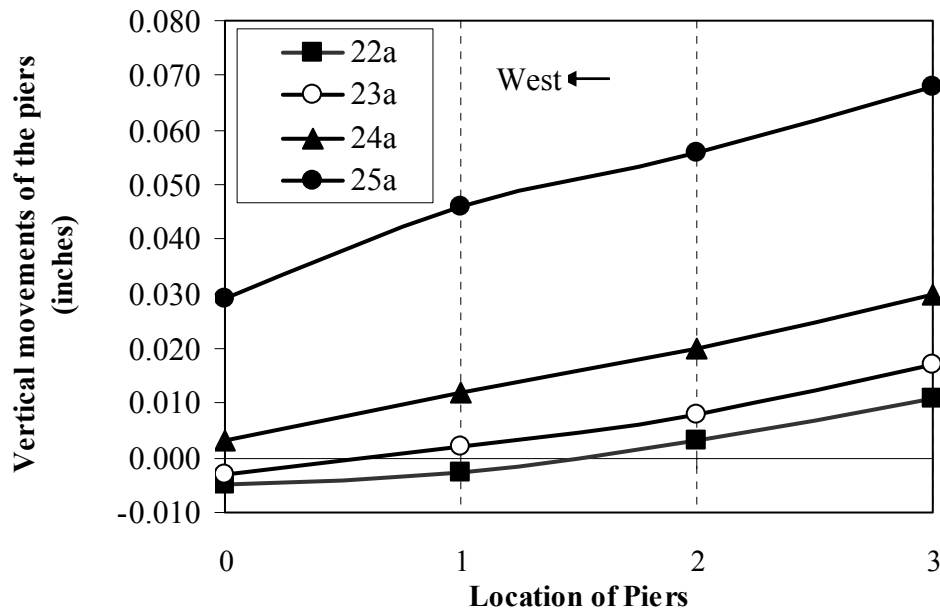


Figure 9.10. Vertical movements of Wall B first floor spandrel when loaded in the push direction to maximum deflection (Cycles 22a – 25a)
X axis: 0 : Pier B-7, 1: Pier B-8, 2: Pier B-9, 3: Pier B-10

Table 9.4. Rigid movements of Wall B first floor spandrel when loaded in the push direction (Cycles 22a to 25a)

Maximum Wall B second floor lateral displacements in the push direction	Movement of Wall B first floor spandrel	
	Vertical movement (in., +: going up)	Rotation (degree, +: counterclockwise)
0.057 (22a)	-0.005	0.0054
0.081 (23a)	-0.003	0.0066
0.117 (24a)	0.003	0.0089
0.189 (25a)	0.029	0.0127

Table 9.4 shows that with increasing lateral (positive) push displacement, the counterclockwise rotation of the Wall B spandrel became larger, reflecting the influence of the global overturning movements. On the other hand, the left side of Wall B first went down, then displaced up with increasing lateral displacement. This indicated that the local rocking of the first story piers was becoming a predominant contributor to the response of Wall B.

The measured maximum vertical movements of the Wall B first floor spandrel in the pull direction (eastward) in Cycles 22a to 25a are shown in Figure 9.11. Similar to the behavior in the push direction, the first floor spandrel exhibited a mixed behavior of global overturning movement and local rocking. Note that the upward movement of Pier B-7 started to slow down relative to the other piers after Test Cycle 23a. This indicated that Pier B-7 was left behind when Wall B first floor spandrel was loaded in the pull direction. If the first floor spandrel was assumed rigid and if its movements could be calculated based on the movements of the three right side piers, its vertical movements on the right side and the rotation angles of this spandrel are as shown in Table 9.5. This table verifies the mixed behavior of Wall B in the pull direction.

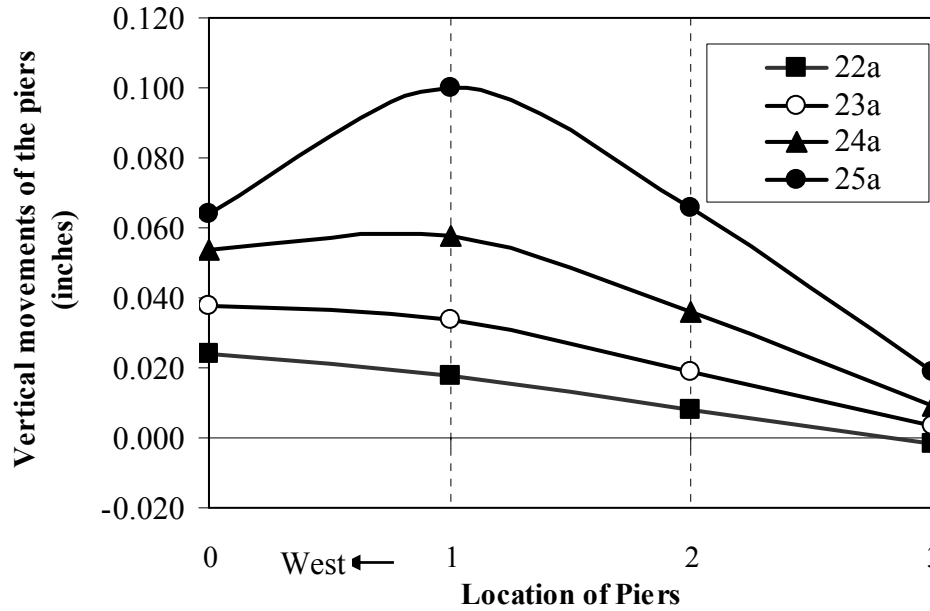


Figure 9.11. Vertical movements of Wall B first floor spandrel when loaded in the pull direction to maximum deflection (Cycles 22a – 25a)
X axis: 0 : Pier B-7, 1: Pier B-8, 2: Pier B-9, 3: Pier B-10

Table 9.5. Rigid movements of Wall B first floor spandrel when loaded in the pull direction (Cycles 22a to 25a)

Maximum Wall B second floor lateral displacements in the pull direction	Movement of Wall B first floor spandrel	
	Vertical movement (in., +: going up)	Rotation (degree, +: counterclockwise)
-0.057 (22a)	-0.0019	-0.01
-0.077 (23a)	0.0035	-0.0153
-0.123 (24a)	0.0089	-0.0246
-0.225 (25a)	0.019	-0.0405

9.3.1.3. Fully developed kinematic mechanism (Cycles 26a and 26b)

In these two cycles, substantial cracks developed in Wall B and the adjacent out-of-plane walls (Figure 9.12). As a result, a kinematic mechanism for Wall B was fully developed. When the building was loaded in the push direction (westward), because of

the flange effects, the uplift of the right side of Wall B introduced large tensile stress in the adjacent Wall 1, and that tension stress cracked the bottom of Wall 1 adjacent to Wall B. Consequently, the entire left (south) portion of Wall 1 was lifted from its base. The lateral push force for Wall B also caused Pier B-7 to rock about its left (west) toe. As a result, a 45^0 crack propagated from the existing cracks at the bottom of Pier B-7, and spread to its left toe.

When the building was loaded in the pull direction (eastward), the uplift on the left side of Wall B caused two diagonal cracks to initiate above the arch lintel of the door opening. These cracks propagated upward and to the left toward the bottom of the Wall 2 second floor fixture steel plate, turned about the corner into Wall 2, and propagated farther at an angle of approximately 45^0 upward and to the left until it reached the top of Wall 2. As a result, the portion of Wall B above these cracks was lifted due to the overturning movement. Meanwhile, the triangular portion of Wall 2 above the crack was also lifted as the flange of Wall B.

During this cycle, flexural cracks were also observed at the top and bottom of the second story piers in Wall B, due to the rocking behavior of these piers. Another interesting phenomenon was that the first floor spandrel of Wall B seemed to slide on the top of Pier B-8 and B-9 during this cycle.

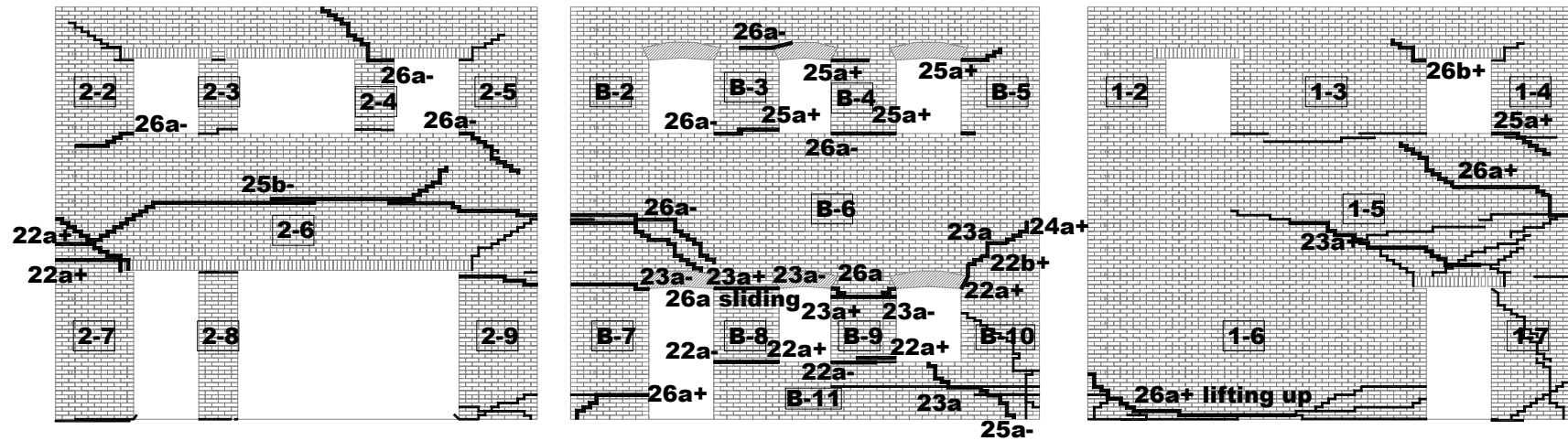


Figure 9.12. Crack pattern of Wall B and adjacent Wall 2 (left) and Wall 1 (right) at the end of Cycle 26b. The crack number corresponds to the test run number. Number IDs of each pier are given in the rectangles.

With all these cracks formed, a kinematic mechanism for Wall B was fully developed. When Wall B was loaded in the push direction, the movement of Wall B is shown in Figure 9.13. Although the bottom horizontal crack in Pier B-7 was above its first header course, the 45° crack at the left toe of this pier indicated that Pier B-7 rocked about its left toe. Pier B-10 separated from the majority of Wall B through the diagonal crack at its top, while the Wall B first floor spandrel and the entire Wall B second story moved upward and rotated counterclockwise under lateral push forces. The two interior piers (Piers B-8 and B-9) also rocked about their left toes.

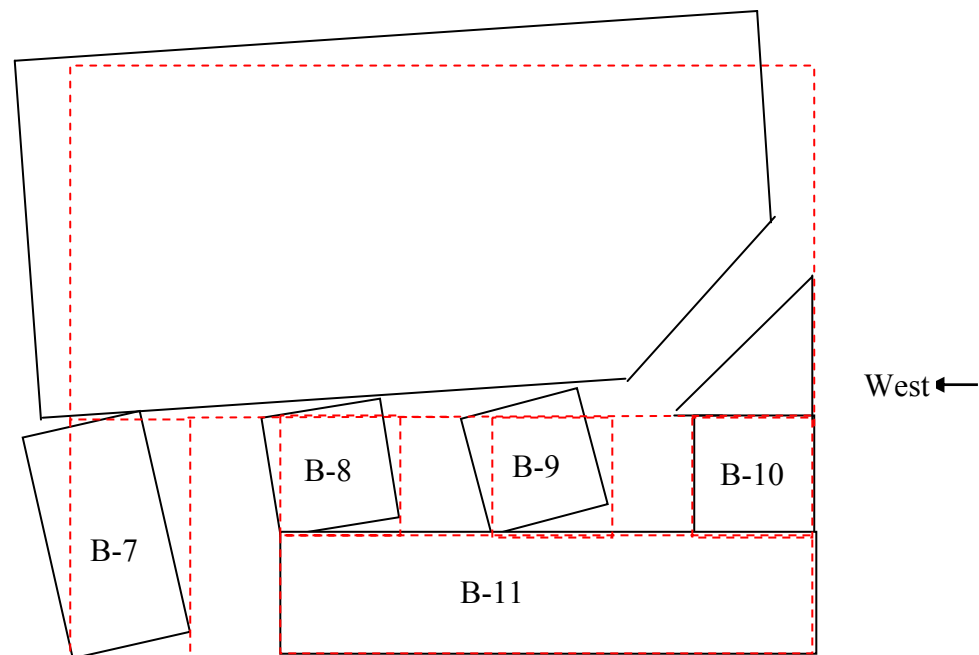


Figure 9.13. Kinematic mechanism of Wall B when loaded in the push direction

Two issues need to be pointed out for this kinematic mechanism. First, although there were signs of rocking for the second floor piers, the damage to the second floor wall was minor compared with that to the first floor piers. Therefore, the entire second floor masonry wall was still assumed rigid in this kinematic mechanism. Second, the rocking of the in-plane Wall B forced the flanges (Walls 1 and 2) to move as well, and caused these walls to crack. The flange effects due to the movement of Walls 1 and 2 made a large contribution to the lateral resistance of the in-plane wall, as discussed in more detail in Section 9.4.

When Wall B was loaded in the pull direction, the kinematic mechanism of Wall B is shown in Figure 9.14. Similar to the push direction, the pier on the tension side (Pier B-7) separated from the majority of the wall through the diagonal crack at its top. The two interior piers rocked about their right toes. The Wall B first floor spandrel and the entire Wall B second story wall moved together as a rigid body upward and rotated clockwise. On the other hand, being slightly different from the push direction case, the pier on the compressive side (Pier B-10) did not rock with its own size. Instead, a 45° crack developed at the left bottom of this pier, and that crack separated Pier B-10 from the lower Wall Section B-11. As a result, Pier B-10 rocked about the right toe of Wall B as a pier with the same aspect ratio as that of Pier B-7. The deformation mechanism of Wall B in the pull direction basically mirrors that in the push direction. More detailed discussion on the effective aspect ratio of the URM piers in this perforated wall is given in Section 9.6.

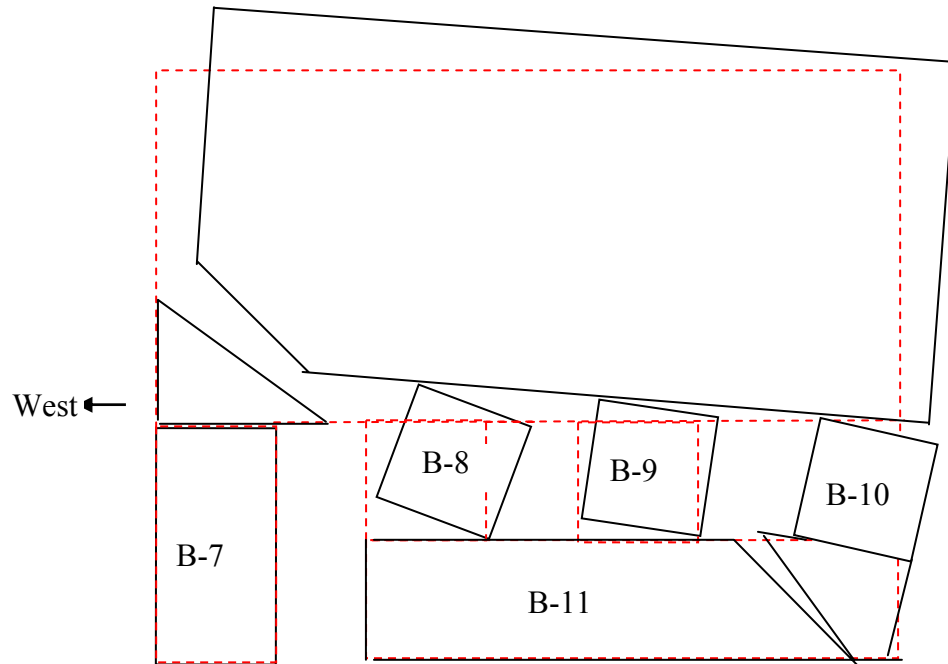
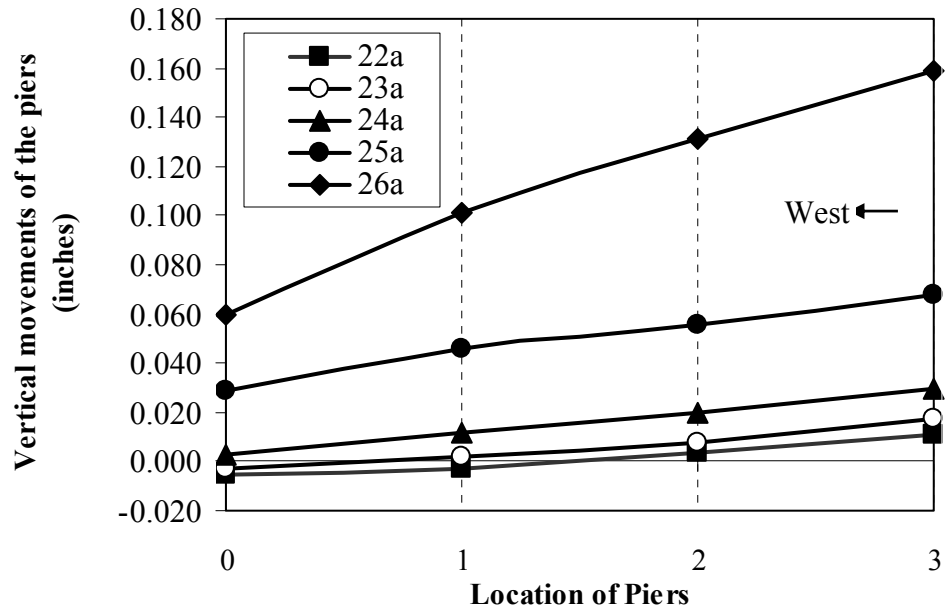
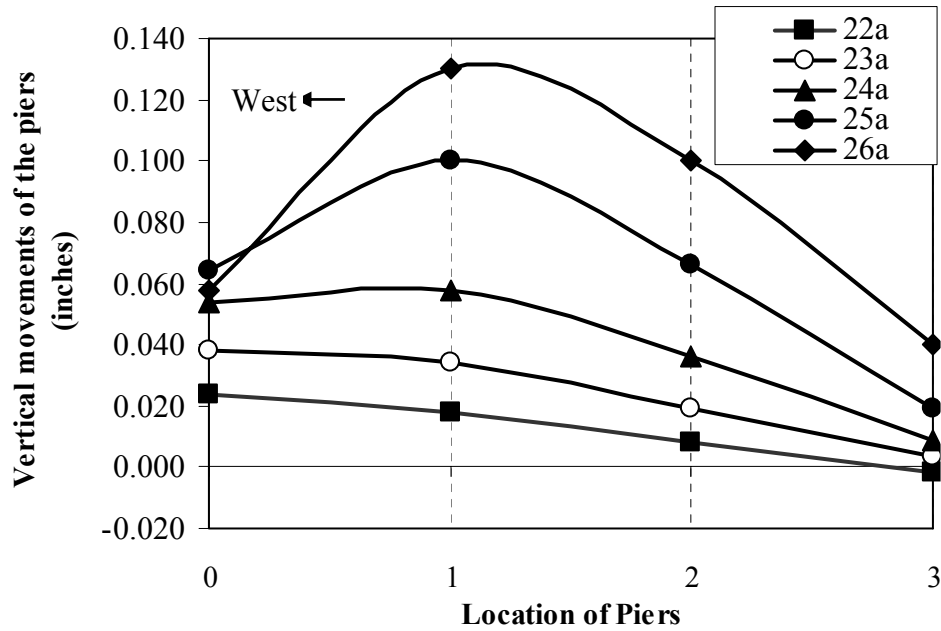


Figure 9.14. Kinematic mechanism of Wall B when loaded in the pull direction

The vertical displacements of the Wall B first floor spandrel in Test Cycle 26a, corresponding to the maximum lateral push and pull displacements are shown in Figure 9.15 (a) and Figure 9.15(b), respectively. The vertical displacements in the previous test cycles are also shown in the figures as a comparison. These figures show that the movement of the spandrel in Test Cycle 26a was basically the same as those in the previous cycles. Its movement exhibited a mixture of global overturning movement and local rocking. Again, Figure 9.15(b) indicates that Pier B-7 was left behind when Wall B was loaded in the pull direction.



(a) Push direction



(b) Pull direction

Figure 9.15. Vertical movements of the Wall B first floor spandrel (up to Cycle 26a)
X axis: 0 : Pier B-7, 1: Pier B-8, 2: Pier B-9, 3: Pier B-10

The lateral displacement–shear force curve for Wall B in all these test cycles is shown in Figure 9.16. When Wall B lateral roof displacement was larger than 0.25 in. (0.09% drift), the lateral strength of Wall B decreased slowly with increasing lateral displacements. On the other hand, the unloading curve exhibited a large energy dissipation capacity. This was consistent with the observed sliding behavior of the first floor spandrel on the top of Pier B-8 and B-9. In Test Cycle 26b, although no new cracks were observed in Wall B, a large strength degradation was observed. The strength degradation in the push direction was 5.2 Kips between Cycles 26a and 26b at a roof displacement level of 0.47 in., and 1.9 Kips between Cycles 26a and 26b in the pull direction at a roof displacement level of -0.52 in. Since the mature kinematic mechanism for the tested wall was observed, the tests for the URM building stopped in Cycle 26b.

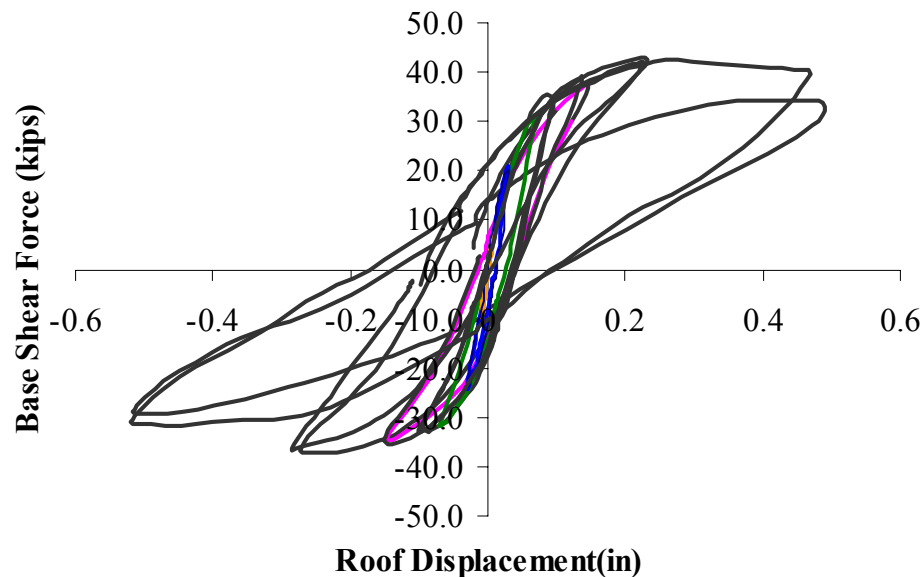


Figure 9.16. Lateral displacement – shear force curves for Wall B in all the test cycles

9.3.2. Wall A

Wall A was identical to Wall B. However, the initial cracks in Wall A were different from those in Wall B. Furthermore, the flange effect for Wall A was also different from that for Wall B due to the unsymmetrical configuration of the out-of-plane Wall 1. As a result, the response of Wall A was different from Wall B. The observed nonlinear properties of Wall A are presented in the following sections, and the response is described at three different levels: the response before the onset of further damage, the accumulation of damage in the walls, and the fully developed kinematic mechanisms.

9.3.2.1. Response of Wall A before further damage (Cycle 20c through 21b)

The existing cracks in Wall A were different from those in Wall B (Figure 9.17). Horizontal cracks through the entire section existed at both the top and the bottom of the two exterior piers (Piers A-7 and A-10), and these cracks propagated into Walls 1 and 2. As a result, the two exterior piers were well defined as the portion between the top and the bottom cracks. Meanwhile, although horizontal cracks cracked the entire top sections of Piers A-8 and A-9, no cracks existed at the bottom of these two piers. As will be seen next sections, these cracks will drive the response of Wall A.

Besides the cracks described above, cracks also existed at the base of Section A-11. However, this crack will not affect the behavior of the wall unless Wall A slides along the foundation. Similarly, there were two diagonal cracks in Wall A on the second floor Wall. These cracks will probably not influence the behavior of Wall A either, as the nonlinear response of Wall A will be determined primarily by the damage of its first story piers.

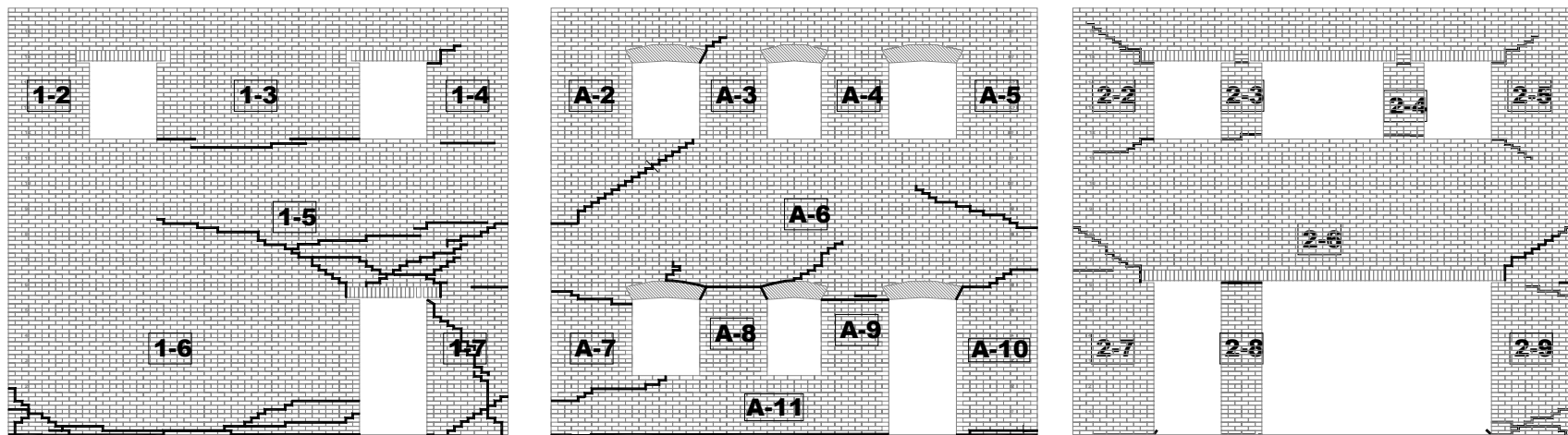


Figure 9.17. Initial cracks in Wall A and adjacent Wall 1 (left) and Wall 2 (right). Number IDs of each pier are given in the rectangles.

As for Wall B, the response of Wall A in Cycles 20c to 21b was essentially elastic. No visual cracks or other damages were observed. The base shear-lateral roof displacement curves for Wall A for these cycles are shown in Figure 9.18.

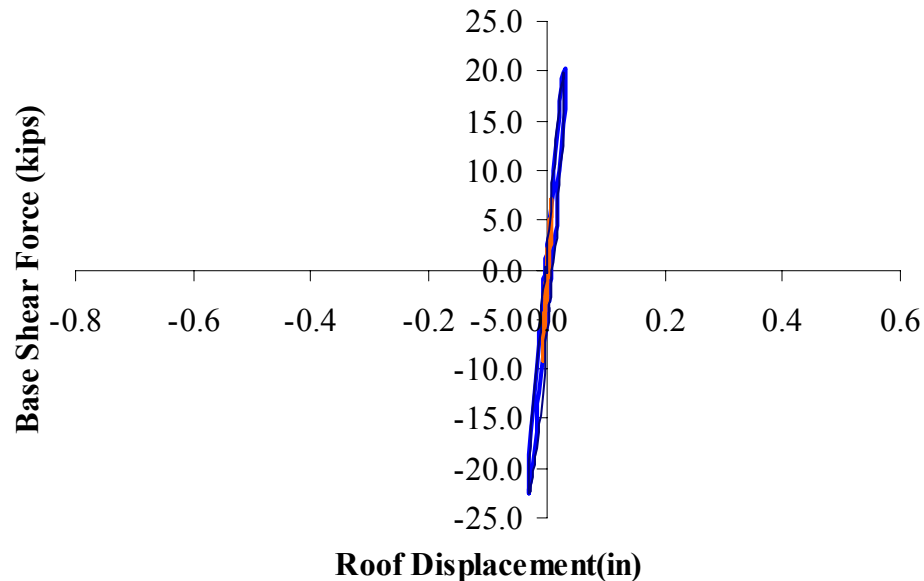


Figure 9.18. Lateral roof displacement-base shear of Wall A (Cycles 20c to 21b)

As was the case for Wall B, the behavior of Wall A in this series of test cycles was governed by a mixture of global overturning movement and local rocking. The measured maximum vertical movements of Wall A first floor spandrel and the vertical strains at the base of the piers exhibited similar behavior as those of Wall B.

9.3.2.2. Accumulation of damage in Wall A (Cycles 22a through 25b)

Substantial damage developed in Wall A during Test Cycles 22a through 25b. The crack pattern in Wall A after Cycle 25b is shown in Figure 9.19. The detailed crack propagation is as follows.

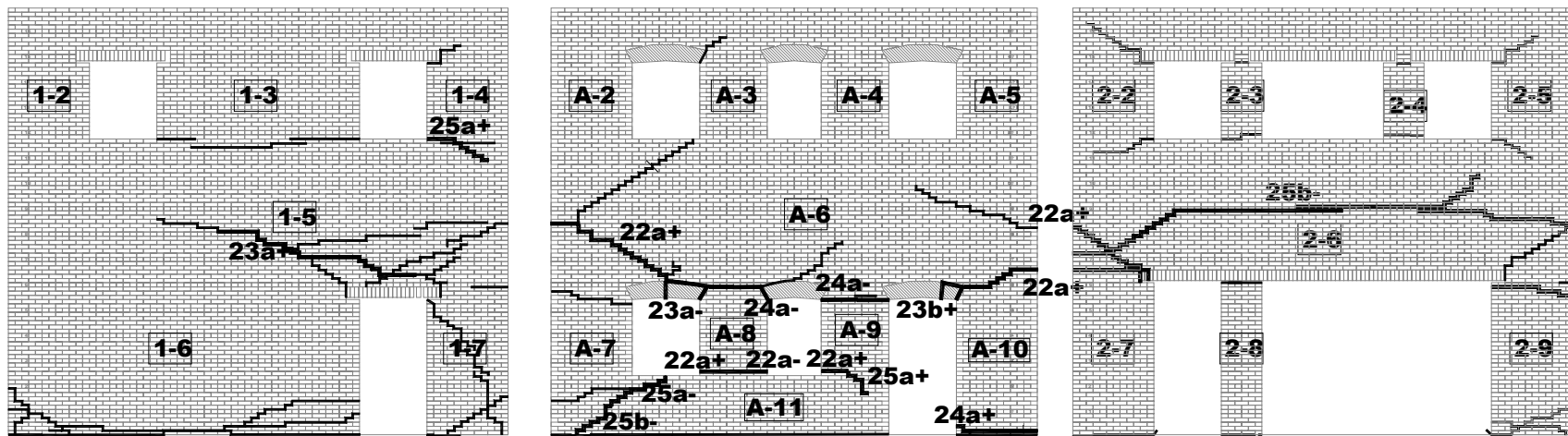


Figure 9.19. Crack pattern of Wall A and adjacent Wall 1 (left) and Wall 2 (right) at the end of Cycle 25b. The crack number corresponds to the test run number. Number IDs of each pier are given in the rectangles.

During Cycle 22a, when Wall A was loaded in the push direction (westward), a crack initiated at the top of the arch lintel of the window opening between Pier A-7 and Pier A-8. This crack propagated at about 45° upward and to the left, reached the corner between Wall 1 and Wall A, and joined an existing crack in that area. As a result, the portion of Wall A above this crack was lifted by the push forces, while Pier A-7 tended to be left behind. Simultaneously, flexural cracks developed at the left bases of Piers A-8 and A-9 due to local rocking. The existing cracks at the top right of these two piers and at the top right and the left bottom of Pier A-10 were observed opening due to the rocking behavior.

In Cycle 23a, when Wall A was loaded in the push direction, the existing cracks on the top right of the arch lintel above the window opening between Piers A-7 and A-8 propagated into the vertical head joint of the arch lintel; the crack completely isolated the right half of this arch lintel from the other portions of Wall A. Meanwhile, the up-lift of the left side of Wall A introduced a large vertical tensile stress in the right portion of Wall 1, and lifted this portion. Thus a crack initiated in the bed joint, three courses above the steel lintel of the door opening in Wall 1. This crack propagated at an angle of approximately 15° upward and to the left, and it joined the existing cracks in Wall A.

In Cycle 24a, when Wall A was loaded in the push direction, a crack developed at the left toe of Pier A-10 two courses above the foundation, due to the large tensile stress induced by the local rocking of this pier.

In Cycle 25a, when the building was loaded in the push direction, the existing crack at the left bottom of Pier A-9 propagated downward and to the left for about 12 in. Meanwhile, the flange effects caused a flexural crack to initiate at the left bottom of Pier

1-4, propagate along the bed joint to the right for about 8 in., then spread farther down and to the right for about 30 in.

When the building was loaded in the pull direction (eastward), another set of cracks developed in the wall. In Cycle 25a, a crack initiated at the middle of the windowsill between Pier A-7 and Pier A-8, propagated at an angle of approximately 30° downward and to the left for about 45 in. In Cycle 25b, this crack propagated farther to the left and towards the bottom until it reached the foundation. This inclined crack was due to the rocking of Pier A-7 about its left toe. Meanwhile, a diagonal crack initiated from the existing horizontal cracks on the top of Pier 2-7, propagated at an angle of about 45° upward and to the right until it reached the mid-height of the Spandrel 2-6. At this point it continued to propagate to the right, and joined another horizontal crack that had propagated from the right side of Wall 2. These cracks formed a large crack, and they separated the entire out-of-plane wall (Wall 2). As a result, the entire second floor of Wall 2 lifted up as the flange of Walls A and B.

Along with the crack propagation, the base shear-lateral roof displacement curve for Wall A exhibited significant nonlinear behavior, as shown in Figure 9.20. Wall A attained a maximum lateral strength of 35.7 kips in the push direction (roof displacement of 0.214 inches) and -40.8 kips in the pull direction (roof displacement of -0.278 inches). The small energy dissipation area for this force-displacement curve indicates that rocking dominated the response of Wall A. This is similar to the behavior of Wall B. On the other hand, in Cycle 25b, the unloading branch from the pull loading peak exhibited a relatively large energy dissipation area. This indicated that a sliding was probably

occurring in this wall, although this behavior could not be visually confirmed during this test cycle.

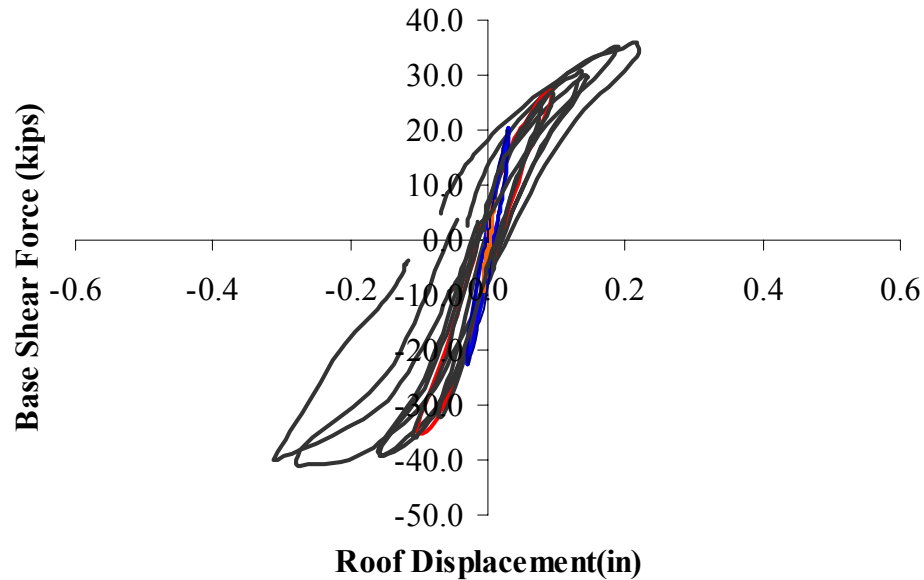


Figure 9.20. Base shear vs. lateral roof displacement for Wall A up to Cycle 25b

The behavior of Wall A (global overturning movement and local rocking) can be seen from the vertical movements of its first floor spandrel, as shown in Figure 9.21 and Figure 9.22. In the two figures, the vertical movement of each pier is calculated by averaging the readings of the two diagonal LVDTs in the pier. For example, the average of the readings of LVDTs PA-8XL and PA-8XR gives the vertical movement of the upper boundary of Pier A-8.

Figure 9.21 and Figure 9.22 show that the behavior of Wall A was similar to that of Wall B. Note that when Wall A was loaded in the push direction, the measured upward movement at the left side of Wall A was quite small compared with the movement at the

mid of the wall. This was attributed to the fact that Pier A-7 was separated from the other portion of Wall A and was being left behind through the diagonal crack on the top of the pier. Pier A-10 exhibited similar behavior when Wall A was loaded in the pull direction.

The vertical movements of Wall A spandrel shown in Figures 9.21 and 9.22 can also be illustrated by the vertical movements at the compressive side of Wall A and the rotation angles of this spandrel. These are shown in Table 9.6 and Table 9.7 for the push and pull directions of loading, respectively. The calculations exclude the piers that were being left-behind; thus only the movements of the three piers in the compressive side of the wall were used to calculate the movement of the spandrel. The tables show that with increasing lateral displacement, the first floor spandrel of Wall A began to displace more vertically. This indicated increasing rocking of the first story piers.

Meanwhile, the rotation of the first floor spandrel of Wall A also increased. This reflected the global overturning movements. Compared with the previous cycles, it is obvious that although the global overturning moment was still governing the response of Wall A, the influence of local rocking of the first story piers was becoming more and more significant. Furthermore, the comparison of the two tables shows that the rotation of the first floor spandrel of Wall A corresponding to the pull direction was more significant than that in the push direction. This can be ascribed to the different kinematic mechanisms in the two directions.

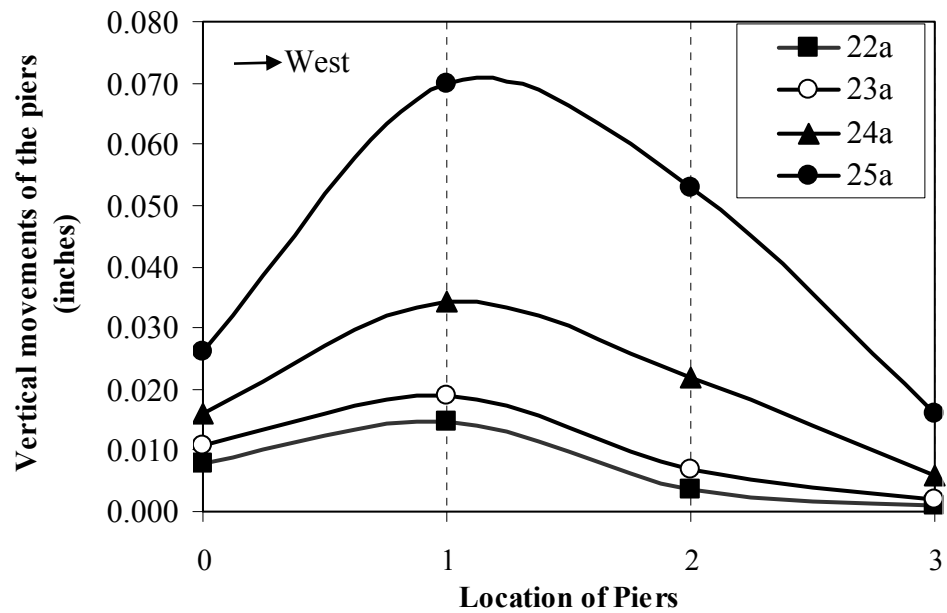


Figure 9.21. Vertical displacement of the first floor spandrel for Wall A when loaded in the push direction to maximum deflection (Cycles 22a to 25a)
X axis: 0 : Pier A-7, 1: Pier A-8, 2: Pier A-9, 3: Pier A-10

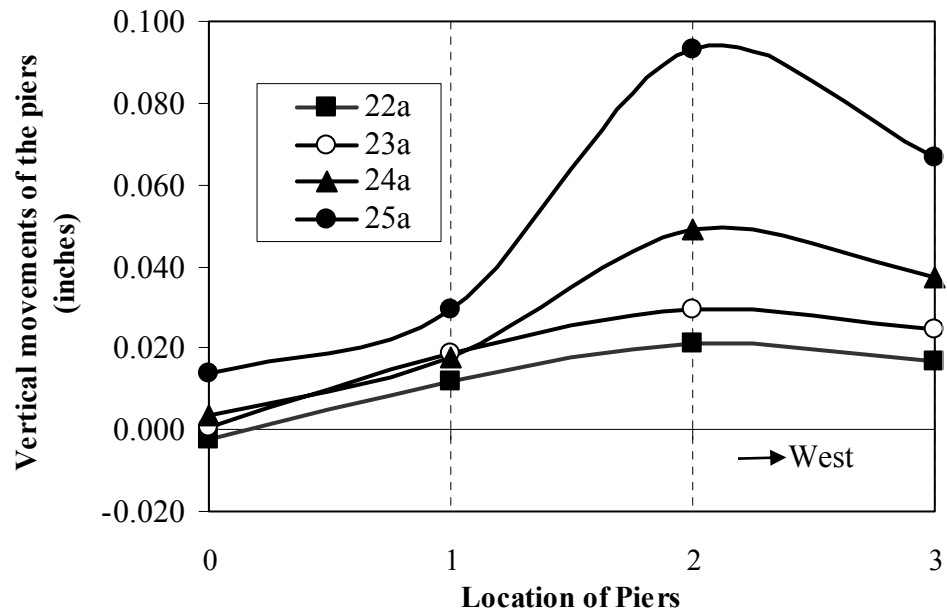


Figure 9.22. Vertical displacement of the first floor spandrel for Wall A when loaded in the pull direction to maximum deflection (Cycles 22a to 25a)
X axis: 0 : Pier A-7, 1: Pier A-8, 2: Pier A-9, 3: Pier A-10

Table 9.6. Rigid movements of First floor spandrel of Wall A when loaded in the push direction (Cycles 22a to 25a)

Maximum Wall A second floor lateral displacements in the push direction	Movement of Wall A first floor spandrel	
	Vertical movement (in., +: going up)	Rotation (degree, +: clockwise)
0.058 (22a)	0.0009	0.0069
0.073 (23a)	0.0019	0.0084
0.111 (24a)	0.006	0.0141
0.186 (25a)	0.0159	0.0271

Table 9.7. Rigid movements of First floor spandrel of Wall A when loaded in the pull direction (Cycles 22a to 25a)

Maximum Wall A second floor lateral displacements in the pull direction	Movement of Wall A first floor spandrel	
	Vertical movement (in., +: going up)	Rotation (degree, +: clockwise)
-0.056 (22a)	-0.0024	0.0117
-0.077 (23a)	0.00043	0.0144
-0.116 (24a)	0.0037	0.0227
-0.206 (25a)	0.0136	0.0397

9.3.2.3. Fully developed kinematic mechanism (Cycles 26a and 26b)

In Cycles 26a and 26b, substantial cracks formed in Wall A and the adjacent out-of-plane walls (Figure 9.23).

During Cycle 26a, when the building was loaded in the push direction (westward), the uplift at the left side of Wall A introduced large tensile stresses in the adjacent Wall 1 due to the flange effects. As a result, the existing crack next to the Wall A second floor fixture steel plate propagated into Wall 1. It continued to propagate at an angle of approximately 30° upward and to the left until it reached the sill level at the second floor.

This crack caused the triangular portion above this crack in Wall 1 to be lifted by the movement of Wall A, and work as the flange of Wall A.

When the building was loaded in the pull direction (eastward), a diagonal crack developed above Pier A-10 because of the overturning movement. However, this crack did not propagate into Wall 2. During this cycle, flexural cracks were also observed at the top and the bottom of the second floor piers in Walls A and B, due to the rocking behavior of these piers.

In Cycle 26b, when the building was loaded in the push direction, a diagonal crack propagated down from the existing flexural crack at the left base of Pier A-9 at an angle of about 45° downward and to the right, and fully cracked this pier. As a result, Pier A-9 rocked about the right toe of A-11. Meanwhile, because of the flange effect, the large tensile stress in Wall 1 caused a diagonal crack to initiate at the top right corner of Pier 1-3, and propagate at the angle of 45° upward and to the left for about 30 in.

Another interesting phenomenon was that in Cycle 26b, when Wall A was loaded in the pull direction, the existing cracks on the top of Pier A-10 propagated into the arch lintel of the door opening. This completely isolated the left one-quarter of this arch lintel from the majority of Wall A; this portion of arch lintel almost collapsed. After this test cycle, a temporary support was provided to prevent a complete collapse (Figure 9.24).

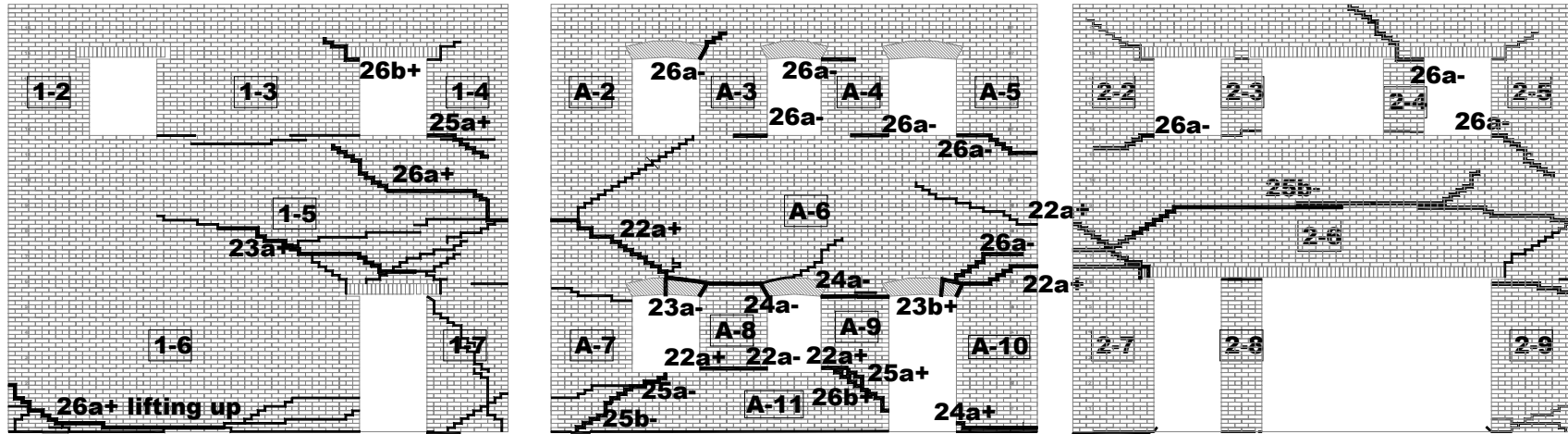


Figure 9.23. Crack pattern of Wall A and adjacent Wall 1 (left) and Wall 2 (right) at the end of Cycle 26b. The crack number corresponds to the test run number. Number IDs of each pier are given in the rectangles.



Figure 9.24. Temporary support for the arch lintel, Pier A-10 on the left (view from inside the building toward north)

With all these formed cracks, a kinematic mechanism for Wall A was fully developed. When Wall A was loaded in the push direction (westward), the deformation mechanism for Wall A is shown in Figure 9.25. Most of the damage concentrated on the first story piers. The first story spandrel and the entire second floor wall moved together as a rigid body. This rigid body rotated in the clockwise direction due to the global overturning moment, and moved upward due to the rocking of the first floor piers. The left pier (Pier A-7) was separated from the majority of the wall by the diagonal crack on the top of this pier. The other three piers at the right side of the wall (Piers A-8, A-9, and A-10) rocked about their right toes. Pier A-9 rocked about the right toe of Section A-11,

indicating that the effective height for Pier A-9 was 84 inches. Detailed explanation for this behavior is given in Section 9.7.

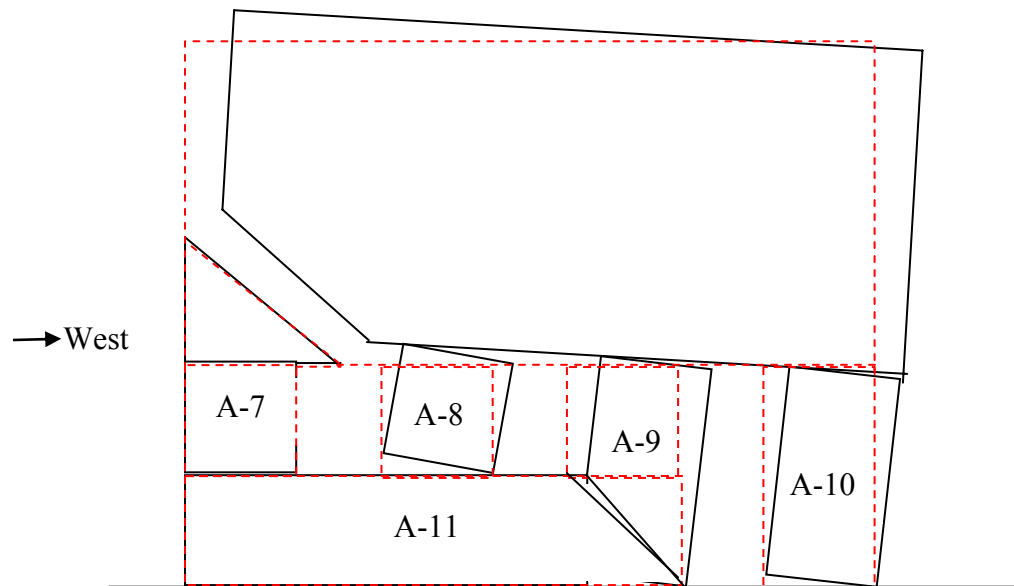


Figure 9.25. Kinematic mechanism of Wall A when loaded in the push direction.

When the building was loaded in the pull direction (eastward), the kinematic mechanism of Wall A is shown in Figure 9.26. Similar to the push direction (westward), most of the damage concentrated on the first story piers. The first floor spandrel of Wall A and the entire second floor wall moved together as a rigid body. They rotated in the counterclockwise direction due to the global overturning moment, and moved upward due to the rocking of the first story piers. The right pier (Pier A-10) was separated from the majority of the wall by a diagonal crack on the top of the pier. The three left piers (Piers A-7, A-8, and A-9) rocked about their left toes. Note that the kinematic mechanism of Wall A in the pull direction is actually identical to that of Wall B in the push direction (Figure. 9.13).

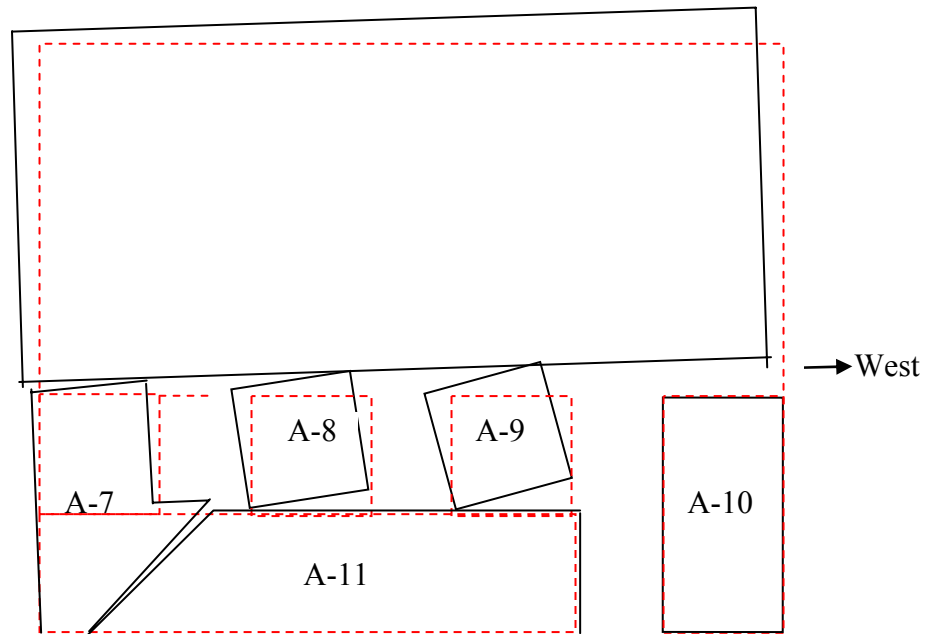
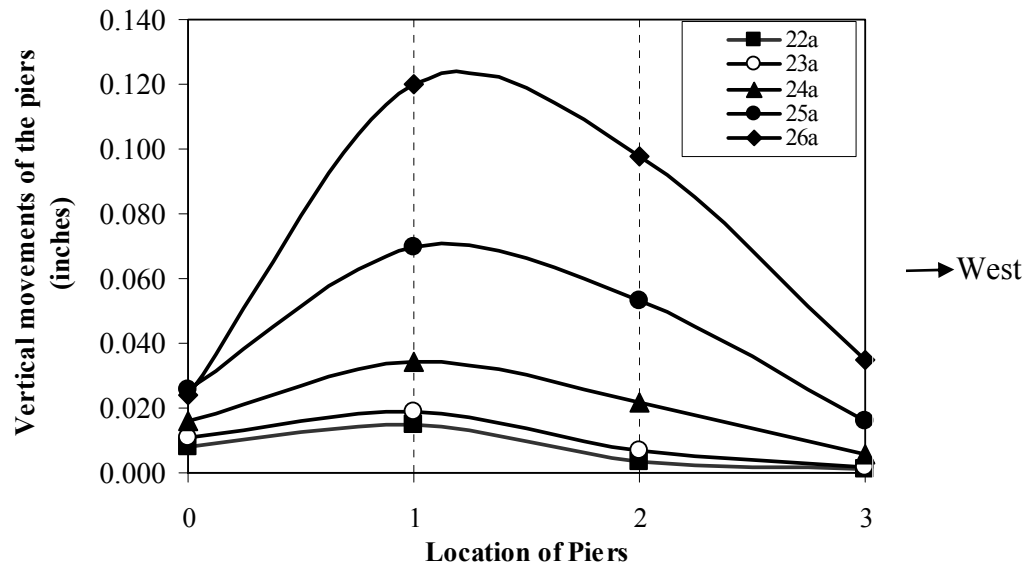


Figure 9.26. Kinematic mechanism of Wall A when loaded in the pull direction.

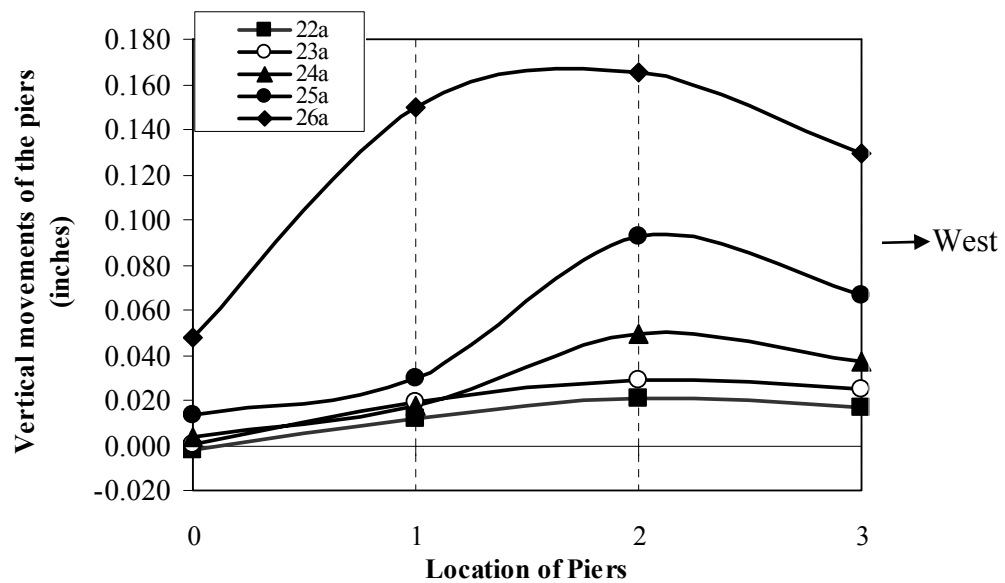
Although there were some signs of rocking for the second floor piers, the damage to the second floor wall was minor compared with that to the first floor piers. Therefore, the entire second floor masonry wall was still assumed rigid in this kinematic mechanism. The participation of flanges observed in the response of Wall A is discussed in more detail in Section 9.5.

The vertical movements of the first floor spandrel of Wall A in Test Cycle 26a corresponding to the maximum lateral push and pull displacements are shown in Figures 9.27 (a) and 9.27(b), respectively. The vertical movements in the previous cycles are also shown in the figures for comparison. These figures show that the movement of the spandrel in Test Cycle 26a was the same as those in the previous cycles. Its movement exhibited a mixture of global overturning movement and local rocking. Again, Figure 9.27 (a) indicates that Pier A-7 was left behind when Wall A was loaded in the push

direction. Figure 9.27(b) indicates that Pier A-10 was left behind when Wall A was loaded in the pull direction.



(a) Push direction



(b) Pull direction

Figure 9.27. Vertical movements of the first floor spandrel of Wall A (up to Cycle 26a)
X axis: 0 : Pier A-7, 1: Pier A-8, 2: Pier A-9, 3: Pier A-10

The lateral displacement-shear force curve for all the test cycles is shown in Figure 9.28. It can be seen when the Wall A lateral roof displacement was larger than 0.21 in. (0.075% drift) in the push direction and 0.28 in. (0.1% drift) in the pull direction, the lateral strength of Wall A decreased slowly with increasing lateral displacements. Meanwhile, the unloading branch of Wall A exhibited a small energy dissipation area. All these observation indicate that the response of Wall A was dominated by rocking.

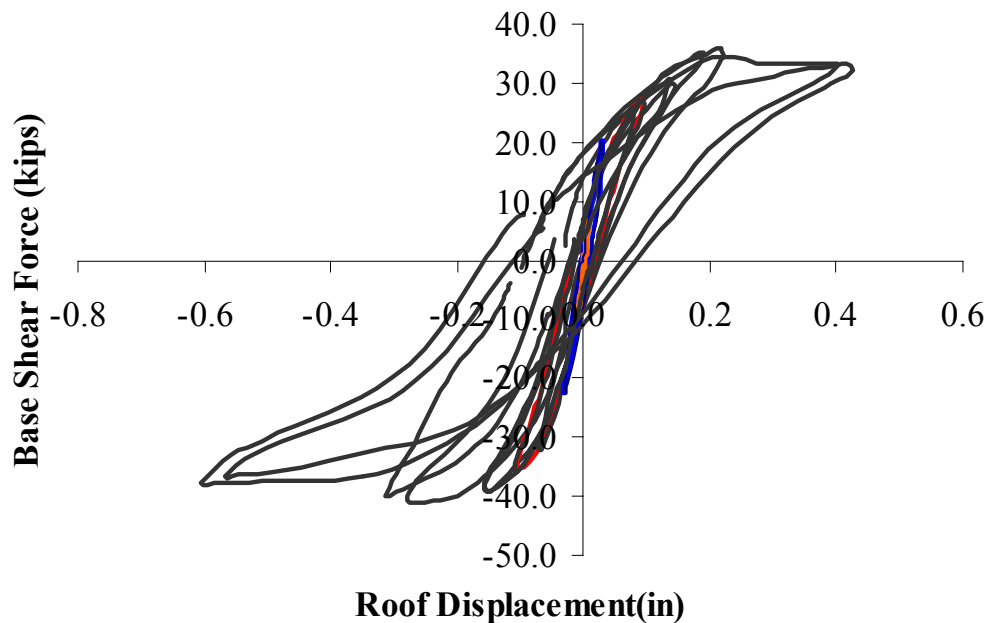


Figure 9.28. Base shear-lateral roof displacement of Wall A in all the test cycles

9.4. FLANGE EFFECTS

Significant flange effects due to the participation of out-of-plane walls were observed in the previous tests parallel to Walls 1 and 2. These flange effects were also

observed in the tests parallel to Walls A and B. However, as opposed to the tests parallel to Walls 1 and 2, there were existing cracks in the masonry walls prior to the tests parallel to Walls A and B. As a result, the flange effects observed in the latter case should be considered as that for a cracked structure. Due to the extensive crack propagation at the base of the masonry walls, the strain gages mounted at the base of the first story piers gave little valuable information on the behavior of the flanges. Nevertheless, the contribution of the flange effects to the kinematic mechanisms and the ultimate strength of Walls A and B can still be understood from the crack propagation in the out-of-plane walls.

The flange effects observed in the tests of Walls A and B and those in the previous test series parallel to Walls 1 and 2 (Section 8.5) can be well explained by the concepts “Pier flange” and “Spandrel flange” as follows.

Figure 9.29 shows a pier and a spandrel on the tensile side of a weak pier-strong spandrel masonry wall. The pier and the spandrel are lifted up due to the external overturning moment. Meanwhile, the pier rocks about its right toe. As a result, cracks develop between the pier and the ground, and between the pier and the spandrel. These cracks propagate into the out-of-plane wall, and divide it into the “pier flange”, the portion between the ground and Crack A, and the “spandrel flange”, the portion above Crack A.

Figure 9.30 shows another case of a flange - a pier and a spandrel at the compressive side of a weak pier-strong spandrel wall. The pier rocks about its left toe and lifts up the spandrel. As a result, cracks develop at both the top and the bottom of the pier

and the flange. These cracks also divide the out-of-plane wall into two different parts (the pier flange and the spandrel flange).

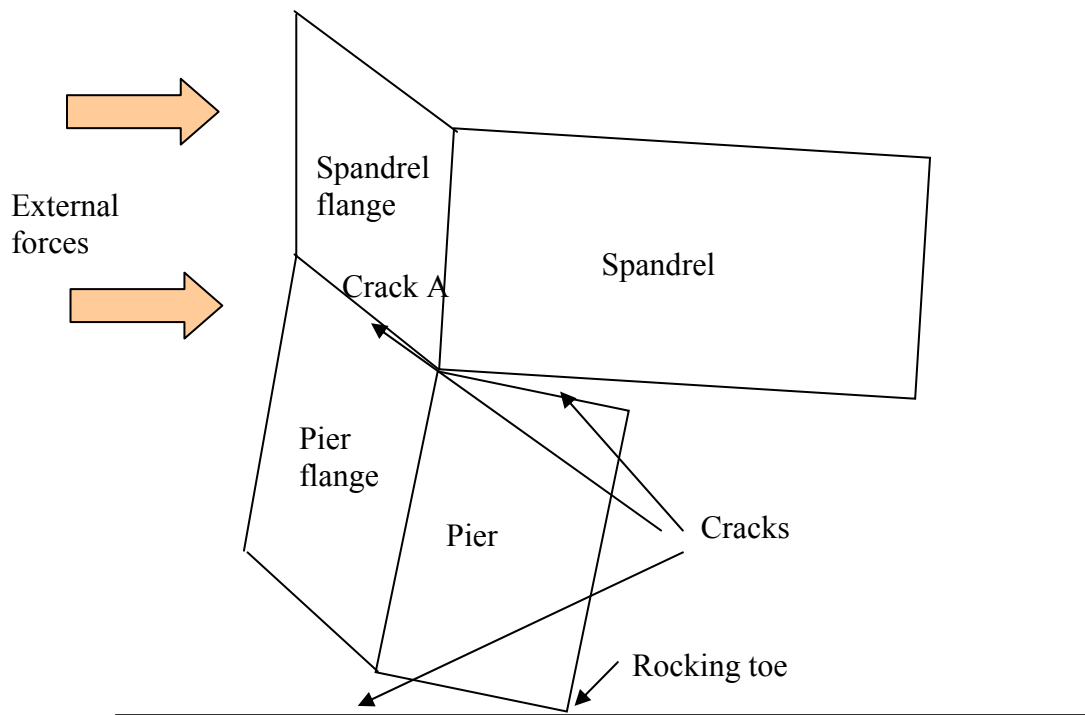


Figure 9.29. Pier flange and spandrel flange in the tensile side of a pier

Note that the flange effects in an individual pier have been discussed in Chapter 5. The conclusions obtained there can be applied for the pier flange discussed herein. When the pier flange is on the tensile side of a wall, the weight center of the flange is located away from the toe of the pier (Figure 9.29). Thus the pier flange will increase the rocking strength of the pier. In contrast, when the pier flange is at the compressive side of the wall, the weight center of the flange is very close to the toe of the pier (Figure 9.30). As a result, it has negligible contribution to the rocking strength of the pier.

In both cases, however, the weight of the spandrel flange is always supported by the pier through the heel of the pier (Figures 9.29 and 9.30). Therefore, the additional vertical compressive force transferred from the spandrel flange to the pier is always away from the toe of the pier and thus increases the rocking strength of this pier.

Another significant difference between the pier flange and the spandrel flange occurs when the spandrel on the tensile side of wall is lifted and separated from the underneath pier due to external overturning moment effects. In this case, the pier, together with its pier flange, is left behind and has no contribution to the lateral resistance of the entire wall. In contrast, the spandrel flange still contributes to the lateral resistance of the wall.

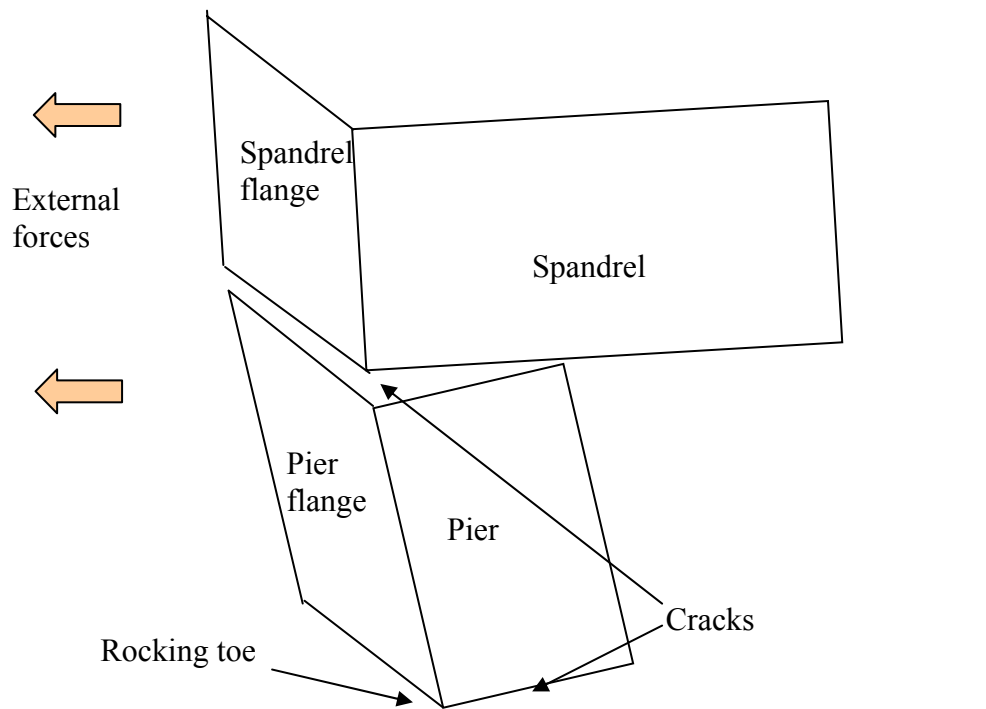


Figure 9.30. Pier flange and spandrel flange on the compressive side of a pier

In the case of a strong pier-weak spandrel wall, the spandrel contributes little to the ultimate strength of the wall. In this case, only the pier flange needs to be considered.

Another issue is the definition of the effective area of a flange. For a case where only a pier flange exists for a pier, the effective flange area has been discussed in Section 5.4 and is illustrated again in Figure 9.36. Rocking causes a crack at the bottom of the pier and the flange. Due to the weight of the flange and/or the forces transferred from other portions of the building, shear stresses exist in the flange. Those shear stresses cause a principal tensile stress about 45° to the vertical edge of the in-plane wall. Since URM is a very brittle material, a crack forms perpendicular to this tensile stress. The exact location of the crack, however, is variable, depending on the distribution of external forces and on the masonry properties. As a simple case, the shadow area shown in Figure 9.31 is the maximum possible effective flange area for this pier. It is formed by a 45° crack initiating at the bottom of the pier, and propagating to up and left until it reaches the top of the wall.

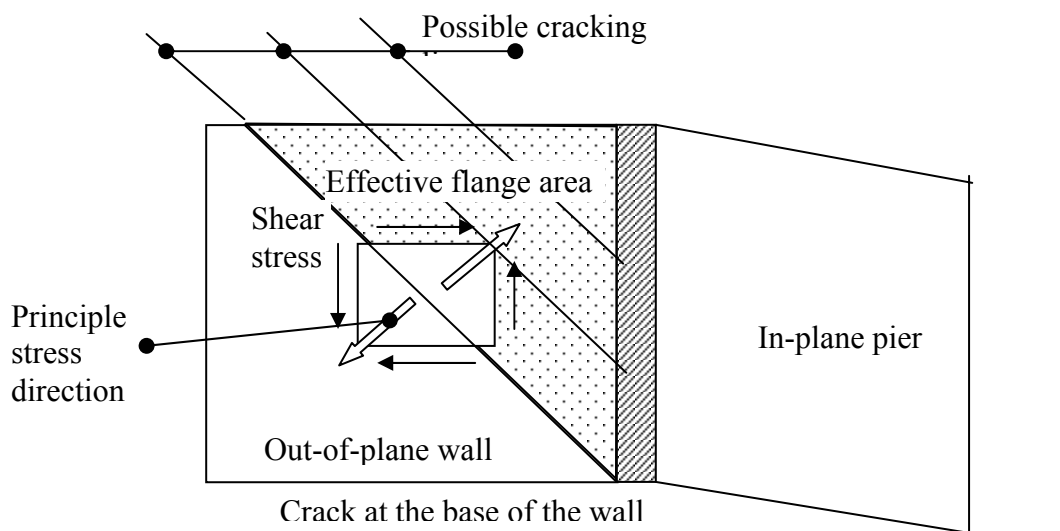


Figure 9.31. Effective area of a pier flange

In the case of a strong spandrel-weak pier wall, the definition of effective flange area is more complex. Taking a pier at the tensile side of a wall for example (Figure 9.32), two cracks are possible to form in the flange. One is the crack initiating from the bottom of the pier (Point C) and propagating at 45° to the top of the wall (Point D); another is the crack propagating from Point A at the top of the in-plane pier to Point B at the top of the flange. As a result, the triangular area above the line AB is the spandrel flange, and the area between Line AB and Line CD is the effective area for the pier flange.

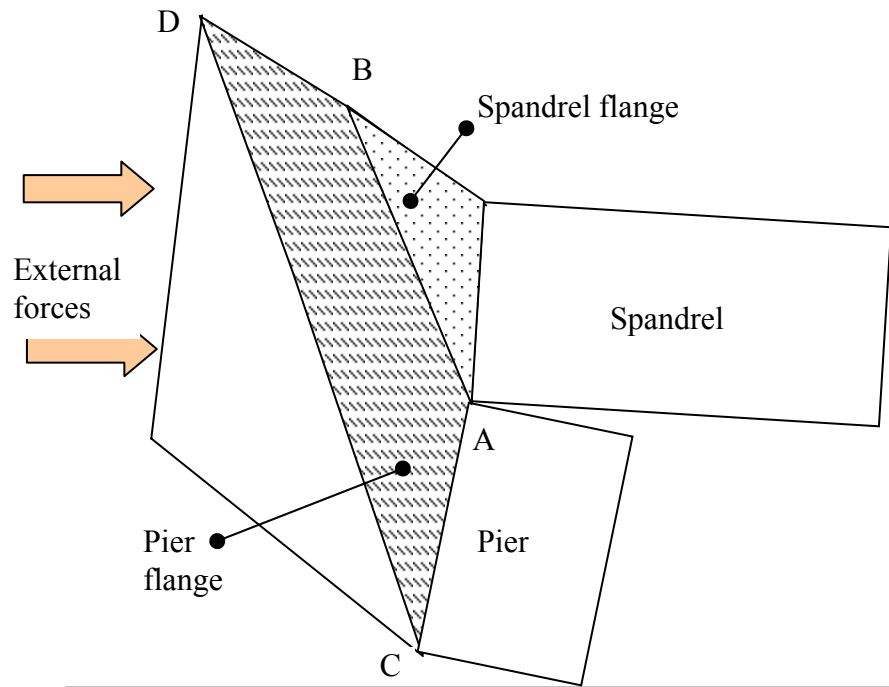


Figure 9.32. Effective area for the pier flange and the spandrel flange in the tensile side of a pier

The determination for the spandrel flange and the pier flange is affected by the distribution of external forces and the crack pattern in the in-plane wall. Figure 9.32 is most likely suitable for a wall with uniformly distributed external forces and the specific in-plane crack pattern shown in the figure. If the flexural crack at the top of the pier is not horizontal, instead going upward and to the left at 45^0 as usually observed in the tests, the area of the spandrel flange will decrease, and the area of the pier flange will increase.

The above discussions are based on a first story exterior pier at the tensile side of a wall. However, the concept also applies to the exterior pier at the higher floors. On the other hand, when the pier is at the compressive side of a wall, the definition for the effective area of the flanges is a little different. As shown in Figure 9.33, the spandrel is lifted due to the rocking of the underneath pier, and thus the effective area for the spandrel flange is defined the same as in the previous case. However, since the pier flange is at the compressive side, no tensile stress is introduced in the flange. In this case, the effective area for the pier flange can be simply determined by the 45^0 line going from the top of the pier to the bottom of the flange, which reflects the flow of the compressive stress in the flange.

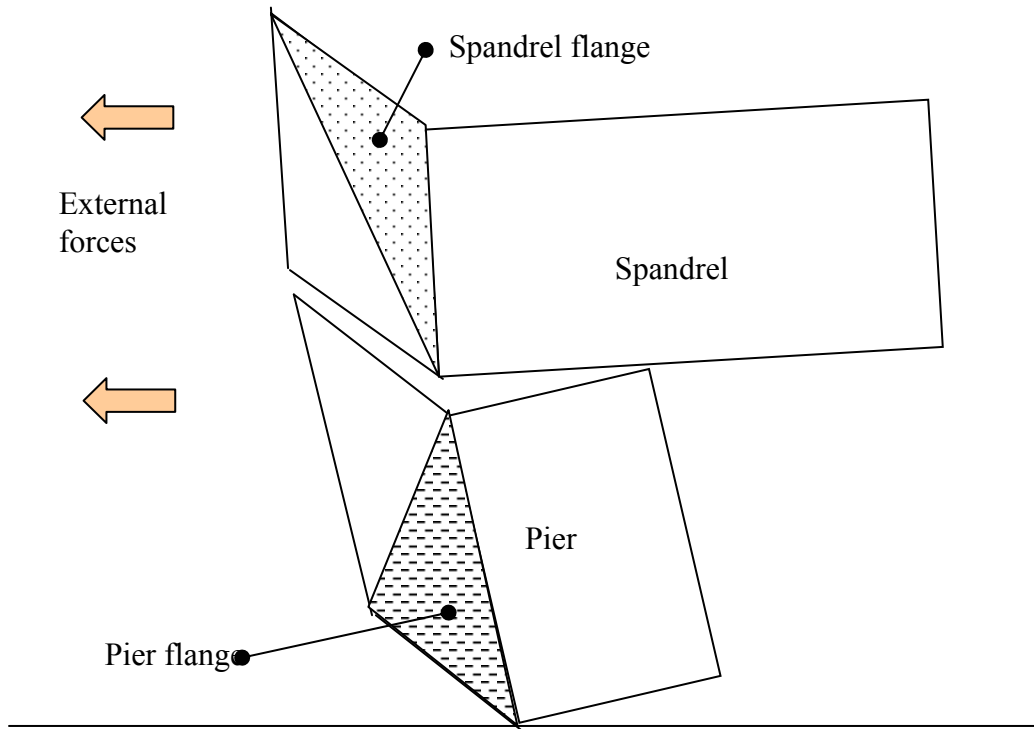


Figure 9.33. Effective area for the pier flange and the spandrel flange in the compressive side of a pier

The last issue that needs to be identified is that the method outlined herein is essentially applicable to a solid out-of-plane wall with large length. When the distance between two parallel in-plane walls is not long enough (see Figure. 5.8), a trapezoid area instead of a triangular one has to be used for the flange of each in-plane wall. On the other hand, when there is a large opening in the out-of-plane wall adjacent to an in-plane pier (Figure. 9.34), the pier flange for this pier is confined inside the local area, since the opening tends to isolate the pier-flange from the other portions of the out-of-plane wall.

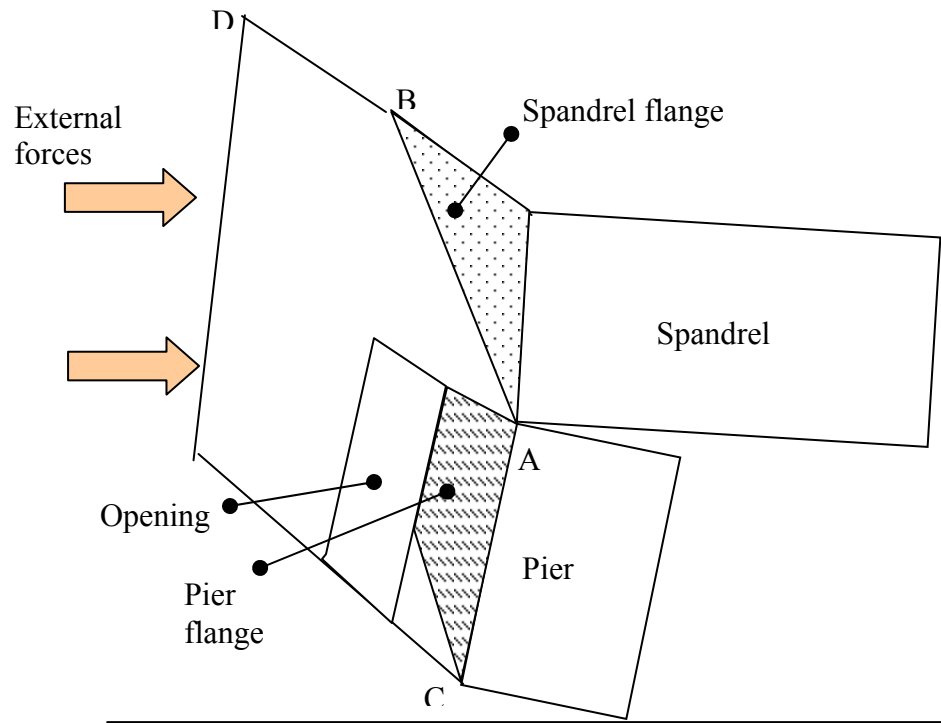


Figure 9.34. Effective flange area for an in-plane pier with adjacent opening in the out-of-plane wall

As an example, the crack patterns in the out-of-plane walls (Walls 1 and 2) observed in this series of tests (shown in Figures 9.12 and 9.23) verifies the above discussion for the particular structure tested in this research project.

In the last URM test cycle (Cycle 26b), when the building was loaded in the push direction (westward), the inclined crack at the top and right of Wall 1 indicates that the triangular portion of masonry wall in Wall 1 above this crack was the ultimate spandrel flange for Pier A-7. At the other side of Wall 1 adjacent to Wall B, the crack defining the flange was not fully developed. Instead, the entire left portion of Wall 1 was lifted up from its base, as shown in Figure 9.12. This crack indicated that much more flange was

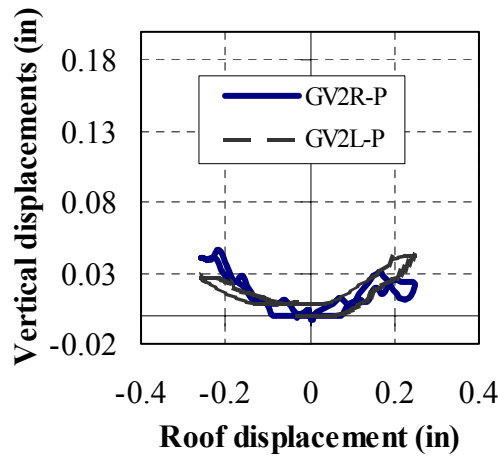
contributing to the lateral resistance of Wall B than of Wall A in this test cycle. This explains the difference in peak lateral shear strength of Wall B in the push direction (39.6 kips) versus that of Wall A (33.0 kips) in this cycle.

When the building was loaded in the pull direction (eastward), as discussed in Section 9.4, a large crack developed at the mid-height of the first spandrel of Wall 2 in Cycle 25b, and separated the entire out-of-plane Wall 2. As a result, the entire second floor of Wall 2 was lifted as the spandrel flange for Walls A and B. In Cycle 26a, another crack propagated from the second floor fixture steel plate in Wall B, and propagated farther at an angle of approximately 45° upward and to the left until it reached the top of Wall 2 (Figure 9.12). As a result, the small triangular portion of Wall 2 above these cracks was lifted as the spandrel flange for Wall B. At this stage there were no new cracks in the flange area of Wall 2 next to Wall A. Therefore, the spandrel flange area for Wall A was larger than that for Wall B. This explains the difference in peak lateral shear strength of Wall A in the pull direction (37.7 kips) versus that of Wall B (33.0 kips) in this cycle.

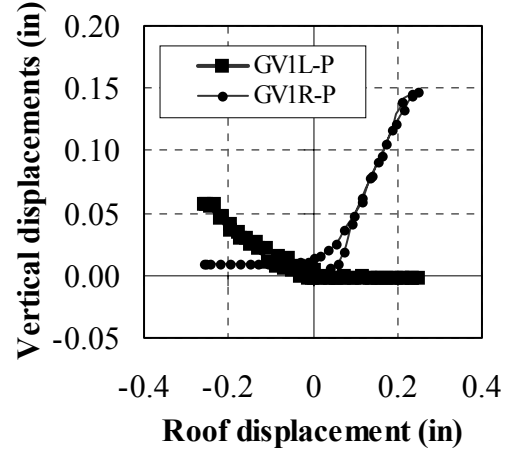
9.5. MIXED BEHAVIOR: GLOBAL OVERTURNING AND LOCAL ROCKING

The vertical movements of Walls 1 and 2 have been discussed in Chapter 8. It is interesting to compare the vertical movements of Walls A and B to those of Walls 1 and 2, as shown in Figure 9.35. When Wall 2 was laterally loaded, the top of both the left side and the right side of Wall 2 were lifted (Figure 9.35a), because Wall 2 was dominated by the local rocking of its first story piers. In contrast, when Wall 1 was laterally loaded, the tensile side of the wall was lifted, while the compressive side of the wall had only small

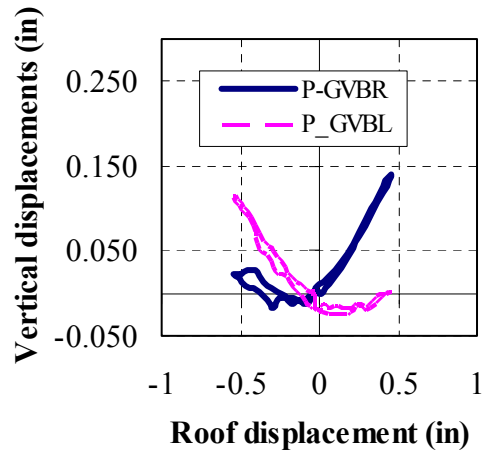
amount of vertical uplift (Figure 9.35b). This is due to the fact that Wall 1 was sliding and rocking globally. The vertical movements of Walls A and B are similar, but are different from those of Walls 1 and 2. When Walls A and B were laterally loaded, the top of the wall at the tensile side was lifted a good amount, and that at the left side was lifted up as well, but with a smaller value (Figure 9.35c,d). This phenomenon indicated that the working mechanisms for Walls A and B were a mixture of global overturning movement and local rocking. The differences in behavior of these four walls are a product of their different configurations. Wall 2 has large openings and slender piers in the first floor. Thus it is easy for this wall to develop component-dominated behavior. In contrast, the small openings in Wall 1 make it easy to develop global-dominated behavior (global overturning and sliding). In the case of Walls A and B, their opening ratios are somewhere between Walls 1 and 2. As a result, their response is a mixed response of global movement and local rocking.



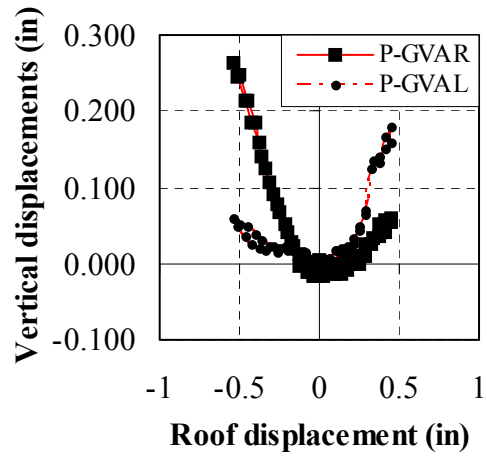
(a) Wall 2



(b) Wall 1



(c) Wall A



(d) Wall B

Figure 9.35. Vertical movements of the masonry walls

9.6. EFFECTIVE PIERS IN A PERFORATED WALL

The effective pier model discussed in Chapters 4 and 5 implies that the response of a URM pier in a perforated wall with weak pier-strong spandrel can be explained by an inclined effective pier defined in the pier. The tests for the ST-11 building parallel to

Walls 1 and 2 indicated that the inclined effective pier for a door pier is different for different loading directions, which can be illustrated as follows.

For an exterior door pier at the right side of the wall, when the wall is loaded from left to right, horizontal cracks develop at the top right and the bottom left of the pier (Figure 9.36). As a result, the aspect ratio for the effective pier is H/L . On the other hand, when the wall is loaded from right to left, a 45° diagonal crack develops from the top left corner of this pier and propagates up and to the right (Figure 9.37). As a result, the aspect ratio for the effective pier is $(H+L)/L$.

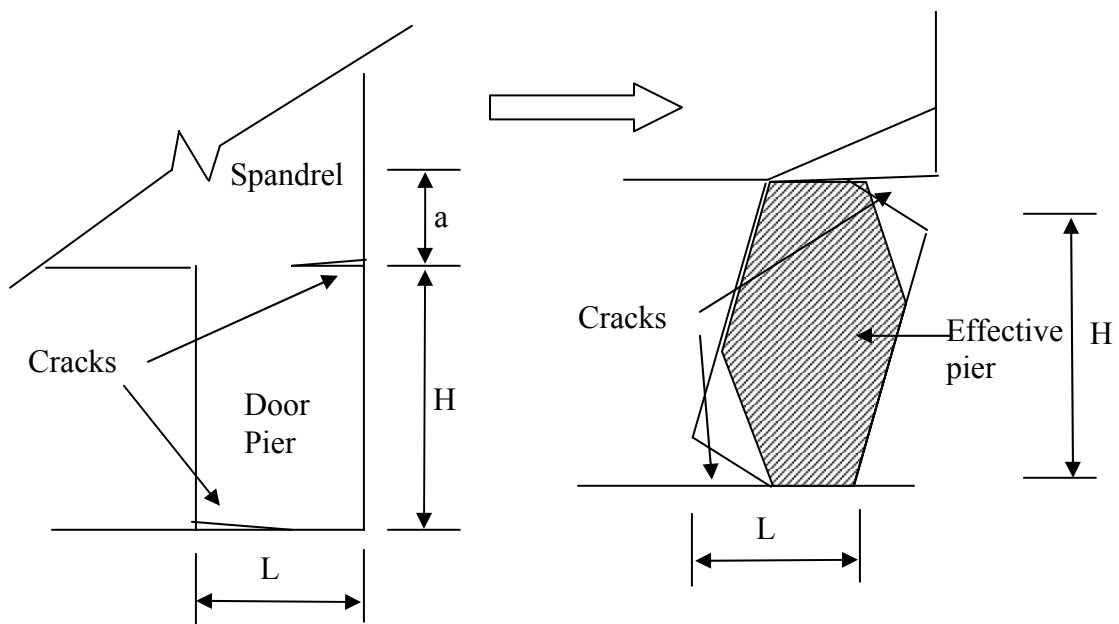


Figure 9.36. Effective pier of a door pier when loaded from left to right

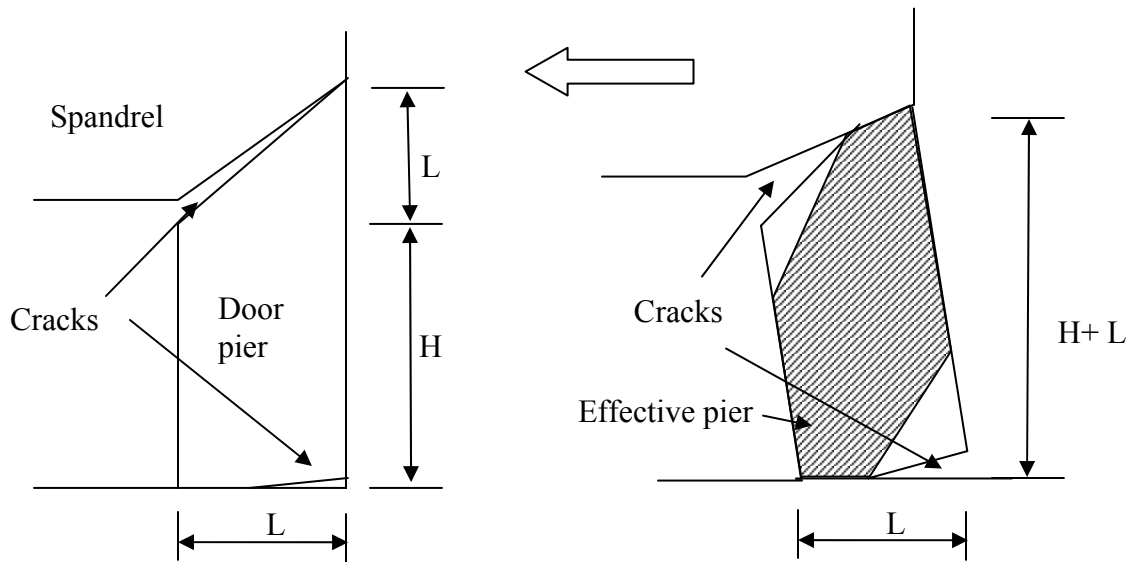
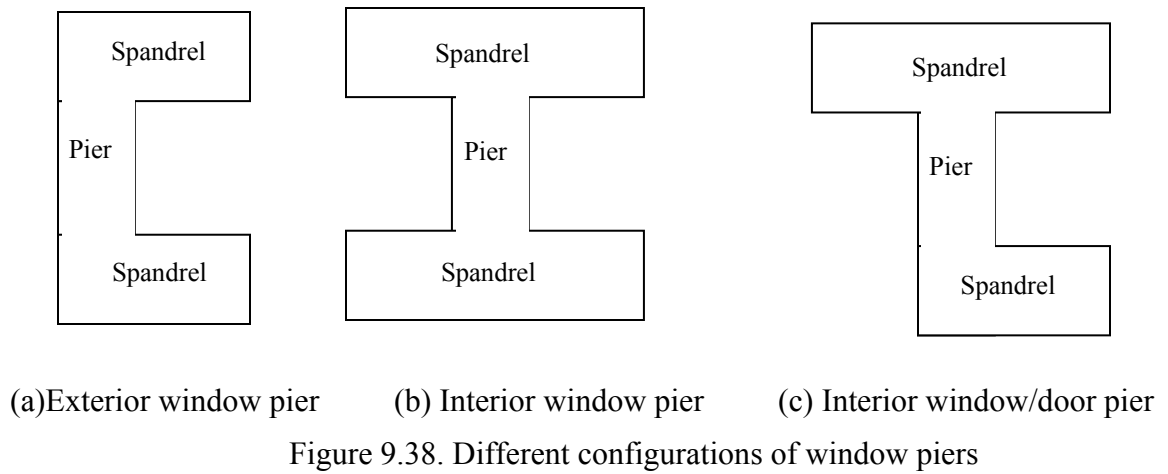


Figure 9.37. Effective pier of a door pier when loaded from right to left

Note that when the exterior door pier is at the left side of the wall, the behavior of the pier is a mirror image to that discussed above. In the case of an interior door pier, it is unlikely for a 45° crack to develop on the top of the pier. Therefore, the aspect ratio for an interior door pier is always H/L .

The tests parallel to Walls A and B gave some information for the determination for an effective pier in a window pier. There are three different types of window piers, which are the exterior window pier (Figure 9.38a), the interior window pier (Figure 9.38b), and the interior window/door pier (Figure 9.38c). The definition of effective pier for those piers can be obtained from the test.



Piers B-9 and A-9 in the test structure are the interior window piers. The tests showed that for an interior window pier rocking caused horizontal cracks to develop at both the top and the bottom of the pier. Therefore, the aspect ratio for this type of pier is always H/L (Figure 9.39).

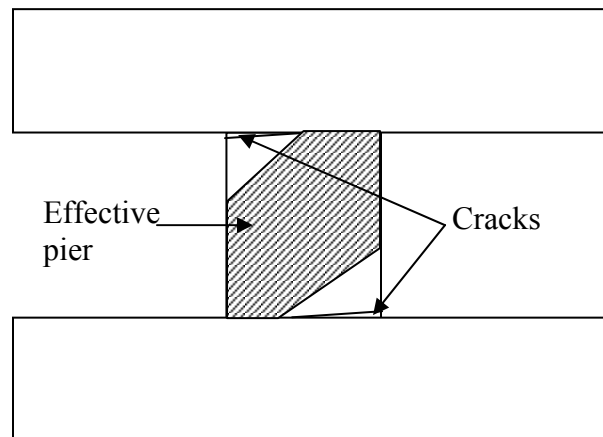


Figure 9.39. Effective pier of an interior window

Piers A-9 and B-8 in the test structure are the interior window/door piers. The tests revealed a quite interesting phenomenon for this type of pier. Taking Pier B-8 as an example, when the pier was laterally loaded so that the side of the pier next to the door opening was in compression, a 45° crack initiated from the bottom window corner, and propagated to the toe next to the door opening (Figure 9.40). Meanwhile, similar to the interior door pier case, a horizontal crack developed at the top of the pier. As a result, the effective pier of this pier went from the top of the pier to the ground, and the aspect ratio of the pier was $(H+a)/L$. On the other hand, when the pier was laterally loaded so that the side of the pier next to the door opening was in tension, the pier worked just like an interior window pier, with horizontal cracks developing at both the top and the bottom of the pier. The aspect ratio of the corresponding effective pier was H/L .

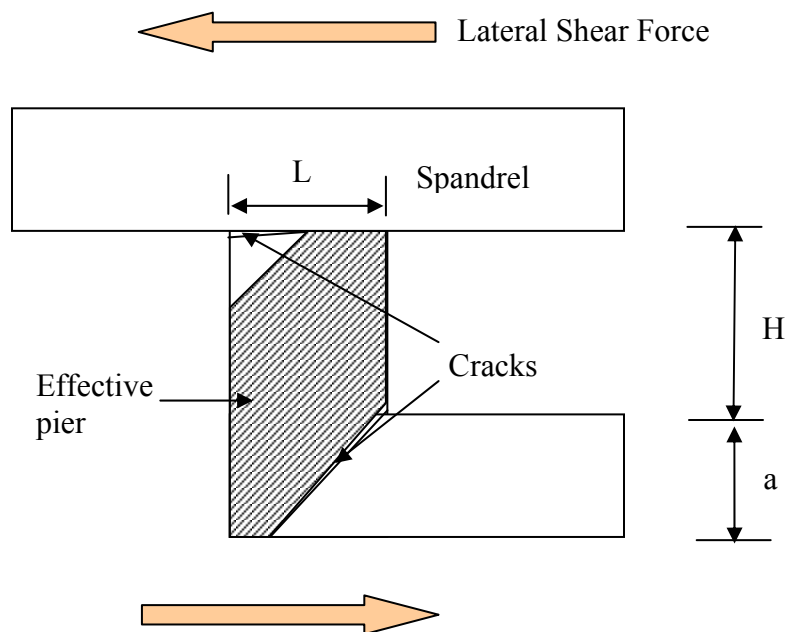


Figure 9.40. Effective pier of a door pier when loaded from right to left

Piers A-7 and B-10 in the test structure are the exterior window piers. The tests showed that their behavior was a combination of exterior door pier and interior window/door pier. Taking Pier B-10 for example. when Wall B was pushed from the right to the left, it worked as an exterior door pier, and a 45° crack initiated at the top left corner of Pier B-10, and propagated upward and to the left (Figure 9.41). Meanwhile, as in an interior window pier, a horizontal crack developed at the right base of the Pier. Therefore, the aspect ratio for the effective pier was $(H+L)/L$. On the other hand, when Wall B was loaded from the left to the right, as an interior window/door pier, a 45° crack initiated at the bottom left corner of this pier, and propagated downward and to the right (Figure 9.42). At the same time, a horizontal crack developed at the right top of the Pier. Therefore, the aspect ratio for the corresponding effective pier was $(H+a)/L$.

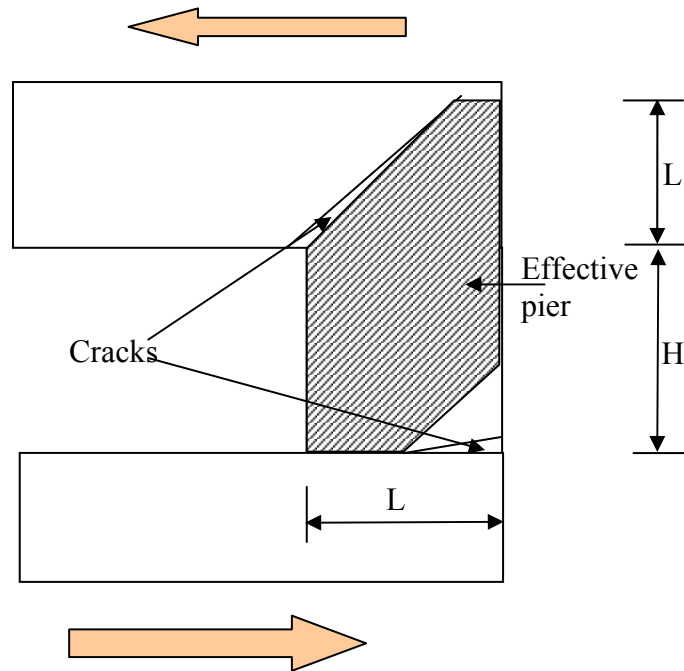


Figure 9.41. Effective pier of an exterior door pier when loaded from right to left

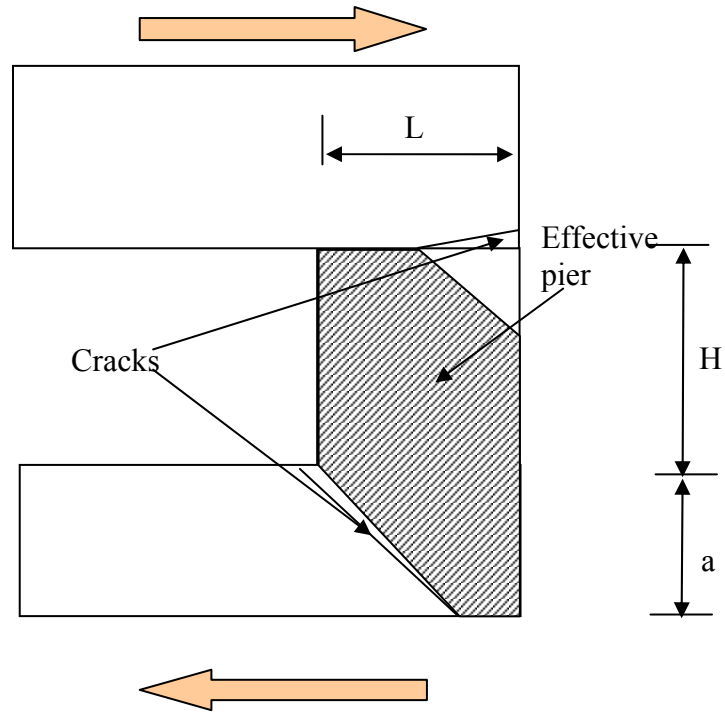


Figure 9.42. Effective pier of an exterior door pier when loaded from left to right

9.7. COMPARISON BETWEEN THE BEHAVIOR OF WALLS A AND B

Walls A and B were identical to each other. The tests showed that their kinematic mechanisms were similar. Moreover, the ultimate crack patterns for the two walls were also similar in spite of different initial cracks. Although flexural cracks were observed in the second floor wall for both walls, the damage for the walls was concentrated in the first story. Both walls exhibited a mixed working mechanism of global overturning and local rocking. When the walls were laterally loaded, the spandrels at the tensile side were lifted above the exterior piers. The latter were left behind and did not resist much lateral shear force. The interior piers rocked, and the exterior piers at the compressive side resisted large vertical compressive and lateral shear forces.

On the other hand, the behavior of the two walls did show some differences. The base shear-lateral roof displacement curves for Walls A and B are compared in Figure 9.43. Wall B reached a maximum lateral strength of 43.0 kips at a displacement of 0.232 in. in the push direction, and 36.9 kips at a displacement of 0.273 in. in the pull direction. In comparison, Wall A reached its maximum lateral strength of 35.70 kips at a displacement of 0.214 in. in the push direction, and 40.8 kips at a displacement of 0.278 in. in the pull direction. As discussed in Section 9.4, the difference sizes in the pier flanges and spandrel flanges between Wall A and Wall B explains the difference in their maximum strengths.

The hysteretic behavior of Wall B exhibited a larger energy dissipation area than that of Wall A. These differences were due to the different flange effects induced by the out-of-plane walls and to the mature level of developed working mechanisms. The larger energy dissipation area of Wall B was also probably due to the relative sliding observed between Wall B first floor spandrel and the tops of Pier B-8 and Pier B-9. Similar behavior was not observed in Wall A. Note that when Wall B was loaded in the push direction, the diagonal crack on the top of Pier B-10, the horizontal cracks on the top of Pier B-8 and B-9, and the diagonal plus horizontal cracks at the bottom of Pier B-7 formed a complete sliding path (Figure 9.12). This allowed the portion of Wall B above and below these cracks to slide. Similarly, when Wall B was loaded in the pull direction, the diagonal crack on the top of Pier B-7, the horizontal cracks on the top of Pier B-8 and B-9, and the diagonal cracks at the mid-height of Pier B-10 developed a complete sliding path again, which allowed Wall B to slide. In contrast, no continuous sliding path formed in Wall A.

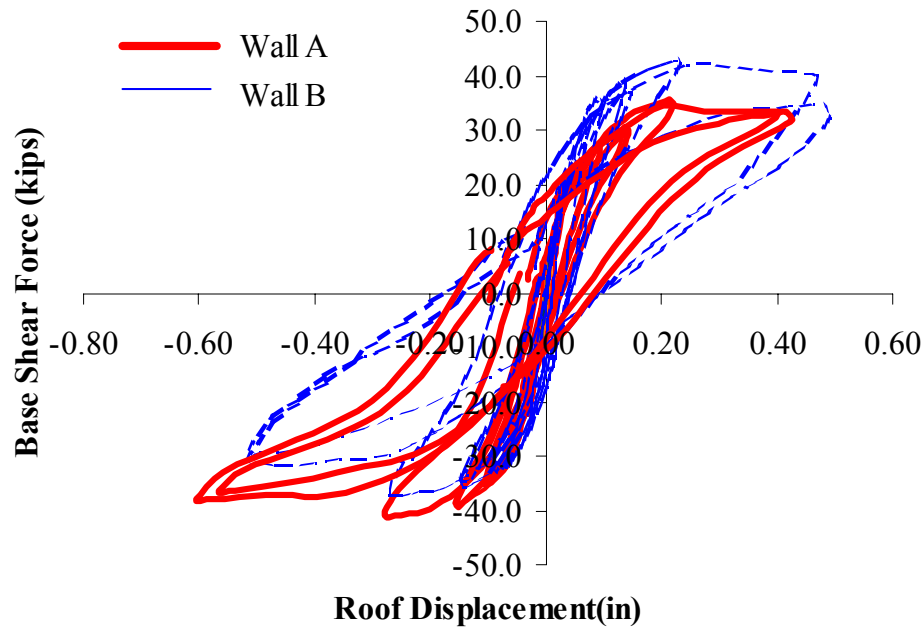


Figure 9.43. Comparison of Wall A and Wall B

It is interesting to compare the response of the test structure parallel to Walls A and B and that parallel to Walls 1 and 2. The maximum lateral strength of the test structure parallel to Walls 1 and 2 was 87 kips in the push direction and 79 kips in the pull direction, which is close to the maximum strength of the test structure parallel to Walls A and B (79 kips in the push direction and 78 kips in the pull direction). This is probably due to the box configuration of the test structure and the contribution of the flange effects. On the other hand, the roof drift corresponding to the peak strength was 0.02% in the direction parallel to Walls 1 and 2 (see Chapter 8), which was much smaller than that in the direction parallel to Walls A and B, 0.07%. The difference was due to the initial damage existing in the structure prior to the tests parallel to Walls A and B.

9.8. EFFECTIVE SECANT ELASTIC MODULUS, NATURAL PERIOD, AND VIBRATION MODES

Following similar procedure as used for the tests parallel to Walls 1 and 2, the effective secant elastic moduli of the tested structure were calculated for each test cycle (Table 9.8). Comparing the values for Walls A and B for secant stiffness to those measured in the previous tests parallel to Walls 1 and 2 (Table 8.13), it is clear that there was initial damage to the building prior to the tests parallel to Walls A and B. With increasing lateral roof displacement, the secant modulus decreased from about 500 ksi in Cycle 20c to about 30 ksi in Cycle 26b.

Table 9.8. Elastic modulus of the test structure parallel to Walls A and B (ksi)

Cycles	Wall A (+)	Wall A (-)	Wall B (+)	Wall B (-)
20c	481	728	563	530
21b	316	322	344	483
22b	170	207	226	204
23b	140	143	175	150
24b	105	102	136	103
25b	79	51	93	52
26b	32	28	28	23

Again, considering each in plane wall (Walls A or B) as a two-degree-of-freedom system with lumped masses at the roof and the second floor levels, the measured lateral displacements and lateral forces are used to calculate its first natural period and the corresponding vibration mode. The calculated results for Walls A and B are listed in Table 9.9. The table shows that the natural periods of both Walls A and B increased from 0.06 seconds to about 0.27 seconds with increasing lateral roof displacements. As a

general trend, the ratio between the second floor displacement and the roof displacement of the vibration mode of Walls A and B increased, because the damage of the walls was concentrated on the first story wall. However, as an exception, the mode shape of Wall A corresponding to the pull direction loading was always about 0.75, probably due to the fact that the global rocking was more prominent in this wall.

Table 9.9. Natural periods and vibration modes of Walls A and B

		Wall A		Wall B	
		Natural Period (seconds)	Vibration mode (second floor/roof)	Natural Period (seconds)	Vibration mode (second floor/roof)
20c	+	0.06	0.77	0.06	0.85
	-	0.06	0.77	0.06	0.76
21b	+	0.075	0.77	0.072	0.83
	-	0.08	0.79	0.08	0.83
22b	+	0.107	0.83	0.093	0.88
	-	0.1	0.78	0.111	0.86
23b	+	0.115	0.86	0.105	0.89
	-	0.114	0.76	0.127	0.86
24b	+	0.153	0.88	0.133	0.92
	-	0.131	0.71	0.145	0.85
25b	+	0.19	0.81	0.193	0.9
	-	0.168	0.72	0.183	0.82
26b	+	0.256	0.89	0.270	0.85
	-	0.266	0.75	0.296	0.91

9.9. DISCUSSIONS

Besides the issues discussed in the above sections, there were some other interesting phenomena that were observed in the test and needed to be pointed out:

9.9.1. Arch lintel

Arch lintels are one of the common types of lintels used in the existing URM buildings. The tests parallel to Walls A and B revealed a potential hazard of this type of lintel. Under external forces, a crack developed at the top of the arch lintel (Crack A in Figure 9.44). Since the header joints are usually weaker than the bed joints, Crack A easily propagates into the header joints, such as Cracks B and C as shown in Figure 9.44. With cyclic loading, the cracks in the arch lintel become larger and larger. As a result, some portion of the arch lintel might lose its stability and fall down. An example of this type of failure is the damaged arch lintel of the door opening in Wall A, as shown in Figure 9.45.

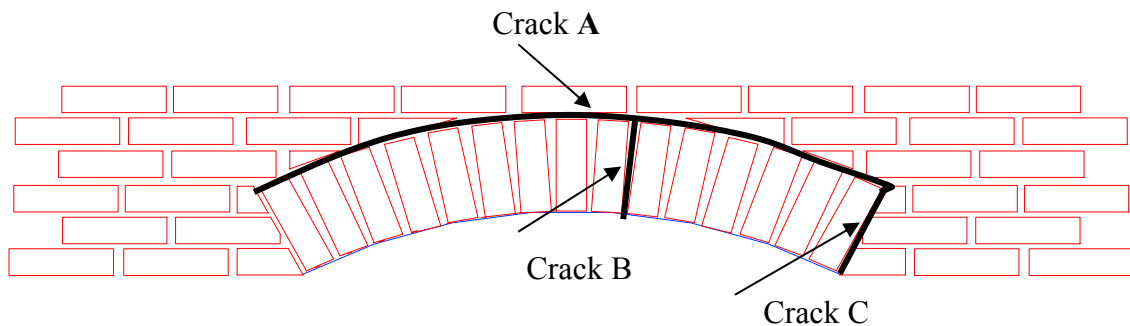


Figure 9.44. Typical cracks in an arch lintel



Figure 9.45. Picture of the damaged arch lintel in Wall A (over Wall A first-story door opening)

9.9.2. Continuous opening of cracks during the cyclic loading

Previous tests for individual pier indicated that although rocking or sliding might occur in a pier, the residual opening of the cracks or the relative sliding in the pier closed or diminished after a complete test cycle. However, this was not true for the cracks in a perforated wall. Large residual crack openings were observed in both the tests parallel to Walls 1 and 2 and in those parallel to Walls A and B. This phenomenon is due to different kinematic mechanisms of the walls in different loading directions. Taking Wall A for example, when the wall was loaded in the push direction, the diagonal crack on the top of A-7 opened due to rocking and sliding (see Figure 9.25). When the wall was loaded in the pull direction, the crack opening on the top of Pier A-7 did not close. Instead, the rocking and sliding deformation of Wall A caused another diagonal crack, which was at the bottom of Pier A-7, to open (see Figure 9.26). The different kinematic mechanisms in different loading directions caused crack widths in a URM building to

grow during cyclic loading. During a seismic event, such growing cracks might eventually cause a masonry wall to lose its stability and collapse.

9.9.3. Toe crushing and diagonal tension cracks

FEMA 356 points out the four typical failure modes of a URM pier: rocking, sliding, toe crushing, and diagonal tension (ATC 2000). For the test structure, the observed failure modes for the piers were rocking and sliding. The other two failure modes, toe crushing and diagonal tension cracks, were not observed. This was due to the small gravity stresses applied to the structure and the relatively small lateral displacements imposed in the tests.

9.10. CONCLUSIONS

Quasi-static cyclic lateral displacements were applied on Walls A and B to investigate the behavior of the test building in the direction parallel to Walls A and B. Some of the main conclusions obtained in the previous tests parallel to Walls 1 and 2 were verified. For example, little coupling between two parallel in-plane walls was evident,; and the mixed behavior of global overturning and local rocking were observed again. On the other hand, some new phenomena and conclusions were obtained from this series of tests. They are as follows:

- The initial effective modulus of masonry parallel to Walls A and B was about 500 ksi. This value was smaller than the initial elastic modulus of 1000 ksi for the tests parallel to Walls 1 and Wall 2. This reduction in E was due to the initial

damage that occurred to the masonry walls prior to the tests parallel to Walls A and B. The effective modulus gradually reduced with increasing lateral displacements to a value of 30 ksi in Cycle 26b. This loss was a clear indication of the damage accumulation in the walls during the tests. The maximum lateral strengths of the test structure were 79 kips in the push direction (36 kips on Wall A and 43 kips on Wall B), and 77 kips in the pull direction (40 kips on Wall A and 37 kips on Wall B). The roof drifts corresponding to the maximum lateral strength were about 0.07%. Compared with the maximum lateral strength (87 kips in the push direction and 79 kips in the pull direction) and the corresponding roof drift (0.02%) obtained in the direction parallel to Walls 1 and 2, the maximum strength values were similar. The similar strengths were probably due to the box configuration of the test structure and the contribution of the flange effects. The response of Walls A and B was softer than that of Walls 1 and 2, again due to the initial damage existing in the walls.

- The response of Walls A and B were similar to each other. Both of them exhibited a mixed kinematic mechanism consisting of a combination of global overturning and local rocking. When the walls were laterally loaded, the spandrels at the tensile side were lifted up above the exterior piers; those exterior piers were left behind and did not resist much lateral shear force. The interior piers rocked, and the exterior piers at the compressive side resisted large vertical compressive and lateral shear forces. The wall behavior fell somewhere between the rocking-dominated response of Wall 2 and the global movement-dominated response of

Wall 1. This was due to the fact that the first-story opening ratios of Walls A and B were between those of Walls 1 and 2.

- On the other hand, the behavior of Walls A and B did show some differences. In the push direction, the maximum strength of Wall B was a little larger than that of Wall A. In the pull direction, the maximum strength of Wall A was a little larger than that of Wall B. This difference was due to the different size of flanges engaged by Walls A and B. Furthermore, the force-displacement curves of Wall B exhibited larger energy dissipation area compared with Wall A. This was probably due to some sliding response observed in Wall B that was not seen in Wall A.
- The flange effects were further investigated in the tests parallel to Walls A and B. Based on the phenomena observed in this series of tests as well as in the previous tests parallel to Walls 1 and 2, it was concluded that the flange effects due to the contribution of the out-of-plane walls could be distinguished between a pier-flange effect and a spandrel-flange effect. The determination of the pier flange and the spandrel flange is different between a strong pier-weak spandrel wall and a weak pier-strong spandrel wall. The two different types of flanges have different effects on the response of a pier depending on whether the flange is on the tensile side or the compressive side of the wall. The method to determine the area of those two flanges is discussed in this chapter.
- Another interesting finding in this series of tests was the method to determine the effective piers in a perforated wall. Depending on the location of a pier and the direction of external forces, cracks with different propagation directions may

develop in a URM pier. This cracking, in turn, determines the size and location of the effective pier. Based on the tests parallel to Walls 1 and 2, a method was given to define the effective pier when a door pier is present. Based on the tests parallel to Walls A and B, a similar method can be used to define the effective pier in a window pier.

- Other important conclusions include that the commonly used arch lintels are prone to damage and that crack widths in a URM building tend to grow during cyclic loading.

CHAPTER 10

PRELIMINARY ANALYSES OF ST-11 BUILDING

10.1. INTRODUCTION

In preparation for the experimental test described in the previous chapters, extensive analytical studies were conducted. This chapter describes the initial analyses conducted for the experimental design and as the test was being carried out. Chapters 11 and 12 describe the more advanced ones that were carried out after the test.

The preliminary analyses were composed of two parts. In the first part, elastic analyses were employed to predict the elastic properties of this test building. This part of analyses includes both a 3D finite element (FE) elastic model and a simplified dynamic conceptual model. The 3D FE elastic model was employed to obtain estimates of elastic properties such as stiffness and to provide insight into three-dimensional effects such as coupling between parallel walls and flange effects in the elastic range. The simplified dynamic conceptual model was developed to analyze the dynamic parameters of the test structure, such as natural frequencies and vibration mode shapes. The response of the test structure to seismic vibrations was also examined with this simple model.

Based on the elastic properties from the above analyses and the results from previous experimental research, the second part of the preliminary analyses utilized simple analytical tools to predict the inelastic properties of this test building. Among those properties are the ultimate strength and the failure modes. This part of analyses started with a performance evaluation based on the pre-standard FEMA 356 (ATC 2000).

Two procedures provided by FEMA 356, the linear static procedure (LSP) and the nonlinear static procedure (NSP), were utilized to evaluate the performance of the test structure in several different seismicity zones. These approaches were assumed to give lower bound prediction as to how the test structure would behave in a real earthquake. Following that, a rigid body analysis, which was based on the observed kinematic mechanism of the test building, was then utilized to analyze the ultimate strength of the test structure. The analyses results were used as a guide prior to testing the ST-11 test structure, and were compared with the experiment results. The assumptions behind these analyses and their results are presented in this chapter.

10.2. THREE DIMENSIONAL ELASTIC FINITE ELEMENT ANALYSIS

As mentioned previously, a three-dimensional FE elastic analysis was utilized to provide insight into the test structure's performance in the elastic range. Specifically, the objectives of this portion of the analysis were to obtain estimates of the following quantities:

- Gravity stresses in each pier
- Out-of-plane elastic stiffness
- In-plane elastic stiffness
- Coupling behavior
- Flange effects
- Locations of highly stressed zones in the masonry walls under lateral forces

The FE model developed included both the perforated masonry walls and the wood floor and roof diaphragms of the ST-11 test structure. Since the stud wall in the

test structure only supported vertical loads and provided negligible lateral stiffness, its strength was ignored in the FE model. After comparing the accuracy and the computational efforts for several different element types and sizes, a 4-node doubly curved, reduced integration shell element (S4R) with a mesh size of 4 inches were used to model the masonry wall and the wood diaphragm (Yi et al. 2002). In the analysis, the density of masonry was taken as 0.06944 lb/in^3 , the elastic modulus was taken as 1000 ksi, and the Poisson's ratio was taken as 0.25.

The model was built using the commercial FE analysis program ABAQUS. The 3D model of the ST-11 building is shown in Figure 10.1. The model consisted of 27,344 nodes, 26,909 elements, and 164,064 degrees of freedom.

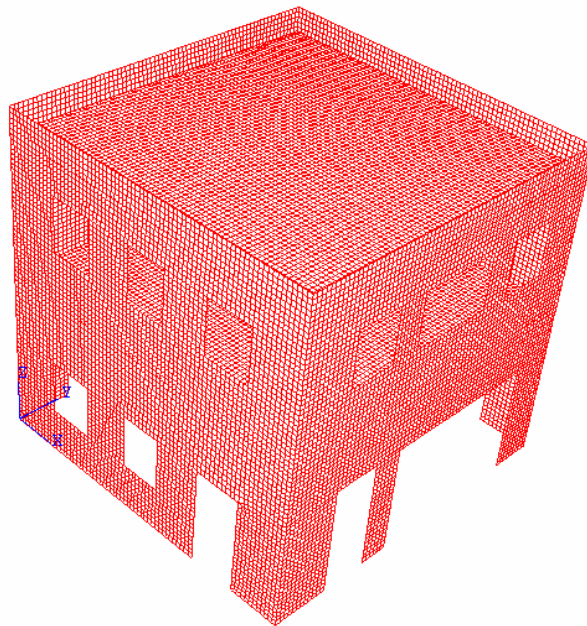


Figure 10.1. Three-dimensional model of the ST-11 building

10.2.1. Diaphragm elastic stiffness

Due to the configuration of the sheathing and joists, the determination of the elastic stiffness of the wood roof and floor diaphragm used in the ST-11 building is not straightforward. Theoretically, this type of diaphragm displays orthotropic behavior since the joists and sheathing run in perpendicular directions. However, in order to keep the model simple, an isotropic material was employed for the diaphragm. The elastic modulus of the isotropic material was selected to provide an elastic stiffness consistent with the results of past experimental research.

MAEC project ST-8 (Peralta et al. 2000) tested several different wood diaphragm systems. One of their test diaphragms, the MAE-2 diaphragm, had a similar configuration to the diaphragms used in the ST-11 building. It should be mentioned that the size of the MAEC-2 diaphragm tested in the ST-8 project (i.e. 24 ft. x 12ft.) was approximately half the size of the diaphragms employed in the ST-11 test structure (i.e. 24 ft. x 24 ft.). Results from the ST-8 testing program showed that the lateral secant stiffness of this diaphragm gradually degraded from 20.6 kips/in to 4.0 kips/in with increasing lateral displacement. Since the diaphragms of the ST-11 structure were twice the size of the diaphragms tested in ST-8, the experimentally measured stiffness was altered to calibrate the model. Based on analysis results obtained through ST-8, the lateral stiffness for the ST-11 roof and floor diaphragms was assumed to be 7.0 kips/in.

In the ST-11 ABAQUS 3D model, S4R shell elements (discussed previously) were used to model the diaphragm. The thickness of the shell element was assumed to be 1 inch. Through trial and error it was determined that an elastic modulus of 2.8 ksi along

with a Poisson's ratio of 0.25 provided a lateral diaphragm stiffness of approximately 7.0 kips/in. As a result, these values were used in the analysis.

10.2.2. Gravity stresses

Estimates of the vertical stress in each pier due to gravity loads were obtained using the 3D elastic FE analysis. The calculated gravity stresses in each pier are listed in Table 10.1. The designation of each pier was given in Figures 6.7 through 6.9.

Table 10.1. Gravity stresses in the piers

Pier	Gravity stress (psi)	Pier	Gravity stress (psi)
A-2	8	B-2	8
A-3	9	B-3	9
A-4	9	B-4	9
A-5	7	B-5	6
A-7	23	B-7	28
A-8	25	B-8	23
A-9	26	B-9	25
A-10	22	B-10	19
1-2	8	2-2	7
1-3	8	2-3	12
1-4	7	2-4	9
1-6	20	2-5	8
1-7	23	2-7	26
		2-8	37
		2-9	30

This table shows that the vertical stresses due to gravity loads in each pier are rather low, with a maximum value of 37 psi. These relatively low vertical stresses are expected, as the gravity load is caused only by the structure's self-weight (i.e. there is no added weight to simulate the building contents).

10.2.3. Elastic out-of-plane wall stiffness

An estimate of the elastic out-of-plane stiffness of each wall of the ST-11 test structure was obtained by utilizing the 3D FE model. The out-of-plane stiffness was defined as:

$$K_o = \frac{V}{u_{center} - 0.5(u_1 + u_2)} \quad (10.1)$$

where, V is the total out-of-plane force, u_{center} is the out-of-plane displacement of the masonry wall at the center point of the roof level, and u_1 , u_2 are the displacements of each in-plane wall at the roof level, respectively (see Figure 10.2).

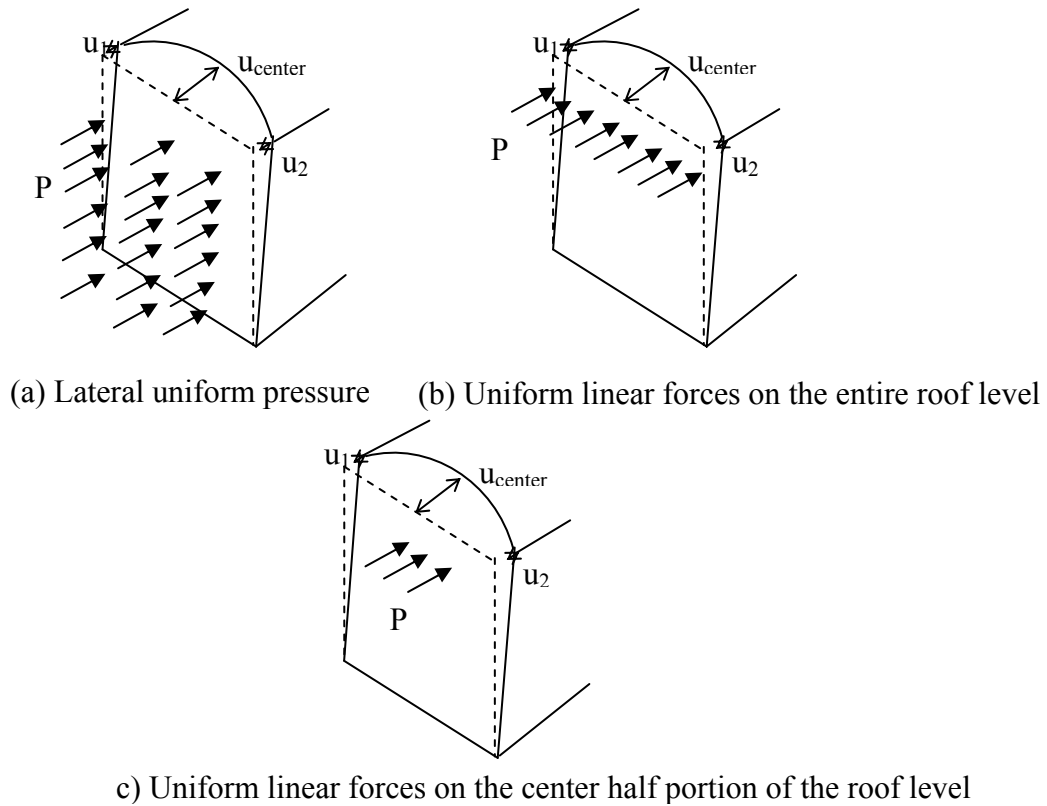


Figure 10.2. Out-of-plane loading of the masonry wall

To simulate possible external force pattern on a URM building, three different loading cases were employed to obtain estimates of the out-of-plane wall stiffness: 1) uniform lateral pressure (Figure 10.2a); 2) uniform linear force applied along the entire roof level (Figure 10.2b); and 3) uniform linear force applied along the center half of the roof level (Figure 10.2c). In addition, to gain insight into the contribution of the roof and floor diaphragms to the out-of-plane stiffness of the masonry walls, the out-of-plane deformations of the masonry walls were calculated both with and without roof/floor diaphragm connections. The results are listed in Table 10.2.

Table 10.2. Out-of-plane stiffness of the masonry walls (kips/in)

Out-of-plane stiffness (kips/in)		Without roof/floor diaphragms	With roof/floor diaphragms	Contributions of roof/floor diaphragms
Wall A	Uniform pressure	-	190.5	-
	Full roof force	75.8	81.2	5.4
	Half roof force	51.5	55.0	3.5
Wall 1	Uniform pressure	-	130.0	-
	Full roof force	44.7	49.6	4.9
	Half roof force	28.5	31.5	3.0
Wall 2	Uniform pressure	-	104.4	-
	Full roof force	39.1	43.8	4.7
	Half roof force	25.0	27.9	2.9

The table shows that the estimated out-of-plane stiffness for Walls A and B are larger than those for Walls 1 and 2. This is expected since Walls A and B are three-wythes in thickness, while Walls 1 and 2 are two-wythe in thickness. Furthermore, the out-of-plane stiffness of Wall 1 is larger than that of Wall 2. This is due to the relatively small wall openings ratio of Wall 1 as compared to that of Wall 2.

The table also shows that the out-of-plane stiffness of the walls is dependent on the distribution of the external force. Uniformly applied pressure leads to a higher stiffness estimate than an applied linear force does. Furthermore, the presence of the floor and roof diaphragms increases the out-of-plane stiffness of the masonry walls. However, this increase is minor because the stiffness of the diaphragms is small compared with that of the masonry walls. In the case of the ST-11 building, the calculated out-of-plane stiffness of the masonry walls are between 4 to 30 times of the stiffness of the diaphragms depending on the type of external forces and the configurations of the walls, which is consistent with the behavior observed in the roof test (see Chapter 7).

10.2.4. Elastic in-plane wall stiffness and coupling behavior

The 3D elastic FE model was used to obtain estimates of the in-plane wall stiffness as well as the coupling effect. Coupling effects refer to the coupling supplied between in-plane walls by either the diaphragm or the out-of-plane walls. This coupling is important because it can cause torsional action in an unsymmetric structure during seismic excitation, and lead to severe damage.

In order to investigate the in-plane stiffness and coupling effects of the walls in the ST-11 test structure, four loading cases were employed. The loading cases were: (1) equal lateral force applied at both the roof and floor levels of the two parallel in-plane walls (Figure 10.3a); (2) equal lateral force applied at the roof level of the two parallel in-plane walls (Figure 10.3b); (3) equal lateral force applied at both the roof and floor level of one in-plane wall, with the displacement of the other in-plane wall constrained (Figure

10.3c); and (4) lateral force applied at the roof level of one in-plane wall, with the displacement of the other in-plane constrained (Figure 10.3d).

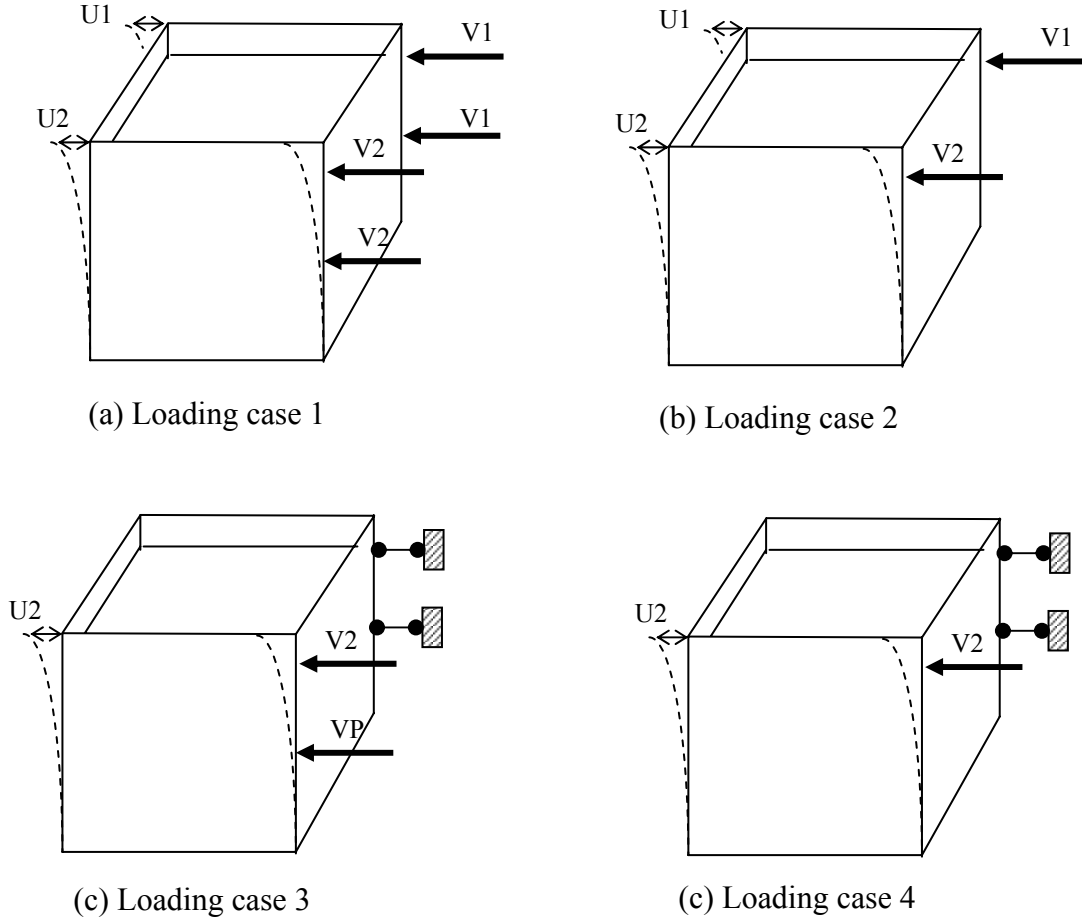


Figure 10.3. Different loading cases for calculation of the in-plane stiffness of masonry walls

The in-plane behavior of the masonry walls can be described by the following equation:

$$\begin{bmatrix} k_{11} & k_{12} \\ k_{12} & k_{22} \end{bmatrix} \begin{Bmatrix} u_1 \\ u_2 \end{Bmatrix} = \begin{Bmatrix} V_1 \\ V_2 \end{Bmatrix} \quad (10.2)$$

where, u_1 and u_2 are the in-plane lateral roof displacements of the in-plane walls; V_1 and V_2 are the lateral in-plane forces applied on the walls, k_{11} and k_{22} are the in-plane stiffness of the masonry walls, and k_{12} is the coupling stiffness. The calculated results are listed in Table 10.3.

Table 10.3. Calculated in-plane stiffness of the masonry walls (kips/in)

		Equal forces at the roof and the floor	Forces applied at the roof
Walls A, B	In-plane stiffness of Wall A	2031	1507
	In-plane stiffness of Wall B	2048	1523
	Coupling stiffness	45	46
Walls 1, 2	In-plane stiffness of Wall 1	2506	1817
	In-plane stiffness of Wall 2	731	588
	Coupling stiffness	2.5	6

Table 10.3 shows that Wall 1 displays the highest stiffness while Wall 2 displays the lowest stiffness. This is expected due to the large differences in the wall openings ratios for these two walls. Comparing Table 10.2 and Table 10.3, it can be seen that the in-plane stiffness of the masonry walls is much higher than their out-of-plane stiffness. The ratios range from 13.4 for Wall 2 to 50.5 for Wall 1. Table 10.3 also shows that the coupling stiffness is negligible compared to the in-plane stiffness, which is consistent with the behavior of the masonry walls observed in the tests (see Chapter 8). As a result, the coupling behavior between two in-plane walls was ignored in further analysis.

10.2.5. Flange effects

In order to facilitate the use of a two-dimensional analysis of in-plane masonry walls, the effect of the out-of-plane wall on the in-plane behavior (i.e. the so-called flange effect) must be assessed. The in-plane stiffness of the walls determined through the 3D analysis in the previous section include this flange effect. For comparison the elastic stiffness of each masonry wall was calculated again as a plane-stress problem without considering the contribution of the out-of-plane walls. The same shell element and the same element size were used in the analysis. The calculated in-plane stiffness of the four walls obtained from both analysis methods are shown in Table 10.4.

Table 10.4. In-plane stiffness of the masonry walls with and without flange effects (kips/in)

		3D analysis	2D analysis	Ratios between 3D analysis and 2D analysis
Wall A	Equal forces on both the roof and the floor	2031	1515	1.34
	Forces applied on the roof	1507	1100	1.37
Wall B	Equal forces on both the roof and the floor	2048	1515	1.35
	Forces applied on the roof	1523	1100	1.39
Wall 1	Equal forces on both the roof and the floor	2506	1606	1.56
	Forces applied on the roof	1817	1157	1.57
Wall 2	Equal forces on both the roof and the floor	731	464	1.58
	Forces applied on the roof	588	379	1.55

The analysis results show that the flange effect can considerably increase the elastic in-plane stiffness of the masonry walls. The increase for the test structure ranges from 34% to 58%.

10.2.6. Locations of Highly Stressed Zones

While the 3D FE elastic analysis cannot model damage, such an analysis can provide information on locations of highly stressed zones in which cracks can be expected to initiate. For such a purpose, equal forces were applied at both the roof and floor levels of each in-plane wall as this is fairly indicative of seismic loading (Calvi et al. 1996). The maximum calculated Von Mises stresses for each of the walls of the ST-11 test structure is shown in Figures 10.4 through 10.6. These figures show that for the selected loading case, the highly stressed zones for each of the walls are located in the first floor piers. This is expected as these piers are subjected to the largest shear force.

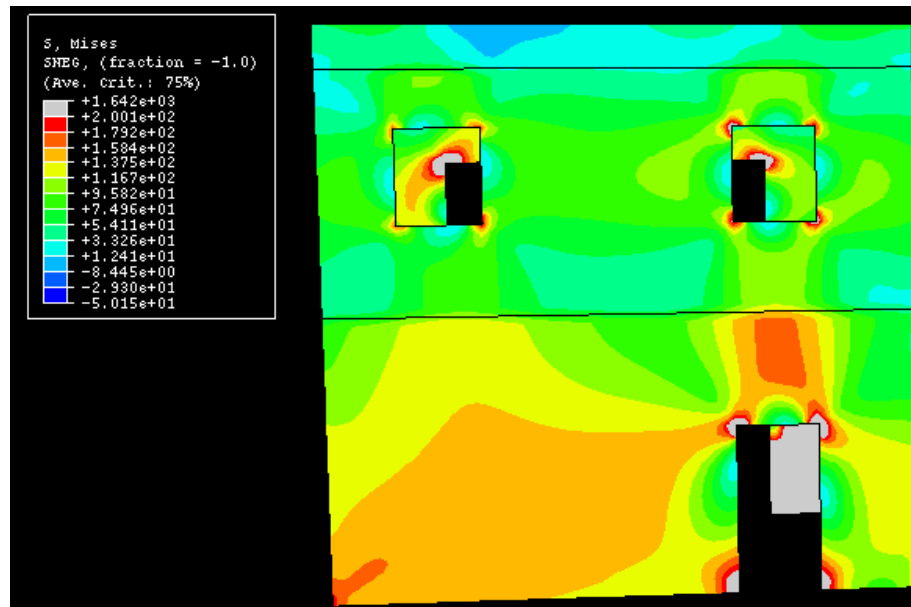


Figure 10.4. Maximum Von Mises stresses in the Wall 1 under in-plane loading (looking west)

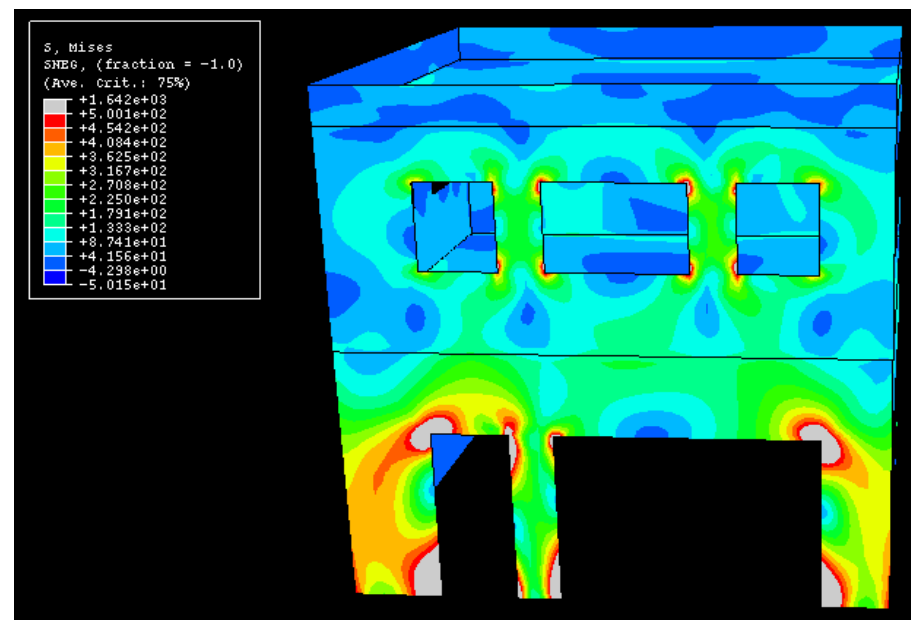


Figure 10.5. Maximum Von Mises stresses in the Wall 2 under in-plane loading (looking east)

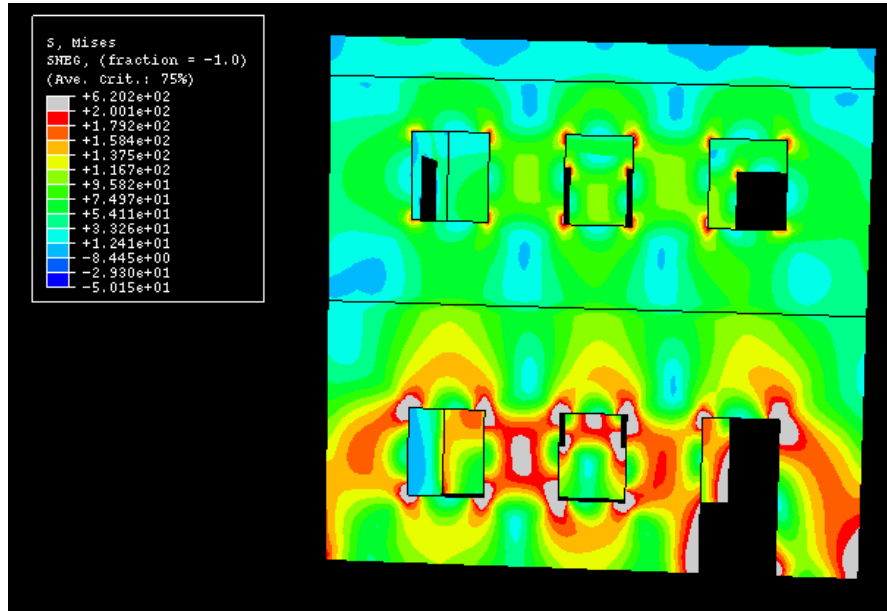


Figure 10.6. Maximum Von Mises stresses in Walls A and B under in-plane loading (looking south)

10.3. DYNAMIC ANALYSIS BASED ON A CONCEPTURAL MODEL

Due to the large number of elements required for the elastic FE model, the investigation of the test structure's dynamic properties based on the previous 3D model is nearly impossible. As a result, a simplified conceptual model was developed. Essentially, the dynamic performance of the test structure as a whole is dominated by the interaction between the in-plane walls, the out-of-plane walls, and the flexible diaphragms. Considering this, a conceptual model containing three lumped masses and four elastic springs can be used to represent the basic components of an URM building (i.e. in-plane wall, out-of-plane wall and floor/roof diaphragm) (Yi et al. 2001). The model is shown in Figure 10.7, which is similar to the model used in Chapter 7 to illustrate the working mechanism of the diaphragm-masonry wall system (see Figure 7.22). However, in order to simplify the analysis, the connection between the out-of-

plane wall and the diaphragm was assumed rigid. The nomenclature for each component can be given in Section 7.5.3.

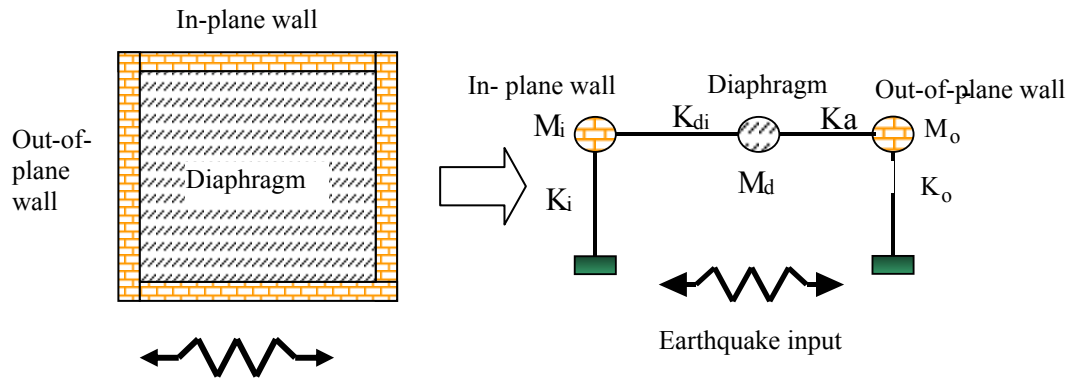


Figure 10.7. Conceptual model of an URM structure

10.3.1. Natural periods and vibration mode shapes of the test structure

The first analysis was conducted assuming that Walls A and B were in-plane and Walls 1 and 2 were out-of-plane. Based on the results of the 3D elastic FE analysis and past experiment data, the properties listed in Table 10.5 were used in the analysis of the ST-11 test structure.

Table 10.5. Structural properties used in analysis with Walls A and B in-plane

Stiffness of in-plane wall: K_i (kips/in)	4079 ⁽¹⁾
Stiffness of out-of-plane wall: K_o (kips/in)	234 ⁽²⁾
Axial stiffness of the floor/roof diaphragm: K_{do} (kips/in)	1740 ⁽³⁾
Shear stiffness of the floor/roof diaphragm: K_{di} (kips/in)	14 ⁽⁴⁾
Weight of the in-plane wall: W_i (kips)	116 ⁽⁵⁾
Weight of the out-of-plane wall: W_o (kips)	69 ⁽⁶⁾
Weight of the diaphragm: W_d (kips)	45 ⁽⁷⁾
<p>Note:</p> <ol style="list-style-type: none"> 1. The stiffness of the in-plane wall was taken as combined in-plane stiffness of Walls A and B assuming equal forces were applied at the roof level and the floor level. 2. The stiffness of the out-of-plane wall was taken as the combined out-of-plane stiffness of Walls 1 and 2 assuming a uniformly applied lateral pressure. 3. The axial stiffness of the floor/roof diaphragm was based on the axial stiffness of the sheathing. 4. The shear stiffness of the diaphragm was the combined shear stiffness of the floor and roof diaphragms, which were both assumed to be 7 kips/in based on the test results of ST-8. 5. The weight of the in-plane wall was taken as the total weight of Walls A and B. 6. The weight of the out-of-plane wall was taken as the total weights Walls 1 and 2. 7. The weight of the diaphragm was taken as the total weight of the floor and roof diaphragms, including 15psf of dead load and 50psf of live load. 	

To assess the possible effects of the inherent variability of the mechanical properties of masonry, two additional sets of stiffness values were used in a sensitivity analysis. One set of the stiffness values represented a lower bound on stiffness (i.e. a flexible structure) while the other represented an upper bound on stiffness (i.e. a stiff structure). The stiffness values used in each case are listed in Table 10.6.

Table 10.6. Elastic stiffness used for sensitivity analysis (Walls A and B in-plane)

	AB-Flexible	AB-Basic	AB-Stiff
K_i (kips/in)	1360	4079	8158
K_o (kips/in)	78	234	468
K_{di} (kips/in)	14	14	140
K_{do} (kips/in)	580	1740	3480

The stiffness and mass matrices of the conceptual model are shown in Eqs. (10.3) and (10.4), respectively. The natural periods of the structure obtained through the solution of the Eigenvalue problem are shown in Table 10.7. The vibration mode shapes of each structure were scaled so that the largest displacement is equal to one and presented in graphical form in Figure 10.8 (note: the y-axis represents each component of the structure with 0 = ground, 1 = in-plane wall, 2 = diaphragm, and 3 = out-of-plane wall, and the x-axis represents displacement in each mode).

$$\begin{bmatrix} K_i + K_{di} & -K_{di} & 0 \\ -K_{di} & K_{di} + K_{do} & -K_{do} \\ 0 & -K_{do} & K_{do} + K_o \end{bmatrix} \quad (10.4)$$

$$\begin{bmatrix} W_i \\ W_d \\ W_o \end{bmatrix} \quad (10.5)$$

Table 10.7. Natural periods of the conceptual model (Walls A and B in-plane)

Natural period (s)	AB-Flexible	AB-Basic	AB-Stiff
Mode 1	0.356	0.218	0.1385
Mode 2	0.093	0.054	0.0378
Mode 3	0.068	0.039	0.0277

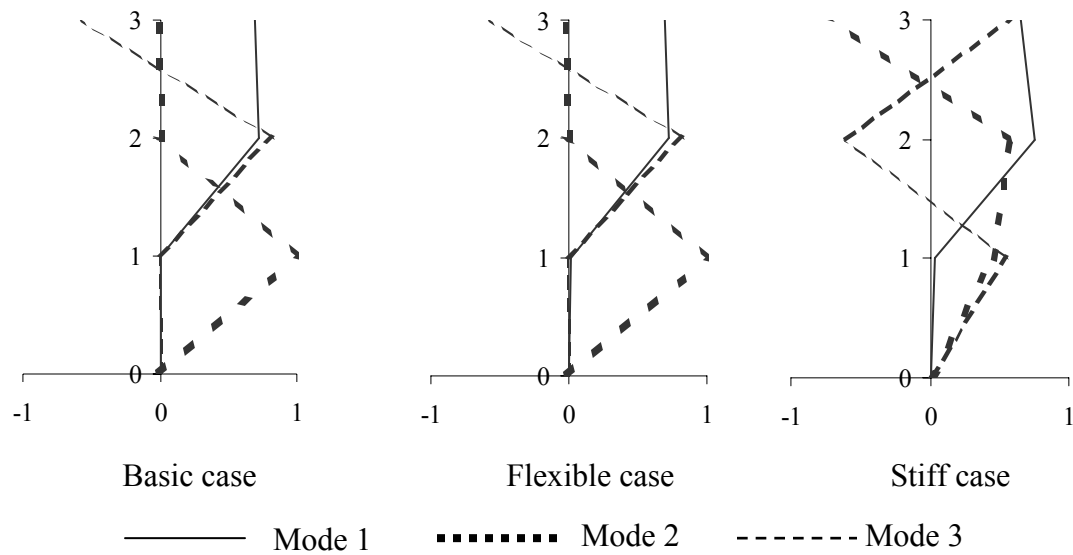


Figure 10.8. Vibration modes for the test structure (Walls A and B in-plane)
(Y axis, 0: ground; 1: in-plane wall; 2: diaphragm; 3: out-of-plane wall)

The second analysis conducted assumed that Walls 1 and 2 were in-plane and Walls A and B were out-of-plane. The properties used in this analysis are shown in Table 10.8 and were determined from the elastic FE analysis.

Again, to assess the effect of the inherent variability of masonry materials, two additional sets of stiffness values were used for a sensitivity analysis. One set of the stiffness values represented a very flexible structure while the other represented a very stiff structure. The stiffness values used in each case are listed in Table 10.9.

The calculated natural periods of the structure are given in Table 10.10. The mode shapes corresponding to each natural period are shown in Figure 10.9. Again, the y-axis represents each component of the structure with 0 = ground, 1 = in-plane wall, 2 =

diaphragm, and 3 = out-of-plane wall, and the x-axis represents displacement in each mode.

Table 10.8. Structural properties used in analysis with Walls 1 and 2 in-plane

Stiffness of in-plane wall K_i (kips/in)	3237 ⁽¹⁾
Stiffness of out-of-plane wall K_o (kips/in)	381 ⁽²⁾
Axial stiffness of the floor/roof diaphragm K_{do} (kips/in)	1740 ⁽³⁾
Shear stiffness of the floor/roof diaphragm K_{di} (kips/in)	14 ⁽⁴⁾
Weight of the in-plane wall W_i (kips)	69 ⁽⁵⁾
Weight of the out-of-plane wall W_o (kips)	116 ⁽⁶⁾
Weight of the diaphragm W_d (kips)	45 ⁽⁷⁾
<p>Note:</p> <ol style="list-style-type: none"> 1. The stiffness of the in-plane wall was taken as combined in-plane stiffness of Walls 1 and 2 assuming equal forces were applied at the roof level and the floor level. 2. The stiffness of the out-of-plane wall was taken as the combined out-of-plane stiffness of Walls A and B assuming a uniformly applied lateral pressure. 3. The axial stiffness of the floor/roof diaphragm was based on the axial stiffness of the sheathing. 4. The shear stiffness of the diaphragm was the combined shear stiffness of the floor and roof diaphragms, which were both assumed to be 7kps/in based on the test results of ST-8. 5. The weight of the in-plane wall was taken as the total weight of Walls 1 and 2. 6. The weight of the out-of-plane wall was taken as the total weights Walls A and B. 7. The weight of the diaphragm was taken as the total weight of the floor and roof diaphragms, including 15psf of dead load and 50psf of live load. 	

Table 10.9. Elastic stiffness used for sensitivity analysis (Walls 1 and 2 in-plane)

	12-Flexible	12-Basic	12-Stiff
K_i (kips/in)	1079	3237	6474
K_o (kips/in)	127	381	762
K_{di} (kips/in)	14	14	140
K_{do} (kips/in)	580	1740	3480

Table 10.10 Natural periods (seconds) of the conceptual model (Walls 1 and 2 in-plane)

	12-Flexible	12-Basic	12-Stiff
Mode 1	0.343	0.205	0.1355
Mode 2	0.08	0.046	0.0326
Mode 3	0.074	0.043	0.0301

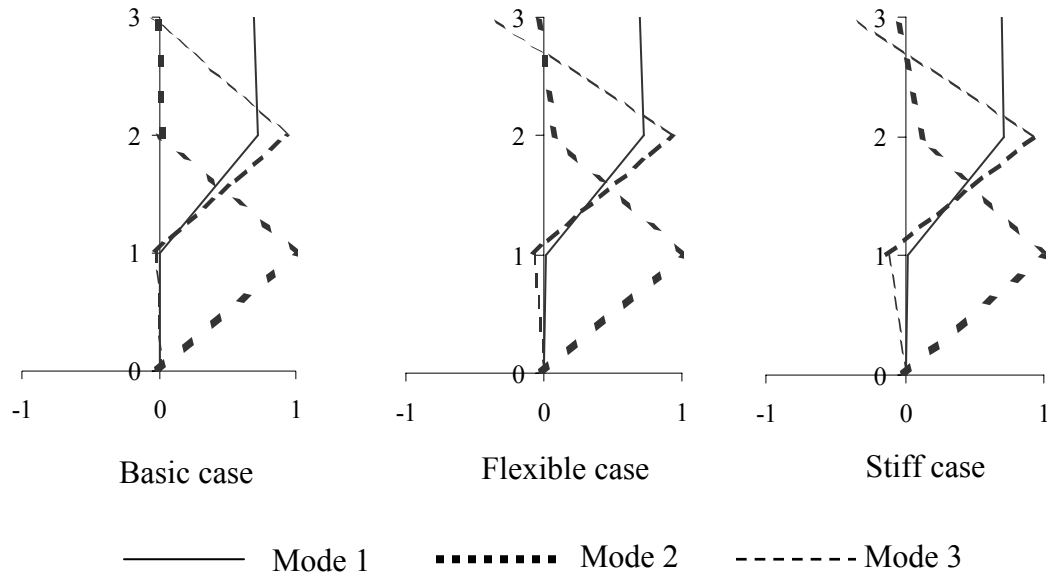


Figure 10.9. Vibration modes for the test structure (Walls 1 and 2 in-plane)
 (Y axis, 0: ground; 1: in-plane wall; 2: diaphragm; 3: out-of-plane wall)

The calculated fundamental natural periods range from 0.14 to 0.36 seconds, which suggests that this URM structure is very stiff. The second and third natural periods of the structure are less than 0.1 seconds, and fall into the decreasing range of the hazard response spectra for Mid-America (ATC 1997, Wen 2001). The low values for the second and third natural periods indicate that the first mode will dominate the behavior of the URM structure under seismic excitation. The analyses results also show that the possible variations in the stiffness of the structure have little effect on the overall mode shapes. In the first vibration mode, the in-plane wall does not move much, while the out-of-plane wall and the floor/roof diaphragm vibrate in phase. Since the first mode dominates the response of the structure, this suggests that out-of-plane masonry walls are most vulnerable to seismic vibrations, as observed in previous seismic events (Bruneau 1994b).

10.3.2. Dynamic analysis based on the conceptual model

Dynamic analyses were also conducted using the conceptual model and two artificial Mid-America ground motions. The first ground motion is indicative of a rock site, with a peak ground acceleration of 0.26g and a predominant period of about 0.1 seconds (Wen 2001). The second ground motion is representative of a soil site, with a peak ground acceleration of 0.50g and a predominant period of about 0.15 seconds. The time histories of the two earthquake motions are shown in Figures. 10.10 and 10.11, respectively.

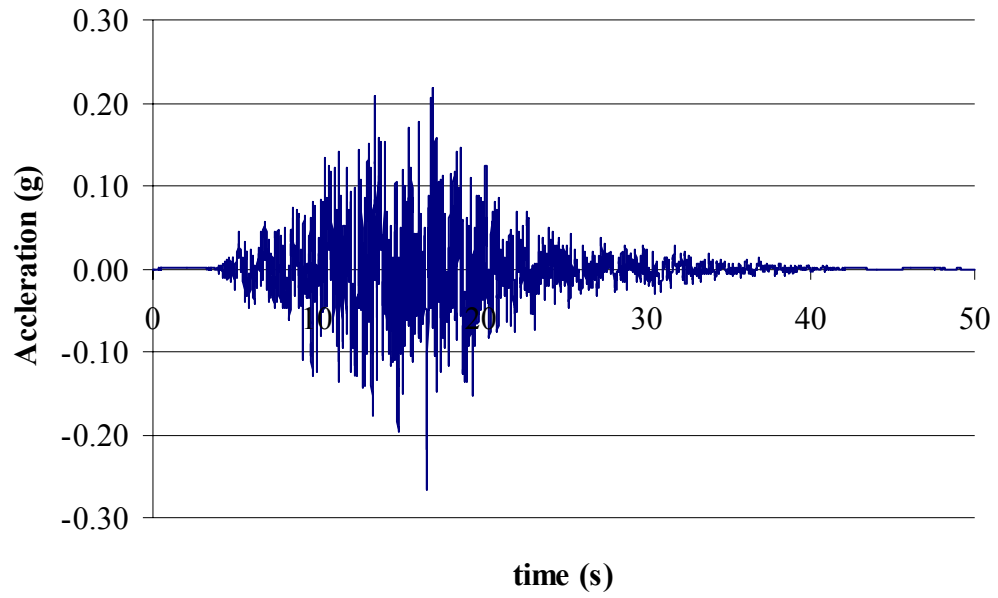


Figure 10.10. Artificial Mid-America ground motion (rock site)

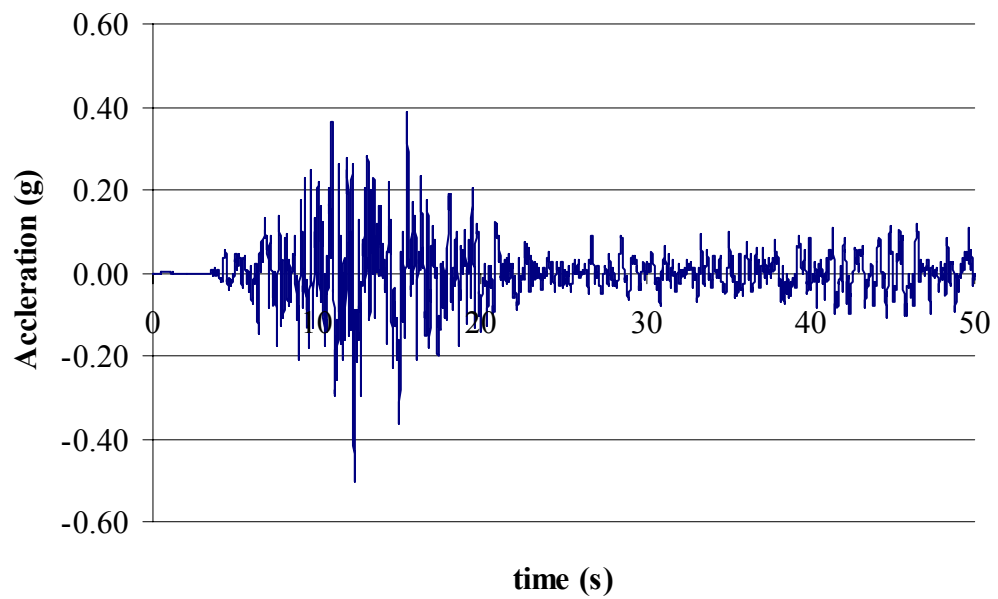


Figure 10.11. Artificial Mid-America ground motion (soil site)

The calculated maximum displacements of each component for the six different structures discussed before are listed in Table 10.11, where $\Delta_{in-plane}$ is the maximum displacement of the in-plane wall relative to the ground, $\Delta_{out-of-plane}$ is the maximum displacement of the out-of-plane wall relative to the ground, and $\Delta_{diaphragm}$ is the maximum displacement of the diaphragm relative to the in-plane wall. This table shows that the displacements of the out-of-plane walls are much larger than those of the in-plane walls. This supports the early contention that the out-of-plane walls are the weak component of a URM structure. Furthermore, the results indicate that the displacements of the in-plane walls are very small. This is expected due to the large stiffness of the in-plane walls.

Table 10.11. Maximum displacements of the URM structure under seismic load

Ground motions	Structure samples	$\Delta_{in-plane}$ (in)	$\Delta_{out-of-plane}$ (in)	$\Delta_{diaphragm}$ (in)
Rock site	AB-flexible	0.035	0.329	0.337
	AB-basic	0.009	0.173	0.179
	AB-stiff	0.006	0.085	0.084
	12-flexible	0.021	0.345	0.347
	12-basic	0.009	0.138	0.150
	12-stiff	0.004	0.082	0.081
Soil site	AB-flexible	0.067	0.979	0.973
	AB-basic	0.013	0.377	0.387
	AB-stiff	0.009	0.154	0.153
	12-flexible	0.039	0.849	0.874
	12-basic	0.010	0.402	0.418
	12-stiff	0.008	0.127	0.125

* Note: all the displacements relative to ground displacements.

The calculated maximum base shears for the in-plane walls, the out-of-plane walls, and the entire structure are listed in Table 10.12 for the six different structures analyzed. The maximum base shears are presented in terms of percentages of the total structural weight. The analyses results show that the maximum base shears for the structure are about 0.3 of the total structural weight in the rock site, and about 0.6 of the total structural weight in the soil site. Compared with the maximum ground acceleration of 0.26g in the case of the rock site, and 0.50g in the case of the soil site, this suggests that the amplification of ground acceleration to URM structures is small.

On the other hand, the table shows that the out-of-plane walls tend to take more seismic base shear than the in-plane walls, which again indicates potential damage to the out-of-plane walls of the URM structure.

Table 10.12. Maximum base shears of the URM structure and each component under seismic loads

Ground motions	Structure samples	The in-plane wall (g)	The out-of-plane wall (g)	The entire structure (g)
Rock site	AB-flexible	0.210	0.113	0.201
	AB-basic	0.162	0.178	0.261
	AB-stiff	0.223	0.132	0.307
	12-flexible	0.099	0.193	0.261
	12-basic	0.123	0.231	0.296
	12-stiff	0.114	0.275	0.376
Soil site	AB-flexible	0.401	0.336	0.606
	AB-basic	0.233	0.388	0.532
	AB-stiff	0.323	0.317	0.568
	12-flexible	0.185	0.475	0.606
	12-basic	0.143	0.674	0.760
	12-stiff	0.228	0.426	0.631

10.4. SEISMIC EVALUATION OF THE TEST STRUCTURE BASED ON FEMA 356 METHDOLOGY

Pre-standard FEMA 356 (ATC 1999) provides a full set of methodologies to evaluate the seismic resistance of an existing building. In this standard, four earthquake hazard levels are defined to describe probabilistic seismic hazard. Among them, the BSE-1 with a 10%/50 year exceedance level and the BSE-2 with a 2%/50 year exceedance level are widely used. For each earthquake hazard levels, four different performance levels, which include the operational performance level (OP), the immediate occupancy performance level (IO), the life safety performance level (LS), and the collapse prevention performance level (CP), are used to describe the performance of an existing building in a possible seismic event.

Based on FEMA 356 methodology, the seismic performance of the test structure was evaluated for four different locations: Memphis, St. Louis, Atlanta, and San Francisco. Among these locations, San Francisco belongs to a high seismicity zone; Memphis and St. Louis belong to moderate seismicity zones; and Atlanta belongs to a low seismicity zone. The short-period response acceleration parameter, S_s , and the long-period response acceleration parameter, S_1 , for the four locations can be obtained for both BSE-1 and BSE-2 from the FEMA ground motion maps published by USGS, and are listed in Tables 10.13 and 10.14.

Table 10.13. Response acceleration parameters (g) (BSE-1)

	Atlanta	Memphis	St. Louis	San Francisco
S_s (g)	0.11	0.28	0.21	1.21
S_1 (g)	0.04	0.07	0.056	0.58

Table 10.14. Response acceleration parameters (g) (BSE-2)

	Atlanta	Memphis	St. Louis	San Francisco
SS (g)	0.26	1.3	0.6	1.81
S1 (g)	0.11	0.4	0.19	1.0

In order to evaluate the seismic resistance of an existing building, four typical analysis procedures are specified in FEMA 356, which include:

- Linear static procedure (LSP),
- Linear dynamic procedure (LDP)
- Nonlinear static procedure (NSP)
- Nonlinear dynamic procedure (NDP)

FEMA 356 also gives the limitations for the use of each procedure (ATC 2000). Considering these limitations, both the LSP and the NSP can be used to analyze the test URM structure. Therefore, both the two procedures were employed to analyze the building. The details of these analyses can be found in Appendices D and E. The main conclusions obtained from the two procedures are presented in the following sections.

10.4.1. LSP

“The linear static procedure (LSP) maintains the traditional use of a linear stress-strain relationship” (ATC 2000). However, adjustment factors are used for the demands and the resistances of the building under analysis to permit better consideration of the nonlinear characteristics of the seismic response. The general procedure for this method is as follows. First, based on the location, the site class, and the general structural characteristics of the building, as well as the seismic hazard level under consideration, the pseudo seismic lateral load for a given horizontal direction of the building (V), can be

determined (FEMA 356, Eq. (3-10)). Second, based on whether the response of the building is deformation-controlled or force-controlled, the deformation-controlled actions (demands), Q_{UD} , or the force-controlled actions (demands), Q_{UF} , for each component of the structure can be calculated through linear analysis (FEMA 356, Eq. (3-18) and Eq. (3-19)). The expected strength of the component for deformation-controlled actions, Q_{CE} , and the lower-bound strength of the component for force-controlled actions, Q_{CL} , can be estimated based on material properties and simplified formulas. Finally, the performance of the building for a particular probabilistic seismic hazard can be checked by the following two acceptance criteria:

For deformation-controlled actions,

$$mkQ_{CE} \geq Q_{UD} \quad (\text{FEMA 356, Eq. (3-20)}) \quad (10-6)$$

For force-controlled actions,

$$kQ_{CL} \geq Q_{UF} \quad (\text{FEMA 356, Eq. (3-21)}) \quad (10-7)$$

For a deformation-controlled action, the possible contribution of the nonlinear ductility of the building is incorporated by the use of the factor m , which depends on the structural type, the failure mechanism and the target performance level. The value of m is larger than 1. For a force-controlled action, the possible contribution of the nonlinear ductility of the building is incorporated by the use of a force-delivery reduction factor J when calculating the seismic demand Q_{UF} . The different treatment is resulted from the different nature of the responses.

For the test structure, the pseudo seismic lateral load V was calculated for both the BSE-1 and BSE-2 ground motions for four different cities. The results are listed in Table 10.15.

Table 10.15. Pseudo seismic lateral load V (kips)

	Atlanta	Memphis	St. Louis	San Francisco
BSE-1: 10% /50 year	24.8	46.8	37.6	301.6
BSE-2: 2% /50 year	62.2	266.5	126.6	465.7

In order to obtain the strength of the test structure, four perforated walls (Walls A, B, 1, and 2) were identified as four structural components and checked for their performance. The elastic model for each wall is conceptually illustrated in Figure 10.12. The model is composed of rigid spandrels and elastic piers.

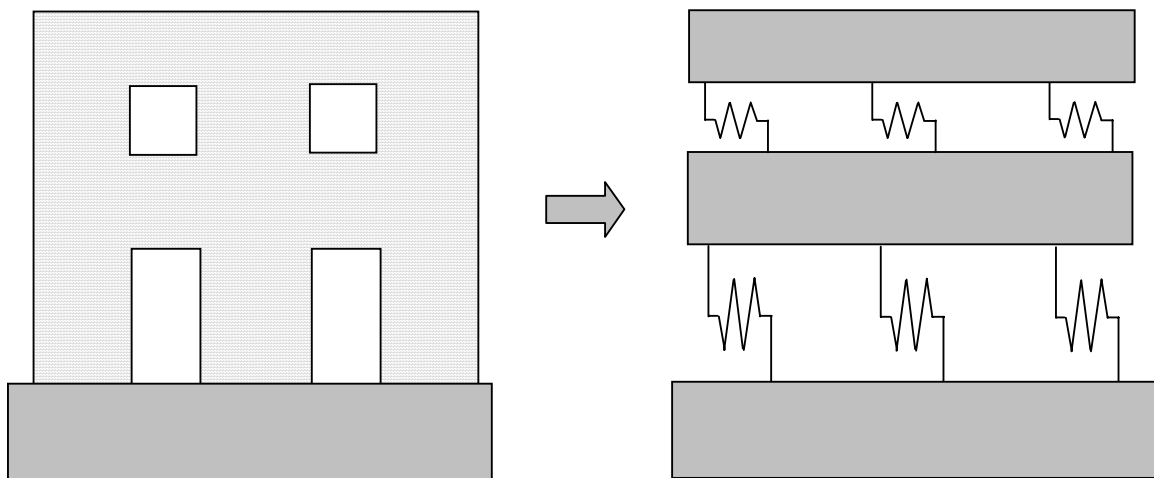


Figure 10.12. Elastic model for each perforated wall

The strength of each perforated wall is determined by the strength of the first-story piers. The possible failure modes for each pier include rocking, sliding, toe crushing and diagonal tension. The first two failure modes are deformation-controlled failure modes, while the latter two failure modes are force-controlled failure modes. FEMA 356

equations (7-3) through (7-6) predict the strength of a pier corresponding to each failure mode. In addition, FEMA 356 assumes that the actual failure mode and the corresponding strength of this pier are controlled by the failure mode with lowest strength (ATC 2000).

The elastic model assumes that the external lateral force applied on a perforated wall is distributed to each pier based on their lateral stiffness. In addition, the wall is assumed to reach its maximum strength when one pier reaches its maximum strength. Furthermore, the controlling mode for the entire wall is also determined by the failure mode of the weakest pier. For example, if Pier 2-7 in Wall 2 is the first pier that reaches its maximum strength and its failure mode is rocking, then the performance of the entire wall is assumed to be deformation-controlled actions. Overturning moment effects and flange effects are not considered in the analysis. The material properties used in the analysis was based on the material test results and can be found in Table 6.3. The calculated strength and controlling mode for each wall are shown in Table 10.16.

Table 10.16. The maximum strengths and the corresponding failure modes for each wall

Wall ID	Maximum Base Shear (kips)	Controlling component and failure modes
Walls A and B	$Q_{CL} = 33$	A-7/B-10, Toe Crushing
Wall 1	$Q_{CE} = 41$	1-7, Rocking
Wall 2	$Q_{CE} = 9.6$	2-7. Rocking

Based on the obtained demands Q_{CE} or Q_{CL} (given in Table 10.16) and resistances Q_{UD} or Q_{UF} (given in Table 10.15), the performance levels of each wall corresponding to

BSE-1 and BSE-2 can be obtained by employing Eqs. 10.6 and 10.7. These results are listed in Tables 10.17 and 10.18, respectively. The performance of the entire building is also listed in the tables.

Table 10.17. Performance level of each wall (BSE-1: 10% /50 year) (based on FEMA 356 equations)

	Atlanta	Memphis	St. Louis	San Francisco
Wall A/B	OP	OP	OP	N.A.*
Wall 1	OP	OP	OP	LS
Wall 2	IO	IO	IO	N.A.
Entire building	IO	IO	IO	N.A.

* N.A. means that the component or building doesn't satisfy CP

Table 10.18. Performance level of each wall (BSE-2: 2% /50 year) (based on FEMA 356 equations)

	Atlanta	Memphis	St. Louis	San Francisco
Wall A/B	OP	N.A.	N.A.	N.A.*
Wall 1	OP	LS	IO	CP
Wall 2	LS	N.A.	CP	N.A.
Entire building	LS	N.A.	N.A.	N.A.

* N.A. means that the component or building doesn't satisfy CP

Tables 10.17 and 10.18 show that the test structure has different performance depending on the locations and seismic level. In the low seismic zone (Atlanta), the test structure can satisfy the IO performance for the BSE-1 Earthquake Hazard Level and the LS performance for the BSE-2 Earthquake Hazard Level. Therefore, the test structure exceeds the Basic Safety Objective (LS for BSE-1 and CP for BSE-2, ATC 2000). No

strengthening would be needed based on these assessments. On the other hand, In the moderate seismic zones, the test structure can satisfy the IO performance for the BSE-1 Earthquake Hazard Level. However, it cannot satisfy CP performance for the BSE-2 Earthquake Hazard Level. Therefore, the test structure cannot achieve the Basic Safety Objective, and thus strengthening of this building is needed. In the high seismic zone (San Francisco), the building is unacceptable for both BSE-1 and BSE-2, and a systematic retrofit is need for this building.

The experimental research outlined in Chapters 8 and 9 revealed that the maximum strength of the test building was around 40 Kips for Walls A and B, 58 kips for Wall 1, and 25 kips for Wall 2. The maximum strength predicted by FEMA 356 as shown in Table 10.16 underestimates the actual strength of the test building. This difference is not due to the ductility considerations. Instead, it is largely due to the fact that the current FEMA methods for URM structure as specified in Chapter 7 of FEMA 356 do not take into account some global characteristics of the test structure such as the flange effects. Moreover, the failure modes predicted by FEMA 356 are significantly different from what was observed for the test structure. This indicates that major improvements are needed for Chapter 7 of FEMA 356.

The evaluation of the test structure was conducted again based on the strength and the failure modes observed during the experiment. Since URM is a brittle material, it is assumed that the ultimate strength obtained from the test can be used as the design elastic strength of the test building. The relevant data are shown in Table 10.19. Note that the responses of all the four walls are deformation-controlled actions.

The performance of the test structure evaluated based on Table 10.19 is given in Tables 10.20 and 10.21 for BSE-1 level and BSE-2 level, respectively. In both moderate and low seismic zones, the test structure satisfies the OP performance for the BSE-1 Earthquake Hazard Level and the LS performance for the BSE-2 Earthquake Hazard Level. No strengthening would be needed. In the high seismic case, although the test structure can satisfy LS for the BSE-1 Earthquake Hazard Level, it cannot satisfy CP for the BSE-2 Earthquake Hazard Level. Therefore, it cannot achieve the Basic Safety Objective, and thus strengthening is needed.

Table 10.19. The observed maximum strengths and failure modes for each wall

Wall ID	Maximum Base Shear (Kips)	Controlling Component and Failure Modes
Wall A/ Wall B	$Q_{CE} = 40$	Rocking
Wall 1	$Q_{CE} = 58$	Rocking
Wall 2	$Q_{CE} = 25$	Rocking

Table 10.20. Performance level of each wall (BSE-1: 10% /50 year) (based on test data)

	Memphis	St. Louis	Atlanta	San Francisco
Wall A/B	OP	OP	OP	LS
Wall 1	OP	OP	OP	LS
Wall 2	OP	OP	OP	LS
Entire building	OP	OP	OP	LS

Table 10.21. Performance level of each wall (BSE-2: 2% /50 year) (based on test data)

	Memphis	St. Louis	Atlanta	San Francisco
Wall A/B	LS	IO	OP	CP
Wall 1	LS	IO	IO	N.A.
Wall 2	LS	IO	IO	N.A.
Entire building	LS	IO	IO	N.A.

10.4.2. NSP

“If the Nonlinear Static Procedure (NSP) is selected for the seismic analysis of a building, a mathematical model directly incorporating the nonlinear load-deformation characteristics of individual components of the building shall be subjected to monotonically increasing lateral loads representing inertia forces in an earthquake until a target displacement is exceeded” (ATC 2000, 3.3.3.1). The target displacement is intended to represent the maximum displacement that the building is likely to experience during the design earthquake.

The general procedure for this method is as follows. The first step is the same as that for the LSP. Based on the location, the site class, and the general structural characteristics of the building, and the considered seismic hazard level, the seismic hazard S_a can be determined. However, instead of determining the pseudo seismic lateral load, the target displacement that the building is likely to experience during a design earthquake is estimated as the next step (FEMA 356, Eq. (3-15)). Following that, this target displacement is then applied to the mathematical model of the building, and the design forces and deformations of each component are calculated. Finally, the

performance of the building for a particular probabilistic seismic hazard can be checked by the following acceptance criteria (ATC 2000):

1) If the primary and secondary components in a URM building were deformation-controlled, the components shall have expected deformation capacities not less than the maximum deformation demands calculated at the target displacement for the building.

2) For a URM building with deformation-controlled primary and secondary components, the base shear for the building at the target displacement, V_t , shall not be less than 80% of the effective yield strength of the structure, V_y .

3) If the primary and secondary components in a URM building were force-controlled, these components shall have lower bound strengths not less than the maximum design forces.

For the test structure, the target displacement, δ_t , at the roof level was calculated for both the BSE-1 and the BSE-2 ground motions for four different cities. The results are listed in Table 10.22.

Table 10.22. Target displacement, δ_t (in)

	Memphis	St. Louis	Atlanta	San Francisco
BSE-1: 10% /50 year	0.31	0.25	0.16	1.98
BSE-2: 2% /50 year	1.75	0.83	0.41	3.06

Since the test URM building featured a flexible diaphragm, the four walls of the test structure, Walls 1, 2, A and B can be checked individually for their performance. The

nonlinear model for a typical URM perforated wall is shown in Figure 10.13. It is similar to the elastic model as shown in Figure 10.12 except that nonlinear pier models are used instead of elastic pier ones. The target displacement, δ_t , is applied at the top of the building. FEMA 356 specifies that at least two lateral load distributions need to be applied to the test structure for the NSP. As a reasonable alternative, two types of displacement profiles with the ratio between the second floor displacement and the roof floor displacement K equal to 1 or 0.5 were applied to each wall. However, it is well known that the nonlinear response of a low-rising URM building is controlled by its first story piers. In this case, the lateral displacement profile with $K = 1$ gives the worse case scenario. Based on these considerations, the design lateral deformation of the critical components in the test structure can be calculated. These values are listed in the following tables:

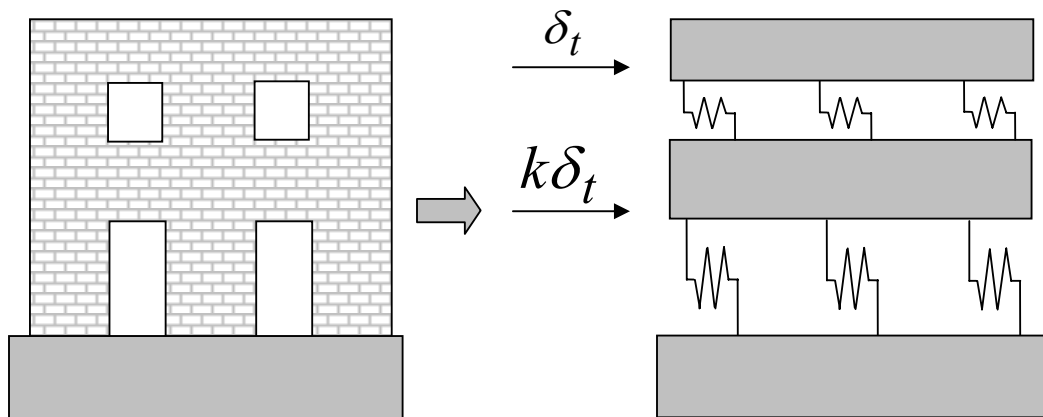


Figure 10.13. Nonlinear model for each perforated wall

Table 10.23. Design displacement drift of each component (%) (BSE-1)

Pier	Atlanta	Memphis	St. Louis	San Francisco
A-7	0.19	0.37	0.30	2.36
A-8	0.34	0.65	0.52	4.15
A-9	0.34	0.65	0.52	4.15
A-10	0.34	0.65	0.52	4.15
1-6	0.19	0.37	0.30	2.36
1-7	0.19	0.37	0.30	2.36
2-7	0.17	0.33	0.27	2.11
2-8	0.17	0.33	0.27	2.11
2-9	0.17	0.33	0.27	2.11

* Wall B is not listed since it is identical to Wall A.

Table 10.24. Design displacement drift of each component (%) (BSE-2)

Pier	Atlanta	Memphis	St. Louis	San Francisco
A-7	0.49	2.09	0.99	3.65
A-8	0.86	3.67	1.74	6.42
A-9	0.86	3.67	1.74	6.42
A-10	0.86	3.67	1.74	6.42
1-6	0.49	2.09	0.99	3.65
1-7	0.49	2.09	0.99	3.65
2-7	0.44	1.86	0.88	3.26
2-8	0.44	1.86	0.88	3.26
2-9	0.44	1.86	0.88	3.26

* Wall B is not listed since it is identical to Wall A.

On the other hand, FEMA 356 points out that deformation-controlled piers and force-controlled piers exhibits different generalized force-deformation relations, as shown in Figure 10.14. Figure 14a is based on a small modification of Figure 7-1 in FEMA 356 due to the following reasons. First, FEMA 356 does not identify the value for point D in its Figure 7-1. For simplicity, a linear relation instead of a bilinear one is used

between Point C and Point E in the current model. Second; FEMA 356 gives a very small value for the strength corresponding to Point E. Again for simplicity, zero strength is assumed for Point E in the current analysis. Figure 14b is used for a force-controlled component. No slope is identified in FEMA for the portion after the peak point. It is assumed in the current model that a URM pier loses its strength as soon as its lateral deformation passes Point B.

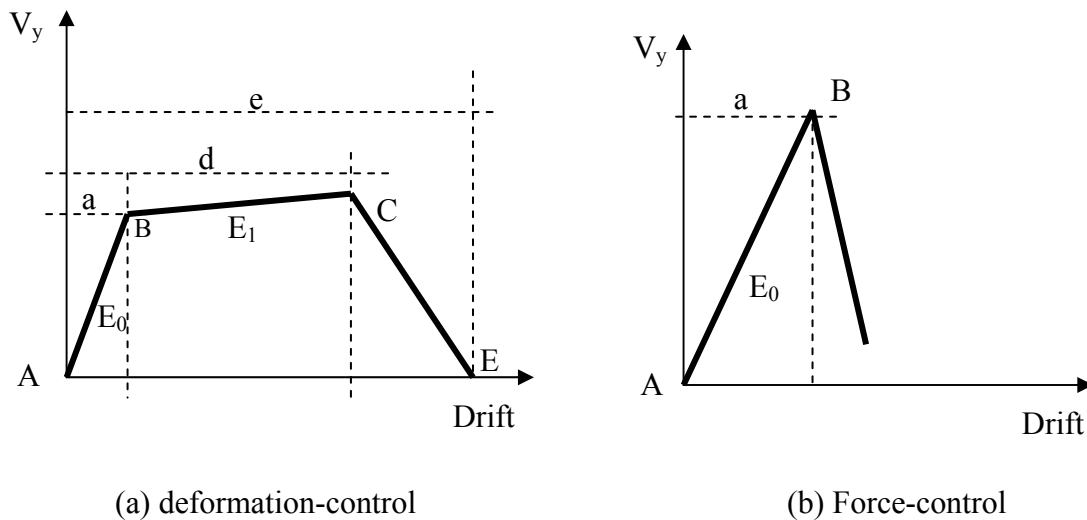


Figure 10.14. Generalized force-deformation relationships for a URM pier

The maximum strength and failure mode for each pier were calculated based on FEMA equations. The force-deformation parameters for all the first story piers are listed in Table 10.25. The acceptance criteria for each deformation-controlled pier, which are derived from Table 7.4 of FEM 356, are also listed in this table.

Table 10.25. Force-deformation parameters for the first story piers

Wall	Pier	Failure mode	V _y (kips)	E1 (kips/in)	a (%)	d (%)	e (%)	IO (%)	LS (%)	CP (%)
A, B	A-7	Rocking	6.81	0	0.011	0.7	1.4	0.1	0.53	0.7
	A-8	Toe Crushing	8.58	-	0.012	-	-	-	-	-
	A-9	Toe Crushing	8.91	-	0.012	-	-	-	-	-
	A-10	Toe Crushing	11.00	-	0.011	-	-	-	-	-
1	1-6	Sliding	52.57	0	0.014	0.4	0.8	0.1	0.3	0.4
	1-7	Rocking	4.33	0	0.011	0.7	1.4	0.1	0.53	0.7
2	2-7	Rocking	4.42	0	0.013	0.8	1.6	0.1	0.6	0.8
	2-8	Rocking	1.57	0	0.026	1.6	3.2	0.1	1.2	1.6
	2-9	Rocking	5.10	0	0.015	0.8	1.6	0.1	0.6	0.8

Comparing Tables 10.23 and 10.24 with Table 10.25, the performance of each pier can be obtained as listed in Table 10.26 and Table 10.27 for the BSE-1 and the BSE-2 levels, respectively. These two tables show that in comparison with the LSP, the NSP gives much conservative predictions on the performance of the test structure. One reason is that the NSP of FEMA predicts that many first floor piers of the test structure, such as Pier A-8, are dominated by toe crushing. This brittle failure mode exhibits a very small deformation capacity, and essentially causes these piers not to contribute to the seismic resistance of the entire building. Again, considering the good performance observed during the test, major improvements are needed for Chapter 7 of FEMA 356.

Table 10.26. Performance level of each component (BSE-1)

Wall	Pier	Atlanta	Memphis	St. Louis	San Francisco
A, B	A-7	LS	LS	LS	NA
	A-8	NA	NA	NA	NA
	A-9	NA	NA	NA	NA
	A-10	NA	NA	NA	NA
1	1-6	LS	LS	LS	NA
	1-7	LS	LS	LS	NA
2	2-7	LS	LS	LS	NA
	2-8	LS	LS	LS	NA
	2-9	LS	LS	LS	NA

* Wall B is not listed since it is identical to Wall A.

Table 10.27. Performance level of each component (BSE-2)

Pier	Atlanta	Memphis	St. Louis	San Francisco
A-7	LS	NA	NA	NA
A-8	NA	NA	NA	NA
A-9	NA	NA	NA	NA
A-10	NA	NA	NA	NA
1-6	NA	NA	NA	NA
1-7	LS	NA	NA	NA
2-7	LS	NA	NA	NA
2-8	LS	NA	CP	NA
2-9	LS	NA	NA	NA

* Wall B is not listed since it is identical to Wall A.

10.5. ULTIMATE STRENGTH BASED ON RIGID BODY ANALYSIS

Since URM is a brittle material and the response of the test structure was observed to be dominated by rigid body movements, a simple analysis based on kinematic analysis and equilibrium equations is used in this section to analyze the ultimate strength of the test structure. The general concepts and procedure for this method are as follows:

- 1) The ultimate failure mechanism for a URM perforated wall is assumed to be composed of rocking or sliding of several rigid bodies; the other two failure modes: diagonal tension and toe crushing, are not considered in the analysis.
- 2) The kinematic mechanism of each masonry wall can be determined based on the experimental observations and the kinematic analysis.
- 3) The size of pier flanges and spandrel flanges for the test structure can be determined based on the experimental observations during the tests or from the rules proposed in Chapter 9.

- 4) The ultimate strength of each wall can be determined by solving a series of equilibrium equations.

The analysis for the ultimate strength of the walls conducted following the above assumptions can be found in Appendix F. In this section only the ultimate strength of Wall 1 in the pull direction is discussed as an example. The analyses results for all the other walls is given and compared to the experimental measurements.

10.5.1. Ultimate strength of Wall 1 in the pull direction

The observed rigid body movement of Wall 1 in the pull direction was slightly different before and after Pier 1-6 slid (see Chapter 8). Before Pier 1-6 slid, both Pier 1-6 and Pier 1-7 rocked about their individual right toes, while the entire second floor wall was lifted and pulled to the right due to the rocking of the first story piers, as illustrated in Figure 10.15. Assuming the left top corners of Piers 1-6 and 1-7 have the same lateral displacement (u), kinematic analysis shows that the vertical uplift of Pier 1-6 (v_6) is larger than that of Pier 1-7 (v_7) due to their different aspect ratios. As a result, the vertical displacement at the left side of Wall 1 was larger than that at the rigid side of Wall 1; this is consistent with the experimental observation.

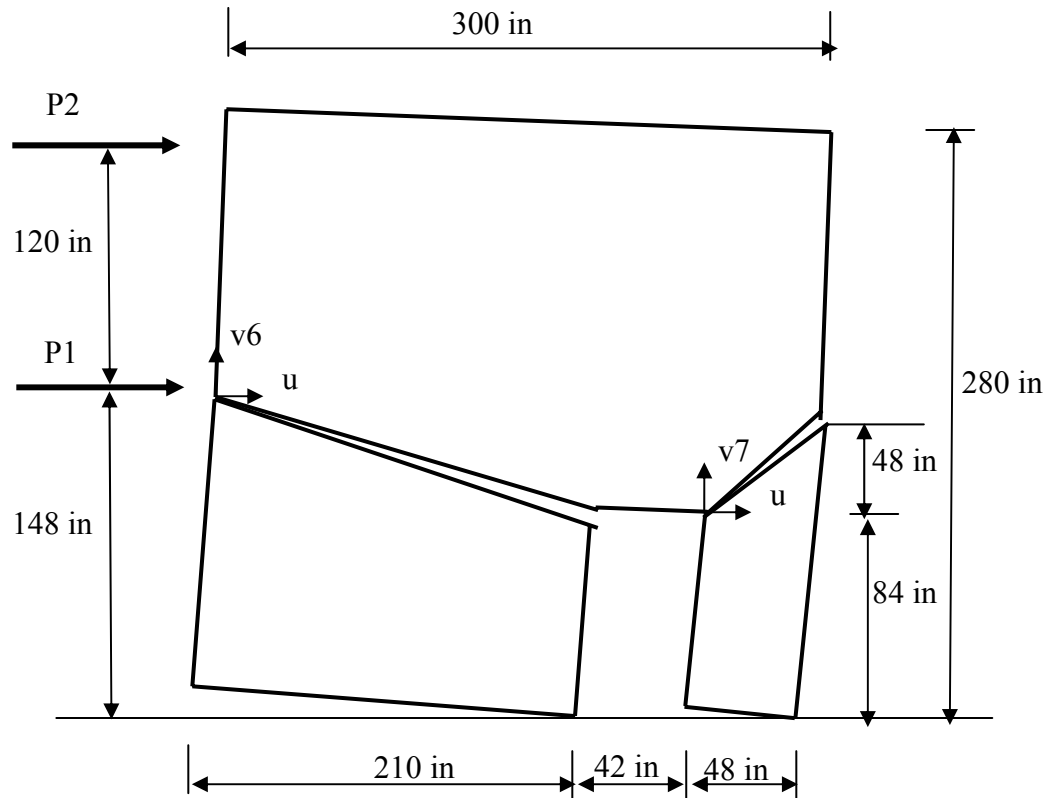


Figure 10.15. Kinematic mechanism of Wall 1 when loaded in the north direction

The internal force distribution for Wall 1 is shown in Figure 10.16. In this figure, F_6 and P_6 are the vertical and lateral internal forces between the spandrel and Pier 1-6, respectively; F_7 and P_7 are the vertical and lateral internal forces between the spandrel and Pier 1-7, respectively; W_{6f} and W_{7f} are the weight of the pier flanges of Pier 1-6 and Pier 1-7, respectively; W_2 and W_3 are the weight of the spandrel flanges at the left side and the right side of Wall 1 spandrel, respectively; W_6 and W_7 are the weight of Pier 1-6 and Pier 1-7, respectively; and W_1 is the weight of the spandrel. The values of each weight and the corresponding calculation rules are listed in Table 10.28.

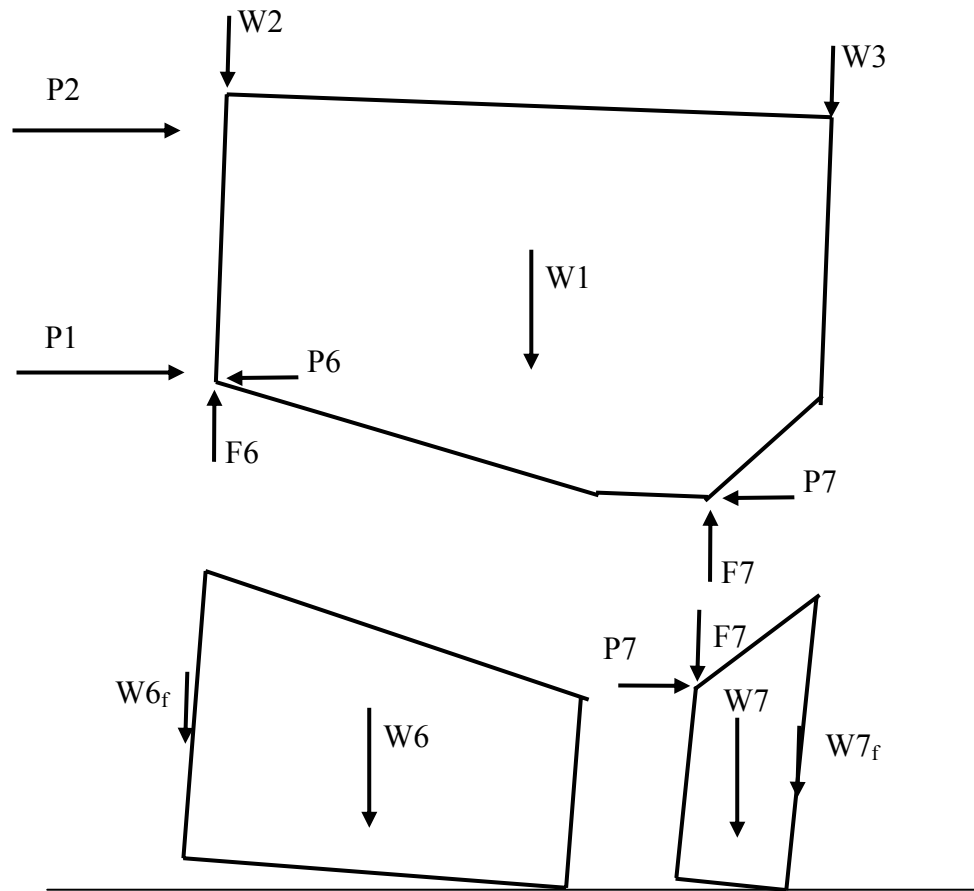


Figure 10.16. Internal force distribution of Wall 1

Table 10.28. Weight calculation for the rigid body analysis for Wall 1

Items	Weight (kips)	Rules
W1	24.3	The weight of the specified area minus window opening
W2	6.44	The weight of the triangular are as shown in Figure 9.23 minus window opening
W3	6.44	The weight of the triangular are as shown in Figure 9.23 minus window opening
W6	13.1	The weight of the specified area of Pier 1-6
W7	3.0	The weight of the specified area of Pier 1-7
W6 _f	23.2	Half the weight of Wall B minus W2 (based on the experimental observation)

Based on the equilibrium equations of the three rigid bodies (Figure 10.16), the following equations can be obtained:

$$210 \cdot F_6 + 210 \cdot W_{6_f} + 105 \cdot W_6 = 148 \cdot P_6$$

$$48F_7 + 24W_7 = 84P_7$$

$$P_6 + P_7 = P_1 + P_2$$

$$F_6 + F_7 = W_1 + W_2 + W_3$$

$$252F_6 + 64P_1 + 184P_2 + 48W_3 = 64P_6 + 252W_2 + 66W_1 \quad (10-7)$$

Moreover, the lateral forces P_1 and P_2 are assumed to be the same:

$$P_1 = P_2 \quad (10-8)$$

Solving Eqs. (10-7) and (10-8), and considering Table 10.28, the base shear corresponding to the rocking failure mechanism of Wall 1 can be calculated to be 56.8 kips, which is close to the experimental result measured in the test (55 kips).

On the other hand, after Pier 1-6 slid, the kinematic mechanism of Wall 1 is still similar to Figure 10.15. However, the uplift of v_6 is smaller because of the sliding of Pier 1-6. Moreover, the first equation in Eq. (10-7) has to be changed to

$$P_6 = \mu(W_{6_f} + W_6 + F_6) \quad (10-7^*)$$

where the shear friction μ is equal to 1.0 based on the material tests discussed in Chapter 6.

Solving Eqs. (10-7), (10-7*), and (10-8), and considering Table 10.28, the base shear of Wall 1 corresponding to the shear failure mechanism of Pier 1-6 can be calculated to be 49.6 Kips, which is also close to the results measured in the test (47 kips).

10.5.2. Calculated strength of each wall based on the rigid body analysis

The ultimate strengths of Walls A, B, 1, and 2 obtained from the rigid body analysis are listed in Table 10.29. Generally the rigid body analysis gives very close prediction to the ultimate strength of the test structure. It verifies that the ultimate failure mechanism of the test structure was indeed governed by the rigid body movements of its components and that the definition role for the effective flange size is correct.

Another important issue is that no bed joint tensile strength is utilized in the analysis. Therefore, the close prediction of the rigid body analysis also indicates that the masonry bed joint tensile strength has negligible effect on the strength of the test URM structure.

Table 10.29. Ultimate strength of each wall (kips)

Items	Rigid body analysis	Experimental results
Wall 2 push and rocking	26.7	27
Wall 2 pull and rocking	26.7	24
Wall 1 push with minor cracks in Wall A	56	60
Wall 1 push with substantial cracks in Wall A, rocking	37.5	40
Wall 1 pull, rocking	56.8	55
Wall 1 pull, rocking/sliding	49.6	47
Wall B push and rocking	46.0	43
Wall B pull and rocking	34.6	37
Wall A pull and rocking	40.2	40
Wall A push and rocking	33.9	36

10.6. DISCUSSIONS

The preliminary analyses reveal some important characteristics of the test structure. These results are consistent with the experimental observations and verify some conclusions obtained from the experimental results.

The first important finding from the 3D elastic FE analyses regards the relative stiffness of the three fundamental components of a URM building: the in-plane wall, the out-of-plane wall, and the diaphragm. The analysis verifies the experimental observation that the stiffness of the three components are significantly different. For the test structure, the wood roof or floor diaphragm exhibits the smallest lateral stiffness with a flexural/shear stiffness around 10 kips/in. The lateral stiffness of URM out-of-plane walls is on the order of 100 kips/in, while the lateral stiffness of URM in-plane walls is on the order of 1000 kips/in. As a result, during a possible seismic event, large lateral displacements will be developed in the out-of-plane walls and in the flexible diaphragms while small displacements will be found in the in-plane walls. This finding explains the many out-of-plane failures reported in previous earthquakes. The dynamic analyses based on the conceptual model gives the same assessments.

On the other hand, the URM in-plane wall is the most important component of a URM building as far as the ultimate strength and the stability of the structure is concerned. The reason is as follows. First, although the simple conceptual model shows that the out-of-plane walls tend to take more seismic forces than the in-plane walls, a large portion of the stiffness of the out-of-plane walls come from the lateral support of the in-plane walls. As a result, a portion of the seismic force resisted by the out-of-plane walls has to be first transferred to the in-plane walls before it goes into the ground.

Second, after the out-of-plane walls crack due to their large lateral deformation under seismic excitation, the stiffness of the out-of-plane walls will reduce, and thus the in-plane walls will resist more seismic forces. This indicates that the URM in-plane walls will become the critical component of a URM building if appropriate approaches have been employed to ensure the deformation capacities and thus prevent the collapse of the out-of-plane walls. This goal has already been successfully fulfilled in many previous retrofit projects, which used various approaches such as tension ties to connect the out-of-plane walls to the diaphragms and the in-plane walls. Based on this consideration, the experimental research that was presented in Chapters 6 through 9 and the analytical investigation that will be presented in Chapters 11 and 12 are mainly focused on the nonlinear in-plane properties of URM building.

The simple conceptual model also reveals that the URM structure is a very stiff building, and, thus its first vibration mode controls the lateral. Note that the natural period and the vibration mode obtained from the simple conceptual model are based on the behavior of an entire URM structure. When only the behavior of one individual URM in-plane wall is of interest, the response of the in-plane wall will be much stiffer because its stiffness is very large. As a result, the fundamental natural period corresponding to each individual URM in-plane wall will be even smaller and thus the first vibration mode will also control its deformation profile.

The results from the analyses presented in this chapter also exhibit significant discrepancies compared with the experimental measurements. This indicates that some improvements are needed for the analytical tools.

Specifically, the analyses showed that the FEMA pre-standard approach does not give a good prediction for URM structures. One reason is that the nonlinear analytical model employed by FEMA does not account for some significant global characteristics observed in the experimental research. In addition, as discussed in Chapter 3, the current FEMA method does not predict the failure mode of each URM pier accurately. For example, the effective pier model (Chapter 4) reveals that the rocking mechanism is actually a normal working mechanism of URM piers and that the toe-crushing failure mode is actually an “ultimate” limit for the rocking mechanism. Therefore, a URM pier could be able to exhibit large deformation capacity before toe-crushing occurs. As a result, the penalty factor 1.6 for the toe-crushing capacity employed by FEMA (see Section 7.4.2.2.2 of FEMA 356) is probably not necessary, and the ultimate strength predictions for a URM pier should be significantly improved. All the issues indicate the importance of developing a more accurate model for the nonlinear analysis of a URM structure.

On the other hand, some unique structural characters of a URM building observed in the test as well as revealed in the preliminary analyses point out a possible direction for the modeling of the nonlinear behavior of a URM structure. They are as follows:

- 1) As discussed previously, if appropriate approaches have been employed to ensure the deformation capacity of out-of-plane walls in a URM building, the evaluation of the performance of an existing building can be focused on its nonlinear in-plane behavior.
- 2) Both the 3D elastic FE analysis and the experimental research have revealed little coupling between two parallel in-plane walls. Therefore, it is possible to use a

simple 2D model instead of a complex 3D model to analyze the nonlinear response of a URM building.

- 3) Since a typical URM building features flexible diaphragm, torsional effects are not significant and thus can be ignored.
- 4) The experimental research, the 3D elastic FE analysis, and the rigid body analysis, all reveal the significant contribution of flange effects. These effects need to be considered in a 2D or 3D model.
- 5) Since URM is a brittle material, the damage to a URM building is governed by several large cracks. The rigid body analysis shows that the ultimate failure mechanism of a URM building is determined by the rigid body movements of several critical components that are defined by these large cracks. Therefore, appropriate modeling of the nonlinear behavior of an entire URM building can be fulfilled by appropriate modeling of these cracks.
- 6) The effective pier model discussed in Chapter 4 and the methodology to define an effective pier in a perforated wall as discussed in Chapter 9 can be used to describe the nonlinear response of each pier.
- 7) Global overturning and local rocking behavior as observed in the test also need to be considered in the nonlinear analysis.

The above issues that arose from both the experimental research and the preliminary analysis are considered in the following, more complete nonlinear analyses presented in Chapters 11 and 12.

10.7. CONCLUSIONS

Preliminary analyses were conducted to predict both the elastic and the inelastic properties of the test structure. The elastic analyses based on both the 3D FE model and the simple conceptual model gave close predictions for the elastic behavior. The rigid body analysis gave very good prediction for the ultimate strength. On the other hand, the FEMA 356 pre-standard approach did not give a good prediction for seismic performance of the URM test structure, mainly because the analytical models and the nonlinear properties of URM piers employed by FEMA 356 are not very accurate.

CHAPTER 11

NONLINEAR FINITE ELEMENT ANALYSIS OF URM STRUCTURE

11.1. INTRODUCTION

As pointed out in the previous chapter, in order to evaluate the nonlinear properties of a URM building, a realistic structural model is needed. The nonlinear FE method is an appropriate and frequently used tool for this purpose. However, due to the unique nonlinear characteristics of a URM structure, such as its brittle behavior and the formation and propagation of large discrete cracks, some specific techniques are needed in the nonlinear FE analysis of URM structures. Two types of nonlinear FE methods are commonly used for URM structures: the discrete-crack model and the smeared-crack model (Bruneau 1994b).

The discrete crack model is a FE model in which a special interface element is introduced to allow the separation of adjacent elements when the tensile strength of masonry is exceeded at this interface. To locate the special interface elements in this FE model, prior knowledge of the ultimate behavior of the URM walls, including the location, direction, and length of possible cracks are needed. Two approaches are generally used to deal with this issue. The first approach assumes that damage to a URM wall is confined to the mortar joints and thus puts the interface elements at each brick-mortar joint (Chiostrini, Foraboschi and Sorace 1989, Lourenco 1996, Martini 1997, 1998). Obviously this approach can give a very detailed description of the damage process for a strong unit-weak mortar masonry component, but at an enormous

computational cost and with the high likelihood of dealing with numerical instabilities problem. In addition, it is neither practical nor necessary to model all brick-mortar joints with interface elements if the goal is to investigate the nonlinear response of entire URM buildings. Therefore, an alternative approach (Chiostrini and Vignoli 1989) is to use interface elements in combination with conventional continuous elements. The continuous elements are used to model the majority of a URM wall, while the interface elements are used in some specific locations to describe possible cracks at those locations. This approach requires significantly less computational cost, but at the price of less accuracy.

Another branch of discrete modeling is the modified distinct element method (MDEM) used by Morales and Delgado (1992) to analyze the failure sequence of an adobe wall. This method was based on Merguro and Hakuno's (1989) work and is widely used in soil mechanics. The MDEM is a numerical method that can follow the behavior of a media from continuous state to complete fracture. However, this method is very time-consuming and special nonlinear programs are needed. As a result, no large-scale URM walls or structures have been found in the current literature review to be analyzed by this method. Recently, a method derived from the block theory originally used for rock mechanics (Goodman and Shi 1985) and called Discontinuous Deformation Analysis (DDA) has been proposed to analyze the nonlinear deformation of a damaged structure. This method accounts for both the contact nonlinearity (opening and sliding) and the deformability of interacting domains (Shi 1993 and 1997). This method was employed by Bicanic et al. (2001) to analyze the nonlinear properties of masonry bridges.

Again, this method requires tremendous computational efforts and special FE coding that is still unavailable in common commercial FE analysis packages.

The smeared-crack model for URM structures is actually a clone of the smeared-crack model used for reinforced concrete structure. It considers the nonlinear effects of the opening and closing of cracks by adjusting the material properties of an equivalent continuous material. It is assumed that the changing of effective elastic modulus and other properties of a continuous element can represent the propagation of cracks inside the element. This method is widely used by European researchers (Chiostrini et al. 1995, Gambarotta et. al. 1995, Koubaa et. al. 1995, Gavarini et. al. 1995, Lourenco 1996, Gambarotta and Lagomarsino 1997, Augarde 2001). The constitutive laws for the equivalent continuous material are either borrowed directly from RC materials, which may fail in representing the behavior of URM particularly due to the URM's anisotropic properties, or based on previous experimental research for the nonlinear behavior of URM materials. Some of these research results were discussed in Chapter 3.

There is still controversy on using the smeared-crack model for URM structures, even when the constitutive laws employed by the model are based on specific URM material tests. This is simply due to the fact that the cracks observed in a damaged URM structure are usually large but only occurring at a small number of discrete locations. This is very different from the case of reinforced concrete, where many small but relatively uniformly distributed cracks are present. This difference may result in significant errors when trying to smear large URM cracks into an entire structure. For example, some particular mechanisms commonly observed in URM structures, such as rocking and sliding, cannot be simulated by the smeared-crack model.

Based on the above considerations, a discrete crack model is used in this chapter to analyze the nonlinear response of the test structure. This model is not intended to model every possible crack at the brick-mortar interfaces. Instead, possible crack locations are pre-defined and the interface elements are employed in those locations. For the rest of the structure, the masonry is modeled by common continuous elements. This model is built in a commercial nonlinear FE analysis package, ABAQUS.

Following this framework, simple two-dimensional models are first established to analyze each masonry in-plane wall and to compare their output with the experimental results. This work is presented in Section 11.2. After that, a more complex three-dimensional model is presented in Section 11.3 to analyze the entire URM test structure. Discussions on the advantages and disadvantages of each model and the conclusions obtained from the analyses also are given in these two sections.

11.2. TWO DIMENSIONAL NONLINEAR FE MODEL

Although the test building is a three-dimensional box structure, previous research has shown that there is little coupling between the two parallel in-plane walls and that such structures exhibit very small torsion response. As a result, it is possible to analyze the nonlinear response of each URM in-plane wall by employing a 2D FE model. The methodology for building a nonlinear model for each URM wall by employing ABAQUS contact element is introduced in the following section. The nonlinear 2D model for each masonry wall is presented after that.

11.2.1. Modeling of URM walls with contact elements

A perforated masonry in-plane wall is composed of two types of members, piers and spandrels (see Figure 2.3). In order to define the possible crack locations in a URM wall, the loading and possible failure modes of each type of member must be fully understood. The failure modes of masonry piers subjected to horizontal shear forces, vertical axial forces, and moments are well documented. Based on numerous past experiments the following four possible failure modes have been identified: rocking, sliding, toe crushing and diagonal tension. These failure modes were discussed in detail in Chapter 4. It is important to note that these failure modes are not mutually exclusive, that is, the failure of in-plane masonry piers is often a combination of these modes.

In contrast, the possible failure modes of masonry spandrels have not been well established. In a perforated wall, the external forces to which a spandrel is subjected are different from those to a pier. The flexural moments and shear forces applied to the spandrel are perpendicular to the head joints instead of the bed joints (Figure 11.1). In addition, the normal forces applied on the head joints of a spandrel are relatively small compared with those applied on the bed joints of a pier (i.e. gravity stress). This distinction of the direction and magnitude of forces between a pier and spandrel is paramount, since masonry is an anisotropic material. As a result, the possible failure modes associated with a spandrel are different from those associated with a pier. For example, the commonly observed pier rocking is not realistic for spandrels. Although the flexural moments on a spandrel place some head-joints in tension and may lead to vertical flexural cracking, the propagation of large flexural cracks associated with rocking is not easy due to the interlocking of bricks in the vertical direction (Figure 11.2).

Moreover, this type of interlocking also prevents the sliding failure mechanism to be observed in piers. That is, in order for a spandrel to slide vertically, the bricks that cross the sliding plane would have to fail in shear. Considering the relatively high strength associated with the brick, the sliding failure mode is not realistic for a spandrel. In addition, the relatively small amount of compressive stress in spandrels suggests that compressive failure of masonry in spandrels is not likely to occur. Following these arguments, it can be concluded that a diagonal tension failure is the only realistic failure mode for a spandrel.

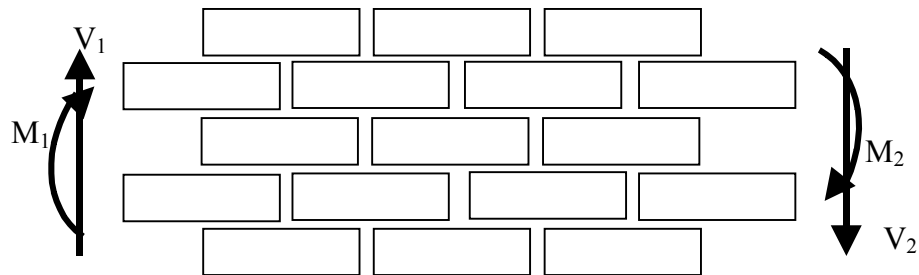


Figure 11.1. Flexural moments and shear forces applied on a spandrel

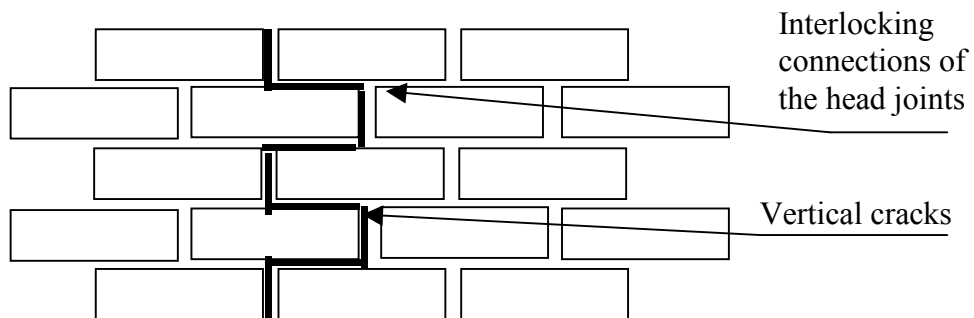


Figure 11.2. Teeth configurations of the head joints

In order to properly address both rocking and sliding failures, non-conventional elements must be employed in the analysis. The reason is that the rigid body motion associated with rocking and sliding cannot be described by conventional FE elements since they are based on an assumption of continuity of deformations. However, a special contact element provided by ABAQUS can be used to model rigid body motions. The contact element defines a pair of surfaces where potential cracking and/or sliding is likely to occur (Figure 11.3). Each surface is defined by a number of nodes and their associated areas. The relative movements of the corresponding nodes between the two surfaces determine the behavior of the pair of surfaces. Initially, the two surfaces are attached to each other. They remain attached (or in contact) until the tensile stress between the surfaces reaches a specified value. Once this value is reached, the surfaces separate and no further normal forces are transferred (Figure 11.4).

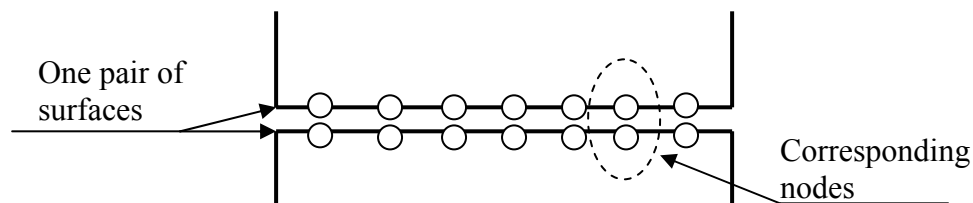


Figure 11.3. Schematic of a contact element

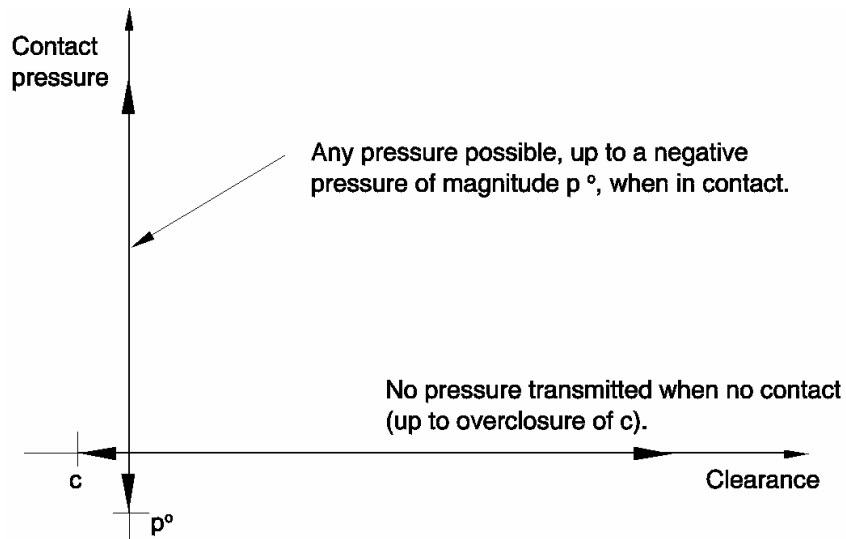


Figure 11.4. Normal forces transmitted between the pair of surfaces (ABAQUS 5.8-19 manual 23.18.37-1)

Prior to separation, the corresponding nodes can transmit shear forces as well as normal forces. Typically the Coulomb friction model is used to describe the shear properties of the contact surface. The corresponding nodes transmit shear forces (or shear stresses for associated areas) up to a specified critical shear value, at which the surfaces slide relative to one another (Figure 11.5). This critical shear value is defined as a fraction of the normal force or stress, which is given by the coefficient of friction (μ). After sliding occurs, the transmitted shear force remains constant, a value given by μ times the normal force. Furthermore, the ABAQUS contact element does not assume an idealized rigid-sliding behavior. Instead, the ABAQUS contact element allows an elastic slip δ_0 to occur prior to actual sliding (Figure 11.5). This modification is necessary in order to ensure the convergence of the solution; however, it decreases the elastic stiffness of the system.

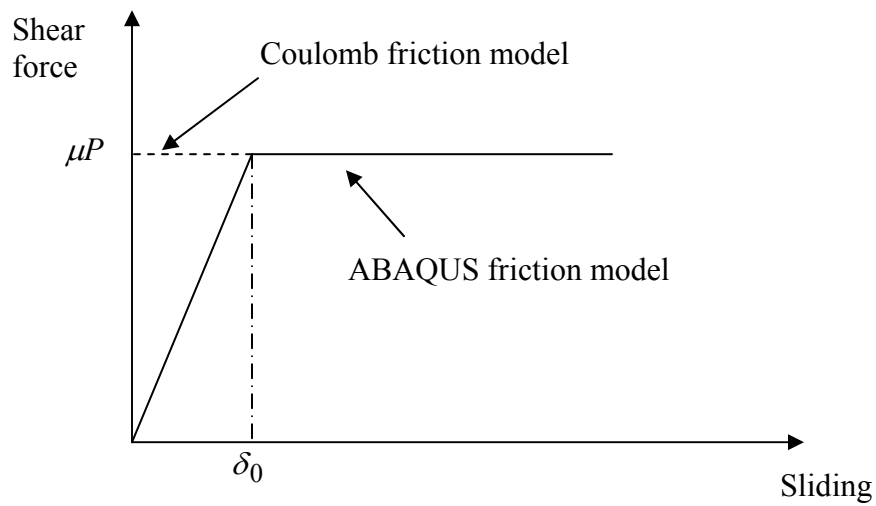


Figure 11.5. Shear force-relative sliding displacement relationship for contact elements

The shear properties described by the Coulomb friction model are different from the actual shear properties of masonry. Essentially the Coulomb friction model ignores the initial shear strength of the bed-joint (τ_o), and thus assumes that the bed-joint is completely cracked. Previous research shows that sliding typically does not develop in piers until after large flexural cracks appear. This suggests that on the onset of sliding the initial shear strength of masonry has been eliminated and only the frictional resistance of the bed-joint remains. Therefore, it appears that the Coulomb friction model can be used to reasonably approximate sliding behavior.

In order to employ the ABAQUS contact element to model rocking and sliding failures of URM piers. Potential rocking and sliding surfaces must be defined. Based on the results of past experimental research, the potential rocking/sliding surfaces are assumed to occur most likely at the top and bottom of the masonry piers. Therefore,

horizontal contact elements were placed at these locations, as shown in Figure 11.6 (Yi et al. 2003).

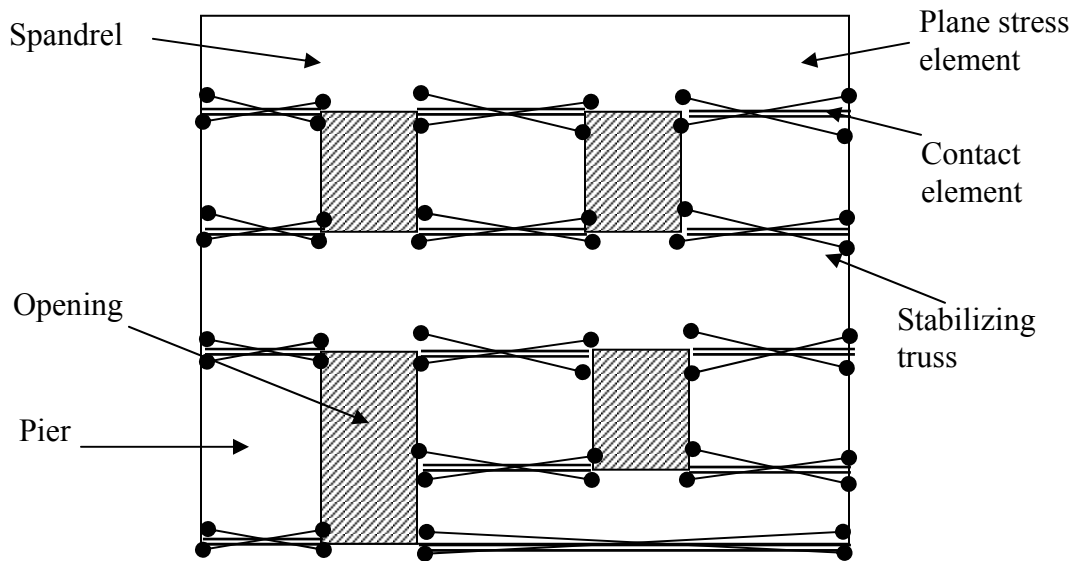


Figure 11.6. Modeling of a perforated wall with contact elements and stabilizing truss elements

During the initial trial analyses it was discovered that the structure quickly became unstable due to its rigid body motion after the contact elements began to slide. To solve this problem, truss elements were added across each contact element to provide a small amount of stiffness (Figure 11.6). The stiffness of the truss elements was set to the smallest value that enabled the structure to remain stable in an effort to minimize the error in the analysis results.

The other two potential failure modes, diagonal tension and toe crushing, were modeled by plane stress elements and the constitutive material properties of concrete contained in ABAQUS. The concrete exhibits a parabolic stress-strain relationship and is

characterized by a maximum compression and tension strength. As a result, this material property is capable of modeling the diagonal tension and toe crushing failure modes. However, the use of the concrete model assumes an isotropic material, which may cause errors since masonry is basically an anisotropic material.

11.2.2. Non-linear FE analysis of the ST-11 test structure

For the analysis of the ST-11 test structure, the elastic modulus of masonry was assumed to be 600 ksi based on the test results of MAEC project ST-6 (Franklin, et al. 2001). To investigate the possible effects of the variations in material properties, two series of analyses were carried out. The first series of analyses investigated the effects of different bed-joint friction coefficients on the overall behavior of the test structure by using 0.4, 0.6, and 0.8 for μ . In order to isolate this effect, this series of analyses were conducted using elastic plane stress elements and the tensile strength normal to the contact element was held constant at 20 psi. The second series of analyses were designed to investigate the effect of the nonlinear properties of the plane stress elements. For these analyses the properties of the contact element were held constant, with the normal tensile strength taken as 20 psi, and the bed-joint friction coefficient taken as 0.6. Two different tensile strengths were used for the concrete material employed. In one set of analyses the strength was set very high (1000 psi) to suppress diagonal tension failures, while the other set of analysis employed a more realistic tensile strength (54 psi). In both cases the compressive strength of the masonry was assumed to be 1800 psi.

To subject the walls of the ST-11 test structure to realistic gravity loads, the density of masonry was assumed to be 0.06944 lb/in³. Lateral loads were applied in the

form of cyclic displacements in order to allow the hysteretic behavior of the walls to be investigated. The displacement ratio between the floor level and the roof level was kept constant throughout loading at 0.85. The maximum roof displacement of 1.12 in. was selected to give a maximum roof drift of 0.4%.

11.2.2.1. Nonlinear FE analysis results for Wall 1

The analyses show that the response of Wall 1 is dominated by sliding. The variations of the bed joints friction coefficient significantly affect the response of this wall (Figure 11.7). For a friction coefficient of 0.4, the maximum strength of Wall 1 is about 16 kips, and its hysteretic response is quite symmetric, which is a typical behavior of sliding. When the shear coefficient is increased to 0.6, the maximum strength of Wall 1 increases to about 24 kips. However, the wall begins to behave asymmetrically. When loading from left to right (i.e. pier 1-6 is at the toe of the wall), sliding dominates the behavior. In contrast, if the wall is loaded in the opposite direction, some rocking behavior is observed, as can be inferred from its nonlinear unloading curve. When the shear coefficient is increased to 0.8, the unsymmetrical behavior of the wall becomes more pronounced. The ultimate strength obtained for Wall 1 is 33 kips and 27 kips when loading Wall 1 to the right and left, respectively.

The unsymmetrical behavior of Wall 1 with high bed joint shear frictions can also be seen from its deformation and stress contours, as shown in Fig 11.8 and Figure 11.9, which correspond to a friction coefficient of 0.8. When pushed to the right, pier 1-7 rocks. When pushed to the left, pier 1-6 slides. The figures also show that the damage is concentrated on the first floor walls. In the case that the wall is loaded to the right, there

are high stress concentration zones at the mid-height of Pier 1-7, and the spandrels above the door opening. This suggests that diagonal cracking is possible in these zones. In the case where the wall is loaded to the left, there are high stress concentration zones at the toe of Pier 1-6. This suggests that a toe crushing failure is possible at this location.

The hysteretic force-displacement behavior of Wall 1 with a bed joint friction coefficient of 0.6 is shown in Figure 11.10 for different masonry properties. The calculated ultimate strengths in both directions are also listed in Table 11.1. The figure and the table show that the use of concrete properties decreases the ultimate strength by a negligible amount. This suggests that neither toe crushing nor diagonal tension dominates the behavior of Wall 1.

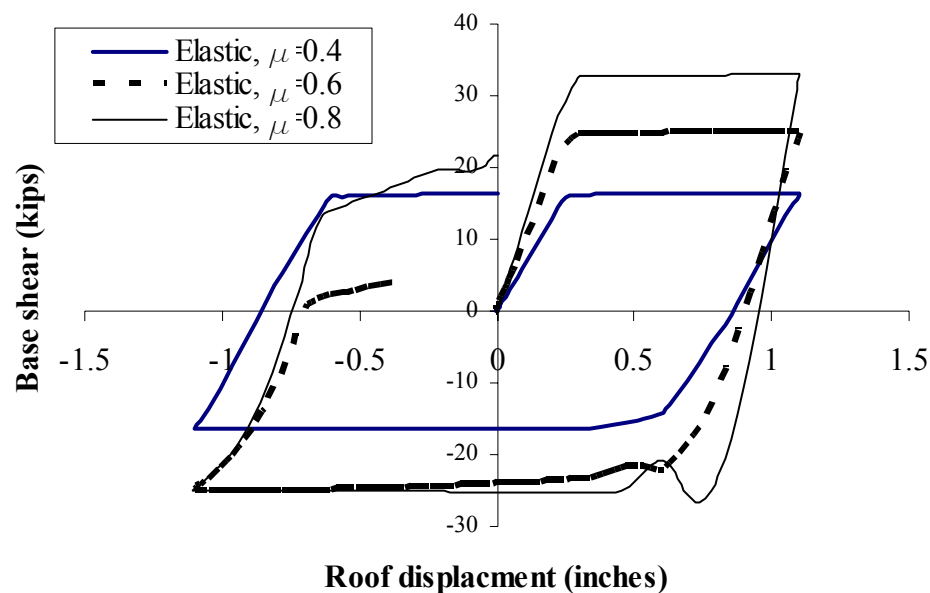
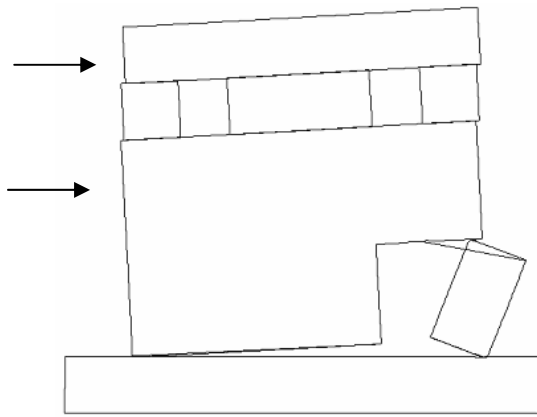
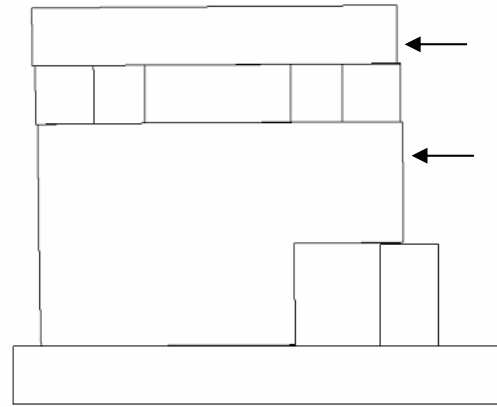


Figure 11.7. Force-displacement response of Wall 1 with different bed joint shear friction coefficients

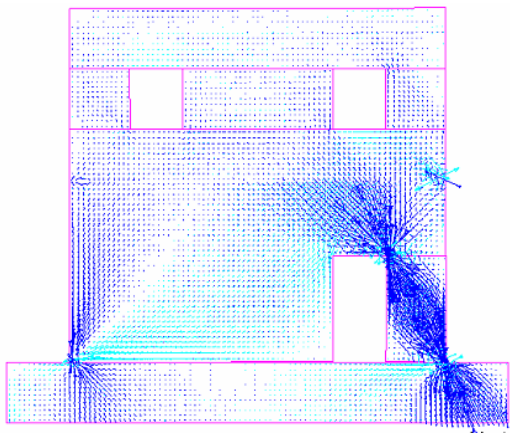


(a) Loaded from left to right

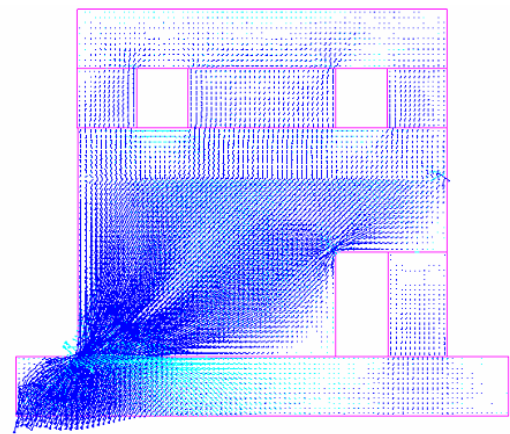


(b) Loaded from right to left

Figure 11.8. Deformed shapes of Wall 1



(a) Loaded from left to right



(b) Loaded from right to left

Figure 11.9. Stress contour of Wall 1

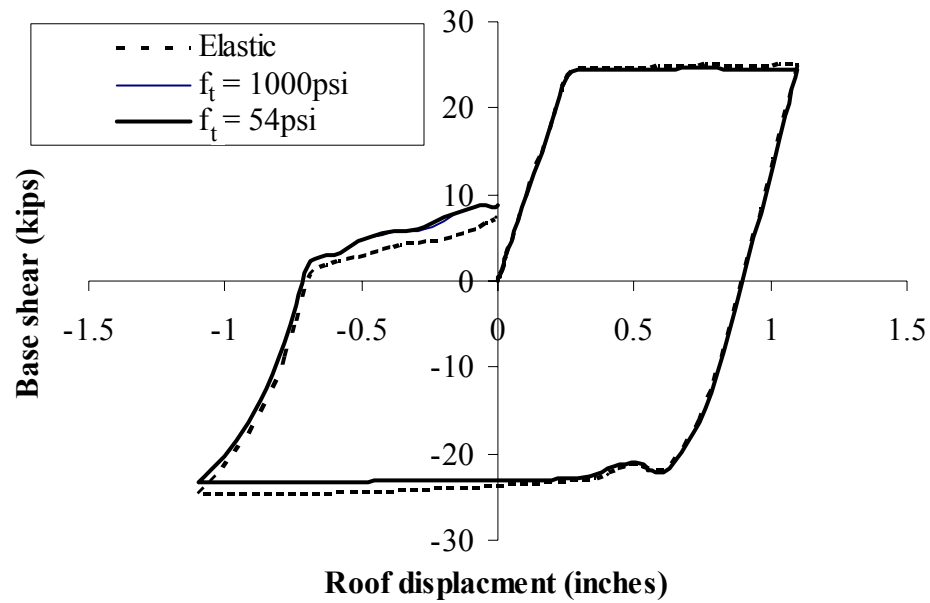


Figure 11.10. Force-displacement response of Wall 1 with different material properties

Table 11.1. Calculated ultimate strength of Wall 1

Methods	Ultimate Strength when pushed to the right (kip)	Ultimate Strength when pushed to the left (kip)
Elastic	25.1	24.6
Concrete material with high tensile strength	24.6	22.8
Concrete material with a tensile strength of 54psi	24.6	22.8

11.2.2.2. Nonlinear FE analysis results for Wall 2

The analyses reveal different influences of the bed-joint friction coefficient on the overall behavior of Wall 2 compared to that on Wall 1 (Figure 11.11). When the friction coefficient is small ($\mu = 0.4$), the hysteresis loop of Wall 2 exhibits a large area and its response is apparently a mixture of rocking and sliding. When the friction coefficient is

increased from 0.4 to 0.6, the maximum strength of Wall 2 increases from 8 kips to about 12 kips. Meanwhile, the hysteresis loops become more pinched. This means less energy is being dissipated and suggests that the behavior is gradually dominated by rocking. When the friction coefficient is increased from 0.6 to 0.8, the maximum strength of Wall 2 exhibits a negligible increase. This is expected since in this case the response of Wall 2 is dominated by rocking and thus the variation of the frictional resistance does not affect rocking strength.

The deformed shapes corresponding to the different loading directions are shown in Figure 11.12, which correspond to a friction coefficient of 0.6. As expected, the first floor piers of Wall 2 are rocking.

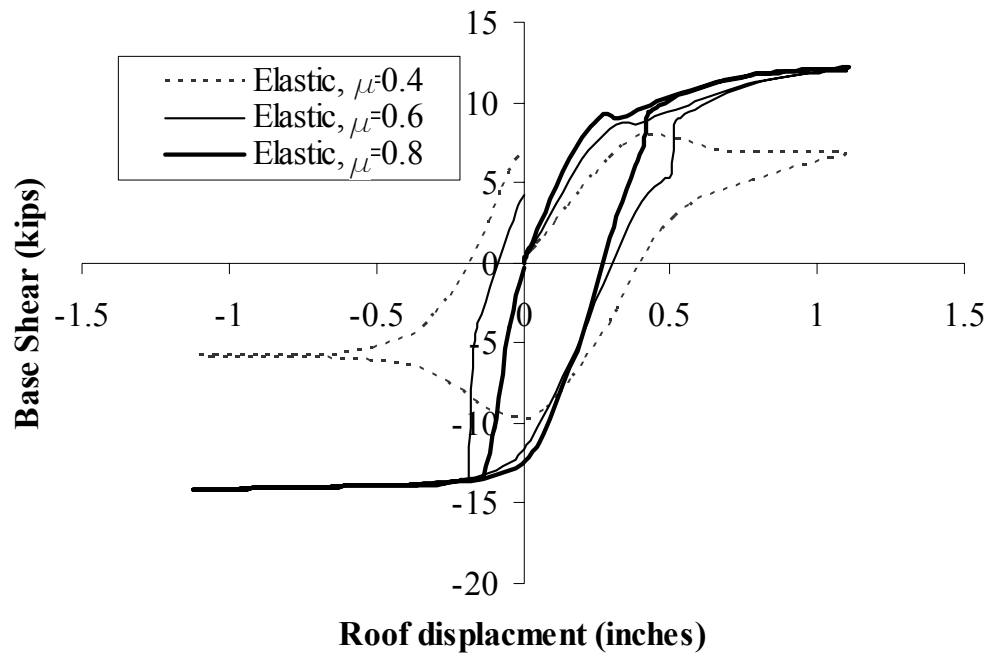


Figure 11.11. Force-displacement response of Wall 2 with different friction coefficients

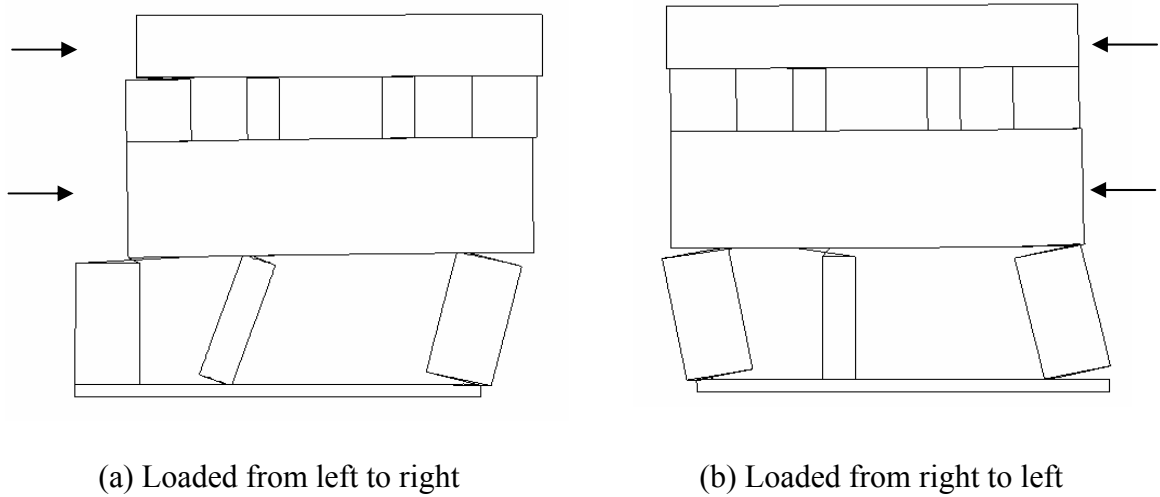


Figure 11.12. Deformed shapes of Wall 2

The hysteretic force-displacement behavior of Wall 2 (with a friction coefficient of 0.6) is shown in Figure 11.13 for different masonry properties. The calculated ultimate strengths for both loading directions are listed in Table 11.2. The figure and the table show that altering the properties of the masonry has a negligible effect on the ultimate strength of Wall 2, just as is the case for Wall 1. This suggests that diagonal tension and toe crushing failures do not govern the behavior of Wall 2.

Table 11.2. Calculated ultimate strength of Wall 2

Methods	Ultimate Strength when pushed to the right (kip)	Ultimate Strength when pushed to the left (kip)
Elastic	12.0	14.2
Concrete material with high tensile strength	11.8	13.5
Concrete material with a tensile strength of 54psi	11.8	13.5

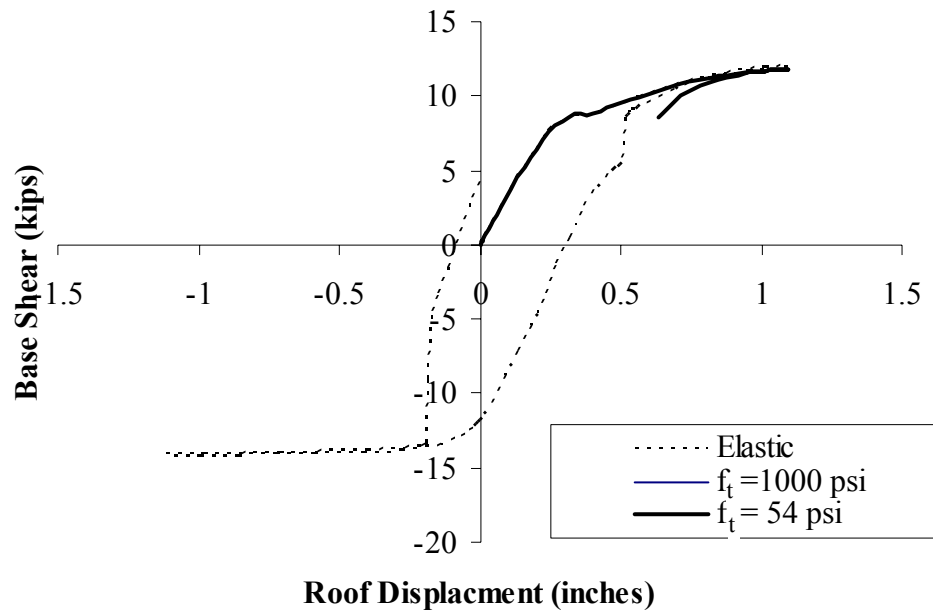


Figure 11.13. Force-displacement response of Wall 2 with different masonry properties

11.2.2.3. Nonlinear FE analysis results for Walls A and B

The same material properties and analysis strategies as those employed for the analyses for Walls 1 and 2 were also used to analyze Walls A and B. Note that since the flange effects are not considered in these analyses, Wall A is identical to Wall B. The analyses show again that increasing the friction coefficient suppresses sliding and causes more rocking (Figure 11.14). When the friction coefficient is 0.4 or 0.6, the failure mode for Walls A and B is a mixture of rocking and sliding. This can be seen from the direct dependence of the ultimate strength on the friction coefficient and the hysteresis energy dissipation area as shown in Figure 11.14. The deformed shapes of Walls A and B as shown in Figure 11.15, corresponding to a friction coefficient of 0.6, also suggest this mixed behavior. This figure shows that the door pier in the first floor rocks, while the

window piers slide. When the friction coefficient is increased to 0.8, the response of Walls A and B is dominated more by its rocking behavior, as shown in Figure 11.14.

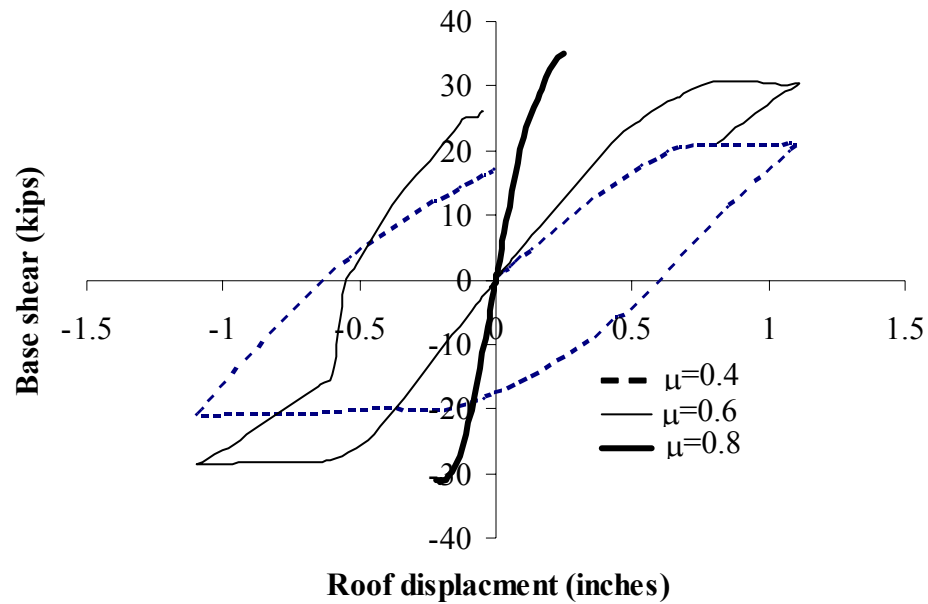


Figure 11.14. Force-displacement response of Walls A and B with different friction coefficients

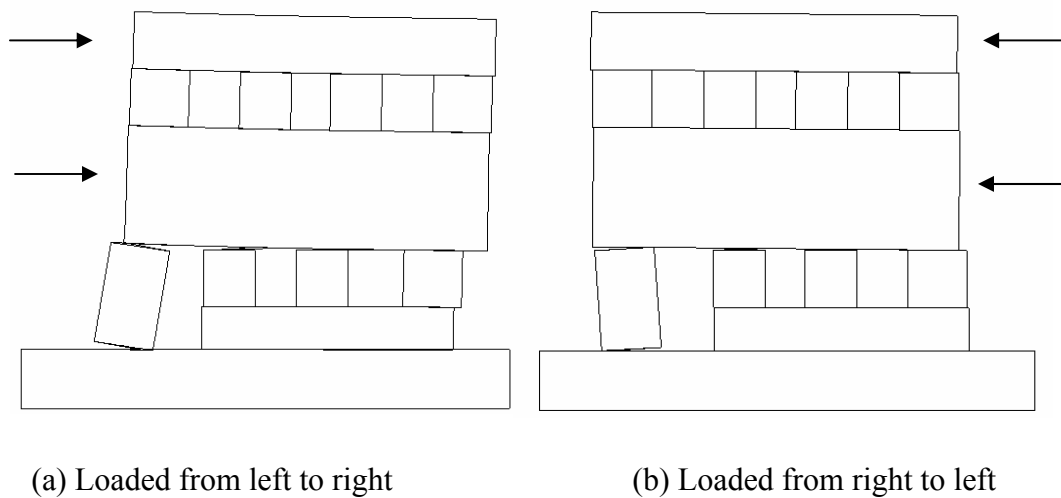


Figure 11.15. Deformed shapes of Walls A and B

The calculated ultimate strengths for Walls A and B in both directions for different masonry properties are listed in Table 11.3. This corresponds to a friction coefficient of 0.6. The table shows that the concrete properties give very similar results as those obtained from modeling masonry as an elastic material. This suggests that toe crushing and diagonal tension are not likely the failure modes for Walls A and B.

Table 11.3. Calculated ultimate strengths of Walls A and B

Methods	Ultimate Strength when pushed to the right (kip)	Ultimate Strength when pushed to the left (kip)
Elastic	30.8	28.6
Concrete material with high tensile strength	30.6	28.3
Concrete material with a tensile strength of 54psi	30.5	28.3

11.2.3. Discussions on the 2D non-linear FE analysis

The 2D non-linear FE model employed for the test structure is a simple and rough model. However, it still gives some valuable insight into the nonlinear working mechanisms of the test structure.

The analyses show that the variations of the bed-joint friction coefficient significantly affect the behavior of each wall. When the bed-joint friction coefficient is low ($\mu = 0.4$), the behavior of each wall is controlled by sliding. With increasing bed-joint friction coefficient, the response of each wall begins to switch towards rocking. Since the bed joint friction coefficient for the test masonry is found to be about 1.0 (see Chapter 6), the 2D nonlinear FE analysis indicates that the behavior of Wall 1 is a

mixture of rocking and sliding, while the behavior of Walls 2, A, and B are dominated by rocking. This assessment is consistent with the experimental observations, as described in Chapters 8 and 9. In addition, the 2D analyses reveal that the damage of the test structure concentrates on the first story walls, which is also observed during the test.

The 2D nonlinear FE analyses reveal that the nonlinear properties of the masonry itself have no significant influences on the nonlinear response of the entire wall. Toe crushing and diagonal tension are not likely controlling failure modes for the test structure. This is consistent with the experimental observations. This conclusion also indicates that the nonlinear analysis for the test structure can be greatly simplified. That is, for a particular case of the test structure, the nonlinear FE model employed can simply use elastic properties for the continuous elements.

On the other hand, the 2D FE model does not give satisfactory predictions for the maximum strength and the local behavior of the test structure. The predicted maximum strength for each Wall is significantly lower than the experimental value. It is due primarily to the fact that the flange effects are not considered in this 2D model. Moreover, the predefined possible crack pattern employed is different from the real crack pattern observed in the test. As a result, some predicted behavior is not consistent with the experimental observations. For example, the 2D model does not define a potential crack on the top of Pier 1-6. Therefore, when Wall 1 is loaded from left to right, the 2D model cannot capture the fact that Pier 1-6 as well as Pier 1-7 is rocking. This indicates that an appropriate predefined crack pattern is very important for the accuracy of the analysis results.

11.3. THREE DIMENSIONAL NONLINEAR FE MODEL

The previous 2D analyses exhibited some important limitations. In order to predict more accurately the nonlinear response of the test structure, a three-dimensional nonlinear model was built. The methodology for building this nonlinear model is first introduced in the following section. The analyses results obtained from this model are presented after that.

11.3.1. Modeling of the test URM structure

The 3D FE model follows the same methodology as that of the 2D FE model. That is, ABAQUS contact elements are used to describe the nonlinear properties of each potential crack, while continuum element is used to describe the other portion of the masonry walls. In this 3D model, both the contact and the continuum elements are three-dimensional. Specifically, a three-dimensional surface-based soft contact element with an isotropic shear friction is used for each potential crack, and an 8-node linear brick, reduced integration 3D continuum element (C3D8R) is used for the masonry wall. Small-stiffness truss elements are also used to stabilize the entire system.

As revealed by the 2D FE analysis, the nonlinear properties of masonry material have no significant effects on the response of the test structure. Therefore, an elastic isotropic material with the elastic modulus of 600 ksi is used for the 3D continuum elements. Based on the material tests, the bed-joint friction coefficient is assumed to be 1.0. The predefined potential crack pattern has important effects on the accuracy of the model. Based on previous experimental research and theoretical investigations, the

following rules are followed when defining the potential crack pattern. The definition of the possible crack pattern in the test structure is shown in Figure 11.16.

- 1) For all the first floor door piers (such as Pier A2-2, 2-7, B2-2, and B1-2), there are possible cracks at the bottom of the piers between the piers and the foundation.
- 2) If a window pier is at the exterior of the wall (such as Piers A1-2, A-1, A2-1, B2-1, and B1-1) or adjacent to a door opening (such as Piers A-7 and Pier B-7), there is a possible crack at the bottom of the pier propagating from the corner adjacent to the window opening to another corner at the foundation level or the floor level.
- 3) If a window pier or door pier is at the exterior of the wall, there is a possible crack at the top of the pier propagating from the corner adjacent to the window opening or the door opening to another corner at the floor level.
- 4) For the other interior window piers or door piers, there are possible horizontal cracks at both the top and the bottom of the pier (the bottom crack for an interior window pier next to a door-opening see Rule 2).
- 5) For the roof spandrel, there are possible cracks propagating from the top interior corners of the window openings upwards at an angle of 45° until they reach the roof.

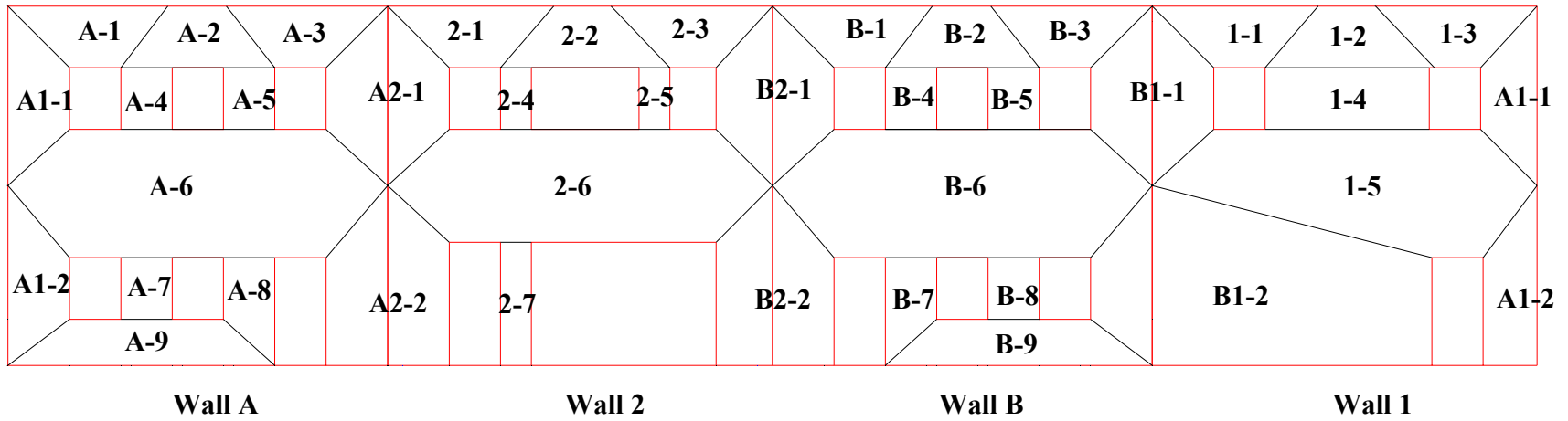


Figure 11.16. Definition of the possible crack pattern in the test structure

The ABAQUS 3D model for the test structure is shown in Figure 11.17. Note that the flexible roof diaphragm and floor diaphragm are not incorporated into this model. This simplification is based on the results from previous research which shows that the existing flexible diaphragms have no significant influences on the behavior of the test structure for the particular in-plane loading cases (see Chapter 10). Similar to the 2D FE model analyses, lateral loads were applied in the form of cyclic displacements in order to allow the hysteretic behavior of the structure to be investigated. The displacement ratio between the floor level and the roof level was kept constant throughout loading at 0.8. Maximum roof displacements of 0.25 inches and 0.5 inches were selected for the directions parallel to Walls 1 and 2, and to Walls A and B, respectively, as employed in the ST-11 building test. The lateral displacements were first applied to the in-plane walls 1 and 2, and then applied to the in-plane walls A and B, to follow the displacement history used in the experimental research. The applied lateral forces are captured by special truss elements employed in the model.

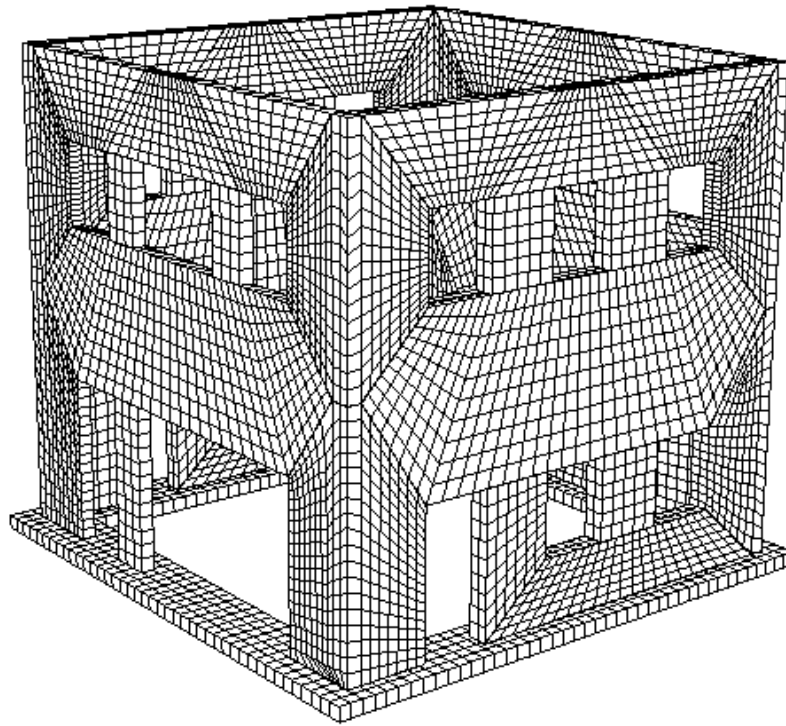


Figure 11.17. ABAQUS 3D contact model for the test structure

11.3.2. Nonlinear FE analysis results parallel to Walls 1 and 2

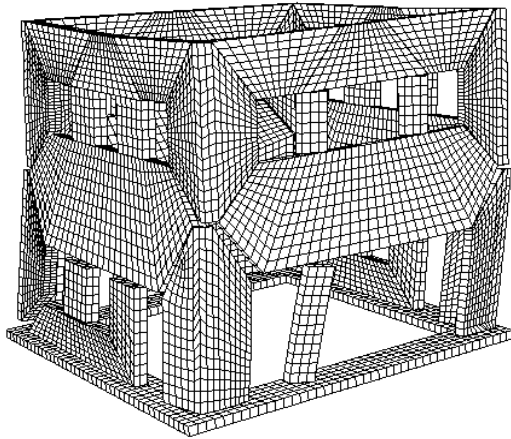
The predicted failure mechanisms of Wall 2 are shown in Figure 11.18, and are similar to what was observed during the test. The damage of the masonry in-plane wall concentrates on the first story piers. All the three first story piers rocked. In addition, the first-story spandrel at the tension side of the wall tended to be lifted above the exterior pier, which implies the importance of the overturning moments. In the out-of-plane wall at the compressive side of the building (for example, Wall B when loaded in the push direction, see Figure 11.18 (b)), the damage was minor. However, the triangular portion above the exterior in-plane pier (for example, the portion B2-1 and B-1 in Wall B when

loaded in the push direction, see Figure 11.16 and Figure 11.18 (b)) tended to be lifted, indicating the movement of the spandrel flange.

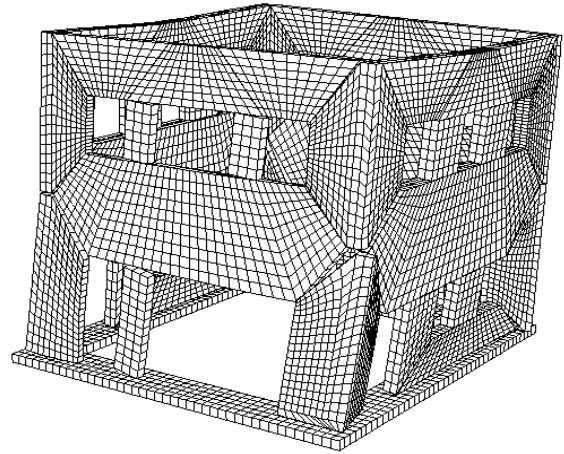
In the out-of-plane wall at the tensile side of the building, the damage is more extensive. For example, when the building was loaded in the push direction, the triangular portion of Wall A above the exterior in-plane pier (A2-1 and A-3) was lifted (see Figure 11.18 (a)). In addition, the entire first-story spandrel of Wall A was also lifted above the first story piers. This reinforces the significance of flange effects.

The calculated base shear-lateral roof displacement relationship for Wall 2 is shown in Figure 11.19. The relationship obtained from the test is also shown as a comparison. Specifically, Figure 11.19 (a) shows the backbone of the test data and the unloading curves at the last cycle, while Figure 11.19 (b) shows the base shear-lateral roof displacement curve corresponding to the test run 10 with a maximum roof displacement of 0.25 inches.

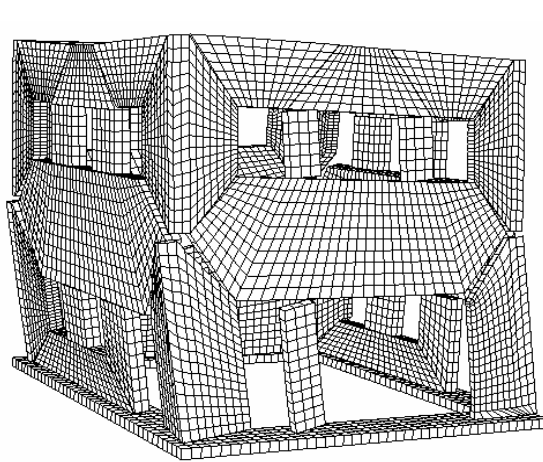
The predicted maximum strengths of Wall 2 by the FE analysis were 33.7 kips and 34.7 kips in the push direction and the pull direction, respectively. They are about 25% and 40% higher than the values obtained in the test (27 kips in the push direction and 24.4 kips in the pull direction). The difference is probably due to the stabilizing truss elements used in the model, which artificially increases the strength of the building. On the other hand, as shown in Figure 11.19 (b), both the analysis result and the test curve exhibit small energy dissipation, which indicates that rocking behavior dominates the response of Wall 2.



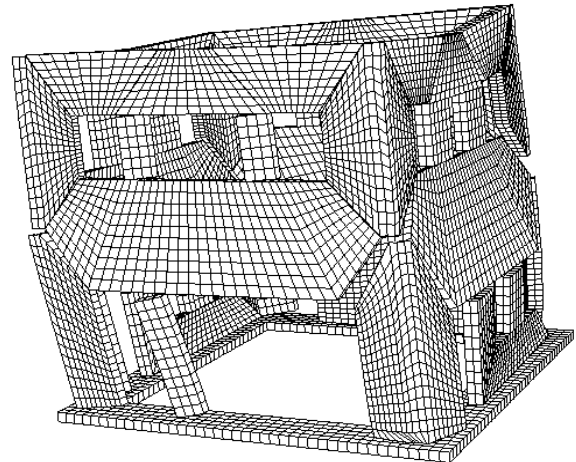
(a) Push direction, left view



(b) Push direction, right view

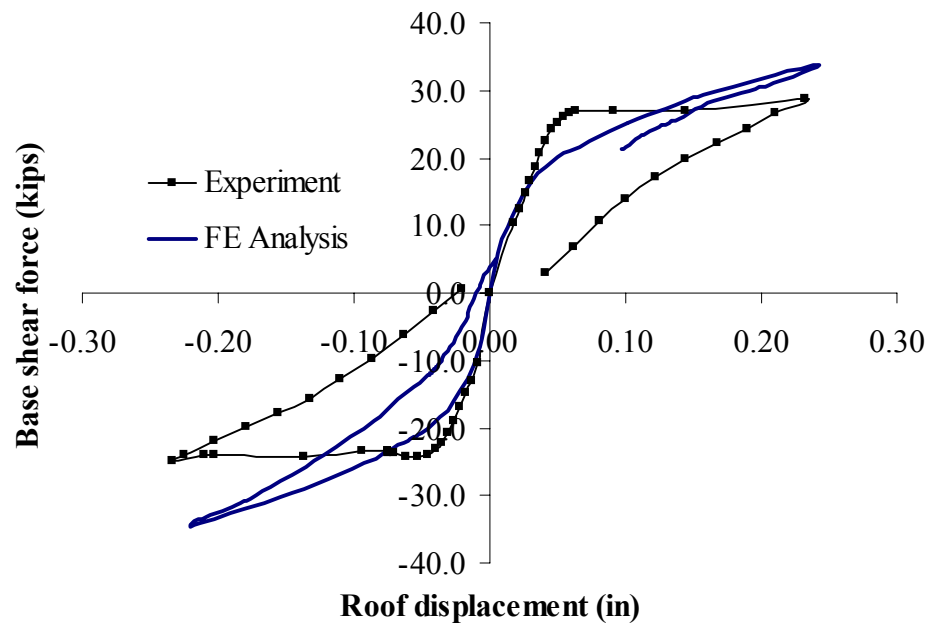


(c) Pull direction, left view

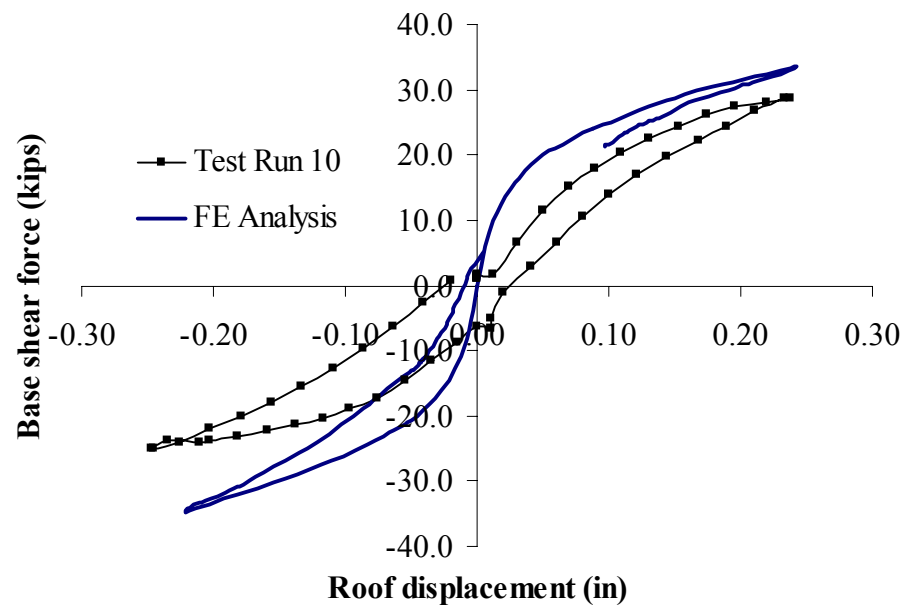


(d) Pull direction, right view

Figure 11.18. Failure mechanisms of Wall 2



(a) Calculated vs. the entire experimental data (backbone)



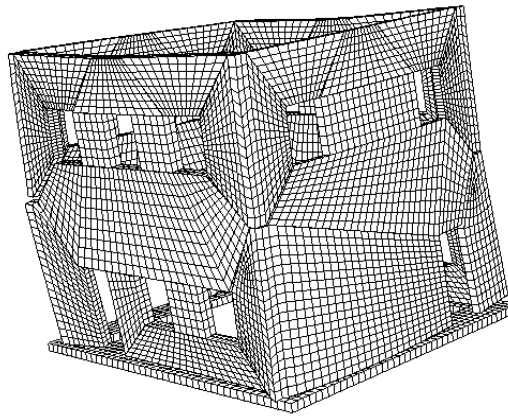
(b) Calculated vs. Test run 10

Figure 11.19. 3D FE analysis vs. measured base shear-lateral roof displacement relationship for Wall 2

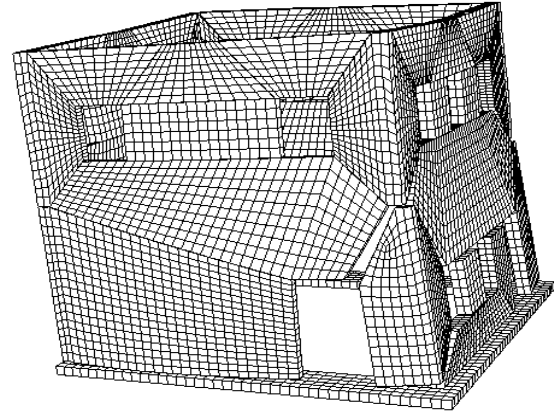
The predicted failure mechanism of Wall 1 in the push direction is shown in Figures 11.20 (a) and (b). It is similar to what was observed during the test. Pier 1-6 (Portion B1-2 in Figure 11.16) slid and rocked to the left, while Pier 1-7 (Portion A1-2 in Figure 11.16) rocked. Meanwhile, the spandrel above Pier 1-6 (Portion A1-1 and A-1) tended to be lifted due to the overturning moment effects. As a result, Pier 1-6 was left behind. A crack also propagated into Wall A and lifted up its upper triangular portion A1-1 and A-1 due to the flange effect. In contrast, the damage to Wall B is insignificant. The predicted failure mechanism of Wall 1 in the pull direction is shown in Figures 11.21 (c) and (d). This is also similar to the test observations, where, Pier 1-6 slid to the right, while Pier 1-7 rocked. However, in contrast to the test observation, the FE analysis shows significant uplift of the spandrel above Pier 1-6. As a result, Pier 1-6 tended to be left behind. The difference is probably due to the fact that the test did not pull the building far enough. Therefore, a through crack could not develop at the top of Pier 1-6, and Pier 1-6 could still rock and slide with increasing lateral displacement.

The calculated base shear-lateral roof displacement relationship for Wall 1 is compared with the test results in Figure 11.21. Specifically, Figure 11.21 (a) shows the backbone of the test data and the unloading curves at the last cycle, while Figure 11.21 (b) shows the base shear-lateral roof displacement curves corresponding to the last test run 10a. Both the analysis result and the test curve exhibit large energy dissipation, which indicates that sliding behavior dominates the response of Wall 1. The predicted maximum strengths of Wall 1 by the FE analysis were 68.0 kips and 63.0 kips in the push direction and the pull direction, respectively. They are about 14% and 15% higher than the values obtained in the test (59.7 kips in the push direction and 54.9 kips in the pull direction).

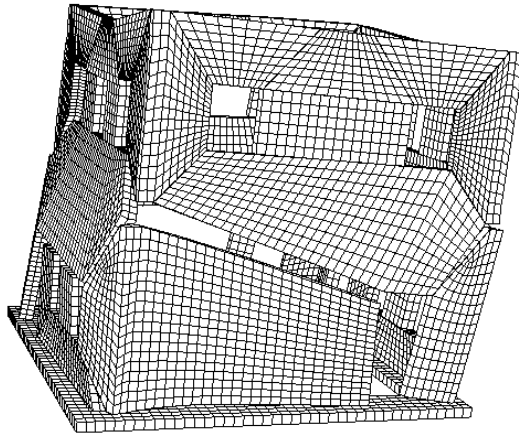
The difference is again due to the utilization of stabilizing truss elements in the FE model.



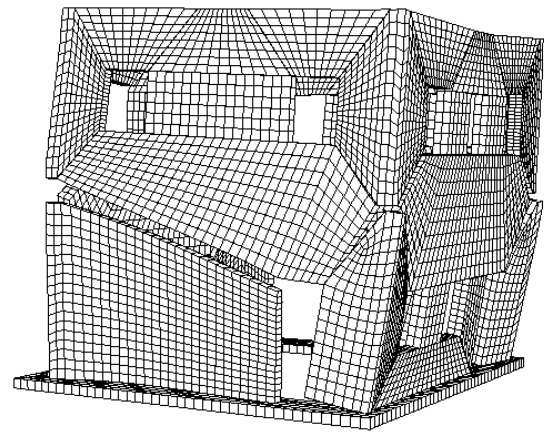
(a) Push direction, left view



(b) Push direction, right view

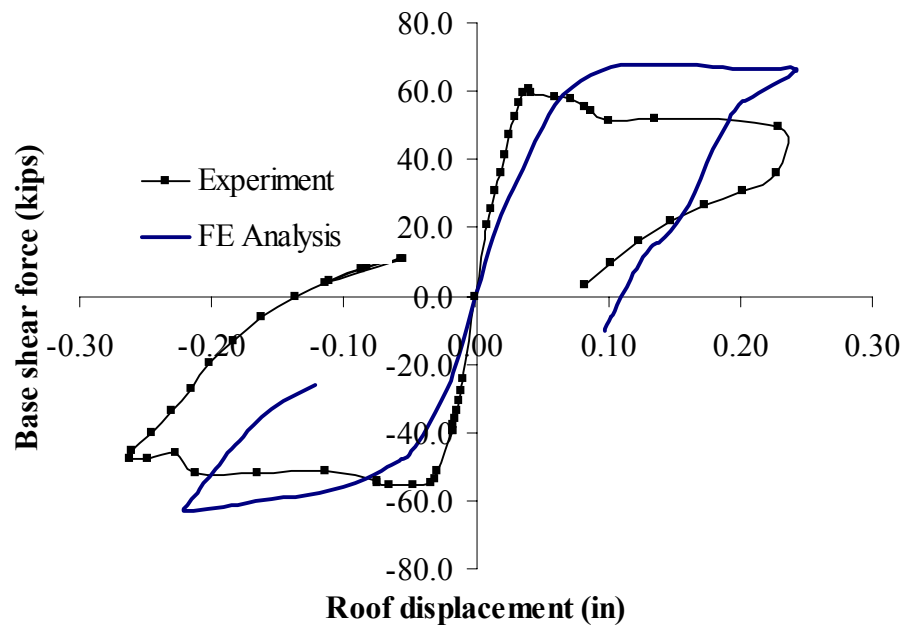


(c) Pull direction, left view

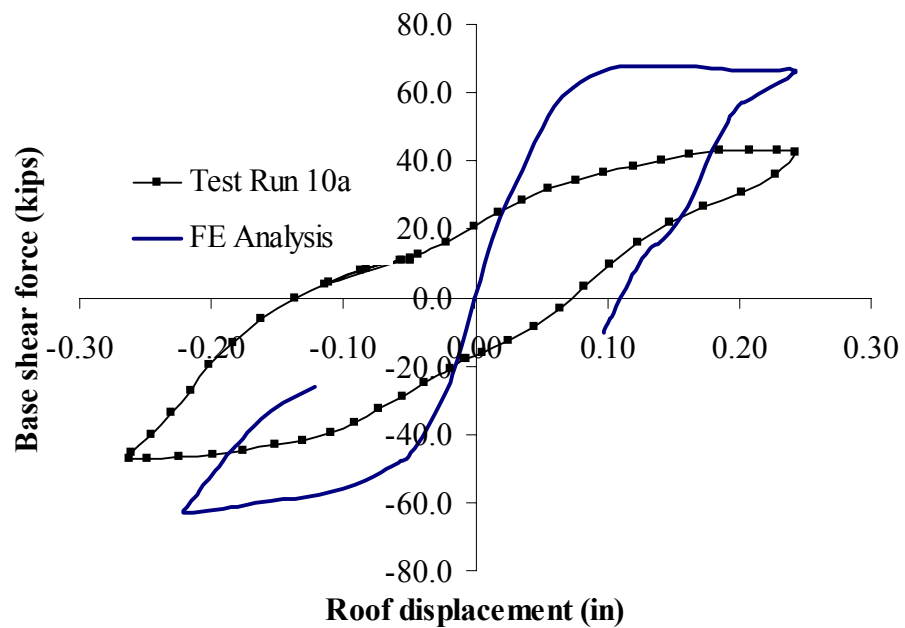


(d) Pull direction, right view

Figure 11.20. Failure mechanism of Wall 1



(a) Calculated vs. the entire experimental data (backbone)



(b) Calculated vs. Test run 10a

Figure 11.21. 3D FE analysis vs. measured base shear-lateral roof displacement relationship for Wall 1

Another interesting result obtained from the FE analysis is the force distribution among the four masonry walls. Figures 11.22, 11.23, and 11.24 show the force distribution among the four walls for the base shear force parallel to Walls 1 and 2, the base shear force perpendicular to Walls 1 and 2, and the vertical compressive force, respectively. The base shear forces in the first two figures are normalized to the total base shear force of the building parallel to Walls 1 and 2, while the vertical force in the last figure is normalized to the total weight of the test structure.

Figure 11.22 shows that at the beginning of loading, the two in-plane walls, Walls 1 and 2, resisted most of the external lateral shear force. When the building was loaded in the pull direction (negative roof displacement), the ratios between the four walls remained relatively constant. In contrast, when the building was loaded in the push direction, with increasing lateral displacement the base shear resisted by the out-of-plane Wall B increased while the base shear resisted by another out-of-plane Wall A and the in-plane wall 1 decreased. This can be explained by the variation of the vertical forces in the four walls, as shown in Figure 11.24. By the end of pull loading, the vertical force distribution among the four walls remained relatively constant. This indicates that the further propagation of cracks in the in-plane walls was not so significant and, thus, the in-plane walls still resisted most of the lateral shear forces. In contrast, by the end of push loading the vertical forces in both Wall 1 and Wall 2 decreased while the vertical forces resisted by the compressive out-of-plane wall, Wall B, increased. This indicates that the crack propagation in the in-plane walls was so extensive that their effective area was significantly reduced. As a result, the uncracked flange of the building (the compressive out-of-plane Wall B) took up more and more vertical and shear force. This redistribution

of vertical force and shear force to the flange area with damage accumulation in the in-plane walls also implies that the assessment of the flange distribution in an elastic structure as discussed in Section 8.6 cannot be simply extended to nonlinear range.

Figure 11.23 shows that the base shear perpendicular to Walls 1 and 2 in each wall was quite small. This indicates that the torsion behavior of the test structure was small, which is consistent with the experimental observation and the elastic analysis.

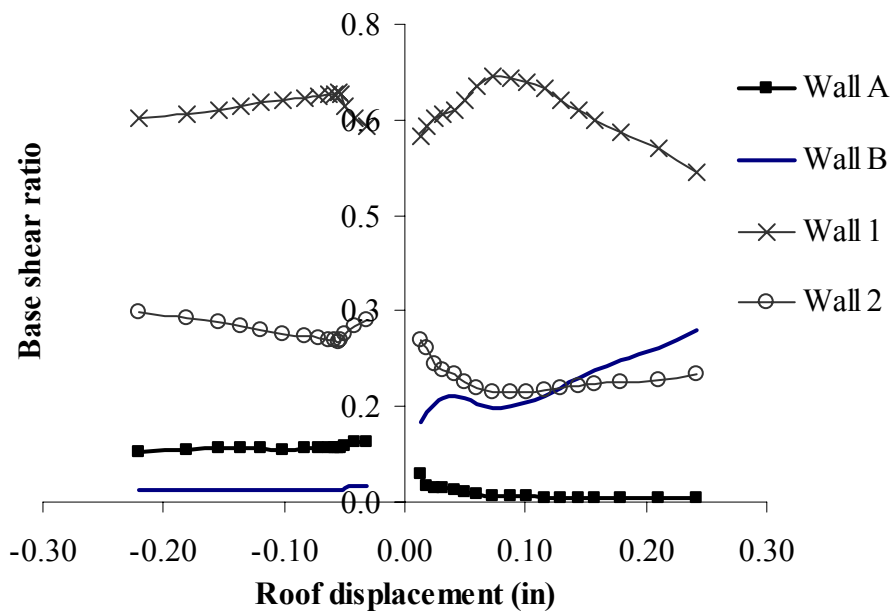


Figure 11.22. Distribution of base shear force parallel to Walls 1 and 2 among four walls

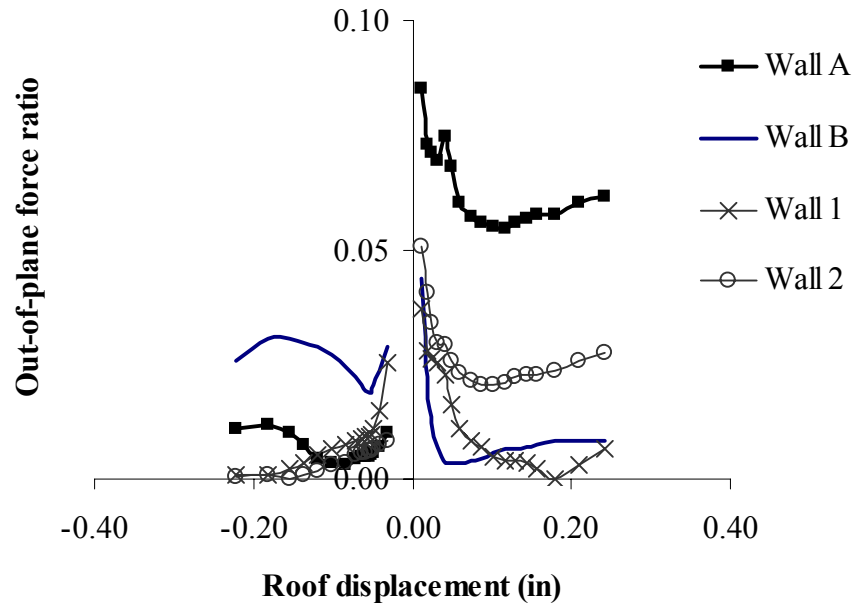


Figure 11.23. Distribution of base shear force perpendicular to Walls 1 and 2 among four walls

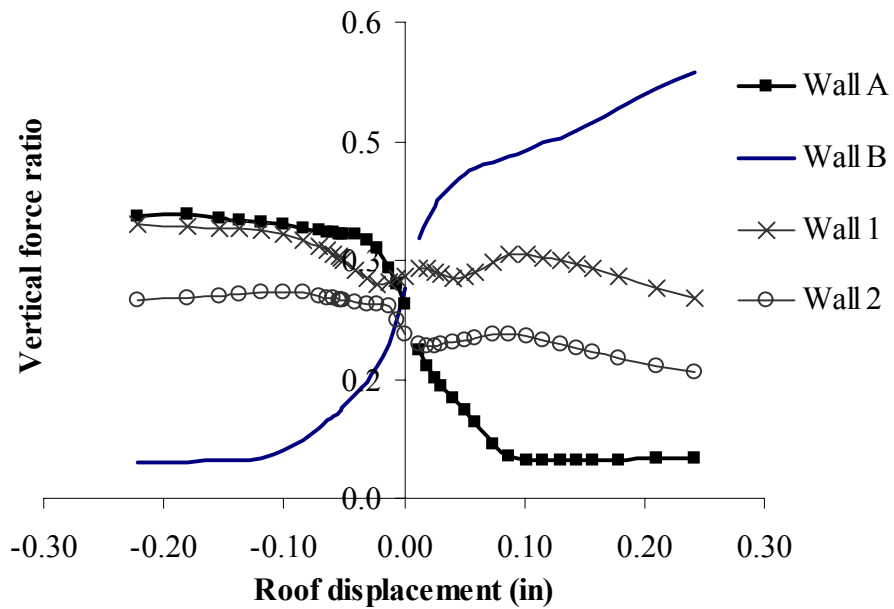


Figure 11.24. Distribution of vertical compressive force among four walls

11.3.3. Nonlinear FE analysis results parallel to Walls A and B

The predicted failure mechanism of Wall B in the push direction is shown in Figures 11.25 (a) and (b), which is similar to the test observation. The three left piers, Pier B-7, B-8, and B-9 rocked to the left. Meanwhile, the first-story spandrel above Pier B-10 tended to be lifted due to the overturning moment effects. As a result, Pier B-10 was left behind. The overturning moment effects and flange effects also introduced large tensile stress in the tensile flange of the building, Wall 1. As a result, Pier 1-6 was lifted up from the foundation and also separated from the Wall 1 first floor spandrel. Note that only the uplift of Pier 1-6 from the foundation was observed in the test, while no separation of Pier 1-6 from the spandrel was recorded (see Section 9.4.1.3). This difference was again probably due to the fact that the building was not displaced sufficiently for the complete mechanism to develop. Minor damage was observed in the compressive flange wall (Wall 2), except that the upper triangular portion adjacent to Wall B (Portion B2-1 and 2-3 in Figure 11.16) was lifted, apparently due to the movement of the spandrel flange.

The predicted failure mechanism for Wall B in the pull direction is shown in Figures. 11.25 (c) and (d). The prediction is in agreement with the test observations, as all four first story piers rocked to the right. Meanwhile, the spandrel above Pier B-7 was lifted due to the overturning moment effects. As a result, Pier B-7 tended to be left behind. The overturning moment effects and flange effects also introduced large tensile stress in the tensile flange of the building (Wall 2). As a result, the Wall 2 first floor spandrel was lifted above the first story piers. The upper triangular portion adjacent to Wall B was also lifted. Minor damage was observed in the compressive flange wall (Wall

1), except that the upper triangular portion adjacent to Wall B (Portion B1-1 and 1-1 in Figure 11.16) was lifted due to the movement of the spandrel flange.

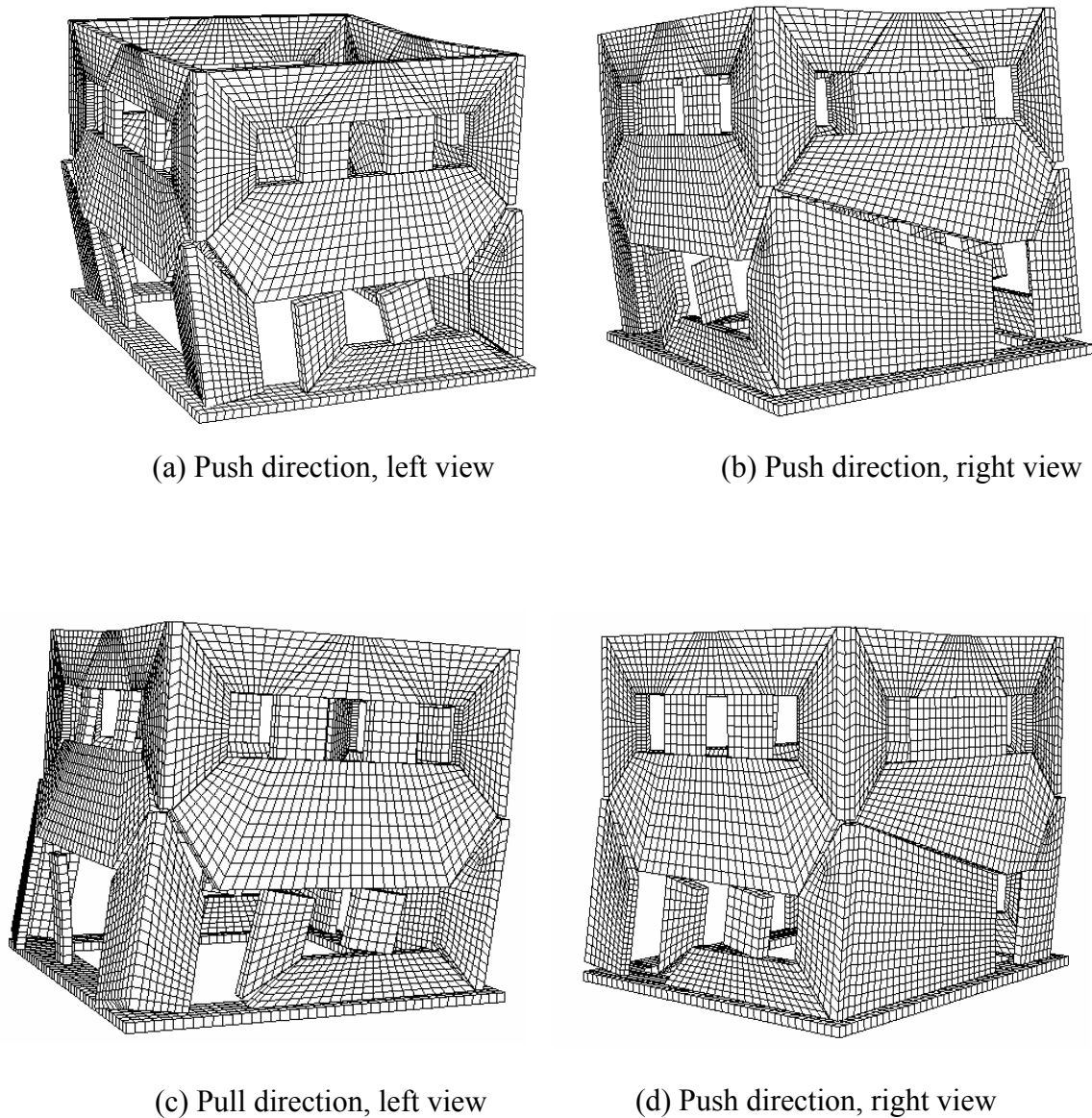
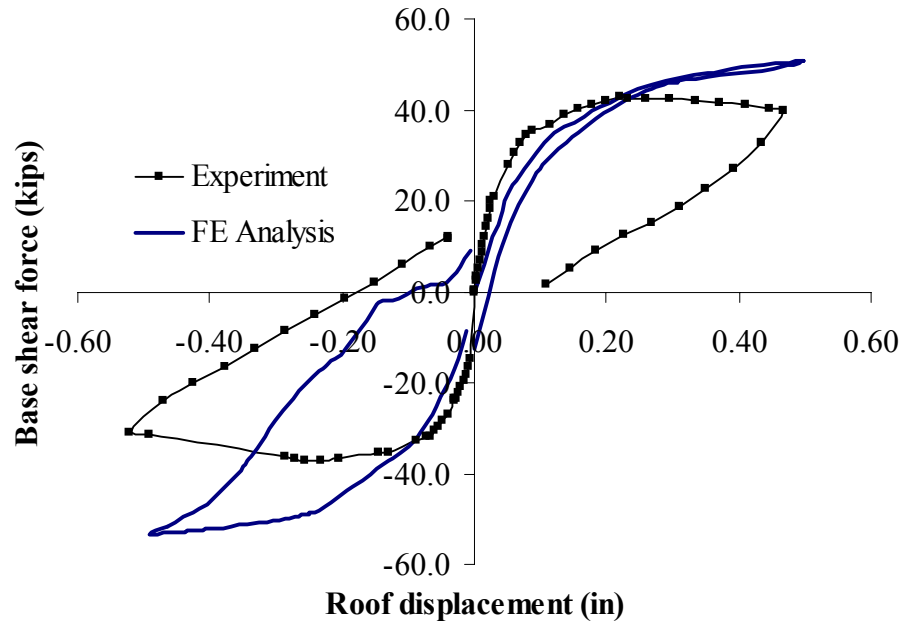
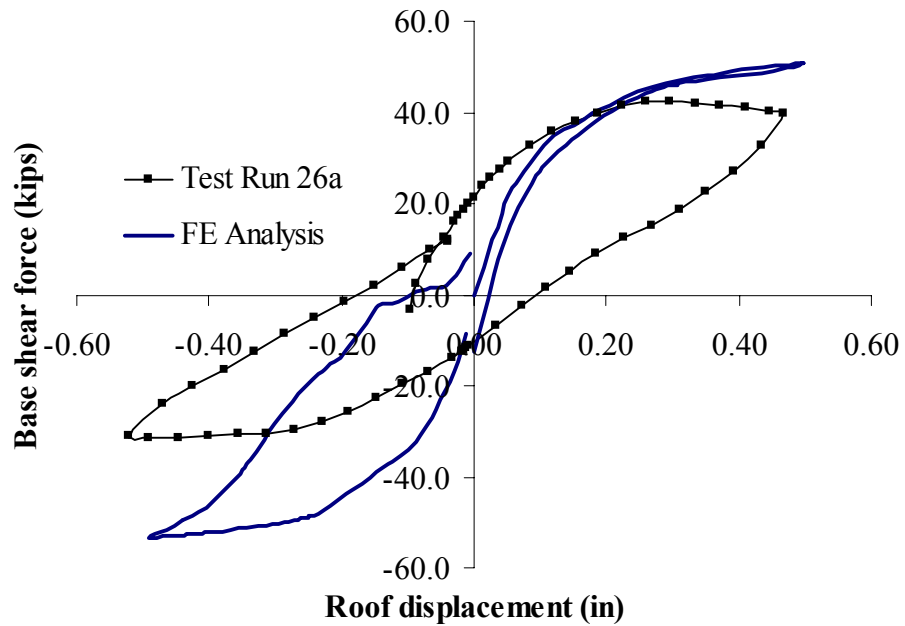


Figure 11.25. Failure mechanism of Wall B

The calculated base shear-lateral roof displacement relationship for Wall B and the corresponding experimental results are compared in Figure 11.26. Figure 11.26 (a) shows the backbone of the test data and the unloading curves at the last cycle, while Figure 11.26 (b) shows the measured base shear-lateral roof displacement relationship corresponding to the last test run 26a. The maximum strengths of Wall B predicted by the FE analysis were 50.7 kips in the push direction and 53.3 kips in the pull direction. These are about 18% and 44% higher than the values obtained in the test (43.0 kips in the push direction and 36.9 kips in the pull direction), respectively. Two reasons may explain the difference. First, as noted before, the utilization of stabilizing truss elements in the model may introduce additional strength to the building. Second, initial damage, induced by the previous tests parallel to Walls 1 and 2, was present in the test structure before the tests parallel to Walls A and B started. Therefore, the measured maximum strength of the building was probably lower than that of an intact building. The measured base shear-lateral roof displacement curves exhibit quite large energy dissipation, which indicates that Wall B was sliding as well as rocking. This response was captured by the FE analyses in the pull direction, but not in the push direction.



(a) Calculated vs. the entire experimental data (backbone)



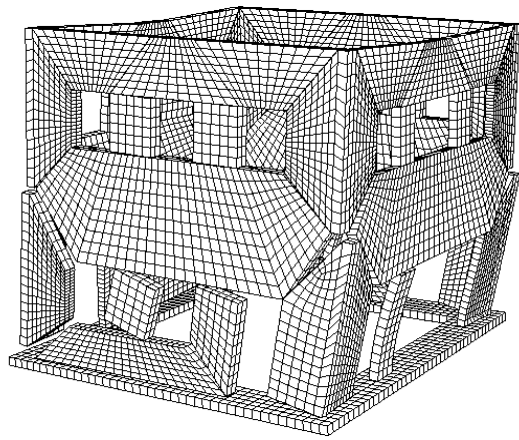
(b) Calculated vs. Test run 26a

Figure 11.26. 3D FE analysis vs. test observation of the base shear-lateral roof displacement relationship for Wall B

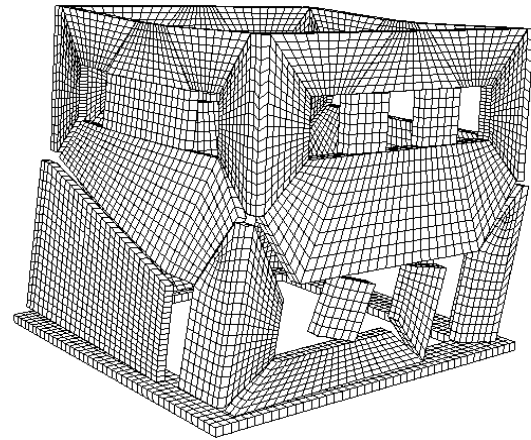
The predicted failure mechanism of Wall A in the push direction is shown in Figures 11.27 (a) and (b). It is similar to what was observed during the test. Three right piers, Pier A-8, A-9, and A-10 rocked to the right. Meanwhile, the spandrel above Pier A-7 was lifted due to the overturning moment effects. As a result, Pier A-7 was left behind. In addition, the overturning moment effects and flange effects also caused the upper triangular portion of Wall 1 adjacent to Wall A (Portion A1-1 and 1-3 in Figure 11.16) to be lifted. Minor damage was observed in the compressive flange wall (Wall 2), except that the upper triangular portion adjacent to Wall A (Portion A2-1 and 2-1 in Figure 11.16) was lifted due to the movement of the spandrel flange.

The predicted failure mechanism of Wall A in the pull direction is shown in Figures. 11.27 (c) and (d). The prediction and observed test behavior are in agreement, as all four first story piers rocked to the left. Meanwhile, the spandrel above Pier A-10 was lifted due to the overturning moment effects. As a result, Pier A-10 tended to be left behind. The overturning moment effects and flange effects also caused the Wall 2 first floor spandrel to be lifted from the Wall 2 first story piers, and the upper triangular portions in Wall 1 and Wall 2 adjacent to Wall A to be lifted.

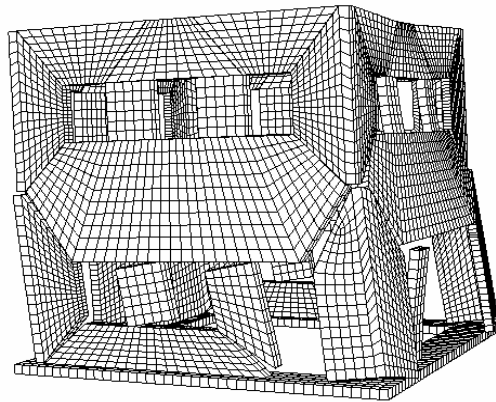
Another interesting phenomenon observed in the analysis is that the door pier A-10 and Pier B-7 rotated out-of-plane no matter the building was loaded in the push direction or the pull direction. It is due to the irregular shape of this pier. This phenomenon was also observed in the test.



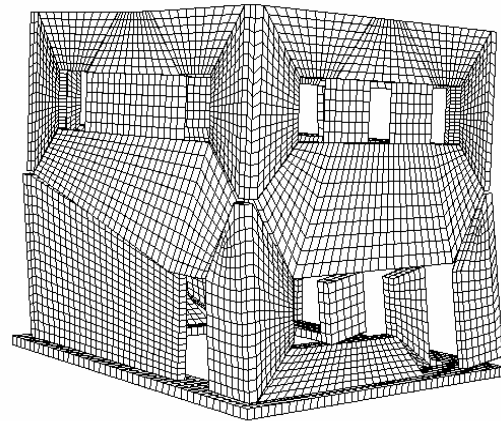
(a) Push direction, left view



(b) Push direction, right view



(c) Pull direction, left view

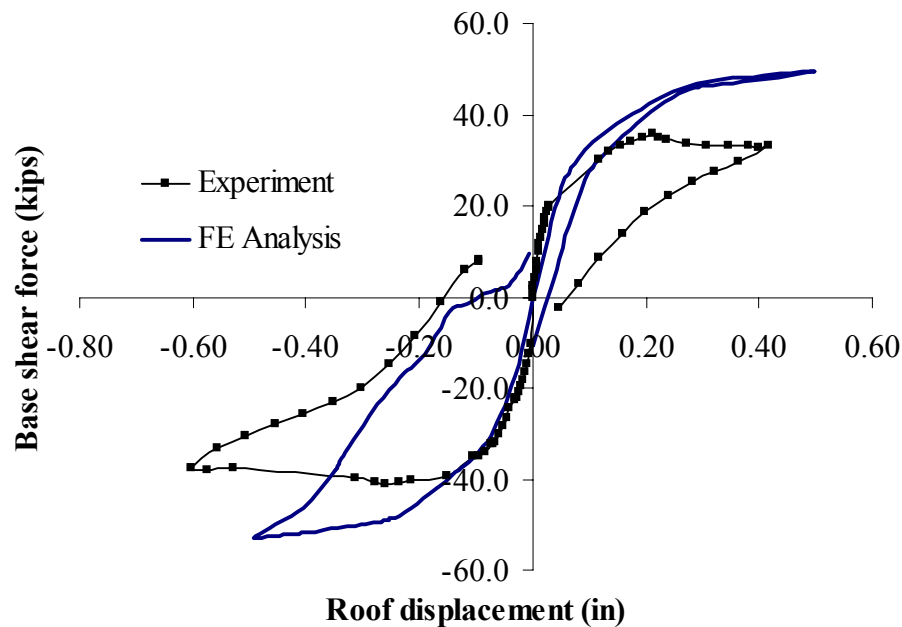


(b) Pull direction, right view

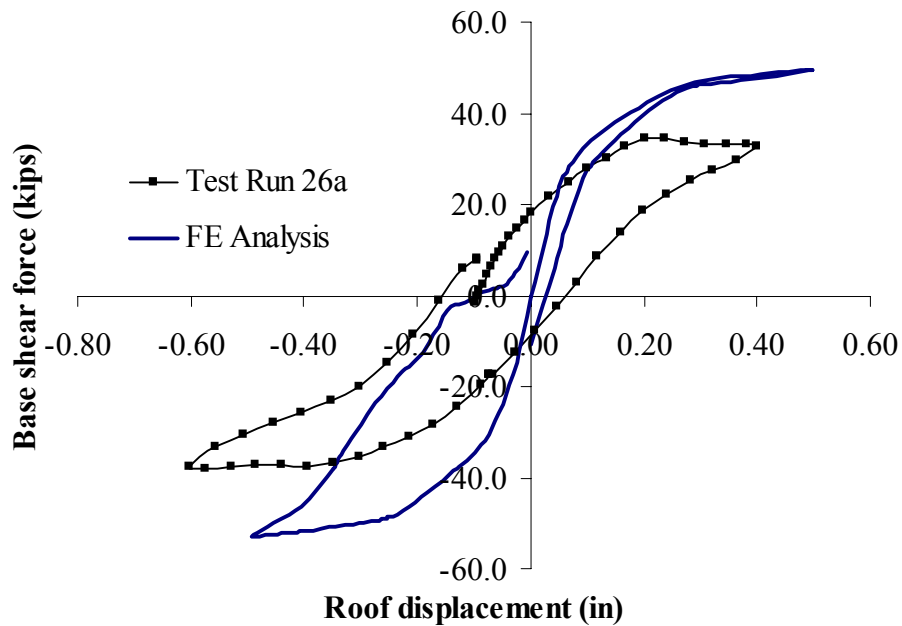
Figure 11.27. Failure mechanisms of Wall A

The calculated base shear-lateral roof displacement relationship for Wall B is compared with the test results in Figure 11.28. Figure 11.28 (a) shows the backbone of the test data and the unloading curves at the last cycle (Cycle 26a), while Figure 11.28 (b) shows the base shear-lateral roof displacement relationship corresponding to the last test run 26a. The maximum strengths of Wall A predicted by the FE analysis were 49.4 kips

in the push direction and 52.8 kips in the pull direction. These are about 38% and 30% higher than the values obtained in the test (35.7 kips in the push direction and 40.8 kips in the pull direction). Again, the utilization of stabilizing truss elements in the model and the existing initial damage in the test structure may explain the difference. The measured base shear-lateral roof displacement curves exhibit quite large energy dissipation, which indicates that Wall A was sliding as well as rocking. As for Wall B, this response was capture by the FE analysis in the pull direction, but not in the push direction.



(a) Calculated vs. the entire experimental data (backbone)



(b) Calculated vs. Test run 26a

Figure 11.28. 3D FE analysis vs. test observation of the base shear-lateral roof displacement relationship for Wall A

Figures 11.29, 11.30, and 11.31 illustrate the force distribution among the four walls for the base shear force parallel to Walls A and B, the base shear force perpendicular to Walls A and B, and the vertical compressive force, respectively. The base shear forces in the first two figures are normalized to the total base shear force of the building parallel to Walls A and B, while the vertical force in the last figure is normalized to the total weight of the test structure. Figure 11.29 shows that with increasing lateral displacement, the base shear resisted by the two in-plane walls decreased; and the base shear resisted by the compressive flange (Wall 2 when loaded in push direction and Wall 1 when loaded in pull direction) increased, while the tensile flange of the building (Wall 1 when loaded in push direction and Wall 2 when loaded in pull direction) essentially

didn't resist any lateral shear force. This is consistent with the variation of vertical forces among the four walls, as shown in Figure 11.31. With increasing lateral displacement, the vertical forces resisted by the tensile flange and the two in-plane walls decreased and the vertical force resisted by the compressive flange increased. Both the variation of the vertical force distribution and the variation of the base shear distribution point out the significant effects of the overturning moment. Similar to the results of the loading parallel to Walls 1 and 2, Figure 11.32 shows that the base shears perpendicular to the loading direction in both Walls A and B was small. Again, this is an indication that the torsional behavior of the test structure was small.

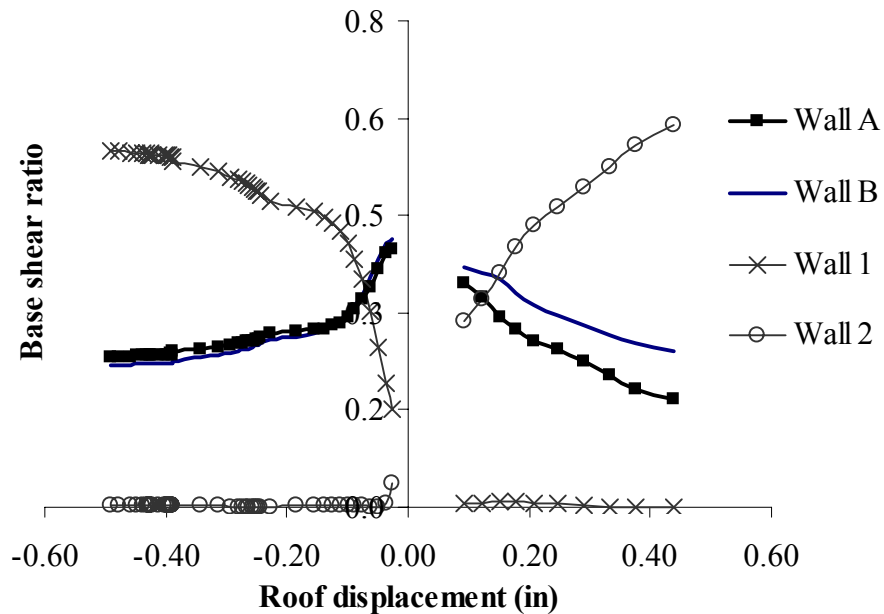


Figure 11.29. Distribution of base shear force parallel to Walls 1 and 2 among four walls

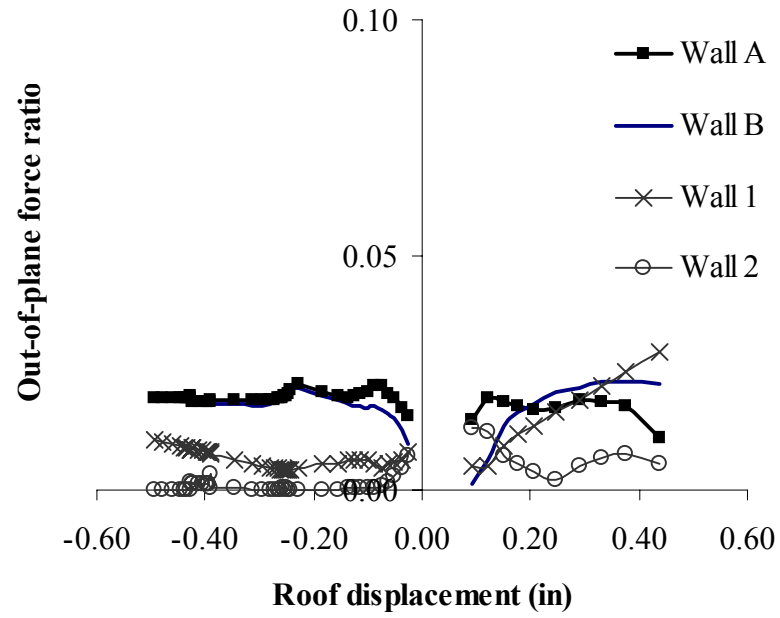


Figure 11.30. Distribution of base shear force perpendicular to Walls 1 and 2 among four walls

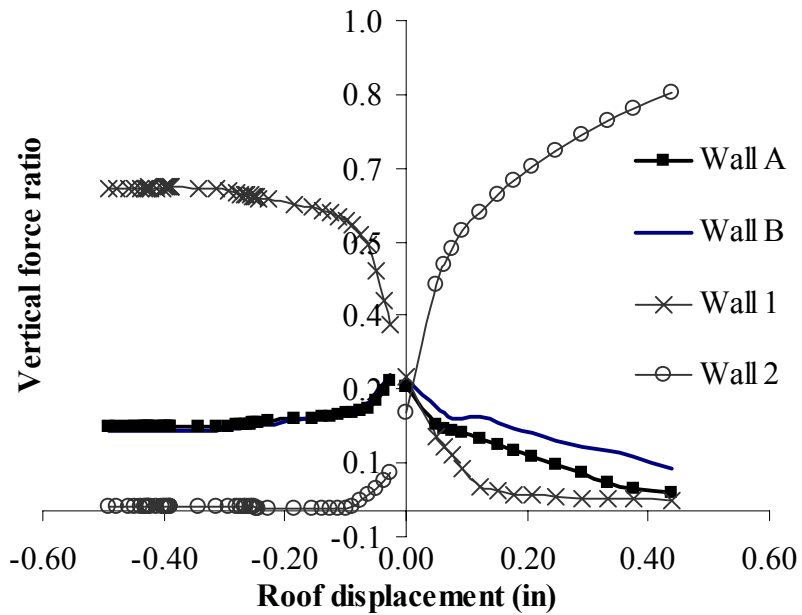


Figure 11.31. Distribution of vertical compressive force among four walls

11.3.4. Discussions of the 3D FE model

The 3D FE analysis for the ST-11 test structure predicted behavior in good agreement with that observed experimentally. The 3D FE model was proven to be an excellent analytical tool for the nonlinear behavior of URM structure for the following reasons:

- The 3D FE model is the only analytical approach that provides insight into the three dimensional behavior of a URM building. For example, the flange effects present in all Walls, the global torsional behavior of the entire URM building, and the local torsion of each individual component can only be satisfactorily examined by this model.
 - The 3D FE model is able to accurately predict the failure mechanisms of this URM structure. The contact element employed provides an excellent means to consider the rocking and sliding of a URM structure.
 - Although the masonry material is assumed to be elastic and thus the diagonal tension failure mechanism and the toe crushing failure mechanism were not considered in the current model for the ST-11 building, these two failure mechanisms can be taken into account by introducing nonlinear material properties into the 3D continuum elements, as demonstrated by their inclusions in the 2D FE model.
 - The 3D FE model can be expanded to consider some other issues associated with a URM structure, such as the effects of rigid diaphragm and the retrofit methods.
- On the other hand, the current 3D FE model has limitation.

- First, the employed FE analysis cannot give an accurate prediction for the maximum strengths of the test structure. The predicted values are always higher than the test values due to the utilization of the elastic stabilizing truss element in the model required to provide numerical stability to the calculations. However, further investigation of the properties of the truss elements employed could solve this problem. For example, if nonlinear properties are introduced, these truss elements can not only be used to stabilize the numerical system but also be used to describe the nonlinear normal tensile strength and the initial shear strength of the crack surfaces.
- Use of a 3D FE model requires great computational efforts and structural expertise. For instance, it takes a significant amount of time to build the structural model and to run the analytical problems. Furthermore, many computational parameters need to be carefully chosen to stabilize the analysis procedure of such a complex nonlinear system. As a result, this method is only suitable for important projects, and it is not recommended for daily design or evaluation projects.

11.4. CONCLUSIONS

Both a 2D discrete-crack FE model and a 3D discrete-crack model were used to analyze the nonlinear properties of the test structure. The 2D discrete-crack FE model could predict the failure mechanism of each in-plane wall moderately well. However, it significantly underestimated the maximum strength of the test structure, because some critical three-dimensional properties, such as the flange effects, could not be considered.

The 3D discrete-crack FE model was built following predefined rules for the potential crack pattern of the URM structure, and directly considered its three dimensional global behavior. It provided a good prediction for the failure mechanisms of the test structure. However, since stabilizing truss elements were used in this model, additional strength was introduced into the model. The maximum strengths predicted by this 3D FE model were 14% to 44% larger than the measured values. Future work could be conducted to vary the properties of the stabilizing truss elements, and to improve the performance of the 3D FE model.

CHAPTER 12

NONLINEAR PUSHOVER ANALYSIS

12.1. INTRODUCTION

The analytical portion of this research was conducted to better understand and evaluate the nonlinear seismic resistance of existing URM buildings. The analytical study included several different nonlinear FE models as discussed in Chapter 11, whose results indicate that appropriate nonlinear FE models can give good predictions of the nonlinear response of existing URM buildings. However, the FE method is usually very time-consuming and requires expertise of the user. As an effective and practical alternative, simplified models were also widely used in previous research (Benedetti and Benzoni 1984, Tomazevic 1987, and Tena-Colunga 1992, to name a few). These simplified methods can be categorized into (a) simplified methods to model an entire URM building and (b) simplified methods to model a perforated URM in-plane wall.

The simplified methods that address an entire URM building were built on a series of major simplifying assumptions. For example, Benedetti and Benzoni (1984) used a non-linear 2D macro model to analyze URM structures for which the response mechanism was assumed to be dominated by shear deformations. The building analyzed was regarded as consisting of a number of substructures. Each substructure was described by means of equivalent homogeneous materials whose properties were derived from experiments. The out-of-plane walls were considered as additional vertical load capacity components which could resist the overturning moments, but their lateral shear resistances were ignored. Tomazevic (1987) suggested that a story mechanism model was

most suitable to define the behavior of masonry buildings with rigid diaphragms and subjected to seismic loading. In his model, the masonry walls were assumed to be fixed at both the top and the bottom, and the masonry walls with composite cross-sections (such as L, T, and H shaped walls) were considered to be separated along the vertical edge. As a result, a masonry building was modeled as a multiply-degree-of-freedom non-linear shear system, with masses concentrated at the floor levels. Story hysteresis envelopes for each story wall were based on the sum of the idealized hysteresis envelopes of the participating walls in the story under consideration. Note that the variation of vertical stress in each pier due to overturning moment was not considered.

A discrete, linear elastic, multi-degree-of-freedom dynamic model was developed by Tena-Colunga (1992) for the dynamic analysis of URM structures with flexible diaphragms. The URM structure was assumed to remain elastic during an earthquake. Masses were lumped at the intersection of the centroidal axes of the walls and the diaphragms, and also at the center of each diaphragm. Flexible diaphragms were represented by elastic shear springs, whose stiffness could be roughly estimated by the in-plane shear and bending stiffness of the floor systems. The in-plane walls were represented by an equivalent condensed beam element with lateral degrees of freedom, whose lateral stiffness was determined by 2D FE analyses. Two generalized springs, one for rotation (rocking) and the other one for direct lateral displacement, represented the foundation flexibility.

A 3D nonlinear model for URM building with flexible roof and floor diaphragms was recently proposed by Kim and White (see MAEC project ST-5). Their model used shear spring elements to simulate in-plane response of masonry walls, and used special

plane elements to simulate shear response of flexible diaphragms. The masses of the out-of-plane walls were lumped at the central axis of the wall, while the stiffness of the out-of-plane walls was considered combined with the stiffness of the floor and roof diaphragms. Moreover, the masonry walls were assumed separated at the corners. The nonlinear shear force-lateral displacement hysteretic curve was provided for each URM pier based on its corresponding failure modes. The shear force-lateral displacement of an entire perforated in-plane wall could be obtained by analyzing this wall based on the response of each pier. The nonlinear shear force-deformation curves for the floor and roof diaphragms were also provided by this model. This model can be used to analyze the nonlinear response of a low-rise URM building under seismic excitation.

Previous experimental research revealed that if the URM out-of-plane walls are appropriately tied to the floor and roof diaphragms and the in-plane walls, the critical component of a URM building is the in-plane walls. As a result, a large amount of works have also been devoted to the simplified modeling of individual URM perforated walls.

The simplified models for a URM perforated in-plane wall can be categorized based on assumptions on the relationship between piers and spandrels. A type of simplified analysis model called the “walls models” (Bruneau, M. 1994) or the “solid spandrel-cracked piers model” (Boussabah, L. 1992) has been applied to strong spandrel-weak pier walls (Figure 12.1). In this type of model, the spandrels were assumed intact and rigid, while the piers could subject to damage. The lateral shear force was distributed to the parallel piers based on relative stiffness, but the overturning moment was usually ignored. The entire perforated wall failed when several or all piers reached their strength capacities.

Another simplified analysis model called the “piers-only model” (Bruneau, M. 1994) or the “solid pier-cracked spandrel model” (Boussabah, L. 1992) has also been developed (Figure 12.2). It was used for a strong pier-weak spandrel wall. This model assumed that the spandrel beams in a perforated wall would crack under very low lateral loads, and thus the continuous piers would work as a cantilever wall fixed at the bottom. This model was originally used for reinforced concrete shear walls and proved to be excessively conservative in case of URM walls (Bruneau, M. 1994(b)).

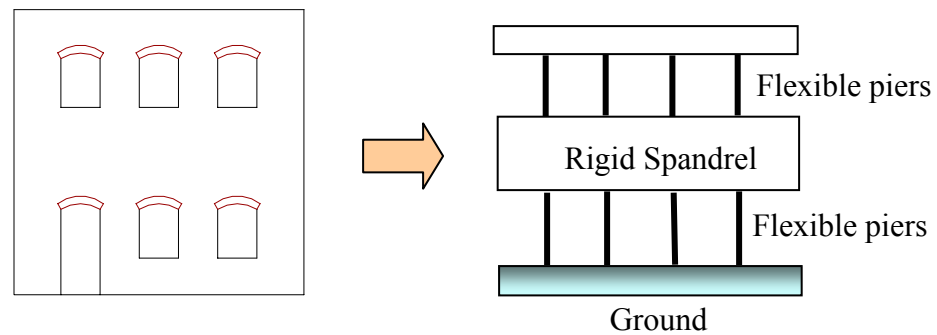


Figure 12.1. Solid spandrel-cracked pier perforated URM wall model

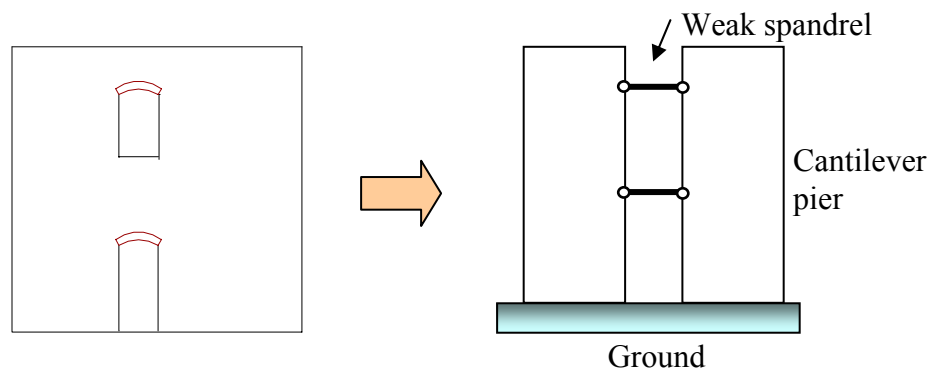


Figure 12.2. Solid pier-cracked spandrel perforated URM wall model

Based on these simplified analysis models, nonlinear pushover analyses have been used to investigate the nonlinear behavior of perforated URM walls. In these models, the nonlinear load-deformation characteristics of individual components were generally directly modeled and embedded into the simplified analysis models. The wall was then subjected to monotonically increasing lateral forces or displacements until either a target displacement was exceeded or the building collapsed (FEMA 356, ATC 2000). One example for this approach was the pushover analysis conducted by Costly and Abrams (1996) for their dynamic test specimens. A solid spandrels-cracked piers model was used in their analysis. In this model, the vertical compressive stress in each pier due to gravity load was considered, but the effect of overturning moments was neglected. The piers were assumed to have perfect elastic-plastic behavior. When an element yielded, the tangential stiffness of this element was assumed to be zero and the incremental loading continued with the reduced structure. Another example is the simple lumped parameter model developed by Park (2002) for the fragility analysis of URM walls (Figure 12.3). Again, a solid spandrel-cracked pier model was used. The piers were assumed fixed at both the top and the bottom. However, the elastic stiffness of each pier was modified accounting for the flexibility of spandrels by either an effective height method or an effective stiffness method (Park 2002). A nonlinear load-deformation hysteresis relationship was also provided for each pier to describe its failure modes and nonlinear behavior.

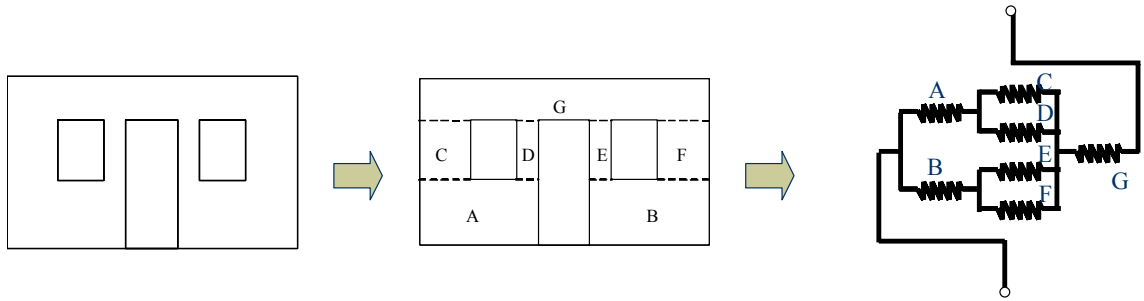


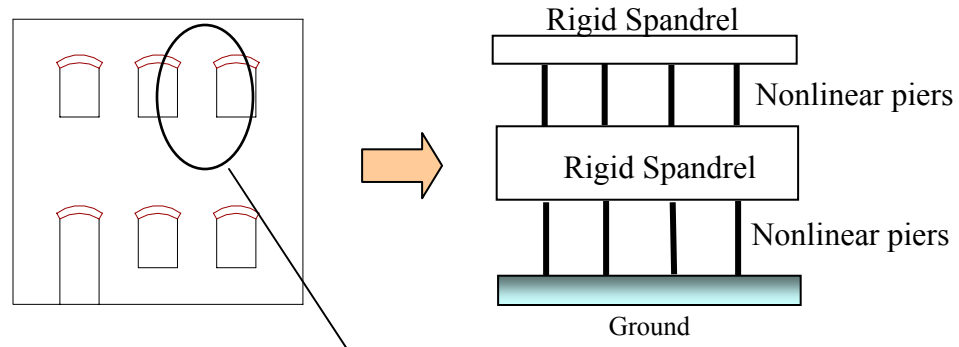
Figure 12.3. Park's simple lumped parameter model (2002)

Those current, available simplified methods for a URM building or a URM perforated in-plane wall generally do not give satisfactory predictions. This is due to the fact that many critical aspects of a URM building behavior, such as the flange effects, the overturning effects, and the typical failure mechanisms of URM pier, are not well addressed in these current models. Considering these limitations, another pushover approach was developed and is presented in this chapter. First, methods to consider the interaction between the piers and the spandrels, the overturning moment effects, and the flange effects are discussed. In addition, the issue of how to simulate the lateral seismic force is addressed. Second, the proposed solutions to these issues are embedded into a new nonlinear pushover program. In this program, two different methods, including the effective pier model outlined in Chapter 4 and another simplified approach, are used to consider the possible failure mechanisms of a URM pier. The proposed nonlinear pushover programs are then used to analyze the test structure discussed in Chapters 6 through 9.

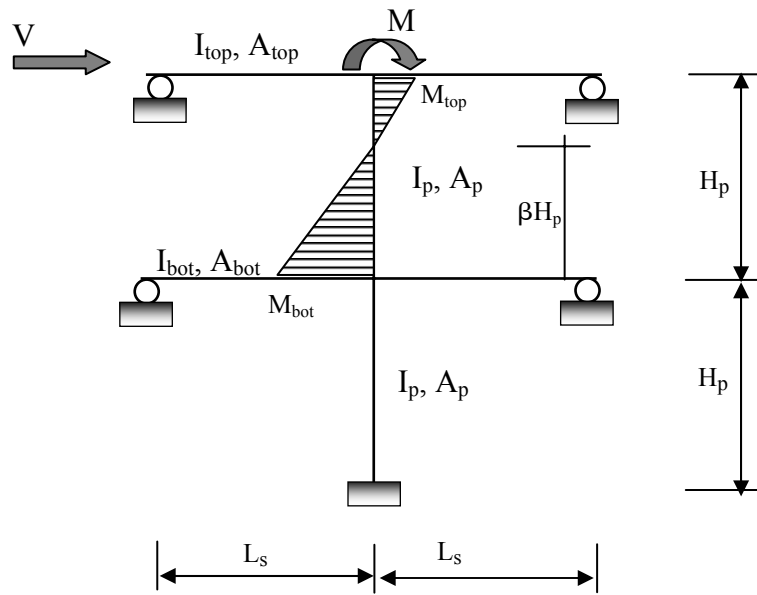
12.2. MODELING OF IN-PLANE WALL AND PIER-SPANDREL INTERACTION

Modeling of a perforated URM wall starts with the description of the interaction between piers and spandrels. Both the piers and the spandrels form part of a loading path transferring the lateral shear forces of the masonry wall to the ground. However, the piers should be more critical than the spandrels, because of their weakened sections due to the presence of door and window openings. Post-earthquake assessments as well as experimental investigations have revealed that once out-of-plane failure is prevented, the final collapse of a URM building is associated with the failure of piers in a critical story (usually the first story). From this point of view, a solid spandrel-cracked pier model is more reasonable than solid pier-cracked spandrel model (Figure 12.4 (a)).

On the other hand, the flexibilities of the spandrels may affect the boundary conditions and thus the elastic stiffness of the piers. A simple model for illustrating the interaction between spandrels and piers is shown in Figure 12.4 (b). The spandrels connected with the pier are modeled as beams simply supported at their inflection points, which are assumed to be located at the mid-span of the spandrels. The effect of the boundary conditions of both the piers above and below the pier under consideration is taken into account. The pier above the one under consideration is replaced by the assumed base shear force (V) and base moment (M) it transfers to the pier being considered. The geometry properties of each element are also shown in Figure 12.4 (b).



(a) Modeling of the perforated



(b) Modeling of the pier

Figure 12.4. Concepts of elastic spandrel-nonlinear pier model

Elastic structural analysis of this model reveals that the height of the inflection point of the pier being considered is dependent on the relative stiffness of the spandrels and the piers as well as the external forces. This can be written in general form as Eq. (12.1):

$$\beta = \beta(M/VH_p, I_p, A_p, H_p, I_{top}, A_{top}, I_{bot}, A_{bot}, L_s) \quad (12.1)$$

In Eq. 12.1, H_p is the height of the pier; I_p is the moment of inertia of the pier; A_p is the area of the pier; L_s is the length of half the spandrel; I_{top} and I_{bot} are the combined moments of inertia of the spandrels above and below the pier, respectively; A_{top} and A_{bot} are the combined areas of the spandrels above and below the pier, respectively. The rather complex form of Eq. 12.1 indicates that it is quite difficult to accurately consider the interaction between piers and spandrels in a pushover analysis. The progressive damage and associated nonlinear behavior of both piers and spandrels with increasing lateral displacement add to this difficulty. On the other hand, previous research shows that with increasing lateral displacement, the damage to a perforated wall generally concentrates on the piers while the spandrels remain essentially intact. As a result, the ratio between the stiffness of the piers and these of the spandrels decreases, and the boundary conditions for the piers become closer to fixed-fixed conditions. As a simplification, a fixed-fixed boundary conditions is assumed for each pier in this proposed pushover analysis.

The overturning moment and the damage of piers alter the behavior of each pier. When only one pier in a certain story remains functional because of the damage of the other piers, the boundary conditions of the remaining pier are changed into that of a cantilever.

Another important issue when describing the response of a pier is the determination of its effective height. The effective height of a pier is dependent on crack propagation, and the effective height can be different from the physical height of a URM pier. This variation of the effective height significantly affects the behavior of a URM

pier. Therefore, it is considered in this pushover analysis. A method outlined in Section 9.6 is used to determine the effective height of a pier.

12.3. OVERTURNING EFFECTS

As revealed in the experimental portion of this research, the overturning moments have a twofold effect on the response of a perforated URM wall. First, these moments introduce additional vertical stress in each pier. Second, these moments also lead to additional global lateral displacements of the wall (see Chapter 8). These two issues will be considered in the pushover analysis.

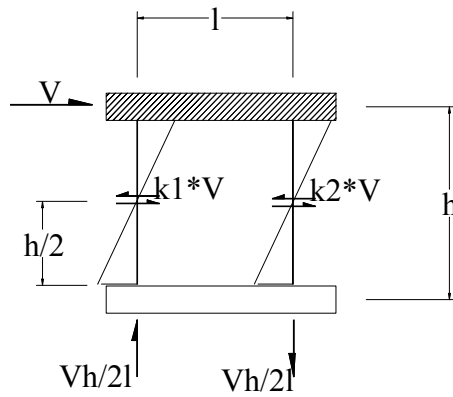
12.3.1. Additional vertical stresses due to overturning moments

Due to the dependence of masonry strength on vertical stress, the effects of overturning moment must be considered in cases where sizable changes in the vertical stress distribution of a URM wall are expected. These cases include structures where the height of the building is similar to its length. This is the case for numerous low-rise URM structures, as represented by the ST-11 test structure.

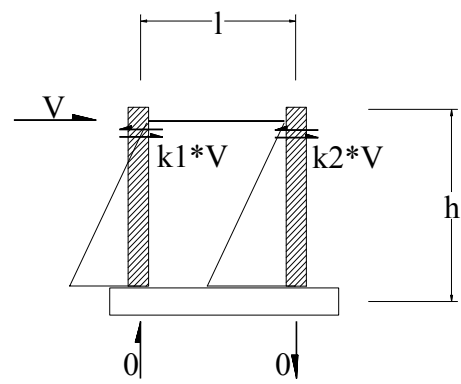
To illustrate how the overturning moments affect a perforated wall, consider four different types of perforated walls as shown in Figure 12.5. Figure 12.5(a) shows an idealized strong spandrel-weak pier structure. The spandrels are rigid and their rotations can be ignored. As a result, the piers work as fixed-fixed columns with their inflection points at the mid-height. For this case, half of the overturning moment is resisted by the internal moment at each end of the piers, while the other half is resisted by the vertical tensile force or compressive force introduced in each pier. Figure 12.5(b) illustrates

another idealized perforated wall, a strong pier-weak spandrel structure. The spandrel is so weak that it can hardly constrain the rotation of the piers. Consequently, the piers work as cantilever columns with the inflection points at the top of the columns and in line with the external lateral forces. This causes the entire overturning moment to be resisted exclusively by the internal moments in the piers, and produces no additional vertical forces in the piers. Figure 12.5(c) shows a third type of idealized perforated wall, which is a mixed structure, with both strong spandrels-weak piers and strong piers-weak spandrels. In this situation, the overturning moments will cause changes in the vertical forces in the fixed-fixed piers, and no variation in the vertical forces in the cantilever piers. As opposed to the idealized boundary conditions shown in Figures 12.5(a) to (c), a real perforated wall is shown in 12.5(d). The height of the inflection point of each pier may be different depending on the relative stiffness values between the spandrels and the piers. This leads to a more complicated distribution of vertical force and moment among the piers.

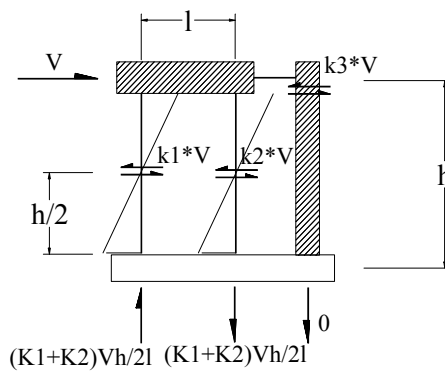
After the height of the inflection point of each pier is determined based on the method discussed in the previous section, the distribution of vertical forces among parallel piers can be calculated. Considering a typical perforated wall with n parallel piers as shown in Figure 12.6, the wall is subjected to a lateral force V acting at a distance h above the base. The shear force in each pier is assumed to be equal to $k_i V$, where k_i is a factor dependent on the secant stiffness of the pier. Therefore, the portion of the overturning moment that is resisted through the change in vertical stresses of the piers can be calculated by subtracting the base moment of each pier from the total overturning moment as:



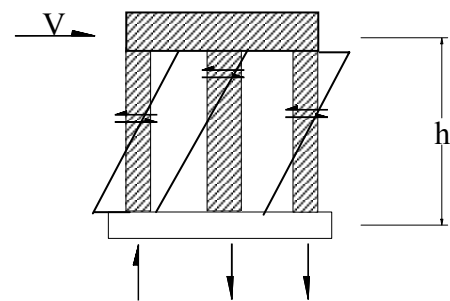
(a) Strong spandrel-weak pier



(b) Strong pier - weak spandrel



(c) Mixed structure



(d) Real structure

Figure 12.5. Effect of overturning moments on different structure configurations

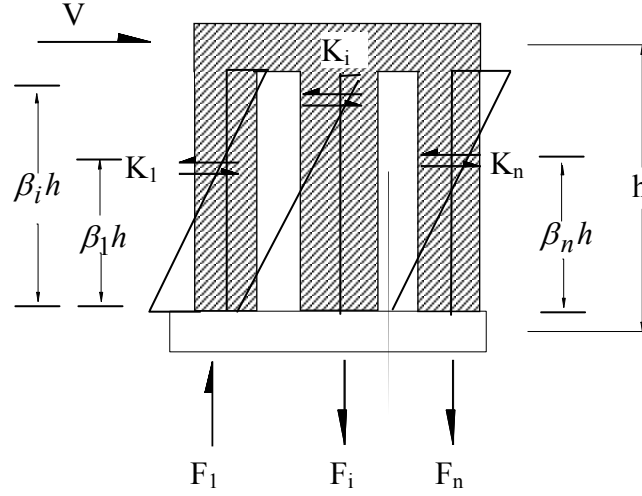


Figure 12.6. Internal forces in an idealized perforated wall

$$M = \left(1 - \sum_{j=1}^n k_j \rho_j \right) Vh \quad (12.2)$$

where h is the height of the wall and ρ_j is the inflection height ratio of each pier. Following the assumptions of beam theory (Gere & Timoshenko 1990) and assuming a linear-elastic material model for masonry, the curvature at the base of the wall can be calculated as:

$$\phi = M / \sum_{j=1}^n A_j d_j^2 \quad (12.3)$$

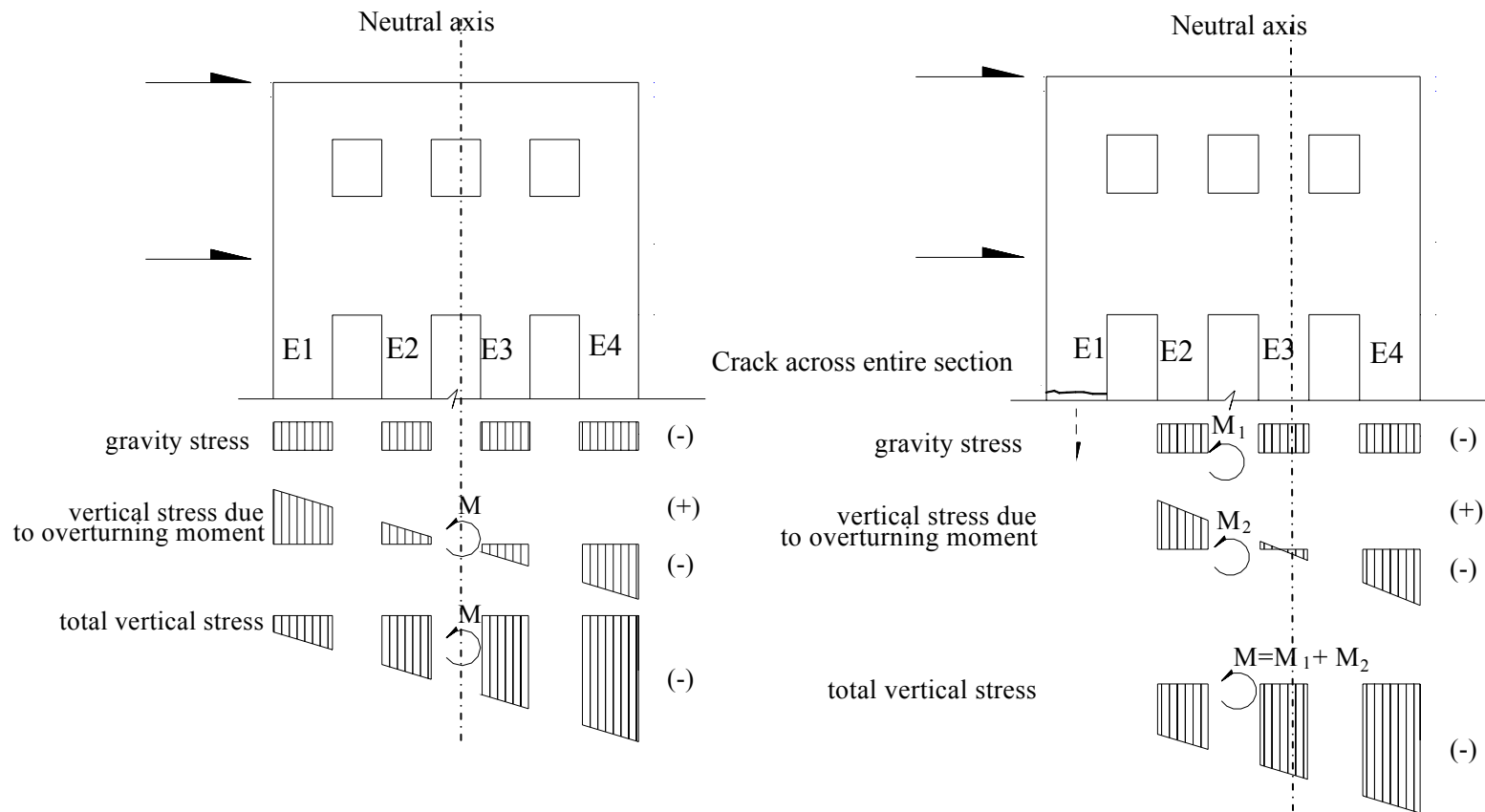
where, A_i is the area of the i th pier and d_i is the distance from the centroid of the i th pier to the neutral axis of the wall. The vertical force in the i th pier induced by the overturning moment is then given by:

$$F_i = A_i d_i \phi = \frac{A_i d_i}{\sum_{j=1}^n A_j d_j^2} M \quad (12.4)$$

Considering Eqs. (12.2) and (12.4), F_i can be written as:

$$F_i = \frac{A_i d_i}{\sum_{j=1}^n A_j d_j^2} (1 - \sum_{j=1}^n k_j \rho_j) Ph \quad (12.5)$$

Figure 12.7(a) illustrates the resulting vertical stress distributions obtained. This distribution is calculated based on the assumed elastic properties of piers and spandrels. However, the damage to the piers can be considered by using the secant stiffness to determine k_i and by limiting the maximum net tension of a pier to the tensile strength of masonry. Once this strength is exceeded the pier is assumed to have cracked across its entire length. As a result, the vertical tensile stress in the pier is assumed to be zero and the only resistance offered by the pier to overturning moment is the initial gravity stress. Figure 12.7(b) illustrates the vertical stress distribution throughout the wall after the tensile strength of a pier has been exceeded.



(a) All piers are in compression

(b) One exterior pier is ignored

Figure 12.7. Distribution of vertical stress under gravity load and lateral force

12.3.2. Lateral displacement of perforated wall due to overturning moments

When calculating the elastic lateral stiffness and the location of the inflection point for each URM pier, the rotation of the elastic spandrel is ignored. This assumption is based on the fact that the rotation of the elastic spandrel is dependent on the axial deformation of each URM pier, which is typically a negligible value. This value, however, may become relevant when a perforated wall is laterally displaced so much that one or several piers are lifted from their bases. In this case, the rotation of the elastic spandrel may become substantial and may lead to additional global lateral displacements of the perforated wall.

Taking the perforated wall shown in Figure 12.6 for example, if the spandrel rotation is neglected, the lateral roof displacement of this perforated wall is exclusively dependent on the lateral deformation of the piers, Δ_{pier} , and can be calculated by:

$$\Delta_{wall} = \Delta_{pier} \quad (12.6)$$

On the other hand, if the spandrel rotation is considered, the lateral roof displacement of this perforated wall has to be calculated as:

$$\Delta_{wall} = \Delta_{pier} + \Delta_{addition} \quad (12.7)$$

where the additional lateral displacement due to the rotation of the spandrel, $\Delta_{addition}$, can be estimated as follows.

1) The vertical axial deformation of Pier i can be calculated by:

$$Y_i = \frac{F_i h}{EA_i} \quad (12.8)$$

where F_i is its additional vertical force as calculated by Eq. (12.5).

2) The rotation of the spandrel is then calculated by:

$$\theta = \frac{Y_1 - Y_n}{L} = \frac{d_1 - d_n}{EL \sum_{j=1}^n A_j d_j^2} (1 - \sum_{j=1}^n k_j \beta_j) Ph^2 \quad (12.9)$$

where Y_1 and Y_n are the vertical displacements of the exterior piers at the tensile side and the compressive side of the wall, respectively. L is the distance between the two piers.

3) Therefore, the additional roof lateral displacement of the perforated URM wall can be calculated as:

$$\Delta_{addition} = \Gamma \cdot \theta \cdot h \quad (12.10)$$

where Γ is a factor dependent on the lateral deformation shape of the wall, which is smaller than or equal to 1. For an elastic cantilever column with the external lateral force on the top of the wall, Γ is equal to 2/3 based on beam theory. For the ultimate state of a URM wall, previous experimental research revealed that the wall rotated as a rigid body around its compression toe. In this case, Γ is equal to 1.

The above method is applied for a single story perforated wall. For a multi-story perforated wall, previous research reveals that the damage to the wall concentrates on the first floor piers. As a result, it can be assumed that the sizable axial deformation will be concentrated on the first floor piers, and thus all the spandrels have the same rotation.

12.4. FLANGE EFFECTS

Flange effects significantly increase both the stiffness and the strength of URM in-plane walls, and need to be considered in the two-dimensional nonlinear pushover analysis. In order to do this, the effective dimensions of the pier flange and the spandrel flange should be determined following the rules outlined in Section 9.5. The contribution of the spandrel flange to the response of the perforated wall can be simply considered by

accounting for the additional vertical forces induced by the spandrels to each URM pier. The contribution of the pier flange to the response of the perforated wall is a little more complex and is discussed in the following section.

12.5. NONLINEAR PROPERTIES OF URM PIERS

The nonlinear properties of a URM perforated wall are dependent on the nonlinear properties of URM piers. Two models, including the effective pier model and the simplified model, are used in the proposed pushover analyses.

12.5.1. Effective pier model

The nonlinear behavior of a URM pier has been illustrated by a comprehensive mechanical model, the effective pier model, as described in detail in Chapter 4. This model was embedded into the pushover analysis frame to analyze the nonlinear response of a URM perforated wall under external lateral forces. The contribution of the pier flange to the stiffness and strength of a URM pier is also considered in the analysis following the method outlined in Chapter 5.

12.5.2. Simplified URM pier model

Besides the effective pier model, another simplified URM pier model is also employed in the pushover analysis. This simplified model is aimed at making the NSP analysis simpler and easier. The principles behind this simplified model are as follows.

The effective pier model presented in Chapter 4 reveals that the failure mechanism of a URM pier is probably a mixed mode of rocking, sliding, toe crushing,

and diagonal tension. Therefore, attributing the damage of a URM pier to one of the four fundamental failure modes identified in FEMA 356 is an oversimplification. On the other hand, FEMA 306 identifies eight possible failure modes for each URM pier. Each mode is one or the combination of the four fundamental failure modes. However, the FEMA 306 identification of failure mode is quite arbitrary and rather difficult to use. A simple and rational method to describe the nonlinear behavior of a URM pier is needed and can be obtained from the analytical results of the effective pier model.

The effective model reveals that the rocking mechanism is actually a normal working mechanism for a URM pier, since it represents the propagation of flexural cracks in the pier. The lateral resistance of a pier remains relatively constant when rocking occurs. Therefore, the shear force-lateral drift of a URM pier can be assumed to be as shown in Figure 12.8. The pier deforms with its initial elastic stiffness until it reaches its rocking strength V_r . After that the lateral strength of the pier remains constant with increasing lateral drift.

When calculating rocking strength of each pier (V_r), the contribution of its flange needs to be considered. By following the procedure outlined in Section 5.4.1, but assuming the pier is fixed-fixed and the self-weight of the pier is neglected, the rocking strength can be calculated as:

$$V_r = 0.9\sigma_n \left(Lt + L_f t_f \right) \frac{L}{H} \quad (12.11)$$

where L , H , and t are the length, height, and thickness of the in-plane pier, respectively; L_f and t_f are the length and the thickness of the flange, respectively; and σ_n is the average vertical compressive stress applied on the top of the pier, including half of the self weight of the pier.

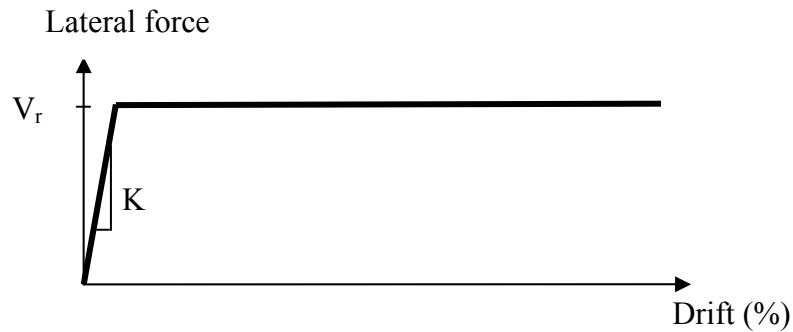


Figure 12.8. Lateral force-drift relationship for rocking

The effective model reveals that the sliding mechanism is more like a plastic working mechanism, since the shear resistance of a pier after sliding is controlled by its normal compressive force and the shear friction coefficient, and does not decrease with increasing lateral displacement. However, the shear force needed to debond the shear surface (V_{bjs}) is usually larger than the Mohr-Coulomb shear force (V_{s2}). Therefore, the shear force-lateral drift of a URM pier corresponding to sliding can be described as shown in Figure 12.9. This figure shows that for a sliding mechanism, the pier first deforms with its initial elastic stiffness until it reaches its initial sliding strength V_{bjs} . Then the lateral shear strength of the pier drops rapidly to its remaining sliding strength V_{s2} . After that the lateral strength of the pier remains constant with increasing lateral drift.

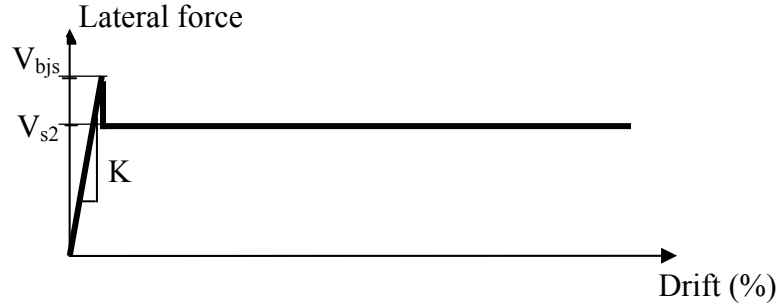


Figure 12.9. Lateral force-drift relationship for sliding

The remaining sliding shear strength of a pier (V_{s2}) can be calculated following Eq. (5.19) to take into account the contribution of flange effects. It can be rewritten as:

$$V_{s2} = \mu_1 \sigma_n (Lt + L_f t_f) \quad (12.12)$$

where μ_1 is the Mohr-Coulomb shear friction coefficient.

Similarly, the initial sliding strength V_{bjs} can be calculated following Eq. (5.20), which can be rewritten as:

$$V_{bjs} = \mu \sigma_n (Lt + L_f t_f) + A_e \tau_0 \quad (12.13)$$

where μ is the effective shear friction coefficient for an intact surface, and A_e is the area of the intact surface. A_e is dependent on external force, and changes with increasing lateral displacement. However, for simplicity, the following A_e is used herein. Before the pier rocks, the intact area is assumed to be 0.75 of the initial area, as implied by FEMA 356 Eq. (7-1). After the pier rocks, since the uncracked area is very small, A_e is assumed to be zero; thus, V_{bjs} is equal to V_{s2} .

FEMA 356 considered the diagonal tension failure mode as a force-controlled mode, because the diagonal tension failure mode shows very brittle behavior. However, previous research has shown that the behavior of a diagonal tension failure mode is dependent on the material properties of URM. For a strong unit-weak mortar material, the URM can still slide along the bed joints after a diagonal crack occurs. Therefore, in the current nonlinear analysis, it is assumed that for a strong unit-weak mortar masonry, the diagonal tension failure mode is still a displacement-controlled mode. The corresponding lateral shear force-lateral drift curve is shown in Figure 12.10. For this particular failure mechanism, the pier first deforms with its initial elastic stiffness until it reaches its initial diagonal tension strength V_{dt} . Then the lateral shear strength of the pier drops rapidly to its remaining diagonal tension strength, which is the same as the remaining sliding strength (V_{s2}). After that the lateral strength of the pier remains constant with the increasing lateral drift.

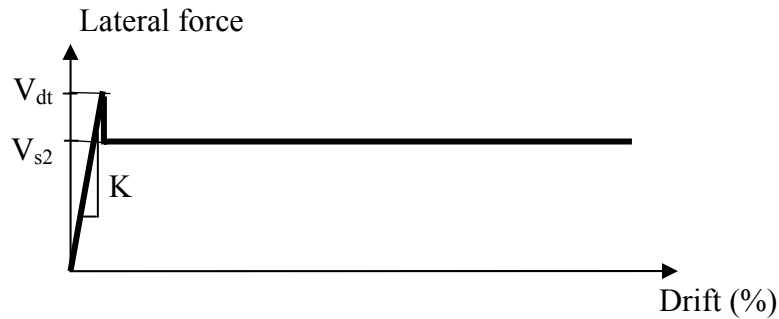


Figure 12.10. Lateral force-drift relationship for diagonal tension

The diagonal tension strength of URM pier is not affected by the flange (see Section 5.3.4), and can be described by Eqs.(5.28) through (5.30). However, for

simplicity, the maximum tensile strength criteria adopted by FEMA 356 as shown in Eq. (4.37) is still used here, as rewritten in Eq. (12.14). The diagonal tension strength of masonry used in the equation, f_t^d , should be obtained from the calibration of appropriate material tests.

$$V_{dia}^{FEMA} = \beta \left(L t f_t^d \right) \sqrt{1 + \frac{\sigma_n}{f_t^d}} \quad (12.14)$$

where β is equal to 0.67 for $L/h < 0.67$, L/h when $0.67 \leq L/h \leq 1.0$, and 1.0 when $L/h > 1.0$.

Both the effective pier model and FEMA 356 consider that toe crushing of a URM pier is due to the excessive compressive stress developed at the toe of a pier, which will lead to the rapid decreasing of the lateral strength of a URM pier. Therefore, it is a force-controlled failure mode. In the current simplified method, the shear force-drift relationship corresponding to the toe crushing mode is not given. Instead, toe crushing strength is treated as a force-limit, and needs to be checked in each step of the analysis. At each analysis step, the maximum compressive stress at the toe of a pier is calculated based on the known internal forces. This maximum compressive stress is then compared with the compressive strength of masonry. If the compressive strength of masonry is reached, the pier is assumed to develop a toe-crushing failure, and the lateral strength of the pier drops to zero, which indicates the pier collapses rapidly.

Another failure mechanism for piers observed in the test but not identified by FEMA 356 is the “left behind” phenomenon repeatedly described in the chapters dealing with the behavior of the test structure. This mechanism is due to the uplift of the spandrel. For this failure mechanism, the lateral shear strength of the pier can be simply assumed to be zero.

A summary of the possible working states of a URM pier discussed above is given in Table 12.1. The identification tag for each of these mechanisms used in the program is also listed in the table. The following rules are followed when describing the evolution of the failure mechanisms of a URM pier:

- A pier starts with an elastic state (0). The first failure mechanism could be: rocking (1), initial sliding (10), initial diagonal cracking (100), toe crushing (1000), or left behind (-1). The latter, “left behind” (-1), occurs only if the vertical stress on the pier reduces to zero,
- If toe crushing (1000) occurs, the pier rapidly collapses (2000).
- If the initial sliding (10) occurs, the next state of the pier must be remaining sliding (20).
- If the initial diagonal tension (100) occurs, the next state of the pier must be remaining diagonal cracking (200).
- When the pier is in the other failure modes, it can be switched to another failure mode with lower lateral strength.

Table 12.1. Working states and the corresponding identification tag of a URM pier

Working state of a URM pier	ID used in the program
No damage or only flexural cracking	0
Left behind	-1
Rocking	1
Preemptive sliding	10
Mature sliding	20
Preemptive diagonal cracking	100
Mature diagonal cracking*	200
Toe crushing	1000
Collapse	2000

* for a strong unit-weak mortar masonry, the remaining diagonal cracking has the same lateral shear resistance as the remaining sliding.

12.6. EXTERNAL LATERAL SEISMIC EXCITATIONS

Two different types of external loads have been used in previous nonlinear pushover analyses: force-controlled analysis and displacement-controlled analysis. In the first case, predetermined increasing external forces are applied on the structure as compared with predetermined increasing roof and floor displacements in the second case. Since force-controlled analysis cannot capture the behavior of a structure after its peak point, displacement-controlled analysis is used in the current analysis.

No special lateral displacement pattern is defined in FEMA 356. However, two vertical distributions of lateral load are recommended by FEMA 356 for force-controlled pushover analysis: one is a uniform pattern while the other is modal pattern (ATC 1999). Both patterns assume that the ratios between forces applied at each floor and/or roof remain constant during loading. This, however, is contrast with the structure behavior observed in the experiments. For example, Paulson conducted a dynamic shaking table test of a one-quarter-scale three-story reinforced masonry building (Paulson 1990). The measured lateral force distributions are shown in Figure 12.11. The specimen gradually changed from an elastic state (Run 1) into a nonlinear range (Runs 2 through 4) with increasing intensity ground motions. It is apparent that the lateral force distributions can be represented with an inverted triangular shape in elastic range (run 1). However, with progressively increasing damage in the building, the force distributions became more and more irregular (Paulson 1990). Similar variation of lateral force distributions were also observed in Costley et al's dynamic test of two two-story URM buildings (Costley and

Abrams 1996), although in the second experiment, the lateral force distributions were closer to a uniform shape present in the elastic range.

These experimental results indicate that a pushover analysis conducted using predetermined displacement profiles may lead to a failure sequence and failure strength different from those in a real earthquake, since the lateral displacement pattern will affect the distribution of shear forces and overturning moments among the stories.

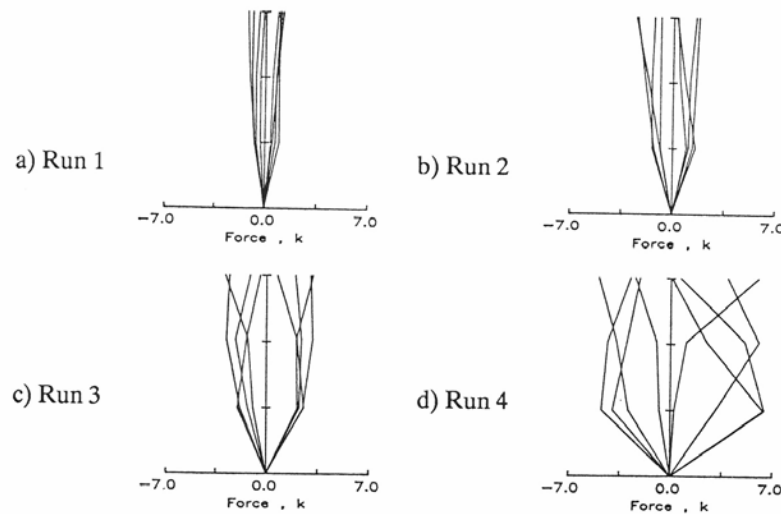


Figure 12.11. Lateral force distributions for all runs in Paulson (1990)'s test

On the other hand, it is rather impractical to use the real lateral displacement pattern in a pushover analysis. First, the real lateral displacement pattern will be different for different ground motions. Second, many factors, including the mass distribution, the stiffness distribution, the damage state of each component will affect the variation of the lateral displacement pattern during each earthquake. This would be rather hard to simulate in the analysis. Fortunately, previous research reveals that for a special type of

structure with rather low natural period, such as low-rise URM building, the first vibration mode should dominate its lateral displacement under seismic excitation (Yi et al., 2002). Therefore, the first vibration mode ϕ_1 can be used as the lateral displacement pattern applied in the displacement-controlled pushover analysis. When damage accumulates unevenly in the building, the stiffness matrix of the building will change. This will lead to changes in its first vibration mode, and as a result the changes of the applied lateral displacement pattern. The scheme for obtaining the updated first vibration mode in this pushover analyses is the same as what is used in the ST-11 in-plane wall tests. More detailed information on the procedure can be found in Section 8.3.1.

12.7. NONLINEAR PUSHOVER ANALYSIS OF THE TEST STRUCTURE

The pushover analyses methods discussed above were applied to the test structure. The results are as follows.

12.7.1. Wall 2

The material properties used in the analysis were based on experimental measurements from material tests. The masonry compressive strength was assumed to be 1458 psi; the initial bed joint shear strength was assumed to be 60psi; and both the initial equivalent shear friction factor and the shear friction factor for a cracked surface were assumed to be 1.0. In addition, the bed joint tensile strength was assumed to be 40 psi, and the initial elastic modulus was assumed to be 1000 ksi.

The program was first used to analyze the nonlinear response of Wall 2 in the test structure. The base shear-lateral displacement relationships of Wall 2 obtained from both

the effective pier model and the simplified pier model are shown in Figure 12.12. The base shear-lateral displacement envelope of Wall 2 measured in the test is also shown in the figure for comparison. Figure 12.12 shows that both analytical models gave a fair prediction of the nonlinear response of the test wall. The effective pier model predicted that the maximum strengths of the test wall corresponding to a roof lateral displacement of 0.25 inches are 27.7 kips and 27.5 kips in the push direction and pull direction, respectively. They are close to the measured values (28.8 kips in the push direction and 25.0 kips in the pull direction). On the other hand, the simplified model gave more conservative predictions. This model predicted that the maximum strengths of the test wall are 23.4 kips and 23.2 kips in the push direction and pull direction, respectively.

The simplified model predicted that all the three first story piers rock when the wall was laterally displaced (see Figure 12.13, Damage ID equal to 1 stands for rocking). In contrast, the effective pier model predicted that only Pier 2-8 rocks during the test, since the flanges of Pier 2-7 and Pier 2-9 delay the propagation of cracks in the two piers. However, the analysis did show that the effective lengths of the two piers decrease with increasing lateral roof displacements. The propagation of horizontal cracks in the piers was consistent with the experimental observation.

Both the effective pier model and the simplified model gave similar predictions for both the variation in vertical stress and the distribution of shear force among the three first story piers. The values predicted by the effective pier model are shown in Figures 12.14 and 12.15. Figure 12.14 shows that at the beginning of lateral loading, there was a rapid change in the vertical stresses in the first story piers. The vertical compressive stress of the pier at the compressive side of the wall increased while that of the pier at the

tensile side of the wall decreased. In addition, the stress variations in the two exterior piers, Pier 2-7 and Pier 2-9, were much more significant than that in the interior pier, Pier 2-8. The vertical stress variation in the piers clearly states the influence of overturning moments.

On the other hand, the analysis also showed that the rate of the variation of vertical stress in the piers decreased with increasing lateral displacement. By the end of loading, the vertical stress variation was actually negligible. This was due to the fact that all the three first story piers tended to rock and the behavior of the entire wall was dominated by the local behavior of these piers.

The base shear force distribution among the three first story piers as shown in Figure 12.15 also exhibited the typical behavior of a rocking mechanism and the influence of overturning moments. With increasing lateral displacement, the base shear in each pier increased but the rate of increase decreased noticeably. This is a typical response of pier rocking, as discussed in Chapter 4.

Figure 12.15 also shows that the pier in the compressive side of wall took more base shear than the pier in the tensile side of the wall. This was because the pier in the compressive side was subjected to larger vertical compressive forces (see Figure 12.14) due to overturning moment and thus its rocking strength increases.

Although the vertical stress and base shear for each pier could not be explicitly measured during the test, the experimental observations of both the vertical and the shear deformations of each pier were in good agreement with the analytical predictions given by the pushover analyses. Detailed description of the experimental observations can be found in Chapter 8.

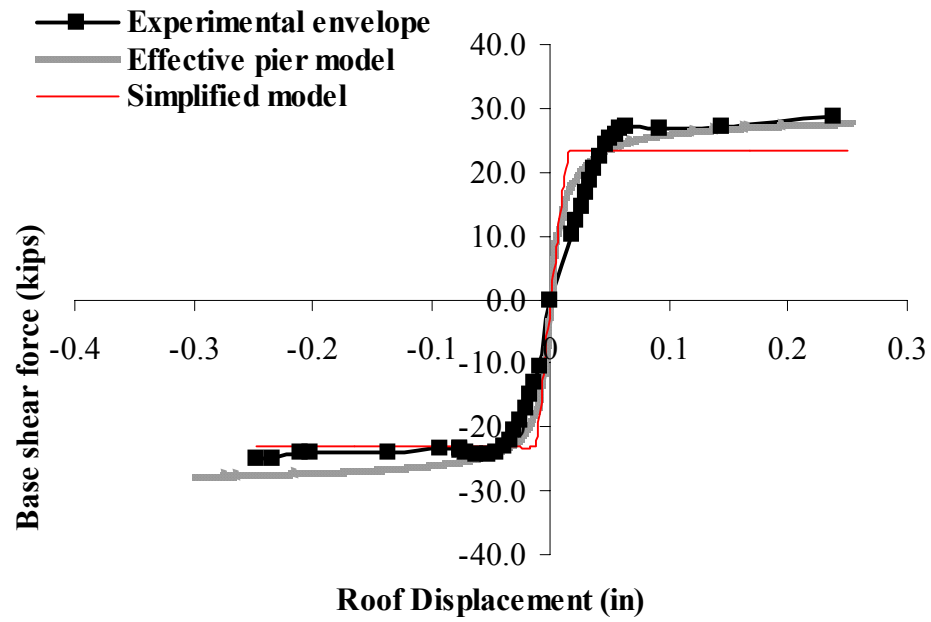


Figure 12.12. Base shear-lateral displacement relationships of Wall 2

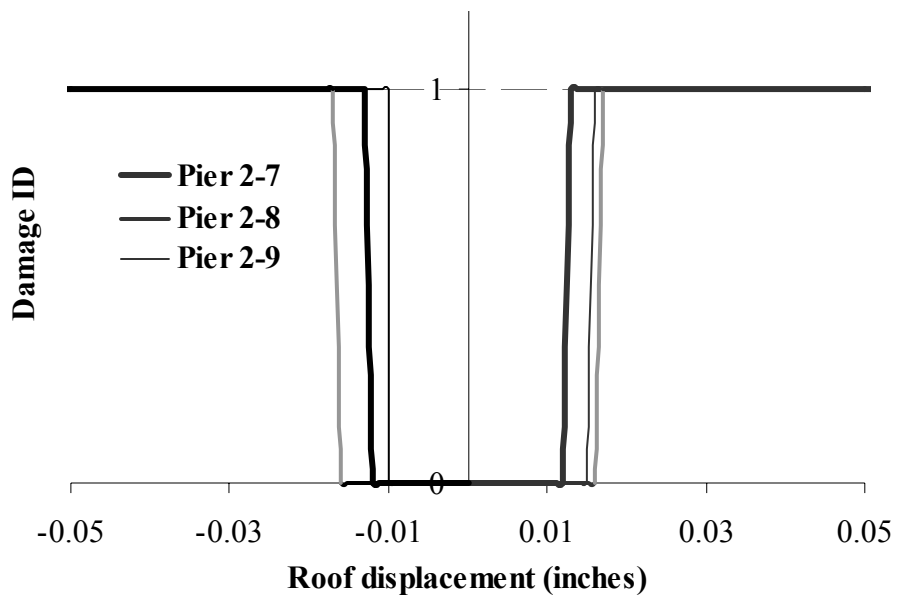


Figure 12.13. Failure mechanisms of Wall 2

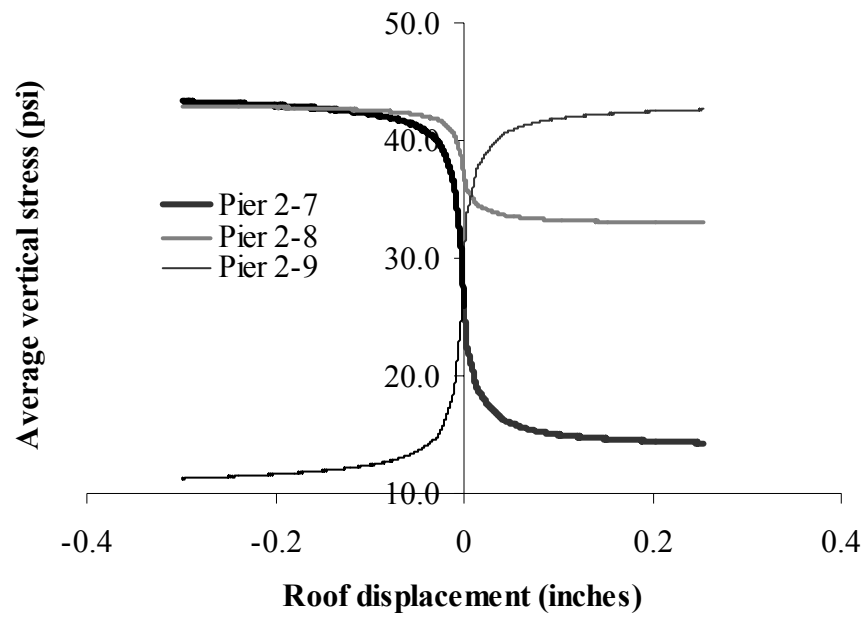


Figure 12.14. Calculated vertical stress variations in Wall 2 first story piers

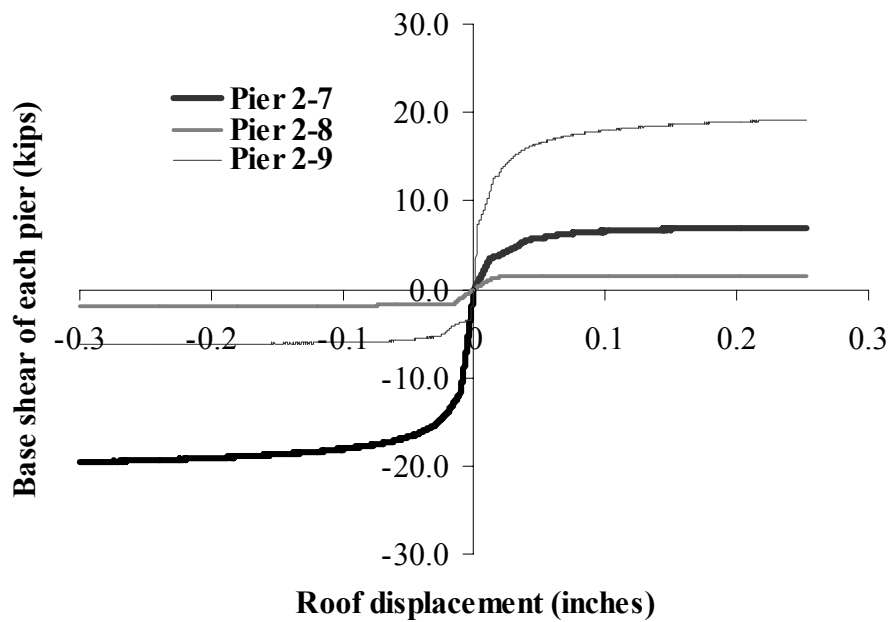


Figure 12.15. Calculated base shear distribution among Wall 2 first story piers

12.7.2. Wall 1

The same material properties as those used for the analysis of Wall 2 were also employed for the pushover analyses of Wall 1. The base shear-lateral displacement relationships of Wall 1 predicted by the pushover analyses are shown in Figure 12.16, along with the measured envelop from the test. Figures 12.17 and 12.18 show the failure mechanisms predicted by the effective pier model and the simplified model, respectively.

Both the effective pier model and the simplified model successfully predicted the behavior of the test wall. When Wall 1 was loaded in the push direction (Pier 1-6 was in compression and the displacements are positive in Figures 12.16 to 12.18), both models predicted that the test wall was quickly lifted above Pier 1-7, and Pier 1-6 started to slide (see Figures 12.17 and 12.18; a Damage ID of -1 means the pier is left behind, 10 means horizontal bed joints sliding and 20 means diagonal sliding). As a result, the test wall rapidly reached its maximum strength, and then dropped down to a stable remaining sliding strength. The effective pier model predicted a maximum strength of 68 kips and a remaining sliding strength of 63 kips, while the simplified model predicted a maximum strength of 70 kips and a remaining sliding strength of 63 kips. Both the predicted values were slightly larger than the experimental observations, which were 61 kips for the maximum strength and 51 kips for the residual sliding strength. The differences could be attributed to the uncertainties in assessing the effective flange sizes and the bed joint shear friction coefficients to be used in the analysis. It could also be attributed to the cyclic loading employed in the tests, since the cyclic loading cracked the masonry bed joint much more rapidly when compared to a monotonic loading.

The formation of an ultimate failure mechanism observed in the test was slower than the analytical prediction suggested. This was probably due to the micro-crack propagation and associated stress redistribution in the test structure which was not addressed in the current model. In addition, the predicted initial lateral stiffness based on an assumed elastic modulus of 1000 ksi for masonry was much larger than the experimental measurements. The difference could be explained again by the propagation of micro-cracks at low stress levels.

When Wall 1 was loaded in the pull direction (Pier 1-7 was in compression and the displacements are negative in Figures 12.16 to 12.18), both models predicted that Pier 1-6 slid (see Figures 12.17 and 12.18). At the same time, the simplified model predicted that the small pier 1-7 rocked, while the effective pier model did not. The reason is that the effective pier model recognized that the existing of flange delays the propagation of cracks in the pier. In addition, the effective pier model predicted a maximum strength of 62 kips, while the simplified model predicted a maximum strength of 41 kips. The former was closer to the test value of 55 kips, while the latter gave a more conservative value.

The behavior of Wall 1 was also clearly illustrated by the vertical stress variation and the base shear distribution among the two first floor piers, as shown in Figures. 12.19 and 12.20. When the wall was loaded in the push direction, the wall was rapidly lifted above pier 1-7 due to the overturning moment effect. As a result, both the vertical stress and the base shear of Pier 1-7 reduced to zero, and the remains of Wall 1, including Pier 1-6 and the second story wall, worked as a single pier with a constant vertical force, sliding and rocking. When the wall was loaded in the pull direction, again due to the overturning moment, a large additional vertical compressive stress was introduced into

Pier 1-7. In the meantime, the vertical compressive stress in Pier 1-6 decreased (see Figure 12.19). As a result of the vertical stress variation, the smaller Pier 1-7 resisted more lateral shear force than the larger Pier 1-6 (see Figure 12.20). On the other hand, after the large Pier 1-6 started to slide, the variation of vertical stresses and base shear between the two piers became smaller.

In conclusion, the analytical predictions on the nonlinear response of Wall 1 were in good agreement with the experimental observations. Detailed description of the experimental observations can be found in Chapter 8.

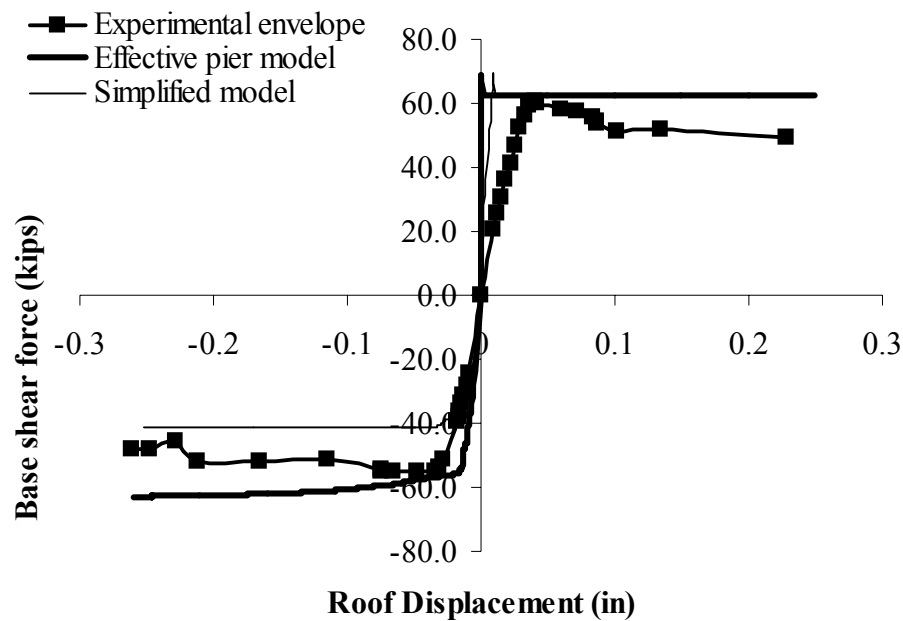


Figure 12.16. Base shear-lateral displacement relationships of Wall 1

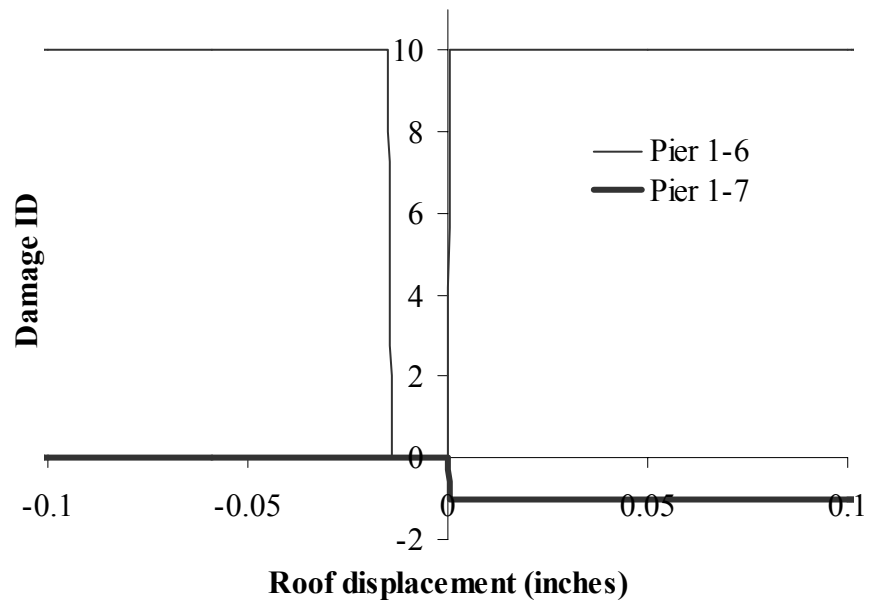


Figure 12.17. Failure mechanism of Wall 1 predicted by the effective pier model

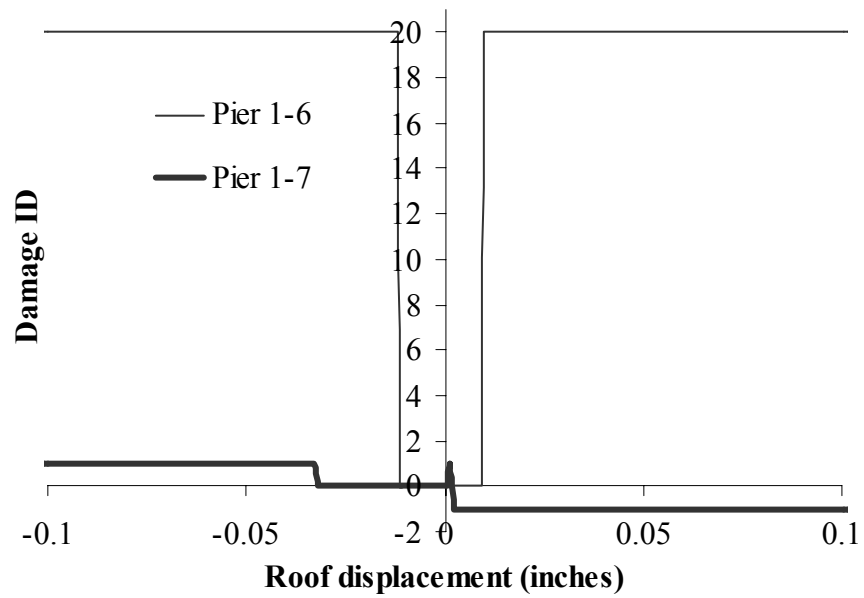


Figure 12.18. Failure mechanism of Wall 1 predicted by the simplified model

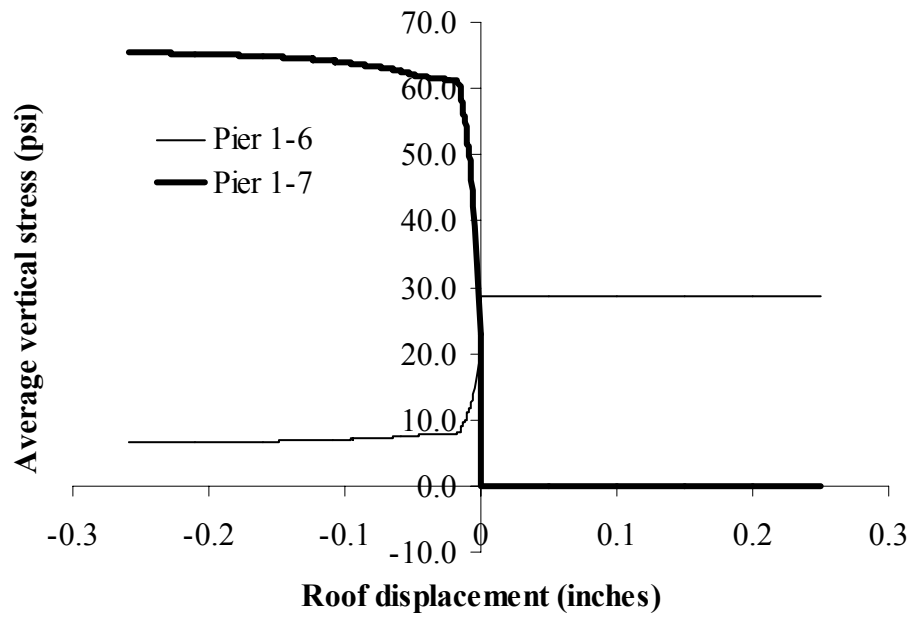


Figure 12.19. Calculated vertical stress variations in Wall 1 first story piers (by the effective pier model)

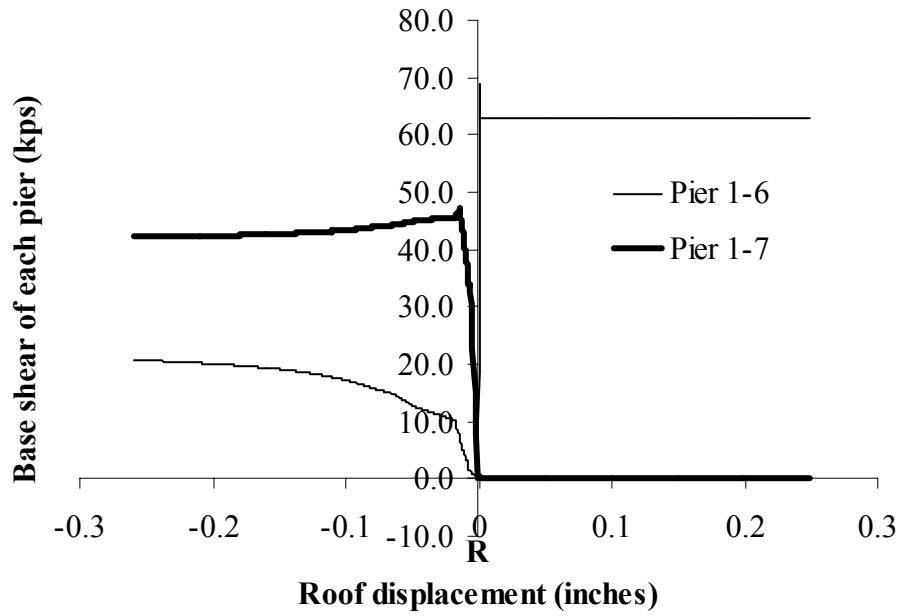


Figure 12.20. Calculated base shear distribution among Wall 1 first story piers (by the effective pier model)

12.7.3. Walls A and B

The configurations of Walls A and B were identical. However, the unsymmetrical openings and existing cracks in Walls 1 and 2 caused different effective flange sizes to Walls A and B. In order to take this effect into account, different flange lengths were used for the exterior piers of Walls A and B in the analyses. The entire length of Pier 1-7 was considered as the effective flange length of Pier A-7 in both loading directions, since the door opening in Wall 1 isolated the possible flange for Pier A-7. On the other hand, in the case of Pier B-10, when Wall B was loaded in the push direction, the large Pier 1-6 tended to move together with Pier B-10. As a result, an effective flange of 99 inches was used for Pier B-10 according to the rules outlined in Chapter 11. When Wall B was loaded in the pull direction, the flange of Pier B-10 was in compression; therefore, a flange length of 48 inches was used for Pier B-10.

The same material properties as those used for the analysis of Walls 1 and 2 were employed to analyze the nonlinear responses of Walls A and B. The predicted base shear-lateral displacement relationships of Walls A and B are shown in Figures 12.21 and 12.22, respectively. The measured base shear-lateral displacement envelopes from the tests are also shown for comparison. The effective pier model predicted that the maximum strengths of Wall A were 35 kips and 42 kips in the push and pull direction, respectively, and the maximum strengths of Wall B were 40 kips and 36 kips in the push and pull direction, respectively. The values are close to the experimental observations, which were 36 kips and 41 kips for Wall A in the push and pull direction, respectively, and 43 kips and 37 kips for Wall B in the push and pull direction, respectively. On the other hand, the simplified method gave more conservative predictions. This method

predicted that the maximum strengths of Wall A were 33 kips and 35 kips in the push and pull direction, respectively, and the maximum strengths of Wall B were 33 kips and 31 kips in the push and pull direction, respectively.

The predicted failure mechanisms of Walls A and B from the pushover analyses are listed in Table 12.2 together with the experimental observations. This table shows that the failure mechanisms of both walls are controlled by rocking, which are consistent with the experimental observations.

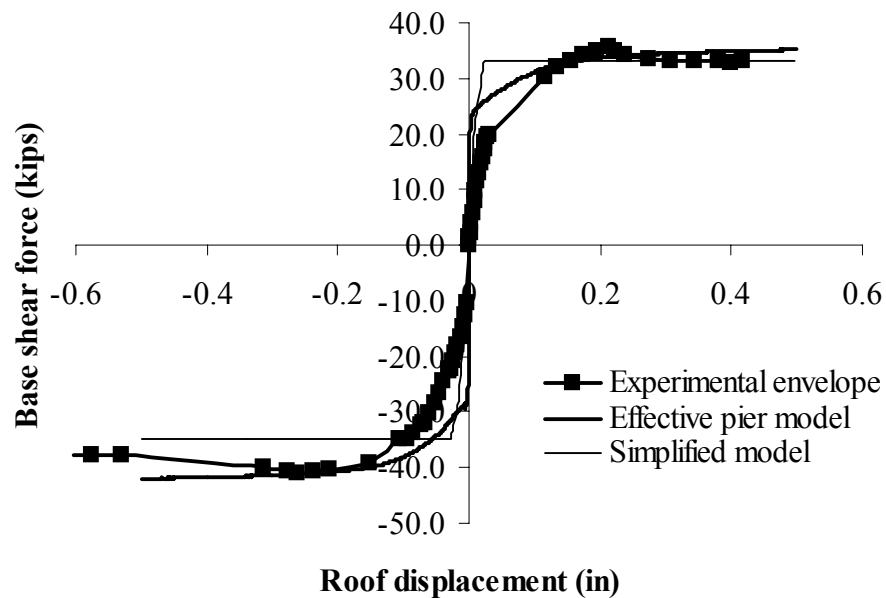


Figure 12.21. Base shear-lateral displacement relationships of Wall A

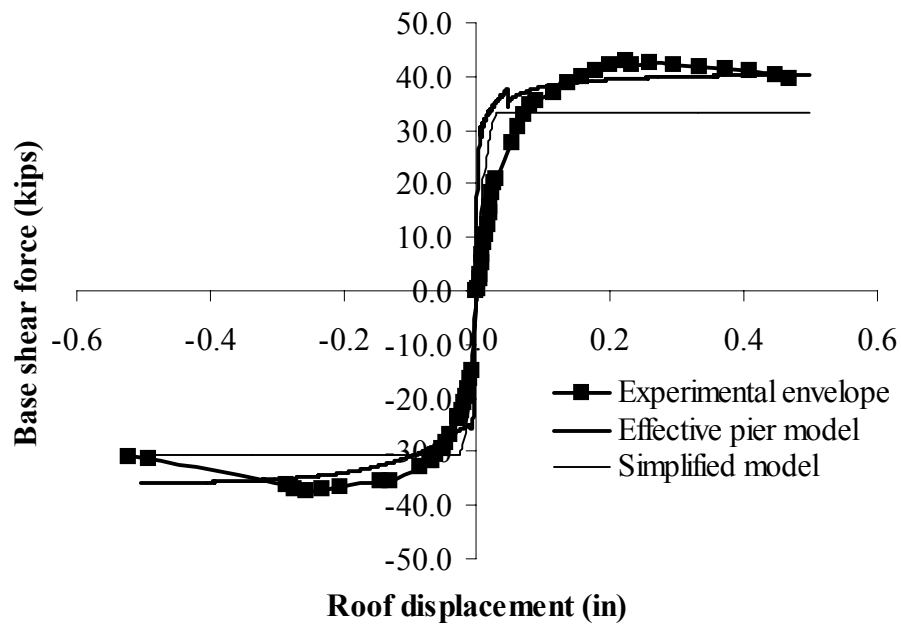


Figure 12.22. Base shear-lateral displacement relationships of Wall B

Table 12.2. Failure mechanisms of Walls A and B

		Effective pier model	Simplified method	Experimental observation
Wall A	Push	Pier A-7 rocks first, followed by the rocking of A-8 and A-9.	Pier A-7 rocks first, followed by the rocking of A-8, A-9, and A-10.	All four first story piers rocked, Pier A-7 tended to be left behind.
	Pull	Pier A-8 rocks first, followed by the rocking of A-7 and A-9.	Pier A-8 rocks first, followed by the rocking of A-7, A-9, and A-10.	All four first story piers rocked
Wall B	Push	Pier B-9 rocks first, followed by the sliding of Pier B-10, and rocking of Pier B-8.	Pier B-10 rocks first, followed by the rocking of B-9, B-8, and B-7.	All four first story piers rocked, Pier B-10 tended to be left behind.
	Pull	Pier B-8 rocks first, followed by the rocking of B-7 and B-9.	Pier B-8 rocks first, followed by the rocking of B-7, B-9, and B-10.	All four first story piers rocked.

Experimentally, when Walls A and B were loaded in the push direction, the piers at the tensile side of the wall, Pier A-7 and Pier B-10, tended to be left behind due to the rotation of the spandrels. This phenomenon was not explicitly predicted by the pushover analyses. However, referring to the calculated vertical stress variations in the Walls A and B first story piers, as shown in Figures 12.23 and 12.24, it can be seen that the vertical stresses in Piers A-7 and B-10 were close to zero at the end of push loading. This indicates that the two piers were close to being left behind. Figure 12.24 shows a small jump in vertical stress in the four first story piers of Wall B when the lateral roof displacement was about 0.045 inches. This jump was due to the switching from rocking to sliding for Pier B-10.

The base shear distribution among the first floor piers in Wall A and Wall B are shown in Figures 12.25 and 12.26, respectively. The two figures reveal similar trends as those in Wall 1 and Wall 2. That is, with increasing lateral displacement, a larger percent of lateral shear force was resisted by the piers at the compressive side of the wall due to overturning moment effects.

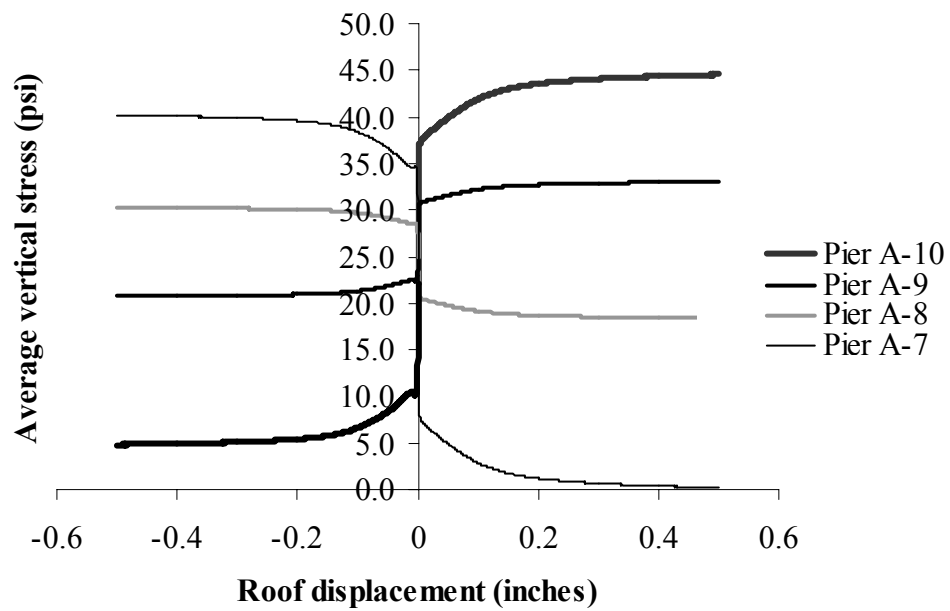


Figure 12.23. Vertical stress variations in Wall A first story piers (by the effective pier model)

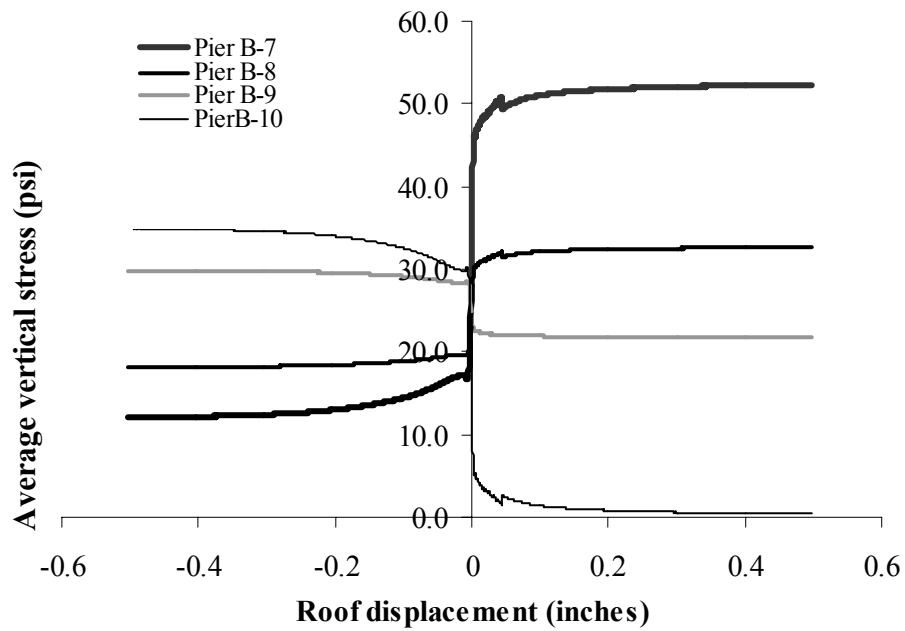


Figure 12.24. Vertical stress variations in Wall B first story piers (by the effective pier model)

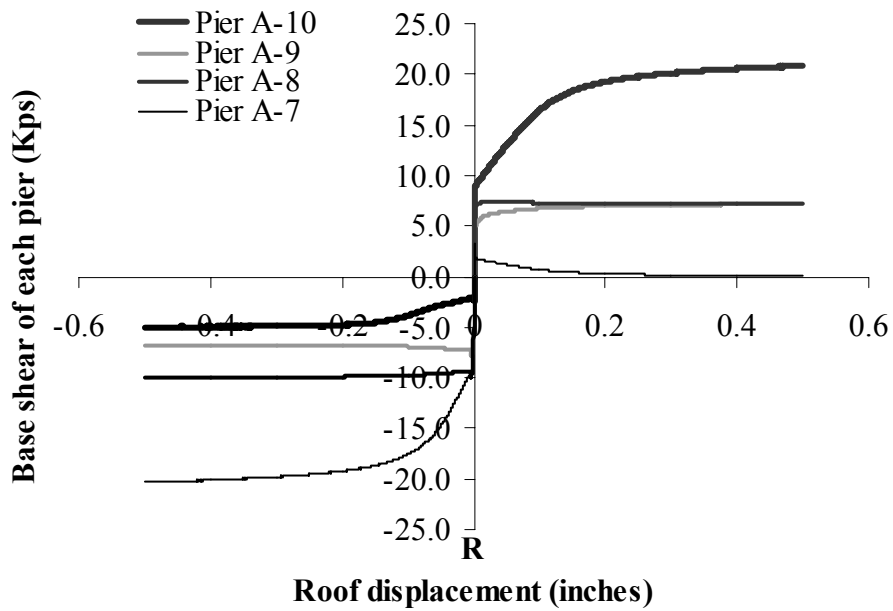


Figure 12.25. Base shear distribution among Wall A first story piers (by the effective pier model)

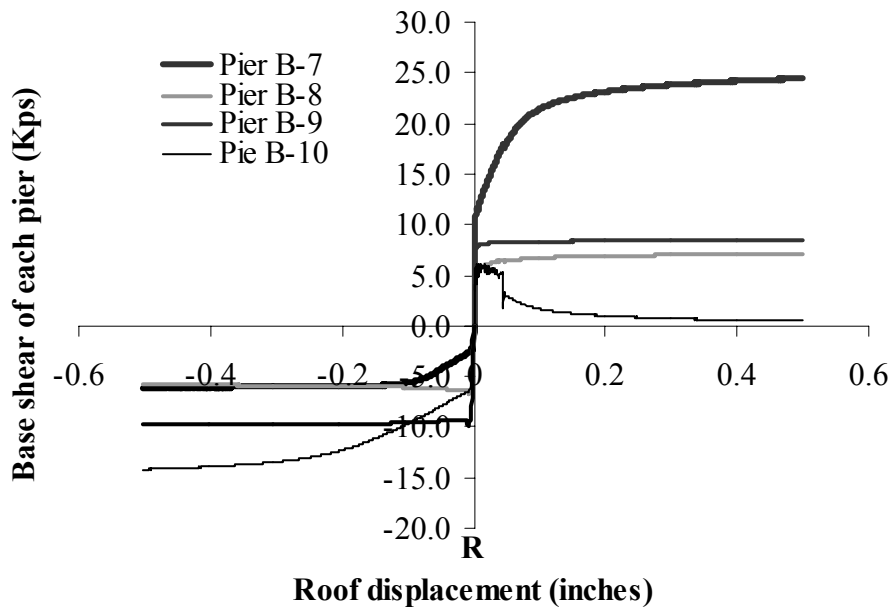


Figure 12.26. Base shear distribution among Wall B first story piers (by the effective pier model)

12.8. CONCLUSIONS

The pushover analysis methods described in this chapter take into account several important issues in the nonlinear analysis for a URM building; the issues include the flange effects, the overturning moments and the effective lateral seismic force. A comprehensive method, the effective pier method, and a simplified method were used in the pushover analysis program to consider the possible failure mechanisms for perforated URM walls. The predicted nonlinear response of the test structure from the pushover analyses were in good agreement with the experimental observations.

CHAPTER 13

RECOMMENDATIONS FOR THE URM SECTION OF FEMA 356

13.1. INTRODUCTION

The FEMA 356 Pre-standard (ATC 2000) provides a full set of methodologies to evaluate and improve the seismic resistance of existing buildings. In this document, the rehabilitation objectives, the general analysis methods and the design procedures are first outlined in Chapters 1 through 3. After that, detailed descriptions for this methodology are given for each structure type, including steel, reinforced concrete, and masonry structures. Specifically, Chapter 7 is devoted to masonry structures. In this chapter, the analysis procedure is organized into the follow sections:

- 7.3 Material properties and condition assessment.
- 7.4 Engineering properties of masonry walls.
- 7.5 Engineering properties of masonry infills
- 7.6 Anchorage to masonry walls
- 7.7 Masonry foundation elements

Section 7.3 is used to describe the masonry material properties, while the other sections are used to describe the behavior of each typical masonry component. The research reported previously in Chapters 2 to 12 of this dissertation concentrated on the in-plane behavior of structural URM walls. Based on this research, some recommendations can be given to improve FEMA 356 Sections 7.3 and 7.4. In addition, although FEMA 356 Chapters 2 and 3 point out that several critical issues need to be considered when analyzing a building, those issues are not discussed in detail for each

specific structure type. Examples of those issues include overturning and interconnection. The research reported in this thesis reveals several unique global structural characteristics preeminent in the nonlinear response of a URM building. These aspects of structural behavior need to be considered in modeling a three-dimensional URM building, and will be emphasized in a proposed new section in FEMA 356 Chapter 7 to be discussed later in this chapter.

The recommendations for modifications to the current FEMA 356 are grouped in several different topics. For each topic, the current FEMA section is first cited, and the proposed modification is given after that. The rationale for the modifications is also stated.

13.2. MATERIAL PROPERTIES AND CONDITION ASSESSMENT (FEMA 356 SECTION 7.3)

13.2.1. Masonry bed joint tensile strength

FEMA 7.3.2.1 General

[2. Masonry tensile strength.]

2. Masonry bed joint tensile strength

FEMA 7.3.2.5 Masonry Flexural Tensile Strength

Expected flexural tensile strength, f_{te} , [for out of plane bending] shall be measured using one of the following three methods:

Rationale

Previous research on masonry material properties has revealed that the tensile strength of masonry is dependent on the loading direction with respect to the masonry bed joints (see Chapter 3). The masonry tensile strength cited by FEMA refers to the tensile strength of masonry in the direction perpendicular to the bed joint. In addition, this tensile strength affects not only the out-of-plane bending strength of masonry, but also its in-plane properties.

13.2.2. Masonry shear strength

FEMA 7.3.2.6 Masonry Shear Strength

The entire section should be changed as the follows:

For URM components, expected masonry shear strength, v_{me} , shall be measured for both uncracked and cracked sections. The corresponding expected shear strength shall be determined in accordance with Equations (7-1a) and (7-1b), respectively:

For uncracked section:
$$v_{me} = \tau_0 + \mu \frac{P_{CE}}{A_n} \quad (\text{FEMA 7-1a})$$

For cracked section:
$$v_{me} = \mu_1 \frac{P_{CE}}{A_n} \quad (\text{FEMA 7-1b})$$

where:

P_{CE} = Expected gravity compressive force applied to a wall or pier component considering load combinations given in Equations (FEMA 3-18) and (FEMA 3-19).

A_n = Area of net mortared/grouted section of a wall or pier.

τ_0 = Masonry bed joint initial shear bond strength.

μ = Masonry bed joint internal frictional resistance.

μ_1 = Shear friction coefficient for cracked masonry bed joint.

The material parameters, τ_0 , μ , and μ_1 , should be determined using an approved 4-brick direct shear test or in-plane shear test. If no test data are available, a value of 1.0 can be assumed for both μ and μ_1 . Values for the masonry bed joint initial shear bond strength, τ_0 , shall not exceed 100 psi for the determination of v_{me} in Equation (7-1a).

The shear tests identified here shall not be used to estimate shear strength of reinforced masonry components. The expected shear strength of reinforced masonry components shall be determined in accordance with FEMA 356 Section 7.4.4.2.

Rationale

The mechanical key model has pointed out that the masonry bed joint shear strengths are different between an uncracked surface and a cracked surface. The corresponding strengths can be illustrated by Eqs. (FEMA 7-1a) and (FEMA 7-1b), respectively. More detailed discussion on this concept can be found in Sections 3.2 through 3.4 in Chapter 3 of this thesis.

For the purpose of comparison, the current FEMA equation (7-1) for masonry shear strength (ATC 2000) can be rewritten as:

$$v_{me} = \frac{0.75 \left(0.75 \tau_0 + \frac{P_{CE}}{A_n} \right)}{1.5} \quad (\text{FEMA 7-1})$$

The above equation gives similar expression as the proposed equation (FEMA 7-1a). It indicates that the current FEMA 356 equation does not distinguish between an uncracked surface and a cracked surface. In addition, the current FEMA equation (7-1) is based on an in-place shear test. Therefore, the contribution of the collar joint to the estimated shear resistance measured by this test must be reduced by the second factor of 0.75. The first factor 0.75 and the factor 1.5 in the current FEMA equation (7-1) are used to convert it to an average stress (ATC 1997). However, the reason for using these two values is not given. When a 4-brick direct shear test is used to determine the material properties, no modification factors are needed.

13.2.3. Diagonal Compression Test

FEMA C7.3.3.3.3 Diagonal compression test

The entire section should be eliminated.

Rationale

The previous research has shown that both the execution of a diagonal compression test and the extrapolation of its test result are difficult. As a result, this material test method is not recommended for masonry structures. More detailed discussion on this topic can be found in Section 3.7 in Chapter 3.

13.3. ENGINEERING PROPERTIES OF MASONRY WALLS (FEMA 356 SECTION 7.4)

13.3.1. Deformation-controlled actions and force-controlled actions

FEMA 2.4.4.3 Deformation- and Force-Controlled Actions

FEMA 2.4.4.4 Expected and Lower-Bound Strength

FEMA 7.4 Engineering Properties of Masonry Walls

These sections should be revised.

Rationale

A fundamental philosophy adopted by the current FEMA 356 is to identify the behavior of an existing structural component as ductile behavior (deformation-controlled behavior) or brittle behavior (force-controlled behavior). In order to evaluate the corresponding strengths, the expected material strength (the statistical mean value) should be used for deformation-controlled behavior, while the lower-bound strength (the statistical mean value minus one standard deviation) should be used for the force-controlled behavior (see FEMA 356 2.4.4.3 and 2.4.4.4). As an application of this philosophy, in the current FEMA 356 Chapter 7 for masonry structures, four different possible failure mechanisms (rocking, sliding, diagonal tension, and toe crushing) are identified for an URM pier. The first two failure mechanisms are considered as deformation-controlled behavior and the corresponding strengths are calculated by using mean material values, while the latter two failure mechanisms are considered as force-controlled behavior and the corresponding strengths are calculated by using lower-bound material values. For example, in order to calculate the toe crushing strength of a URM pier, “ the lower bound masonry compressive strength, f_m' , shall be taken as the expected

strength, f_{me} , determined in accordance with Section 7.3.2.3, divided by 1.6 “ (See FEMA 356 Section 7.4.2.2.2).

This philosophy is suitable for designing a new building, since it will ensure the response of a designed new building to be ductile (deformation-controlled actions) by artificially decreasing the usable strength of its possible force-controlled actions. However, when this method is used to analyze an existing building, the response of the analyzed structure seems to be always controlled by the force-controlled actions. This result, again, is because the strengths for the force-controlled actions are artificially penalized. One example for this result can be found in Section 10.5. As a result, this method should not be used to analyze the response of an existing building, since it will not only greatly underestimate the maximum strength of an existing building, but also misjudge the controlling failure mechanisms of this building. This in turn will lead to possible inappropriate rehabilitation techniques, because in many cases the appropriate rehabilitation techniques are dependent on the dominating failure mechanisms of an existing structure.

As an alternative, it is proposed herein that for analysis purposes, mean material values should always be used, as this will lead to the best predictions for the failure mechanisms and the maximum strengths of the analyzed structure. Following that, the response of the entire structure can be considered as deformation-controlled behavior or force-controlled behavior, and the corresponding strengths and other performance parameters can be modified by using safety factors for the purpose of performance checking.

13.3.2. Elastic Stiffness and story shear distribution

FEMA 7.4.2.1 Stiffness

The following two paragraphs should be changed as shown below.

For linear procedures, the stiffness of a URM wall or pier resisting lateral forces parallel to its plane shall be considered to be linear and proportional with the geometrical properties of the uncracked section excluding veneer wythes but including flange effects.

For linear procedures, story shears in perforated shear walls shall be distributed to piers in proportion to the relative lateral uncracked stiffness of each pier. For nonlinear procedures story shears in perforated shear walls shall be distributed to piers in proportion to the relative secant stiffness of each pier.

Rationale

Both the experimental investigation (see Chapters 8 and 9) and the theoretical research (see Chapter 5) reveal the significant effects of flanges on the stiffness as well as the strength of a URM pier. As a result, the flange effects should be considered in the analysis.

The method for dealing with the distribution of story shears in a perforated shear wall is different between Linear Static Procedure (LSP) and Nonlinear Static Procedure (NSP). In the case of LSP, the shear force is distributed to piers in proportion to the elastic stiffness of each pier. In the case of NSP, the shear force is distributed to piers in proportion to the secant stiffness of each pier, which is dependent on their nonlinear

responses. More detailed discussion on the story shear distribution in a NSP can be found in Section 12.2 in Chapter 12.

13.3.3. Strengths and nonlinear properties (FEMA 7.4.2.2)

FEMA 7.4.2.2 Strength

The entire section should be changed as follows.

7.4.2.2 Strength and Nonlinear Properties

7.4.2.2.1 Effective pier model of unreinforced masonry walls and piers

Expected lateral strength, Q_{CE} , and deformation capacities of existing URM walls or pier components shall be determined by the effective pier model. Flange effects should be considered in the model.

7.4.2.2.2 Simplified methods for unreinforced masonry walls and piers

As an alternative method, for linear procedures, the expected lateral strength, Q_{CE} , of existing URM walls or pier components shall be the lowest of the lateral strengths based on expected bed-joint sliding shear strength, rocking strength, diagonal tension strength, and toe crushing strength, calculated in accordance with Equations (7-3), (7-4), (7-5) and (7-6), respectively:

$$V_{bjs} = v_{me}(Lt + L_f t_f) \quad (\text{FEMA 7-3})$$

$$V_r = 0.9\alpha\sigma_n(Lt + L_f t_f)\frac{L}{H} \quad (\text{FEMA 7-4})$$

$$\frac{\sigma_1}{0.5f_t + 0.8\tau_0} + \frac{\sigma_2}{0.85f_m} = 1 \quad (\text{FEMA 7-5})$$

$$\sigma_2^{\max} = \xi \cdot f_m \quad (\text{FEMA 7-6})$$

where:

H = Height of the pier

L = Length of wall or pier

L_f = Length of flange

t = Thickness of wall or pier

t_f = Thickness of flange

v_{me} = Expected bed-joint sliding shear strength in accordance with Section 7.3.2.6

V_{bjs} = Expected shear strength of wall or pier based on bed-joint sliding shear strength

V_r = Strength of wall or pier based on rocking

α = Factor equal to 0.5 for fixed-free cantilever wall, or equal to 1.0 for fixed-fixed pier

σ_n = Average vertical stress in the wall or pier

σ₁ = Principle tensile stress at the mid panel of the wall or pier

σ₂ = Principle compressive stress at the mid panel of the wall or pier

σ₂^{max} = Maximum compressive stress at the toe of the wall or pier

ξ = Local compressive strength increase factor

In the above equations, the stress values σ₁, σ₂, and σ₂^{max} should

be calculated based on plane-stress assumptions and external forces applied on the wall or pier.

For nonlinear procedures, component force deformation responses shall be represented by appropriate nonlinear force-deformation relations. Force-deformation relations shall be based on the maximum strengths calculated by Eqs. (FEMA 7-3) to (FEMA 7-6) and appropriate treatment of stiffness degradation and failure mechanisms evolution.

Rationale

The effective pier model discussed in Chapter 4 is able to describe not only the maximum strength but also the nonlinear deformation capacity of individual URM components. In addition, it provides a rational explanation for the working mechanisms and the interactions of the four fundamental failure modes. Therefore, it is a reasonable method to calculate the nonlinear response of individual URM piers utilizing nonlinear procedures. More discussion on the effective pier model can be found in Chapter 4 and Chapter 5.

On the other hand, in order to ease the job of structural engineers, a simplified method is proposed based on the effective pier model. In this method, force-deformation relations are given respectively for rocking, sliding, and diagonal cracking failure modes for each individual URM pier. Toe crushing is treated as a force limit for the response of the pier. A simple rule is given for possible failure mechanisms evolution. More detailed information on this simplified method can be found in Section 12.9.1.

13.4. PROPOSED MATHEMATICAL MODEL FOR A THREE DIMENSIONAL URM BUILDING

FEMA 7.0 Masonry

The following section is proposed to be added to Chapter 7 of FEMA 356.

7.9 Mathematical modeling of three-dimensional URM building

A three-dimensional URM building with flexible diaphragms should be modeled by a nonlinear three-dimensional FE model or two separate two-dimensional models parallel to each principal axis of the building.

Horizontal torsion needs not to be considered in URM buildings with flexible diaphragms.

The definition of the effective dimensions of each URM pier in a perforated wall should be dependent on the possible crack pattern of the pier.

The pier flange for each pier and the spandrel flange for each story should be considered in the model.

Two different outcomes of the overturning moment caused by seismic forces should be considered in the model. The first one is the additional vertical force induced in each pier; and the second one is the induced global lateral displacement of the building.

Rationale

Although FEMA 356 Chapters 2 and 3 have pointed out that some global characteristics of a structure, such as horizontal torsion, overturning, and interconnection between two elements, should be considered in the mathematical modeling of this

structure, no detailed guidelines are given for URM structures. On the other hand, both the experimental investigation of a two-story URM structure and the corresponding analytical examinations reported in the previous chapters have revealed some unique features of typical URM buildings. These findings are proposed to be added to FEMA pre-standard to enhance the mathematical modeling of URM structures.

Both the experimental research (see Chapters 8 and 9) and the elastic analysis (see Chapter 10) have revealed negligible coupling between the two parallel in-plane walls. In addition, the torsion behavior of a URM building is minor. Therefore, a regular 3D URM building can be simply modeled by 2D model.

In modeling each perforated masonry in-plane wall, several issues have to be considered. First, the adjacent out-of-plane wall has a significant influence on the initial stiffness and the maximum strength of a URM pier. As a result, the flange effects have to be considered in the model. Detailed analytical investigation of the flange effects can be found in Chapter 5. The experimental investigation can be found in Chapters 8 and 9. In order to consider the flange effects, the effective area of each flange should be determined; some basic rules can be found in Section 9.5. The calculation of the stiffness and maximum strength of a URM pier considering flange effects can be found in Chapter 5 and Section 12.9.1.

The second issue is the determination of the effective dimensions for each pier. The tests of the two-story URM building revealed that specific diagonal cracks might develop at the top or bottom of a URM pier, which alter the behavior of this pier significantly. The rules for determining the effective piers in a perforated wall can be found in Section 9.7. The third issue is the effect of the overturning moment, which was a dominating

phenomenon observed in the tests (see Chapters 8 and 9). The combined effects of overturning moment, i.e., the additional vertical force in the pier and the additional global lateral displacements to the building, should be considered following the approaches described in Section 12.4.

13.5. OTHER ISSUES

This research was centered on an experimental and analytical investigation of a box-type, two-story URM building. As a result, not enough information is available to make recommendations for the acceptance criteria of the performance of URM buildings at large. However, current FEMA 356 gives acceptance criteria only in terms of two failure mechanisms: bed-joint sliding and rocking (see FEMA 356 Section 7.4.2.3). Based on the proposed new FEMA provisions, these existing acceptance criteria are not sufficient for checking the performance of a structure. Thus, more research is needed in this area.

In addition, FEMA 356 gives several typical drift values in Table C1-3 to illustrate the overall structural response associated with various structural performance levels. Specifically, for unreinforced masonry walls, the values of 0.3%, 0.6%, and 1% were used for Immediate Occupancy, Life Safety, and Collapse Prevention performance level, respectively. Again, sufficient information is not available to make recommendations for drift values for a URM wall. However, comparing the values given in FEMA Table C1-3 to the response of the two-story URM building tested, it seems that FEMA Table C1-3 gives a much higher estimation. As an alternate, the values of 0.01%, 0.15%, and 0.3% should be used for Immediate Occupancy, Life Safety, and Collapse Prevention

performance level, respectively. They correspond to the elastic response limit, the forming of full mechanism, and the point at which large strength degradation occurred in the test.

13.6. SUMMARY

Several recommendations have been proposed for the URM section of FEMA 356 based on the knowledge obtained from the research reported in Chapters 2 to 12. The recommendations will enhance the estimation of the seismic resistance of existing URM buildings. Future research needs for the FEMA URM section are also pointed out in this chapter.

CHAPTER 14

CONCLUSIONS AND FUTURE RESEARCH

This research was aimed at investigating the seismic resistance of existing URM structures at three different levels: the material level, the individual structural component level and the global structural level. The conclusions are grouped into the following topics:

- URM materials
- URM components
- Structural characteristics of URM buildings
- Modeling of URM buildings
- Proposed modifications to FEMA provisions

Some recommendations for future research also are proposed.

14.1. URM MATERIALS

Numerous investigations have been conducted on masonry material properties from both the experimental and analytical standpoints. In spite of this, some fundamental behavior of URM materials, such as the failure mechanisms at the interface between masonry units and mortar, still remain unclear. A mechanical key model was proposed in this research to illustrate the tensile and shear strengths of the interface between masonry units and mortar. This model revealed that both the tensile failure and the shear failure of the interface between masonry units and mortar can be attributed to the tensile failure of

mechanical keys at the interface. When combined with a biaxial masonry failure criterion, this model can be used to illustrate the complete failure envelope of a masonry bed joint. In addition, the following conclusions also were drawn from this model:

- A distinction needs to be made between the initial equivalent internal shear friction coefficient for the uncracked bed joints and the shear friction factor for the cracked bed joints, since the two parameters are associated with different mechanical mechanisms.
- The upper-boundary estimate for the initial equivalent internal shear friction coefficient is 1.0.
- The initial bed joint shear bond strength is roughly twice the initial bed joint tensile strength.

For a strong unit-weak mortar masonry, the behavior of the masonry bed joints controls the response of the entire URM assemblage. In this case the mechanical key model was extended to explain the failure mechanism for the entire URM assemblage, and the following conclusions could be drawn:

- Diagonal cracking is either due to the sliding and splitting of masonry joints, or due to the compressive failure of the URM assemblage. This mode of failure cannot be characterized by a simple diagonal tensile strength.
- The diagonal compression test is not recommended for measuring the material properties of masonry.

14.2. URM STRUCTURAL COMPONENTS

URM piers are the most important structural components in a URM building. A macro model, termed the effective pier model, was developed in this research to describe the nonlinear in-plane behavior of individual URM piers. This model can describe the failure mechanisms, the maximum strength, and the deformation capacity of a URM pier. A nonlinear pushover analysis program was developed based on the effective pier model and used to analyze URM piers investigated in previous experiments. Strength, force-displacement behavior, and failure modes were all in close agreement with observed behavior. In addition, with some simplifications to the model, strength expressions were derived for URM piers corresponding to each of the four primary failure modes. These strength expressions were in close agreement with FEMA 356.

On the other hand, compared with FEMA 356, the effective pier model provides more reasonable explanations for the nonlinear behavior of individual URM piers. The effective pier model is able to accurately describe both single and mixed failure modes of URM piers, which cannot be modeled by current analytical procedures such as the one outlined by FEMA 356. Moreover, the effective pier model shows that the rocking mechanism is actually a normal working mechanism for URM piers and that the toe-crushing failure mode is a limit for the rocking mechanism.

Adjacent, transverse walls may significantly increase both the initial stiffness and the maximum lateral strength of a URM pier. In order to consider this contribution, the effective pier model was modified to account for non-rectangular cross section URM pier. Based on this modified effective pier model, the maximum strengths of a URM pier corresponding to each of the four primary failure mechanisms were investigated. The

analyses showed that flange effects significantly increase the rocking strength and the shear sliding strength of a URM pier. In contrast, a non-rectangular cross section has no significant effects on the diagonal tension strength of a URM pier. Furthermore, the analyses also revealed that the location of the transverse wall has a remarkable influence on the response of a URM pier.

14.3. STRUCTURAL CHARACTERISTICS OF URM BUILDING

A two-story URM bearing wall structure with timber floor and roof diaphragms was tested in quasi-static fashion to investigate the seismic resistance of a typical, existing URM building in the Mid-America region. The main conclusions obtained from this test are as follows:

14.3.1. Interactions between masonry walls and flexible roof and floor diaphragms

- The stiffness of the basic components of a URM building (the in-plane walls, the out-of-plane walls, the flexible diaphragms, and the connections between the diaphragms and masonry walls) determine the response of this diaphragm-wall system. The tests revealed that the interaction mechanisms between the timber diaphragm and the masonry walls are different in the directions parallel and perpendicular to the floor joists.
- The lateral flexural and shear stiffness of the roof diaphragm is smaller than that of the masonry out-of-plane wall, while the axial stiffness of the roof diaphragm is larger than that of the masonry out-of-plane wall.

- The stiffness of the masonry in-plane wall is much larger than the stiffness of the roof diaphragm and of the masonry out-of-plane wall.
- At low levels of lateral force, there are large relative movements between the roof diaphragm and the masonry out-of-plane walls due to the flexible connection details typically employed.
- Tension ties connect the diaphragm with the masonry out-of-plane walls, and they help to distribute the lateral forces from the diaphragm to the out-of-plane walls.

14.3.2. Nonlinear properties of URM buildings

14.3.2.1 Failure mechanisms, maximum strength, and ductility

- The test structure exhibited very stiff response before substantial cracking occurred. When the building was loaded parallel to Walls 1 and 2, the maximum lateral strengths of the test structure were 87 kips in the south direction (60 kips on Wall 1 and 27 kips on Wall 2), and 79 kips in the north direction (55 kips on Wall 1 and 24 kips on Wall 2). The lateral drift at the roof level corresponding to the maximum lateral strengths was about 0.02%. When the building was loaded parallel to Walls A and B, the maximum lateral strengths of the test structure were 79 kips in the west direction (36 kips on Wall A and 43 kips on Wall B), and 77 kips in the east direction (40 kips on Wall A and 37 kips on Wall B). The lateral drift at the roof level corresponding to the maximum lateral strength was about 0.07%. After the test building reached its maximum lateral strengths, several large cracks rapidly developed and the secant stiffness decreased quickly.

- The damage to the masonry walls was characterized by several large, discrete cracks due to the brittle behavior of the URM material.
- The failure mechanism for each masonry wall depended on the configuration of the masonry wall. Wall 2 was a perforated wall with large openings and slender piers in the first story. It exhibited a component-dominated rocking mechanism, with all three first floor piers rocking and the entire second floor wall moving laterally and vertically as a monolithic portion on top of the first story piers. In contrast, Wall 1 was a fairly solid wall with only a small door opening in the first floor. The behavior of Wall 1 was significantly affected by a global overturning moment, and the behavior changed significantly throughout the loading. The opening ratios of Walls A and B were between those of Walls 1 and 2. Both Walls A and B exhibited a mixed response of global overturning and local rocking. When the walls were laterally loaded, the spandrels on the tensile side were lifted above the exterior piers. These piers were “left behind” and did not resist much lateral shear force. The interior piers rocked, and the exterior piers on the compressive side resisted large vertical compressive and lateral shear forces.

14.3.2.2 Coupling

- The coupling stiffness between two parallel masonry shear walls was small and can be ignored for all practical purposes.

14.3.2.3 Torsion

- The torsional response of the test structure that featured flexible roof and floor diaphragms was small and did not contribute significantly to the observed performance.

14.3.2.4 Flange effects

- The compression and tension flange effects due to the contribution of the out-of-plane walls exhibited significant influence on the behavior of the in-plane walls. As a result, although Walls A and B had identical configuration, their behavior was different due to the different sizes of flanges activated by those two walls.
- The flange effects should be distinguished between a pier flange and a spandrel flange. The two different types of flanges have different effects on the response of a pier depending on whether the flange is on the tensile or compressive side of the pier. Based on the experimental observations, a set of rules was given for the determination of the sizes of the pier flange and the spandrel flange.

14.3.2.5 Overturning moment

- The overturning movement induced by the lateral forces had significant effects on the response of the test structure. The effects were twofold. First, the overturning moment introduced additional vertical stresses in the piers and altered their response. Second, the overturning movement caused additional lateral displacements to the building and global rocking of the entire wall.

14.3.2.6 Effective piers

- The flexural cracks induced by the rocking of a pier generally did not propagate into the horizontal bed joint. Instead, these cracks propagated perpendicular to the direction of the maximum tensile stresses at the corner of openings. This led to different effective aspect ratios of the pier when the pier was loaded in different directions, and consequently altered the response of the pier. Based on the experimental observation, a method was determined to define effective pier dimensions in a perforated wall.

14.3.2.7 Details

- Compared to steel lintels, masonry arch lintels appeared to be more prone to damage and collapse.
- Pocket grouting did not significantly affect the behavior of the diaphragm in the direction perpendicular to the joists.

14.4. MODELING OF URM BUILDINGS

Along with the experimental investigation, several analytical models were employed to predict the responses of the test structure. The main conclusions from the analytical studies are as follows:

14.4.1. Elastic analysis

- A three-dimensional elastic finite element model gave good predictions for the elastic properties of the test structure, including the relative stiffness of the three basic components of a URM building: diaphragm, out-of-plane walls, and in-

plane walls. However, this approach could not describe the nonlinear behavior of a URM building.

- The elastic dynamic conceptual model revealed that the URM structure was a very stiff building; and, thus, its first vibration mode controlled the lateral deformation of the test structure.

14.4.2. Rigid body analysis

- The rigid body analysis gave good predictions for the ultimate strengths of the test structure. This analysis also verified the significant flange effects observed in the experimental research. However, this method could not consider either the toe crushing or the diagonal tension failure modes. As a result, the ultimate strengths estimated by this method should be considered as an upper-bound value.

14.4.3. Nonlinear FE analysis

- Since the damage to a URM building is characterized by several large cracks, appropriate FE modeling of the nonlinear behavior of a URM building can be accomplished by the appropriate modeling of these cracks.
- A 2D discrete-crack FE model gave a reasonable prediction for the failure mechanisms of the URM in-plane walls. However, it significantly underestimated the maximum strengths of the test structure, because some critical three-dimensional properties of the test structure, such as the flange effects, could not be considered in this model.
- A 3D discrete-crack FE model, built following predefined rules of the potential crack pattern for the structure, provided a good prediction for the failure mechanisms of the test structure. However, since stabilizing truss elements were

used in this model to resolve numerical convergence problems, the maximum strengths predicted by this FE model were 14% to 44% larger than the measured values.

14.4.4. 2D nonlinear pushover analysis

- If the roof and floor diaphragms in a URM building are flexible, the coupling between two parallel in-plane walls and the torsion of the entire building can be neglected. In this case, if out-of-plane damage to masonry walls can be prevented or ignored, the nonlinear behavior of an existing building can be analyzed reasonably well by using a two-dimensional nonlinear pushover model.
- The effects of flanges and overturning moments on the response of a URM building have to be considered in a pushover analysis.
- The nonlinear response of URM piers in a perforated wall should be considered by the effective pier model or a similar simplified method.

14.5. FEMA 356 PROVISIONS

The FEMA 356 pre-standard provides a full set of methodologies to evaluate the performance of existing buildings. However, this method does not give good prediction for URM structures because some critical issues were not considered in the current FEMA 356 document. Several recommendations are proposed to improve FEMA 356:

- It is recommended that mean material values be used for both displacement-controlled actions and force-controlled actions when analyzing the behavior of an existing building.

- An improved calculation method for the bed joint shear strength is proposed. It recognizes the difference between the behavior of an uncracked surface and a cracked bed joint surface.
- The effective pier model and a simplified method are proposed to describe the nonlinear properties of URM piers.
- It is recommended that a section is added to FEMA 356, Chapter 7, to provide guidelines for the mathematical modeling of a three-dimensional URM building. Specifically, flange effects and overturning moment effects should be considered.

14.6. ADDITIONAL RESEARCH NEEDS

Although this research added to the understanding of the seismic behavior of URM buildings, additional research is needed. This is particularly true in the following areas:

- Experimental investigations of the nonlinear behavior of URM piers with flanges: although an analytical solution for the flange effects of a URM pier has been developed, little experimental investigation is available to verify the proposed theory. Therefore, a series of tests to study the flange effects on the response of a URM pier, considering different flange sizes, locations, and different vertical stresses, need to be conducted.
- Experimental and analytical investigations on the nonlinear behavior of URM spandrels: in the current research, the URM spandrel was assumed to be elastic since a typical spandrel in a URM building is deep and strong. However, spandrel damage has been observed in previous seismic events. Having different force and deformation boundary conditions compared with a URM pier, a URM spandrel

might exhibit working mechanisms and nonlinear behavior different from a URM pier. Research is needed on the nonlinear response of URM spandrels in general.

- Quasi-static testing of a URM building with different controlling failure mechanisms: the failure of the test structure in the current research was controlled by rocking and sliding. The other two failure mechanisms for URM piers, i.e., diagonal tension and toe crushing, were not significant phenomena in this test. These two failure modes can be investigated by testing a building or a perforated wall with higher gravity stress and different pier aspect ratios. In addition, the spandrel in the current test structure was strong and thus no damage was observed. A URM perforated wall with weaker spandrel should also be the topic of a future experimental research project.
- Dynamic testing of URM buildings: due to the limits of quasi-static testing, the effects of different characteristics of seismic excitation on the nonlinear response of a URM building could not be fully investigated in this research. This problem can be solved by dynamic testing of a URM building. A shaking table test of a reduced scale URM building with similar configurations to the full-scale test structure reported herein has been conducted in CERL. A comparison between the responses of the two structures could provide an insight into the effects of the seismic excitations.
- Investigation of the properties of stabilizing trusses on the response of nonlinear three-dimensional FE model: it has been found in the current research that the stiffness of a stabilizing truss has a sizable influence on the response of nonlinear


three-dimensional FE model. More research is needed on this effect along with the potential of applying it for modeling FRP retrofits in a URM building.

- Macro model for URM perforated wall: the two-dimensional push-over model employed in this research gave good predictions of the response of the test structure. However, this model assumes an elastic spandrel, which limits its applicability to other wall configurations, as in the case where the spandrels are weak and vulnerable to damage. A macro panel model that is similar to the effective pier model for the pier but which also considers the nonlinear behavior of spandrels is a good candidate for analyzing the nonlinear response of perforated URM walls with weak spandrels.
- Dynamic analysis of URM structures under seismic excitation: the analyses conducted in the current research were aimed at simulating the nonlinear response of a URM building under quasi-static lateral forces. A dynamic analysis model can be used to analyze the “true” response of a URM building under seismic excitation. Such an analytical model can be built by modifying the nonlinear pushover model employed in the current research. Another candidate is the modification of the rigid-body-analysis model.

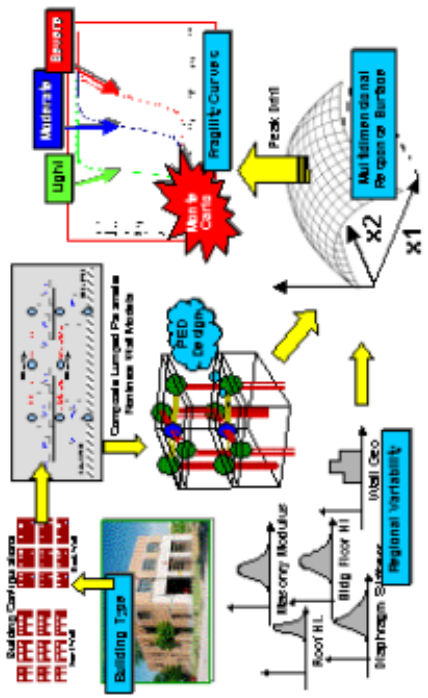
APPENDIX A.

QUAD CHARTS FOR RELATED MAEC PORJECTS

<p>Research Program: Regional Damage Synthesis</p> <p>Project Title: Inventories of Essential Facilities in Mid-America</p> <p>MAE Project Number: SE-1</p> <p>Start Date: 1-98 End Date: 6-00</p>	
<p>Project Goals and Objectives:</p> <ul style="list-style-type: none"> The purpose of this project is to develop a representative inventory of essential facilities in Mid-America. Once this data is collected, these facilities should be entered into a GIS database. Results should be provided to experimental researchers to guide their laboratory testing program. <p>Project Milestones and Deliverables:</p> <ul style="list-style-type: none"> Evaluate existing inventory databases Develop a comprehensive list of facilities and contact information Develop a telephone survey instrument based on ATC-21 Pretest survey instrument Produce a final report, with maps and summary data on facilities and key characteristics Disseminate inventory data via the Internet 	<p>Project Personnel:</p> <p>Pt. S. P. French Co-Pt. R. Olshansky Graduate RAs: W. Ross, M Stallings, A Goodwin, C. Young, B. O'Malley, T. Severe, R. Barlette, S. Lewis, M. Chan, F. Hu Undergraduates: C. LeBlanc External Collaborators: C. Cutrell, IL Emergency Mgt Agency, Ed Gray, Missouri Emergency Mgt. Agency</p> <p>Project Methodology:</p> <ul style="list-style-type: none"> The project will adapt the structural classification system developed in ATC-21 for use in a telephone survey format. Building owners and managers of a representative sample of essential facilities in Mid-America will be contacted to determine the age, structural class, number of stories and other salient characteristics of the building. The survey data will be analyzed to produce a descriptive analysis of the building inventory in mid-America. The essential facilities will be geocoded into a GIS database so their location can be compared with expected ground motion and known geotechnical conditions. This database will be designed to be compatible with FEMA's HAZUS software so that loss assessments can be performed in later projects (SE-5, SE-6, SE-7).
<p>Project Scope:</p> <ul style="list-style-type: none"> The project will assemble GIS inventories of essential facilities for the MAE Center study area. The location and key characteristics of hospitals, schools, police and fire stations will be determined based on a sample of facilities from the region. <p>Project Plan:</p> <ul style="list-style-type: none"> The project will generate descriptive statistics on the size, age, function, and physical structure of these facilities and will be located on a GIS database. The GIS database has been designed to be compatible with the MAE Center hazard maps and with HAZUS loss estimation system, which can be used to conduct a large-scale risk assessment. It is also compatible with the database developed for the transportation inventory (Project SE-3). Furthermore, the inventory will provide the MAE Center with a better understanding of the age and structural characteristics of the overall building stock in Mid-America. This will help guide the design of laboratory testing of prototypical buildings for risk assessment. 	

<p>Research Program: Regional Damage Synthesis</p> <p>Project Title: Inventories of Essential Facilities in Mid-America</p> <p>MAE Project Number: SE-1</p>	
<p>Co-Dependency with Other MAE Center projects:</p> <ul style="list-style-type: none"> This project provides basic information to other researchers in the Essential Facilities Program. The loss estimation projects (SE-5, SE-7, SE-9) depend directly on information collected in this project. The characteristics of the building stock discovered in this project also provide basic guidance to the research on structural systems and mitigation techniques (ST-4, ST-5, ST-9). <p>How project differs from similar work done elsewhere:</p> <ul style="list-style-type: none"> No research on the characteristics of the essential facilities building inventory existed prior to the formation of the MAE Center. Several states had developed partial inventories, but most were not georeferenced or based on a consistent structural classification system that is compatible with existing loss assessment models. 	<p>Publications:</p> <p>French, S.P. and Robert Olschansky. 2000. Inventory of Essential Facilities in Mid-America. Project Se-1 Final Report. Mid-America Earthquake Center.</p>
<p>Research Advances:</p> <ul style="list-style-type: none"> Produced first quantitative description of the age, type and composition of essential facilities in Mid-America Adapted ATC-21 methodology to telephone survey format <p>Potential Impact of Project:</p> <p>This project provides MAE Center researchers, state emergency managers and local elected officials with detailed information on the characteristics of the building supply. This helps to document the vulnerability of Mid-America and is basic information needed to craft realistic mitigation strategies.</p>	

Research Program: Building Owners Research Project Title: Response Modification Applications for Essential Facilities		NBAE Project Number: ST-4 Start Date: 1-98 End Date: 4-01
Project Goals and Objectives: <ul style="list-style-type: none"> Identify building structural characteristics for essential facilities in region Develop passive response modification methods for rehabilitation <ul style="list-style-type: none"> identify most promising passive energy dissipater (PED) technologies develop analytical modeling & design methods Validate approaches using ST-10 and ST-11 test results Assess potential regional fragility reduction using passive response modification for essential facilities Project Milestones and Deliverables: <ul style="list-style-type: none"> Identified low-rise URM structures with flexible floor diaphragms as most common essential facility and selected firehouses as a baseline configuration. Developed energy-based design method and selected base PED concepts that are activated by flexible diaphragm and diaphragm-wall interaction. Developed a composite nonlinear model for URM inplane wall response. Developed an improved probabilistic method for fragility assessment incorporating structural variability. 	Project Personnel: Pt. J.I. Craig Co-Pt. B. J. Goodno Graduate RAs: P. Towashiraporn, J. Park Undergraduates: K. Duose External Collaborators: C. Lindbergh, Charleston SC; J. Willmer, Willmer Engineering Inc., Atlanta GA; J. Hayes, USACERL, Urbana IL; R. Howe; Stanley D. Lindsey & Associates, Nashville TN	
Project Scope: <ul style="list-style-type: none"> Study how to achieve FEMA Level 1 performance objectives in URM essential facilities using passive energy dissipation approaches for response modification. Assess potential regional improvements in fragility for a class of URM essential facilities using passive energy dissipation approaches. Project Plan: <ul style="list-style-type: none"> Identify structural characteristics of essential facilities in region. <ul style="list-style-type: none"> regional inventory from SE-1 meetings with end users Develop simple 2D nonlinear URM numerical design models. Develop passive response modification approaches for target structures. <ul style="list-style-type: none"> energy-based design methodology floor diaphragm response modification inplane wall response modification Assess performance improvements for rehabilitated structures. <ul style="list-style-type: none"> improved serviceability reduced fragility Evaluate approaches using in ST-10 dynamic wall tests. 	Project Methodology: <ul style="list-style-type: none"> Analyzed SE-1 inventory as well as other sources and end-users. Developed selection of PED's suitable for use in typical URM buildings. Adapted energy-based PED design methodology from previous cladding work. Developed simple nonlinear bldg design models (with limited DOF's) <ul style="list-style-type: none"> URM inplane wall models with ST-5 flexible floor diaphragms using ST-8 results Studied performance of different PED's in baseline URM building model to assess range of improvements in structural fragility that can be achieved. Developed probabilistic method to assess potential fragility improvement across the essential facilities regional inventory. <ul style="list-style-type: none"> used design-of-experiments and response surfaces methods to model bldg behavior as function of design parameters chosen from Pareto diagrams. used Monte Carlo simulation to model response variability and assess fragility across region. 	

<p>Research Program: Building Owners Research</p> <p>Project Title: Response Modification Applications for Essential Facilities</p>	<p>Co-Dependency with Other NAE Center projects:</p> <ul style="list-style-type: none">SE-1: used regional inventory of essential facilitiesRR-2/SG-8: used synthesized ground motionsST-5: used flexible floor diaphragm models; co-developed nonlinear URM wall models for inplane responseST-9: incorporated out-of-plane URM wall models for nonstructural and architectural elementsST-10/11: recommended PED's for incorporation in testsRR-3: provided models of URM bldgs with added PED's <p>How project differs from similar work done elsewhere:</p> <ul style="list-style-type: none">The project focused on use of passive energy dissipation in certain types of URM essential facilities to achieve FEMA Level 1 (immediate occupancy) performance objectives.A method was developed to incorporate structural variability in the estimation of response modification improvements across a regional inventory of buildings.	<p>Five of the Most Relevant Publications:</p> <ol style="list-style-type: none">1. Craig, J. I., Goodno, B. J., Towehingom, P., and Dogan, T., "Hazard Mitigation for Long Recurrence Interval Earthquakes Using Passive Response Modification," <i>A New Advance in Seismic Solution: Energy Dissipation and Control of Structures</i>, Z. Fulin & B. F. Spencer, Jr., Editors, Seismological Press, Beijing, China, 1999, pp. 180-187.2. Goodno, B. J., Craig, J. I., Towehingom, P., and Losiribak, T., "Passive Response Modification for Low Rise Buildings in Mid-America," <i>Proceedings of The US Korea Workshop on New Frontiers in Infrastructure and Seismic Engineering</i>, Seoul, Korea, August 24-26, 1999, pp. 167-175 (published by Techno-Press, Korea, 2000).3. Craig, J. I., Goodno, B. J., Towehingom, P., and Dogan, T., "Ductile Cladding Systems for Seismic Design," <i>Proceedings, 12th World Conference on Earthquake Engineering (12WCEE)</i>, Auckland, New Zealand, on January 30-February 4, 2000 (CD-ROM).4. Goodno, B. J., Craig, J. I., Towehingom, P., Dogan, T., and Losiribak, T., "Response Modification for Essential Facilities Hazard Mitigation in Mid-America," <i>Proceedings 12th World Conference on Earthquake Engineering (12WCEE)</i>, Auckland, New Zealand, on January 30-February 4, 2000 (CD-ROM).5. P. Towehingom, J. Park, J. I. Craig, & B. J. Goodno, "Fragility Reduction for URM Buildings Using Passive Response Modification," abstract submitted in March 2001 for review for possible presentation at Seventh U.S. National Conference on Earthquake Engineering (NCEE), Boston, July 21-25, 2002.
<p>Research Advances:</p> <ul style="list-style-type: none">Simplified design method for passive response modification of URM bldgs.Design models for ductile energy dissipation devices.Nonlinear design models for inplane response of URM walls.Improved nonlinear URM inplane wall response model in DRAIN-2dx using new Pak 3 parameter nonlinear spring elements.Assessment of potential reduction in fragility of URM essential facilities using passive response modification (30-60% reduction in accelerations, drift).Improved methodology for fragility assessment across regional inventory incorporating structural variability.Plans for experimental validation of passive response modification approaches for URM buildings using experimental Test Beds (ST-10/11). <p>Potential Impact of Project:</p> <ul style="list-style-type: none">Methods for evaluating performance improvements in certain kinds of URM bldgs using passive energy dissipation.Methods for incorporating structural variability in regional assessments of building performance for seismic disturbances.	 <p>http://www.naecc.gatech.edu/EFP</p>	

Research Program: Building Owners Research Project Title: MDOF Response of Low Rise Buildings NBAE Project Number: ST-5 Start Date: 4-98 End Date: 12-01	
<p>Project Goals and Objectives:</p> <ul style="list-style-type: none"> The goal of the project is to develop and apply low degree-of-freedom models for calculation of the nonlinear dynamic response of low-rise buildings with unreinforced masonry (URM) walls and flexible diaphragms. Research objectives are to: (a) capture key phenomena associated with out-of-plane excitation and three-dimensional torsional coupling of wall systems via models suitable for rapid assessment and simulation, (b) conduct parameter studies to assess the effect of flexible floor diaphragms on building response, and (c) develop guidelines for evaluating the response of these types of structures. <p>Project Milestones and Deliverables:</p> <ul style="list-style-type: none"> Development and testing of Version 1.0 of the software was completed in December 1999. Refinements to the models, and development of a Java-based platform for access to and interpretation of simulation results was completed in January 2001. Parameter studies on a number of buildings have been performed. Final reports on the models, software system, and parameter studies will be completed by August 2001. A report on guidelines will be completed by October 2001, and proposed updates to FEMA 273/356 will be submitted by November 2001. 	<p>Project Personnel:</p> <p>PI: D. White Co-PI: K. Hjeltnad Graduate RAs: S.-C. Kim, J. Lewis Undergraduates: External Collaborators: J. Hayes, CERL, US Army Engineering Development and Research Center.</p>
<p>Project Scope:</p> <ul style="list-style-type: none"> A new approach for three-dimensional low degree-of-freedom nonlinear modeling of low-rise buildings with flexible floor and roof diaphragms was developed. The models are verified versus prior and new experimental test data on buildings and building wall and diaphragm components. Parametric sensitivity studies are conducted to evaluate the effect of flexible diaphragm characteristics on building response. <p>Project Plan:</p> <ul style="list-style-type: none"> Flexibility-based diaphragm models were developed which allow characterization of diaphragm bending and shear-racking response using six degrees-of-freedom (dof) per diaphragm. Low-dof wall models, and a methodology for characterization of the stiffness and strength of complex wall geometries based on simplified FEMA 273/356 type equations were created. Correlation with results of building tests are conducted. Parametric studies are performed to ascertain the sensitivity of the seismic responses to variations in building characteristics. 	<p>Project Methodology:</p> <ul style="list-style-type: none"> A six degree-of-freedom flexibility-based diaphragm element is developed which incorporates deformations due to bending as well as shear racking associated with coupling of lateral-load resisting wall systems. Force-deformation models are created to represent various types of wood and metal deck diaphragms. Low-degree of freedom wall models (one in-plane degree of freedom per story) are developed based on the assumption of negligible out-of-plane wall stiffness. Methodologies for characterization of the stiffness, strength and hysteretic response of complex wall geometries, using simplified FEMA 273/356 type equations, are investigated within the context of the proposed low-dof wall models, and recommendations are specified. A Java-based software platform is developed to facilitate access to the results of simulation studies by research and design engineers. Verification studies are conducted based on field as well as laboratory data on buildings and their wall and diaphragm components. Parametric sensitivity studies are conducted on selected building geometries to determine the effects of changes in stiffness, strength and mass of the floor diaphragms on the building response, and to support development of guidelines for evaluation of these types of buildings.

Research Program: Building Owners Research

Project Title: MDOF Response of Low Rise Buildings

NBAE Project Number: ST-5

Co-Dependency with Other NBAE Center projects:

- The software developed within this project is being used by Project RR-3 in the development of fragility curves for existing and retrofitted URM building structures in mid-America. The software has been utilized for initial analysis and design of the prototype building structure to be tested within ST11. Data from projects ST6 and ST8 has been utilized for calibration and assessment of the low-dof diaphragm and wall models. The synthetic ground motions developed in projects RR-2 and SG-8 are employed within the analysis parametric studies. Data from SE8 was utilized in determining specific building configurations for the parametric studies.

How project differs from similar work done elsewhere:

- No research has been conducted on creation and application of three-dimensional low-degree of freedom models that allow consideration of both out-of-plane wall excitations as well as torsional coupling of wall systems associated with diaphragm response.

Research Advances:

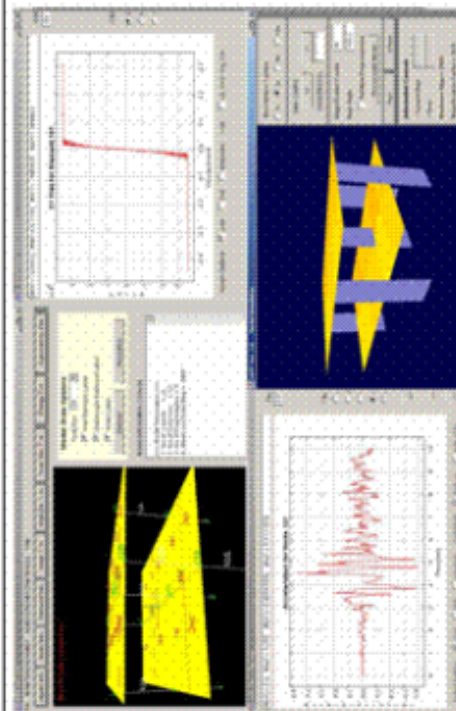
- The flexibility-based diaphragm element addresses the analysis of nonlinear flexible diaphragm response due to out-of-plane wall excitation and the lateral and torsional coupling of in-plane wall actions with only six degrees of freedom per diaphragm. The methodologies proposed for definition of low-dof wall models address the rational application of simple FEMA 273/356 equations to complex wall configurations. Studies to date indicate reasonable correlation with field and laboratory data.

Potential Impact of Project:

- Project results will have an impact on future updates of national guidelines for seismic rehabilitation (FEMA 273/356). The software developed in this project is a useful simplified tool that can be utilized by research and design engineers for three-dimensional simulation of the time-history response of low-rise URM buildings with flexible floor diaphragms.

Five of the Most Relevant Publications:

- Kim, S.-C. and White, D.W., "Three-Dimensional Non-Linear Time History Analysis of Low-Rise Buildings with Flexible Diaphragms," Seventh US National Conference on Earthquake Engineering, Boston, MA, July 2002.
- White, D.W., "Seismic Assessment of Existing Unreinforced Masonry Buildings," Korean Earthquake Engineering Research Center - Mid-America Earthquake Center Workshop, University of Illinois, Urbana, IL, August 2001.
- White, D.W., Alomdar, B.N., and Nohela, P.K.V., "Mixed finite elements for three-dimensional nonlinear analysis of steel frames," Proc., First Int. Conf. Structural Stability and Dynamics, Taipei, Taiwan, December 2000, 131-140.
- Alomdar, B.N., White, D.W., and Leon, R.T., "Cyclic nonlinear analysis of partially-restrained composite framing systems using component-based connection models," Proceedings, Composite Construction in Steel and Concrete IV, Engineering Foundation Conference, Banff, Alberta, May 28-June 2, 2000, (in press).
- Alomdar, B.N. and White, D.W., "Anisotropic co-rotational finite element for three-dimensional nonlinear frame analysis," First MIT Conference on Computational Fluid and Solid Mechanics, Cambridge, MA, June 2000.




Research Program: Building Owners Research Project Title: Performance of Rehabilitated URM Components NBAE Project Number: ST-6 Start Date: 4-98 End Date: 12-00	
<p>Project Goals and Objectives:</p> <ul style="list-style-type: none"> The goal of the project is to explore possible alternatives for adding both seismic strength and deformation capacity to unreinforced clay-unit masonry buildings. Research objectives are to: (a) assess strength and behavior of URM pier and wall components before rehabilitation, (b) examine possible improvements in strength or deformation capacity with various rehabilitation methods and (c) propose updates to national rehabilitation guidelines (FEMA 273 or 356). <p>Project Milestones and Deliverables:</p> <ul style="list-style-type: none"> Testing of wall and pier specimens was completed in February 2001. Load-deflection data and summaries of these tests are available by download from the project website. Final reports on the flexural series and the shear series of tests will be completed by August 2001. Proposed updates to FEMA 273/356 will be submitted by November 2001. 	<p>Project Personnel:</p> <p>Pt. D.P. Abrams Co-Pt. T. Hanson Graduate RAs: S. Franklin, O. Ebbay, J. Lynch Undergraduates: D. Ford External Collaborators: C. Lindbergh, Charleston SC; D. Shapiro, SOHA Engineers, San Francisco, CA; P. Stukas, B&B Engineers, Sacramento, CA</p> <p>Project Methodology:</p> <ul style="list-style-type: none"> Full-scale test piers and walls are constructed within Newmark Structural Engineering Laboratory for the purpose of testing to failure under a controlled series of lateral-load tests. Horizontal forces are applied at the top of a test specimen to simulate lateral seismic story shears. Vertical force is applied at the top of a test specimen as well to simulate gravity loads. The resulting lateral force-deflection relations, or hysteresis curves, from these experiments are used to judge the relative effectiveness of various rehabilitation methods in terms of strength and deformation capacity. Photos and measurements indicating the level of damage and performance at various drift levels are used to support development of future guidelines for seismic rehabilitation of URM buildings.
<p>Project Scope:</p> <ul style="list-style-type: none"> A series of unreinforced clay-unit masonry piers and shear walls were tested to determine seismic performance characteristics with and without rehabilitation. Data analysis is done to evaluate effectiveness of rehabilitation methods. <p>Project Plan:</p> <ul style="list-style-type: none"> Strength, stiffness, and deformation capacities of URM walls and piers are evaluated through a series of static, load-reversal tests on full-scale specimens. Mechanisms for non-rehabilitated test specimens are examined with respect to rocking, toe crushing, bed-joint sliding and diagonal tension. Flexural mechanisms are examined for piers rehabilitated with shotcrete overlays, ferrocement coatings, FRP strips and center-core reinforcement. In addition, shear mechanisms for squat walls are studied. 	



Research Program: Building Owners Research Project Title: Performance of Rehabilitated URM Components		NMAE Project Number: ST-6
Co-Dependency with Other NMAE Center projects: <ul style="list-style-type: none"> Observed and measured behavior of URM test piers is being used to develop computational models of building response in Project ST-5. Rehabilitation methods explored in ST-6 are used as a basis for selection of strengthening methods for a large-scale building test (ST-11) and a shake-table test of a replicate half-scale building (ST-22). 	Five of the Most Relevant Publications: <ol style="list-style-type: none"> Abrams, D.P., "Rehabilitating Unreinforced Masonry Buildings with Ductility," <i>Proceedings of Eighth North American Masonry Conference</i>, University of Texas at Austin, June 1999. Abrams, D.P., "New Perspectives on Seismic Rehabilitation," Proc. of International Workshop on Annual Commemoration of Chi-Chi Earthquake, National Center for Research on Earthquake Engineering, Taipei, September 2000. Abrams, D.P., "Seismic Rehabilitation Methods for Unreinforced Masonry Walls," Proc. of Third Multilateral Workshop on Development of Earthquake and Tsunami Disaster Mitigation Technologies and Their Integration for the Asia-Pacific Region, Manila, Philippines, November 2000. Ehbay, O., and D.P. Abrams, "Seismic Rehabilitation of Unreinforced Masonry Shear Walls," <i>Proceedings of Ninth Canadian Masonry Symposium</i>, University of New Brunswick, June 2001. Abrams, D.P., "Performance Based Engineering Concepts for Unreinforced Masonry Structures," <i>Journal on Progress in Structural Engineering</i>, June 2001. 	
How project differs from similar work done elsewhere: <ul style="list-style-type: none"> No research on masonry rehabilitation is being done at the other EERCs. Some research is being done at USA CERL and the University of Wyoming on the use of FRP strips for strengthening masonry buildings. ST-6 has adapted technologies from this research, but has focused on how FRP strips alter mechanisms for rocking of slender piers from a perspective of performance-based design. 	Accomplishments <ul style="list-style-type: none"> New rehabilitation technologies have been developed for improving the seismic performance of unreinforced clay-unit masonry buildings. 	Core Research Benefits <ul style="list-style-type: none"> Provides improved seismic performance to allow rehabilitated fragility curves to be developed for comparing effects of community actions with and without consequence minimization.
Research Advances: <ul style="list-style-type: none"> Data on cyclic strength and behavior in rocking mode confirms FEMA 273 assumptions. Deformation capacity with toe crushing redefined from present national guidelines. Ferrocement coatings not effective in increasing strength or deformation capacity. FRP strips increase strength but limit deformation capacity. Anchorage problems with center-core technique found. Bed-joint sliding behavior of shear walls proves to be excellent energy dissipation mechanism. 	Potential Impact of Project: <ul style="list-style-type: none"> Research results will have an impact on future updates of national guidelines for seismic rehabilitation (FEMA 273/556). New information from research will enhance future rehabilitation of URM buildings. Examples include the current upgrade of the National Civil Rights Museum in Memphis and the Sacramento Municipal Utility District historical Station A power plant. 	
Persistence to CBE Framework Development: <ul style="list-style-type: none"> This project will advance utilization of Consequence-Based Engineering by providing new rehabilitation strategies for consequence minimization interventions. 		

Research Program: Building Owners Research Project Title: Performance of Rehabilitated Floor and Roof Diaphragms		MAE Project Number: ST-8 Start Date: 9-98 End Date: 12-01
<p>Project Goals and Objectives:</p> <ul style="list-style-type: none"> The goal of the project is to examine the strength, stiffness and deformation capacities of existing floor and roof diaphragms for essential facilities in mid-America, with a focus on pre-1950's unreinforced masonry (URM) buildings. In addition, rehabilitation strategies for existing diaphragms are assessed for improved overall structural performance during seismic excitations. <p>Project Milestones and Deliverables:</p> <ul style="list-style-type: none"> Project milestones included the experimental verification of the basic seismic behavior of existing and rehabilitated wood diaphragms, which was completed in 12/99. Various methods of retrofit for existing URM structures included stiffening, strengthening and response modification. A project report documenting the results of this experimental program is under review within the MAE Center. 	<p>Project Personnel:</p> <p>PI: Joseph M. Bracci</p> <p>Co-PI: Mary Beth D. Hushe</p> <p>Grad. RA's: David Peraha, Amber Grubbs</p> <p>Undergrads: Bill Beason, Joel Barron, Brian Dahn, John Everett, and David Pfingsten</p> <p>External: Alan Scott and Ted Preuss (BOE Intl, St. Louis, MO),</p> <p>Collaborators: Jack Hayes (USACERL)</p>	
<p>Project Scope:</p> <ul style="list-style-type: none"> Three large-scale wood diaphragm specimens were built, tested, retrofitted and retested again under quasi-static reversed cyclic loading. A total of four retrofit methods were used to strengthen and stiffen the specimens. Limits of flexible/rigid diaphragm behavior based on in-plane stiffness, chord discontinuities due to openings, and connection characteristics were investigated, as well as rehabilitation techniques for improving lateral force distribution to vertical elements. <p>Project Plan:</p> <ul style="list-style-type: none"> The project initially identified typical details and deficiencies found in existing diaphragms found in pre-1950's URM essential facilities. Each specimen developed for testing was also tested again using at least two retrofit techniques to assess the corresponding increase in stiffness and strength. Additional analytical studies will be performed to evaluate the effect of diaphragm retrofit on the overall building response under seismic loading for selected case study structures. 	<p>Project Methodology:</p> <ul style="list-style-type: none"> The project focused on experimentally investigating the strength, stiffness and deformation capacities of existing and rehabilitated wood diaphragms subject to quasi-static reversed cyclic loading during years 1 and 2. Test specimens were developed from collaborative research projects within the center on essential facility inventory in mid-America (SE-1) and MDOF response of low-rise buildings (ST-5) and through discussions with structural engineers in St. Louis. The details for the specimens representing existing construction were based on pre-1950's URM building construction. Test results are reported consistent with parameters given in FEMA 273. Year 4 funding is dedicated to the analytical component of this project. This work will provide a basis for identifying areas in which analysis and design guidelines are needed to evaluate pre-1950's URM buildings for seismic retrofit, with a focus on the floor and roof diaphragms. The impact of selected retrofits on the overall building response will be evaluated analytically and recommendations will be formulated. 	

<p>Research Program: Building Owners Research</p> <p>Project Title: Performance of Rehabilitated Floor and Roof Diaphragms</p> <p>MAE Project Number: ST-8</p>	
<p>Co-Dependency with Other MAE Center projects:</p> <ul style="list-style-type: none"> Results from this project are being used by MAE Center project ST-5 to calibrate diaphragm computational models, project ST-10 in identifying diaphragm stiffness for existing infrastructure, and project ST-11 to define a shaketable model for a low-rise building system. <p>How project differs from similar work done elsewhere:</p> <ul style="list-style-type: none"> The researchers are not aware of similar work being done at the other EERCs. However, work on wood diaphragms is being performed as part of the CUREE-Cal Tech wood frame project. 	<p>Five of the Most Relevant Publications:</p> <ol style="list-style-type: none"> Peraha, D., Hueste, M.D., and Bracci, J.M. "Seismic Performance of Rehabilitated Floor and Roof Diaphragms in Pre-1950's Unreinforced Masonry Buildings," submitted to the 7th U.S. National Conference on Earthquake Engineering, July 2002. Peraha, D., Bracci, J.M., and Hueste, M.D. "Seismic Performance of Rehabilitated Floor and Roof Diaphragms," MAE Technical Report, in review. Peraha, D., Bracci, J.M., and Hueste, M.D. "Performance of Rehabilitated Floor and Roof Diaphragms," 1999 EERI Annual Meeting, Poster Session. Project web page: http://keep.rofs.tamule.edu/bracci/mae/mse.html
<p>Research Advances:</p> <ul style="list-style-type: none"> Experimental seismic behavior for existing and rehabilitated floor and roof wood diaphragms, with a focus on details found in pre-1950's URM buildings in mid-America. Assessment of new and traditional methods of seismic retrofit for stiffening and strengthening wood diaphragms. Development of backbone curves of in-plane response and comparison to FEMA-273 guidelines. <p>Potential Impact of Project:</p> <ul style="list-style-type: none"> Project results will impact future updates of the national guidelines for seismic rehabilitation (FEMA 273) and new information will enhance future rehabilitation of wood diaphragms in older URM buildings. 	 <p>Diaphragm Test for Specimen with Single Straight Square-Edged Sheathing on Wood Joists Retrofitted with Blocked Plywood Overlay</p>

Research Program: Building Owners Research Project Title: Performance Objectives for Essential Facilities		NBAE Project Number: ST-9 Start Date: 10-98 End Date: 12-01
Project Goals and Objectives: <ul style="list-style-type: none"> • Inventory types of non-structural components found in typical EF • Define performance objectives for life safety, immediate occupancy, and operational performance levels in FEMA 273/274 (356/357) • Identification of cost effective rehabilitation strategies for partial height partitions • Specify permissible amounts of damage to nonstructural elements • Prepare results in a consistent format with Chapter 11 of FEMA 273 (356) Project Milestones and Deliverables: <ul style="list-style-type: none"> • Completed inventory of 7 Atlanta area school buildings to identify partial height URM partitions in April 1999; focused on ceiling and partition systems • Developed simple and complex finite element models of URM partitions using DRAIN-2dx and ABAQUS by August 1999 • Developed analytical model of rehab device and conduct parametric studies to assess its effectiveness for various wall geometries by November 1999 • Currently developing: improved failure models for out-of-plane wall behavior for inclusion within ST-4 & ST-5 analytical models & ST-11 & ST-22 test structures; and possible expanded & improved guidelines for use within FEMA 273 (356) 	Project Personnel: PI: B. J. Goodno Co-PI: J. I. Craig Graduate RA's: T. Lostribak Undergraduates: K. Duose; A. Williamson External Collaborators: C. Lindberg, Charleston SC; J. Wilhoit, Wilhoit Engineering Inc., Atlanta GA; J. Hayes, USACEEL, Urbana IL; R. Howe, Stanley D. Lindsey & Associates, Nashville TN; J. Riley, Fulton Co Schools, Atlanta GA	
Project Scope: <ul style="list-style-type: none"> • Develop limited inventory of nonstructural components, with a focus on URM partial height partitions in school buildings in Mid-America; assemble both simple & complex nonlinear models to establish failure patterns and criteria, and develop rehab guidelines and procedures to meet performance objectives within the framework of FEMA 273 (356) Project Plan: <ul style="list-style-type: none"> • Analyze SE-1 & SE-5 inventories as well as local school survey & end-users • Focus assessment of non-structural performance on partial height URM partitions of varying geometry and support conditions • Develop nonlinear models which predict first crack and failure for URM partitions using ABAQUS and nonlinear static push over analysis • Develop suitable simple nonlinear design models (limited DOFs) which are compatible with low-rise analytical (ST-5) and test (ST-10) models for dynamic analysis • Specify performance limits/measures consistent with FEMA 273 • Determine potential improvement in partition fragility due to cost effective rehabilitation measures 	Project Methodology: <ul style="list-style-type: none"> • Conduct inventory of "typical" essential facilities to identify classes of nonstructural components organized around the categories found in FEMA 273 (356) • Perform analyses on selected components using FEMA 273 (356) Analytical Procedures • Confirm results of FEMA 273 (356) evaluations using more complex models and analysis (linear, nonlinear) procedures and existing software (ABAQUS, nonlinear static push over analysis) • Develop simplified analysis procedures, improved rehabilitation guidelines, and performance measures • Implement the results in the form of a nonstructural database or enhance existing databases, as appropriate • Disseminate results on ST-9 web page (www.nbae.gatech.edu/EFP) 	

<p>Research Program: Building Owners Research</p> <p>Project Title: Performance Objectives for Essential Facilities</p> <p>MAE Project Number: ST-9</p>	
<p>Co-Dependency with Other MAE Center projects:</p> <ul style="list-style-type: none"> • SE-1, 5: use regional inventory of essential facilities • RR-2/SG-8: use ground motions; RR-3: use fragility methodology • ST-5, ST-10: integrate nonlinear out-of-plane wall models of varying geometries (developed here) with generic low-rise building models • ST-10 & ST-11: provide input to low-rise URM building model full-scale building laboratory testing • ST-4, ST-5: development of nonlinear URM wall models for out-of-plane response in collaboration with work to develop models for in-plane response • ST-10: joint work to develop out-of-plane wall models (DRAIN-2dnt) • ST-22 & ST-11: explore opportunities to incorporate nonstructural systems in MAE-CREL shake table test & in full-scale test <p>How project differs from similar work done elsewhere:</p> <ul style="list-style-type: none"> • The focus on inventorying partial height URM partitions in school buildings, modeling their out-of-plane behavior, and developing economical rehab procedures and guidelines is unique to this MAE project 	<p>Four of the Most Relevant Publications:</p> <ol style="list-style-type: none"> 1. Goodno, B. J., Craig, J. I., Towashiraporn, P., and Losrihik, T., "Passive Response Modification for Low Rise Buildings in Mid-America," <i>Proceedings of The US Korea Workshop on New Frontiers in Architectural and Seismic Engineering</i>, Seoul, Korea, August 24-26, 1999, pp. 167-175 (published by Techno-Press, Korea, 2000). 2. Goodno, B. J., Craig, J. I., Towashiraporn, P., Dugan, T., and Losrihik, T., "Response Modification for Essential Facilities Hazard Mitigation in Mid-America," <i>Proceedings, 12th World Conference on Earthquake Engineering (I2WCEE)</i>, held in Auckland, New Zealand, on January 30-February 4, 2000, (CD-ROM). 3. T. Losrihik, B. J. Goodno, & J. I. Craig, "Seismic Response of Partial Height URM Walls," abstract submitted in March 2001 for review for possible presentation at <i>Seventh U.S. National Conference on Earthquake Engineering (2001)</i>, Boston, July 21-25, 2002 4. Goodno, B. J., Craig, J. I., & Losrihik, T., "Seismic Vulnerability Of Partial Height URM Partitions," abstract submitted for review for possible presentation at <i>Ninth European Conference on Earthquake Engineering (ECEE)</i>, London, Sept. 9-13, 2002. <p>Accomplishments:</p> <ul style="list-style-type: none"> • An inventory of construction types for interior walls of school buildings. • Advanced failure models were developed for out-of-plane wall behavior. • Cost effective rehabilitation techniques were developed for interior free standing walls.
<p>Research Advances:</p> <ul style="list-style-type: none"> • Obtained data on nonstructural components in essential facilities in Mid-America (i.e., 7 Atlanta area schools) & share with investigators on SE-1 and SE-5 (augment data from Case Study Communities: Silerston, MO & Carbondale, IL) to improve nonstructural databases and performance limits within HAZUS • Development of failure models for URM nonlinear out-of-plane wall behavior for varying support conditions; develop representative simple (DRAIN-2dnt) & complex (ABAQUS) models which predict wall failure for various wall geometries • Identification/evaluation of cost effective rehabilitation strategies for partial height partitions <p>Potential Impact of Project:</p> <p>Based on an inventory of school buildings, partial height URM partitions were judged most critical among other nonstructural components in essential facilities in Mid-America. A rehabilitation technique, which utilizes a special compression strut device, was developed in this study, and was shown to increase the out of plane strength of URM partitions by up to 30%.</p>	

Research Program: Building Owners Research Project Title: Dynamic Tests of Low-Rise Buildings NSAE Project Number: ST-10 Start Date: 1-99 End Date: 5-02	
<p>Project Goals and Objectives:</p> <ul style="list-style-type: none"> The goal of the project is to determine the influence of diaphragm flexibility on the dynamic response of low-rise buildings. Research objectives are (1) to obtain empirical data on the response of representative low rise buildings having different diaphragm properties through shake-table testing, (2) to develop and validate analytical methods for simulating observed response data, (3) to relate measured response to estimates made using the linear and nonlinear procedures of FEMA-273/356; and (4) formulate recommendations for assessing when rehabilitation is warranted. <p>Project Milestones and Deliverables:</p> <ul style="list-style-type: none"> Shake table testing of the as-built specimen was completed in February 2001. Summaries of response data are available for viewing on the project web site. Models for simulating response will be finalized by August 2001. Comparisons of response with the provisions of FEMA 273/356 will be completed by November 2001. Proposed updates to FEMA 273/356 will be submitted by February 2002. A final report will be completed by May 2002. 	<p>Project Personnel:</p> <p>Pt. M. Aschheim Co-Pt. D. Abrams Graduate RAs: C. Simsir, C. Wissawapaisal Undergraduates: R. Senese, E. Bretz, David Pfington External Collaborators: C. Lindbergh, Charleston SC; Alan Scott, St. Louis, and John Thesis, St. Louis.</p> <p>Project Methodology:</p> <ul style="list-style-type: none"> Inventories of essential facilities were reviewed to determine the most common low-rise building type. An idealized model was constructed on the shake-table in Newmark Laboratory using half-scale concrete block for walls and a steel tube simulating the diaphragm. The diaphragm beam was instrumented and calibrated prior to installation, to determine the distribution of inertial loads between the components of the building. Displacement transducers and accelerometers were used to record response; data was compared to that generated using complex models in Drain-2DX and simplified models in USEE for simulating the response to the measured input motions. Tests were done with different ground motions scaled to different intensities and with diaphragm beams that represented different diaphragm stiffnesses. Results were used to improve the computational models. Subsequent analytical studies using validated models will explore parametric variations for representative building configurations to understand behavior patterns; these results will help to formulate recommendations for engineering practice.
<p>Project Scope:</p> <ul style="list-style-type: none"> A idealized specimen representing key features of low rise essential facilities was tested on a shake table using recorded and synthetic ground motions. Analytical methods are being applied to simulate the observed response and to establish expected performance of full-scale structures. Applicable provisions of FEMA-273/356 will be compared to experimental results; where indicated, updates to these provisions will be formulated. Methods for rehabilitation of the unreinforced masonry walls were to have been tested, but it has not been possible to damage the walls sufficiently to rehabilitate them; only minor rocking has occurred with drifts exceeding 3%. <p>Project Plan:</p> <ul style="list-style-type: none"> Record the acceleration and displacement responses at multiple locations of the test structure as it is subjected to base motions of increasing severity. Perform frequency sweep tests to monitor the change in specimen properties with increasing damage. Develop accurate nonlinear SDOF and detailed fiber element models to simulate the recorded responses. 	

Research Program: Building Owners Research
Project Title: Dynamic Tests of Low-Rise Buildings

NIAE Project Number: ST-10

Co-Dependency with Other NIAE Center projects:

- Inventory data from SE-1 was used to determine that a mixed reinforced and unreinforced masonry bearing wall structure would be tested. Synthetic ground motions from RE-2 were applied to the structure. Models for the out-of-plane response of the unreinforced masonry walls were shared with ST-9. The influence of wood diaphragm hysteretic behavior determined in ST-3 will be explored in the analytical studies. The response data from ST-10 is being used by ST-5 and ST-11. The idealized specimen was the target of studies to determine optimal response modification devices in ST-4. Had failure of the walls occurred, rehabilitation of the diaphragm using these devices and the rehabilitation technologies of ST-6 would have been explored further.

How project differs from similar work done elsewhere:

- Previous studies of building systems did not examine the influence of diaphragm stiffness on the stability of unreinforced masonry walls. Previous studies on unreinforced masonry walls did not account for interaction between the diaphragm and load-bearing walls.

Research Advances:

- Detailed fiber models for simulating response were developed and validated.
- Simplified techniques for estimating peak displacement response were applied successfully.
- The lack of significant damage to the out-of-plane walls indicates that current provisions for allowable limits on wall slenderness are too conservative.
- The ability of the walls to tolerate drifts exceeding 3% with damage consisting of only minor rocking at their bases indicates that limits on drift associated with operational performance can be increased substantially for out-of-plane response.

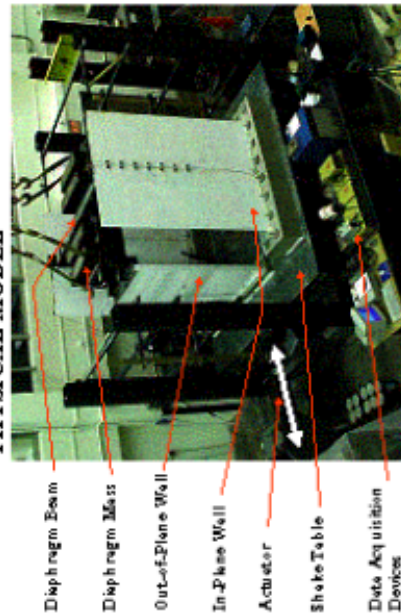
Potential Impact of Project:

- Project results will impact the evaluation and rehabilitation of low-rise buildings with flexible diaphragms.

Relevant Publications:

- Smsir, C., Accheini, M., and D.P. Abrams, "Influence of Diaphragm Flexibility on the Out-of-Plane Response of Unreinforced Masonry Walls," Proceedings of Ninth Canadian Masonry Symposium, University of New Brunswick, June 2001.
- Smsir, C., Accheini, M., and D.P. Abrams, "Response of Unreinforced Masonry Walls Subjected Normal to the Direction of Seismic Motions," Proceedings of Seventh US National Conference on Earthquake Engineering, Boston, July 2002.

PHYSICAL MODEL



Research Program: Building Owners Research Project Title: Large-Scale Tests of Low-Rise Building Systems MAE Project Number: ST-11 Start Date: 10-99 End Date: 12-01	
<p>Project Goals and Objectives:</p> <ul style="list-style-type: none"> The goal of the project is to examine the structural performance of existing unreinforced masonry buildings and to explore the effectiveness of several rehabilitation approaches for this type of structure. The research objectives are to: (a) assess strength, deformation capacity, critical components behavior and failure modes of existing URM structures at the system level, (b) determine the effectiveness of several rehabilitation techniques on URM building performance, including FRP and vertical pre-stressing strengthening of individual piers and its effects on the overall performance of the system, and (c) verify and propose updates to standard codes (FEMA 273/356) and advanced analysis tools for calculating the behavior of existing and rehabilitated URM buildings. <p>Project Milestones and Deliverables:</p> <ul style="list-style-type: none"> Two planning meetings were held in 1998 and 1999, with a final one held in September, 2000. Design of the test structure completed at the end of 2000. Southern Brick Institute has donated construction materials in the amount of \$35,000. The test structure's foundation and stud walls were completed in early March, 2001, and construction of the structure is set to begin in late May. Tests aimed at determining the material properties of the test structure are currently underway. The large-scale test will be finished by Fall 2001 and the final report will be completed by 3/02. 	<p>Project Personnel:</p> <p>PI: Roberto Leon Co-PI: Larry Kalm Graduate RA's: Tianyi Yi, Franklin Moon Undergraduates: Tito Del-Valle, Maholn Foss External Collaborators: Greg Borchelt (Brick Institute of America); Bill Kjoslein, (Southern Brick Institute)</p> <p>Project Methodology:</p> <ul style="list-style-type: none"> Full-scale two-story unreinforced masonry structure with flexible wood diaphragm will be built and tested in the Georgia Tech Structural and Materials Lab. The structure will be fixed to the strong floor through a RC foundation mat to allow for vertical pre-stressing. Horizontal forces will be slowly applied at the roof and floor level of the masonry wall and/or at the center of the diaphragm to simulate lateral seismic force. Extensive instrumentation, in the form of load cells, displacement transducers, and strain gages will be used to measure the performance of the structure. Photos and visual observation will also be used to record the progression of damage and performance at various drift levels. Some non-structural elements will be incorporated to assess their performance limits. FEMA 273/356 and advanced analysis tools based on the research results of other MAEC ST projects will be used to predict the performance of the structure. The measured data from the test will be used to verify the analysis tools and to support development of future guidelines for seismic rehabilitation of URM buildings.

Research Program: Building Owners Research

Project Title: Large-Scale Tests of Low-Rise Building Systems

MAE Project Number: ST-11

Co-Dependency with Other MAE Center projects:

- Project ST-11 incorporates and synthesizes the knowledge developed in other MAE Center projects including: (1) ST-6, which conducted research on the behavior of single in-plane URM wall piers with or without rehabilitation; (2) ST-4 which provided analysis tools for the in-plane strength and deformation capacity of perforated masonry walls; (3) ST-10 which conducted experimental research on out-of-plane strength and deformation of masonry walls; (4) ST-9 which provided analysis tools for the out-of-plane strength and deformation capacity of masonry walls with and without transverse walls; (5) ST-8 which conducted experimental and analytical research on existing and rehabilitated wood diaphragms; and (6) ST-5 which provided analysis tools for the elastic and inelastic behavior of wood diaphragms and its interaction with masonry structures. Finally, ST-11 is closely coordinated with ST-22, a parallel project focused on the dynamic test of a similar half-scale building to be conducted at CERL.

How project differs from similar work done elsewhere:

- No research on full-scale URM building test is being done at the other EERCs. A small, full-scale single-story URM building test has recently been completed at the University of Ottawa. The main strength of project ST-11 comes from the integration of a series of related MAEC ST projects. As such, ST-11 is intended to be a "capstone" of various research projects on the rehabilitation of existing URM structures.

Research Advances:

This project intends to develop advances in the following areas:

- Verification of advanced analytical models - this project is unique in that the effect of local repairs to the overall performance of a highly redundant but brittle system can be assessed experimentally and serve as back-calculation to the numerous tests available on individual URM piers and floor diaphragms.
- Verification of the effect of selective retrofit techniques on the overall structural system response. In particular, it will attempt to show that retrofitting to allow for rocking and sliding can result in satisfactory seismic performance

Potential Impact of Project:

- This project will serve as proof-of-concept at a large scale for the evaluation and retrofit strategies developed by other MAE Center researchers. Tests of this type are essential to show building code officials and the profession at large that research results based on reduced-scale models or component tests can be extended to entire structural systems. Research results will have an impact on future updates of national guidelines for seismic rehabilitation (FEMA 273/356). New information from research will enhance future rehabilitation of URM buildings.

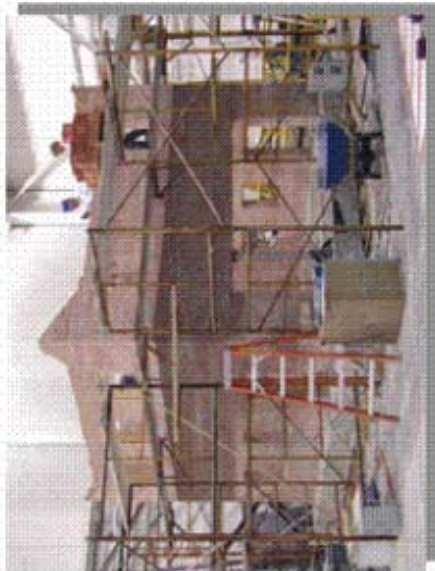
Relevant Publication:

1. Moon, F., Yi, T., Leon, R.T. and Kahn, L. "Retrofit of URM Structures with FRP Overlays and Post-Tensioning," Proceedings of the NSF-COHEMIS Workshop on Repair and Rehabilitation of Buildings and Bridges, University of Puerto Rico - Mayaguez, April 2001



Mid-America Earthquake Center

<p>Research Program: Building Owners Research</p> <p>Project Title: Performance of Rehabilitated URM Building Systems</p> <p>NWAE Project Number: ST-22</p> <p>Start Date: 10-00 End Date: 9-02</p>	
<p>Project Goals and Objectives:</p> <ul style="list-style-type: none"> The goals of this project are to verify analytical models developed through component tests, verify standard code and simplified analysis tools for calculating behavior of existing and rehabilitated URM buildings, determine system response at different levels of deformation (performance-based design), assess diaphragm and diaphragm-wall connection behavior, assess effectiveness of proposed rehabilitation schemes (FRP, prestressing), and correlate static and dynamic testing results and full-scale vs. half-scale modeling techniques <p>Project Milestones and Deliverables:</p> <ul style="list-style-type: none"> Building design was completed in April 2001. Model will be constructed by September 2001. Testing will be completed by November 2001. Analysis of test results will be completed by May 2002. Proposed updates to FEMA 273/356 will be submitted by August 2002. 	<p>Project Personnel:</p> <p>Pt Steve Sweeney Co-Pt Dan Abrams, Jack Hayes Graduate RAs: S. Orton, S. Moses Undergraduates: External Collaborators: US Army Engineer Research and Development Center</p>
<p>Project Scope:</p> <ul style="list-style-type: none"> A single half-scale URM model will be built and tested on the US Army ERDC shake table to represent the full scale structure tested under ST11. <p>Project Plan:</p> <ul style="list-style-type: none"> Strength, stiffness, and deformation capacities of URM walls and piers are evaluated through a series of tests of increasing magnitude (level of shaking). As limits are approached for building elements, they will be retrofitted to mitigate deficiencies and testing will continue. Mechanisms for non-rehabilitated test specimens are examined with respect to rocking, toe crushing, bed-joint sliding and diagonal tension. Flexural mechanisms are examined for piers rehabilitated with FRP strips. Diaphragm behavior will be studied with respect to stiffness and wall connectivity. Effectiveness of stiffening, damping, and anchorage to walls will be evaluated. 	<p>Project Methodology:</p> <ul style="list-style-type: none"> The half scale model will be based on the full scale model tested at Georgia Tech in ST11. Masonry units: 1-1/8 inch x 3-3/4 inch x 1-3/4 inch will be placed with nominal 1/4 inch mortar joints using standard type O mortar. The model will include one interior wood partition wall, and the roof and floor diaphragm will be 1 x 3 decking nailed perpendicular to the joists. Joists will initially be supported in beam pockets without positive attachment to wall. The unreinforced model will first be tested using white noise and sine sweep to characterize fundamental frequencies and elastic response. The model will then be subjected to simulated earthquakes of increasing magnitude both uni-axially and bi-axially. Response will be closely monitored to determine when the limits of walls or diaphragms are being approached. Incremental strengthening will be conducted as limits are approached, white noise and sine sweep tests will be repeated, and testing will continue until the objectives have been achieved.

Research Program: Building Owners Research Project Title: Performance of Rehabilitated URM Building Systems NBAE Project Number: ST-22	
<p>Co-Dependency with Other NBAE Center projects:</p> <ul style="list-style-type: none"> Computational models of building response developed in Project ST5. Rehabilitation methods explored in ST6 are used as a basis for selection of strengthening methods. Ground motions developed in RE2 will be used for testing. Results from ST8 on the behavior and strengthening of building diaphragms. Results will be compared to full-scale static test (ST11). It is also expected that non-structural walls will be added to the interior of the model and subjected to earthquake simulations, in support of ST-9. <p>Performance Objectives for Essential Facilities. Both as-built and rehabilitated wall sections will be tested in support of ST-9.</p> <p>How project differs from similar work done elsewhere:</p> <ul style="list-style-type: none"> This project builds on the work from several other projects. The most significant difference is the use of dynamic loading on the US Army ERDC shaking table. It will provide information on the dynamic response of components and full scale models tested in other projects, and provide information on the total system response. 	<p>Relevant Publication:</p> <ol style="list-style-type: none"> Ottom, S.L., Abrams, D.P., Hayes, J., "Performance of Rehabilitated Unreinforced Masonry Systems," Proceedings of Ninth Canadian Masonry Symposium, University of New Brunswick, June 2001.
<p>Potential Impact of Project:</p> <ul style="list-style-type: none"> Research results will have an impact on future updates of national guidelines for seismic rehabilitation (FEMA 273/356). New information from research will enhance future rehabilitation of URM buildings by taking a system total building approach and by studying the effect of incremental strengthening on building response. URM is the most prominent construction type for existing buildings owned by the Department of the Army that require mitigation. Verify analytical models developed through component tests Verify standard code and simplified analysis tools for calculating behavior of existing and rehabilitated URM buildings Determine system response at different levels of deformation (performance-based design) Assess diaphragm and diaphragm-wall connection behavior Assess effectiveness of proposed rehabilitation schemes (FRP, prestressing) Correlate static and dynamic testing results and full-scale vs. half-scale modeling techniques 	

APPENDIX B

DETERMINATION OF TYPE K' MORTAR

A first series of tests were conducted using a Type N mortar according to ASTM E519-00 (ASTM 2000) with the exception that the specimens tested were 2 ft by 2 ft as opposed to the specified 4 ft by 4 ft. This modification was made as a result of the difficulties inherent in testing a large 4 ft by 4 ft masonry panel. This mix consisted of a one to three ratio of bagged Type N masonry cement to sand. A total of 16 specimens were tested including 8 constructed of solid bricks and 8 constructed of cored brick. Table B.1 shows a summary of the results of this series of tests.

Table B.1. Summary of diagonal compression test results (Type N)

Type of Brick	Specimen Number	Mean Shear Strength (psi)	Standard Deviation	Coefficient of Variation
Solid	8	123	63	0.51
Cored	7	88	30	0.35

The tests resulted in the failures in the mortar. No cracking of the bricks was observed. While a good deal of scatter was expected, the large coefficient of variation associated with this series of tests is troublesome. Furthermore, the Type N mortar cubes tested gave a compressive strength of only 360 psi, which is far below the expected 750 psi compressive strength for a typical Type N mortar. It was concluded that the

exceptionally high coefficient of variation along with the poor mortar compressive strength was most likely due to the use of a commercial bagged masonry cement.

As a result, a second series of tests employed a Type O mortar, which was comprised of a Portland cement to lime to sand ratio of 1:2:9. A total of 10 specimens were tested including 5 constructed of cored brick and 5 constructed of solid brick. The results of this series of tests are shown in Table B.2.

Table B.2. Summary of diagonal compression test results (Type O)

Type of Brick	Specimen Number	Mean Shear Strength (psi)	Standard Deviation	Coefficient of Variation
Solid	5	284	41	0.14
Cored	6	154	36	0.23

The coefficient of variation is much lower for this Type O mortar, and the shear strength increased. More important than the apparent increase in shear strength is the fact that this Type O mortar caused cracks to go through the bricks in some cases (Figure B.1). Based on field studies it seems that this failure mode is not consistent with existing URM structures in Mid-America. That is, if the ST-11 test structure were constructed with this Type O mortar a “strong brick-weak mortar” behavior would not be guaranteed. In addition, the compressive strength of the Type O mortar cubes was found to be 517 psi, which is considerably higher than the expected 350 psi compressive strength for a typical Type O mortar.



Figure B.1. Photograph of shear failure through brick

As a result, a third series of tests were conducted aimed at obtaining a mortar mix that would cause a “strong brick-weak mortar” behavior. To accomplish this, the amount of Portland cement was varied while keeping the amount of sand and lime constant. The three mortars mixes that were tested were in ratios of 0.25: 2: 9, 0.5: 2: 9 and 1: 2: 9 (Portland cement: lime: sand). In all nine specimens were tested, three of each type of mortar (one solid and two cored). To speed up the test schedule, the direct shear test discussed in Chapter 3 was used instead of the diagonal compression test. Table B.3 gives a summary of the results.

The 0.25: 2: 9 mortar was first eliminated from consideration because of the difficult in handling the specimens (it was easy to fail the test specimens during installation) and exceptionally large scatter in the data (i.e. coefficient of variation of 0.77). The Type O mortar was also eliminated because it was still too strong as shown by the previous diagonal compression test. In the end, the 0.5: 2: 9 mortar was chosen for construction because it gave a reasonable bed joint shear strength. In addition, the

compressive strength of this mortar cubes was found to be 41 psi, which is close to the value for Type K mortar used before 1950. Since this mortar mixture is close to that specified for Type K mortar (Portland cement: lime: sand ratio of 0.25: 2: 7.5), this mortar is designated as a Type K' mortar.

Table B.3. Summary of direct shear tests

Type of Brick	Mortar (Portland cement:lime:sand)	Specimen Number	Shear Strength (psi)	Standard Deviation
Cored	0.25:2:9	3	22	17
Solid	0.25:2:9	1	22	-
Cored	0.5:2:9	3	53	16.5
Solid	0.5:2:9	1	60	-
Cored	1:2:9 (Type O)	3	87	12
Solid	1:2:9 (Type O)	1	118	-

APPENDIX C

DESIGN OF FOUNDATION SLABS

The reinforced concrete (RC) foundation blocks for the ST-11 building were designed to transfer the base shear from the structure to the strong floor and to anchor the post-tensioning tendons used for retrofit.

The design of this foundation is shown in Figures C.1 and C.2. This foundation was composed of six individual RC slabs in order to allow them to be easily moved by the overhead cranes in the laboratory. The dimensions and weight of each RC slab are listed in Table C.1. The thickness of the foundation slabs is 20 in., which ensures sufficient development length for the post-tensioning anchor bolts to be used for retrofit. The slabs were cast with groups of four holes spaced at 4 ft on center in order to allow the foundation to be post-tensioned to the strong floor, which contains the same pattern of tie downs.

Table C.1 Dimensions and weights of the RC slabs

Slab	Dimension (in x in x in)	Volume (in ³)	Weight (lb)
1	222 x 66 x 20	293040	25438 (11.4 ton)
2	222 x 66 x 20	293040	25438 (11.4 ton)
A-1	177 x 66 x 20	233640	20282 (9.06 ton)
A-2	177 x 66 x 20	233640	20282 (9.06 ton)
B-1	177 x 66 x 20	233640	20282 (9.06 ton)
B-2	177 x 66 x 20	233640	20282 (9.06 ton)
Total		1520640	132001 (59.1 ton)

The RC slabs were designed in accordance with the minimum reinforcement requirement of ACI318-95 (ACI, 1995). The governing loading case was due to the self-weight of the concrete when the crane was lifting the slab.

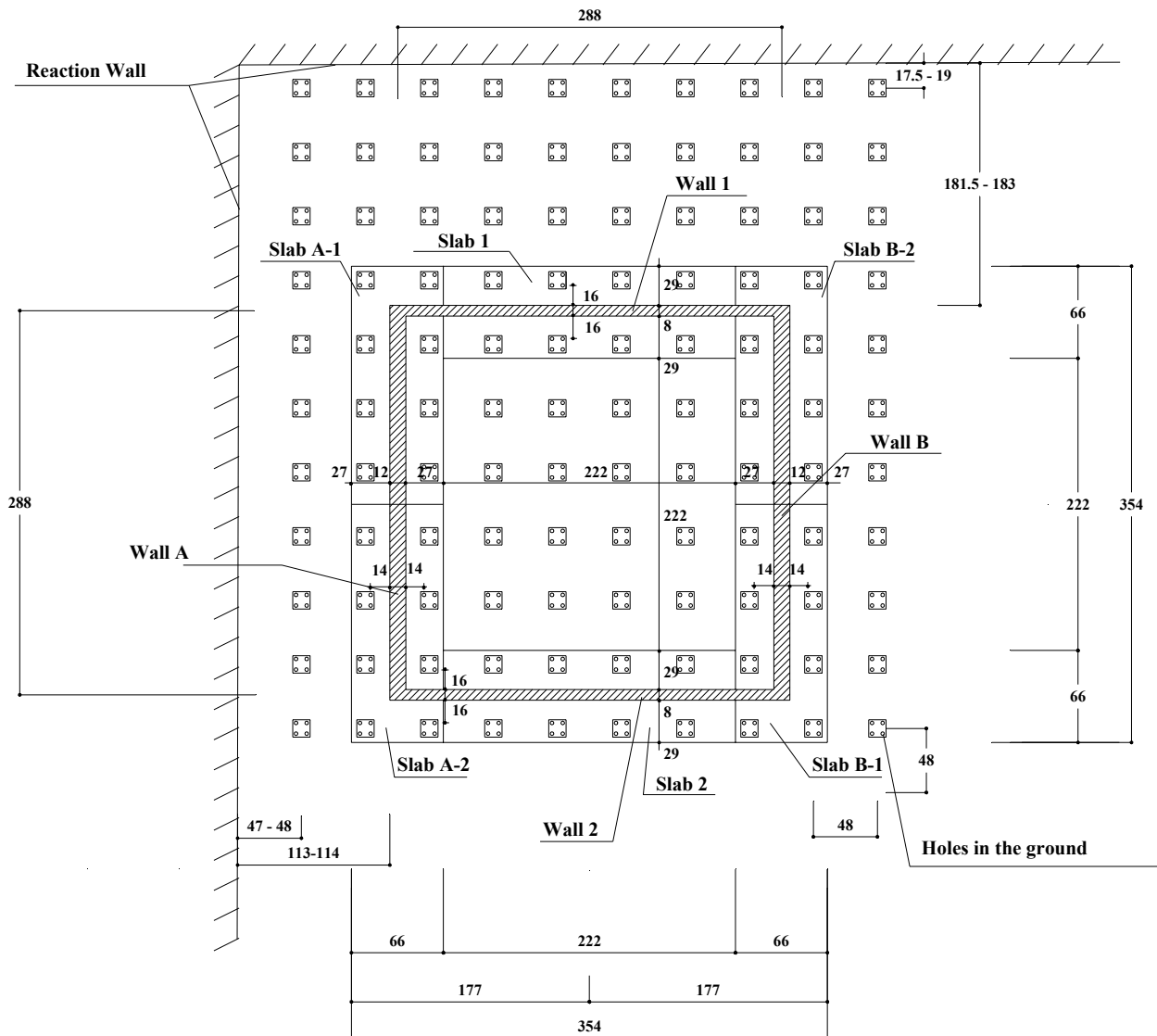
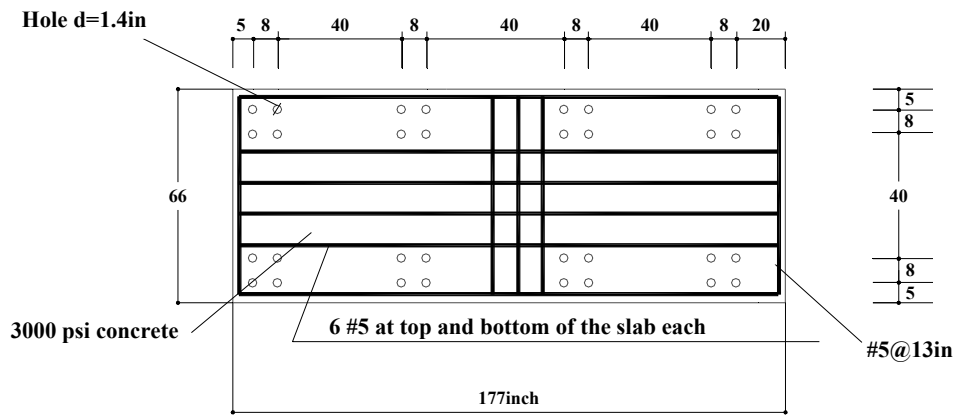
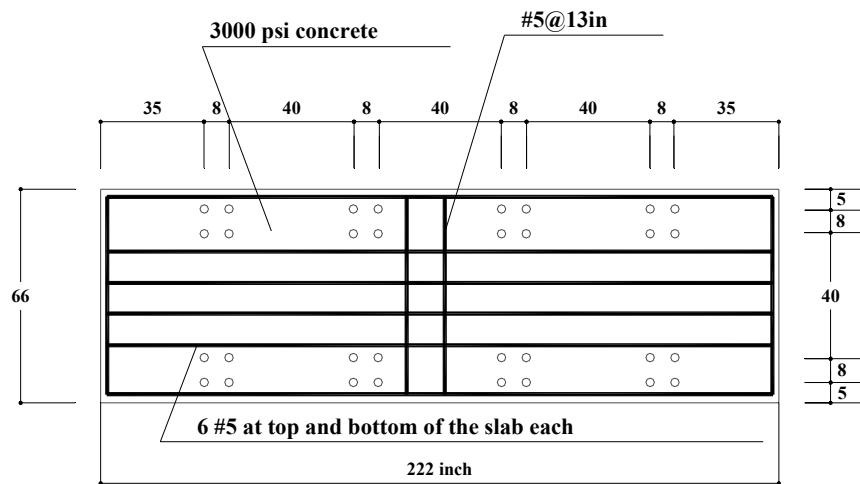


Figure C.1. Plan view of foundation layout (dimensions are in inches)



Slab A-1, A-2, B-1, B-2



Slab 1,2

Figure C.2. Reinforcement details of the foundation slabs (dimensions are in inches)

APPENDIX D

LINEAR STATIC DESIGN PROCEDURE FOR THE TEST STRUCTURE

D.1 Introduction

A Linear Static Procedure (LSP) is permitted for buildings without irregularities in plan and elevations. The test building satisfies the requirements for the use of LSP as listed in FEMA 356 2.4.1 (ATC 2000). As a result, a LSP with the following assumptions was used to analyze the test structure:

- All the piers are considered as primary elements in the structure.
- The test building can be analyzed using a 2D model since it has a flexible diaphragm (FEMA 356 3.2.2.1). Although FEMA 356 requires that the three dimensional features of components and elements shall be considered when calculating stiffness and strength properties, no detailed provisions are given in FEMA 356. Therefore, the flange effects were not considered in the analysis.
- Torsion need not be considered in buildings with flexible diaphragms.
- Since the structure was very stiff, P- Δ effects were not considered.
- Overturning effects were not considered.

Based on FEMA 356 provisions, two different earthquake hazard levels were considered in the analyses:

- BSE-1: 10% /50 year
- BES-2: 2% /50 year

D.2. Seismic hazard and pseudo seismic lateral load

The seismic hazard and the corresponding seismic lateral loads for the test structure were determined as follows.

D.2.1 Model characteristics

The following characteristics were assumed in the analyses of the test structure:

- Site class: B
- 5% effective viscous damping, $BS=B1=1.0$
- $C2: 1.0$ (FEMA 356 3.2.10.1)
- $C3: 1.0$ (FEMA 356 3.2.10.1)
- $C_m: 1.0$ (FEMA 356 3.2.10.1)
- Self weight W : 201 kips

D.2.2 Period estimation

Two methods were used to estimate the natural period of the test structure.

1) Method 1-Analytical

An eigenvalue (dynamic) analysis for the building was conducted based on a simple conceptual model (see Chapter 10). The fundamental natural period obtained for the test building was 0.22 seconds parallel to Walls A and B, and 0.21 seconds parallel to Walls 1 and 2.

2) Method 2-Approximate

FEMA 356 Eq. (3-9) is based on the deformation and the associated vibration period of a flexible diaphragm structure. If the lateral stiffness of diaphragm is assumed

to be 14 kips/in, and the weight of diaphragm is assumed to be 16 kips, the fundamental natural period of the test building can be calculated as:

$$T = (0.078 \cdot 16 / 14)^{0.5} = 0.3$$

A value of 0.3 seconds was chosen for the natural period of the test building, since it was close to the values obtained for the flexible diaphragm case of the conceptual model. Note that in this case, the stiffness of the masonry wall is less than elastic value. This is consistent with the specification of FEMA 356, which points out that instead of elastic stiffness, the secant stiffness corresponding to the maximum strength should be chosen to model the structure for LSP (FEMA 356 3.3.1.1, ATC 2000).

D.2.3 Pseudo seismic lateral load (V)

The pseudo lateral load (V) can be calculated by:

$$V = C_1 \cdot C_2 \cdot C_3 \cdot C_m \cdot S_a \cdot W \quad (\text{FEMA 356 3-10})$$

The calculation procedure and the results obtained are listed in Tables D.1 and D.2 for the BSE-1 level and the BSE-2 level, respectively.

Table D.1. Seismic forces for the test structure at the BSE-1 level

	Atlanta	Memphis	St. Louis	San Francisco
S_s (g)	0.11	0.28	0.21	1.21
S_1 (g)	0.04	0.07	0.056	0.58
F_a	1.0	1.0	1.0	1.0
F_v	1.0	1.0	1.0	1.0
$S_{XS} = F_a S_s$	0.11	0.28	0.21	1.21
$S_{X1} = F_v S_1$	0.04	0.07	0.056	0.58
Seismicity Zone (1.6.3.1)	Low	Moderate	Moderate	High
$T_s = (S_{X1} B_s / S_{XS} B_1)$	0.364	0.25	0.27	0.48
T_0	0.0728	0.05	0.054	0.096

Table D.1 (cont')

S _a (g)	0.11	0.233	0.187	1.21
C1	1.12	1.0	1.0	1.24
Pseudo lateral load V Kips (3.10)	24.8	46.8	37.6	301.6
Vertical force distribution (P2/P1)	1/2	1/2	1/2	1/2

* S_s and S₁ for BSE-1 should be less than 2/3 of the corresponding values of BSE-2.

Table D.2. Seismic forces for the test structure at the BSE-2 level

	Atlanta	Memphis	St. Louis	San Francisco
S _s (g)	0.26	1.3	0.6	1.81
S ₁ (g)	0.11	0.4	0.19	1.0
F _a	1.0	1.0	1.0	1.0
F _v	1.0	1.0	1.0	1.0
S _{XS} =F _a S _s	0.26	1.3	0.6	1.81
S _{X1} =F _v S ₁	0.11	0.4	0.19	1.0
Seismicity Zone (1.6.3.1)	Low	Moderate	Moderate	High
T _s =(S _{X1} B _s /S _{XS} B ₁)	0.423	0.31	0.32	0.553
T ₀ =0.2 T _a	0.0846	0.062	0.064	0.111
S _a (g) (Fig. 1-1)	0.26	1.3	0.6	1.81
C1 (3.3.1.3.1)	1.19	1.02	1.05	1.28
Pseudo lateral load V Kips (3.10)	62.2	266.5	126.6	465.7
Vertical force distribution (P2/P1)(3.3.1.3.5)	1/2	1/2	1/2	1/2

D.2.4 Design earthquake actions for each component (Q_E)

Four basic components, Walls 1, 2, A and B were identified for the test structure. Walls A and B were identical to each other. Since the test URM building had flexible diaphragms, the external lateral seismic force was distributed to each wall based on their tributary loads (see FEMA 356 3.3.1.3.5). Therefore, the design earthquake actions (Q_E)

for each component can be calculated as shown in Tables D.3 and D.4 for the BSE-1 level and the BSE-2 level, respectively.

Table D.3. Design earthquake actions Q_E for each wall at the BSE-1 level (in kips)

	Atlanta	Memphis	St. Louis	San Francisco
Wall A/B	12.4	23.4	18.8	150.8
Wall 1	12.4	23.4	18.8	150.8
Wall 2	12.4	23.4	18.8	150.8

Table D.4. Design earthquake actions Q_E for each wall at the BSE-2 level (in kips)

	Atlanta	Memphis	St. Louis	San Francisco
Wall A/B	31.1	133.3	63.3	232.9
Wall 1	31.1	133.3	63.3	232.9
Wall 2	31.1	133.3	63.3	232.9

D.3. Elastic strength and controlling mode of the test structure

An elastic model composed of rigid spandrels and elastic piers, as shown in Figure D.1 modeled each wall.

The strength of each wall was governed by the strength of the piers. The possible failure modes for each pier include rocking, sliding, toe crushing and diagonal tension. The first two failure modes are deformation-controlled failure modes, while the latter two failure modes are force-controlled failure modes. Based on FEMA 356 Eqs. (7.3) to (7.6), the strength of the pier corresponding to each failure mode can be calculated. The actual strength and the failure mode of each pier were dominated by the lowest value of the four failure modes. On the other hand, it was assumed that the external lateral force applied on

the wall was distributed to each pier proportionally to the lateral stiffness of each pier. Therefore, the wall was assumed to reach its maximum strength when one of the piers of this perforated wall reaches its maximum strength. Furthermore, the controlling mode for the entire wall was also determined by the failure mode of that pier.

The analysis assumed that the ratio of the lateral forces applied on the roof and the second floor is 1 to 2 (see FEMA 356 3.3.1.3.5). The material properties used in the analysis was based on the material test results and can be found in Table 6.3. The results obtained for each wall are shown in Table D.5.

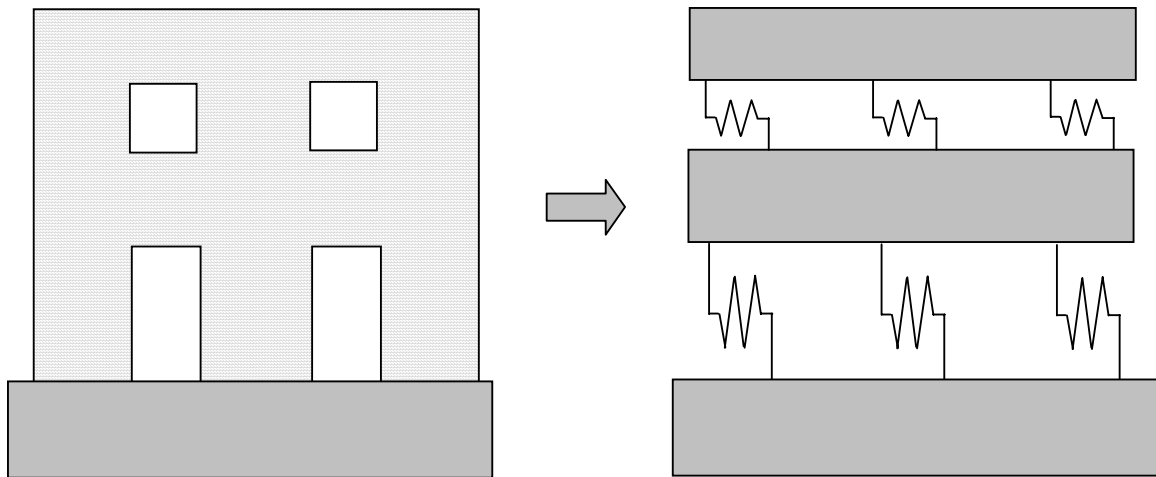


Figure D.1. Analytical model for the URM wall

Table D.5. The maximum strengths and the corresponding failure modes for each wall

Wall ID	Maximum base shear (kips)	Controlling component and failure modes
Walls A and B	$Q_{CL} = 33$	A-7/B-10, Toe Crushing
Wall 1	$Q_{CE} = 41$	1-7, Rocking
Wall 2	$Q_{CE} = 9.6$	2-7, Rocking

D.4. Acceptance Criteria

Table D.5 shows that Walls A and B are force-controlled, while Walls 1 and 2 is deformation-controlled. Based on Tables D.3 and D.4, and the following equations, the design actions for each wall can be calculated.

For deformation-controlled actions:

$$Q_{UD} = Q_G \pm Q_E \quad (\text{FEMA 356 3-18})$$

For force-controlled actions:

$$Q_{UF} = Q_G \pm \frac{Q_E}{C_1 C_2 C_3 J} \quad (\text{FEMA 356 3-19})$$

Note that the action due to design gravity loads Q_G in the above equations can be assumed as zero, since gravity load does not cause lateral shear force. The factors C_1 , C_2 , C_3 and the force-delivery reduction factor J are determined based on the building location and its seismic level, as well as the target performance level. The factors employed in the analyses are listed in Table D.6.

Table D.6. Factors for determining the design actions of the test structure

	Atlanta	Memphis	St. Louis	San Francisco
C1 (BSE-1)	1.12	1.0	1.0	1.24
C1 (BSE-2)	1.19	1.02	1.05	1.28
C2	1.0	1.0	1.0	1.0
C3	1.0	1.0	1.0	1.0
J (OP, IO)	1.0	1.0	1.0	1.0
J (LS, CP)	1.0	1.5	1.5	2.0

Using the parameters listed in Table D.6, the design actions Q_{UD} or Q_{UF} for each wall can be calculated as listed in Tables D.7 and D.8 for BSE-1 level and BSE-2 level, respectively.

Table D.7. Design actions for each wall at BSE-1 level (in kips)

	Atlanta	Memphis	St. Louis	San Francisco
Walls A and B(Q_{UF}) (LS, CP)	11.1	15.6	12.5	60.8
Walls A and B(Q_{UF}) (OP, IO)	11.1	23.4	18.8	121.6
Wall 1 (Q_{UD})	12.4	23.4	18.8	150.8
Wall 2 (Q_{UD})	12.4	23.4	18.8	150.8

Table D.8. Design actions for each wall at BSE-2 level (in kips)

	Atlanta	Memphis	St. Louis	San Francisco
Walls A and B(Q_{UF}) (LS, CP)	26.1	87.1	40.2	91.0
Walls A and B(Q_{UF}) (OP, IO)	26.1	130.7	60.3	182.0
Wall 1 (Q_{UD})	31.1	133.3	63.3	232.9
Wall 2 (Q_{UD})	31.1	133.3	63.3	232.9

The acceptance criteria of each component can be checked by:

For deformation-controlled actions:

$$mkQ_{CE} \geq Q_{UD} \quad (\text{FEMA 356 3-20})$$

For force-controlled actions:

$$kQ_{CL} \geq Q_{UF} \quad (\text{FEMA 356 3-21})$$

Note that based on Table 2-1 of FEMA 356, the knowledge factor k is equal to 1.0. The component demand modifier for the deformation-controlled action, m , is determined by the building's performance levels and failure modes, and can be calculated based on Table 7-3 of FEMA 356. The results for Walls 1 and 2 are listed in Table D.9:

Table D.9. m factor for Wall 2

	OP	IO	LS	CP
Wall 1	1	2.6	5.2	6.9
Wall 2	1	3	6	8

Based on Tables D.5, D.7, D.8, and D.9, the performance level of each wall can be estimated as follows:

Table D.10. Performance level of each wall (BSE-1)

	Atlanta	Memphis	St. Louis	San Francisco
Walls A and B	OP	OP	OP	N.A.
Wall 1	OP	OP	OP	LS
Wall 2	IO	IO	IO	N.A.

Table D.11. Performance level of each wall (BSE-2)

	Atlanta	Memphis	St. Louis	San Francisco
Walls A and B	OP	N.A.	N.A.	N.A.
Wall 1	OP	LS	IO	CP
Wall 2	LS	N.A.	CP	N.A.

D.5. Evaluation based on experimental observation

The evaluation of the test structure was conducted again based on the strength and failure modes observed during the experiment. Since URM is a brittle material, it is assumed that the ultimate strength obtained from the test can be used as the design elastic strength of the test building. The related data is shown in Table D.12. It is apparent that the responses of all the four walls are deformation-controlled actions.

Table D.12. The observed maximum strengths and failure modes for each wall

Wall ID	Maximum Base Shear (Kips)	Controlling Component and Failure Modes
Walls A and B	$Q_{CE} = 40$	Rocking
Wall 1	$Q_{CE} = 58$	Rocking
Wall 2	$Q_{CE} = 25$	Rocking

Therefore, the design actions Q_{UD} for each wall can be calculated as shown in Tables D.13 and D.14 for the BSE-1 level and the BSE-2 level, respectively. The m factors for each wall are listed in Table D.15.

Table D.13. Design actions for each wall at the BSE-1 level (based on test, in kips)

	Atlanta	Memphis	St. Louis	San Francisco
Walls A and B(Q_{UD})	12.4	23.4	18.8	150.8
Wall 1 (Q_{UD})	12.4	23.4	18.8	150.8
Wall 2 (Q_{UD})	12.4	23.4	18.8	150.8

Table D.14. Design actions for each wall at the BSE-2 level (based on test, in kips)

	Atlanta	Memphis	St. Louis	San Francisco
Walls A and B(Q_{UD})	31.3	133.3	63.3	232.9
Wall 1 (Q_{UD})	31.3	133.3	63.3	232.9
Wall 2 (Q_{UD})	31.3	133.3	63.3	232.9

Table D.15. m factor for each wall

	OP	IO	LS	CP
Wall 2	1	3	6	8
Wall 1*	1	1.4	2.8	3.7
Wall AB	1	2.6	5.2	6.9

* Global rocking, use the height and the length of the entire wall to calculate the value of the factor m.

Based on Tables D.12, D.13, D.14, and D.15, the performance level for each wall can be estimated as listed in Tables D.16 and D.17 for the BSE-1 level and BSE-2 level, respectively.

Table D.16. Performance level of each wall (based on test, BSE-1)

	Atlanta	Memphis	St. Louis	San Francisco
Walls A and B	OP	OP	OP	LS
Wall 1	OP	OP	OP	LS
Wall 2	OP	OP	OP	LS

Table D.17. Performance level of each wall (based on test, BSE-2)

	Atlanta	Memphis	St. Louis	San Francisco
Walls A and B	OP	LS	IO	CP
Wall 1	OP	LS	IO	N.A.
Wall 2	IO	LS	IO	N.A.

APPENDIX E

NOLINEAR STATIC DESIGN PROCEDURE FOR THE TEST STRUCTURE

E.1 Introduction

The Nonlinear Static Procedure (NSP) uses simplified nonlinear techniques to estimate the deformation of a structure under lateral forces, including seismic loads. In order to use this procedure, the higher order modes of the structure should not have significant effects on its response (FEMA 356 2.4.1, ATC 2000). The URM building tested satisfies this requirement. Therefore, NSP was used to analyze the test structure. Similar assumptions as those used for LSP were used for NSP. Again, two different earthquake hazard levels, including BSE-1 and BSE-2, were considered in the analysis.

E.2. Seismic hazard and target displacement

The seismic hazard and the corresponding target displacements for the test structure were determined as follows.

E.2.1 Model characteristics

The following characteristics were assumed in the analyses of the test structure:

- Site class: B
- 5% effective viscous damping, $BS=B1=1.0$
- W : 201 kips

In addition, similar to the LSP, a fundamental period of 0.3 seconds was assumed for the test structure.

E.2.2. Target Displacements

The target displacements for the test structure can be calculated by:

$$\delta_t = C_0 C_1 C_2 C_3 S_a \frac{T_e^2}{4\pi^2} g \quad (\text{FEMA 356 3-15})$$

where C_0 is given by FEMA 356 Table 3-2. For the tested two-story shear building, C_0 was assumed to be 1.5. The values of C_m , C_2 and C_3 were assumed to be 1.0. The same value as that used for LSP was used for C_1 herein, since V_y was unknown.

Based on the above equation, the target displacements for the test structure were calculated and are listed in Tables E.1 and E.2 for the BSE-1 and the BSE-2 levels, respectively.

Table E.1. Target displacements for the test structure at the BSE-1 level

	Atlanta	Memphis	St. Louis	San Francisco
S_s (g)	0.11	0.28	0.21	1.21
S_1 (g)	0.04	0.07	0.056	0.58
F_a	1.0	1.0	1.0	1.0
F_v	1.0	1.0	1.0	1.0
$S_{XS}=F_a S_s$	0.11	0.28	0.21	1.21
$S_{X1}=F_v S_1$	0.04	0.07	0.056	0.58
Seismicity Zone (1.6.3.1)	Low	Moderate	Moderate	High
$T_s=(S_{X1}B_s/S_{XS}B_1)$	0.364	0.25	0.27	0.48
T_0	0.0728	0.05	0.054	0.096
S_a (g)	0.11	0.233	0.187	1.21
C_1	1.12	1.0	1.0	1.24
δ_t (in)	0.16	0.31	0.25	1.98

* S_s and S_1 for BSE-1 should be less than 2/3 of the corresponding values of BSE-2.

* $1g = 386 \text{ in/s}^2$

Table E.2. Target displacements for the test structure at the BSE-2 level

	Atlanta	Memphis	St. Louis	San Francisco
S_s (g)	0.26	1.3	0.6	1.81
S_1 (g)	0.11	0.4	0.19	1.0
F_a	1.0	1.0	1.0	1.0
F_v	1.0	1.0	1.0	1.0
$S_{XS}=F_a S_s$	0.26	1.3	0.6	1.81
$S_{X1}=F_v S_1$	0.11	0.4	0.19	1.0
Seismicity Zone (1.6.3.1)	Low	Moderate	Moderate	High
$T_s=(S_{X1}B_s/S_{XS}B_1)$	0.423	0.31	0.32	0.553
$T_0=0.2 T_a$	0.0846	0.062	0.064	0.111
S_a (g) (Fig. 1-1)	0.26	1.3	0.6	1.81
C_1 (3.3.3.3.2)	1.19	1.02	1.05	1.28
δ_t (in)	0.41	1.75	0.83	3.06

E.3. Component design deformations

Since the test URM building features flexible roof and floor diaphragms, the four walls of the test structure, Walls 1, 2, A and B can be checked individually for their performance. A nonlinear model for a typical URM perforated wall is shown in Figure E.1. It is composed of rigid spandrels and nonlinear piers. The target displacement, δ_t , was applied at the top of the building. For the second floor lateral displacement, two types of displacement profiles, with the ratio (K) between the second floor displacement and the roof floor displacement equal to 1 or 0.5, were applied to each wall.

The design deformation for each pier is easy to obtain since the spandrel is assumed rigid and all the lateral displacement of the wall concentrates on the piers. The design displacements for each pier are listed in Tables E.3 through E.6 for the different K values and earthquake levels.

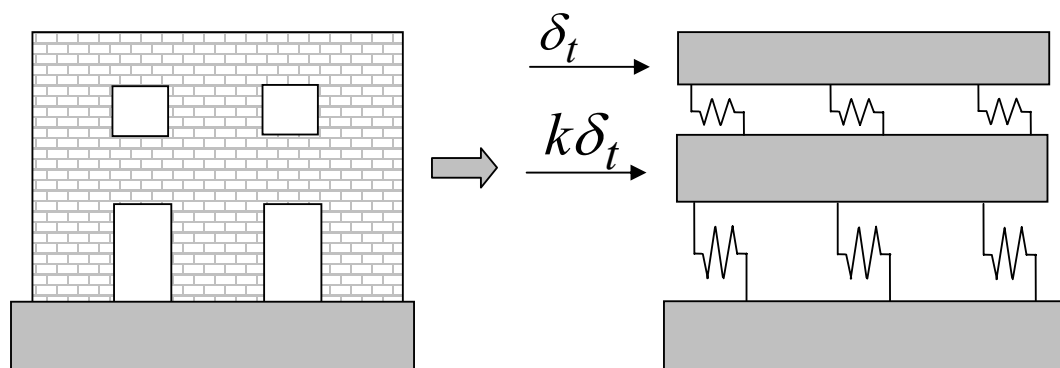


Figure E.1. Nonlinear pushover model for a perforated URM wall

Table E.3. Design displacements for each component (in.) (BSE-1 and K=1)

Pier	Atlanta	Memphis	St. Louis	San Francisco
A-2	0	0	0	0
A-3	0	0	0	0
A-4	0	0	0	0
A-5	0	0	0	0
A-7	0.16	0.31	0.25	1.98
A-8	0.16	0.31	0.25	1.98
A-9	0.16	0.31	0.25	1.98
A-10	0.16	0.31	0.25	1.98
1-2	0	0	0	0
1-3	0	0	0	0
1-4	0	0	0	0
1-6	0.16	0.31	0.25	1.98
1-7	0.16	0.31	0.25	1.98
2-2	0	0	0	0
2-3	0	0	0	0
2-4	0	0	0	0
2-5	0	0	0	0
2-7	0.16	0.31	0.25	1.98
2-8	0.16	0.31	0.25	1.98
2-9	0.16	0.31	0.25	1.98

* Wall B is not listed since it is identical to Wall A.

Table E.4. Design displacement for each component (in.) (BSE-1 and K=0.5)

Pier	Atlanta	Memphis	St. Louis	San Francisco
A-2	0.08	0.16	0.13	0.99
A-3	0.08	0.16	0.13	0.99
A-4	0.08	0.16	0.13	0.99
A-5	0.08	0.16	0.13	0.99
A-7	0.08	0.16	0.13	0.99
A-8	0.08	0.16	0.13	0.99
A-9	0.08	0.16	0.13	0.99
A-10	0.08	0.16	0.13	0.99
1-2	0.08	0.16	0.13	0.99
1-3	0.08	0.16	0.13	0.99
1-4	0.08	0.16	0.13	0.99
1-6	0.08	0.16	0.13	0.99
1-7	0.08	0.16	0.13	0.99
2-2	0.08	0.16	0.13	0.99
2-3	0.08	0.16	0.13	0.99
2-4	0.08	0.16	0.13	0.99
2-5	0.08	0.16	0.13	0.99
2-7	0.08	0.16	0.13	0.99
2-8	0.08	0.16	0.13	0.99
2-9	0.08	0.16	0.13	0.99

Table E.5. Design displacement for each component (in.) (BSE-2 and K=1)

Pier	Atlanta	Memphis	St. Louis	San Francisco
A-2	0	0	0	0
A-3	0	0	0	0
A-4	0	0	0	0
A-5	0	0	0	0
A-7	0.41	1.75	0.83	3.06
A-8	0.41	1.75	0.83	3.06
A-9	0.41	1.75	0.83	3.06
A-10	0.41	1.75	0.83	3.06
1-2	0	0	0	0
1-3	0	0	0	0
1-4	0	0	0	0
1-6	0.41	1.75	0.83	3.06
1-7	0.41	1.75	0.83	3.06
2-2	0	0	0	0
2-3	0	0	0	0
2-4	0	0	0	0

Table E.5 (cont')

2-5	0	0	0	0
2-7	0.41	1.75	0.83	3.06
2-8	0.41	1.75	0.83	3.06
2-9	0.41	1.75	0.83	3.06

Table E.6. Design displacements for each component (in.) (BSE-1 and K=0.5)

Pier	Atlanta	Memphis	St. Louis	San Francisco
A-2	0.22	0.88	0.42	1.53
A-3	0.22	0.88	0.42	1.53
A-4	0.22	0.88	0.42	1.53
A-5	0.22	0.88	0.42	1.53
A-7	0.22	0.88	0.42	1.53
A-8	0.22	0.88	0.42	1.53
A-9	0.22	0.88	0.42	1.53
A-10	0.22	0.88	0.42	1.53
1-2	0.22	0.88	0.42	1.53
1-3	0.22	0.88	0.42	1.53
1-4	0.22	0.88	0.42	1.53
1-6	0.22	0.88	0.42	1.53
1-7	0.22	0.88	0.42	1.53
2-2	0.22	0.88	0.42	1.53
2-3	0.22	0.88	0.42	1.53
2-4	0.22	0.88	0.42	1.53
2-5	0.22	0.88	0.42	1.53
2-7	0.22	0.88	0.42	1.53
2-8	0.22	0.88	0.42	1.53
2-9	0.22	0.88	0.42	1.53

Based on previous research, it is well known that the nonlinear response of a low-rise URM building is controlled by its first story piers. For the first story piers, the lateral displacement profile with $K = 1$ gives the worst case scenario. In this case, the design lateral deformations of the controlling components of the test structure are listed in terms of drift in Tables E.7 and E.8 for the BSE-1 and the BSE-2 levels, respectively.

Table E.7. Design displacement drift for each component (%) (BSE-1)

Pier	Atlanta	Memphis	St. Louis	San Francisco
A-7	0.19	0.37	0.30	2.36
A-8	0.34	0.65	0.52	4.15
A-9	0.34	0.65	0.52	4.15
A-10	0.34	0.65	0.52	4.15
1-6	0.19	0.37	0.30	2.36
1-7	0.19	0.37	0.30	2.36
2-7	0.17	0.33	0.27	2.11
2-8	0.17	0.33	0.27	2.11
2-9	0.17	0.33	0.27	2.11

* Wall B is not listed since it is identical to Wall A.

Table E.8. Design displacement drift for each component (%) (BSE-2)

Pier	Atlanta	Memphis	St. Louis	San Francisco
A-7	0.49	2.09	0.99	3.65
A-8	0.86	3.67	1.74	6.42
A-9	0.86	3.67	1.74	6.42
A-10	0.86	3.67	1.74	6.42
1-6	0.49	2.09	0.99	3.65
1-7	0.49	2.09	0.99	3.65
2-7	0.44	1.86	0.88	3.26
2-8	0.44	1.86	0.88	3.26
2-9	0.44	1.86	0.88	3.26

E.4. Force-deformation relationship for each component

Based on FEMA 356, a deformation-controlled pier and a force-controlled pier exhibit different generalized force-deformation relationships. They are shown in Figure E.2.

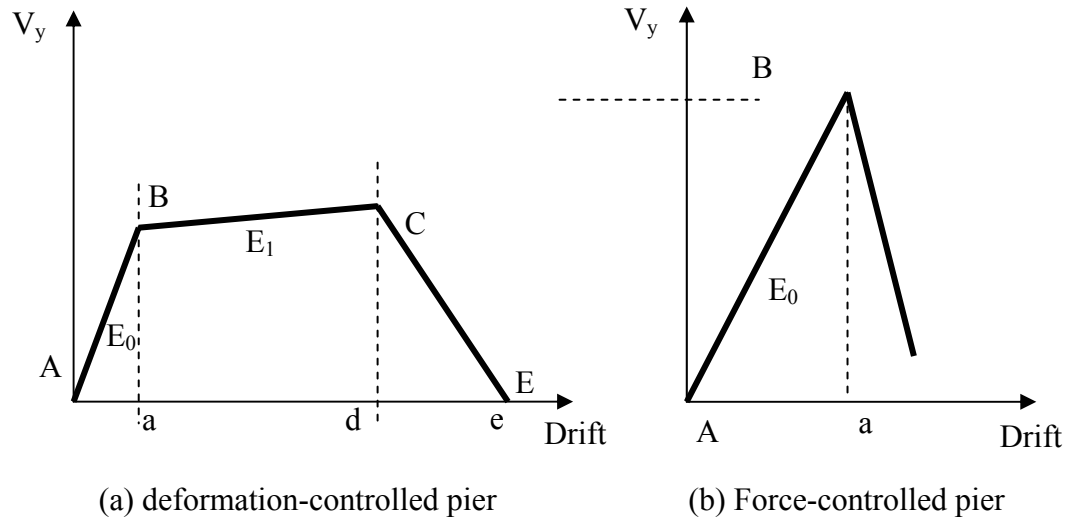


Figure E.2. Force-displacement relationship for a URM pier

Figure E.2 (a) is based on a small modification of Fig. 7-1 of FEMA 356 for the following reasons. First, FEMA 356 does not identify the value of point D in Fig. 7-1. Therefore, a linear relation instead of a bilinear relation is used between Point C and Point E herein. Second, FEMA gives a very small value for the strength corresponding to Point E. To make the analysis simple, a zero strength is assumed for Point E in the current analysis. Figure E.2 (b) is used for a force-controlled component. No slope is identified in FEMA 356 for the portion after the peak point. Therefore, it is assumed that the pier will rapidly lose its strength as soon as its lateral deformation passes Point B.

The maximum strength and failure mode for each pier were calculated based on FEMA equations. The force-deformation relationships obtained for all the first story piers are listed in Table E.9.

Table E.9. Force-deformation relationships for all the first-story piers

Wall	Pier	Failure mode	V_y (kips)	EI (kips/in)	a (%)	d (%)	e (%)	IO (%)	LS (%)	CP (%)
A B	A-7	Rocking	6.81	0	0.011	0.7	1.4	0.1	0.53	0.7
	A-8	Toe Crushing	8.58	-	0.012	-	-	-	-	-
	A-9	Toe Crushing	8.91	-	0.012	-	-	-	-	-
	A-10	Toe Crushing	11.00	-	0.011	-	-	-	-	-
1	1-6	Sliding	52.57	0	0.014	0.4	0.8	0.1	0.3	0.4
	1-7	Rocking	4.33	0	0.011	0.7	1.4	0.1	0.53	0.7
2	2-7	Rocking	4.42	0	0.013	0.8	1.6	0.1	0.6	0.8
	2-8	Rocking	1.57	0	0.026	1.6	3.2	0.1	1.2	1.6
	2-9	Rocking	5.10	0	0.015	0.8	1.6	0.1	0.6	0.8

E.5. Acceptance criteria

The acceptance criteria for the performance of the test structure gave a particular probabilistic seismic hazard can be checked according to the following rules:

1) In the case of primary and secondary components with deformation-controlled actions, the components shall have expected deformation capacities not less than maximum deformation demands calculated at the target displacement.

2) In the case of primary and secondary components with deformation-controlled actions, the base shear at the target displacement, V_t , shall not be less than 80% of the effective yield strength of the structure, V_y .

3) In the case of primary and secondary components with force-controlled actions, primary and secondary components shall have lower bound strengths not less than the maximum design forces.

The acceptance criteria obtained for each pier in the test structure are listed in Tables E.10 and E.11 for the BSE-1 and BSE-2 levels, respectively.

Table E.10. Performance of each component (BSE-1)

Wall	Pier	Atlanta	Memphis	St. Louis	San Francisco
A, B	A-7	LS	LS	LS	NA
	A-8	NA	NA	NA	NA
	A-9	NA	NA	NA	NA
	A-10	NA	NA	NA	NA
1	1-6	LS	LS	LS	NA
	1-7	LS	LS	LS	NA
2	2-7	LS	LS	LS	NA
	2-8	LS	LS	LS	NA
	2-9	LS	LS	LS	NA

* Wall B is not listed since it is identical to Wall A.

Table E.11. Performance of each component (BSE-2)

Pier	Atlanta	Memphis	St. Louis	San Francisco
A-7	LS	NA	NA	NA
A-8	NA	NA	NA	NA
A-9	NA	NA	NA	NA
A-10	NA	NA	NA	NA
1-6	NA	NA	NA	NA
1-7	LS	NA	NA	NA
2-7	LS	NA	NA	NA
2-8	LS	NA	CP	NA
2-9	LS	NA	NA	NA

* Wall B is not listed since it is identical to Wall A.

APPENDIX F

F.1. Wall 2 in the push direction and the pull direction

The observed kinematic movement of Wall 2 when loaded from left to right (in the push direction) is illustrated in Figure F.1. The three first story piers rocked about their individual right toes, while the entire second floor wall was lifted and pushed to the right due to the movement of the first story piers.

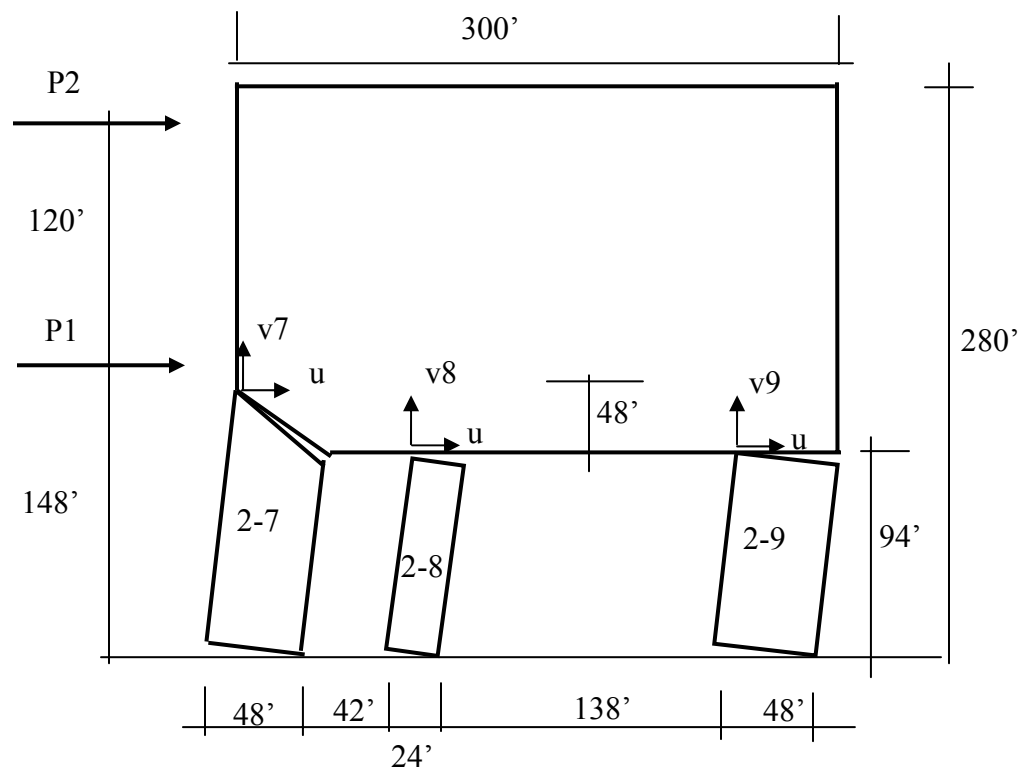


Figure F.1. Kinematic movement of Wall 2 when loaded in the push direction

Assuming the three first story piers exhibit the same lateral displacement, u , at the top of the piers, the vertical movements at the tops of the piers can be calculated as:

$$v_7 = 48u/142 = 0.338u, \quad v_8 = 24u/94 = 0.255u, \quad v_9 = 48u/94 = 0.511u \quad (F.1)$$

Apparently, since v_8 is less than v_7 and v_9 , Pier 2-8 is actually separated from the spandrel and left behind. It has no contribution to the lateral resistance of the wall. As a result, the internal force distribution of Wall 2 can be assumed as shown in Figure F.2. The following equations can be used to describe the equilibrium of the three rigid bodies:

$$\begin{aligned} 48 \cdot F_7 + 48 \cdot W_7^f + 24 \cdot W_7 &= 142 \cdot P_7 \\ 48F_9 + 24W_9 &= 94P_9 \\ P_7 + P_9 &= P_1 + P_2 \\ F_7 + F_9 &= W_1 + W_2 + W_3 \\ 252F_7 + 54P_1 + 174P_2 + 48W_3 &= 48P_7 + 252W_2 + 102W_1 \end{aligned} \quad (F.2)$$

The weight of each component, including the flange weight W_2 , W_3 , W_7^f , and W_9^f (the superscript indicates the flange portions), can be calculated based on the crack pattern observed in the test and the rules specified in Chapter 9. The results are listed in Table F.1.

Table F.1. Weight used in the right body analysis for Wall 2 (push direction)

	W1	W2	W3	W7	W9	W7 ^f
Weight (kips)	25.43	7.93	14.41	3.05	2.43	5.68

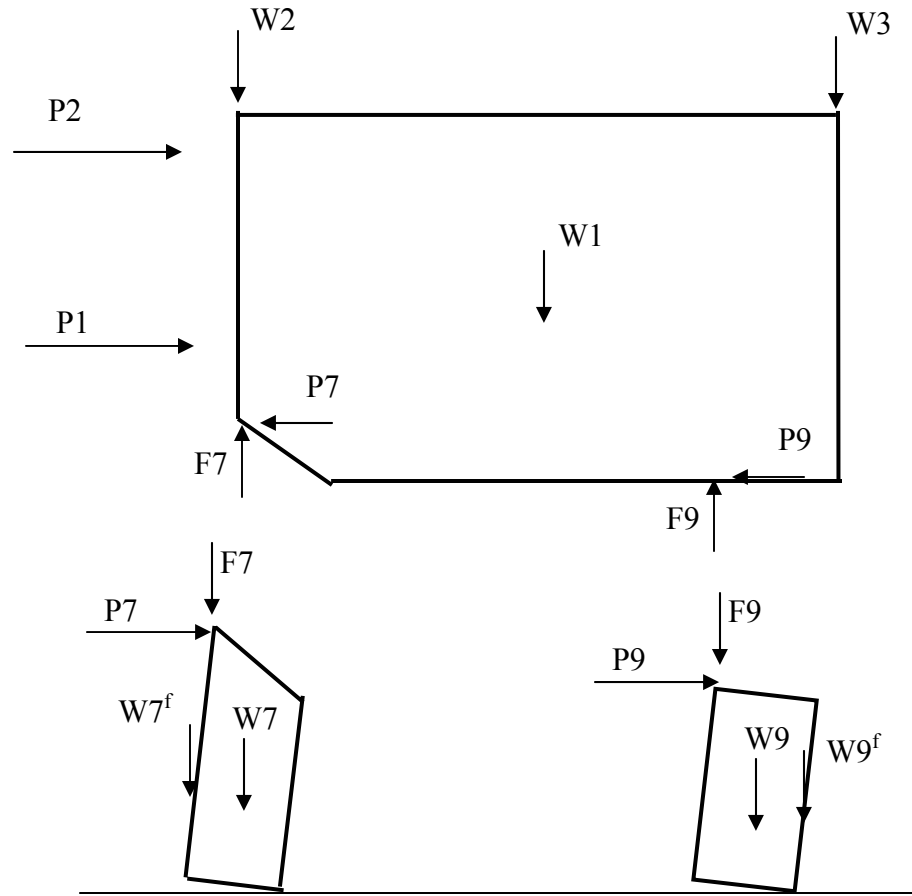


Figure F.2. Internal force distribution in Wall 2 when loaded from left to right

Assuming the lateral force applied on the roof is the same as that applied on the second floor, i.e.,

$$P1 = P2 \quad (F.3)$$

Substituting Eq. (F.3) into Eq. (F.2) and assuming the values from Table F.1, the lateral force corresponding to the kinematic mechanism shown in Figure F.2 can be calculated to be 26.7 kips, which is close to the values measured in the test (27 kips). When Wall 2 is loaded in the pull direction, the kinematic mechanism is basically the

mirror image of what is shown in Figure F.1. The flange sizes for the wall are the same as those listed in Table F.1. As a result, the predicted ultimate base shear for Wall 2 in the pull direction is 26.7 kips, which is also close to the measured results (24 kips).

F.2. Wall 1 in the push direction

The observed kinematic movement and the corresponding internal and external force distribution in Wall 1 when loaded in the push direction are illustrated in Figure F.3. The majority of Wall 1 rocks about its left toe, while Pier 1-7 is left behind.

The moment equilibrium equation about the left toe of Pier 1-6 gives:

$$150W_1 + 300W_2 = 148P_1 + 268P_2 \quad (F.4)$$

The external forces P_1 is assumed equal to P_2 , i.e.,

$$P_1 = P_2 \quad (F.3)$$

The self-weight of W_1 can be calculated as 37.4 kips. There are two estimates for the flange weight W_2 as listed in Table F.2.

Solving Eqs. (F.3) and (F.4) and considering Table F.2, the maximum lateral force for the push direction is 56 kips for Cycle 6 when no substantial crack is observed, and is 37.5 kips corresponding to the ultimate failure mechanism as shown in Figure F.3. Both the values are close to the measured values obtained from the test (60 kips maximum and 40 kips ultimate).

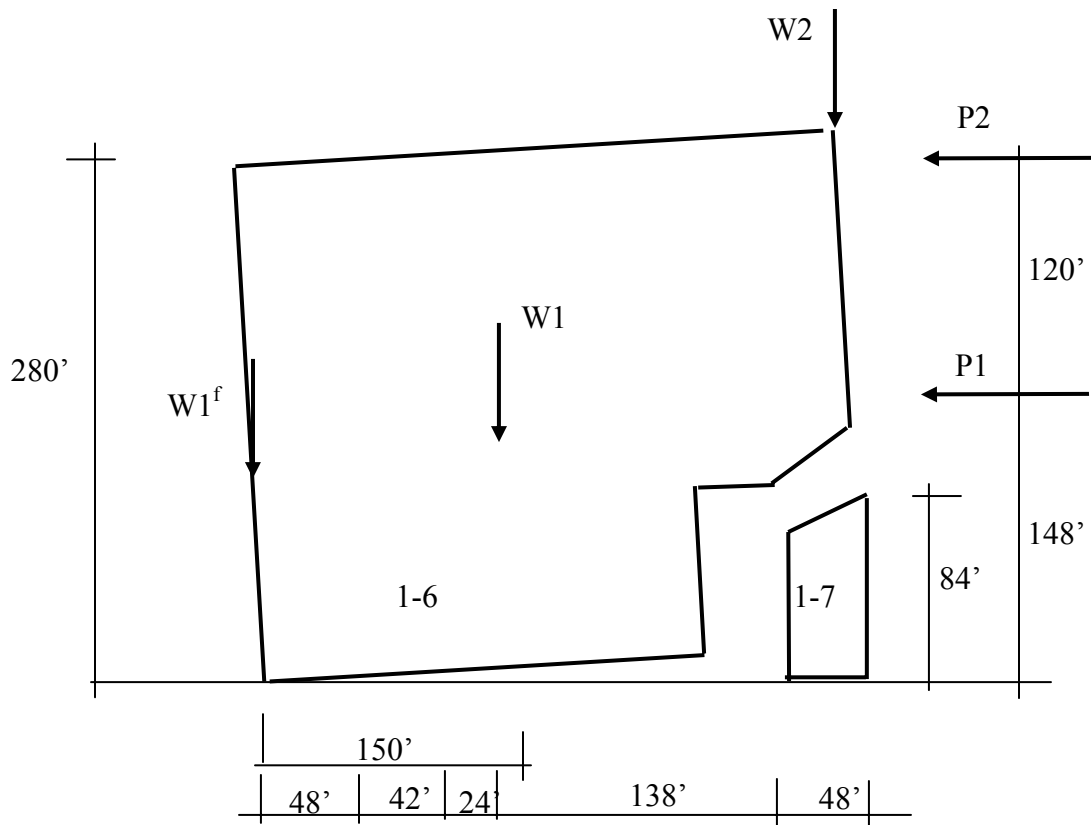


Figure F.3. Kinematic movements and internal force distribution in Wall 1 when loaded in the push direction

Table F.2. Weights used in the right body analysis for Wall 1 (push direction)

Cycle 6	The weight of a trapezoid from the bottom of Wall 1 before any cracks in Wall 1 is observed. = 20.3 kips
> Cycle 7	Triangular weight at the second floor of Wall 1 due to the ultimate crack = 7.3 kips

F.3. Wall 1 in the pull direction

The observed kinematic movement of Wall 1 in the pull direction is slightly different before and after Pier 1-6 slides. Before Pier 1-6 slides, the kinematic

mechanism of Wall 1 is illustrated in Figure F.4. Both Pier 1-6 and Pier 1-7 rocked around their individual right toes, while the entire second floor wall was lifted and pulled to the right due to the movement of the first story piers. Since v_6 is larger than v_7 due to the different aspect ratio between Piers 1-6 and 1-7, the lift up at the left side of Wall 1 is larger than that at the rigid side of Wall 1.

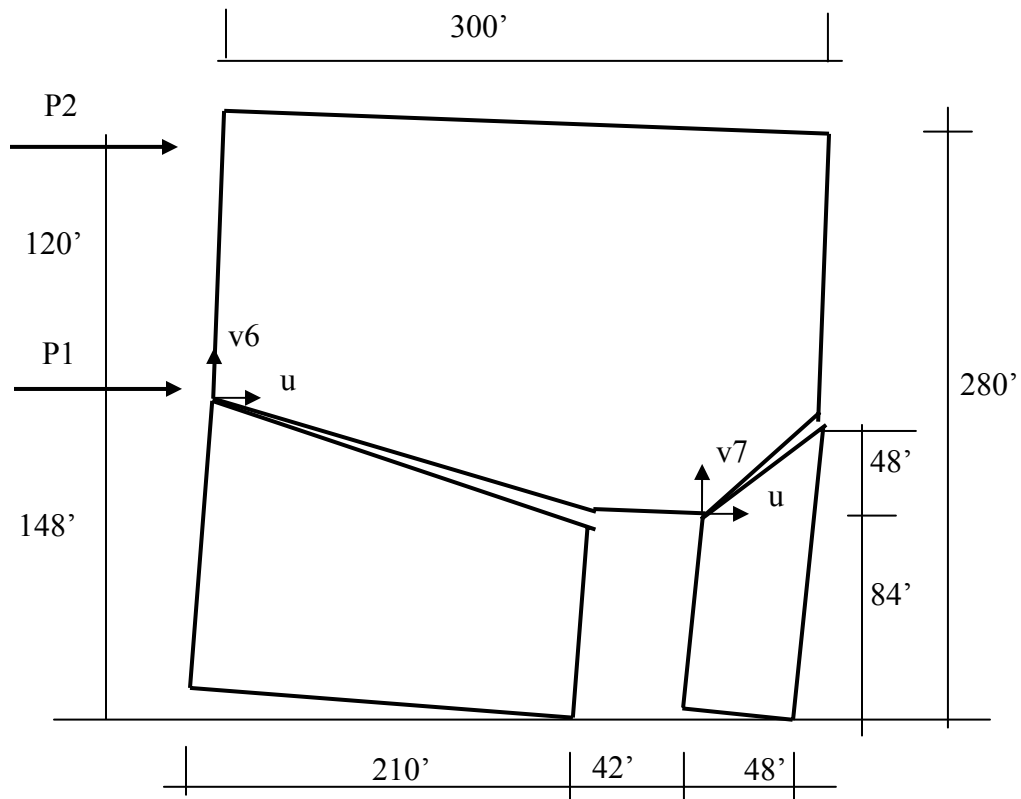


Figure F.4. Kinematic movement of Wall 1 before Pier 1-6 slides (pull direction)

The internal force distribution of Wall 1 is shown in Figure F.5. The following equations can be used to describe the equilibrium of the three rigid bodies:

$$210 \cdot F6 + 210 \cdot W6^f + 105 \cdot W6 = 148 \cdot P6$$

$$48F7 + 24W7 = 84P7$$

$$P6 + P7 = P1 + P2$$

$$F6 + F7 = W1 + W2 + W3$$

$$252F6 + 64P1 + 184P2 + 48W3 = 64P6 + 252W2 + 66W1 \quad (F.5)$$

The weight of each component, including the flange weight $W2$, $W3$, $W7^f$, and $W9^f$, can be calculated based on the crack pattern observed in the test and the rules specified in Chapter 9. The results are listed in Table F.3.

Substituting Eq. (F.3) into Eq. (F.5) and introducing the values listed in Table F.3, the lateral shear corresponding to the rocking failure mechanism can be calculated to be 56.8 kips, which is close to the measured value (55 kips).

On the other hand, after Pier 1-6 slides, although the kinematic mechanism of Wall 1 is still similar to Figure F.4, the uplift of $v6$ is smaller because of the sliding of Pier 1-6. The first equation in Eq. (F.5) has to be changed to

$$P6 = \mu(W6^f + W6 + F6) \quad (F.5^*)$$

where the shear friction μ is assumed to be 1.0 based on the material test discussed in Chapter 3.

Changing Eq. (F.5) based on Eq. (F.5*), and considering Eq. (F.3) and Table F.3, the lateral forces corresponding to the shear failure mechanism can be calculated to be 49.6 kips, which is close to the values measured in the test (47 kips).

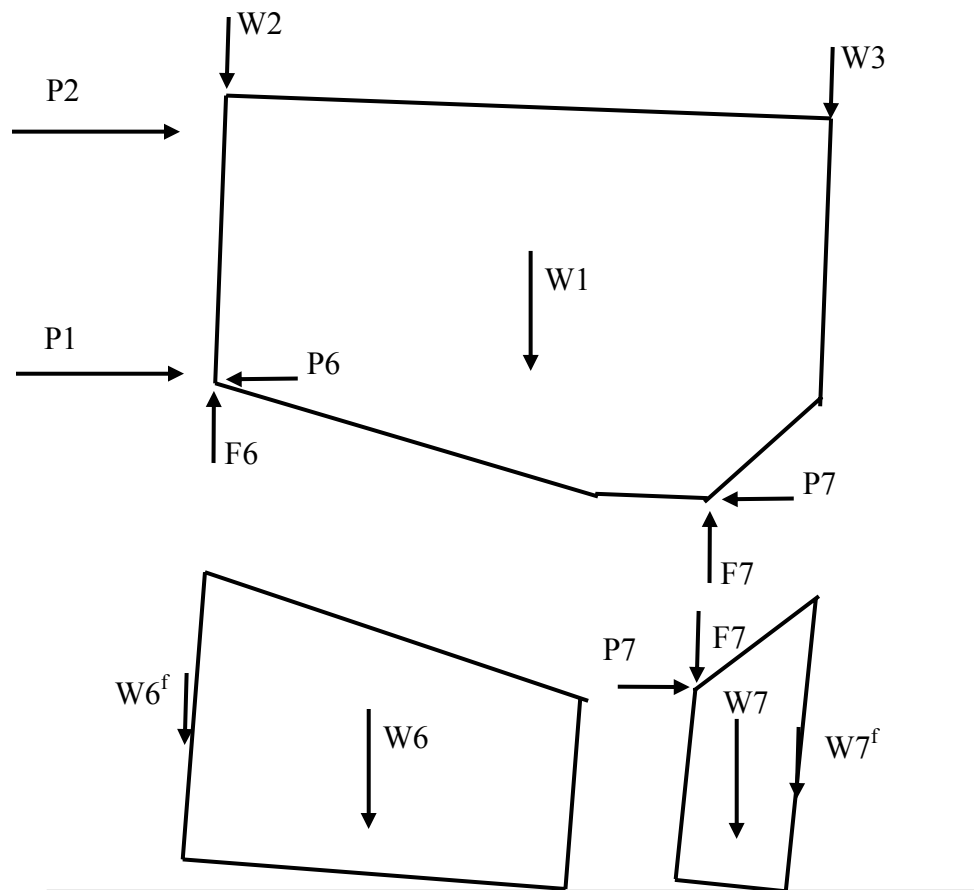


Figure F.5. Internal force distribution in Wall 1 before Pier 1-6 slides (pull direction)

Table F.3. Weights used in the right body analysis for Wall 1 (pull direction)

	W1	W2	W3	W6	W7	W6 ^f
Weight (kips)	24.3	6.44	6.44	13.1	3.0	23.2

F.4. Wall B in the push and pull directions and Wall A in the pull direction (rocking)

Wall B in both the push and pull directions and Wall A in the pull direction exhibited similar kinematic mechanisms but with different flange weights. As a result, they are discussed as a group here. Taking Wall B as an example, when the wall was loaded in the pull direction, the ultimate kinematic mechanism is shown in Figure F.6. All three first story piers on the left side of the wall rock, while Pier B-10 is left behind. However, since v_9 is smaller than v_8 , only Pier B-7 and B-8 support the second floor wall.

The internal force distribution of Wall B is shown in Figure F.7. Based on the equilibrium equations of the three rigid bodies, the following equations can be obtained:

$$48 \cdot F_7 + 24 \cdot W_7 = 84 \cdot P_7$$

$$41F_8 + 20.5W_8 = 48P_8$$

$$P_7 + P_8 = P_1 + P_2$$

$$F_7 + F_8 = W_1 + W_2 + W_3$$

$$82F_8 + 64P_1 + 184P_2 + 48W_3 = 248W_2 + 100W_1 \quad (F.6)$$

The weight of each component, including the flange weight W_2 , W_3 , W_7^f , and W_9^f , can be calculated based on the crack pattern observed in the test and the rules specified in Chapter 9. The results are listed in Table F.4. The weights for the other cases are also listed in this table.

Solving Eq. (F.6), Eq. (F.3) and considering Table F.4, the base shear corresponding to the three cases can be calculated and listed in Table F.5. The experimental measurements are also listed in the table as a comparison. Again the analyses provide close predictions for the maximum strengths of the test.



	W1	W2	W3	W7	W8
Wall B Push	42.6	14.8	9.8	3.4	1.6
Wall B Pull	42.6	4.5	5.9	3.4	1.6
Wall A Push	42.6	10.4	4.8	3.4	1.6

	Rigid body analysis	Experimental results
Wall B Push	46.0	43
Wall B Pull	34.6	37
Wall A Push	40.2	40

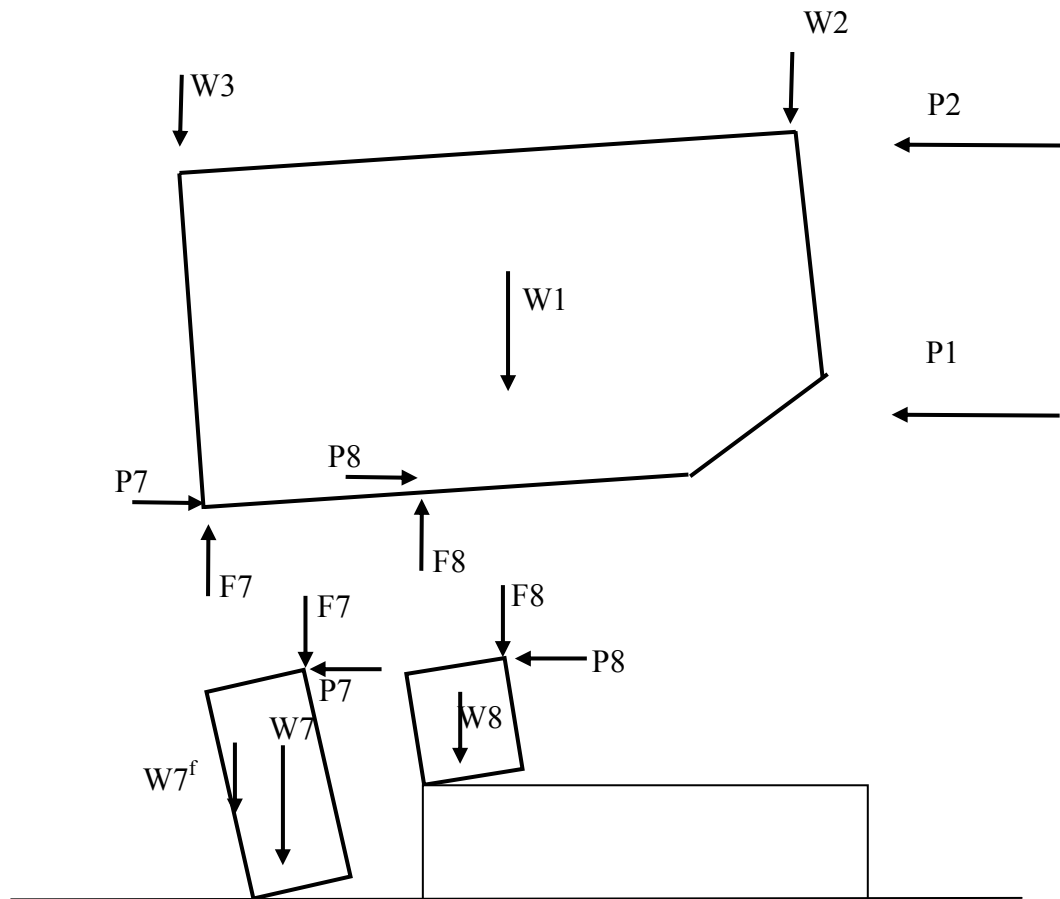


Figure F.7. Internal force distribution in Wall B when loaded in the push direction

F.5. Wall B in the push and pull directions (sliding)

Relative sliding between Wall B first floor spandrel and the first floor piers is a possible kinematic mechanism for Wall B. In this case three first floor piers are engaged, as shown in Figure F.8.

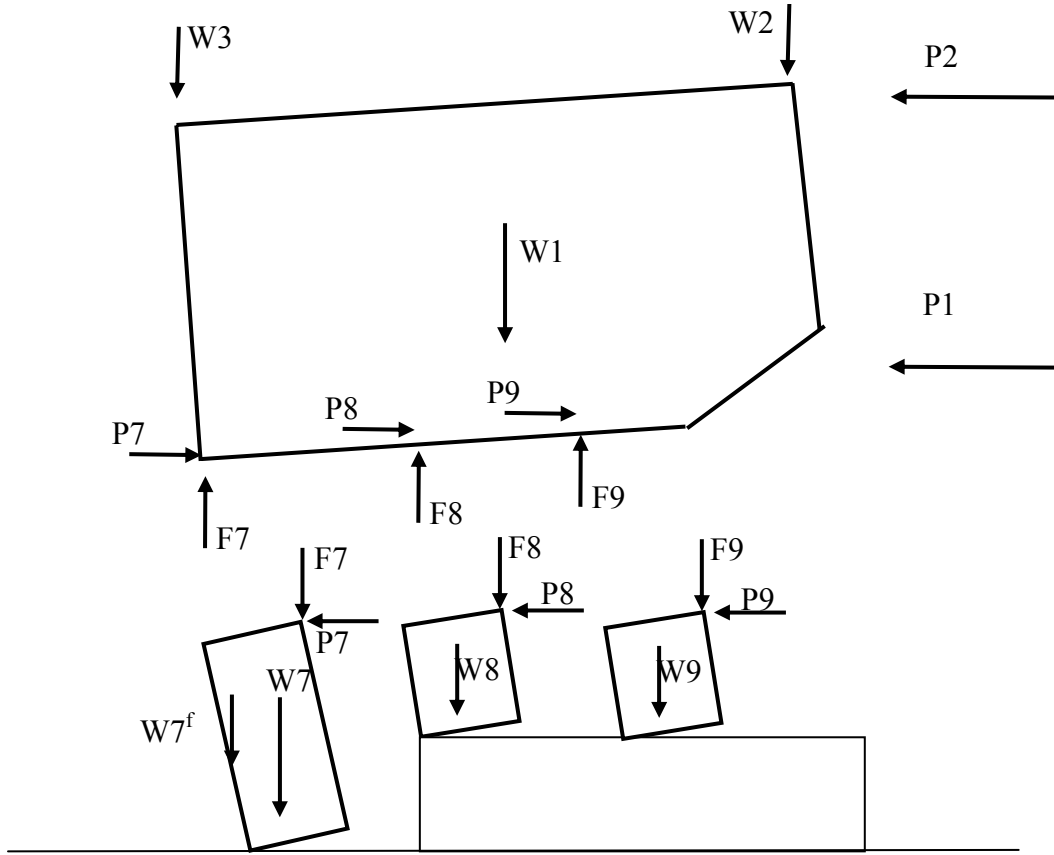


Figure F.8 Kinematic movement of Wall B with sliding between spandrel and piers (push direction)

Based on the equilibrium equations of the four rigid bodies, the following equations can be obtained:

$$48 \cdot F7 + 24 \cdot W7 = 84 \cdot P7$$

$$41F8 + 20.5W8 = 48P8$$

$$41F9 + 20.5W9 = 48P9$$

$$P7 + P8 + P9 = \mu(W1 + W2 + W3)$$

$$P7 + P8 + P9 = P1 + P2$$

$$F7 + F8 + F9 = W1 + W2 + W3$$

$$82F8 + 159F9 + 64P1 + 184P2 + 48W3 = 248W2 + 100W1 \quad (F.7)$$

The weight of each component, including the flange weight W_2 , W_3 , W_7^f , and W_9^f , can be calculated based on the crack pattern observed in the test and the rules specified in Chapter 9. The results are listed in Table F.6.

Table F.6 Weights used in the right body analysis for Wall B sliding (kips)

	W1	W2	W3	W7	W8	W9
Wall B Push	42.6	14.8	9.8	3.4	1.6	1.6

Solving Eq. (F.7), Eq. (F.3) and considering Table F.6, the maximum strengths of Wall B calculated corresponding to the three cases are listed in Table F.7. The rigid body analysis points out that if the shear friction is 1.0 and the Wall B first floor spandrel slides on the top of the first floor piers, the ultimate strength of Wall B in the push direction is 67 kips. Even if the shear friction factor is reduced to 0.7, the ultimate strength of Wall B is still 47 kips. Both the values are larger than the measured values. As a result, sliding is unlikely as a kinematic mechanism for Walls A and B.

Table F.7. Analyzed vs. measured maximum strengths for Wall B

	Rigid body analysis	Experimental results
Wall B Push	66.0	43

F.6. Wall A in the push direction

The kinematic mechanism of Wall A in the push direction is slightly different from that in the pull direction. Again, all the three first story piers at the right side of the

wall tended to rock, while Pier A-7 was left behind. However, since there was a diagonal crack at the base of Pier A-9, the effective aspect ratio of Pier A-9 was the same as that of Pier A-10. As a result, the rigid body analysis shows that Pier A-9 separated from the second floor wall and only A-8 and A-10 support the displaced second floor wall. The ultimate kinematic mechanism is shown in Figure. F.9.

The internal force distribution of Wall A in the push direction is shown in Figure F.10. Based on the equilibrium equations of the three rigid bodies, the following equations can be obtained:

$$48 \cdot F_{10} + 24 \cdot W_{10} = 84 \cdot P_{10}$$

$$41F_8 + 20.5W_8 = 48P_8$$

$$P_{10} + P_8 = P_1 + P_2$$

$$F_{10} + F_8 = W_1 + W_2 + W_3$$

$$159F_8 + 64P_1 + 184P_2 + 48W_3 = 248W_2 + 100W_1 \quad (F.8)$$

The weight of each component, including the flange weight W_2 and W_3 , can be calculated based on the crack pattern observed in the test and the rules specified in Chapter 9. The results are listed in Table F.8.

Solving Eqs. (F.8) and (F.3), and considering Table F.8, the base shear of Wall A in the push direction was calculated to be 33.9 kips. This value is the same as the measured value of 33.9 kips.

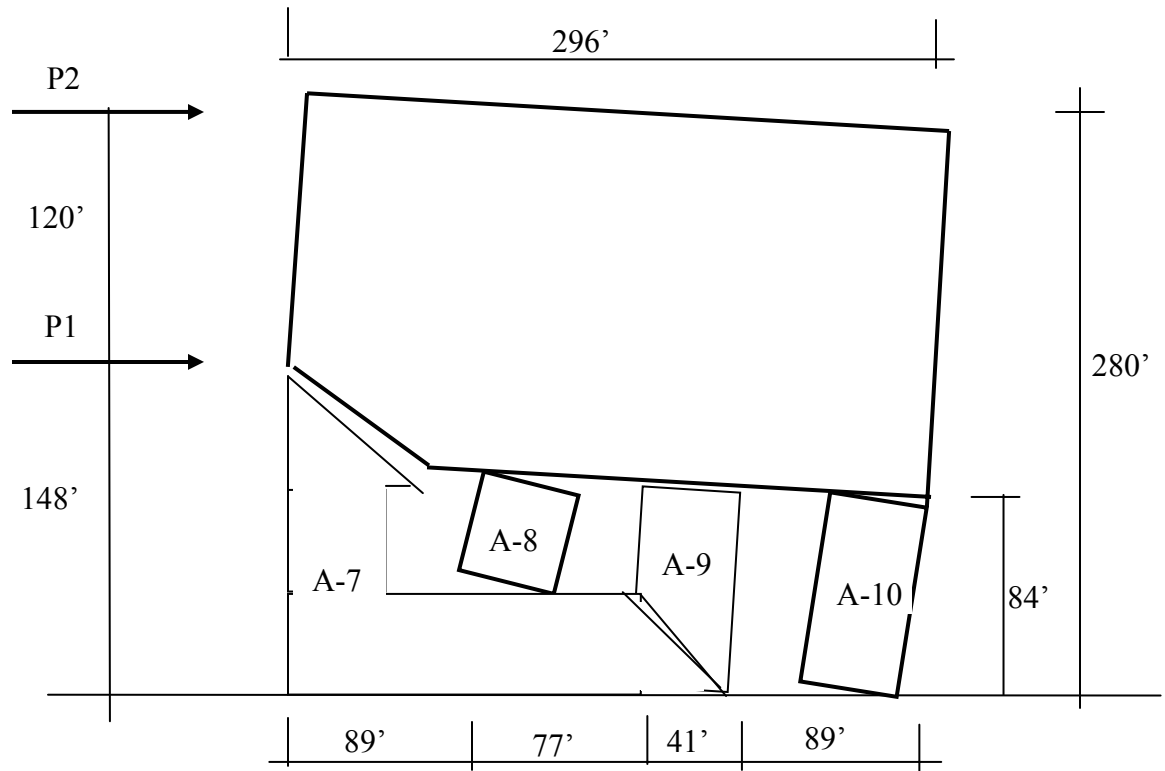


Figure F.9. Kinematic movement of Wall A (push direction)

Table F.8. Weights used in the right body analysis for Wall A (push direction) (kips)

W1	W2	W3	W10	W8
42.6	4.84	5.3	3.4	1.6

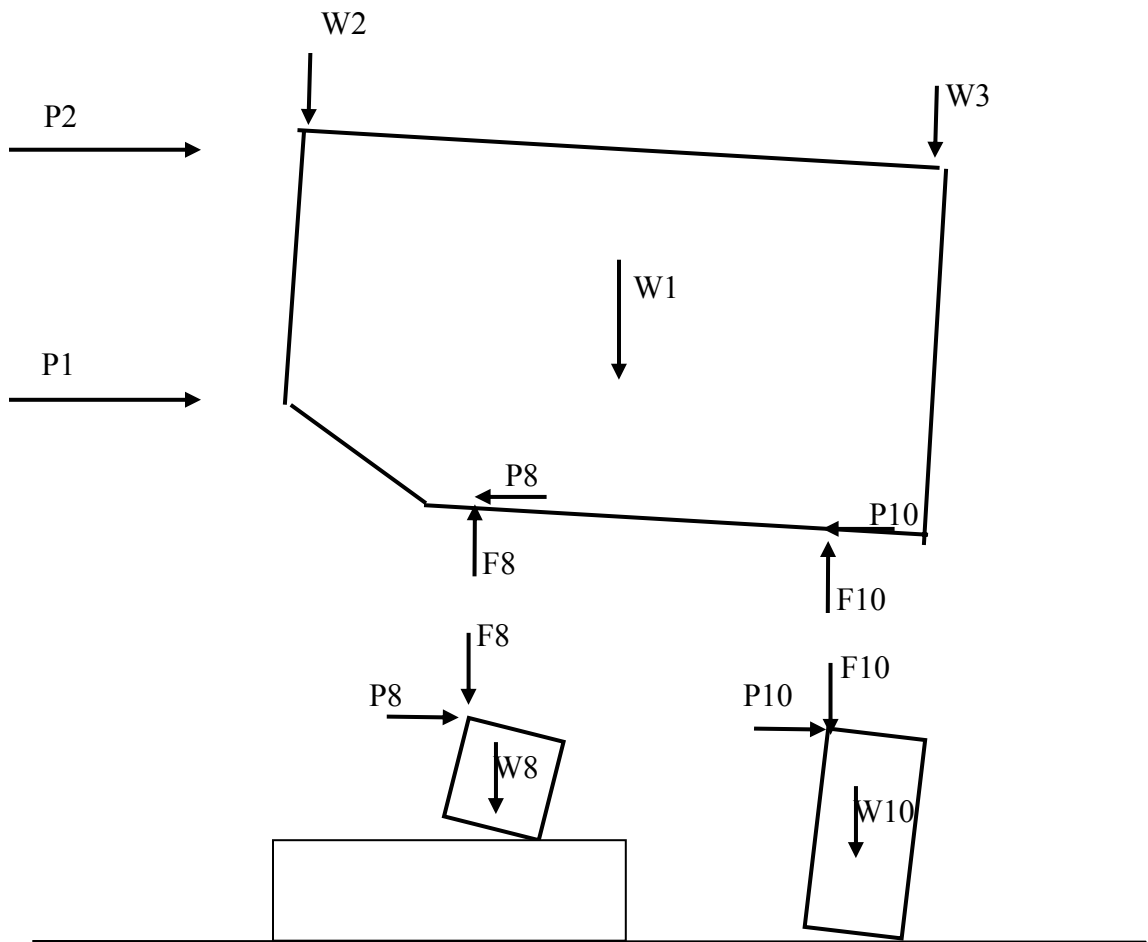


Figure F.10. Internal force distribution in Wall A (push direction)

REFERENCES

Abell, A.B. and Lange, D.A. (1998). Fracture Mechanics Modeling Using Images of Fracture Surfaces. *International Journal of Solids and Structure*. Vol. 35, No. 31-32, pp. 4025-4034.

ABK. (1981a). Methodology for Mitigation of Seismic Hazards in Existing Unreinforced Masonry Buildings: Diaphragm Testing. ABK-TR-03, Agbabian & Associates, S.B. Barnes & Associates, and Kariotis & Associates, El Segundo, CA.

ABK. (1981b). Methodology for Mitigation of Seismic Hazards in Existing Unreinforced Masonry Buildings: Wall Testing, Out-of-plane. ABK-TR-04, Agbabian & Associates, S.B. Barnes & Associates, and Kariotis & Associates, El Segundo, CA.

ABK. (1984). Methodology for Mitigation of Seismic Hazards in Existing Unreinforced Masonry Buildings: the Methodology. ABK-TR-08, Agbabian & Associates, S.B. Barnes & Associates, and Kariotis & Associates, El Segundo, CA.

Abrams, D. P. (1992). Strength and Behavior of Unreinforced Masonry Elements. 10th World Conference on Earthquake Engineering, Madrid, Spain, pp. 3475-3480.

Abrams, D.P. and Shah, N. (1992). Cyclic Load Testing of Unreinforced Masonry Walls. College of Engineering, University of Illinois at Urbana, Advanced Construction Technology Center Report #92-26-10.

ACI Committee 318 (2002). Building Code Requirements for Structural Concrete (ACI 318-02) and Commentary (318R-02). American Concrete Institute, Farmington Hills, Mich.

ACI Committee 530 (2002). Building Code Requirements for Masonry Structures (ACI 530-02) and Specification for Masonry Structures (530.1-02). American Concrete Institute, Farmington Hills, Mich.

Alshebani, Milad M. and Sinha, S.N. (1999). Stress-Strain Characteristics of Brick Masonry under Uniaxial Cyclic Loading. Journal of Structural Engineering, ASCE., Vol. 125, No.6, June 1999, pp. 600-604.

Andrean, U., and Ceradini, G. (1992). Failure Modes of Solid Brick Masonry under In-plane Loading. Masonry International, Vol. 6, No. 1, pp.4-8.

Andrean, U. (1996). Failure Criteria for Masonry Panels under In-plane Loading. Journal of Structural Engineering. ASCE., Vol. 122, No.1, Jan 1996, pp. 37-46.

Anthoine, A., Magonette, G. and Magenes, G. (1995). Shear-Compression Testing and Analysis of Brick Masonry Walls. Proceedings of the 10th European Conference on Earthquake Engineering, Duma, the Netherlands.

APA-the Engineered Wood Association (1985). Design/Construction Guide Residential and Commercial. Tacoma, Washington.

APA-the Engineered Wood Association (1986). Plywood Design Specification. Tacoma, Washington.

Applied Technology Council (ATC) (1987). Evaluating the Seismic Resistance of Existing Buildings. Report ATC-14, Applied Technology Council, Redwood City, CA.

Applied Technology Council (ATC) (1989). A Hand Book for Seismic Evaluation of Existing Buildings. Report ATC-22, Applied Technology Council, Redwood City, CA.

Applied Technology Council (ATC) (1997a). NEHRP Guidelines for the Seismic Rehabilitation of Buildings. Publication No. 273, Federal Emergency Management Agency, Washington, D.C. (FEMA-273).

Applied Technology Council (ATC) (1997b). NEHRP Commentary on the Guidelines for the Seismic Rehabilitation of Buildings. Publication No.274, Federal Emergency Management Agency, Washington, D.C. (FEMA-274).

Applied Technology Council (ATC) (1999a). Evaluation of Earthquake Damaged Concrete and Masonry Wall Buildings, Basic Procedures Manual. Publication No.306, Federal Emergency Management Agency, Washington, D.C. (FEMA-306).

Applied Technology Council (ATC) (1999b). Evaluation of Earthquake Damaged Concrete and Masonry Wall Buildings, Technical Resources. Publication No.307, Federal Emergency Management Agency, Washington, D.C. (FEMA-307).

Applied Technology Council (ATC) (2000). Prestandard and Commentary for the Seismic Rehabilitation of Buildings. Publication No.356, Federal Emergency Management Agency, Washington, D.C. (FEMA-356).

ASTM C270-57T (1958). Tentative Specification for Mortar for Unit Masonry. West Conshohocken, Pennsylvania.

ASTM E447 (1997). Test Methods for Compressive Strength of Masonry Prisms. West Conshohocken, Pennsylvania.

ASTM E111 (1997). Test Method for Young's Modulus, Tangent Modulus, and Chord Modulus. West Conshohocken, Pennsylvania.

ASTM C67 (1998). Standard Test Methods for Sampling and Testing Brick and Structural Clay Tile. West Conshohocken, Pennsylvania.

ASTM E519 (2000). Method for Diagonal Tension (Shears in Masonry Assemblages). West Conshohocken, Pennsylvania.

ASTM C1072 (2000). Standard Test Method for Measurement of Masonry Flexural Bond Strength. West Conshohocken, Pennsylvania.

ASTM E72 (2002). Method for Conducting Strength Tests of Panels for Building Construction. West Conshohocken, Pennsylvania.

Atkinson, R.H., Amadei, B.P., Saeb, S. and Sture, S. (1989). Response of Masonry Bed Joints in Direct Shear. Journal of Structural Engineering. ASCE., Vol. 115, No. 9, pp. 2276-2296.

Augarde, C. (2001). Settlement Induced Damage to Masonry Buildings, in Computational Modeling of Masonry, Brickwork and Blockwork Structures. Edited by Bull, J.W., Saxe-Coburg Publications, UK.

Bariola, J., Ginocchio, J.F., and Quiun, D. (1990). Out-of-plane Response of Brick Walls. Proceedings of the Fifth North American Masonry Conference, Urbana-Champaign, Ill, Vol.1, pp. 429-439.

Benedetti, D. and Benzoni, G.M. (1984). A Numerical Model for Seismic Analysis of Masonry Buildings: Experimental Correlations. Earthquake Engineering and Structural Dynamics, Vol.12, pp. 817-831.

Benjamin, J.R. and Williams, H. (1958). The Behavior of One-Story Brick Shear Walls. Journal of the Structural Division, Proceedings of the ASCE, Paper 1723, ST4, July.

Bicanic, N., Ponniah, D. and Robinson, J. (2001). Discontinuous Deformation Analysis of Masonry Bridges, in Computational Modeling of Masonry, Brickwork and Blockwork Structures. Edited By Bull, J.W., Saxe-Coburg Publications, U.K.

Boussabah, L. and Bruneau, M. (1992). Review of the Seismic Performance of Unreinforced Masonry Wall. 10th World Conference on Earthquake Engineering, Madrid, Spain, pp. 4537-4540.

Bruneau M. (1994a). Seismic Evaluation of Unreinforced Masonry Buildings – a State-of-the-Art Report. Canadian Journal of Civil Engineering. Vol. 21, pp. 512-539.

Bruneau M. (1994b). State-of-the-Art Report on Seismic Performance of Unreinforced Masonry Buildings. Journal of Structural Engineering, ASCE., Vol. 120, No. 1, pp. 230-251.

Bruneau M. (1995). Performance of Masonry Structures during the 1994 Northridge (Los Angeles) Earthquake. Canadian Journal of Civil Engineering. Vol. 22, pp. 378-402.

Bull J.W. (Editor). Computational Modeling of Masonry, Brickwork and Blockwork Structures. Saxe-Coburg Publications, Stirling, Scotland, 2001, pp. 53-77.

Calvi, G.M., Magenes, Gi, Magenes, Gu and Pavese, A. (1995). Experimental and Numerical Investigation on a Brick Masonry Building Prototype, Report 3.0, Numerical Prediction of the Experiment. Gruppo Nazionale Per La Difesa Dai Terremoti.

Calvi, G. M., Gregory, R. K. and Magenes, G. (1996). Testing of Masonry Structures for Seismic Assessment. Earthquake Spectra, Vol. 12, No.1, pp. 145-162.

Chiostrini. S. and Vignoli, A. (1989). An Application of a Numerical Method to Study Masonry Panels with Various Geometry under Seismic Loads. Proceedings of the First International Conference on Structural Repair & Maintenance of Historical Buildings, Florence, Italy.

Chiostrini, S., Foraboschi, P. and Sorace, S. (1989). Problems Connected with the Arrangement of a Non-Linear Finite Element Method to the Analysis of Masonry Structures. Proceedings of the First International Conference on Structural Repair & Maintenance of Historical Buildings, Florence, Italy, pp. 525-534.

Chiostrini, S., Maestrelli, L. and Vignoli, A. (1995). Numerical Simulation of Destructive Tests on a Full-Scale Brick-Masonry Prototype, in Experimental and Numerical Investigation on a Brick Masonry Building Prototype. Report 3.0, Gruppo Nazionale La Difesa Dai Terremoti.

Clemson University (2000). Test Results for Bricks and Mortar Samples. The National Brick Research Center, Clemson University, SC.

Clough, R. H., Mayes R. L. and Gulkan, P. (1979). Shaking Table Study of Single-Story Masonry Houses, Vol.3: Summary, Conclusions, and Recommendations. Report No. UCB/EEERC-79/25, University of California, Berkeley, CA.

Costley, A.C. and Abrams, D.P. (1996). Dynamic Response of Unreinforced Masonry Buildings with Flexible Diaphragms. NCEER-96-0001, University of Buffalo, Buffalo, N.Y.

Countryman, D. (1952). Lateral Tests on Plywood Sheathed Diaphragms. Laboratory Report 55, Douglas Fir Plywood Association, Tacoma, Washington.

Deppe, K. (1988). The Whittier Narrows, California Earthquake of October 1, 1987-Evaluation of Strengthened and Unstrengthened Unreinforced Masonry in Los Angeles City. *Earthquake Spectra*, Vol. 4, No.1, pp. 157-180.

Dialer, C. (1991). Some Remarks on the Strength and Deformation Behavior of Shear Stressed Masonry Panels under Static Monotonic Loading. *Proceeding of the 9th IBMAC*, Berlin, German, Vol. 1, pp. 276-283.

Dhanasekar, M., Page, A. W. and Kleeman, P. W. (1985a). The Failure of Brick Masonry under Biaxial Stresses. *Proceedings Institution of Civil Engineers*, London, U.K., Part 2, pp. 295-313.

Dhanasekar, M., Page, A. W. and Kleeman, P. W. (1985b). The Behavior of Brick Masonry under Biaxial Stresses with Particular Reference to Infill Frames. *Seventh Boume*, Australia, Vol. 2, pp. 815-824.

Drysdale, R. G., Vanderkeyl, R.V., and Hamid, A. A. (1979). Shear Strength of Brick Masonry Joints. *Proceeding of 5th International Brick Masonry Conference*, Paper II-13, Washington, D.C.

Drysdale, R. G. and Hamid, A. A. (1984). Tensile Failure Criteria for Plain Concrete Masonry. *Journal of Structural Engineering*, ASCE., Vol.110, No.2, pp. 228-244.

Drysdale, R. G. and Essawy, S. (1988). Out-of-plane Bending of Concrete Block Walls. *Journal of Structural Engineering*, ASCE., Vol. 114, No.1, pp.121-133.

Ehsani, M. and Wight, J. K. (1985). Effects of Transverse Beams and Slab on Beam-to-Column Connections. *ACI Structural Journal*, Vol. 82, No. 2, pp. 188-195.

Epperson, G.S. and Abrams, D.P. (1989). Nondestructive Evaluation of Masonry Buildings. *College of Engineering, University of Illinois at Urbana, Advanced Construction Technology Center*, Report #89-26-03.

Epperson, G.S. and Abrams, D.P. (1992). Evaluating of Lateral Strength of Existing Unreinforced Brick Piers in the Laboratory. The Masonry Society Journal, February, pp. 86-93.

Erbay, O. and Abrams, D. P. (2002). Seismic Rehabilitation of Unreinforced Masonry Shear Walls. Seventh U.S. National Conference on Earthquake Engineering, July 21-25, Boston, USA.

Eurocode 6 (1995). Design of Masonry Structures, Part 1-1: General Rules for Buildings. Rules for Reinforced and Unreinforced Masonry, ENV. 1996-1-1: 1995, CEN, Brussels.

Evans, H.R. and Taherian, A.R. (1980). A Design Aid for Shear Lag Calculations. Proceedings Institution of Civil Engineers, Part 2, Vol. 69, pp. 403–24.

FEMA (1992a). NEHRP Handbook for the Seismic Evaluation of Existing Buildings. Federal Emergency Management Agency, Washington, D.C.

FEMA (1992b). NEHRP Handbook of Techniques for the Seismic Rehabilitation of Existing Buildings. Federal Emergency Management Agency, Washington, D.C.

Franklin, S., Lynch, J. and Abrams, D. P. (2001). Performance of Rehabilitated URM Shear Walls: Flexural Behavior of Piers. Department of Civil Engineering, University of Illinois at Urbana-Champaign Urbana, Illinois.

Frederick, P., Spalding, A., Lincoln, H. and Robinson, E. F. (1926). Masonry Structures. Press of Braunworth & Co., Inc., New York.

Gambarotta, L., Lagomarsino, S. and Morbiducci, R. (1995). Two-Dimensional Finite Element Simulation of a Large Scale Brick Masonry Wall through a Continuum Damage Model, in Experimental and Numerical Investigation on a Brick Masonry Building Prototype. Report 3.0, Gruppo Nazionale La Difesa Dai Terremoti.

Gambarotta, L. and Lagomarsino, S. (1997). Damage Models for the Seismic Response of Brick Masonry Shear Walls, Part I: the Mortar Joint Model and Its Applications. Earthquake Engineering and Structure Dynamics, Vol. 26, pp. 423-439.

Ganz, H. R. (1985). Mauerwerksscheiben Unter Nonnaikraft Und Schub. Bericht- Nr. 148, Institut Filr Baustatik Und Konstruktion Eth, Zcirich, Switzerland (In German).

Ganz, H. R. (1989). Failure Criteria for Masonry. Proceeding of 5th Canada Masonry Symposium, Vol.1, pp. 65-77.

Ganz, H. R. and Thurlimann, B. (1982). Versuche Uber Die Festigkeit Von Zweiachsig Beanspruchtem Mauerwerk. Bericht Nr. 7502-3, Institut Fur Baustatik Und Konstruktion Eth, Zurich, Switzerland (In German).

Ganz, H. R. and Thurlimann, B. (1984). Bruchbedingung Fur Zweiachsig Beanspruchtes Mauerwrk Bericht Nr. 143, Institut Fur Baustatik Und Konstruktion Eth, Zurich, Switzerland (In German).

Gavarini, C., Andreaus, U., Carriero, A., Asdia, P.D., Dayala, D., Ippoliti, L., Mollaioli, F., Valente, G. and Viskovic, A. (1995). Numerical Modeling of Unreinforced Masonry Building, in Experimental and Numerical Investigation on a Brick Masonry Building Prototype. Report 3.0, Gruppo Nazionale La Difesa Dai Terremoti.

Gere, J.M. and Timoshenko, S. P. (1990). Mechanics of Materials. 3rd, Boston, Pws-Kent Pub. Co.

Goodman, R.E. (1980). Introduction to Rock Mechanics. John Wiley & Sons, Hoboken, NT.

Goodman, R.E. and Shi, G. (1985). Block Theory and Its Application to Rocking Engineering, Prentice-Hall, Inc., Englewood Cliffs, New Jersey.

Gulkan, P., Ray, H., Mayes, R. L. and Clough, R. W. (1979). Shaking Table Study of Single-Story Masonry Houses, Vol. 1: Test Structures 1 and 2. Report No. UCB/EERC-79/23, University of California, Berkeley, CA.

Gulkan, P., Ray, H., Mayes, R. L. and Clough, R. W. (1979). Shaking Table Study of Single-Story Masonry Houses, Vol. 2: Test Structures 3 and 4. Report No. UCB/EEERC-79/24, University of California, Berkeley, CA.

Gulkan, P., Clough, R. W., Mayes, R. L. and Manos, G. C. (1990). Seismic Testing of Single-Story Masonry Houses. Part 1, Journal of Structural Engineering, ASCE, Vol. 116, No. 1, pp. 235-256.

Hamid, A. A., Drysdale, R. G. and Heidebrecht, A. C. (1979). Shear Strength of Concrete Masonry Joints. Journal of Structural Engineering, ASCE., Vol. 105, No.7, pp. 1227-1240.

Hamid, A. A. and Drysdale, R. G. (1980). Behavior of Brick Masonry under Combined Shear and Compression Loading. Proceeding of the 2nd Canada Masonry Symposium, pp. 51-64.

Hamid, A. A. and Drysdale, R. G. (1981). Proposed Failure Criteria for Concrete Block Masonry under Biaxial Stresses. Journal of Structural Engineering, ASCE., Vol. 107, No.8, pp. 1675-1687.

Hamid, A. A. and Drysdale, R. G. (1982). Proposed Failure Criteria for Brick Masonry under Combined Stresses. Proceeding of the 2nd North American Masonry Conference, College Park, Md., pp. 9.2- 9.11.

Hamid, A. A., Ziab, G. and Naway, O. E. (1987). Modulus of Elasticity of Concrete Block Masonry. The 4th North American Masonry Conference, Los Angeles, USA, Aug.

Hassan, M. and Ei-Tawil, S. (2003). Tension Flange Effective Width in Reinforced Concrete Shear Walls. ACI Structural Journal, Vol. 100, No. 3, pp. 349-356.

Hegemeir, G. A., Nunn, R. O., and Arya, S. K. (1978). Behavior of Concrete Masonry under Biaxial Stress. Proceeding of the 1st North American Masonry Conference, Boulder, Colo., pp.1-24.

Hosoyama, H., Abe, I., Kitagawa, Y. and Okada, T. (1995). Shaking Table Tests of Three-Dimensional Scale Models of Reinforced Concrete High-Rise Frame Structures with Wall Columns. ACI Structural Journal, Vol. 92, No. 6, pp. 765-780.

ICBO (1997). Uniform Code for Building Conservation. International Conference of Building Officials, Whittier, CA.

Jonhson, J. W. (1956). Lateral Tests on Full-Scale Lumber and Plywood-Sheathed Roof Diaphragms. The American Society of Mechanical Engineers (ASME), Paper No. 56-S-16.

Johnson, F.B. and Thompson, J.N. (1969). Development of Diametric Testing Procedures to Provide a Measure of Strength Characteristics of Masonry Assemblages. In *Designing, Engineering and Constructing with Masonry Products*, Gulf Publishing Co., Houston, TX.

Kampf, L. (1963). Factors Effecting Bond of Mortar to Brick. Symposium on Masonry Testing (ASTM STP 320), pp. 127-141.

Kariotis, J.C., Ewing, R. D. and Johnson, A.W. (1985). Strength Determination and Shear Failure Modes of Unreinforced Brick Masonry with Low Strength Mortar. Proceeding of the 7th International Brick Masonry Conference, Melbourne, Australia, Feb.

Kim, S.C. and White, D.W. (2003). MDOF Response of Low-Rise Buildings. ST-5 Project Final Report, Mid-America Earthquake Center, Georgia Institute of Technology, Atlanta.

Koubaa, B., Nappi, A. and Papa, E. (1995). Numerical Analysis of Masonry Structures by Using Material Models Based on Damage Mechanics, in *Experimental and Numerical Investigation on a Brick Masonry Building Prototype*. Report 3.0, Gruppo Nazionale La Difesa Dai Terremoti.

Kristek V. (1979). Folded Plate Approach to Analysis of Shear Wall Systems and Frame Structures. *Proceedings Institution of Civil Engineers, Part 2, Vol. 67*, pp. 1065-1075.

Kristek V., Studnicka J. and Skaloud M. (1981). Shear Lag in Wide Flanges of Steel Bridges. *ACTA Technica CSAV, Vol. 26*, pp. 464-488.

Lange, D.A., Deford, H.D. and Werner, A.M. (1999). Microstructural Investigation of Mortar/Unit Interaction. *The Masonry Society Journal*, Nov., pp. 31-42.

Lawrence, S.J. and Cao, H.T. (1987). An Experimental Study of the Interface Between Brick and Mortar. The 4th North American Masonry Conference, Los Angeles, Aug.

Lourenco, P.B. (1996). Computational Strategies for Masonry Structures. Delft University Press, the Netherlands.

Magenes, G. and Calvi, G. M. (1992). Cyclic Behavior of Brick Masonry Walls. Tenth World Conference on Earthquake Engineering, Madrid, Spain, pp. 3517-3522.

Magenes, G. and Calvi, G.M. (1995). Shaking Table Tests on Brick Masonry Walls. Proceedings of the 10th European Conference on Earthquake Engineering, Duma, the Netherlands.

Magenes, G., Kingsley, G. R., and Calvi, G. M (1995). Seismic Testing of a Full-Scale, Two-story Masonry Building: Test Procedure and Measured Experimental Response, in Experimental and Numerical Investigation on a Brick Masonry Building Prototype. Report 3.0, Gruppo Nazionale La Difesa Dai Terremoti.

Mann, W. and Muller, H. (1982). Failure of Shear-Stressed Masonry - An Enlarged Theory, Tests and Application to Shear Walls. Proceedings BCS., Loading-bearing Brickwork, Vol.7, No. 30, pp. 223- 235.

Manzouri, T., Shing, P.B., Amadei, B., Schuller, M. and Atkinson, R. (1995). Repair and Retrofit of Unreinforced Masonry Walls: Experimental Evaluation and Finite Element Analysis. Department of Civil, Environmental and Architectural Engineering, University Of Colorado: Boulder, Colorado, Report CU/SR-95/2

Martini, K. (1997). Finite Element Studies in the Out-of-plane Failure of Unreinforced Masonry. Proceedings of the International Conference on Computing in Civil and Building Engineering, Korea, Vol.1, pp. 179-184.

Martini, K. (1998). Finite Element Studies in the Two-Way Out-of-plane Failure of Unreinforced Masonry. 6th U.S. National Conference of Earthquake Engineering, Seattle, WA.

Mayes, R.L. and Clough, R.W. (1975). State-of-the-art in Seismic Shear Strength of Masonry – An Evaluation and Review. EERC 75-21, University of California, Berkeley, CA.

McDowell, E.L. Mckee, K.E. and Sevin, E. (1956). Arching Action Theory of Masonry Walls. Journal of Structural Division, ASCE. ST2, Mar., pp. 915-1 – 915-18.

Meli, R. (1973). Behavior of Masonry Walls under Lateral Loads. Proceedings of the 5th World Conference on Earthquake Engineering, Rome, Italy, pp. 853-862.

Merguro, K. and M. Hakuno. (1989). Fracture Analysis of Concrete Structures by the Modified Distinct Element Method. Structural Engineering and Earthquake Engineering, Japan Society of Civil Engineers, Vol. 6, No.2, pp. 283s-284s.

Moon, F., Yi, T., Leon, R. and Kahn, L. (2003). Large-Scale Tests of an Unreinforced Masonry Low-Rise Building. Ninth North American Masonry Conference, Clemson, SC.

Moon, F. (2004). Seismic Strengthening of Low-Rise Unreinforced Masonry Buildings. Ph.D. Thesis, Georgia Institute of Technology, Atlanta, GA.

Morales, R. and Delgado, A. (1992). Feasibility of Construction of Two-Story Adobe Buildings in Peru. Proceedings of the Tenth World Conference on Earthquake Engineering, Madrid, Spain, Vol. 6, pp. 3545-3550.

Mulligan, John A. (1931). Brick Masonry Construction. Press of Oscar A. Randel, Inc.

Naraine, K. and Sinha, S. (1989). Behavior of Brick Masonry under Cyclic Compressive Loading. Journal of Construction Engineering and Management, Vol. 115, No.2, June, pp. 1432-1445.

Naraine, K. and Sinha, S. (1991). Model for Cyclic Compressive Behavior of Brick Masonry. ACI Structural Journal, Vol. 88, No 5, Sep-Oct, pp. 603-609.

Nuss, L.K., Noland, J.L. and Chinn, J. (1978). The Parameters Influencing Shear Strength between Clay Masonry Units and Mortar. Proceeding of the First North American Masonry Conference, Boulder, Colo., Aug.

Page, A. W. (1980). A Biaxial Failure Criterion for Brick Masonry in the Tension-Tension Range. International Journal of Masonry Construction, Vol. 1, pp. 245-259.

Page, A. W. (1981). The Biaxial Compressive Strength of Brick Masonry. Proceedings Institution of Civil Engineers, Part 2, Vol. 71, pp. 893-906.

Page, A. W. (1982). An Experimental Investigation of the Biaxial Strength of Brick Masonry. Proceedings of the Sixth International Brick Masonry Conference, Rome, Italy, pp. 3-15.

Page, A. W. (1983). The Strength of Brick Masonry under Biaxial Compression-Tension. International Journal of Masonry Construction, 3(1), pp. 26-31.

Page, A. W., Samarasinghe, W. and Hendry, A. W. (1982). The In-plane Failure of Masonry - A Review. Proceedings BCS., Load-bearing Brickwork (7), No. 30, pp. 90-100.

Pantazopoulou, S. J., and French, C. W. (2001). Slab Participation in Practical Earthquake Design of Reinforced Concrete Frames. ACI Structural Journal, Vol. 98, No. 7, July-Aug., pp. 479-489.

Pantazopoulou, S. J. and Moehle, J. P. (1990). Identification of Effect of Slabs on Flexural Behavior of Beams. Journal of Engineering Mechanics, ASCE., Vol. 116, No. 1, pp. 91-104.

Paquette J. and Bruneau, M. (1999). Seismic Resistance of Full Scale Single Story Brick Masonry Building Specimen. 8th North American Masonry Conference, June 6-9, Austin, Texas, pp. 227-234.

Paquette, J. and Bruneau, M. (2000). Pseudo-Dynamic Testing of Unreinforced Masonry Buildings with Flexible Diaphragm. 12th World Conference of Earthquake Engineering, Auckland, New Zealand.

Paquette J. and Bruneau M. (2003). Pseudo-Dynamic Testing of Unreinforced Masonry Buildings with Flexible Diaphragm. *Journal of Structural Engineering*, ASCE., Vol. 129, No. 6, pp. 708-716.

Park, J., Craig, J. I. and Goodno, B. J. (2002). Simple Nonlinear In-Plane Response Models for Assessing Fragility of URM Walls. *Seventh U.S. National Conference on Earthquake Engineering*, Boston, Massachusetts.

Paulson, T.J. and Abrams, D.P. (1990). Correlation between Static and Dynamic Response of Model Masonry Structures. *Earthquake Spectra*, Vol. 6, No 3, pp. 573-591.

Peralta, D. F., Bracci, J. M., and Hueste, M. B. D. (2000). Seismic Performance of Rehabilitated Floor and Roof Diaphragms. ST-8 Project Final Report, Mid-America Earthquake Center, Texas A&M University, College Station, TX.

Pook, R.L., Stylianou, M.A. and Dawe, J.L. (1986). Experimental Investigation of the Influence of Compression on the Shear Strength of Masonry Joints. *Proceedings of the 4th Canada Masonry Symposium*, Fredericton, N.B., Canada, June.

Prawel, S.P., and Lee, H.H. (1990a). The Performance of Upgraded Brick Masonry Piers Subjected to Out-of-plane Motion. *Proceedings of the Fourth National Conference on Earthquake Engineering*, Palm Springs, California, Vol. 3, pp.273-281.

Prawel, S.P. and Lee, H.H. (1990b). The Performance of Upgraded Brick Masonry Piers Subjected to Out-of-plane Motion. *Proceedings of the Fifth North American Masonry Conference*, Urbana-Champaign, III, Vol.1, pp. 411-427.

Priestley M.J. and He, L. (1995). Seismic Response of T-Section Masonry Shear Walls. *The Masonry Society Journal*, Vol. 9, No 1, pp. 10-19.

Qi, X. and Pantazopoulou, S. I. (1991). Response of RC Frames under Lateral Loads. *Journal of Structural Engineering*, ASCE., Vol. 117, No. 4, pp. 1167-1188.

Reisner, E. (1964). Analysis of Shear Lag in Box Beams by Principle of Minimum Potential Energy. *Quarterly Journal of Mechanics and Applied Mathematics*, Vol. 4, No. 3, pp. 268-278.

Riddington, J.R. and Ghazali, M.Z. (1990). Hypothesis for Shear Failure in Masonry Joints. Proceedings Institution of Civil Engineers, U.K., Part 2, Mar., pp. 89-102.

Sahlin, S. (1971). Structural Masonry. Prentice-Hall, Inc., Englewood Cliffs, New Jersey.

Samarasinghe, W. (1980). The In-Plane Failure of Brickwork. Ph.D. thesis, the University of Edinburgh, U.K.

Samarasinghe, W. and Hendry, A. W. (1982). The Strength of Brickwork under Biaxial Tensile and Compressive Stress. Proceedings BCS. Load-Bearing Brickwork (7); No. 30, pp. 129-139.

Sinha, B.P. (1978). A Simplified Ultimate Load Analysis of Laterally Loaded Orthotropic Brickwork Panels of Low Tensile Strength. Structural Engineer, Part B, Vol. 56b, No.4, pp. 81-84.

Sinha, B P., and Hendry, A. W. (1969). Racking Tests on Story-Height Shear-Wall Structures: with Openings, Subjected to Pre-Compression. Design Engineering & Construction with Masonry Products, Gulf Publishing Co., Houston, TX., pp. 192-199.

Shahrooz, B. M. and Pantazopoulou, S. J. (1992). Modeling Slab Contribution in Frame Connections. Journal of Structural Engineering, ASCE, Vol. 118, No. 9, pp. 2475-2492.

Shi, G. (1993). Block System Modeling by Discontinuous Deformation Analysis. WIT Press, Southampton UK and Boston USA.

Shi, G. (1997). Numerical Manifold Method and Discontinuous Deformation Analysis. Tsinghua University Press, P.R. China (in Chinese).

Smith, B.S. and Carter, C. (1971). Hypothesis of Shear Failure of Brickwork. ASCE., ST4, Vol. 97, pp. 1055-1063.

Smith, B.S. and Hofmann, P. (1986). Tests on the Shear-Bond Behavior in the Bed Joints of Masonry. *Masonry International*, Vol. 9, Dec., pp. 1-15.

Stoddard, R.P. (1946). *Brick Structures, How to Build Them*. McGraw-Hill Book Company, Inc., New York.

Structural Clay Products Institute (1949). *Handi-Guide on Brick and Structural Tile Wall Assemblies*. Canton, Ohio.

Syrmakezis, C.A., Chronopoulos, M.P., Sophocleous, A.A. and Asteris, P.G. (1995). Structural Analysis Methodology for Historical Buildings. *Proceedings of the Fourth International Conference on Structural Studies of Historical Buildings, STREMA 95*, Vol.1, pp. 373-382.

Tahan N. and Pavlovic M. (1997). Shear Lag Revisited: the Use of Single Fourier Series for Determining the Effective Breadth in Plated Structures. *Computers and Structures*, Vol.63, pp. 759–67.

Tassios, Th. P., and Vachliotis, Ch. (1989). Failure of Masonry under Heterosemous Biaxial Stresses. *Proceedings of International Conference on Conservation of Stone, Masonry-Diagnosis, Repair and Strengthening*. Athens, Greece.

Tena-Colunga, A. (1992). Seismic Evaluation of Unreinforced Masonry Structures with Flexible Diaphragms. *Earthquake Spectra*, Vol. 8, No. 2, pp. 305-318.

Timoshenko, S. P. and Goodier, J. N. (1969). *Theory of Elasticity*. 3rd, McGraw-Hill College, New York.

Tissell, J. R. (1967). 1966 Horizontal Plywood Diaphragm Tests. *Laboratory Report 106*, American Plywood Association, Tacoma, Washington.

Todeschini, C.E., Bianchini, A.C. and Kesler, C.E. (1964). Behavior of Concrete Column Reinforced with High Strength Steels. *ACI Journal*, Vol. 61, No. 6, pp. 701-716.

Tomazevic, M. (1987). Dynamic Modeling of Masonry Buildings: Storey Mechanism Model as a Simple Alternative. *Earthquake Engineering and Structural Dynamic*, Vol.15, pp.731-749.

Tomazevic, M., Modena, C., Velechovsky, T. and Weiss, P. (1990). The Influence of Structural Layout and Reinforcement on the Seismic Behavior of Masonry Buildings: An Experimental Study. *The Masonry Society Journal*, August, pp. 26-50.

Tomazevic, M., Lutman, M. and Weiss, P. (1993). The Seismic Resistance of Historical Urban Buildings and the Interventions in their Floor Systems: An Experimental Study. *The Masonry Society Journal*, August, pp. 77-86.

Tomazevic, M. (1999). *Earthquake-Resistant Design of Masonry Buildings*. Imperial College Press, London, U.K.

Yi, T., Moon, F., Leon, R. and Kahn, L. (2002). Performance Characteristics of Unreinforced Masonry Low-Rise Structure Before and After Rehabilitation. Seventh U.S. National Conference on Earthquake Engineering, Boston, Massachusetts.

Yi, T., Moon, F., Leon, R. and Kahn, L. (2003). Structural Analysis of a Prototype Unreinforced Masonry Low-Rise Building. Ninth North American Masonry Conference, Clemson, SC.

Yokel, F. Y. and Fattal, S. G. (1976). Failure Hypothesis for Masonry Shear Walls. *Journal of Structural Division, ASCE*, Vol. 102, No.3, pp. 515-532.

Zagajeski, S., Halvorsen, G. T., Gangarao, H. V.S., Luttrell, L. D., Jewell, R. B., Corda, D., N. and Roberts, J. D. (1984). Theoretical and Experimental Studies on Timber Diaphragms Subject to Earthquake Loads. Department of Civil Engineering, West Virginia University, Morgantown, West Virginia.

Zhang, X., Singh S. S., Bull, D. K. and Cooke, N. (2001). Out-of-plane Performance of Reinforced Masonry Walls with Openings. *Journal of Structural Engineering, ASCE*, Vol.127, No 1, pp. 51-57.

Wen, Y.K. and Wu, C.L. (2001). Uniform Hazard Ground Motions for Mid-America Cities. *Earthquake Spectra*, Volume 17, No. 2, pp. 359-384.

VITA

Tianyi Yi was born in HuNan province, P.R. China in 1971. He received his bachelor degree and master degree in the structural engineering from Tongji University, P.R. China in 1993 and 1996, respectively. In 1999, he came to the United States and started to pursue his Ph.D. in the School of Civil and Environmental Engineering at Georgia Institute of Technology under the supervision of Dr. Roberto Leon.